UNIVERSIDADE FEDERAL DO RIO GRANDE DO NORTE
CENTRO DE CIÊNCIAS EXATAS E DA TERRA
PROGRAMA DE PÓS-GRADUAÇÃO EM GEODINÂMICA E GEOFISICA

TESE DE DOUTORADO

TERREMOTOS PROFUNDOS NA REGIÃO AMAZÔNICA (ACRE): MECANISMOS FOCAIS E PARÂMETROS DE FONTE

Autor:

GILBERTO DA SILVA LEITE NETO

Orientador:

PROF. DR. JORDI JULIÀ CASAS

Coorientador:

PROF. DR. GERMÁN ANDRES PRIETO GOMEZ

Tese nº 87/PPGG

Julho de 2024
Natal, RN

UNIVERSIDADE FEDERAL DO RIO GRANDE DO NORTE
CENTRO DE CIÊNCIAS EXATAS E DA TERRA
PROGRAMA DE PÓS-GRADUAÇÃO EM GEODINÂMICA E GEOFISICA

TESE DE DOUTORADO

TERREMOTOS PROFUNDOS NA REGIÃO AMAZÔNICA (ACRE): MECANISMOS FOCAIS E PARÂMETROS DE FONTE

Autor:

GILBERTO DA SILVA LEITE NETO

Tese apresentada em 12 de julho de 2024 ao Programa de Pós-Graduação em Geodinâmica e Geofísica (PPGG) da Universidade Federal do Rio Grande do Norte (UFRN) como requisito à obtenção do Título de Doutor em Geodinâmica e Geofísica, Área de Concentração Geofísica.

BANCA EXAMINADORA:

Prof. Dr. Jordi Julià Casas - Presidente/Orientador (DGEF-UFRN)

Prof. Dr. Aderson Farias do Nascimento - Membro Interno (DGEF-UFRN)

Prof. Dr. Francisco Hilário Rego Bezerra - Membro Interno (DG-UFRN)

Prof. Dr. Marcelo Souza de Assumpção - Membro Externo (IAG-USP)

Dr. Juraci Mário de Carvalho - Membro Externo (IG-UNB)

Julho de 2024
Natal, RN

Universidade Federal do Rio Grande do Norte - UFRN
Sistema de Bibliotecas - SISBI
Catalogação de Publicação na Fonte. UFRN - Biblioteca Setorial Prof. Ronaldo Xavier de Arruda - CCET

Leite Neto, Gilberto da Silva.
Terremotos profundos na região amazônica (Acre): mecanismos focais e parâmetros de fonte / Gilberto da Silva Leite Neto. - 2024.
304 f.: il.

Tese (doutorado) - Universidade Federal do Rio Grande do Norte, Centro de Ciências Exatas e da Terra, Programa de Pós-Graduação em Geodinâmica e Geofísica. Natal, RN, 2024.
Orientação: Prof. Dr. Jordi Julià Casas.
Coorientação: Prof. Dr. Germán Andres Prieto Gomez.

1. Geofísica - Tese. 2. Terremotos profundos - Tese. 3. América do Sul - Tese. 4. Mecanismos focais - Tese. 5. Parâmetros de fonte - Tese. I. Casas, Jordi Julià. II. Gomez, Germán Andres Prieto. III. Título.

RN/UF/CCET CDU 550.3(043.2)

Elaborado por Joseneide Ferreira Dantas - CRB-15/324

AGRADECIMENTOS

A Deus, quem sempre guiou minha trajetória.

Ao meu orientador – Prof. Jordi Julià – por confiar no meu potencial e pela sua total dedicação ao desenvolvimento desta pesquisa.

A mi co-supervisor, el Prof. Germán Prieto, por recibirme en la Universidad Nacional de Colombia y por guiarme en el desarrollo de esta investigación.

Ao Prof. José Moreira, por ter me incentivado no bacharelado a seguir na carreira acadêmica.

Aos Profs. Aderson do Nascimento e Francisco Hilário Bezerra, os quais sempre me incentivaram e torceram pelo meu sucesso.

À Banca Examinadora, pela disponibilidade em participar da minha defesa de Tese.

À CAPES, pelas bolsas de doutorado no Brasil e doutorado sanduíche no exterior.

À UFRN, por toda estrutura que usufruí por mais de dez anos, do bacharelado ao doutorado.

Aos técnicos e colegas do Laboratório de Sismologia – Eduardo Menezes, Flauber Costa, André Tavares, Rômulo Brito e Suzara Sena – por todo apoio prestado.

À minha família, pelo suporte ao longo de todos esses anos – Neide Nair, Beniza Pessoa, Genivaldo Leite, Siomara Priscilla, Altamiro Junior, Giovanni Miro e Raquel Pessoa.

Aos meus padrinhos – Elaine Ciabotti e Humberto Gois – que foram fundamentais para a minha educação.

Aos meus amigos – Thaise Carvalho, Vanessa Torres, Gabriel Bulhões, Antonio Alexandre, Matheus Amaral, Rafael Linhares, Amanda Nobre, Vinícius Calazans, Laís Queiroz, Giovanna Medeiros, Márcia Clementino, Daniel Medeiros, Rafael Azevedo, Débora Everly, Izaias Magnus e Victória Cedraz.

A mis amigas Sandra Mesa y Lindsay Ramirez, a quienes les debo que el intercambio doctoral haya sido aún más especial.

A Ana Nemocón, por toda la atención que me brindó mientras estuve en Bogotá.

A todos los profesores de la UNAL por toda la atención mientras estuve allí – Profs. Clemencia Gómez, Ariel Cadena, Daniel Hernández-Deckers, Alexander Caneva y Carlos Alberto Vargas.

RESUMO

Terremotos profundos ocorrem em profundidades superiores a 70 km, no núcleo frio da litosfera subduzida, onde as condições extremas de pressão e temperatura deveriam impedir o falhamento. Portanto, algum mecanismo ainda não compreendido é necessário para explicar esses eventos. Em profundidades que excedem 300 km, os terremotos são atribuídos ao *transformational faulting*, um mecanismo que depende da presença de uma cunha de olivina metaestável (MOW), típica de placas suficientemente frias. No entanto, esses eventos também ocorrem em placas quentes, como na América do Sul, o que torna a explicação desses fenômenos ainda mais desafiadora. Este estudo busca investigar o mecanismo gerador na América do Sul determinando mecanismos focais e parâmetros de fonte para uma sequência de 42 eventos de foco profundo na região amazônica entre o Peru e o Brasil (2014-2022). Para isso, foram utilizados dados de várias estações banda-larga distribuídas pelo continente que garantiram uma cobertura inédita desses eventos. Inicialmente, foram determinados mecanismos focais e profundidades de centroide para um total de 28 eventos (Mw 4.2-7.5) utilizando o método *Cut-and-Paste*. Os mecanismos revelam uma predominância de falhas normais, refletindo um regime de compressão ao longo do mergulho da placa (DDC). Os planos nodais, orientados a aproximadamente 45º do eixo de compressão máxima, indicam a formação de novas falhas, consistente com *transformational faulting*. As profundidades do centroide mostram uma zona sísmica confinada entre 557 e 659 km. Essas observações sugerem que a sismicidade pode ser resultado de *transformational faulting* em uma MOW que foi preservada por um segmento mais frio acoplado em profundidade à placa de Nazca. Momentos sísmicos, frequências de esquina e energias irradiadas foram determinados para 13 eventos (Mw 4.8-7.4) por meio dos espectros observados. Com esses parâmetros, foram calculados *stress drops* (5-90 MPa) e eficiências de irradiação (0.1-1.4) que revelaram variações importantes. A variabilidade nas eficiências sugere a coexistência de rupturas eficientes e dissipativas na região, possivelmente influenciadas pelo grau de derretimento na zona de falha, que pode ser favorecido pela desidratação de regiões hidratadas próximas à fonte. Assim, este trabalho sugere que terremotos de foco profundo na região resultam da combinação entre *transformational faulting* e *thermal runaway*, este último envolvendo mais ou menos derretimento dependendo da presença de água próximo à fonte.

Palavras-chave: Terremotos profundos; América do Sul; *Transformational faulting*; Mecanismos focais; Parâmetros de fonte.

ABSTRACT

Deep earthquakes occur at depths greater than 70 km, in the cold core of the subducting lithosphere, where the extreme pressure and temperature conditions should prevent brittle failure. Thus, alternative physical processes are necessary in order to explain the occurrence of these events. At depths exceeding 300 km, earthquakes are attributed to transformational faulting, a mechanism that relies on the presence of a metastable olivine wedge (MOW) in cold slabs. However, these events also occur in warm slabs, such as the Nazca plate, which makes explaining these phenomena even more challenging. This study aims to investigate the generating mechanism in South America by determining focal mechanisms and source parameters for a sequence of 42 deep-focus events in the Amazonian region between Peru and Brazil (2014-2022). To achieve this goal, data from several broadband stations distributed across the continent were utilized, ensuring unprecedented coverage of these events. Initially, focal mechanisms and centroid depths were determined for a total of 28 events (Mw 4.2-7.5) using the Cut-and-Paste method. The mechanisms reveal a predominance of normal faults reflecting a down-dip compression (DDC) regime. Nodal planes, oriented approximately 45º from the axis of maximum compression, indicate the formation of new faults, consistent with transformational faulting. Centroid depths demonstrate a seismic zone confined between 557 and 659 km. These observations suggest that seismicity may result from transformational faulting within a MOW preserved by a colder slab segment attached at depth to a warmer Nazca Plate. Seismic moments, corner frequencies, and radiated energies were determined for 13 events (Mw 4.8-7.4) from P- and S-wave spectra. From these parameters, stress drops (5-90 MPa) and radiation efficiencies (0.1-1.4) were calculated, revealing significant variations. The variability in radiation efficiencies suggests the coexistence of brittle and dissipative ruptures, possibly influenced by the degree of melting in the fault zone and favored by the dehydration of hydrous phases near the source. Thus, this work suggests that deep-focus earthquakes in the region result from the combination of transformational faulting and thermal runaway, the latter involving more or less melting depending on the presence of water near the source.

Keywords: Deep earthquakes; South America; Transformational faulting; Focal mechanisms; Source parameters.

LISTA DE FIGURAS

CAPÍTULO 1

Figura 1. Distribuição de terremotos profundos (h > 70 km) pelo planeta entre 1970 e 2020 de acordo com o catálogo ISC-EHB (Engdahl et al., 1998, 2020; International Seismological Centre, 2024; Weston et al., 2018). Os epicentros estão coloridos pela profundidade, ressaltando as zonas de Wadati-Benioff. 19

Figura 2. Sismicidade profunda em uma zona de subducção: a) distribuição de terremotos ocorridos entre 1976 e 2018 com a profundidade, de acordo com o catálogo do GCMT. O histograma em vermelho representa a sismicidade apenas na zona de subducção de Tonga enquanto o histograma em azul representa a sismicidade global. Nos histogramas estão indicados os intervalos de profundidades que definem os eventos de foco intermediário e profundo; b) distribuição de terremotos de foco intermediário ao longo de uma zona sísmica dupla, formada pelas zonas sísmicas superior e inferior, e de terremotos de foco profundo na cunha de olivina metaestável (MOW). Os regimes de esforço ao longo da placa estão indicados por setas e os planos de ruptura associados a esses regimes estão representados em vermelho. Figura adaptada de Zhan (2020). …….....20

Figura 3. Mecanismo de *dehydration embrittlement*; a) a desidratação de minerais hidratados leva a formação de poros preenchidos com fluidos que concentram esforços distensivos; b) os poros evoluem para uma estrutura chamada *microcrack* paralelo ao esforço compressivo máximo (σ_1) com esforços distensivos concentrados em suas pontas; c) a auto-organização de vários *microcracks* leva à formação de uma zona de falha. Figura modificada de Green & Marone (2002) e Frohlich (2006).…….....21

Figura 4. O mecanismo de *transformational faulting*; a) estrutura lenticular perpendicular ao esforço compressivo máximo preenchida com fase spinel mais densa e superplástica (*anticrack*) resultante da transformação de fase da olivina; b) auto-organização dos *anticracks* por meio dos esforços compressivos em suas extremidades em uma zona de falha orientada a aproximadamente 45º do eixo de máxima compressão. Figura modificada de Zhan (2020)..…….....24

Figura 5. Mecanismo de *thermal runaway*: a-b) o cisalhamento ao longo de uma zona de fraqueza preexistente provoca o aumento local de temperatura por fricção que resulta na diminuição local da viscosidade. O *feedback* positivo entre essa diminuição da viscosidade e o cisalhamento promove a instabilidade; c-d) é possível que o aumento local de temperatura seja elevado o suficiente para produzir derretimento parcial na zona de falha. Figura adaptada de John et al. (2009) e Zhan (2020) 27

Figura 6. Mecanismo duplo para a gênese de terremotos de foco profundo: a) Lei de Gutemberg-Richter para eventos em profundidades maiores que 500 km para placa fria (Tonga), em quadrados e losangos verdes, e para placas quentes: AS: América do Sul; PH: Filipinas; JK: Japão-Curilhas e IBM: Izu-Bonin-Marianas, em círculos vermelhos (b = 0.49) e azuis (b = 0.95); b) Modelo de mecanismo duplo para placas frias e quentes. Círculos representam a área de ruptura e a cor representa o mecanismo dominante. Em cinza é mostrada a espessura da MOW disponível na placa subduzida, que é mais espessa em placas frias que em placas quentes. Note que, para placas frias, as rupturas são dominadas pelo *transformational faulting*, e são compreendidas pela MOW. No caso de placas quentes, as rupturas se iniciam por *transformational faulting* e continuam a se propagar fora da MOW por *thermal runaway*. No caso de grandes eventos (Mw > 6.5), o mecanismo de *thermal runaway* tem um papel ativo, dominando o processo de ruptura (círculos laranja). Figura modificada de Zhan (2017). 28

Figura 7. Distribuição espacial de grandes terremotos (Mw > 7) de foco intermediário (a) e profundo (b), entre 1900 e 2004 de acordo com os catálogos do GCMT (círculos escuros), Abe (1981) e Engdahl & Villaseñor (2002) (círculos claros), e a distribuição da sismicidade de foco profundo na América do Sul ao longo de quatro segmentos (c). A geometria da placa de Nazca em subducção é simplificada por áreas de subducção plana e normal. As localizações aproximadas dos grandes terremotos da Colômbia (Mw 8.1, 1970) e da Bolívia (Mw 8.3, 1994) são mostradas no mapa. Figura modificada de Frohlich (2006). 29

Figura 8. a) A Rede Sismográfica Brasileira (RSBR) e a sua expansão em direção à região amazônica desde 2014; b) a sequência sísmica de 2014-2022 no segmento Peru-Brasil de acordo com o catálogo do USGS. 30

Figura 9. Histograma mostrando o número de eventos por ano desde 2014 no segmento Peru-Brasil, de acordo com o USGS. Note o número desproporcional de eventos ocorridos apenas em 2015. 31

CAPÍTULO 2

Figure 1. a) Moment tensor solutions for deep earthquakes (d > 70 km and Mw > 5) in South America according to the GCMT catalog (1977-2022). The focal solutions in this map are colored by depth and sized by magnitude. Plate boundaries are from Bird (2003) and convergence rate of the Nazca plate in cm/yr are from DeMets et al. (2010). Contours from Slab 2 delineate the geometry of the subducting Nazca plate (Hayes et al., 2018). Main oceanic ridges in Nazca plate: CR – Carnegie Ridge, NR – Nazca Ridge, IR – Iquique Ridge and JFR – Juan Fernandez Ridge, are shown in light gray (Gutscher et al., 2000; Rosenbaum et al., 2005). The inferred continuation of the Nazca Ridge (PN) and location of the postulated Inca Plateau (IP) are drawn in dark gray (Bishop et al., 2017; Gutscher et al., 1999, 2000). Distribution of broadband stations from the Brazilian Seismic Network (RSBR) for different time periods are shown as open (1980-2013) and closed (2014-2022) squares; b) 42 deep-focus earthquakes (d > 300 km) within the period of 2014 to 2022 according to the USGS catalog. 45

Figure 2. Examples of waveform fitting produced by the focal mechanisms determined for the 2015 deep-focus doublet, events 8 and 9; a) map showing the preferred solution for event 8 and the distribution of stations that were used in the inversion. Dashed circles indicate radii of 5º and 30º from epicenter; b) distribution of focal mechanisms with investigated centroid depths. The preferred solution, which is the one that produced the best fit to observations is indicated by the vertical dashed line; c) examples of waveform matches produced by this preferred solution. Black and red waveforms denote observations and synthetics, respectively. Station names, azimuths and distances are shown above each station panel. Time shifts (top) and cross-correlation coefficients (bottom) are shown in blue at the lower right corner of each panel. Wave segments (Pr, Pz, SVr, SH and SVz) are identified at the upper

right corners; d-f) the same as in a-c but for event 9. For the complete waveform matches, see Figures S4 and S5. 53

Figure 3. Focal mechanisms determined for 28 events in the 2014-2022 deep-focus sequence. a) Distribution of the obtained focal solutions sized by magnitude and colored in grayscale by quality (A, B, C and D) (Table 2). Each solution in the map is identified by event number in Tables S1 and 2. The epicenters are colored by centroid depths. Dashed lines delineate the Nazca slab depth from Slab 2 (Hayes et al., 2018); b) nodal planes from 39 GCMT focal mechanisms in the Peru-Brazil region occurred between 1977 and 2022 and 5.1 ≤ Mw ≤ 7.6 (Figure 1a) plotted on a stereonet using FaultKin (Allmendinger et al., 2012; Marrett & Allmendinger, 1990). The fault zone orientation, striking 160º and dipping 60º, as proposed by Zahradnik et al. (2017) is shown in red (FPZ); c) nodal planes from the solutions obtained in this study. Planes are colored in grayscale according to quality, as in a; d) Principal axes (P, T and B) from the GCMT solutions and e) principal axes from this study. Another version of this figure with focal mechanisms colored by faulting style can be found in supplementary material Figure S30. 54

Figure 4. Examples of waveform inversions for the two frequency ranges used in this study, 0.02-0.05 Hz (event 12, from a to c), and 0.3-1.0 Hz (event 14, from d to f). Features in this figure are the same described in Figure 2. 55

Figure 5. Focal mechanisms for deep-focus earthquakes in the Peru-Brazil border region classified according to the seismic moment tensor main axes plunges: a) solutions from this study, 28 earthquakes with 4.2 ≤ Mw ≤ 7.5 from 2014 to 2022 and b) solutions available in the GCMT catalog, 39 events with 5.1 ≤ Mw ≤ 7.6 from 1977 to 2022. The FMC program (Álvarez-Gómez, 2019) was used to classify the focal mechanisms and draw the diagrams, which are based on the Kaverina projection (Kaverina et al., 1996). The classification allows for up to seven styles of faulting: normal (N), normal with strike-slip (N-SS), strike-slip with normal (SS-N), strike-slip (SS), strike-slip with reverse (SS-R), reverse with strike-slip (R-SS) and reverse (R).....58

Figure 6. Nodal plane poles displayed on stereographic projection: a) GCMT solutions (solid black circles) plotted with the inverted stresses (colored squares). The two fault

planes poles predicted by the inverted stresses are plotted as blue crosses while the pole of the regional fault plane proposed by Zahradník et al. (2017) is plotted as a red cross; and b) the same as in a but with solutions from this study colored according to quality. 66

Figure 7. Histograms of the number of nodal planes as a function of the angle between these planes and the main compression axis. a) histogram considering only GCMT solutions for the study region and b) considering only A-quality solutions obtained in this study. 66

Figure 8. Schematic model proposed to explain deep-focus seismicity in the Peru-Brazil region. The model illustrates the South American subduction zone and the main features observed in the study region, the Peruvian flat slab, and the concentration of deep-focus earthquakes in a narrow fault zone. The Nazca ridge termination, as suggested by Bishop et al. (2017), is indicated by the red dashed line at ~500 km depth. The ridge termination marks the transition from a warmer to a colder Nazca slab segment. In the colder segment, we propose that a MOW could be preserved and thus allowing for earthquake nucleation (red stars) in the MTZ. 68

CAPÍTULO 3

Figure 1. Distribution of the 55 seismic stations and 42 DFEs used in this study. Stations are colored by network. Black and gray stations belong to the RSBR subnetworks (NB and BR). Network codes follow the International Federation of Digital Seismograph Networks (FDSN) standards. A table with station information can be found in the Supporting Information (Table S2). Epicenters for the 2014-2022 deep-focus sequence are color-coded by depth and sized by magnitude, as reported in the USGS catalog (Table S1)…….....87

Figure 2. Selection of observed and predicted spectra for event 32 (7.0 Mw). On the map (a), the red star represents the epicenter, while red triangles indicate the stations selected for display in the figure (b). For each selected station, the black, red and light gray lines respectively represent the observed, modeled and background noise spectra. Segments of the observed spectra with low SNR are shown in dark gray and were not considered for inversion. The complete set of stations used in the inversion is displayed in Figure S17.....91

Figure 3. P- and S-wave corner frequencies as a function of seismic moment for the 14 events listed in Table 1. The uncertainties in f_c and M_0 are represented by vertical black bars and horizontal gray bars, respectively. Dashed black lines are for reference stress drops of 1, 10 and 100 MPa.....92

Figure 4. Average Δσ for the 13 events in Table 1 plotted against the corresponding seismic moments. Solutions are numbered as in Tables 1 and S1. Vertical bars represent the estimate's uncertainties. Gray squares represent estimates from Poli & Prieto (2016), comprising 180 DFEs ($5.8 \leq Mw \leq 7.8$) from several subduction zones between 2000 and 2016.....93

Figure 5. Estimates of E_R from the 13 events in Table 1. a) energy radiated as P-wave, E_R^P; b) energy radiated as S-wave, E_R^S; c) total radiated energy, E_R; and d) ratio between E_R^S and E_R^P as a function of the seismic moment. Events are numbered as in Table 1 and color-coded by the amount of extrapolated energy in E_R. Solid gray line in c represents the $E_R = 1.6 \times 10^{-5} M_0$ empirical relationship from Choy & Boatwright (1995).……..96

Figure 6. Scaled energy plotted as function of magnitude. Events are color-coded by the amount of extrapolation and labeled as in Table 1. Gray squares are estimates from Poli & Prieto (2016).....97

Figure 7. Radiation efficiency plotted as function of the seismic moment. Events are color-coded by the amount of extrapolation and labeled as in Table 1. Gray squares are estimates calculated based on the apparent stresses and stress drops of Poli & Prieto (2016).....97

Figure 8. Comparison between vertical seismograms for event 32 and event 34 at station CZSB at different frequency ranges. P- and S-wave arrivals are shown as dashed red and blue lines on the broadband seismograms (upper panels). The frequency ranges used for filtering are shown in the upper right corner of each panel. 100

Figure 9. Schematic model proposed to explain variable η_R for DFEs in the Peru-Brazil segment. Outer rise faults promote localized deep hydration of mantle rocks that can survive down to MTZ depths in the form of small-scale slab heterogeneities. DFEs are explained as the result of transformational faulting and thermal runaway

controlled by the dehydration reactions in such hydrated regions near the source. Transformational faulting in a preserved MOW could explain the confinement of DFEs to a narrow depth range (~500-700 km). The more or less dissipative behavior of the rupture is thus explained by the amount of melting involved in the thermal runaway step, which is possibly controlled by the amount of fluids released by the dehydration reactions when available. 103

LISTA DE TABELAS

CAPÍTULO 2

Table 1. Description of the cutting scheme employed in this work to obtain the body-wave segments to be modeled. …….....50

Table 2. Earthquake focal mechanisms determined in this study for a total of 28 deep-focus events from the 2014-2022 sequence. …….....59

CAPÍTULO 3

Table 1. Inverted parameters for 14 selected events in the 2014-2022 deep-focus sequence…….. 93

SUMÁRIO

AGRADECIMENTOS iii

RESUMO iv

ABSTRACT v

LISTA DE FIGURAS vi

LISTA DE TABELAS xiii

SUMÁRIO. xiv

CAPÍTULO 1 17

1. Introdução 17

1.1. Apresentação e estrutura da Tese 17

1.2. Terremotos profundos 18

1.3. Principais mecanismos propostos para eventos profundos 19

1.3.1. *Dehydration embrittlement* 19

1.3.2. *Transformational faulting* 22

1.3.3. *Thermal runaway* 26

1.3.4. O mecanismo duplo 27

1.4. Terremotos profundos no Acre 28

1.5. Objetivo da Tese 31

Referências 31

CAPÍTULO 2 40

MANUSCRITO 1 40

Key Points 40

Abstract 40

Plain language summary 41

2.1. Introduction 41

2.2. The 2014-2022 deep-focus earthquake sequence 45

2.3. Data selection, data processing, and Green's functions 47

2.4. Waveform modeling details 48

2.5. Results 51

2.5.1. The great 2015 deep-focus doublet 51

2.5.2. The 2014-2022 deep-focus sequence 53

2.5.2.1. Goodness of fit 54

2.5.2.2. Focal mechanisms 56

2.5.2.3. Seismic moment 57

2.5.2.4. Centroid depths 57

2.5.2.5. Qualitative grading scheme 59

2.6. Discussion 60

2.6.1. Variability in faulting style 60

2.6.1.1. Variability within normal faulting 61

2.6.1.2. Deviations from normal faulting 62

2.6.2. Stresses in the subducting Nazca plate 63

2.6.2.1. DDC and flat-slab subduction 64

2.6.2.2. Viability of transformational faulting 65

2.6.3. Thermal structure and deep-focus nucleation 66

2.6.3.1. Composite thermal structure at the Peru-Brazil border 67

2.6.3.2. A generalized, composite thermal structure for South America? 69

2.7. Conclusions 70

Acknowledgments 71

Open research 71

References 72

CAPÍTULO 3 83

MANUSCRITO 2 83

Key Points 83

Plain language summary 84

Abstract 84

3.1. Introduction 85

3.2. Data 87

3.3. Seismic moments, corner frequencies and stress drops 88

3.3.1. Determination of source and background spectra 88

3.3.2. Seismic moments and corner frequencies 89

3.3.3. Stress drops 91

3.4. Radiated energies, scaled energies and radiation efficiencies 94

3.4.1. Radiated energies from body-wave spectra 94

3.4.2. Radiation efficiency 95

3.5. Discussion 98

3.5.1. Variability in Δσ, radiated energy and seismic efficiency 98

3.5.2. Nucleation of DFEs along the Peru-Brazil segment 101

3.6. Conclusions 104

Acknowledgments 104

Open research 105

References 105

CAPÍTULO 4 116

CONCLUSÕES 116

APÊNDICE A 119

APÊNDICE B 149

APÊNDICE C 169

APÊNDICE D 268

CAPÍTULO 1

1. Introdução

1.1. Apresentação e estrutura da Tese

Esta Tese de Doutorado é requisito para a obtenção do título de Doutor em Geodinâmica e Geofísica pelo Programa de Pós-Graduação em Geodinâmica e Geofísica (PPGG) da Universidade Federal do Rio Grande do Norte (UFRN). O trabalho foi desenvolvido sob a supervisão do Prof. Dr. Jordi Julià Casas, do Departamento de Geofísica da UFRN, e do Prof. Dr. Germán Andres Prieto Gomez, do Departamento de Geociências da *Universidad Nacional de Colombia* (UNAL).

A Tese está dividida em quatro capítulos, compreendendo um capítulo introdutório, dois capítulos que descrevem os resultados da pesquisa de Doutorado na forma de manuscritos, e um capítulo final com as conclusões gerais.

O Capítulo 1 tem como objetivo: i – contextualizar o leitor sobre o tema de terremotos profundos; ii – descrever os principais mecanismos físicos propostos para explicá-los; e iii – destacar a motivação e os objetivos da tese.

O Capítulo 2 apresenta o manuscrito submetido ao periódico *Earth and Space Science* da AGU em março de 2024, intitulado "*Deep-focus earthquake mechanisms at the subducting Nazca plate (Peru-Brazil border): Cold slab behavior in a warm plate*". Este artigo representa a etapa inicial da caracterização da sequência de eventos profundos estudada e descreve observações baseadas em mecanismos focais.

O Capítulo 3 compreende o manuscrito com os resultados da segunda etapa da caracterização dos eventos profundos, intitulado "*Deep-Focus Earthquakes in Warm Slabs: Seismic Source Parameters in the Peru-Brazil Region*". Este trabalho descreve os parâmetros de fonte obtidos para a sequência sísmica e foi submetido em julho de 2024 ao periódico *Journal of Geophysical Research: Solid Earth*.

O Capítulo 4 apresenta as conclusões da pesquisa de doutorado, além de propor temas para investigações futuras.

Por fim, o Apêndice A contém um terceiro manuscrito, publicado em 2023 na revista *Journal of South American Earth Sciences*, intitulado: *Determination of intraplate focal mechanisms with the Brazilian Seismic Network: a simplified Cut-and-Paste approach.* Esse artigo foi elaborado durante a etapa de desenvolvimento dos códigos utilizados na inversão de mecanismos focais para os terremotos profundos (Capítulo 2).

Naquele momento, observou-se que a metodologia poderia ser empregada para solucionar outro problema importante: a determinação de mecanismos focais robustos para terremotos intraplaca usando estações esparsamente distribuídas da Rede Sismográfica Brasileira (RSBR) e modelos de velocidade imprecisos.

1.2. Terremotos profundos

Terremotos profundos, eventos que ocorrem em profundidades maiores que 70 km, compreendem menos de 25% da sismicidade global (Frohlich, 2006). Esses eventos ocorrem em várias zonas de subducção em profundidades que podem atingir ~700 km, delineando a geometria da placa subduzida, as chamadas zonas de Wadati-Benioff (Figura 1). Devido às grandes profundidades nas quais ocorrem, geralmente representam um baixo perigo sísmico. Apesar disso, a exemplo do terremoto de 2013 no Mar de Okhotsk (8.3 Mw), grandes eventos ainda podem ser amplamente sentidos pelo globo devido à baixa atenuação das ondas sísmicas no manto (Frohlich, 1989, 2006; Houston, 2015; Zhan, 2020).

De acordo com Frohlich (2006), eventos profundos diferem dos eventos rasos: i - no sismograma, apresentando pouca ou quase nenhuma onda de superfície, além de ondas de corpo mais claras e impulsivas, o que está diretamente ligado à profundidade focal; ii - na produção de *aftershocks*, sendo bem menos produtivos que eventos rasos de tamanhos comparáveis; e iii – nas condições de pressão e temperatura sob as quais ocorrem, que são completamente distintas daquelas próximas à superfície, indicando que eventos rasos e profundos são mecanicamente diferentes (Frohlich, 1989). Apesar disso, observações sismológicas mostram que eventos rasos e profundos podem ser igualmente explicados por rupturas ao longo de superfícies planas, isto é, ambos tem mecanismos focais que podem ser explicados por um modelo de duplo-binário (Zhan, 2020).

Devido às extremas condições de pressão e temperatura onde ocorrem, o falhamento deveria ser impossível, uma vez que a pressão confinante atuaria impedindo o processo de ruptura e a temperatura favoreceria o comportamento dúctil (Green & Marone, 2002; Griggs & Handin, 1960; Officer & Secco, 2020). Dessa maneira, terremotos profundos devem ser fundamentalmente diferentes dos eventos rasos, necessitando de algum mecanismo físico que viabilize o falhamento nessas condições. Esse mecanismo, no entanto, permanece mal compreendido (Zhan, 2020). Os mecanismos frequentemente propostos são: *dehydration embrittlement*, *transformational faulting* e *thermal runaway* (Frohlich, 2006; Houston, 2015; Zhan, 2020).

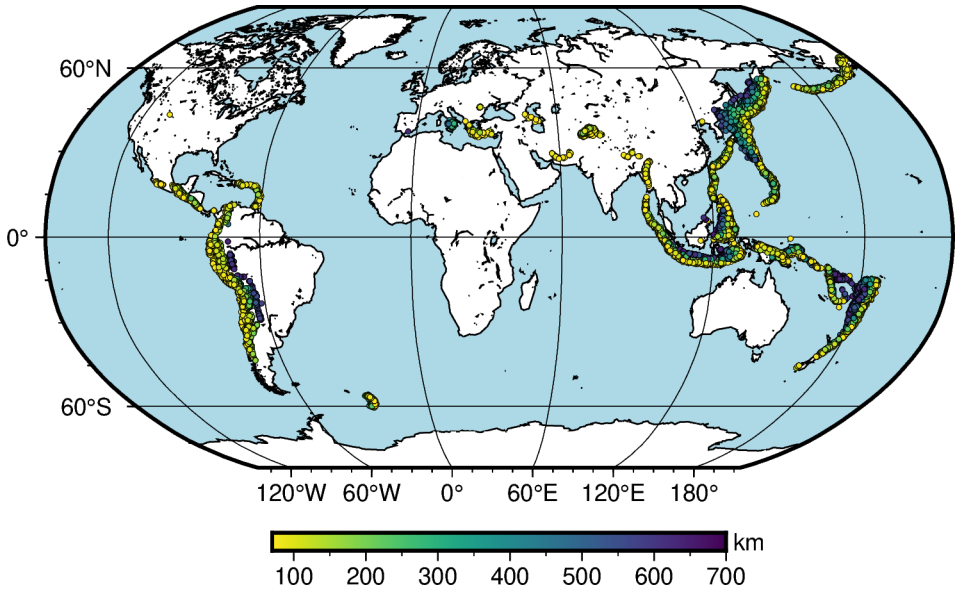

Figura 1. Distribuição de terremotos profundos (h > 70 km) pelo planeta entre 1970 e 2020 de acordo com o catálogo ISC-EHB (Engdahl et al., 1998, 2020; International Seismological Centre, 2024; Weston et al., 2018). Os epicentros estão coloridos pela profundidade, ressaltando as zonas de Wadati-Benioff.

A distribuição dos eventos profundos com a profundidade mostra uma diminuição exponencial da sismicidade até cerca de 300 km, seguida por um novo aumento em torno de 500 km e cessando em 700 km (Figura 2a) (Shirey et al., 2021). Esse padrão bimodal serve de base para a classificação dos terremotos profundos em eventos de foco intermediário, que ocorrem entre 70 e 300 km, e de foco profundo, que ocorrem em profundidades maiores que 300 km (Frohlich, 2006; Houston, 2015). Essa distribuição sugere ainda que diferentes mecanismos atuam na gênese desses grupos de eventos (Zhan, 2020).

1.3. Principais mecanismos propostos para eventos profundos

1.3.1. *Dehydration embrittlement*

Dehydration embrittlement é o mecanismo no qual o falhamento em regime dúctil é viabilizado por meio da desidratação de fases hídricas quando submetidas a determinadas condições de pressão e temperatura (Green & Marone, 2002; Meade & Jeanloz, 1991; Raleigh & Paterson, 1965). Como importantes reações de desidratação são esperadas na litosfera subduzida em profundidades menores que 300 km (Hacker et al., 2003), esse mecanismo é muitas vezes proposto para explicar a gênese de eventos de foco

intermediário (e.g., Dobson et al., 2002; Hacker et al., 2003; Jung et al., 2004; Okazaki & Hirth, 2016; Raleigh, 1967; Shao et al., 2023). O decaimento exponencial da atividade sísmica com a profundidade (Figura 2a) seria o resultado da progressiva desidratação da placa até esgotar o seu conteúdo de água a ~300 km de profundidade (Zhan, 2020).

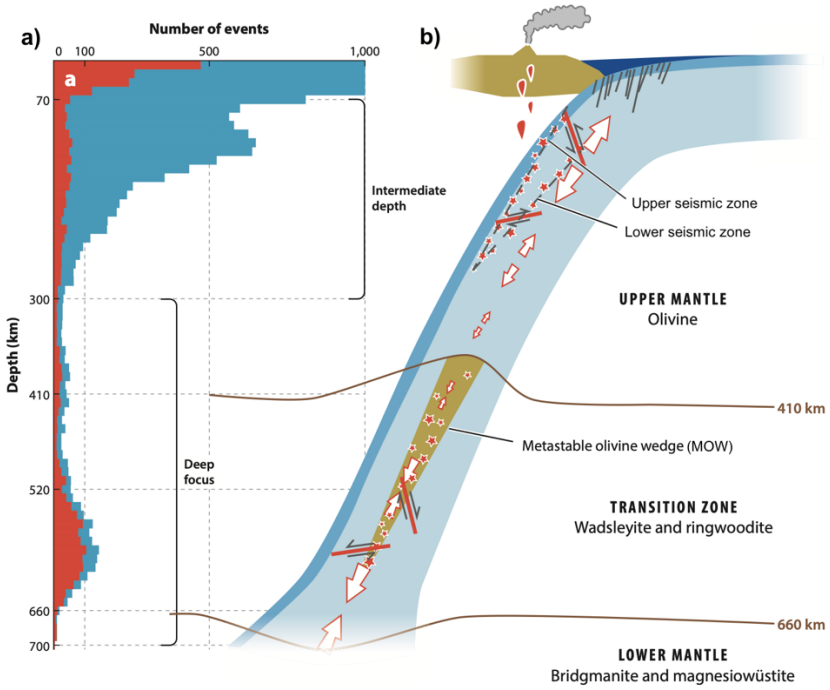

Figura 2. Sismicidade profunda em uma zona de subducção: a) distribuição de terremotos ocorridos entre 1976 e 2018 com a profundidade, de acordo com o catálogo do GCMT. O histograma em vermelho representa a sismicidade apenas na zona de subducção de Tonga enquanto o histograma em azul representa a sismicidade global. Nos histogramas estão indicados os intervalos de profundidades que definem os eventos de foco intermediário e profundo; b) distribuição de terremotos de foco intermediário ao longo de uma zona sísmica dupla, formada pelas zonas sísmicas superior e inferior, e de terremotos de foco profundo na cunha de olivina metaestável (MOW). Os regimes de esforço ao longo da placa estão indicados por setas e os planos de ruptura associados a esses regimes estão representados em vermelho. Figura adaptada de Zhan (2020).

A hidratação da crosta oceânica pode ocorrer tanto durante a sua formação, nas dorsais oceânicas, quanto devido às falhas de flexão que são produzidas no *outer rise*. Essas falhas, em particular, teriam um papel fundamental na hidratação da litosfera subduzida, sendo capazes de promover serpentinização profunda atingindo as porções superiores do manto litosférico (Peacock, 2001; Ranero et al., 2003).

Acredita-se que a desidratação da crosta e do manto litosférico da placa subduzida esteja diretamente relacionada aos terremotos nas zonas sísmicas superior e inferior,

respectivamente, que compõem as chamadas zonas sísmicas duplas, feições globais típicas de terremotos de foco intermediário (Figura 2b) (Zhan, 2020). Zonas sísmicas duplas são definidas por dois planos de sismicidade que estão separados por até 40 km de zona assísmica ou de baixa atividade que eventualmente se interceptam com o aumento da profundidade (Hacker et al., 2003).

O *dehydration embrittlement* propõe que o excesso de pressão gerado por poros preenchidos com fluidos, os quais resultam da desidratação de minerais hídricos presentes na placa oceânica (e.g. serpentina, lawsonita e antigorita) durante a subducção, levaria à concentração de esforços distensivos ao redor do poro (Figura 3a). Esses esforços permitiriam o desenvolvimento de uma estrutura de *microcrack* orientado na direção da compressão máxima (Figura 3b). Uma vez formado, o *microcrack* permaneceria aberto devido aos fluidos em seu interior e cresceria por meio dos esforços concentrados nas extremidades. O falhamento seria possibilitado através da auto-organização de vários *microcracks* pela interação dos esforços distensivos nas suas pontas, formando uma zona de falha (Figura 3c) (Green & Marone, 2002).

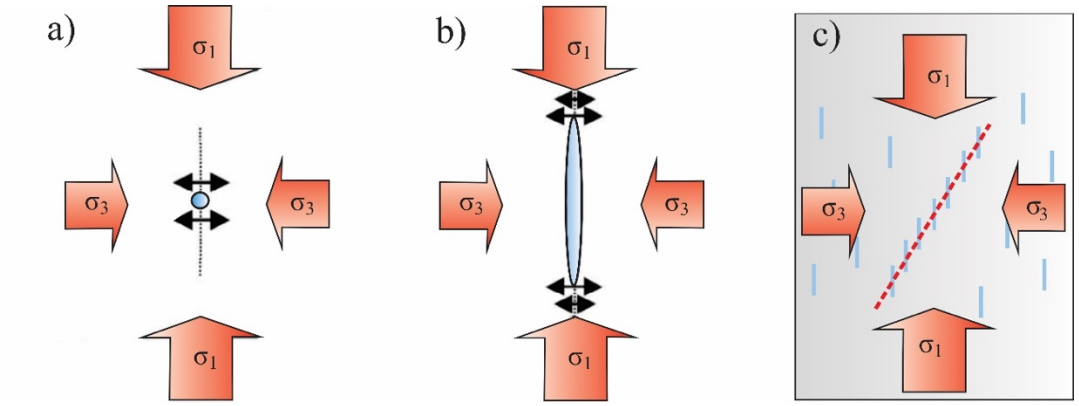

Figura 3. Mecanismo de *dehydration embrittlement*; a) a desidratação de minerais hidratados leva a formação de poros preenchidos com fluidos que concentram esforços distensivos; b) os poros evoluem para uma estrutura chamada *microcrack* paralelo ao esforço compressivo máximo (σ_1) com esforços distensivos concentrados em suas pontas; c) a auto-organização de vários *microcracks* leva à formação de uma zona de falha. Figura modificada de Green & Marone (2002) e Frohlich (2006).

A principal limitação desse mecanismo é que requer uma variação de volume positiva, o que só acontece para profundidades menores que ~70 km. Em maiores profundidades, as reações de desidratação apresentam sinal negativo devido à compressibilidade do fluido (Green & Marone, 2002). No entanto, experimentos laboratoriais observam que o falhamento devido à desidratação da antigorita, principal

mineral hidratado na placa oceânica (Ferrand et al., 2017), ocorre sob maiores condições de pressão (e.g., Gasc et al., 2017; Reinen et al., 1998). Dessa forma, se faz necessário um mecanismo alternativo que explique o falhamento resultante da desidratação de fases hídricas com variações volumétricas negativas (Green & Marone, 2002).

Alternativamente, Ferrand et al. (2017) propuseram o mecanismo de *dehydration-driven stress transfer* para explicar os eventos de foco intermediário, em particular aqueles da zona sísmica inferior. Com base em experimentos laboratoriais de desidratação de amostras sintéticas de peridotito serpentinizado (olivina + antigorita), esses autores sugerem que, na verdade, o falhamento é mais provável de ocorrer a partir de variações volumétricas negativas. Segundo o mecanismo proposto, o falhamento na matriz de olivina resultaria da transmissão de esforços elevados produzidos pela desidratação de clusters de antigorita, bem como da instabilidade promovida pelos produtos nano cristalinos dessas reações (Shirey et al., 2021). Nesse sentido, para que o falhamento ocorra, seria necessário um conteúdo de antigorita suficiente para transmitir uma quantidade crítica de esforço à matriz de olivina.

Como geralmente não é esperado que haja conteúdo suficiente de água na placa subduzida em profundidades maiores que 300 km, esse mecanismo é muitas vezes limitado a explicar eventos de foco intermediário (Zhan, 2020). No entanto, alguns estudos indicam a água ainda pode ter um papel importante na gênese de terremotos de foco profundo (e.g., Barcheck et al., 2012; Shirey et al., 2021; Zhang et al., 2021). Shirey et al. (2021), por exemplo, associam esses terremotos à liberação de fluidos entre 300 e 700 km, a qual é evidenciada por diamantes sublitosféricos.

1.3.2. *Transformational faulting*

O *transformational faulting* ou *anticrack faulting* consiste em um mecanismo de alta pressão observado em laboratório que viabiliza o falhamento em regime dúctil por meio de estruturas chamadas *anticracks*. Esses *anticracks* são lentes preenchidas com material superplástico que resultam de uma transformação de fase exotérmica, como a mudança da olivina para suas fases mais densas: wadsleyita ou ringwoodita. Como terremotos de foco profundo ocorrem em profundidades referentes à zona de transição do manto (MTZ), caracterizada por importantes transformações de fase da olivina, a origem desses eventos é muitas vezes atribuída ao *transformational faulting* em uma cunha de olivina metaestável (MOW) (Figura 2b) (Green & Burnley, 1989; Green & Marone, 2002; Green & Zhou, 1996).

Com o aumento da pressão, a olivina (α-$(Mg,Fe)_2SiO_4$) – um dos minerais mais abundantes no manto superior – se transforma de maneira exotérmica em seus polimorfos mais densos de fase spinel: wadsleyita (β-$(Mg,Fe)_2SiO_4$) e ringwoodita (γ-$(Mg,Fe)_2SiO_4$). A transformação em wadsleyita produz a descontinuidade sísmica que marca o topo da MTZ, a aproximadamente 410 km de profundidade, enquanto a transformação em ringwoodita está possivelmente relacionada a uma descontinuidade intermediária a ~520 km. Finalmente, a transformação endotérmica da ringwoodita em bridgemanita + magnésio-wustita a ~660 km define a base da MTZ e o topo do manto inferior (Green & Houston, 1995; Shearer, 2000; Tsujino et al., 2019; Zhan, 2020).

Em zonas de subducção, no entanto, a litosfera oceânica produz uma condição de desequilíbrio devido às menores temperaturas em seu interior. Nesse contexto, o núcleo frio dessa placa poderia permitir que a olivina penetre de maneira metaestável na MTZ, formando uma MOW capaz de nuclear terremotos por *transformational faulting* (Figura 2b) (e.g., Bina et al., 2001; Devaux et al., 2000).

A existência da MOW, especialmente nas placas mais frias, é fundamental para a hipótese de *transformational faulting* como mecanismo gerador de eventos de foco profundo (Green & Burnley, 1989; Green & Houston, 1995; Houston, 2015; Kirby et al., 1996; Zhan, 2020), uma vez que permitiria reações exotérmicas de α para β e α para γ capazes de gerar instabilidade (Green & Zhou, 1996). Essa hipótese, obviamente, só seria possível para profundidades maiores que 350 km, uma vez que o limite olivina-spinel é localmente elevado pela placa fria em subducção (Figura 2b) (Houston, 2015), e assim explicaria naturalmente o aumento na frequência de terremotos nessas profundidades e o confinamento deles à MTZ (Green & Zhou, 1996; Zhan, 2020). O término abrupto da sismicidade próximo ao topo do manto inferior seria devido ao falhamento por *anticracks* não ser esperado, uma vez que as transformações possíveis ou são endotérmicas (γ para perovskita + magnésio-wustita ou ilmenita para perovskita) ou são lentas o suficiente (α to perovskita + magnésio-wustita e granada para perovskita) (Houston, 2015).

O processo de transformação da olivina em suas fases spinel leva à formação de *anticracks*, lentes preenchidas com a fase mais densa e superplástica orientadas de maneira perpendicular ao eixo de máxima compressão (Figura 4a). Os *anticracks* crescem e interagem entre si por meio dos esforços compressivos concentrados em suas extremidades, formando uma zona de falha orientada a mais ou menos 45º do eixo principal de compressão (Figura 4b). Nesse contexto, o preenchimento superplástico seria

o responsável por garantir a instabilidade, atuando como um lubrificante na falha (Green & Marone, 2002; Green & Zhou, 1996).

Para que ocorra a formação de *anticracks*, é condição necessária que a mudança de fase envolvida seja exotérmica. Esse tipo de reação resulta em um aumento local da temperatura do meio, o que por sua vez favorece a nucleação de *anticracks* necessários para o falhamento. Desse modo, há um *feedback* positivo entre o aumento local da temperatura devido à transformação e a nucleação de *anticracks* (Green & Marone, 2002; Green & Zhou, 1996). Note que, embora a reação exotérmica seja necessária, ela não é suficiente para viabilizar o *transformational faulting*. Green & Zhou (1996) sugerem que reações exotérmicas, tal como a de olivina para perovskita + magnésio-wustita, podem ocorrer de maneira assísmica uma vez que a reação não é rápida o suficiente para produzir *anticracks*, e consequentemente, instabilidade. Assim, a transformação de fase, além de ser exotérmica, deve ser suficientemente rápida para viabilizar o mecanismo (Green & Marone, 2002).

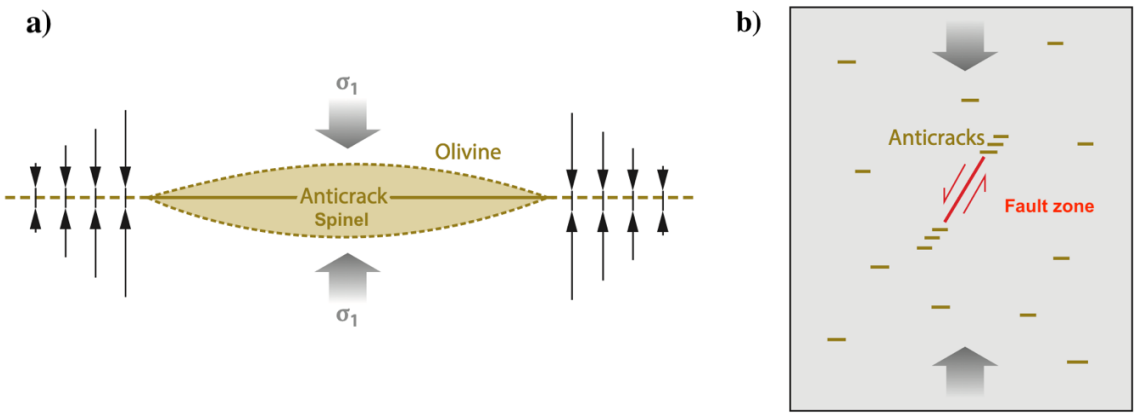

Figura 4. O mecanismo de *transformational faulting*; a) estrutura lenticular perpendicular ao esforço compressivo máximo preenchida com fase spinel mais densa e superplástica (*anticrack*) resultante da transformação de fase da olivina; b) auto-organização dos *anticracks* por meio dos esforços compressivos em suas extremidades em uma zona de falha orientada a aproximadamente 45º do eixo de máxima compressão. Figura modificada de Zhan (2020).

Alguns estudos no Japão têm apresentado evidências sismológicas que suportam a existência de MOW (Furumura et al., 2016; Jiang & Zhao, 2011; Kawakatsu & Yoshioka, 2011; Shen & Zhan, 2020). Shen & Zhan (2020), por exemplo, conseguiram delimitar uma MOW de ~30 km de espessura a 410 km que se estenderia até 580 km por meio de interferometria entre fontes (Curtis et al., 2009; Tonegawa & Nishida, 2010). No entanto, ainda há poucas evidências sismológicas em outras zonas de subducção (e.g., Kaneshima et al., 2007) para concluir sobre a existência da MOW (Zhan, 2020).

A temperatura da placa exerce um papel fundamental na preservação de olivina em estado metaestável na MTZ, uma vez que controla a taxa de transformação desse mineral (Green & Marone, 2002; Green & Zhou, 1996). Dessa maneira, não é esperada a ocorrência de MOW em placas quentes, pois as altas temperaturas favoreceriam as transformações de fase e consequentemente evitariam a metaestabilidade (e.g., Devaux et al., 1997; Mosenfelder et al., 2001). No entanto, terremotos de foco profundo são observados em profundidades próximas à base da MTZ tanto em placas quentes quanto frias (Houston, 2015).

Para contornar essa limitação da MOW, a hipótese de *transformational faulting* iniciado em uma cunha de enstatita metaestável (MEW) foi levantada por Hogrefe et al. (1994). A enstatita representa ~25% do volume total da placa oceânica e poderia persistir metaestavelmente até profundidades maiores que a olivina. Nesse contexto, a transformação exotérmica de enstatita para ilmenita, que é acompanhada por uma diminuição significativa de volume de ~12%, poderia resultar em *transformational faulting*, explicando eventos de foco profundo nas placas quentes.

Além da estrutura térmica da placa subduzida, o conteúdo de água na placa também exerce um papel importante na viabilidade da MOW. Experimentos laboratoriais mostram que mesmo uma pequena quantidade de água pode acelerar consideravelmente a transformação de fase da olivina (Du Frane et al., 2013; Hosoya et al., 2005; Kubo et al., 1998). Dessa maneira, acredita-se que a presença de uma MOW deve estar necessariamente atrelada à uma litosfera oceânica seca, consequentemente tornando incompatível a ocorrência simultânea de *dehydration embrittlement* e *transformational faulting* (Du Frane et al., 2013; Kawakatsu & Yoshioka, 2011; Shen & Zhan, 2020; Zhan, 2020).

Por outro lado, um estudo recente mostrou que fase hídrica A pode coexistir com a olivina e a wadsleyita na MTZ, atuando como uma esponja na placa subduzida até temperaturas de 1000 ºC, evitando a saturação desses minerais e preservando a MOW (Ishii & Ohtani, 2021). A desidratação de fase hídrica A hidrataria a olivina metaestável e serviria como catalisador para o *transformational faulting*. O papel da água como catalisador de terremotos de foco profundo na borda superior da MOW foi proposto por Mao et al. (2022) após observar que a litosfera oceânica altamente hidratada (em Izu e Honshu) está associada a um relativamente maior valor *b* para pequenos eventos de foco profundo ($3.0 \leq Mw \leq 3.8$).

De acordo com Zhan (2020), assumindo a existência de uma MOW, a ruptura por *transformational faulting* deveria: i - estar totalmente confinada na MOW; e ii - não deveria ocorrer mais de uma vez ao longo de um mesmo plano de falha. O confinamento de rupturas dentro da MOW é previsto, naturalmente, pelo fato de que a formação de *anticracks* só seria possível no volume metaestável. Porém, estudos laboratoriais recentes e observações a partir de grandes eventos tem demonstrado que rupturas conseguem se propagar fora da MOW, possivelmente por meio de um mecanismo secundário, como *thermal runaway* (seção 1.3.3) (Gasc et al., 2022; Green & Zhou, 1996; Silver et al., 1995; Wiens, 2001). Uma vez que a transformação de fase tem caráter irreversível, não seriam esperadas múltiplas rupturas ao longo de uma mesma zona de falha. Essa hipótese, no entanto, é difícil de ser testada, uma vez que o mecanismo de *transformational faulting* parece necessitar de apenas uma fina camada de material spinel para promover falhamento (Schubnel et al., 2013; Wang et al., 2017). Portanto, a existência de uma MOW, especialmente em placas quentes, permanece em debate, assim como a viabilidade de *transformational faulting*.

1.3.3. *Thermal runaway*

O mecanismo *thermal runaway* descreve o falhamento como resultado de um *feedback* positivo entre o cisalhamento e o aumento local de temperatura, podendo envolver derretimento parcial ou não (Green & Marone, 2002; Zhan, 2020). Esse mecanismo geralmente é proposto tanto para eventos de foco intermediário (e.g., Poli et al., 2016) quanto para eventos de foco profundo (e.g., Ogawa, 1987), e provavelmente serve como um mecanismo auxiliar à propagação da ruptura (e.g., Zhan, 2017). Em especial, o terremoto de 1994 da Bolívia (Mw 8.3), ocorrido a 637 km de profundidade, é evidência de um processo altamente dissipativo que, provavelmente, envolveu fusão parcial na zona de falha (Kanamori et al., 1998).

O *Thermal runaway* ocorre quando a viscosidade diminui devido ao aumento local de temperatura causado pelo aquecimento durante o cisalhamento, gerando uma instabilidade por meio do *feedback* entre esses dois fatores (Figura 5) (Green & Marone, 2002; Kanamori et al., 1998). Para que ocorra falhamento a partir desse mecanismo deve haver tanto uma elevada taxa de deformação local quanto um *feedback* térmico considerável (Karato et al., 2001).

Esse mecanismo, no entanto, não parece ser capaz de explicar a nucleação de novas rupturas, necessitando de zonas de fraqueza ou heterogeneidades preexistentes

(John et al., 2009; Kelemen & Hirth, 2007). Assim, é geralmente empregado como um mecanismo auxiliar que promove a propagação da ruptura já iniciada por *dehydration embrittlement* ou *transformational faulting* (Zhan, 2017).

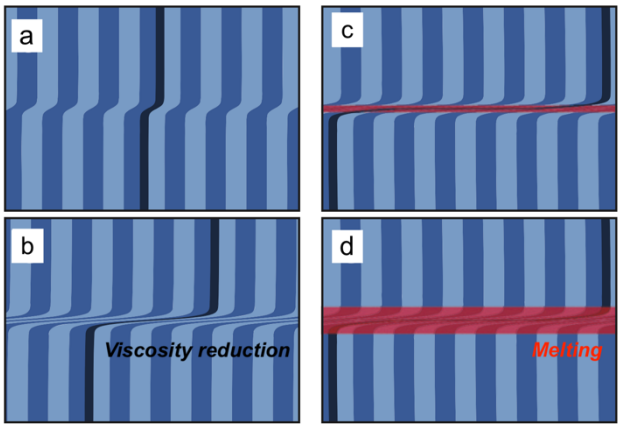

Figura 5. Mecanismo de *thermal runaway*: a-b) o cisalhamento ao longo de uma zona de fraqueza preexistente provoca o aumento local de temperatura por fricção que resulta na diminuição local da viscosidade. O *feedback* positivo entre essa diminuição da viscosidade e o cisalhamento promove a instabilidade; c-d) é possível que o aumento local de temperatura seja elevado o suficiente para produzir derretimento parcial na zona de falha. Figura adaptada de John et al. (2009) e Zhan (2020).

1.3.4. O *mecanismo duplo*

A hipótese de mecanismo duplo foi introduzida por Zhan (2017) com base nas variações espaciais do valor *b* da Lei de Gutemberg-Richter e no estado térmico das placas subduzidas, representado pelo parâmetro térmico Φ. Este parâmetro é o produto da idade da placa, do ângulo de mergulho e da taxa de convergência da placa oceânica, expresso em quilômetros. Placas consideradas frias, como a placa de Tonga, tendem a apresentar um Φ maior, enquanto placas quentes, como a placa sul-americana, tendem a ter um Φ menor (Frohlich, 2006; Kirby et al., 1991).

Zhan (2017) observou uma clara relação entre o valor *b* de eventos Mw < 6.5 abaixo de 500 km com o Φ, onde $b \sim 1$ em placas frias e $b \sim 0.5$ em placas quentes, sugerindo uma forte relação entre a sismicidade e as temperaturas na placa. Além disso, verificou que há uma mudança abrupta de $b \sim 0.5$ para $b \sim 1$ em torno de Mw 6.5 nas placas quentes, o que não foi observado em placas frias (Figura 6a) e que poderia estar sugerindo um mecanismo gerador diferente para os grandes eventos (Mw > 6.5) (e.g., Giardini, 1988; Okal & Kirby, 1995; Wiens & Gilbert, 1996).

Nesse sentido, Zhan (2017) propõe que rupturas em placas quentes ocorrem inicialmente por *transformational faulting* em uma fina MOW, e posteriormente se propagam para fora da MOW por *thermal runaway* (Figura 6b). Grandes eventos em placas quentes seriam então explicados como rupturas que são dominadas pelo segundo mecanismo, possivelmente envolvendo derretimento na zona de falha. Em placas frias, por outro lado, a maior parte das rupturas estaria sendo acomodada pela MOW mais espessa, envolvendo pouca ou nenhuma contribuição de *thermal runaway*.

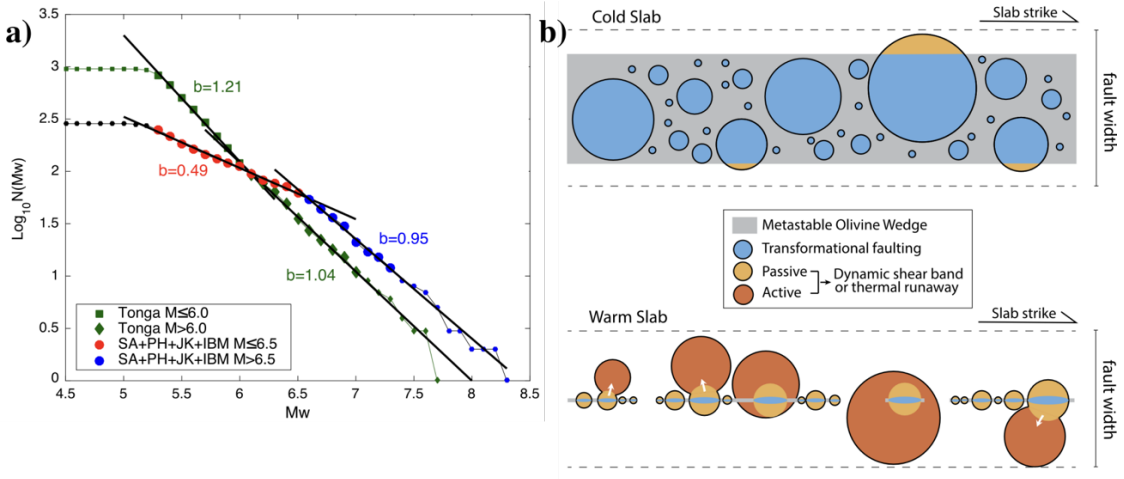

Figura 6. Mecanismo duplo para a gênese de terremotos de foco profundo: a) Lei de Gutemberg-Richter para eventos em profundidades maiores que 500 km para placa fria (Tonga), em quadrados e losangos verdes, e para placas quentes: AS: América do Sul; PH: Filipinas; JK: Japão-Curilhas e IBM: Izu-Bonin-Marianas, em círculos vermelhos (b = 0.49) e azuis (b = 0.95); b) Modelo de mecanismo duplo para placas frias e quentes. Círculos representam a área de ruptura e a cor representa o mecanismo dominante. Em cinza é mostrada a espessura da MOW disponível na placa subduzida, que é mais espessa em placas frias que em placas quentes. Note que, para placas frias, as rupturas são dominadas pelo *transformational faulting*, e são compreendidas pela MOW. No caso de placas quentes, as rupturas se iniciam por *transformational faulting* e continuam a se propagar fora da MOW por *thermal runaway*. No caso de grandes eventos (Mw > 6.5), o mecanismo de *thermal runaway* tem um papel ativo, dominando o processo de ruptura (círculos laranja). Figura modificada de Zhan (2017).

1.4. Terremotos profundos no Acre

Terremotos de foco intermediário ocorrem ao longo de várias zonas de subducção pelo mundo (Figura 7a). Por outro lado, eventos de foco profundo estão limitados a cerca de uma dúzia de regiões, uma delas localizada na América do Sul (Figura 7b). Nesse continente, a sismicidade de foco profundo se distribui ao longo de até quatro segmentos:

Colômbia-Peru, Peru-Brasil, Peru-Bolívia e Bolívia-Argentina (Figura 7c). Dentre esses, apenas os segmentos Peru-Brasil e Bolívia-Argentina apresentam atividade sísmica regular, alinhada paralelamente à trincheira. Por outro lado, os outros segmentos são caracterizados por enormes eventos que ocorrem de maneira isolada e em grandes profundidades (Frohlich, 2006). Como exemplos, temos o terremoto de 9 de junho de 1994 (Mw 8.3), a 647 km de profundidade na Bolívia, e o terremoto de 31 de julho de 1970 (Mw 8.1), a 623 km, na Colômbia (Figura 7c) (Houston, 2015).

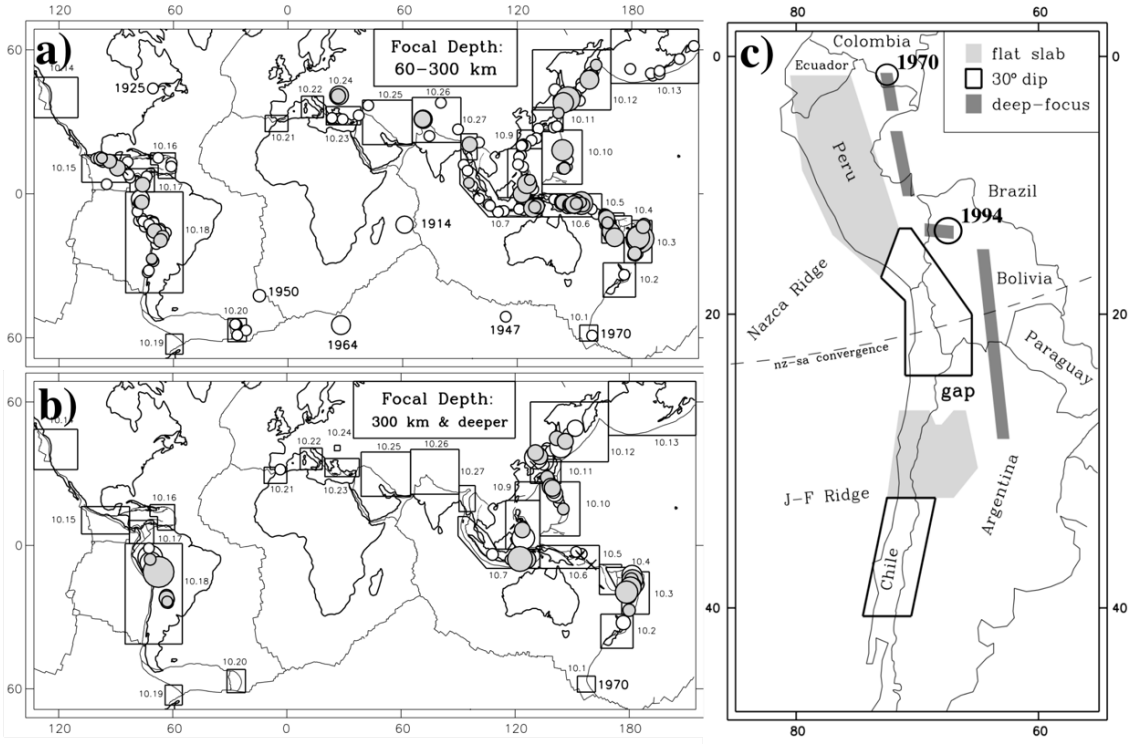

Figura 7. Distribuição espacial de grandes terremotos (Mw > 7) de foco intermediário (a) e profundo (b), entre 1900 e 2004 de acordo com os catálogos do GCMT (círculos escuros), Abe (1981) e Engdahl & Villaseñor (2002) (círculos claros), e a distribuição da sismicidade de foco profundo na América do Sul ao longo de quatro segmentos (c). A geometria da placa de Nazca em subducção é simplificada por áreas de subducção plana e normal. As localizações aproximadas dos grandes terremotos da Colômbia (Mw 8.1, 1970) e da Bolívia (Mw 8.3, 1994) são mostradas no mapa. Figura modificada de Frohlich (2006).

O segmento Peru-Brasil, que atravessa o Estado do Acre, é conhecido por terremotos que ocorrem em profundidades maiores que 500 km. Esses eventos têm origem em uma porção da placa de Nazca que subduz quase verticalmente em direção ao manto inferior (e.g., Portner et al., 2020; Rodríguez et al., 2020) após cerca de 500 km de subducção plana (e.g., Bishop et al., 2017). Os terremotos na região são geralmente

caracterizados por falhas normais, indicativas de um regime uniforme de compressão ao longo do mergulho da placa (Frohlich, 2006). Esse regime é frequentemente interpretado como resultado da resistência encontrada pela placa ao penetrar o manto inferior (e.g., Isacks & Molnar, 1971).

Em 2014, teve início a instalação de várias estações da Rede Sismográfica Brasileira (RSBR) na região amazônica (Figura 8a). Desde então, essas estações têm proporcionado uma melhor cobertura de terremotos de foco profundo ao longo do segmento Peru-Brasil, permitindo a amostragem de ambos os hemisférios, superior e inferior. Essa cobertura é crucial para a caracterização desses sismos e, consequentemente, para uma melhor compreensão do mecanismo físico por trás de eventos profundos.

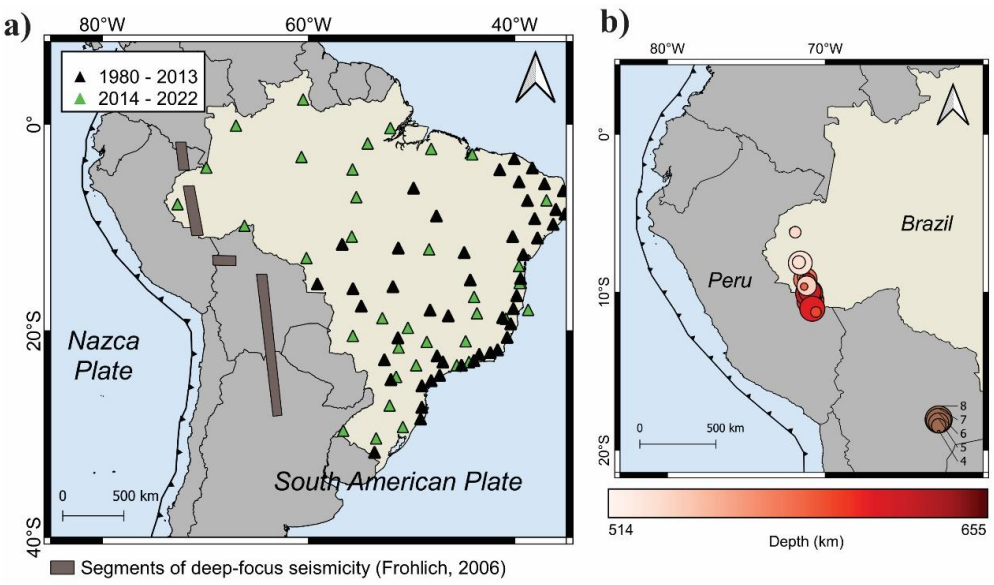

Figura 8. a) A Rede Sismográfica Brasileira (RSBR) e a sua expansão em direção à região amazônica desde 2014; b) a sequência sísmica de 2014-2022 no segmento Peru-Brasil de acordo com o catálogo do USGS.

O catálogo do USGS lista um total de 42 terremotos de foco profundo nesse segmento entre 2014 e 2022. Tais eventos têm magnitudes de Mw 4.0 a 7.6 e profundidades variando entre 515 e 655 km (Figura 8b). Vale ressaltar que, apenas em 2015, 25 terremotos foram registrados, compreendendo um *doublet*, um par de eventos Mw 7.6 separados por ~50 km e 5 minutos, e seus *aftershocks* de menores magnitudes (Figura 9) (Jiménez et al., 2021; Ruiz et al., 2017; Ye et al., 2016; Zahradník et al., 2017). Assim, a cobertura do hemisfério superior garantida por estações da RSBR e a ocorrência de um ano de atividade sísmica anômala fornecem uma chance única de investigar o

mecanismo físico por trás de terremotos de foco profundo. Isso é ainda mais importante no sentido de entender o mecanismo atuante em placas quentes, como a placa de Nazca.

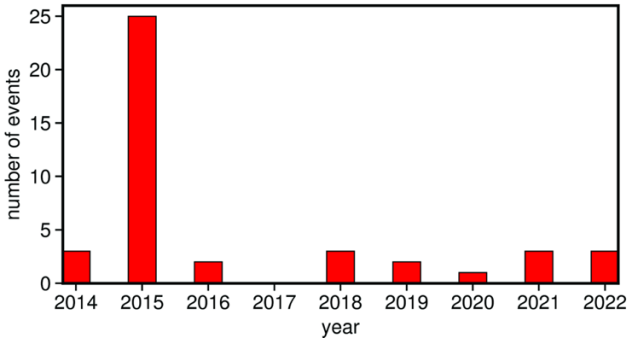

Figura 9. Histograma mostrando o número de eventos por ano desde 2014 no segmento Peru-Brasil, de acordo com o USGS. Note o número desproporcional de eventos ocorridos apenas em 2015.

1.5. Objetivo da Tese

Considerando que a origem de terremotos de foco profundo permanece enigmática e constitui um problema importante para diversas áreas das geociências, esta Tese de Doutorado visa investigar o mecanismo gerador desses eventos, em particular daqueles que ocorrem em placas quentes como na América do Sul. O objetivo principal é caracterizar a sequência sísmica ocorrida entre 2014 e 2022 na região amazônica entre o Peru e o Brasil, aproveitando a cobertura sem precedentes proporcionada pelas estações da Rede Sismográfica Brasileira (RSBR) e de redes internacionais vizinhas. Essa caracterização inclui a determinação de mecanismos focais e de parâmetros de fonte sísmica, os quais são apresentados na forma de dois manuscritos (Capítulos 3 e 4).

Referências

Abe, K. (1981). Magnitudes of large shallow earthquakes from 1904 to 1980. Physics of the Earth and Planetary Interiors, 27(1), 72–92. https://doi.org/10.1016/0031-9201(81)90088-1

Barcheck, C. G., Wiens, D. A., van Keken, P. E., & Hacker, B. R. (2012). The relationship of intermediate- and deep-focus seismicity to the hydration and dehydration of subducting slabs. Earth and Planetary Science Letters, 349–350, 153–160. https://doi.org/10.1016/j.epsl.2012.06.055

Bina, C. R., Stein, S., Marton, F. C., & Van Ark, E. M. (2001). Implications of slab mineralogy for subduction dynamics. Physics of the Earth and Planetary Interiors, 127(1–4), 51–66. https://doi.org/10.1016/S0031-9201(01)00221-7

Bishop, B. T., Beck, S. L., Zandt, G., Wagner, L., Long, M., Antonijevic, S. K., et al. (2017). Causes and consequences of flat-slab subduction in southern Peru. Geosphere, 13(5), 1392–1407. https://doi.org/10.1130/GES01440.1

Curtis, A., Nicolson, H., Halliday, D., Trampert, J., & Baptie, B. (2009). Virtual seismometers in the subsurface of the Earth from seismic interferometry. Nature Geoscience, 2(10), 700–704. https://doi.org/10.1038/ngeo615

Devaux, J. P., Schubert, G., & Anderson, C. (1997). Formation of a metastable olivine wedge in a descending slab. Journal of Geophysical Research: Solid Earth, 102(B11), 24627–24637. https://doi.org/10.1029/97JB02334

Devaux, J. P., Fleitout, L., Schubert, G., & Anderson, C. (2000). Stresses in a subducting slab in the presence of a metastable olivine wedge. Journal of Geophysical Research: Solid Earth, 105(B6), 13365–13373. https://doi.org/10.1029/1999JB900274

Dobson, D. P., Meredith, P. G., & Boon, S. A. (2002). Simulation of Subduction Zone Seismicity by Dehydration of Serpentine. Science, 298(5597), 1407–1410. https://doi.org/10.1126/science.1075390

Engdahl, E. R., & Villaseñor, A. (2002). Global Seismicity: 1900-1999. In W. H. K. Lee, H. Kanamori, P. C. Jennings, & C. Kisslinger (Eds.), International Handbook of Earthquake and Engineering Seismology (pp. 665–690). Academic Press.

Engdahl, E. R., van der Hilst, R., & Buland, R. (1998). Global teleseismic earthquake relocation with improved travel times and procedures for depth determination. Bulletin of the Seismological Society of America, 88(3), 722–743. https://doi.org/10.1785/BSSA0880030722

Engdahl, E. R., Di Giacomo, D., Sakarya, B., Gkarlaouni, C. G., Harris, J., & Storchak, D. A. (2020). ISC-EHB 1964–2016, an Improved Data Set for Studies of Earth Structure and Global Seismicity. Earth and Space Science, 7(1). https://doi.org/10.1029/2019EA000897

Ferrand, T. P., Hilairet, N., Incel, S., Deldicque, D., Labrousse, L., Gasc, J., et al. (2017). Dehydration-driven stress transfer triggers intermediate-depth earthquakes. Nature Communications, 8(1), 15247. https://doi.org/10.1038/ncomms15247

Du Frane, W. L., Sharp, T. G., Mosenfelder, J. L., & Leinenweber, K. (2013). Ringwoodite growth rates from olivine with ~75ppmw H2O: Metastable olivine must be nearly anhydrous to exist in the mantle transition zone. Physics of the Earth and Planetary Interiors, 219, 1–10. https://doi.org/10.1016/j.pepi.2013.04.001

Frohlich, C. (1989). The Nature Of Deep-Focus Earthquakes. Annual Review of Earth and Planetary Sciences, 17, 227–254. https://doi.org/10.1146/annurev.earth.17.1.227

Frohlich, C. (2006). Deep Earthquakes. Cambridge: Cambridge University Press. https://doi.org/10.1017/CBO9781107297562

Furumura, T., Kennett, B. L. N., & Padhy, S. (2016). Enhanced waveguide effect for deep-focus earthquakes in the subducting Pacific slab produced by a metastable olivine wedge. Journal of Geophysical Research: Solid Earth, 121(9), 6779–6796. https://doi.org/10.1002/2016JB013300

Gasc, J., Hilairet, N., Yu, T., Ferrand, T., Schubnel, A., & Wang, Y. (2017). Faulting of natural serpentinite: Implications for intermediate-depth seismicity. Earth and Planetary Science Letters, 474, 138–147. https://doi.org/10.1016/j.epsl.2017.06.016

Gasc, J., Daigre, C., Moarefvand, A., Deldicque, D., Fauconnier, J., Gardonio, B., et al. (2022). Deep-focus earthquakes: From high-temperature experiments to cold slabs. Geology. https://doi.org/10.1130/G50084.1

Giardini, D. (1988). Frequency distribution and quantification of deep earthquakes. Journal of Geophysical Research: Solid Earth, 93(B3), 2095–2105. https://doi.org/10.1029/JB093iB03p02095

Green, H. W., & Burnley, P. C. (1989). A new self-organizing mechanism for deep-focus earthquakes. Nature, 341, 733–737. https://doi.org/10.1038/341733a0

Green, H. W., & Houston, H. (1995). The Mechanics of Deep Earthquakes. Annual Review of Earth and Planetary Sciences, 23, 169–213. https://doi.org/10.1146/annurev.ea.23.050195.001125

Green, H. W., & Marone, C. (2002). Instability of Deformation. Reviews in Mineralogy and Geochemistry, 51(1), 181–199. https://doi.org/10.2138/gsrmg.51.1.181

Green, H. W., & Zhou, Y. (1996). Transformation-induced faulting requires an exothermic reaction and explains the cessation of earthquakes at the base of the mantle transition zone. Tectonophysics, 256(1–4), 39–56. https://doi.org/10.1016/0040-1951(95)00164-6

Griggs, D., & Handin, J. (1960). Chapter 13: Observations on Fracture and a Hypothesis of Earthquakes*. In Rock Deformation (A Symposium) (79th ed., pp. 347–364). Geological Society of America. https://doi.org/10.1130/MEM79-p347

Hacker, B. R., Peacock, S. M., Abers, G. A., & Holloway, S. D. (2003). Subduction factory 2. Are intermediate-depth earthquakes in subducting slabs linked to metamorphic dehydration reactions? Journal of Geophysical Research: Solid Earth, 108(B1). https://doi.org/10.1029/2001JB001129

Hogrefe, A., Rubie, D. C., Sharp, T. G., & Seifert, F. (1994). Metastability of enstatite in deep subducting lithosphere. Nature, 372, 351–353. https://doi.org/10.1038/372351a0

Hosoya, T., Kubo, T., Ohtani, E., Sano, A., & Funakoshi, K. (2005). Water controls the fields of metastable olivine in cold subducting slabs. Geophysical Research Letters, 32(L17305). https://doi.org/10.1029/2005GL023398

Houston, H. (2015). Deep Earthquakes. In Treatise on Geophysics (pp. 329–354). Elsevier. https://doi.org/10.1016/B978-0-444-53802-4.00079-8

International Seismological Centre. (2024). ISC-EHB dataset.

Isacks, B., & Molnar, P. (1971). Distribution of stresses in the descending lithosphere from a global survey of focal-mechanism solutions of mantle earthquakes. Reviews of Geophysics, 9(1), 103–174. https://doi.org/10.1029/RG009i001p00103

Ishii, T., & Ohtani, E. (2021). Dry metastable olivine and slab deformation in a wet subducting slab. Nature Geoscience, 14, 526–530. https://doi.org/10.1038/s41561-021-00756-7

Jiang, G., & Zhao, D. (2011). Metastable olivine wedge in the subducting Pacific slab and its relation to deep earthquakes. Journal of Asian Earth Sciences, 42(6), 1411–1423. https://doi.org/10.1016/j.jseaes.2011.08.005

Jiménez, C., Calvo, C., Saavedra, M., Moggiano, N., & Molina, W. (2021). Source characteristics of Peruvian deep focus seismic doublet of November 24, 2015. Journal of South American Earth Sciences, 105(102919). https://doi.org/https://doi.org/10.1016/j.jsames.2020.102919

John, T., Medvedev, S., Rüpke, L. H., Andersen, T. B., Podladchikov, Y. Y., & Austrheim, H. (2009). Generation of intermediate-depth earthquakes by self-localizing thermal runaway. Nature Geoscience, 2(2), 137–140. https://doi.org/10.1038/ngeo419

Jung, H., Green II, H. W., & Dobrzhinetskaya, L. F. (2004). Intermediate-depth earthquake faulting by dehydration embrittlement with negative volume change. Nature, 428, 545–549. https://doi.org/10.1038/nature02412

Kanamori, H., Anderson, D. L., & Heaton, T. H. (1998). Frictional Melting During the Rupture of the 1994 Bolivian Earthquake. Science, 279(5352), 839–842. https://doi.org/10.1126/science.279.5352.839

Kaneshima, S., Okamoto, T., & Takenaka, H. (2007). Evidence for a metastable olivine wedge inside the subducted Mariana slab. Earth and Planetary Science Letters, 258(1–2), 219–227. https://doi.org/10.1016/j.epsl.2007.03.035

Karato, S. -i., Riedel, M. R., & Yuen, D. A. (2001). Rheological structure and deformation of subducted slabs in the mantle transition zone: implications for mantle circulation and deep earthquakes. Physics of the Earth and Planetary Interiors, 127(1–4), 83–108. https://doi.org/10.1016/S0031-9201(01)00223-0

Kawakatsu, H., & Yoshioka, S. (2011). Metastable olivine wedge and deep dry cold slab beneath southwest Japan. Earth and Planetary Science Letters, 303(1–2), 1–10. https://doi.org/10.1016/j.epsl.2011.01.008

Kelemen, P. B., & Hirth, G. (2007). A periodic shear-heating mechanism for intermediate-depth earthquakes in the mantle. Nature, 446, 787–790. https://doi.org/10.1038/nature05717

Kirby, S. H., Durham, W. B., & Stern, L. A. (1991). Mantle Phase Changes and Deep-Earthquake Faulting in Subducting Lithosphere. Science, 252, 216–225. https://doi.org/10.1126/science.252.5003.216

Kirby, S. H., Stein, S., Okal, E. A., & Rubie, D. C. (1996). Metastable mantle phase transformations and deep earthquakes in subducting oceanic lithosphere. Reviews of Geophysics, 34(2), 261–306. https://doi.org/10.1029/96RG01050

Kubo, T., Ohtani, E., Kato, T., Shinmei, T., & Fujino, K. (1998). Effects of Water on the α-β Transformation Kinetics in San Carlos Olivine. Science, 281(5373), 85–87. https://doi.org/10.1126/science.281.5373.85

Mao, G. L., Ferrand, T. P., Li, J., Zhu, B., Xi, Z., & Chen, M. (2022). Unsupervised machine learning reveals slab hydration variations from deep earthquake distributions beneath the northwest Pacific. Communications Earth & Environment, 3:56, 1–9. https://doi.org/10.1038/s43247-022-00377-x

Meade, C., & Jeanloz, R. (1991). Deep-Focus Earthquakes and Recycling of Water into the Earth's Mantle. Science, 252(5002), 68–72. https://doi.org/10.1126/science.252.5002.68

Mosenfelder, J. L., Marton, F. C., Ross, C. R., Kerschhofer, L., & Rubie, D. C. (2001). Experimental constraints on the depth of olivine metastability in subducting lithosphere. Physics of the Earth and Planetary Interiors, 127(1–4), 165–180. https://doi.org/10.1016/S0031-9201(01)00226-6

Officer, T., & Secco, R. A. (2020). Detection of high P,T transformational faulting in Fe2SiO4 via in-situ acoustic emission: Relevance to deep-focus earthquakes. Physics of the Earth and Planetary Interiors, 300, 106429. https://doi.org/10.1016/j.pepi.2020.106429

Ogawa, M. (1987). Shear instability in a viscoelastic material as the cause of deep focus earthquakes. Journal of Geophysical Research: Solid Earth, 92(B13), 13801–13810. https://doi.org/10.1029/JB092iB13p13801

Okal, E. A., & Kirby, S. H. (1995). Frequency-moment distribution of deep earthquakes; implications for the seismogenic zone at the bottom of slabs. Physics of the Earth and Planetary Interiors, 92(3–4), 169–187. https://doi.org/10.1016/0031-9201(95)03037-8

Okazaki, K., & Hirth, G. (2016). Dehydration of lawsonite could directly trigger earthquakes in subducting oceanic crust. Nature, 530(7588), 81–84. https://doi.org/10.1038/nature16501

Peacock, S. M. (2001). Are the lower planes of double seismic zones caused by serpentine dehydration in subducting oceanic mantle? Geology, 29(4), 299. https://doi.org/10.1130/0091-7613(2001)029<0299:ATLPOD>2.0.CO;2

Poli, P., Prieto, G. A., Yu, C. Q., Florez, M., Agurto-Detzel, H., Mikesell, T. D., et al. (2016). Complex rupture of the M 6.3 2015 March 10 Bucaramanga earthquake: evidence of strong weakening process. Geophysical Journal International, 205(2), 988–994. https://doi.org/10.1093/gji/ggw065

Portner, D. E., Rodríguez, E. E., Beck, S., Zandt, G., Scire, A., Rocha, M. P., et al. (2020). Detailed Structure of the Subducted Nazca Slab into the Lower Mantle Derived From Continent-Scale Teleseismic P Wave Tomography. Journal of Geophysical Research: Solid Earth, 125(5). https://doi.org/10.1029/2019JB017884

Raleigh, C. B. (1967). Tectonic Implications of Serpentinite Weakening. Geophysical Journal of the Royal Astronomical Society, 14(1–4), 113–118. https://doi.org/10.1111/j.1365-246X.1967.tb06229.x

Raleigh, C. B., & Paterson, M. S. (1965). Experimental deformation of serpentinite and its tectonic implications. Journal of Geophysical Research, 70(16), 3965–3985. https://doi.org/10.1029/JZ070i016p03965

Ranero, C. R., Phipps Morgan, J., McIntosh, K., & Reichert, C. (2003). Bending-related faulting and mantle serpentinization at the Middle America trench. Nature, 425(6956), 367–373. https://doi.org/10.1038/nature01961

Reinen, L. A., Green, H. W., & Nielsen, S. K. (1998). Dehydration embrittlement of antigorite serpentinite at high pressures: Implication for intermediate depth earthquakes. In EOS, Trans Am Geophys Union 79:F853.

Rodríguez, E. E., Portner, D. E., Beck, S. L., Rocha, M. P., Bianchi, M. B., Assumpção, M., et al. (2020). Mantle dynamics of the Andean Subduction Zone from continent-scale teleseismic S-wave tomography. Geophysical Journal International, 224(3), 1553–1571. https://doi.org/10.1093/gji/ggaa536

Ruiz, S., Tavera, H., Poli, P., Herrera, C., Flores, C., Rivera, E., & Madariaga, R. (2017). The deep Peru 2015 doublet earthquakes. Earth and Planetary Science Letters, 478, 102–109. https://doi.org/10.1016/j.epsl.2017.08.036

Schubnel, A., Brunet, F., Hilairet, N., Gasc, J., Wang, Y., & Green, H. W. (2013). Deep-Focus Earthquake Analogs Recorded at High Pressure and Temperature in the Laboratory. Science, 341(6152), 1377–1380. https://doi.org/10.1126/science.1240206

Shao, T., Song, M., Ma, X., Ding, X., Liu, S., Zhou, Y., et al. (2023). Potential link between antigorite dehydration and shallow intermediate-depth earthquakes in hot subduction zones. American Mineralogist, 108(1), 127–139. https://doi.org/10.2138/am-2022-8271

Shearer, P. M. (2000). Upper mantle seismic discontinuities. In Geophysical Monograph Series (pp. 115–131). https://doi.org/10.1029/GM117p0115

Shen, Z., & Zhan, Z. (2020). Metastable Olivine Wedge Beneath the Japan Sea Imaged by Seismic Interferometry. Geophysical Research Letters, 47(6). https://doi.org/10.1029/2019GL085665

Shirey, S. B., Wagner, L. S., Walter, M. J., Pearson, D. G., & van Keken, P. E. (2021). Slab Transport of Fluids to Deep Focus Earthquake Depths—Thermal Modeling Constraints and Evidence From Diamonds. AGU Advances, 2(2). https://doi.org/10.1029/2020AV000304

Silver, P. G., Beck, S. L., Wallace, T. C., Meade, C., Myers, S. C., James, D. E., & Kuehnel, R. (1995). Rupture Characteristics of the Deep Bolivian Earthquake of 9 June 1994 and the Mechanism of Deep-Focus Earthquakes. Science, 268(5207), 69–73. https://doi.org/10.1126/science.268.5207.69

Tonegawa, T., & Nishida, K. (2010). Inter-source body wave propagations derived from seismic interferometry. Geophysical Journal International, 183(2), 861–868. https://doi.org/10.1111/j.1365-246X.2010.04753.x

Tsujino, N., Yoshino, T., Yamazaki, D., Sakurai, M., Sun, W., Xu, F., et al. (2019). Phase transition of wadsleyite-ringwoodite in the Mg2SiO4-Fe2SiO4 system. American Mineralogist, 104(4), 588–594. https://doi.org/10.2138/am-2019-6823

Wang, Y., Zhu, L., Shi, F., Schubnel, A., Hilairet, N., Yu, T., et al. (2017). A laboratory nanoseismological study on deep-focus earthquake micromechanics. Science Advances, 3(7), e1601896. https://doi.org/10.1126/sciadv.1601896

Weston, J., Engdahl, E. R., Harris, J., Di Giacomo, D., & Storchak, D. A. (2018). ISC-EHB: reconstruction of a robust earthquake data set. Geophysical Journal International, 214(1), 474–484. https://doi.org/10.1093/gji/ggy155

Wiens, D. A. (2001). Seismological constraints on the mechanism of deep earthquakes: temperature dependence of deep earthquake source properties. Physics of the Earth and Planetary Interiors, 127(1–4), 145–163. https://doi.org/10.1016/S0031-9201(01)00225-4

Wiens, D. A., & Gilbert, H. J. (1996). Effect of slab temperature on deep-earthquake aftershock productivity and magnitude–frequency relations. Nature, 384(6605), 153–156. https://doi.org/10.1038/384153a0

Ye, L., Lay, T., Kanamori, H., Zhan, Z., & Duputel, Z. (2016). Diverse rupture processes in the 2015 Peru deep earthquake doublet. Science Advances, 2(6). https://doi.org/10.1126/sciadv.1600581

Zahradník, J., Čížková, H., Bina, C. R., Sokos, E., Janský, J., Tavera, H., & Carvalho, J. (2017). A recent deep earthquake doublet in light of long-term evolution of Nazca subduction. Scientific Reports, 7(45153). https://doi.org/10.1038/srep45153

Zhan, Z. (2017). Gutenberg–Richter law for deep earthquakes revisited: A dual-mechanism hypothesis. Earth and Planetary Science Letters, 461, 1–7. https://doi.org/10.1016/j.epsl.2016.12.030

Zhan, Z. (2020). Mechanisms and Implications of Deep Earthquakes. Annual Review of Earth and Planetary Sciences, 48, 147–174. https://doi.org/10.1146/annurev-earth-053018-060314

Zhang, H., van der Lee, S., Bina, C. R., & Ge, Z. (2021). Deep Dehydration as a Plausible Mechanism of the 2013 Mw 8.3 Sea of Okhotsk Deep-Focus Earthquake. Frontiers in Earth Science, 9. https://doi.org/10.3389/feart.2021.521220

CAPÍTULO 2

MANUSCRITO 1

Este manuscrito foi submetido em 4/3/2024 ao periódico *Earth and Space Science*, da AGU. O material suplementar deste manuscrito se encontra no Apêndice C.

Deep-focus earthquake mechanisms at the subducting Nazca plate (Peru-Brazil border): Cold slab behavior in a warm plate

[1]Leite Neto, G. S., [1,2]Julià J., [3]Prieto, G. A.

[1]Programa de Pós-Graduação em Geodinâmica e Geofísica, Universidade Federal do Rio Grande do Norte, Natal, Brasil
[2]Departamento de Geofísica, Universidade Federal do Rio Grande do Norte, Natal, Brasil
[3]Departamento de Geociencias, Universidad Nacional de Colombia, Bogotá, Colombia

Key Points

- We determined focal mechanisms and centroid depths for 28 deep-focus earthquakes along the Peru-Brazil border from 2014 to 2022.
- Deep-focus earthquakes in South America are possibly nucleated from transformational faulting in a metastable olivine wedge.
- Depth distribution of deep-focus earthquakes is possibly controlled by the subduction of the aseismic ridges and flat subduction.

Abstract

We develop focal mechanisms and centroid depths for deep-focus earthquakes (DFEs) along the Peru-Brazil border with the aim to gain insight into the physical mechanism responsible for their nucleation. We obtained a total of 28 focal solutions for events with magnitudes between 4.2 and 7.5 Mw and occurring between 2014 and 2022. Focal mechanisms indicate predominance of normal faulting, demonstrating a rather uniform down-dip compression (DDC) regime within the plate. The orientations of the nodal planes suggest that earthquakes tend to occur along faults parallel to the local slab strike, although other fault types are documented. Stress orientations derived from the focal mechanisms agree with patterns

expected if faulting were initiated by transformational faulting on a metastable olivine wedge (MOW) under DDC. Centroid depths range between 557 and 659 km, defining a narrow seismic zone within the lower portion of the subducting plate and an aseismic upper portion. We suggest that DFEs nucleate through transformational faulting within a narrow MOW preserved at a colder slab segment right above the lower mantle and juxtaposed to a shallower, warmer segment at around 500 km depth. This thermal complexity was possibly produced through flat subduction due to the subduction of the Nazca Ridge. We speculate that subduction of other aseismic ridges is possibly controlling the thermal state of the Nazca slab as a whole and, consequently, the depth distribution of DFEs along the South America subduction front.

Plain language summary

Aiming to investigate the generating mechanism behind deep earthquakes, we studied mechanisms and depths for deep-focus earthquakes (DFEs) from 2014 to 2022 at the Peru-Brazil border. We determined focal mechanisms for 28 events, which indicate the predominance of normal faulting and demonstrate that the Nazca plate is under down-dip compression regime (DDC). Stresses from these mechanisms agree with patterns expected if faulting were initiated by the transformational faulting mechanism on a metastable olivine wedge (MOW) under DDC. Events' depths ranged from 557 to 659 km, defining a narrow seismic zone within the plate. We suggest that DFEs are nucleating through transformational faulting in a narrow MOW preserved at a colder slab segment right above the lower mantle and connected to a warmer segment at around 500 km depth. Thermal complexity possibly resulted from the flat subduction associated with the Nazca Ridge. We speculate that subduction of other aseismic ridges is possibly controlling the thermal state of the Nazca slab as a whole and, consequently, the depth distribution of DFEs along the South America subduction front.

2.1. Introduction

Deep-focus earthquakes (d > 300 km) are limited to a few subduction zones worldwide and are generally confined within the cold core of the subducting oceanic plates. Due to the extreme pressure and temperature conditions in which these events take place, brittle failure as we know it should be inhibited (Houston, 2015); thus, deep earthquakes must be mechanically different from ordinary shallow earthquakes and have a physical mechanism that accounts for faulting at such great depths. Although several physical processes have been

identified, this mechanism remains largely unresolved due to the limitations in each proposed mechanism to explain all observations (Frohlich, 1989, 2006; Houston, 2015; Zhan, 2020).

The mechanisms traditionally proposed for deep-focus earthquakes include transformational faulting (Green & Burnley, 1989; Green & Marone, 2002; Green & Zhou, 1996) and thermal runaway (Kanamori et al., 1998; Ogawa, 1987). Transformational faulting is basically a high-pressure, self-organizing shear instability that requires an exothermic phase change to nucleate small anti-cracks. Those are microscopic lenses filled with superplastic and denser material that form and grow under compressive stress regimes, the instability resulting from the superplastic filling (Green & Burnley, 1989; Green & Marone, 2002; Green & Zhou, 1996). Transformational faulting would require deep-focus earthquakes to nucleate at the relatively lower temperatures inside subducting oceanic plates, where olivine can be metastably preserved down to mantle transition zone (MTZ) depths within the so-called Metastable Olivine Wedge (MOW) (e.g., Bina et al., 2001; Devaux et al., 2000). Under this hypothesis, the expected exothermic transformations from olivine to wadsleyite (~410 km) and from wadsleyite to ringwoodite (~520 km) could be responsible for triggering transformational faulting, thus explaining deep-focus earthquake confinement around MTZ depths (Green & Zhou, 1996; Houston, 2015; Zhan, 2020). Based on laboratory observations in Ge-olivine, Gasc et al. (2022) suggested that, once transformational faulting is initiated, faulting can propagate beyond the MOW through melting-assisted processes. They also noted that transformational faulting would have to take place within a narrow range of temperatures (600-700 ºC) in both cold and warm slabs. Moreover, this range would depend on strain rate and favor nucleation along the borders of the MOW, possibly explaining the existence of double seismic zones and higher b-values in cold plates. An important physical constraint is that transformational faulting would require that olivine remains sufficiently dry within the oceanic lithosphere, as its transformation into denser polymorphs is catalyzed in the presence of even small amounts of water (e.g., Du Frane et al., 2013; Hosoya et al., 2005; Kubo et al., 1998). Interestingly, recent studies have pointed out that olivine can remain dry within the MTZ thanks to the presence of hydrous phase A under water-undersaturated conditions (Ishii & Ohtani, 2021), and thus that water may actually play an important role in promoting earthquake nucleation in the MOW (e.g., Mao et al., 2022).

Thermal runaway, on the other hand, would be the result of a positive thermal feedback between the heat generated by shearing and viscosity reduction, which might or might not culminate in melting (Green & Marone, 2002; Zhan, 2020). This mechanism, however, seems to lack the ability to nucleate ruptures by itself (Green & Marone, 2002; Kelemen & Hirth,

2007) and thus is often regarded as an auxiliary mechanism to transformational faulting that extends deep-focus earthquakes beyond the MOW (e.g., Zhan, 2017). The very low seismic efficiency found for the 1994 Mw 8.2 Bolivia earthquake is generally invoked as strong evidence for the co-existence of such a dissipative process in the genesis of this large deep-focus earthquake (Kanamori et al., 1998).

Slab temperature plays a fundamental role in the ability of these mechanisms to trigger deep-focus earthquakes (Billen, 2020; Houston, 2015). As mentioned above, transformational faulting is strongly linked to the preservation of a MOW within the subducting slab, which is in turn dependent on the slab's thermal state through the dependence of phase transformation rates on temperature (Green & Marone, 2002; Green & Zhou, 1996). The slab's thermal state is often described through the thermal parameter, an oversimplification of its thermal structure obtained as the product of age, dip, and convergence rate (Frohlich, 2006; Kirby et al., 1991). According to this parameter, only the coldest plates (e.g. Tonga) are expected to retain a MOW down to the base of the MTZ (~660 km) (Devaux et al., 1997; Mosenfelder et al., 2001). Despite that, earthquakes at such depths are also observed in warmer slabs (Devaux et al., 1997; Houston, 2015). To account for this limitation, transformational faulting on a metastable enstatite wedge (MEW) has been proposed, which could explain earthquakes over a depth range beyond that of the MOW (Green & Zhou, 1996; Hogrefe et al., 1994). Thermal runaway, on the other hand, naturally requires sufficiently high temperatures to allow for sufficient viscosity reduction and subsequent instability (Green & Marone, 2002; Houston, 2015). Thermally induced instability could explain dissipative events occurring predominantly - but not exclusively - in warmer slabs (Tibi et al., 2003; Zhan, 2020; Zhan et al., 2014). In this sense, bigger ruptures would be initiated by transformational faulting in a thin MOW in warmer slabs and further propagate through thermal runaway (Zhan, 2017).

Nonetheless, because the slab thermal parameter is an oversimplification, assessing the viability of the mechanisms might not be as straightforward. For young, slow lithosphere, for example, deep-focus seismicity ($d > 300$ km) is generally absent (Myhill, 2013; Wortel, 1982); yet, the Nazca plate, which clearly falls at the warm end of the thermal parameter spectrum of subducting slabs, does host deep-focus ruptures (Houston, 2015). It has been proposed that the subducting Nazca slab might have a composite thermal structure consisting of a cold, deeper portion attached to a warm, shallower portion - with the transition possibly happening at 500 km depth - and that the cold portion of this composite structure might meet the requirements for hosting a MOW and trigger deep-focus earthquakes (Collier & Helffrich, 2001; Engebretson & Kirby, 1992; Kirby et al., 1995; Okal & Bina, 1994; Zahradník et al., 2017).

Moreover, while this bottom segment may have remained cold enough to effectively retain olivine metastably to MTZ depths, olivine in the warmer segment may have been completely transformed aseismically near the nominal transformation depth, thus impeding metastability and explaining the prominent seismic gap between 300 and 500 km depth and the corresponding concentration of deep-focus events at depths larger than 500 km (Kirby et al., 1995). If this composite structure is correct, then mechanisms usually proposed for cold slabs (e.g., transformational faulting on a MOW) could be viable in the Nazca slab despite its nominally low thermal parameter.

Since 2014, several broadband stations have been installed in the Amazon region of Brazil as part of the national Brazilian Seismographic Network (RSBR) (Bianchi et al., 2018). The coverage provided by these stations (Figure 1a), together with that provided by other national and international networks, offers a unique opportunity to closely investigate deep-focus earthquakes in the Peru-Brazil region. Luckily, the RSBR stations were installed right before an unusual year of rather intense seismic activity (2015), which comprised a rare doublet and a relatively large number of aftershocks. In this work, we determine focal mechanisms and centroid depths for 28 deep-focus earthquakes along the Peru-Brazil border (Figure 1b), with the aim to investigate the stress conditions under which deep-focus earthquakes take place and, consequently, obtain insights into the physical mechanisms that trigger them. We found that deep-focus earthquakes in this region occur within a narrow depth-range (587-659 km) and under a predominant down-dip compression (DDC) regime, consistent with nucleation inside a relatively narrow MOW at the bottom of the subducting slab. Moreover, most fault planes are found to be at ~45º from a near-vertical direction of maximum compression, as expected from nucleation through superplastically-filled anti-cracks in transformational faulting (Warren et al., 2007). Also, although nodal planes are found to be striking preferentially in the N-S direction, some fault planes deviate from this preferred orientation. These are typically events in the lower magnitude range that occurred shortly after a larger magnitude event, which might have locally affected horizontal stresses within the slab. Finally, we speculate that a composite thermal structure might be present in other flat-slab segments along the South American subduction front, as they display gaps in the distribution of deep earthquakes analogous to the one observed in the Nazca slab.

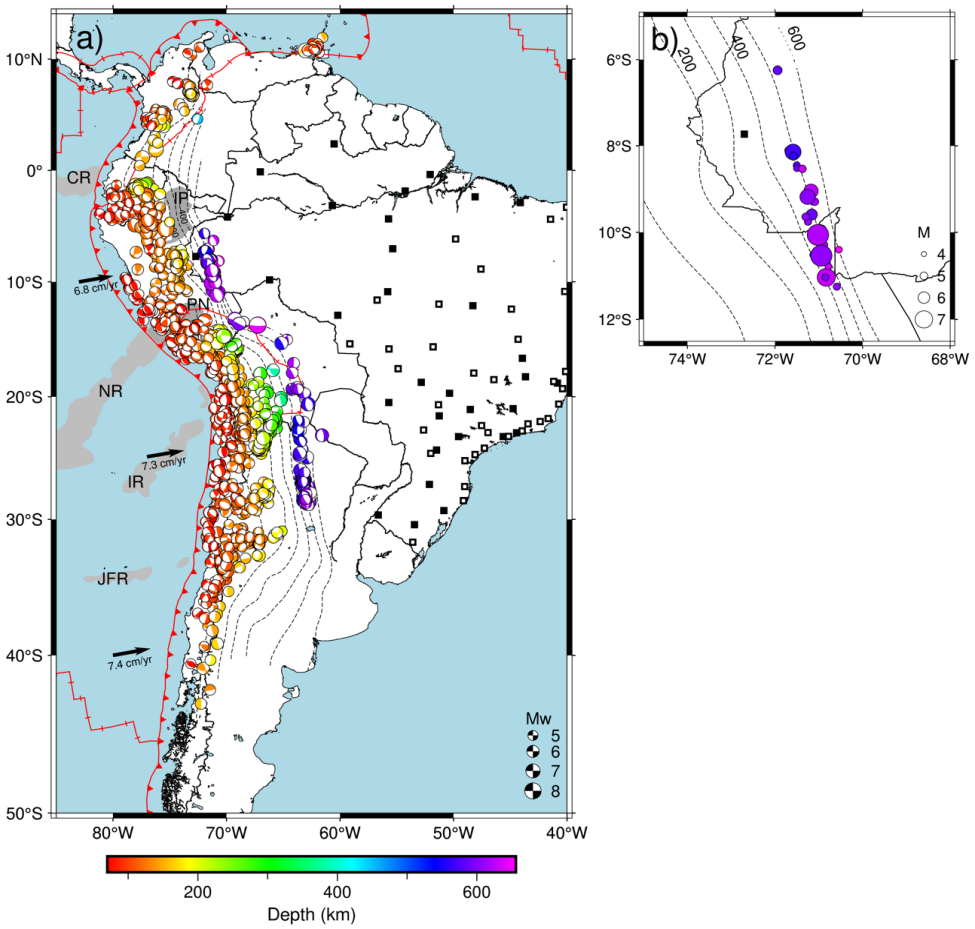

Figure 1. a) Moment tensor solutions for deep earthquakes (d > 70 km and Mw > 5) in South America according to the GCMT catalog (1977-2022). The focal solutions in this map are colored by depth and sized by magnitude. Plate boundaries are from Bird (2003) and convergence rate of the Nazca plate in cm/yr are from DeMets et al. (2010). Contours from Slab 2 delineate the geometry of the subducting Nazca plate (Hayes et al., 2018). Main oceanic ridges in Nazca plate: CR – Carnegie Ridge, NR – Nazca Ridge, IR – Iquique Ridge and JFR – Juan Fernandez Ridge, are shown in light gray (Gutscher et al., 2000; Rosenbaum et al., 2005). The inferred continuation of the Nazca Ridge (PN) and location of the postulated Inca Plateau (IP) are drawn in dark gray (Bishop et al., 2017; Gutscher et al., 1999, 2000). Distribution of broadband stations from the Brazilian Seismic Network (RSBR) for different time periods are shown as open (1980-2013) and closed (2014-2022) squares; b) 42 deep-focus earthquakes (d > 300 km) within the period of 2014 to 2022 according to the USGS catalog.

2.2. The 2014-2022 deep-focus earthquake sequence

Since the deployment of RSBR broadband stations in the Amazon region of Brazil in 2014, a total of 42 deep-focus events have been reported in the region by the USGS (Figure 1b), with magnitudes and depths ranging from 4.0 mb to 7.6 Mw and 515 to 655 km, respectively (see Table S1 for catalog information). A total of 25 of these events occurred only

in 2015, just a year following the installation of the first RSBR stations (Figure S39a-b). Most of these 25 events occurred by the end of November and included an earthquake doublet consisting of two Mw 7.6 events separated ~5 min apart and ~50 km from each other. The doublet occurred on November 24th, it was preceded by a single 4.3 mb foreshock and was followed by nearly 20 aftershocks with magnitudes ranging from 4.0 mb to 6.7 Mw (Figure S39c-d) (Ruiz et al., 2017; Ye et al., 2016). Up to 16 of these aftershocks took place within a time span of one week and followed shortly after the Mw 7.6 mainshocks (Jiménez et al., 2021; Ye et al., 2016; Zahradník et al., 2017).

Other large events within the 2014-2022 sequence had magnitudes in the $5.9 \leq Mw \leq 7.1$ range. Those included events 32, 34, 38 and 41 (Table S1), each followed by at least one small ($mb < 5$) aftershock (events 33, 35, 39 and 42, respectively). These aftershocks occurred from nearly an hour to a few months after their corresponding mainshocks. Only event 30, with Mw 6.4, showed no aftershocks – within the USGS catalog threshold (4 mb) - despite its relatively large magnitude. Temporally and spatially clustered deep events are relatively common along the South American subduction zone (Okal & Bina, 1994; Ruiz et al., 2017; Ye et al., 2016). A low productivity of aftershocks is a common characteristic of warm slabs (Tibi et al., 2003), so the large number of aftershocks after the November 24th doublet is most unusual.

Studies on the source mechanism of deep-focus earthquakes in this region generally focused on the 2015 great doublet. Those studies revealed two consistent normal fault mechanisms with negligible non-double-couple (NDC) components and intermediate stresses aligned with the approximately N-S regional trend of deep-focus epicenters (Jiménez et al., 2021; Ye et al., 2016; Zahradník et al., 2017). They also indicated that both ruptures probably occurred along the same west-dipping fault plane (160º strike and 60º dip, parallel to inferred slab strike), but in a segmented manner, with the first event rupturing towards SE and the second one rupturing towards NW (Ruiz et al., 2017; Ye et al., 2016; Zahradník et al., 2017). Aftershock distribution was observed to follow the regional N-S trend but failed to constrain the actual fault plane (Ruiz et al., 2017). Ye et al. (2016) suggested that the second event of the doublet was probably dynamically triggered by the S-wave from the first event, while Zahradník et al. (2017) proposed that the second event was triggered by static stress changes resulting from the first event. Jiménez et al. (2021), on the other hand, suggested that both events constituted mainshocks. Regarding their rupture processes, Ye et al. (2016) first suggested diversity of rupture, in which the second event would have been more dissipative than the first one and possibly nucleated under different conditions. This was in contraposition to the findings of Ruiz et al. (2017), who reported similar rupture parameters for both events.

Apart from the great doublet, a total of 8 events ($5.2 \leq Mw \leq 7.1$) of this sequence have focal mechanisms available in either the USGS or GCMT catalogs (see events 1, 19, 30, 32, 34, 35, 38 and 41, in Table S3). It is worth noting that they all exhibit a radiation pattern remarkably similar to that obtained for the 2015 doublet. Furthermore, this observation is generally consistent with GCMT solutions available for events in the Peru-Brazil region that occurred since 1977 (Figure 1a). This suggests a quite uniform ambient stress regime for the triggering of these events, characterized by a predominant down-dip P-axes, along-strike B-axes and slab-normal T-axes (Kirby et al., 1995).

2.3. Data selection, data processing, and Green's functions

We collected seismograms from several broadband stations belonging to various networks operating in the continent ($\Delta \leq 45°$): the Brazilian Seismic Network (RSBR), which provided upper-hemisphere coverage for the deep events, especially through stations in the Amazonian region (see black squares in Figure 1a); other national (e.g., Colombia, Chile and Ecuador) and international (GSN, GEOFON and GEOSCOPE) permanent networks, for which data were openly available through the EarthScope Consortium Wilber 3 (https://ds.iris.edu/wilber3/); and, finally, temporary stations deployed under the 3-basins Project (Assumpção et al., 2016; Chagas de Melo et al., 2018), which included stations in Uruguay, Argentina, Paraguay, Bolivia and Brazil. We did not include stations outside the South American continent to avoid using waveforms traveling through complex tectonic settings (e.g., the Caribbean) which could potentially introduce artifacts in our inversions. Our data selection thus contemplated local ($\Delta \leq 5°$), regional ($5° < \Delta < 30°$) and teleseismic ($\Delta \geq 30°$) waveforms recorded within South America. Those data provided sufficient azimuthal coverage to tightly constrain the radiation pattern of the deep-focus events.

Theoretical arrival times were obtained for the main phases (P, S, sP and pP) using the TauP utility (Crotwell et al., 1999) and the reference velocity model ak135 (Kennett et al., 1995). Seismograms were then cut within time windows starting at 70 s before the P-wave arrival and lengths that included the direct P and S phases as well as the pP and sP depth phases. More accurate first arrival were visually picked after simulating the WWSSN short-period response on the vertical seismogram. The mean and trend were next removed, and a 5% cosine taper was applied before removal of the instrument response. The resulting displacement waveforms were then rotated into the great-circle-path, to naturally separate P and SV energy from SH energy. Seismograms were all decimated to 10 samples per second (s.p.s.). We

carefully checked our data for errors in the reported instrument responses and/or component orientations and removed those for which metadata was found inaccurate.

For the computation of Green's functions, we used the wavenumber-integration method of Bouchon (1981), as implemented in the Computer Programs in Seismology (CPS) package of Herrmann (2013). We considered epicenters from the USGS catalog and, aiming at improving on the source-depth estimates for each event, we computed synthetics for a range of focal depths around the nominal values given in the catalog, at 10 km intervals (Table S1). The synthetic waveforms were obtained considering an impulsive source and the AK135-F reference Earth model, which consists of the AK135 velocity model of Kennett et al. (1995) with density and attenuation (Q) estimates added from free-oscillation data in Montagner and Kennett (1996). Synthetics started 70 s before the P-wave, with a sampling interval of either 0.5 s or 0.2 s, depending on the frequency range considered for inversion (0.02-0.05 Hz or 0.3-1.0 Hz, respectively), as explained later in the Methodology section. When using a sampling interval of 0.5 s, the total length of the synthetics was set to either 512 ($\Delta < 900$ km) or 1024 ($\Delta \geq 900$ km) points; on the other hand, when using a sampling interval of 0.2 s, the total length was set to 1024 ($\Delta < 900$ km) or 2048 ($\Delta \geq 900$ km) points. These parameters allowed us to produce synthetic waveforms with sufficiently long time windows to include both P and S waves and the corresponding depth phases. The theoretical arrivals in the synthetic waveforms were determined using TauP (Crotwell et al., 1999).

2.4. Waveform modeling details

For the determination of the earthquake source mechanisms, we used the Cut-and-Paste (CAP) approach of Zhao & Helmberger (1994) and Zhu & Helmberger (1996). The CAP method assumes a pure double-couple (DC) source mechanism and performs a grid-search over the fault-parameter space (strike, dip, and rake) that yields the best fault orientation and slip direction for a given earthquake. We regard this assumption as valid for deep earthquakes because it is now accepted that no significant isotropic component is to be expected (Kawakatsu, 1991), and any significant NDC contributions are likely to result from either multiple faulting events (Frohlich, 1994; Houston, 2015) or from shear faulting in a highly anisotropic medium (J. Li et al., 2018). The CAP approach models the body-wave (P and S) segments independently and uses time shifts determined through waveform cross-correlation to optimize the alignment between observations and predictions (Chang et al., 2019). These time shifts represent an efficient manner to account for inaccuracies in origin time, location,

and model velocities during computation of the Green's functions (Zhao & Helmberger, 1994; Zhu & Helmberger, 1996).

To perform the inversions, we initially aligned observed waveforms and Green's functions by cutting both from 55 s before the P-wave arrival to 100 s after the S-wave arrival. We then applied a zero-phase Butterworth band-pass filter with corner frequencies of 0.02 and 0.05 Hz (e.g., Zahradník et al., 2017) and decimated the observed seismograms to 2 s.p.s. This frequency range was selected after extensive testing aimed at determining the lowest possible frequency content with a signal-to-noise ratio (SNR) high-enough to model body waves. For the smallest events (mb < 5), we had to use a relatively higher frequency range between 0.3 and 1.0 Hz, and a sampling rate of 5 s.p.s. to obtain waveforms with a SNR suitable for waveform modeling. The use of this higher frequency range for small-magnitude events was critical because, as shown in the next section, it allowed us to determine focal mechanisms for 14 events for which there were no previously published solutions (events 6, 10-13, 17-18, 29, 31, 33, 37, 39-40 and 42, in Tables 1 and S1).

Next, following the CAP approach, we split the filtered seismograms and their respective Green's functions into separate body-wave segments to be modeled individually. We extracted the P- and SV-wave segments from the radial (Pr and SVr) and vertical (Pz and SVz) components, while the SH segment was extracted from the transverse component, resulting in up to five traces to be modeled for a given station (Chang et al., 2019; Zhan & Kanamori, 2016).

Modeling time windows were set according to epicentral distance and frequency range for P and S, as described in Table 1. The windows were based on the main arrival times on the seismograms (P, S and sP), and were defined to include the target phase while avoiding unwanted phases. Naturally, we used narrower windows in the higher frequency range when compared to the lower frequency range. For teleseismic stations ($\Delta \geq 30°$), we ensured that the depth phases (sP and pP) were included in the P-wave window to be modeled. This was done to improve event depth estimation during inversion, as the temporal separation between P, sP and pP is known to strongly constrain source depth (e.g., Chu et al., 2009; Heyburn et al., 2013). Note that we did not consider teleseismic body wave windows in the higher frequency range (0.3 – 1.0 Hz) because they were not suitable for inversion due to very low SNRs. Similarly, we disregarded regional SV segments due to complications related to sP phase propagation.

Table 1. Description of the cutting scheme employed in this work to obtain the body-wave segments to be modeled.

Frequency range	Distance range[1]	Phase	Windows cut description[2]
0.02 – 0.05 Hz	local	P	[tP – 55 s] to [tP + (tS – tP)/2]
		S	[tS – (tS – tP)/2] to [tS + 100 s]
	regional	P	[tP – 55 s] to [tP + (tsP – tP)/2]
		S	[tS – (tS – tP)/2] to [tS + 100 s]
	teleseismic	P	[tP – 55 s] to [tP + (tS – tsP)/2]
		S	[tS – (tS – tsP)/2] to [tS + 100 s]
0.3 – 1.0 Hz	local	P	[tP – (tS – tP)/8] to [tP + (tS – tP)/8]
		S	[tS – (tS – tP)/8] to [tS + (tS – tP)/8]
	regional	P	[tP – (tsP – tP)/8] to [tP + (tsP – tP)/8]
		S	[tS – (tS – tP)/8] to [tS + (tS – tP)/8]

[1]Local stations are those at $\Delta \leq 5°$, regional are those within $5° < \Delta < 30°$, and teleseismic those at $\Delta \geq 30°$; [2]The windows were cut based on the arrival times of P, S and sP, identified as tP, tS and tsP, respectively.

Only windows with SNR above a given threshold were used in our inversions. The thresholds were determined experimentally according to the magnitude of the event regardless of segment type: SNR ≥ 5 for $4.0 \leq M < 5.0$; SNR ≥ 10 for $5.0 \leq M < 6.0$; and SNR ≥ 15 for $6.0 \leq M < 7.0$. For the largest events ($7.0 \leq Mw \leq 7.6$), however, we were able to use thresholds of SNR ≥ 20 and SNR ≥ 30, for P and S windows, respectively, due to the relatively larger amount of data available for inversion. Realize that the use of lower thresholds for the smaller events was expected, as SNR decreases with earthquake size.

The grid-search to determine the focal mechanism was carried out by varying each fault angle by 10° and computing the average misfit between predicted and observed seismograms for all possible fault orientations and slip directions. The solution with the least average misfit was selected as the best focal mechanism for the target earthquake. The scalar seismic moment was then obtained from the average scale factor between observed and predicted seismograms for all components, and the moment magnitude was determined following the relationship given in Hanks & Kanamori (1979). Waveform misfits were assessed using the L2-norm of the difference between observations and predictions after normalizing by the number of data points, which ensured that different time windows contribute equally to the average misfit.

Recall that the CAP method allows for empirical time shifts between synthetic and observed waveforms before computation of the RMS misfit. This procedure is very efficient to overcome misalignment between observations and predictions resulting from imprecise velocity models and/or inaccuracies in event location (Leite Neto & Julià, 2023). These time shifts are determined from waveform cross-correlation and can lead to either an advance or a delay in the synthetics with respect to the observed seismograms. After considerable testing, we defined a correlation window length of 75% of the observed waveform window and constrained the time shifts to ±25 s or ±2 s, depending on whether the frequency range was 0.02-0.05 Hz or 0.3-1.0 Hz, respectively. Note that such discrepancy between the time tolerances is merely empirical, as we observed that small time shifts were required to align waveforms in the higher frequency range. We also avoided employing unnecessarily large tolerances since it might result in phase skipping during the inversions.

2.5. Results

All focal mechanisms, described by the three fault angles: strike (S), dip (D) and rake (R), and their preferred centroid depths (CD) determined in this study are summarized in Table 2. To illustrate our inversion results, we first describe the modeling for the 2015 deep-focus doublet (events 8 and 9, in Table 2), which represent the largest and most studied deep-focus earthquakes within the 2014-2022 sequence. After that, we briefly describe our results for the rest of the deep-focus sequence. To facilitate comparison with previous studies, focal mechanisms are classified in Table 2 according to the Focal Mechanism Classification (FMC) criterion of Álvarez-Gómez (2019), which conducts a double-couple (DC) classification based on the orientation of the P, T and B axes.

2.5.1. The great 2015 deep-focus doublet

For the first event of the doublet (event 8), we inverted a total of 332 waveform segments from 132 stations in the 0.02-0.05 Hz frequency range (Figures 2 and S4). We obtained a normal fault solution (350°±0º, 40°±0º, -80°±0º) and a preferred centroid depth of 616±10 km, with a scalar seismic moment of 1.81±0.02e+27 dyne-cm, which corresponds to a moment magnitude of Mw 7.5 (Table 2 and Figure 2a). This solution showed remarkable stability within the entire range of investigated source depths (Figures 2b and S4b). Also, most of the synthetic waveforms produced with this solution were in excellent agreement with the observed traces. This excellent match includes stations at teleseismic distances, for which we included depth phases in the P-wave segments (see some examples in Figure 2c and all matches

in Figure S4c). For this event, we excluded teleseismic SV waveforms due to its contamination with the P-wave from event 9 at those distances. However, we still managed to use S-wave segments taken from the teleseismic transverse recordings (SH), since events 8 and 9 have virtually the same location (only ~50 km apart) and consequently little P-wave energy was leaked onto the transverse (SH) components after rotation. The uncertainties in this work were all assessed through jackknife resampling (Miller, 1974; Quenouille, 1949, 1956), after removing one station at a time.

For the second event (event 9), we obtained a very similar normal fault solution (350°±0º, 30°±0º, -90°±0º), centroid depth (621±13 km), and scalar seismic moment (1.93±0.02e+27 dyne-cm), again corresponding to a magnitude of Mw 7.5. Those results were achieved using the same frequency range (Table 2 and Figure 2d) as for the previous event. This solution was again remarkably stable within the studied depth range and produced excellent synthetic waveform matches with most of the 88 observed waveforms (Figures 2 and S5). Note that, for this event, we had to use less waveforms in our inversion when compared to event 8. First, P-wave recordings were often contaminated with signal-generated noise from the first event, which led to a considerable reduction of the SNRs for regional P-wave segments. Second, as explained before, the contamination of the P-wave from this event with the S-wave from event 8 at teleseismic distances rendered teleseismic P-wave segments unusable. Additionally, this contamination prevented us from including depth phases in our analysis; despite that, the preferred centroid depth of 621 km was well defined in the misfit curve (Figures 2e and S5b). We note, nonetheless, that a second minimum occurs in the misfit curve at 661 km depth, which is probably caused by the abrupt change in velocity at ~660 km.

The focal mechanisms obtained in this study for the earthquake doublet are consistent with those determined in independent works using a variety of approaches and datasets (Jiménez et al., 2021; Ye et al., 2016; Zahradník et al., 2017), and with solutions reported in the USGS and GCMT catalogs (see Table S2 for comparison). Overall, we observed that our results are in closer agreement to those in the GCMT catalog. Regarding centroid depths, our estimates generally agree with previous estimates (Table S2). Centroid depths in Jiménez et al. (2021), however, were considerably deeper, suggesting that both events happened around the base of the mantle transition zone (~660 km). Our depth estimates suggest centroids were just ~5 km apart, closer than indicated in previous studies. We stress that we included depth phases in our inversion for event 8, which were satisfactorily modeled (see some examples in Figure 2c), thus ensuring accurate depth estimates. Finally, regarding seismic moments, we observed that our estimates for events 8 and 9 are very similar, around Mw 7.5 (Table 2 and S2),

suggesting similar sizes. Compared to previous estimates, we obtained smaller moments for the doublet (Table S2).

In summary, our results suggest that the 2015 deep-focus doublet was composed of two events with very similar ruptures, in terms of focal mechanism, centroid depth, and size. This observation substantiates previous claims that both events ruptured along the same fault plane (e.g., Zahradník et al., 2017).

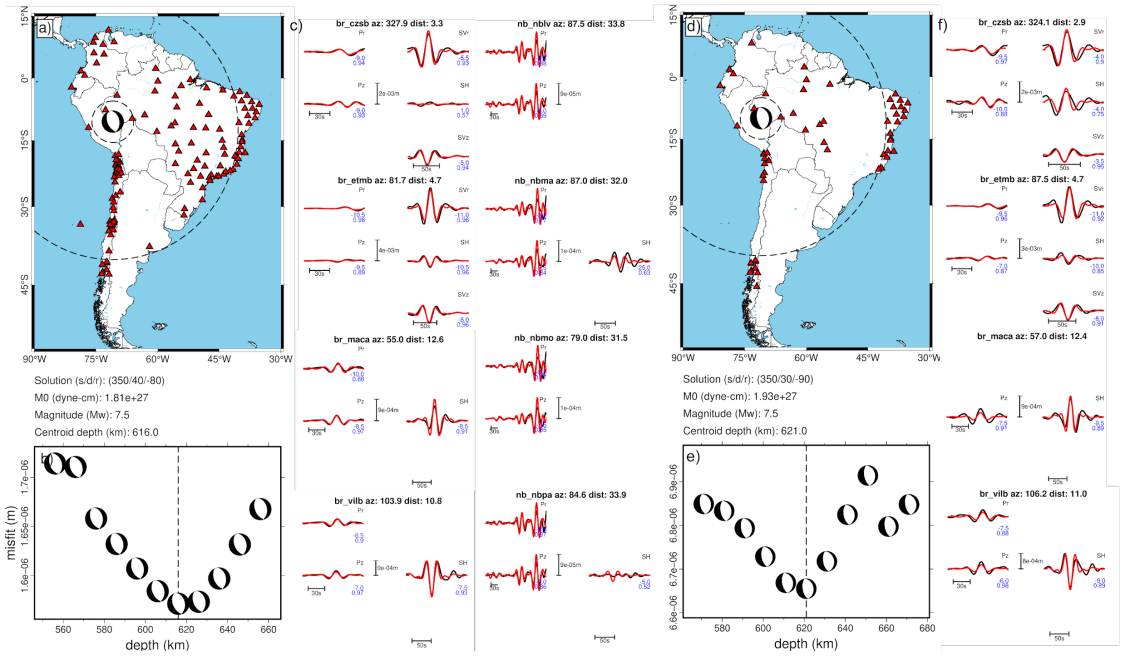

Figure 2. Examples of waveform fitting produced by the focal mechanisms determined for the 2015 deep-focus doublet, events 8 and 9; a) map showing the preferred solution for event 8 and the distribution of stations that were used in the inversion. Dashed circles indicate radii of 5º and 30º from epicenter; b) distribution of focal mechanisms with investigated centroid depths. The preferred solution, which is the one that produced the best fit to observations is indicated by the vertical dashed line; c) examples of waveform matches produced by this preferred solution. Black and red waveforms denote observations and synthetics, respectively. Station names, azimuths and distances are shown above each station panel. Time shifts (top) and cross-correlation coefficients (bottom) are shown in blue at the lower right corner of each panel. Wave segments (Pr, Pz, SVr, SH and SVz) are identified at the upper right corners; d-f) the same as in a-c but for event 9. For the complete waveform matches, see Figures S4 and S5.

2.5.2. The 2014-2022 deep-focus sequence

Regarding the whole seismic sequence, we were able to determine focal mechanisms and centroid depths for 28 of the 42 deep-focus events listed in Table S1 (see Figure 3). In general,

our inversions with the CAP approach led to robust solutions that provided reasonable fits to observed seismograms (Figures S1-S28). These events span a relatively wide magnitude range, from Mw 4.2 to Mw 7.5 (Table 2). In the following, we briefly describe our inversions and compare our focal mechanisms and centroid depths with independent assessments when available.

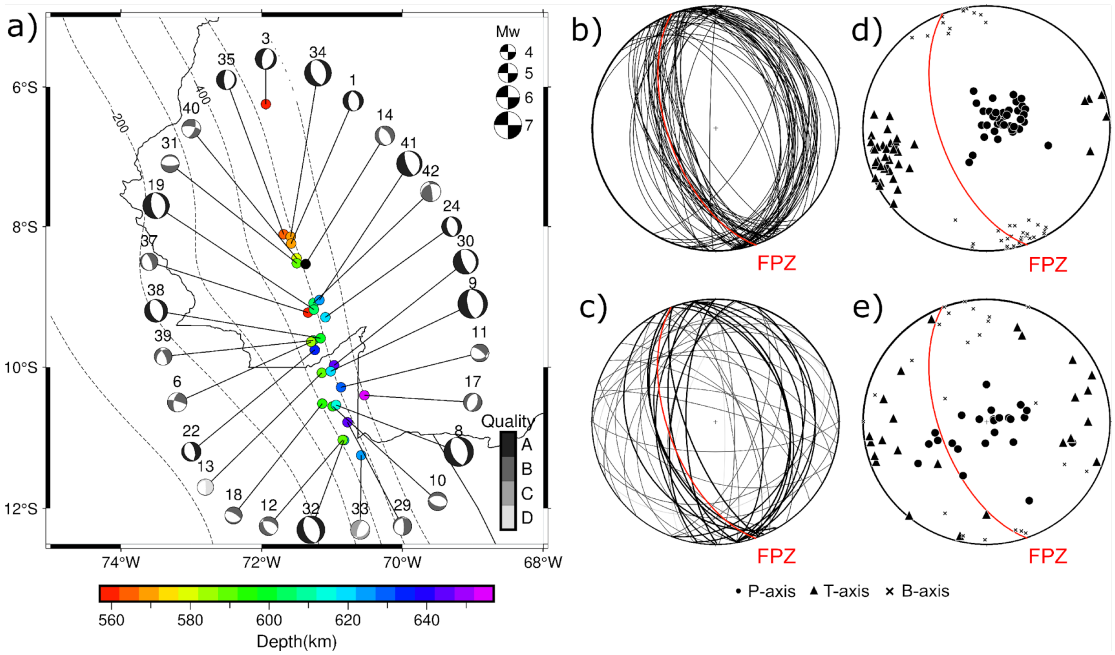

Figure 3. Focal mechanisms determined for 28 events in the 2014-2022 deep-focus sequence. a) Distribution of the obtained focal solutions sized by magnitude and colored in grayscale by quality (A, B, C and D) (Table 2). Each solution in the map is identified by event number in Tables S1 and 2. The epicenters are colored by centroid depths. Dashed lines delineate the Nazca slab depth from Slab 2 (Hayes et al., 2018); b) nodal planes from 39 GCMT focal mechanisms in the Peru-Brazil region occurred between 1977 and 2022 and 5.1 ≤ Mw ≤ 7.6 (Figure 1a) plotted on a stereonet using FaultKin (Allmendinger et al., 2012; Marrett & Allmendinger, 1990). The fault zone orientation, striking 160º and dipping 60º, as proposed by Zahradnik et al. (2017) is shown in red (FPZ); c) nodal planes from the solutions obtained in this study. Planes are colored in grayscale according to quality, as in a; d) Principal axes (P, T and B) from the GCMT solutions and e) principal axes from this study. Another version of this figure with focal mechanisms colored by faulting style can be found in supplementary material Figure S30.

2.5.2.1. Goodness of fit

As explained before, inversions were performed at either the 0.02-0.05 Hz frequency range or the 0.3-1.0 Hz frequency range (Table 2), depending on magnitude. In general, we observed good waveform matches at either frequency range (see Figures S1-S28), as illustrated through waveform fits for events 14 (Figure 4f) and 12 (Figure 4c), respectively. Note that

both events utilized the same number of stations (5) at both local and regional distances, and that both were aftershocks of the 2015 doublet (Table S1). It is worth mentioning that the use of a higher frequency range for smaller-magnitude events was critical, as it allowed us to determine focal mechanisms for (smaller) events that showed poor SNRs in the 0.02-0.05 Hz frequency range.

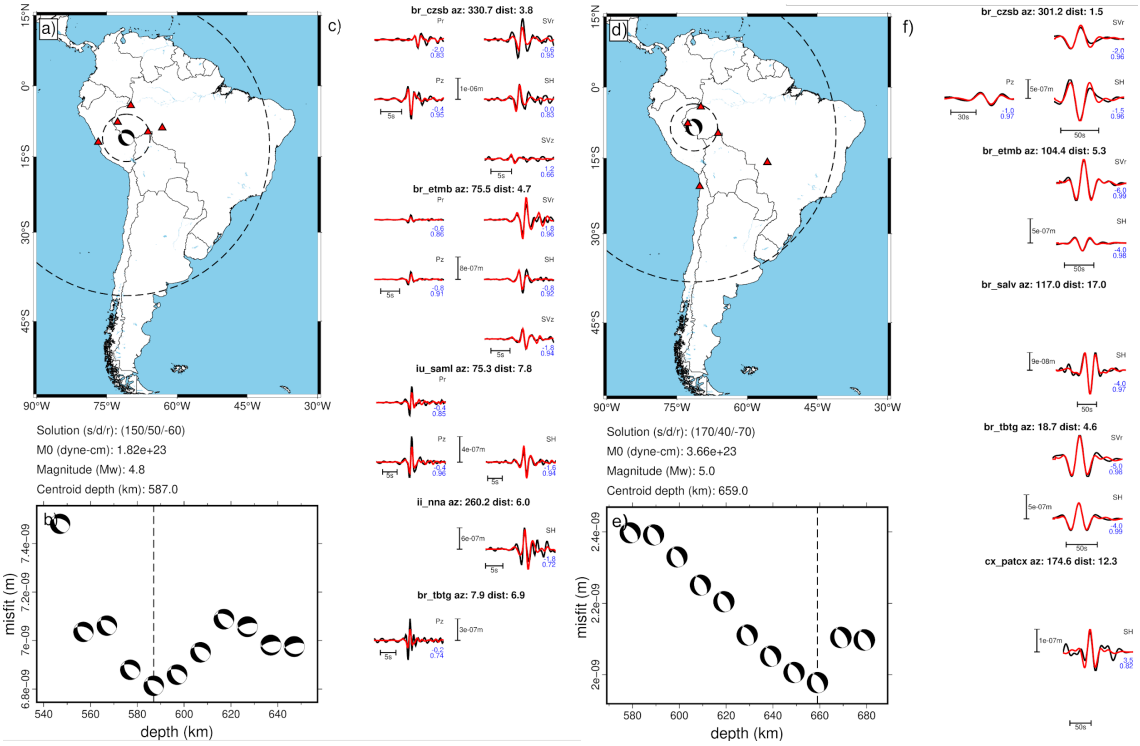

Figure 4. Examples of waveform inversions for the two frequency ranges used in this study, 0.02-0.05 Hz (event 12, from a to c), and 0.3-1.0 Hz (event 14, from d to f). Features in this figure are the same described in Figure 2.

Although our inversions in the lower frequency range were quite straightforward, the inversions in the higher frequency range were found to be more challenging. The most important challenge was presented by the contamination of P- and S-wave segments at regional distances, which resulted in waveform complications. This contamination was verified through computation of travel-times, revealing up-going and down-going direct phases at similar times or multiple P or S reflections present in the recordings. As these waveforms were difficult to model, we simply removed them from inversion. At lower frequencies, on the other hand, this contamination appeared to be less critical, as we did not observe any difficulties in matching synthetic and observed waveforms.

A second challenge arose from the use of an inaccurate attenuation model. We noticed that our attenuation model was perhaps too severe on the higher frequency range, as it made amplitudes decay faster than actually required. This severity can be noticed in some waveform

fits as discrete, unmodelled high-frequency features in the observed waveforms (see for example Figures S16 and S25). This observation suggests that the attenuation model in AK135-F might have to be tailored to our study region in order to improve waveform fits in the higher frequency range. In any case, as demonstrated through Figures S1-S28, our solutions display acceptable waveform fits and are quite robust, showing little variation in focal mechanism within the investigated depth ranges.

2.5.2.2. Focal mechanisms

From the 28 focal mechanisms determined in this study, 22 of them describe pure normal faulting, while the other 6 mechanisms describe different types of oblique faulting: 3 normal with strike-slip component, 2 strike-slip with normal component, and 1 reverse with strike-slip component (see Figure 5a and Table 2).

Only 10 out of the 28 inverted events in Table 2 have source mechanisms available in either the USGS or the GCMT catalogs. Generally, these catalogs provide focal solutions for events with magnitudes greater than Mw ~5.0. Comparing the available solutions with ours, we observed that the agreement is excellent (see Table S3). The only strong disagreement was perhaps found for the fault strike of event 1, which deviates about ~35º from that reported in the GCMT catalog, but the fault type remained roughly the same. This difference might be due to the few traces available (14 traces from 7 stations), since this event happened in the beginning of 2014 when RSBR stations in the Amazonian region were not yet installed (Table S4 and Figure S1). Also, compared with the GCMT orientation, our fault strike is in relatively better agreement with the observed N-S trend of the B-axes (see mechanism 1 in Figure 3a).

We now compare our results, which span from 2014 to 2022, with GCMT solutions within the extended period from 1977 to 2022 (Dziewonski et al., 1981; Ekström et al., 2012). According to the 39 moment tensors available in the GCMT catalog ($5.1 \leq Mw \leq 7.6$) for this extended period, earthquake focal mechanisms along the Peru-Brazil border are usually normal, with only two cases of normal to strike-slip faulting (Figure 5b). Interestingly, there seems to be a slight dependency with depth in terms of faulting orientation for this set of solutions. Shallower events seem to show B-axis plunges deviating a little more from the horizontal than deeper events. In our set of solutions, in Figure 5a, we did not observe this trend, but our results also indicated the predominance of normal faults with a few normal with strike-slip faults. Contrary to GCMT solutions, we observe two strike-slip with normal component faults, events 6 and 40, and an oblique reverse fault, event 42 (Figure 5a). The

robustness of these disparate focal mechanisms is investigated later in the manuscript (section 6.1.2).

2.5.2.3. Seismic moment

The values found for seismic moments ranged from 2.27±4.57e+22 to 1.93±0.02e+27 dyne-cm, corresponding to magnitudes from Mw 4.2 to 7.5 (Table 2). Regarding these seismic moments, we obtain values between 3% and 92% smaller than those provided by the two catalogs (~26% smaller on average, see Table S3). Note that, in general, uncertainties in M0 are small and do not explain such discrepancies. For event 19, a Mw 6.7, our M0 estimate (1.27±0.01e+26 dyne-cm) was remarkably close to those from USGS (1.21e+26 dyne-cm) and GCMT (1.34e+26 dyne-cm), being ~5% larger and ~5% smaller, respectively; for event 35, a Mw 5.1, on the other hand, our estimate (4.76±0.22e+23 dyne-cm) was very different from the previous estimate from GCMT (1.36e+24 dyne-cm, corresponding to Mw 5.4), being almost three times smaller. The only exception occurs for event 1 (Mw 5.2), for which uncertainties in M0 (7.36±1.06e+23 dyne-cm) can explain values from 9% to 46% smaller than the estimate given by the GCMT catalog (9.18e+23 dyne-cm).

We investigated whether such systematic smaller values were due to overestimation of Q values in the reference model, by systematically reducing Q in 10% steps until it reached 50% of its original values (Table S5). We applied the same reduction for both P and S attenuation. Our tests showed that overestimation in Q structure does not account for the systematically smaller seismic moments found in this study. It is still possible that these systematically smaller values result from an inaccurate attenuation model that is not representative of the complex setting of the South America subduction zone and the large range of distances used in our inversions. Nevertheless, it is noteworthy that our inversions used considerably more data and a wider range of distances than other independent studies, providing solutions that showed good fit to local, regional and teleseismic observations.

2.5.2.4. Centroid depths

Centroid depths were determined by selecting the global minimum in the misfit curves. In the best cases, we observed well-behaved misfit curves with a single minimum, unambiguously indicating the optimal depth for the event (see for example Figures S1 and S13). In some other cases, the curves were a bit more challenging, with more than one minimum; but, as their shapes were relatively simple, we could also identify a global minimum

with good accuracy and settle on a centroid depth (see for example Figures S5 and S20). Finally, in the worst-case scenario (events 10, 13, 17, 18, 31, 37, 40 and 42), the curve shape was found to be cumbersome, and we could not determine the preferred depth with any degree of confidence (see Figures S9 and S26 as examples). In such cases we fixed centroid depths to the USGS hypocentral depth and used the corresponding focal solution as our preferred mechanism (see Table 2).

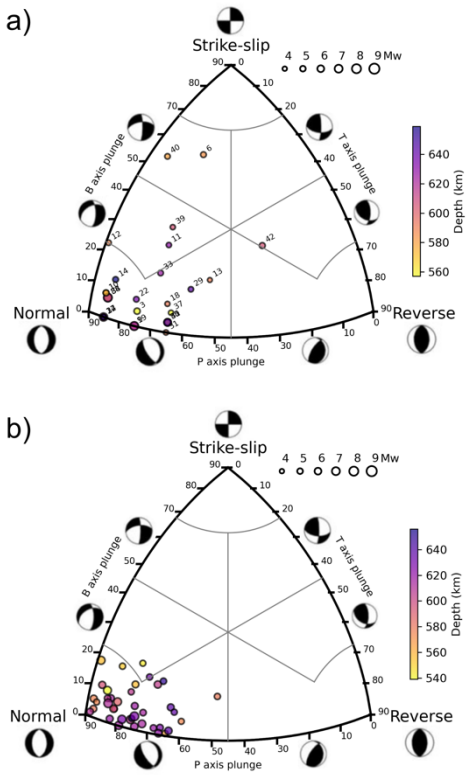

Figure 5. Focal mechanisms for deep-focus earthquakes in the Peru-Brazil border region classified according to the seismic moment tensor main axes plunges: a) solutions from this study, 28 earthquakes with $4.2 \leq Mw \leq 7.5$ from 2014 to 2022 and b) solutions available in the GCMT catalog, 39 events with $5.1 \leq Mw \leq 7.6$ from 1977 to 2022. The FMC program (Álvarez-Gómez, 2019) was used to classify the focal mechanisms and draw the diagrams, which are based on the Kaverina projection (Kaverina et al., 1996). The classification allows for up to seven styles of faulting: normal (N), normal with strike-slip (N-SS), strike-slip with normal (SS-N), strike-slip (SS), strike-slip with reverse (SS-R), reverse with strike-slip (R-SS) and reverse (R).

An abrupt decrease in the rms misfit was observed around 660 km depth when that depth was included in the investigated depth range (see for example Figure S19). In Figure S15, for instance, such a decrease almost became a global minimum. We sometimes observed abrupt increases in the rms around those depths as well (see Figure S10, as an example). Such features are probably artifacts due to the source being placed near the 660 km seismic discontinuity.

Because deep events are not expected to occur below those depths, we disregarded such minima as physically unfeasible. In particular, for event 35 (Figure S22), we had to expand the investigated depth range up to 684 km to check if the observed decrease in rms from 614 to 634 km would lead towards a global minimum, which was not the case.

We stress that the inclusion of depth phases in our inversions was only possible for earthquakes with Mw ≥ 5.4, which showed clear P, sP and pP observations at teleseismic distances. Centroid depths estimated with the help of depth phases are indicated in Table 2. Overall, we observed centroid depths ranging from 557 to 659 km, defining a quite narrow (~100 km thick) zone of deep-focus seismicity. Note that events with fixed centroid depths are all within this estimated depth range (Table 2).

2.5.2.5. Qualitative grading scheme

Finally, prior to interpretation, we qualitatively graded our solutions according to fault mechanism robustness and depth resolution (Figure 3a). In our qualitative classification, we assigned qualities from A to D to our 28 solutions (Table 2). We attributed quality A to the more reliable solutions, in which both the mechanism and centroid depth are well determined. For example, for the 2015 doublet (events 8 and 9), we were able to easily determine their preferred depths and observed consistent mechanisms across the investigated depth range (Figures S4b and S5b). Quality B was assigned to events for which faulting style was observed to be robust within the investigated depth range, but preferred depth was ambiguous due to an ill-defined minimum (see e.g. Figure S23b). Quality C was attributed to solutions with non-robust mechanisms but well-resolved depths (Figure S20, event 33). Finally, quality D was given to those solutions with both unreliable mechanisms and inaccurate depths (Figure S9b, event 13). Most of our solutions were qualified as either A or B (see Table 2). Notably, all solutions that included depth phases in the inversion were found to be of A quality; only two events, event 33 (C) and event 13 (D), did not qualify as A or B.

Table 2: Earthquake focal mechanisms determined in this study for a total of 28 deep-focus events from the 2014-2022 sequence.

Event	S (º)	D (º)	R (º)	CD (km)	M0 (dyne-cm)	Mw	Type	Quality	FR (Hz)
1	180±8	50±7	-80±11	571±18	7.36±1.06e+23	5.2±0.04	N	A	0.02-0.05
3	20±4	30±0[c]	-80±4	557[b]±9	1.36±0.02e+24	5.4±0.004	N	A	0.02-0.05
6	190±8	60±10	-10±6	584±13	3.28±0.77e+23	5.0±0.07	SS-N	B	0.3-1.0

8	350±0	40±0	-80±0	616[b]±10	1.81±0.02e+27	7.5±0.003	N	A	0.02-0.05
9	350±0	30±0	-90±0	621±13	1.93±0.02e+27	7.5±0.003	N	A	0.02-0.05
10	110±20	50±9	-80±8	595[a]	1.63±0.34e+23	4.8±0.05	N	B	0.3-1.0
11	310±64	70±35	-60±28	629±17	9.61±0.76e+22	4.6±0.03	N-SS	B	0.3-1.0
12	150±32	50±18	-60±35	587±8	1.82±0.27e+23	4.8±0.04	N-SS	B	0.3-1.0
13	250±145	20±0	-20±67	590[a]	2.27±4.57e+22	4.2±0.22	N	D	0.3-1.0
14	170±4	40±0	-70±0	659±4	3.66±0.11e+23	5.0±0.01	N	B	0.02-0.05
17	200±41	40±5	-90±24	655[a]	1.25±0.67e+23	4.7±0.11	N	B	0.3-1.0
18	300±111	70±11	-80±15	592[a]	4.60±2.17e+22	4.4±0.11	N	B	0.3-1.0
19	350±0	30±0	-90±0	603[b]±9	1.27±0.01e+26	6.7±0.002	N	A	0.02-0.05
22	350±0	60±0	-80±0	636±15	2.75±0.03e+23	4.9±0.003	N	A	0.02-0.05
24	170±2	50±2	-90±3	617±13	5.44±0.19e+23	5.1±0.01	N	A	0.02-0.05
29	230±131	20±23	-40±15	643±8	1.24±0.78e+23	4.7±0.17	N	B	0.3-1.0
30	350±0	20±0	-80±0	642[b]±19	4.72±0.01e+25	6.4±0.001	N	A	0.02-0.05
31	90±35	70±19	-90±59	590[a]	7.79±2.94e+22	4.6±0.08	N	B	0.3-1.0
32	340±1	40±1	-90±1	620[b] ±14	4.83±0.02e+26	7.1±0.001	N	A	0.02-0.05
33	60±26	30±8	-50±9	626±8	2.58±0.55e+23	4.9±0.06	N	C	0.3-1.0
34	350±1	40±0	-80±2	570[b]±12	1.64±0.02e+26	6.8±0.003	N	A	0.02-0.05
35	10±4	20±0	-80±3	564±5	4.76±0.22e+23	5.1±0.01	N	A	0.02-0.05
37	180±66	20±30	-70±42	557[a]	5.59±6.04e+22	4.5±0.17	N	B	0.3-1.0
38	350±0	40±0	-80±0	599[b]±18	9.31±0.12e+24	5.9±0.004	N	A	0.02-0.05
39	220±21	40±28	-30±7	605±5	7.26±3.24e+22	4.5±0.10	N-SS	B	0.3-1.0
40	280±58	70±30	-30±24	580[a]	1.70±0.66e+23	4.8±0.13	SS-N	B	0.3-1.0
41	350±0	20±0	-80±0	623[b]±12	6.16±0.08e+25	6.5±0.004	N	A	0.02-0.05
42	350±69	80±0	60±56	605[a]	7.80±0.65e+23	5.2±0.02	R-SS	B	0.3-1.0

[a]The centroid depth was fixed to be the hypocenter depth given by the USGS catalog. In these cases, there was no clear minimum in the misfit curve and thus we could not select a preferred depth. [b]The centroid depth was determined with the inclusion of depth phases in the inversion. [c]An error of 0º means that uncertainties are estimated to be within the grid-search steps (10º), that is, that fault angles did not change after removal of one station.

2.6. Discussion

2.6.1. Variability in faulting style

The predominant faulting style in our data set closely follows that of the 2015 doublet (Figures S6b-S9b) and is consistent with the faulting style displayed by the CGMT solutions. The solutions indicate that normal-faulting (22 events out of 28), with a near vertical P-axis and near horizontal B- and T-axis (see Figures 3, 5a and S30a) is predominant. We emphasize that, due to the coverage provided by our set of stations, we were able to determine focal mechanisms for events as small as Mw 4.2, so our set of solutions expand the range for which this faulting style is observed. For most of these normal-faulting solutions (17 events), B-axes orientations vary about the N-S direction, roughly following the strike of the linear distribution of deep-focus earthquakes in the region, while T-axes are oriented almost perpendicular to them (specifically events 1, 3, 8, 9, 13, 14, 17, 19, 22, 24, 30, 32, 34, 35, 37, 38 and 41) (Figure 3a and e). In fact, we noted that all events with Mw > 5.2 were pure normal faults, in reasonable agreement with the predominant configuration of the P, T and B axes.

2.6.1.1. Variability within normal faulting

Some of our solutions in the lower-magnitude range display a normal faulting style that is rotated with respect to the predominant style around the compressional axis. Solutions 3 and 17 presented small deviations from the predominant B-axis orientation, with B-axes tending to move a bit towards NE. Note that such small deviations also occur within the GCMT solutions (Figure 3d). Event 17, however, has relatively high uncertainties in its fault angles that could explain such deviation; but event 3 is one of the best constrained solutions in our set (Table 2). Events 10, 18, 29, 31 and 33, on the other hand, display substantial deviations from the predominant B-axis orientation, suggesting a change from strike-parallel B-axis to strike-parallel T-axis (Figure 3a and b). Events 10, 18, 29 and 33 were clearly small aftershocks (Mw from 4.4 to 4.9) in our sequence, as events 10, 18, and 29 occurred shortly after the 2015 doublet, and event 33 followed event 32 (Mw 7.1); event 31, on the other hand, occurred more than a year after event 30 (Mw 6.4) and nearly five months before event 32 (Mw 7.1) (Table S1). Note that the mechanisms found for events 10, 18 and 31 are very similar (Figure 3a). Uncertainties for some of these events were very high (events 18 and 29), but uncertainties for events 10, 31 and 33 suggest that their mechanisms are reasonably stable. Note, however, that the solution found for event 33 was assigned a C quality, which means the focal mechanism is not robust.

To further investigate the robustness of events 10 and 31, we performed a constrained grid-search, so that strike, dip, and rake were restricted to vary from 330º to 30º, from 25º to 65º and from -90º to -40º, respectively, forcing the search for normal mechanisms consistent

with the predominant pattern. For event 31, we observed that the unconstrained solution produced a better fit to observations (see Figure S35 and COHC, MCRA, CHSH, ANTS, VCES, PUYO in Figure S36c), suggesting that anomalous, orthogonal normal faulting might have occurred in the region. For event 10, the constrained mechanism provided a better amplitude fit to SAML, and correctly reproduced the observed P-wave polarity in ETMB (Figure S34); on the other hand, the unconstrained solution showed better amplitude fit in NNA, but both solutions produced the correct polarity for this station (Figure S33c and f). Thus, a normal faulting style consistent with the regional pattern, cannot be ruled out.

2.6.1.2. Deviations from normal faulting

Most interestingly, a few of our solutions present significant deviations from the predominant normal-faulting style. These events, all with Mw ≤ 5.2, consist of six oblique faults, mainly normal with a small strike-slip component (events 11, 12 and 39), but also include strike-slip faults with a small normal component (events 6 and 40), and a single event showing reverse faulting with a small strike-slip component (event 42). The three normal with strike-slip faults (from Mw 4.5 to 4.8) still display a near vertical P-axis but with variable B-axis orientations: approximately N-S for event 39, NW-SE for event 12, and E-W for event 11 (Figure 3a). Events 11 and 12 are aftershocks of the 2015 doublet and event 39 is an aftershock from a Mw 5.9 (Table S1). Because two normal with strike-slip faults were also present among the 1977-2022 GCMT solutions in the Peru-Brazil segment (Figure 5b), we can conclude that such a pattern is plausible but unusual in this region. This pattern seems relatively more common in the Argentina-Bolivia segment (Figure S29a).

The two strike-slip with normal component faults, events 6 and 40 (Mw 5.0 and 4.8, respectively), on the other hand, show opposite slip directions but basically the same orientation of the nodal planes. Both preceded great ruptures in our sequence, the Mw 7.5 doublet and event 41 (Mw 6.5), respectively. It is noteworthy that there is no evidence of such faulting style in any deep-focus seismicity segment in South America within the reference catalog (Figure S29a). The radiation pattern found for event 40 was observed to be poorly constrained, where uncertainties in rake can change its strike-slip with normal mechanism (280º±58º, 70º±30º, -30º±24º) to either pure strike-slip or normal with strike-slip.

On the other hand, the small uncertainties in the fault angles of the oblique strike-slip mechanism obtained for event 6 suggests that it is a reliable observation (190º±8º, 60º±10º, -10º±6º). As for event 10, we run a constrained inversion to verify the robustness of our solution. We observed that both solutions (constrained and unconstrained) produced very similar

waveform matches, but our unconstrained solution was the one that provided the best fit for the P waveform of station TBTG (compare Figures S31c and f). As shown in Figure S32, TBTG is the only station that expects a substantial change in polarity between the two solutions (Figure S32a and b) and is clear that the constrained solution does not provide the correct polarity for the P-wave at TBTG (Figure S32c). Although this event preceded the 2015 doublet by nearly a month (Table S1), it is not clear to us how such unusual faulting could be explained. Interestingly, event 6 preceded the great doublet Mw 7.5, in October 2015.

Finally, the single case of reverse fault mechanism (Mw 5.2 event 42 in Figure 3a) suggests a notable change to a near horizontal P-axis and a near vertical T-axis. The radiation pattern for this event was found to be unstable, since uncertainties in rake can explain from reverse to strike-slip faulting (350º±69º, 80º±0º, 60º±56º). Note that although this solution has relatively large uncertainties, there are some reverse faulting observations in other deep-focus segments in South America, in Bolivia and Argentina (see Figure S29a).

Because most of the solutions that deviated from the normal faulting regime were small-magnitude aftershocks (Mw ≤ 5.2), we suggest that such deviations could be due to stress changes imposed by their respective mainshocks. Thus, our results indicate that oblique strike-slip, oblique reverse, and orthogonal normal faulting may also occur along the predominant normal style in the Peru-Brazil segment of deep-focus seismicity if the predominant stress field is perturbed. It is noteworthy that event 6, the oblique strike-slip mechanism, does not seem to be an aftershock from any event within our sequence (Table S1), and thus it is not clear to us how the ambient stresses changed before event nucleation.

2.6.2. Stresses in the subducting Nazca plate

The observed pattern of near-vertical P-axes within the near-vertical subducting slab (e.g., Portner et al., 2020; Rodríguez et al., 2020) indicates that the deep-focus earthquakes in the Peru-Brazil region are occurring predominantly under down-dip compression (DDC). This type of regime was already recognized for events with Mw > 5 (see Figure 3d), and our results now show that the same regime holds for a wider range of magnitudes (4.2 ≤ Mw ≤ 7.5) (Figure 3e). Despite our solutions presenting more variability in B and T axes orientations, as discussed before, P-axes in general are near vertical, reflecting the predominance of normal faulting among our solutions and supporting a dominant DDC regime (Figure 3e). DDC is the dominant stress regime for subduction zones around the globe holding deep-focus seismicity (d > 400 km) (Houston, 2015), and is mainly attributed to the lower mantle resisting penetration of the subducting plate under its own weight (Isacks & Molnar, 1971).

2.6.2.1. DDC and flat-slab subduction

The Nazca plate (< 50 Myr) is presently converging against the South American plate at a rate of ~7 cm/yr (DeMets et al., 2010; Müller et al., 2008) (Figure 1a). Near the Peruvian coast, the Nazca plate initially sinks at an angle of nearly 30º until it reaches a depth of ~100 km, after which it continues to subduct almost horizontally for nearly 700 km under northern Peru, and 500-600 km under central and southern Peru, to finally drop almost vertically (~75º) down to MTZ depths. The locus of the deep-focus events is precisely at the bottom of this vertically subsiding segment of the slab (Gutscher et al., 2000; Kirby et al., 1995). Laterally, such geometry extends for ~1500 km in the NS direction, between 2ºS and 15ºS, and defines a flat slab segment within the Nazca plate (Bishop et al., 2017; Gutscher et al., 2000). The flat slab geometry seems to be directly linked to the subduction of overthickened oceanic crust, especially the Nazca Ridge to the south and, possibly, a postulated Inca Plateau to the north (Gutscher et al., 1999, 2000). The positive buoyancy of such anomalous features likely prevents the slab from sinking at an angle and keeps it moving horizontally until significant eclogitization occurs and becomes negatively buoyant (Antonijevic et al., 2015; Gutscher et al., 2000).

It's worth noting that the presence of an anomalously thick oceanic crust, although necessary, is not sufficient to explain flat subduction extending for more than 300 km from the trench. As demonstrated by previous modeling studies (e.g., Espurt et al., 2008; Manea et al., 2012), a combination of other effects such as trench retreat is required (Antonijevic et al., 2015). Seismic tomography studies also suggested that a marked slow velocity anomaly beneath the Peruvian flat slab, extending from 165 to 650 km depth and possibly reflecting hot and buoyant mantle material, might be supporting the observed flat geometry (e.g., Portner et al., 2017, 2020; Rodríguez et al., 2020; Scire et al., 2016). This support would explain why the Nazca slab remains flat far beyond the expected eclogitization limit (~350 km from the trench) (Bishop et al., 2017). Note that subduction velocity in the MTZ should be decreased due to flat slab subduction, effectively reducing slab penetration into the lower mantle, and possibly reducing the stresses associated with lower mantle resistance. If this were the case, we would expect relatively lower strain rates at MTZ depths, and buoyancy alone might not be strong enough to trigger DDC within the slab.

As demonstrated by independent numerical modeling studies, DDC is usually predicted at MTZ depths for a plate under both equilibrium and disequilibrium phase transformation conditions, the last one meaning the presence of metastable phase in the MTZ (e.g., Bina et al.,

2001; Devaux et al., 2000; Guest et al., 2003). Under equilibrium conditions, DDC is expected to occur inside the subducting slab due to the buoyancy forces generated by the density contrasts at both top and bottom of the MTZ, which are caused by the elevation and depression of the main phase boundaries that define the MTZ. Under disequilibrium conditions, such a regime is also predicted by volumetric changes due to olivine phase transformations. Moreover, stresses from volumetric changes will dominate over buoyancy stresses (e.g., Devaux et al., 2000) becoming the most important source of stress behind deep-focus earthquakes. Because the slab should be considerably dehydrated after the anomalously long horizontal subduction - which goes far beyond the eclogitization limit – the persistence of a MOW could be making a significant contribution to the strain rates responsible for deep-focus earthquakes.

2.6.2.2. Viability of transformational faulting

Transformational faulting naturally requires the formation of new faults in the MOW, which would in turn be controlled by the slab stress field (Warren et al., 2007). According to Warren et al. (2007), conjugate ruptures in DDC regimes are expected to occur along planes oriented ±Φ from the slab dip (or from the P-axis), Φ being the angle of internal friction (see their figure 1). Their findings for the Tonga-Kermadec subduction zone suggest that Φ is close to 45º, consistent with Anderson's prediction when no internal friction is acting on the fault plane and with other previous laboratory and seismological studies (Jiao et al., 2000; Kirby, 1987). To find the angle of internal friction, we first invert the principal stresses from the 39 GCMT solutions available in the Peru-Brazil segment, using the STRESSINVERSE package (Vavryčuk, 2014), which performs the inversion according to Michael's methodology (Michael, 1984, 1987). After that, we plot the conjugate plane poles predicted by these stresses. In Figure 6a the poles from GCMT solutions can be separated into two clusters, each of them centered around one of the two expected 45º planes, and the regional fault plane proposed by Zahradník et al. (2017) shows remarkable agreement with the relatively more vertical west-dipping plane. The histogram in Figure 7a shows that there is a marked concentration of GCMT nodal planes around 45º from the main compression axis. Thus, GCMT nodal planes are in reasonable agreement with fault planes expected from transformational faulting. Note, however, that this region lacks evidence of faulting along the east-dipping and more horizontal plane. In Figure 6b, A-quality solutions from this study are clearly clustering similar to those from the GCMT catalog, and there is also a clear concentration of nodal planes at ~45º (Figure

7b). B- to D-quality solutions show the previously explained variability, which can be due to uncertainties or to variations in the dominant stress field.

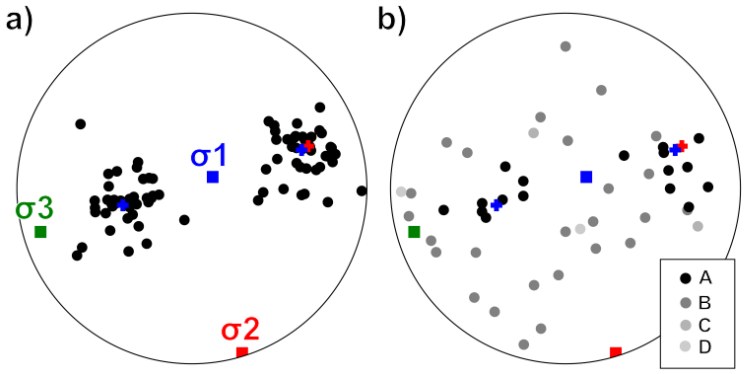

Figure 6. Nodal plane poles displayed on stereographic projection: a) GCMT solutions (solid black circles) plotted with the inverted stresses (colored squares). The two fault planes poles predicted by the inverted stresses are plotted as blue crosses while the pole of the regional fault plane proposed by Zahradník et al. (2017) is plotted as a red cross; and b) the same as in a but with solutions from this study colored according to quality.

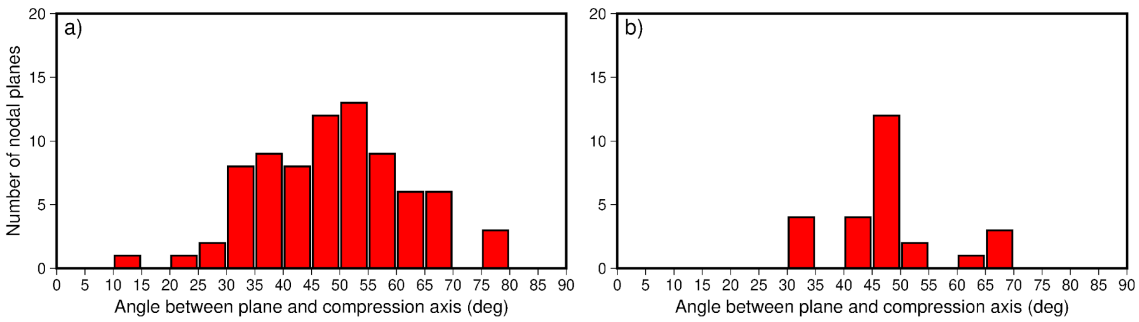

Figure 7. Histograms of the number of nodal planes as a function of the angle between these planes and the main compression axis. a) histogram considering only GCMT solutions for the study region and b) considering only A-quality solutions obtained in this study.

2.6.3. Thermal structure and deep-focus nucleation

For young and slow lithosphere deep seismicity is commonly restricted to less than 300 km depth (Myhill, 2013; Wortel, 1982). Assuming that deep-focus earthquakes are nucleated in a MOW within the subducting slab, the inability of such a hot lithosphere to preserve olivine at those depths would explain why deep-focus seismicity would be inhibited. As the Nazca plate is regarded as a warm endmember within the subduction zone spectrum (e.g., Frohlich, 2006; Wiens & Gilbert, 1996), deep-focus seismicity would not be expected. The thermal classification of the Nazca plate, however, is based on estimates of the thermal parameter, which characterizes the thermal structure of the whole plate based on its properties –

subduction speed and age – at the trench (Frohlich, 2006), which does not characterize thermal structure in detail.

2.6.3.1. Composite thermal structure at the Peru-Brazil border

Kirby et al. (1995), in their study of the great 1994 Bolivian earthquake, noted that the Nazca plate might have an anomalous thermal structure, consisting of a hot upper portion and a cold lower portion. Such composite structure would have resulted from the juxtaposition of younger, Tertiary-age lithosphere currently entering the trench and older, Mesozoic-age lithosphere in the deeper portions of the slab. According to Okal & Bina (1994) the older portion would have originated at the Pacific-Farallon spreading center at ~50-65 Ma and would be presently sitting at 500 – 700 km depth. The idea, first suggested by Engebretson & Kirby (1992), would thus explain the composite thermal structure through abrupt variation in slab age.

Alternatively, the composite thermal structure could be the result of a reduction in subduction velocity due to subduction of the Nazca ridge. Aseismic ridges, which are characterized by anomalously thick oceanic crust, have been invoked to explain segmentation by flat-slab subduction along the South American Pacific border (Espurt et al., 2008; Gutscher et al., 2000; Hu et al., 2016; McGeary et al., 1985), and might in turn have been responsible for slowing subduction along those segments due to their enhanced buoyancy (Espurt et al., 2008). In the Peru-Brazil region, it has been estimated that the tip of the aseismic Nazca Ridge would currently be at ~500 km depth (Bishop et al., 2017). In this alternative scenario, the composite thermal structure would be the result of a warm upper portion from slow, flat-style subduction juxtaposed to a cold lower portion from faster (and older), normal-style subduction (Collier & Helffrich, 2001; Engebretson & Kirby, 1992; Kirby et al., 1995; Okal & Bina, 1994).

Regardless of the nature of the postulated composite thermal structure, an abrupt transition from warm to cold is thus to be expected at around 500 km depth. Interestingly, one of the main findings of this study is that deep-focus seismicity along the Peru-Brazil border is confined between 557 and 659 km depth (557 and 642 if only A-quality solutions are considered) within the Nazca slab, well beyond the depth at which the abrupt thermal transition is postulated (Table 2). The concentration of deep-focus seismicity below 500 km depth, and the corresponding paucity above that depth, is consistent with the composite thermal structure mentioned above (Engebretson & Kirby, 1992; Kirby et al., 1995). The deeper and colder portion of the slab may have remained sufficiently cold during subduction to preserve olivine

metastably down to MTZ depths, while the shallower and warmer portion may have inhibited metastability and completely transformed olivine aseismically near the nominal equilibrium depth. The preservation of a MOW in the deeper portion would have permitted the nucleation of deep-focus earthquakes through transformational faulting while the lack of an MOW in the shallower portion would have prevented their nucleation (Figure 8).

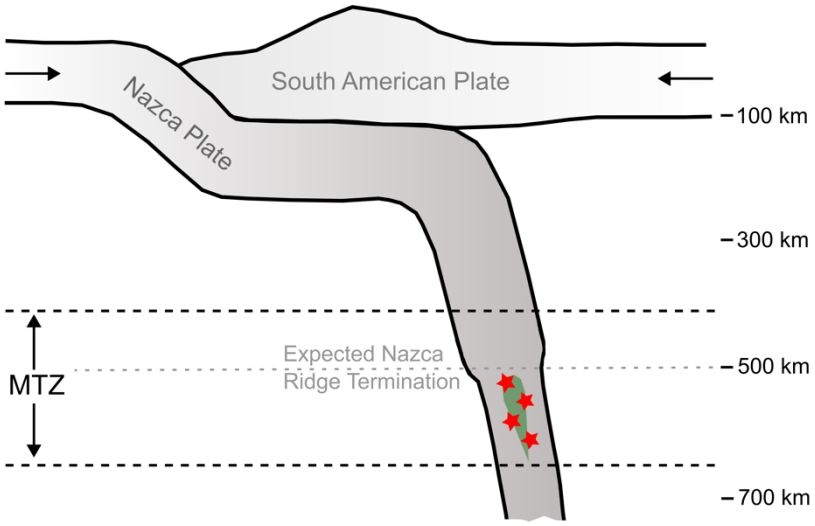

Figure 8. Schematic model proposed to explain deep-focus seismicity in the Peru-Brazil region. The model illustrates the South American subduction zone and the main features observed in the study region, the Peruvian flat slab, and the concentration of deep-focus earthquakes in a narrow fault zone. The Nazca ridge termination, as suggested by Bishop et al. (2017), is indicated by the red dashed line at ~500 km depth. The ridge termination marks the transition from a warmer to a colder Nazca slab segment. In the colder segment, we propose that a MOW could be preserved and thus allowing for earthquake nucleation (red stars) in the MTZ.

Moreover, if the composite thermal structure were correct, mechanisms commonly proposed for colder slabs (i.e., transformational faulting) would also become viable for the nominally warmer Nazca slab. Realize that even a thin MOW would be sufficient to nucleate deep-focus ruptures, as they could propagate beyond the MOW through some complementary mechanism such as thermal runaway (Zhan, 2017). A recent experiment has demonstrated that after a rupture is initiated by transformational faulting, it can propagate outside from the metastable nucleus when accompanied by melting (Gasc et al., 2022). Indeed, the largest deep-focus ruptures in South America have been explained through this dual-mechanism. For the Bolivia earthquake of 1994 (Mw 8.2 and 637 km), for example, the extremely low seismic efficiency determined by Kanamori et al. (1998) clearly attests to a very dissipative process during its rupture, possibly involving melting.

Alternatively, Billen (2020) suggested that the large gaps in deep-focus seismicity observed in South America and Java-Sumatra could be explained through a combination of regions of high strain rates and cold temperatures within the slab. The seismic gaps observed in many subduction zones would thus be the result of sluggish deformation rather than high temperature alone. Similarly, the abrupt paucity in seismicity around the top of the more viscous lower mantle could be due to minimum strain rates predicted at such depths. For the Peruvian and Chilean segments, for example, high strain rates could explain the concentration of events at around 600 km, probably due to phase transformations around those depths. Slab temperature, nonetheless, would still be a major factor influencing slab rheology, as warmer slabs would be expected to deform more plastically (Billen, 2020).

2.6.3.2. A generalized, composite thermal structure for South America?

Along the whole of the South America subduction front, deep-focus seismicity is clearly limited to regions where the subducting Nazca plate is imaged at depth. Some tomography models show that the Nazca plate is continuous from the north of Peru down to central Argentina, comprising the observed deep-focus segments (see models SAM5_P_2019, UU_P07, MITP08 and DETOX-P1 in figure 9 from Mohammadzaheri et al., 2021) (Amaru, 2007; C. Li et al., 2008; Mohammadzaheri et al., 2021; Portner et al., 2020). The apparent absence of this oceanic lithosphere further north and south could explain the absence of deep-focus seismicity in these regions. Additionally, it has been demonstrated that the Nazca plate does penetrate the lower mantle all along its strike, which would in turn explain the predominant DDC regime for these kind of earthquakes in South America (Portner et al., 2020).

As with the Peru-Brazil segment, it is possible that a thermally composite Nazca plate may be responsible for allowing deep-focus earthquakes in other segments as well. In Figure 1a, it is notable that the subduction of three aseismic ridges (Nazca, Iquique, and Juan Fernandez) seems to be related to the distribution of deep earthquakes with depth. Note that regions characterized by the subduction of these anomalously thick oceanic crusts are displaying marked gaps in deep seismicity, from nearly 200 km to ~500/600 km: In Peru, related to the Nazca Ridge; in central Bolivia, related to the Iquique Ridge; and in central Chile, related to the Juan Fernandez Ridge. Another marked gap is also observed further north of the Chilean-Pampean flat-slab, which could be associated with the subduction of the Copiapó Ridge. Although the Chilean-Pampean flat slab is often attributed to the subduction of the Juan Fernandez Ridge alone, it is possible that the Copiapó Ridge also contributed to the formation

of this feature at its northern limit (Álvarez et al., 2015; Gimenez et al., 2019). Other regions, on the other hand, show almost continuous distributions of events with depth (see, for instance, northern Chile and southern Bolivia).

Note, however, that flat subduction is only observed in Peru and central Chile, linked to the subduction of the Nazca Ridge and Juan Fernandez Ridge. The subduction of the Carnegie and Iquique Ridges, on the other hand, is not associated to flat subduction, probably because the subduction of such features began too recently (1-2 Ma ago) (Espurt et al., 2008). In Central Bolivia, where Iquique Ridge is subducting, a marked gap in deep seismicity is observed, flanked by two regions with continuous distribution of earthquakes (Figure 1a). In this case, it is possible that the plate is currently under a slab flattening process (Espurt et al., 2008). This process could be now reducing subduction velocity and consequently increasing temperatures in the oceanic plate, but since slab flattening is not complete, it is not clear if our model could explain seismicity in this region. It is notable that this region is marked by very few available mechanisms (Figure 1a). In fact, regions marked by flat subduction are presenting a higher seismic activity in the MTZ compared to this Northern Bolivia-Peru segment (see the Peru-Brazil and Northern Argentina-Bolivia segments of deep-focus seismicity in Figure 1).

2.7. Conclusions

In this work we determined focal mechanisms and centroid depths for a total of 28 deep-focus earthquakes that occurred in the Peru-Brazil region from 2014 to 2022. This sequence included the great 2015 Mw 7.5 doublet and its aftershocks. We observed a predominant pattern of normal faults in our solutions, describing a pattern of near-vertical P-axis, strike-parallel B-axis, and slab-normal T axis consistent with DDC within the Nazca slab. We also observed some normal solutions deviating from this general pattern, probably resulting from local stress changes brought by larger events, as well as more severe variations in faulting style that include oblique strike-slip and an oblique reverse mechanisms. The DDC regime is consistent with other regions in the world hosting deep-focus seismicity and we observed that this regime holds for a wider range of magnitudes ($4.2 \leq Mw \leq 7.5$) than previously observed ($Mw > 5$). The observed stress regime is consistent with both equilibrium and disequilibrium conditions within the subducting slab, and thus does not necessarily imply the existence of a MOW. Nevertheless, the expected influence of the flat-slab subduction in the stress regime and the observation of fault-plane orientations at ~45º from the main axis of compression -

suggesting they are consistent with newly formed faults – is found consistent with transformational faulting on a MOW.

The viability of transformational faulting in a MOW is discussed in the light of a thermally composite Nazca slab. In this hypothesis, the young and warmer Nazca plate that is being subducted is attached at ~500 km to an older and colder lithosphere segment in the MTZ. This thermal anomaly would be responsible for allowing metastable material to penetrate deep into the MTZ, and consequently allowing for transformational faulting to occur. This would explain the observed narrow band of deep-focus seismicity and could also explain both the pronounced seismic gap at ~300-500 km, where the warmer slab is subducting, and the lack of seismicity at the top of the lower mantle.

Acknowledgments

We thank Marcelo Assumpção, Marcelo Bianchi and Bruno Collaço for facilitating access to data from the temporary XC network. We also thank C.J. Ammon for making his inversion codes available. GSLN thanks the Coordenação de Aperfeiçoamento de Pessoal de Nível Superior (CAPES) for his PhD scholarship at Universidade Federal do Rio Grande do Norte (UFRN) and for his exchange scholarship (Programa de Doutorado Sanduíche no Exterior - PDSE/CAPES) to study at Universidad Nacional de Colombia (UNAL). JJ also thanks the Conselho Nacional de Desenvolvimento Científico e Tecnológico (CNPq) for support through a research grant (award n. 434807/2018-4) and a continued research fellowship (award n. 308644/2019-0).

Open research

All seismograms used in this work were collected from a variety of sources and are made available at a Zenodo repository (10.5281/zenodo.10685297). Data from the permanent Brazilian Seismographic Network (RSBR, comprising network codes BL, BR, NB and ON) are distributed at http://rsbr.on.br, while data from the temporary 3-basins Project (network code XC) can be obtained through the USP Seismological Center (USPSC) FDSNWS server (http://seisrequest.iag.usp.br/fdsnws/dataselect/1/) (Assumpção & Bianchi, 2016). Seismic data from the other networks were all acquired through the EarthScope Consortium Wilber 3 system (https://ds.iris.edu/wilber3/), including networks: IU (Albuquerque Seismological Laboratory/USGS, 2014), II (Scripps Institution of Oceanography, 1986), G (Institut de Physique du Globe de Paris (IPGP) and École et Observatoire des Sciences de la Terre de Strasbourg (EOST), 1982), GE (GEOFON Data Centre, 1993), C (Chilean National Seismic

Network), C1 (Universidad de Chile, 2012), CX (GFZ German Research Centre for Geosciences; Institut des Sciences De l'Univers-Centre National de la Recherche CNRS-INSU, 2006), CM (Servicio Geológico Colombiano, 1993) and EC (Ecuador Seismic Network).

References

Albuquerque Seismological Laboratory/USGS. (2014). Global Seismograph Network (GSN - IRIS/USGS) [Dataset]. International Federation of Digital Seismograph Networks. https://doi.org/10.7914/SN/IU

Allmendinger, R. W., Cardozo, N., & Fisher, D. M. (2012). Structural Geology Algorithms: Vectors and Tensors. Cambridge University Press.

Álvarez, O., Gimenez, M., Folguera, A., Spagnotto, S., Bustos, E., Baez, W., & Braitenberg, C. (2015). New evidence about the subduction of the Copiapó ridge beneath South America, and its connection with the Chilean-Pampean flat slab, tracked by satellite GOCE and EGM2008 models. Journal of Geodynamics, 91, 65–88. https://doi.org/10.1016/j.jog.2015.08.002

Álvarez-Gómez, J. A. (2019). FMC—Earthquake focal mechanisms data management, cluster and classification. SoftwareX, 9, 299–307. https://doi.org/10.1016/j.softx.2019.03.008

Amaru, M. L. (2007). Global travel time tomography with 3-D reference models. Utrecht University.

Antonijevic, S. K., Wagner, L. S., Kumar, A., Beck, S. L., Long, M. D., Zandt, G., et al. (2015). The role of ridges in the formation and longevity of flat slabs. Nature, 524, 212–215. https://doi.org/10.1038/nature14648

Assumpção, M., Bianchi, M., Rocha, M., & Azevedo, P. A. D. (2016). The "3-Basins" Project in Mid South America and the Geometry of the Deep Nazca Subducted Slab. In American Geophysical Union, Fall Meeting 2016.

Assumpção, M. S., & Bianchi, M. B. (2016). Pantanal, Chaco and Paraná (PCPB) structural studies network [Dataset]. USP Seismological Center (USPSC). https://doi.org/10.7914/8scf-yd39

Bianchi, M. B., Assumpção, M., Rocha, M. P., Carvalho, J. M., Azevedo, P. A., Fontes, S. L., et al. (2018). The Brazilian Seismographic Network (RSBR): Improving Seismic Monitoring

in Brazil. Seismological Research Letters, 89(2A), 452–457. https://doi.org/10.1785/0220170227

Billen, M. I. (2020). Deep slab seismicity limited by rate of deformation in the transition zone. Science Advances, 6(22). https://doi.org/10.1126/sciadv.aaz7692

Bina, C. R., Stein, S., Marton, F. C., & Van Ark, E. M. (2001). Implications of slab mineralogy for subduction dynamics. Physics of the Earth and Planetary Interiors, 127(1–4), 51–66. https://doi.org/10.1016/S0031-9201(01)00221-7

Bird, P. (2003). An updated digital model of plate boundaries. Geochemistry, Geophysics, Geosystems, 4(3). https://doi.org/10.1029/2001GC000252

Bishop, B. T., Beck, S. L., Zandt, G., Wagner, L., Long, M., Antonijevic, S. K., et al. (2017). Causes and consequences of flat-slab subduction in southern Peru. Geosphere, 13(5), 1392–1407. https://doi.org/10.1130/GES01440.1

Bouchon, M. (1981). A simple method to calculate Green's functions for elastic layered media. Bulletin of the Seismological Society of America, 71(4), 959–971. https://doi.org/10.1785/BSSA0710040959

Chagas de Melo, B., Assumpção, M., & "3-Basins" Project Team. (2018). Mantle anisotropy and asthenospheric flow around cratons in southeastern South America. Geophysical Journal International, 215, 494–506. https://doi.org/10.1093/gji/ggy288

Chang, Y., Warren, L. M., Zhu, L., & Prieto, G. A. (2019). Earthquake focal mechanisms and stress field for the intermediate-depth Cauca cluster, Colombia. Journal of Geophysical Research: Solid Earth, 124, 822–836. https://doi.org/https://doi.org/10.1029/2018JB016804

Chu, R., Zhu, L., & Helmberger, D. V. (2009). Determination of earthquake focal depths and source time functions in central Asia using teleseismic P waveforms. Geophysical Research Letters, 36(L17317), 1–4. https://doi.org/10.1029/2009GL039494

Collier, J. D., & Helffrich, G. R. (2001). The thermal influence of the subducting slab beneath South America from 410 and 660 km discontinuity observations. Geophysical Journal International, 147(2), 319–329. https://doi.org/10.1046/j.1365-246X.2001.00532.x

Crotwell, H. P., Owens, T. J., & Ritsema, G. (1999). The TauP Toolkit: Flexible Seismic Travel-time and Ray-path Utilities. Seismological Research Letters, 70(2), 154–160. https://doi.org/https://doi.org/10.1785/gssrl.70.2.154

DeMets, C., Gordon, R. G., & Argus, D. F. (2010). Geologically current plate motions. Geophysical Journal International, 181(1), 1–80. https://doi.org/10.1111/j.1365-246X.2009.04491.x

Devaux, J. P., Schubert, G., & Anderson, C. (1997). Formation of a metastable olivine wedge in a descending slab. Journal of Geophysical Research: Solid Earth, 102(B11), 24627–24637. https://doi.org/10.1029/97JB02334

Devaux, J. P., Fleitout, L., Schubert, G., & Anderson, C. (2000). Stresses in a subducting slab in the presence of a metastable olivine wedge. Journal of Geophysical Research: Solid Earth, 105(B6), 13365–13373. https://doi.org/10.1029/1999JB900274

Dziewonski, A. M., Chou, T.-A., & Woodhouse, J. H. (1981). Determination of earthquake source parameters from waveform data for studies of global and regional seismicity. Journal of Geophysical Research: Solid Earth, 86(B4), 2825–2852. https://doi.org/10.1029/JB086iB04p02825

Ekström, G., Nettles, M., & Dziewoński, A. M. (2012). The global CMT project 2004–2010: Centroid-moment tensors for 13,017 earthquakes. Physics of the Earth and Planetary Interiors, 200–201, 1–9. https://doi.org/10.1016/j.pepi.2012.04.002

Engebretson, D. C., & Kirby, S. H. (1992). Deep Nazca slab seismicity: why is it so anomalous? Eos, Trans. Amer. Geophys. Un., 73(43), 379 [abstract].

Espurt, N., Funiciello, F., Martinod, J., Guillaume, B., Regard, V., Faccenna, C., & Brusset, S. (2008). Flat subduction dynamics and deformation of the South American plate: Insights from analog modeling. Tectonics, 27(TC3011). https://doi.org/10.1029/2007TC002175

Du Frane, W. L., Sharp, T. G., Mosenfelder, J. L., & Leinenweber, K. (2013). Ringwoodite growth rates from olivine with ~75ppmw H2O: Metastable olivine must be nearly anhydrous to exist in the mantle transition zone. Physics of the Earth and Planetary Interiors, 219, 1–10. https://doi.org/10.1016/j.pepi.2013.04.001

Frohlich, C. (1989). The Nature Of Deep-Focus Earthquakes. Annual Review of Earth and Planetary Sciences, 17, 227–254. https://doi.org/10.1146/annurev.earth.17.1.227

Frohlich, C. (1994). Earthquakes with Non-Double-Couple Mechanisms. Science, 264(5160), 804–809. https://doi.org/10.1126/science.264.5160.804

Frohlich, C. (2006). Deep Earthquakes. Cambridge: Cambridge University Press. https://doi.org/10.1017/CBO9781107297562

Gasc, J., Daigre, C., Moarefvand, A., Deldicque, D., Fauconnier, J., Gardonio, B., et al. (2022). Deep-focus earthquakes: From high-temperature experiments to cold slabs. Geology. https://doi.org/10.1130/G50084.1

GEOFON Data Centre (1993). GEOFON Seismic Network [Dataset]. Deutsches GeoForschungsZentrum GFZ. https://doi.org/10.14470/TR560404

GFZ German Research Centre for Geosciences; Institut des Sciences De l'Univers-Centre National de la Recherche CNRS-INSU (2006). IPOC Seismic Network [Dataset]. Integrated Plate boundary Observatory Chile – IPOC. https://doi.org/10.14470/PK615318

Gimenez, M., Acosta, G., Alvarez, O., Pesce, A., Lince Kinger, F., & Folguera, A. (2019). The subduction of the Copiapó aseismic ridge, is the causing of the formation of metallic minerals deposits in north of Chile and Argentina? Geodesy and Geodynamics, 10(6), 471–476. https://doi.org/10.1016/j.geog.2019.04.007

Green, H. W., & Burnley, P. C. (1989). A new self-organizing mechanism for deep-focus earthquakes. Nature, 341, 733–737. https://doi.org/10.1038/341733a0

Green, H. W., & Marone, C. (2002). Instability of Deformation. Reviews in Mineralogy and Geochemistry, 51(1), 181–199. https://doi.org/10.2138/gsrmg.51.1.181

Green, H. W., & Zhou, Y. (1996). Transformation-induced faulting requires an exothermic reaction and explains the cessation of earthquakes at the base of the mantle transition zone. Tectonophysics, 256(1–4), 39–56. https://doi.org/10.1016/0040-1951(95)00164-6

Guest, A., Schubert, G., & Gable, C. W. (2003). Stress field in the subducting lithosphere and comparison with deep earthquakes in Tonga. Journal of Geophysical Research: Solid Earth, 108(B6). https://doi.org/10.1029/2002JB002161

Gutscher, M.-A., Olivet, J.-L., Aslanian, D., Eissen, J.-P., & Maury, R. (1999). The "lost Inca Plateau": cause of flat subduction beneath Peru? Earth and Planetary Science Letters, 171, 335–341. https://doi.org/10.1016/S0012-821X(99)00153-3

Gutscher, M.-A., Spakman, W., Bijwaard, H., & Engdahl, E. R. (2000). Geodynamics of flat subduction: Seismicity and tomographic constraints from the Andean margin. Tectonics, 19(5), 814–833. https://doi.org/10.1029/1999TC001152

Hanks, T. C., & Kanamori, H. (1979). A moment magnitude scale. Journal of Geophysical Research, 84(B5), 2348–2350. https://doi.org/10.1029/JB084iB05p02348

Hayes, G. P., Moore, G. L., Portner, D. E., Hearne, M., Flamme, H., Furtney, M., & Smoczyk, G. M. (2018). Slab2, a comprehensive subduction zone geometry model. Science, 362(6410), 58–61. https://doi.org/10.1126/science.aat4723

Herrmann, R. B. (2013). Computer Programs in Seismology: An Evolving Tool for Instruction and Research. Seismological Research Letters, 84(6), 1081–1088. https://doi.org/10.1785/0220110096

Heyburn, R., Selby, N. D., & Fox, B. (2013). Estimating earthquake source depths by combining surface wave amplitude spectra and teleseismic depth phase observations. Geophysical Journal International, 194, 1000–1010. https://doi.org/10.1093/gji/ggt140

Hogrefe, A., Rubie, D. C., Sharp, T. G., & Seifert, F. (1994). Metastability of enstatite in deep subducting lithosphere. Nature, 372, 351–353. https://doi.org/10.1038/372351a0

Hosoya, T., Kubo, T., Ohtani, E., Sano, A., & Funakoshi, K. (2005). Water controls the fields of metastable olivine in cold subducting slabs. Geophysical Research Letters, 32(L17305). https://doi.org/10.1029/2005GL023398

Houston, H. (2015). Deep Earthquakes. In Treatise on Geophysics (pp. 329–354). Elsevier. https://doi.org/10.1016/B978-0-444-53802-4.00079-8

Hu, J., Liu, L., Hermosillo, A., & Zhou, Q. (2016). Simulation of late Cenozoic South American flat-slab subduction using geodynamic models with data assimilation. Earth and Planetary Science Letters, 438, 1–13. https://doi.org/10.1016/j.epsl.2016.01.011

Institut de Physique du Globe de Paris (IPGP) and École et Observatoire des Sciences de la Terre de Strasbourg (EOST) (1982). GEOSCOPE, French Global Network of Broad Band Seismic Stations [Dataset]. Institut de Physique du Globe de Paris (IPGP), Université de Paris. https://doi.org/10.18715/GEOSCOPE.G

Isacks, B., & Molnar, P. (1971). Distribution of stresses in the descending lithosphere from a global survey of focal-mechanism solutions of mantle earthquakes. Reviews of Geophysics, 9(1), 103–174. https://doi.org/10.1029/RG009i001p00103

Ishii, T., & Ohtani, E. (2021). Dry metastable olivine and slab deformation in a wet subducting slab. Nature Geoscience, 14, 526–530. https://doi.org/10.1038/s41561-021-00756-7

Jiao, W., Silver, P. G., Fei, Y., & Prewitt, C. T. (2000). Do intermediate- and deep-focus earthquakes occur on preexisting weak zones? An examination of the Tonga subduction zone. Journal of Geophysical Research: Solid Earth, 105(B12), 28125–28138. https://doi.org/10.1029/2000JB900314

Jiménez, C., Calvo, C., Saavedra, M., Moggiano, N., & Molina, W. (2021). Source characteristics of Peruvian deep focus seismic doublet of November 24, 2015. Journal of South American Earth Sciences, 105(102919). https://doi.org/https://doi.org/10.1016/j.jsames.2020.102919

Kanamori, H., Anderson, D. L., & Heaton, T. H. (1998). Frictional Melting During the Rupture of the 1994 Bolivian Earthquake. Science, 279(5352), 839–842. https://doi.org/10.1126/science.279.5352.839

Kaverina, A. N., Lander, A. V., & Prozorov, A. G. (1996). Global creepex distribution and its relation to earthquake-source geometry and tectonic origin. Geophysical Journal International, 125(1), 249–265. https://doi.org/10.1111/j.1365-246X.1996.tb06549.x

Kawakatsu, H. (1991). Insignificant isotropic component in the moment tensor of deep earthquakes. Nature, 351(6321), 50–53. https://doi.org/10.1038/351050a0

Kelemen, P. B., & Hirth, G. (2007). A periodic shear-heating mechanism for intermediate-depth earthquakes in the mantle. Nature, 446, 787–790. https://doi.org/10.1038/nature05717

Kennett, B. L. N., Engdahl, E. R., & Buland, R. (1995). Constraints on seismic velocities in the Earth from traveltimes. Geophysical Journal International, 122(1), 108–124. https://doi.org/10.1111/j.1365-246X.1995.tb03540.x

Kirby, S. H. (1987). Localized polymorphic phase transformations in high-pressure faults and applications to the physical mechanism of deep earthquakes. Journal of Geophysical Research: Solid Earth, 92(B13), 13789–13800. https://doi.org/10.1029/JB092iB13p13789

Kirby, S. H., Durham, W. B., & Stern, L. A. (1991). Mantle Phase Changes and Deep-Earthquake Faulting in Subducting Lithosphere. Science, 252, 216–225. https://doi.org/10.1126/science.252.5003.216

Kirby, S. H., Okal, E. A., & Engdahl, E. R. (1995). The 9 June 94 Bolivian Deep Earthquake: An exceptional event in an extraordinary subduction zone. Geophysical Research Letters, 22(16), 2233–2236. https://doi.org/10.1029/95GL01802

Kubo, T., Ohtani, E., Kato, T., Shinmei, T., & Fujino, K. (1998). Effects of Water on the α-β Transformation Kinetics in San Carlos Olivine. Science, 281(5373), 85–87. https://doi.org/10.1126/science.281.5373.85

Leite Neto, G. S., & Julia, J. (2023). Determination of intraplate focal mechanisms with the Brazilian Seismic Network: A simplified Cut-and-Paste approach. Journal of South American Earth Sciences, 121, 104149. https://doi.org/10.1016/j.jsames.2022.104149

Li, C., Van der Hilst, R. D., Engdahl, E. R., & Burdick, S. (2008). A new global model for P wave speed variations in Earth's mantle. Geochemistry, Geophysics, Geosystems, 9(5). https://doi.org/10.1029/2007GC001806

Li, J., Zheng, Y., Thomsen, L., Lapen, T. J., & Fang, X. (2018). Deep earthquakes in subducting slabs hosted in highly anisotropic rock fabric. Nature Geoscience, 11, 696–700. https://doi.org/10.1038/s41561-018-0188-3

Manea, V. C., Pérez-Gussinyé, M., & Manea, M. (2012). Chilean flat slab subduction controlled by overriding plate thickness and trench rollback. Geology, 40(1), 35–38. https://doi.org/10.1130/G32543.1

Mao, G. L., Ferrand, T. P., Li, J., Zhu, B., Xi, Z., & Chen, M. (2022). Unsupervised machine learning reveals slab hydration variations from deep earthquake distributions beneath the northwest Pacific. Communications Earth & Environment, 3:56, 1–9. https://doi.org/10.1038/s43247-022-00377-x

Marrett, R., & Allmendinger, R. W. (1990). Kinematic analysis of fault-slip data. Journal of Structural Geology, 12(8), 973–986. https://doi.org/10.1016/0191-8141(90)90093-E

McGeary, S., Nur, A., & Ben-Avraham, Z. (1985). Spatial gaps in arc volcanism: The effect of collision or subduction of oceanic plateaus. Tectonophysics, 119(1–4), 195–221. https://doi.org/10.1016/0040-1951(85)90039-3

Michael, A. J. (1984). Determination of stress from slip data: Faults and folds. Journal of Geophysical Research: Solid Earth, 89(B13), 11517–11526. https://doi.org/10.1029/JB089iB13p11517

Michael, A. J. (1987). Use of focal mechanisms to determine stress: A control study. Journal of Geophysical Research: Solid Earth, 92(B1), 357–368. https://doi.org/10.1029/JB092iB01p00357

Miller, R. G. (1974). The Jackknife - A Review. Biometrika, 61(1), 1–15. https://doi.org/10.2307/2334280

Mohammadzaheri, A., Sigloch, K., Hosseini, K., & Mihalynuk, M. G. (2021). Subducted Lithosphere Under South America From Multifrequency P Wave Tomography. Journal of Geophysical Research: Solid Earth, 126(6). https://doi.org/10.1029/2020JB020704

Montagner, J.-P., & Kennett, B. L. N. (1996). How to reconcile body-wave and normal-mode reference earth models. Geophysical Journal International, 125(1), 229–248. https://doi.org/10.1111/j.1365-246X.1996.tb06548.x

Mosenfelder, J. L., Marton, F. C., Ross, C. R., Kerschhofer, L., & Rubie, D. C. (2001). Experimental constraints on the depth of olivine metastability in subducting lithosphere. Physics of the Earth and Planetary Interiors, 127(1–4), 165–180. https://doi.org/10.1016/S0031-9201(01)00226-6

Müller, R. D., Sdrolias, M., Gaina, C., & Roest, W. R. (2008). Age, spreading rates, and spreading asymmetry of the world's ocean crust. Geochemistry, Geophysics, Geosystems, 9(4), n/a-n/a. https://doi.org/10.1029/2007GC001743

Myhill, R. (2013). Slab buckling and its effect on the distributions and focal mechanisms of deep-focus earthquakes. Geophysical Journal International, 192, 837–853. https://doi.org/10.1093/gji/ggs054

Ogawa, M. (1987). Shear instability in a viscoelastic material as the cause of deep focus earthquakes. Journal of Geophysical Research: Solid Earth, 92(B13), 13801–13810. https://doi.org/10.1029/JB092iB13p13801

Okal, E. A., & Bina, C. R. (1994). The deep earthquakes of 1921–1922 in Northern Peru. Physics of the Earth and Planetary Interiors, 87, 33–54. https://doi.org/10.1016/0031-9201(94)90020-5

Portner, D. E., Beck, S., Zandt, G., & Scire, A. (2017). The nature of subslab slow velocity anomalies beneath South America. Geophysical Research Letters, 44(10), 4747–4755. https://doi.org/10.1002/2017GL073106

Portner, D. E., Rodríguez, E. E., Beck, S., Zandt, G., Scire, A., Rocha, M. P., et al. (2020). Detailed Structure of the Subducted Nazca Slab into the Lower Mantle Derived From

Continent-Scale Teleseismic P Wave Tomography. Journal of Geophysical Research: Solid Earth, 125(5). https://doi.org/10.1029/2019JB017884

Quenouille, M. H. (1949). Approximate tests of correlation in time-series 3. Mathematical Proceedings of the Cambridge Philosophical Society, 45(3), 483–484. https://doi.org/10.1017/S0305004100025123

Quenouille, M. H. (1956). Notes on Bias in Estimation. Biometrika, 43(3/4), 353–360. https://doi.org/10.2307/2332914

Rodríguez, E. E., Portner, D. E., Beck, S. L., Rocha, M. P., Bianchi, M. B., Assumpção, M., et al. (2020). Mantle dynamics of the Andean Subduction Zone from continent-scale teleseismic S-wave tomography. Geophysical Journal International, 224(3), 1553–1571. https://doi.org/10.1093/gji/ggaa536

Rosenbaum, G., Giles, D., Saxon, M., Betts, P. G., Weinberg, R. F., & Duboz, C. (2005). Subduction of the Nazca Ridge and the Inca Plateau: Insights into the formation of ore deposits in Peru. Earth and Planetary Science Letters, 239, 18–32. https://doi.org/10.1016/j.epsl.2005.08.003

Ruiz, S., Tavera, H., Poli, P., Herrera, C., Flores, C., Rivera, E., & Madariaga, R. (2017). The deep Peru 2015 doublet earthquakes. Earth and Planetary Science Letters, 478, 102–109. https://doi.org/10.1016/j.epsl.2017.08.036

Scire, A., Zandt, G., Beck, S., Long, M., Wagner, L., Minaya, E., & Tavera, H. (2016). Imaging the transition from flat to normal subduction: variations in the structure of the Nazca slab and upper mantle under southern Peru and northwestern Bolivia. Geophysical Journal International, 204(1), 457–479. https://doi.org/10.1093/gji/ggv452

Scripps Institution of Oceanography (1986). Global Seismographic Network – IRIS/IDA [Dataset]. International Federation of Digital Seismograph Networks. https://doi.org/10.7914/SN/II

Servicio Geológico Colombiano (1993). Red Sismologica Nacional de Colombia [Dataset]. International Federation of Digital Seismograph Networks. https://doi.org/10.7914/SN/CM

Tibi, R., Bock, G., & Wiens, D. A. (2003). Source characteristics of large deep earthquakes: Constraint on the faulting mechanism at great depths. Journal of Geophysical Research: Solid Earth, 108(B2). https://doi.org/10.1029/2002JB001948

Universidad de Chile (2012). Red Sismologica Nacional [Dataset]. International Federation of Digital Seismograph Networks. https://doi.org/10.7914/SN/C1

Vavryčuk, V. (2014). Iterative joint inversion for stress and fault orientations from focal mechanisms. Geophysical Journal International, 199, 69–77. https://doi.org/10.1093/gji/ggu224

Warren, L. M., Hughes, A. N., & Silver, P. G. (2007). Earthquake mechanics and deformation in the Tonga-Kermadec subduction zone from fault plane orientations of intermediate- and deep-focus earthquakes. Journal of Geophysical Research: Solid Earth, 112(B5). https://doi.org/https://doi.org/10.1029/2006JB004677

Wiens, D. A., & Gilbert, H. J. (1996). Effect of slab temperature on deep-earthquake aftershock productivity and magnitude–frequency relations. Nature, 384(6605), 153–156. https://doi.org/10.1038/384153a0

Wortel, R. (1982). Seismicity and rheology of subducted slabs. Nature, 296, 553–556. https://doi.org/10.1038/296553a0

Ye, L., Lay, T., Kanamori, H., Zhan, Z., & Duputel, Z. (2016). Diverse rupture processes in the 2015 Peru deep earthquake doublet. Science Advances, 2(6). https://doi.org/10.1126/sciadv.1600581

Zahradník, J., Čížková, H., Bina, C. R., Sokos, E., Janský, J., Tavera, H., & Carvalho, J. (2017). A recent deep earthquake doublet in light of long-term evolution of Nazca subduction. Scientific Reports, 7(45153). https://doi.org/10.1038/srep45153

Zhan, Z. (2017). Gutenberg–Richter law for deep earthquakes revisited: A dual-mechanism hypothesis. Earth and Planetary Science Letters, 461, 1–7. https://doi.org/10.1016/j.epsl.2016.12.030

Zhan, Z. (2020). Mechanisms and Implications of Deep Earthquakes. Annual Review of Earth and Planetary Sciences, 48, 147–174. https://doi.org/10.1146/annurev-earth-053018-060314

Zhan, Z., & Kanamori, H. (2016). Recurring large deep earthquakes in Hindu Kush driven by a sinking slab. Geophysical Research Letters, 43(14), 7433–7441. https://doi.org/10.1002/2016GL069603

Zhan, Z., Kanamori, H., Tsai, V. C., Helmberger, D. V., & Wei, S. (2014). Rupture complexity of the 1994 Bolivia and 2013 Sea of Okhotsk deep earthquakes. Earth and Planetary Science Letters, 385, 89–96. https://doi.org/10.1016/j.epsl.2013.10.028

Zhao, L.-S., & Helmberger, D. V. (1994). Source estimation from broadband regional seismograms. Bulletin of the Seismological Society of America, 84(1), 91–104. https://doi.org/https://doi.org/10.1785/BSSA0840010091

Zhu, L., & Helmberger, D. V. (1996). Advancement in source estimation techniques using broadband regional seismograms. Bulletin of the Seismological Society of America, 86(5), 1634–1641. https://doi.org/https://doi.org/10.1785/BSSA0860051634

CAPÍTULO 3

MANUSCRITO 2

Este manuscrito foi submetido em 10/7/2024 ao periódico *Journal of Geophysical Research: Solid Earth*, da AGU. O material suplementar deste manuscrito se encontra no Apêndice D.

Deep-Focus Earthquakes in Warm Slabs: Seismic Source Parameters in the Peru-Brazil Region

G. S. Leite Neto[1*], G. A. Prieto[2], and J. Julià[1,3]

[1]Programa de Pós-Graduação em Geodinâmica e Geofísica, Universidade Federal do Rio Grande do Norte, Natal, Brasil.

[2]Departamento de Geociencias, Universidad Nacional de Colombia, Bogotá, Colombia.

[3]Departamento de Geofísica, Universidade Federal do Rio Grande do Norte, Natal, Brasil.

Corresponding author: Gilberto S. Leite Neto (leitenetogs@gmail.com)

Key Points

- Seismic source parameters were determined for 13 deep-focus earthquakes in the Peru-Brazil region
- Significant variations in stress drop and radiation efficiency were found to occur within a narrow seismic zone in our study region
- We propose that water may play a role in explaining the coexistence of dissipative and brittle-like ruptures in the Peru-Brazil region

Plain language summary

Deep-focus earthquakes are puzzling because they occur under extreme pressure and temperature conditions that should inhibit brittle-failure. Transformational faulting is often regarded as the likely mechanism, but it faces limitations in explaining ruptures in warm slabs like Nazca. Aiming at understanding conditions and processes driving deep seismicity in warm slabs, we assessed seismic source parameters for 13 deep-focus events with magnitudes from 4.8 to 7.4 Mw in the Peru-Brazil border region. We found significant variations in terms of both stress drop (5-90 MPa) and radiation efficiency (0.1-1.4) within the slab segment. We propose that variable efficiencies reflect different degrees of melting involved in the rupture process, possibly controlled by the release of water from hydrous phases in the source region. Dehydration reactions would be triggered by either the latent heat released from transformational faulting or by shear heating, establishing an interplay between thermal runaway enhanced by melting and phase transformations promoted by the release of water.

Abstract

Deep-focus earthquakes pose a significant challenge because their occurrence under extreme pressure and temperature conditions should inhibit nucleation through conventional brittle-failure. Transformational faulting is generally accepted as a most plausible mechanism to explain deep-focus seismicity, but it encounters limitations in warm slabs like Nazca because warm temperatures may hinder the preservation of a metastable olivine wedge. Aiming at elucidating the conditions and processes driving deep seismicity in warm slabs, we determined seismic source parameters (stress drop, seismic moment, radiated energy, seismic efficiency) for 13 deep-focus earthquakes ($4.8 \leq Mw \leq 7.4$) in the Peru-Brazil border region. Our results suggest that variations in stress drop can be significant (5-90 MPa) and that scaling between stress drop and seismic moment holds for a wider range of magnitudes (Mw 4.8 to 7.4) than previously reported. Radiated energies are in the 6.8×10^{10}-1.9×10^{16} J range, with earthquakes in the 6.4-7.4 Mw magnitude range displaying the largest values (4.2×10^{14}-1.9×10^{16} J). Most importantly, variable radiation efficiencies (0.1-1.4) suggest the coexistence of dissipative and brittle-like ruptures within the slab segment. We propose that these values reflect different degrees of melting involved in the rupture process, possibly controlled by the release of water from hydrous phases in the source region. Moreover, dehydration reactions would be triggered by either the latent heat released from phase transformations or by shear heating, establishing

an interplay between thermal runaway enhanced by melting and phase transformations promoted by the release of water.

3.1. Introduction

Deep earthquakes are defined as those happening at depths of 70 km or larger, and their very occurrence has puzzled seismologists due to their nucleation under pressure and temperature conditions where brittle fracture is inhibited (Frohlich, 1989, 2006). Down to 300 km depth, it is believed that the release of water from hydrated minerals within the slab enables embrittlement through increased pore pressured, which in turn reduces normal stress and cohesive strength within cracks (Raleigh, 1967) and/or pre-existing faults (Ranero et al., 2003); at depths larger than 300 km, however, the progressive dehydration of the slab's crust and the negative sign of the volumetric changes of the reactions makes this mechanism more unlikely (Houston, 2015; Zhan, 2020). At larger depths, the origin of deep-focus earthquakes (DFEs) is often attributed to transformational faulting, which results from the formation and self-organization of anticracks – microscopic lenses filled with fine-grained superplastic material formed by transformation of olivine into its high-pressure polymorphs wadsleyite and ringwoodite – into a shear instability (Green & Burnley, 1989; Green & Marone, 2002; Green & Zhou, 1996; Ohuchi et al., 2022). Most importantly, this mechanism requires the preservation of a metastable olivine wedge (MOW) within the core of a subducted slab at mantle transition zone (MTZ) depths, where delayed phase transformations capable of triggering a shear instability would allow the nucleation of earthquakes at great depths (Green & Zhou, 1996; Zhan, 2020).

The existence of a MOW strongly depends on the thermal state of the subducting plate (Green & Marone, 2002; Green & Zhou, 1996), which is often described by the thermal parameter $\boldsymbol{\phi}$ calculated from the age and subduction speed of the oceanic lithosphere (Frohlich, 2006; Kirby et al., 1991, 1996). Warm plates such as Nazca ($\boldsymbol{\phi}$ < 2500 km) (Frohlich, 2006), are not expected to host a MOW because their higher temperatures would favor olivine phase transformations close to nominal depths, thereby limiting the depth extent of the MOW within the MTZ. Numerical experiments show that only the coldest slabs (e.g., Tonga with $\boldsymbol{\phi}$ > 10000 km) (Frohlich, 2006) would be able to sustain a MOW down to the base of the MTZ (Devaux et al., 1997; Mosenfelder et al., 2001), but, surprisingly, some warm slabs such as Nazca also exhibit DFEs at such depths (Frohlich, 2006). Recent studies have provided seismological evidence of a MOW in the Pacific slab under Japan (e.g., Furumura et al., 2016; Jiang & Zhao, 2011; Kawakatsu & Yoshioka, 2011; Shen & Zhan, 2020), which is characterized by a thermal

parameter of ϕ~5000-7000 km (Frohlich, 2006). Although no such evidence has been reported for the Nazca slab, the existence of a MOW that nucleates DFEs has been postulated from analysis of focal plane solution and centroid depths (Leite Neto & Julià, 2022).

The Brazilian Seismographic Network (RSBR) started operations in 2011, slowly expanding seismic coverage to the West through deployment of broadband stations in the Amazonian region since 2014 (Bianchi et al., 2018). These stations have provided an unprecedented coverage of DFEs with epicenters in the Peru-Brazil region, one of the two segments with regular DFE seismicity in South America (Figure 1) (Frohlich, 2006). Between 2014 and 2022, a total of 42 DFEs with magnitudes between 4.0 and 7.6 Mw and depths between 515 and 655 km occurred in this region, according to the USGS. A total of 25 events happened only in 2015, a year of anomalously intense seismic activity that included a well-studied 7.6 Mw doublet and several aftershocks (e.g., Jiménez et al., 2021; Ruiz et al., 2017; Ye et al., 2016; Zahradník et al., 2017). It is worth noting that studies of DFE sequences spanning a broad range of magnitudes have been uncommon, likely due to the lack of adequate seismic coverage at close distances. Most studies on DFEs, including those in South America, have thus usually focused on the largest ruptures (e.g., Estabrook, 1999; Kanamori et al., 1998; Zahradník et al., 2017). Moreover, a comparison of the reported parameters has often been difficult due to the variety of approaches utilized for retrieving them (e.g., Tibi et al., 2003). Therefore, the unprecedented additional coverage provided by RSBR, coupled with the occurrence of unusual seismic activity in 2015, represents a unique opportunity to investigate the physical mechanisms responsible for the nucleation of DFEs in a warm slab.

In this work we study the seismic source parameters for these 42 DFEs, with the aim of investigating the physical mechanism behind the occurrence of DFEs under South America. We were able to determine seismic moments, corner frequencies, stress drop, radiated energies and radiation efficiencies for a total of 13 events with magnitudes from 4.8 to 7.4 Mw. We show that variations in stress drop and radiation efficiency can be considerable within our study region, reflecting the coexistence of dissipative and brittle rupture. We argue that more dissipative ruptures are controlled by localized hydrated regions near the source, which can eventually dehydrate and induce melting within the fault zone. The occurrence of DFEs is then explained as the result of rupture initiation by transformational faulting followed by thermal runaway. The amount of melting during this last stage would be controlled by the amount of water that can be released through dehydration reactions (e.g., hydrous phase A), through either the latent heat released by the reaction or by shear heating near the fault zone. Moreover, we think that our interpretation reconciles the presence of water in the MTZ, as evidenced by

sublithospheric diamonds, with the existence of a MOW responsible for the nucleation and observed depth-span of DFEs.

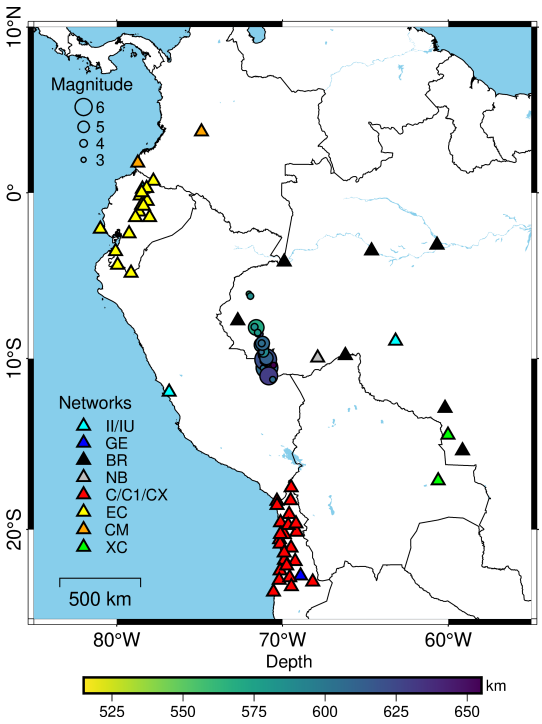

Figure 1. Distribution of the 55 seismic stations and 42 DFEs used in this study. Stations are colored by network. Black and gray stations belong to the RSBR subnetworks (NB and BR). Network codes follow the International Federation of Digital Seismograph Networks (FDSN) standards. A table with station information can be found in the Supporting Information (Table S2). Epicenters for the 2014-2022 deep-focus sequence are color-coded by depth and sized by magnitude, as reported in the USGS catalog (Table S1).

3.2. Data

Our dataset comprises recordings from several broadband stations in South America (Table S2), including those belonging to the international GSN (network codes II and IU) and GEOFON (GE) networks, as well as data from the national networks of Brazil (BR and NB), Colombia (CM), Ecuador (EC), and Chile (C and C1). It also included recordings from the temporary 3-Basin Project (XC) deployment, with stations installed in Uruguay, Argentina, Paraguay, Bolivia and Brazil, and the IPOC seismic network in Chile (CX) (Figure 1). Note that stations from the RSBR (black and gray triangles) were essential to provide upper-hemisphere coverage of the seismic focal sphere. Further details on the dataset can be found in the Open Research section.

As mentioned above, our dataset consisted of 42 DFEs with depths between 515 and 655 km and magnitudes between 4.0 and 7.6 Mw, as reported in the USGS catalog after 2014, coinciding with the deployment of RSBR stations in the Amazon region. As a pre-processing step, P- and S-wave arrival times were marked on the seismograms using the TauP algorithm (Crotwell et al., 1999) and based on the AK135 velocity model (Kennett et al., 1995). We used these times to cut the seismograms into windows starting 2 minutes before the P-wave arrival and lengths equal to one S-P interval after the S-wave arrival time. This time window was found sufficient to encompass the entirety of P- and S-wave energy in the recordings. The instrument responses were then deconvolved from the corresponding seismograms, after removal of the mean and trend and the application of a 5% cosine taper. Next, displacement recordings were rotated into the great-circle-path to ensure the separation of P-SV and SH amplitudes into the rotated components (see examples in Figures S1 and S2).

3.3. Seismic moments, corner frequencies and stress drops

3.3.1. Determination of source and background spectra

To calculate the spectra for each source-station pair we selected all local and regional stations at less than 1500 km from the epicenter and cut the P- and S-wave segments from the corresponding seismograms using time windows of 40 s and 100 s, respectively. These time windows were chosen to comprise the full body wave signal and were set with tolerances of 10% and 20% around the P- and S-wave arrival times, respectively. We retrieved P-wave windows from the vertical components only, while S-wave windows were obtained from all three components. The corresponding noise segments were obtained using the same window lengths, but stopping just right before the beginning of the P-wave window (e.g., Prieto et al., 2004). After the signal and noise segments were obtained, the mean and trend from each of these segments were removed before computing the spectra, which was obtained using the multitaper algorithm available in the open-source Multitaper python package (Prieto, 2022). This algorithm effectively minimizes the inherent limitations of non-parametric approaches (spectral leakage and high variance of the spectrum estimate) by applying multiple tapering and then averaging the resulting spectra employing an adaptive weighting (Thomson, 1982). We adopted a time-bandwidth product of 4 and a total of 6 tapers in all our estimations.

Based on the individual noise spectra computed for each source-station pair, an average background noise spectrum was developed for each station. These spectra are used to assess the signal-to-noise ratio (SNR) at a given station with respect to the individual P- and S-wave

spectra for a given event. After analyzing station averages obtained from the arithmetic mean, the geometric mean, and the median of the individual noise spectra, we selected the geometric mean plus one standard deviation as the background noise spectrum for each station. Estimates from the arithmetic mean were found to be unsuitable due to their sensitivity to outliers; the median and the geometric mean provided similar results, so we chose the geometric mean plus one standard deviation to ensure a careful SNR evaluation (see Figure S3). Note that the method models individual source spectra, so average source spectra were not developed.

Finally, source and background noise spectra were resampled to display uniformly spaced values in the logarithmic scale (e.g., Ide et al., 2003). Note that, if spectra were left with uniformly spaced values in the linear scale, higher frequencies would be more densely sampled in the logarithmic scale and bias the source parameters estimates obtained from them. Additionally, the original number of points for both P- and S-wave spectra was reduced from 4000 and 10000, respectively, to just 100, which were found enough for modeling purposes. To make sure that the spectra can be minimally modeled, only those with at least one decade in the log scale with points above the SNR threshold (SNR ≥ 3) were considered. Also, only events with spectra from at least 5 stations were considered for analysis, ensuring that events are minimally covered azimuthally.

3.3.2. Seismic moments and corner frequencies

To determine the seismic moment ($\boldsymbol{M_0}$) and corner frequency ($\boldsymbol{f_c}$) for the events making up the seismic sequence, we employed the Cluster-Event Method (CEM) of Ko et al. (2012). This method considers clusters of nearby events to empirically constrain Q structure while ensuring stability of the inversion parameters by requiring that: (i) all spectra within a given cluster have the same Q for a given station; and (ii) all spectra for a given event are described by the same values of $\boldsymbol{M_0}$ and $\boldsymbol{f_c}$. These constraints significantly reduce the number of parameters to be inverted and increase the robustness of the inversion. In our implementation, considering the small number of relatively close events, we assumed a single cluster and constrained $\boldsymbol{M_0}$, $\boldsymbol{f_c}$, and Q to be within reasonably tight ranges to speed convergence. Thus, M_0 was forced to stay within ±20% from the previous estimate from either the USGS catalog or the waveform inversion study of Leite Neto & Julià (2022), whichever was available (Table S1), $\boldsymbol{f_c}$ was allowed to vary in a broad range from 0.01 to 50 Hz, and Q was allowed to vary between 100 and 2000. We observed that Q was poorly constrained in most of our inversions, introducing a systematic decrease in the $\boldsymbol{f_c}$ estimates due to the trade-off between $\boldsymbol{f_c}$ and Q

(e.g., Ko et al., 2012). Thus, we decided to fix Q to 1000 for every event-station pair and carry the inversion only for $\boldsymbol{M_0}$ and $\boldsymbol{f_c}$ (see Text S1 for more details).

The misfit function, defined as the L1-norm between observed and modeled spectra, was evaluated with respect to the Brune circular fault model (Brune, 1970; Havskov & Ottemoller, 2010). For each source-station pair, a general misfit was calculated as the sum of the individual misfits for the single P-wave spectrum, which was determined from the vertical seismogram, and up to three S-wave spectra, corresponding to the radial, transverse and vertical components. To prevent S-wave spectra from dominating in the inversion, we adjusted the weighting on the P spectrum based on the number of S spectra being utilized. We solved for the global minimum using the Dual Annealing optimization algorithm implemented in the Scipy Optimization subpackage, which is a global optimization routine based on the combination of the Classic Simulated Annealing (CSA) and the Fast Simulated Annealing (FSA) (Tsallis, 1988; Tsallis & Stariolo, 1996; Xiang et al., 1997). After the classical simulated annealing process, this approach performs a local search around its solution, increasing the accuracy. We configured this routine to perform a maximum of 100 iterations and use an initial temperature of 100000, high enough to avoid entrapment by a local minimum. Uncertainties in $\boldsymbol{M_0}$ and $\boldsymbol{f_c}$ were assessed through bootstrap resampling (Efron & Tibshirani, 1991). For each event, we constructed 100 ensembles, each comprising randomly selected samples from the original set of stations with replacement. The inversion was then performed for every ensemble, allowing us to evaluate the variability and confidence in our estimates.

Using the approaches described above, we were able to determine $\boldsymbol{M_0}$ and $\boldsymbol{f_c}$ for a total of 14 events out of 42, as listed in Table 1. The remaining portion of the sequence did not meet our criteria for analysis due to either spectra with low SNR and/or fewer than five stations available for inversion. In general, the inverted parameters provided satisfactory fits to our observations, especially for the larger events (see Figure 2 and Figures S10-S23). We found $\boldsymbol{f_c^P}$ ranges from 0.16 to 3.7 Hz, $\boldsymbol{f_c^S}$ from 0.13 to 2.7 Hz, and $\boldsymbol{M_0}$ from 2.08 x 10^{16} to 1.54 x 10^{20} N.m (Mw between 4.8 and 7.4). While $\boldsymbol{M_0}$ is well constrained for all events, $\boldsymbol{f_c}$ tends to be less accurate for the smaller events (Mw < 6). More in particular, four events showed considerable uncertainties: event 22 (4.9 Mw), in both $\boldsymbol{f_c^P}$ and $\boldsymbol{f_c^S}$ estimates; event 35 (5.1 Mw), in the $\boldsymbol{f_c^P}$ estimate; and event 3 (5.4 Mw) and event 33 (4.8 Mw) in $\boldsymbol{f_c^S}$ (Figure 3). Therefore, we decided to disregard event 22 from our analysis but retain $\boldsymbol{f_c^S}$ for event 35 and $\boldsymbol{f_c^P}$ for events 3 and 33, thus proceeding with only 13 events. Note that these results show that $\boldsymbol{f_c}$ decreases with $\boldsymbol{M_0}$, but not exactly as $\boldsymbol{M_0 \propto f_c^{-3}}$, suggesting they are not self-similar (e.g., Prieto et al., 2004).

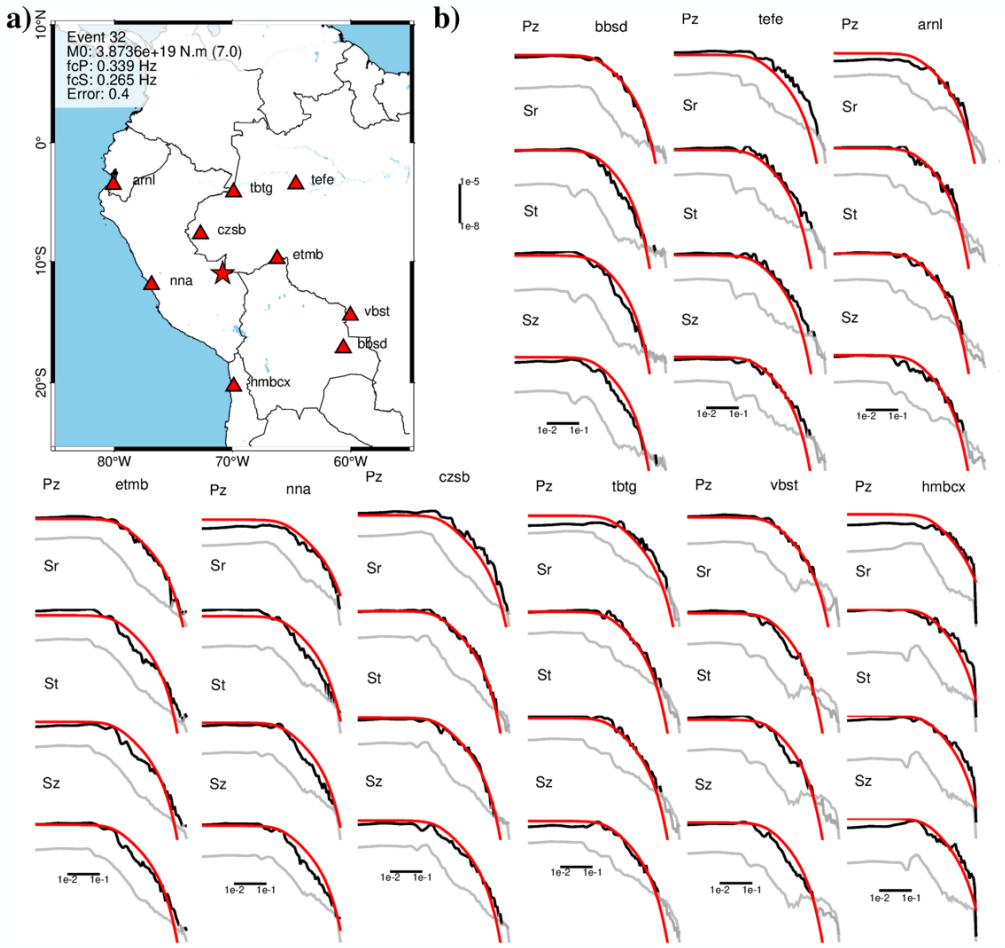

Figure 2. Selection of observed and predicted spectra for event 32 (7.0 Mw). On the map (a), the red star represents the epicenter, while red triangles indicate the stations selected for display in the figure (b). For each selected station, the black, red and light gray lines respectively represent the observed, modeled and background noise spectra. Segments of the observed spectra with low SNR are shown in dark gray and were not considered for inversion. The complete set of stations used in the inversion is displayed in Figure S17.

3.3.3. Stress drops

The static stress drop ($\Delta\boldsymbol{\sigma}$) is an important parameter that quantifies the change in stress around the fault during its rupture (Lay & Wallace, 1995; Venkataraman & Kanamori, 2004). We determined $\Delta\boldsymbol{\sigma}$ from $\boldsymbol{M_0}$ and $\boldsymbol{f_c}$ estimates for each event after assuming a circular source as (Brune, 1970; Eshelby, 1957; Kaneko & Shearer, 2014; Madariaga, 1976):

$$\Delta\boldsymbol{\sigma} = \frac{7}{16}\boldsymbol{M_0}\left(\frac{\boldsymbol{f_c}}{\boldsymbol{k\beta}}\right)^{\mathbf{3}} \quad (1)$$

in which $\boldsymbol{f_c}$ is the corner frequency, $\boldsymbol{\beta}$ is the S-wave velocity, and k is a constant that depends on wave type and the assumed theoretical model (Brune, 1970; Kaneko & Shearer, 2014;

Madariaga, 1976). We used the model derived by Kaneko & Shearer (2014), which considers a circular rupture with a cohesive zone to avoid stress singularity at the rupture front (Madariaga, 1976). For a rupture velocity of $\boldsymbol{V_R = 0.9\beta}$, they found that $\boldsymbol{k = 0.38}$ for P waves, and $\boldsymbol{k = 0.26}$ for S waves. $\boldsymbol{\beta}$ was obtained from the AK135 velocity model based on event's depth (Kennett et al., 1995). Uncertainties in $\boldsymbol{\Delta\sigma}$ were evaluated after propagating uncertainties in both $\boldsymbol{M_0}$ and $\boldsymbol{f_c}$ through differentiation of eq. (1) (e.g., Prieto et al., 2007).

The $\boldsymbol{\Delta\sigma}$ estimated from $\boldsymbol{f_c^P}$ range from 5.1 to 72.1 MPa, while estimates from $\boldsymbol{f_c^S}$ range from 2.8 to 107.6 MPa (Table 1). We determined the average $\boldsymbol{\Delta\sigma}$ for each event based on the individual P and S corner frequency estimates, which resulted in variable values ranging between 5 and 90 MPa. Our confidence bounds are generally small, which reflects the accuracy of our $\boldsymbol{f_c}$ and $\boldsymbol{M_0}$ estimates (Figure 4). It is worth noting that event 32 (Mw 7.0) shows the maximum $\boldsymbol{\Delta\sigma}$ estimate, around 89.8 MPa. We also observed high $\boldsymbol{\Delta\sigma}$ for the two biggest ruptures (Mw 7.4), corresponding to events 8 (43.8 MPa) and 9 (50.3 MPa), and event 34 (Mw 6.7, 34.8 MPa). The rest of the events, on the other hand, showed smaller values, $\boldsymbol{\Delta\sigma} \leq 17$ MPa, with the minimum $\boldsymbol{\Delta\sigma}$ found for event 3 (5.4 Mw, 5.1 MPa). Overall, there appears to be a trend of $\boldsymbol{\Delta\sigma}$ increasing with $\boldsymbol{M_0}$, albeit with considerable dispersion (Figure 4).

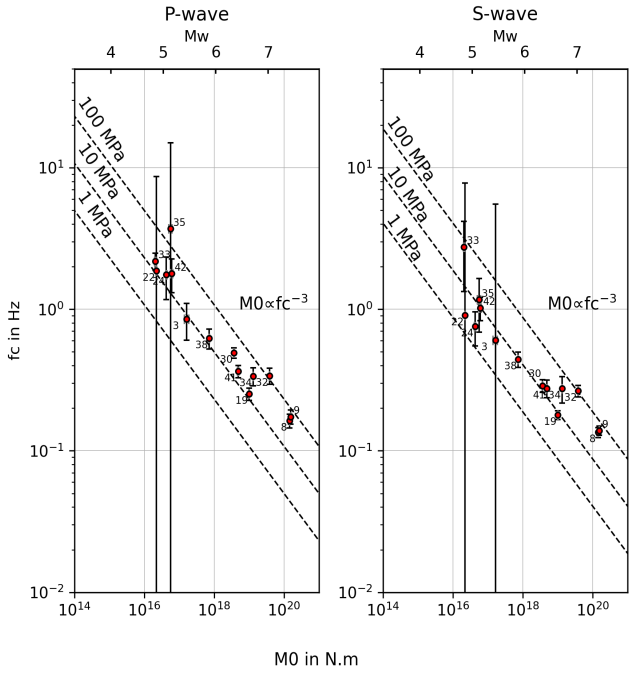

Figure 3. P- and S-wave corner frequencies as a function of seismic moment for the 14 events listed in Table 1. The uncertainties in $\boldsymbol{f_c}$ and $\boldsymbol{M_0}$ are represented by vertical black bars and horizontal gray bars, respectively. Dashed black lines are for reference stress drops of 1, 10 and 100 MPa.

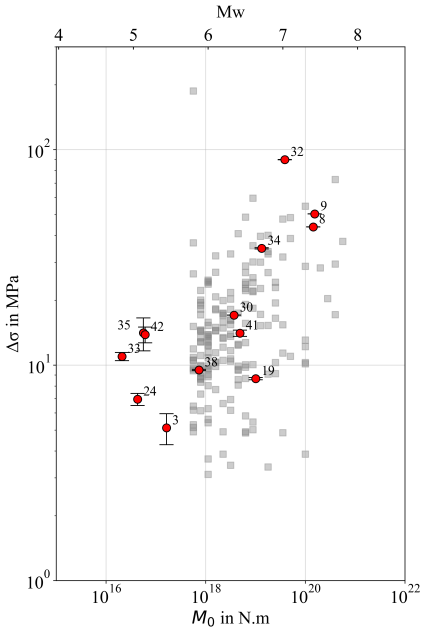

Figure 4. Average $\Delta\boldsymbol{\sigma}$ for the 13 events in Table 1 plotted against the corresponding seismic moments. Solutions are numbered as in Tables 1 and S1. Vertical bars represent the estimate's uncertainties. Gray squares represent estimates from Poli & Prieto (2016), comprising 180 DFEs ($5.8 \leq Mw \leq 7.8$) from several subduction zones between 2000 and 2016.

Event	f_c^P(Hz)	f_c^S(Hz)	M_0 (N.m)	M_w	$\Delta\sigma^P$(MPa)	$\Delta\sigma^S$(MPa)	$\Delta\sigma$(MPa)	E_R(J)	ext%	η_R
3	0.851 ± 0.246	0.604 ± 4.921	$1.64x10^{17}$±$0.23x10^{17}$	5.4	5.1±0.84	-[1]	5.1±0.84	$5.80x10^{12}$	67	1.58
8	0.163 ± 0.018	0.135 ± 0.011	$1.44x10^{20}$±$0.16x10^{5}$	7.4	31.6±0.04	56.0±0.03	43.8±0.04	$1.06x10^{16}$	43	0.38
9	0.174 ± 0.02	0.139 ± 0.010	$1.54x10^{20}$±$0.15x10^{5}$	7.4	38.8±0.06	61.8±0.02	50.3±0.04	$1.23x10^{16}$	32	0.37
19	0.252 ± 0.025	0.179 ± 0.013	$1.01x10^{19}$±$0.11x10^{18}$	6.6	8.2±0.10	9.1±0.11	8.6±0.10	$1.49x10^{14}$	22	0.39
22	1.87 ± 6.783	0.908 ± 6.878	$2.23x10^{16}$±$0.43x10^{15}$	4.9	-[1]	-[1]	-	-	-	-
24	1.756 ± 0.583	0.756 ± 0.205	$4.30x10^{16}$±$0.13x10^{16}$	5.1	11.1±0.76	2.8±0.14	6.9±0.45	$4.31x10^{11}$	59	0.34
30	0.491 ± 0.041	0.288 ± 0.029	$3.70x10^{18}$±$0.51x10^{3}$	6.3	20.9±0.01	13.2±0.01	17.0±0.01	$4.81x10^{13}$	39	0.18
32	0.339 ± 0.044	0.265 ± 0.025	$3.87x10^{19}$±$0.82x10^{4}$	7.0	72.1±0.16	107.6±0.09	89.8±0.12	$1.95x10^{16}$	49	1.33
33	2.184 ± 0.301	2.757 ± 1.420	$2.08x10^{16}$±$0.86x10^{15}$	4.8	11.0±0.48	-[1]	11.0±0.48	$6.79x10^{10}$	68	0.07
34	0.336 ± 0.049	0.276 ± 0.059	$1.33x10^{19}$±$0.20x10^{4}$	6.7	25.5±0.08	44.2±0.43	34.8±0.25	$1.13x10^{15}$	25	0.56
35	3.698 ± 11.315	1.167 ± 0.480	$5.61x10^{16}$±$0.59x10^{16}$	5.1	-[1]	14.1±2.46	14.1±2.46	$2.06x10^{12}$	52	0.59
38	0.625 ± 0.101	0.442 ± 0.055	$7.30x10^{17}$±$0.31x10^{16}$	5.9	9.0±0.08	10.0±0.06	9.5±0.07	$1.15x10^{13}$	47	0.38

41	0.364 ± 0.037	0.276 ± 0.039	$4.88 \times 10^{18} \pm 0.15 \times 10^{18}$	6.4	11.9±0.38	16.2±0.55	14.1±0.46	4.23×10^{14}	50	1.40
42	1.784 ± 0.475	1.022 ± 0.192	$6.07 \times 10^{16} \pm 0.42 \times 10^{16}$	5.2	17.4±1.55	10.2±0.78	13.8±1.17	3.92×10^{11}	25	0.10

[1]High uncertainties in the corresponding $\boldsymbol{f_c}$ precluded the correct determination of the $\Delta\boldsymbol{\sigma}$.

Table 1. Inverted parameters for 14 selected events in the 2014-2022 deep-focus sequence.

3.4. Radiated energies, scaled energies and radiation efficiencies

3.4.1. Radiated energies from body-wave spectra

The radiated energy ($\boldsymbol{E_R}$) was determined for each event as the sum of the P- and S-wave radiation energies, $\boldsymbol{E_R^P}$ and $\boldsymbol{E_R^S}$ respectively (Boatwright & Fletcher, 1984; Mayeda & Walter, 1996; Prieto et al., 2004). We used the P-wave vertical displacement spectrum to determine $\boldsymbol{E_R^P}$, and the vectorial sum of the radial, transverse, and vertical S-wave displacement spectra to determine $\boldsymbol{E_R^S}$. All displacement spectra were corrected for attenuation and geometrical spreading and then transformed into moment rate spectra by differentiation (Havskov & Ottemoller, 2010). We then calculated an average spectrum for each phase based on all available spectra for a given event. In this step, only portions of the spectra with SNR ≥ 3 were considered. From the average moment-rate spectrum, $\boldsymbol{\omega M(\omega)}$, we determined the energy in the frequency domain following (Baltay et al., 2010; Mayeda & Walter, 1996):

$$\boldsymbol{E_R^{P,S} = \frac{1}{4\pi^2 \rho c^5} \int_0^\infty |\omega M(\omega)|^2 d\omega} \quad (2)$$

where $\boldsymbol{\omega}$ is the angular frequency, $\boldsymbol{M(\omega)}$ is the moment spectrum, $\boldsymbol{c}$ is either $\boldsymbol{\alpha}$ (P-wave velocity) or $\boldsymbol{\beta}$ (S-wave velocity), and $\boldsymbol{\rho}$ is density. To assess the integral in eq. (2), the moment-rate spectrum was extrapolated to both low and high frequencies using a low-frequency average and a $\boldsymbol{\omega^{-1}}$ fall-off rate, respectively, and $\boldsymbol{\rho}$, $\boldsymbol{\alpha}$ and $\boldsymbol{\beta}$ were estimated from the AK135 velocity model (Kennett et al., 1995) according to hypocentral depth. We set the extrapolation limits for each average spectrum to the highest and lowest spectral amplitude values that were above the SNR threshold, keeping a record of the amount of energy that was extrapolated for future interpretations.

$\boldsymbol{E_R}$ estimates vary from 6.8 x 10^{10} J to 1.9 x 10^{16} J among the sequence (Table 1). In general, most $\boldsymbol{E_R}$ values represent $\boldsymbol{E_R^S}$ (Figure 5a-c), which can range from 3 to 120 times $\boldsymbol{E_R^P}$ (Figure 5d). From Figure 5c, it is clear that $\boldsymbol{E_R}$ is roughly proportional to $\boldsymbol{M_0}$, although we observed that some similar-sized earthquakes show quite different values of $\boldsymbol{E_R}$. First, $\boldsymbol{E_R}$ from event 41 (6.4 Mw) is notably 9 times larger than the estimate from event 30 (6.3 Mw). Second, our estimate for event 32 (Mw 7.0), 1.9 x 10^{16} J, is slightly larger than our estimate for the

largest ruptures in the sequence (events 8 and 9, 7.4 Mw) which showed remarkably similar $\boldsymbol{E_R}$ values of 1.06 x 10^{16} J and 1.23 x 10^{16} J, respectively. Finally, event 34 (6.7 Mw) showed much higher $\boldsymbol{E_R}$ than event 19 (6.6 Mw). Nevertheless, we note that more than 50% of the $\boldsymbol{E_R}$ for events 3, 24, 33, and 35 came from the extrapolated, high-frequency portion of the moment-rate spectra and, therefore, must be considered with care.

The scaled energy ($\boldsymbol{E_R/M_0}$) was also examined and observed to be quite variable within the sequence (Figure 6). Clearly, event 32 showed the highest value, displaying a disproportionate release of energy from its rupture process. Events 8, 9, 34 and 41 also showed relatively high energy-to-moment ratios, while the rest of the sequence showed considerably smaller values. The scaled energy found for event 35 (5.1 Mw) is considerably higher than estimates from similar-size DFEs (events 24 and 42). Disregarding event 33, for which a 68% of the energy was contributed by the extrapolated portion of the spectrum, event 42 displayed the smaller scaled energy. Overall, scaled energies display a suggestive but not clear trend of scaled energy increasing with magnitude (Figure 6).

3.4.2. Radiation efficiency

Based on the $\boldsymbol{M_0}$, $\boldsymbol{\Delta\sigma}$, and $\boldsymbol{E_R}$ estimates for each event, we determined the radiation efficiency ($\boldsymbol{\eta_R}$) as (e.g., Kanamori & Brodsky, 2004):

$$\boldsymbol{\eta_R = \frac{2\mu}{\Delta\sigma}\frac{E_R}{M_0}} \tag{3}$$

in which the shear modulus ($\boldsymbol{\mu}$) was calculated based on the S-wave velocity value at the source. The $\boldsymbol{\eta_R}$ quantifies the proportion of energy released as elastic waves relative to the energy dissipated in the rupture process (Poli & Prieto, 2016). By definition $\boldsymbol{\eta_R}$ varies between 0, meaning that no energy was radiated as seismic waves, and 1, when no energy was dissipated mechanically and all energy budget, after subtracting the energy lost by friction, is transmitted as seismic waves (Kanamori & Brodsky, 2004). Values of $\boldsymbol{\eta_R}$ larger than 1 can sometimes be obtained, possibly reflecting either imprecise estimates of $\boldsymbol{E_R}$ and/or $\boldsymbol{\Delta\sigma}$, a complex stress release process, the use of an inaccurate model to calculate $\boldsymbol{\eta_R}$, or an undershoot rupture (Nishitsuji & Mori, 2014; Venkataraman & Kanamori, 2004).

We observed quite variable $\boldsymbol{\eta_R}$ values for the sequence under study, with values ranging from as high as 1.58 to as low as 0.07 (Figure 7). The smallest $\boldsymbol{\eta_R}$ value was found for event 33, which is the smallest event in the sequence, while the maximum value was observed for event 3 (5.4 Mw). These two events, however, had almost 70% of their $\boldsymbol{E_R}$ extrapolated and may not be reliable. Aside from these two extreme events, $\boldsymbol{\eta_R}$ values still vary considerably

(0.1 to 1.4); however, if we disregard efficiency values above 1.0, all estimates are roughly between 0.2 and 0.6. Within this reduced range, events 34 and 35 had relatively high $\boldsymbol{\eta_R}$ of ~0.6, while the rest of the events showed $\boldsymbol{\eta_R}$ < 0.4 and an average $\boldsymbol{\eta_R}$ of 0.3, meaning that most of the events involved relatively small $\boldsymbol{\eta_R}$ values (Table 1). We did not find any size dependency for $\boldsymbol{\eta_R}$; in fact, similar-size events showed quite different efficiencies (see for instance events 30, 41, 19 and 34 showing $\boldsymbol{\eta_R}$ equal to 0.2, 1.4, 0.4 and 0.6, respectively).

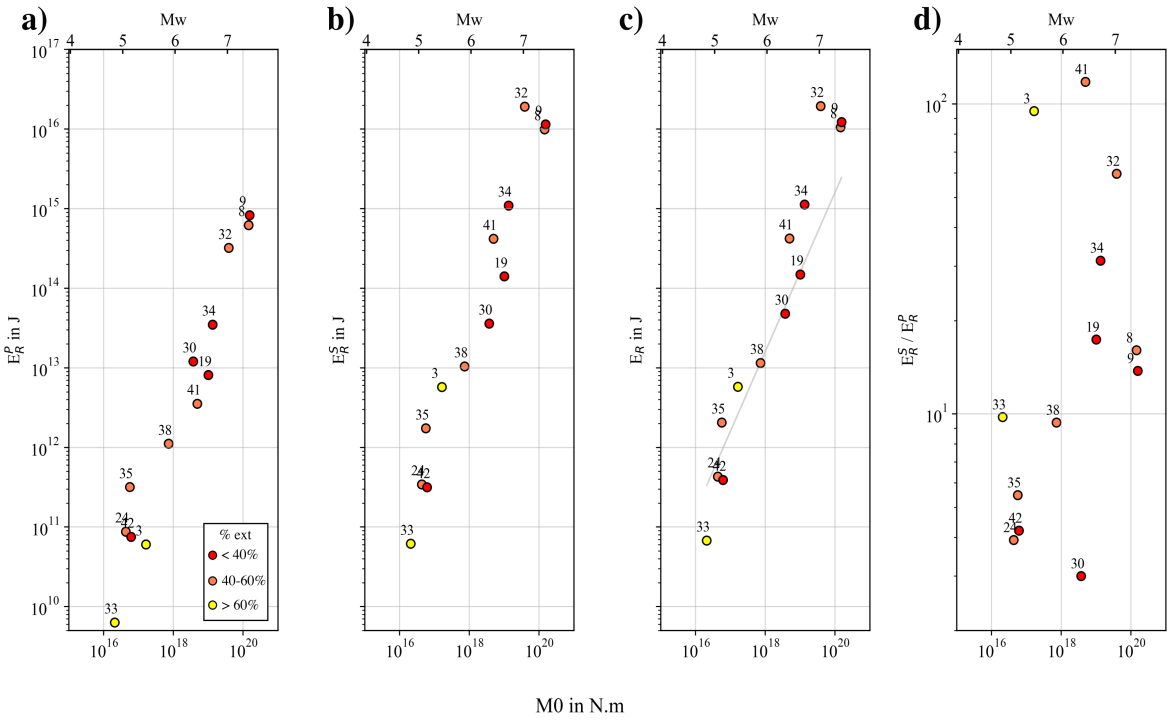

Figure 5. Estimates of $\boldsymbol{E_R}$ from the 13 events in Table 1. a) energy radiated as P-wave, $\boldsymbol{E_R^P}$; b) energy radiated as S-wave, $\boldsymbol{E_R^S}$; c) total radiated energy, $\boldsymbol{E_R}$; d) ratio between $\boldsymbol{E_R^S}$ and $\boldsymbol{E_R^P}$ as a function of the seismic moment. Events are numbered as in Table 1 and color-coded by the amount of extrapolated energy in $\boldsymbol{E_R}$. Solid gray line in c represents the $\boldsymbol{E_R}$ = 1.6 x 10^{-5} $\boldsymbol{M_0}$ empirical relationship from Choy & Boatwright (1995).

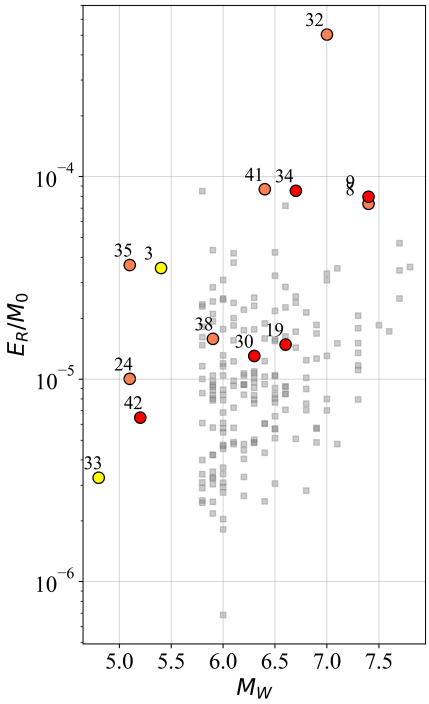

Figure 6. Scaled energy plotted as function of magnitude. Events are color-coded by the amount of extrapolation and labeled as in Table 1. Gray squares are estimates from Poli & Prieto (2016).

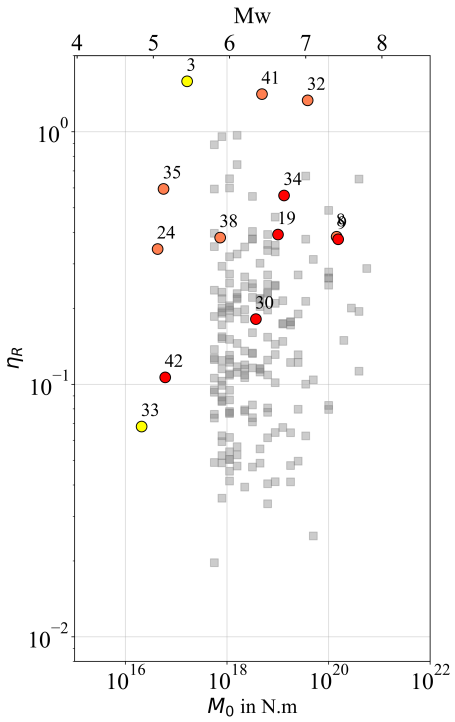

Figure 7. Radiation efficiency plotted as function of the seismic moment. Events are color-coded by the amount of extrapolation and labeled as in Table 1. Gray squares are estimates calculated based on the apparent stresses and stress drops of Poli & Prieto (2016).

3.5. Discussion

3.5.1. Variability in Δσ, radiated energy and seismic efficiency

As shown in Figure 4, Δσ calculated from $\boldsymbol{f_c}$ and $\boldsymbol{M_0}$ (5-90 MPa) are all within the expected range of 1-100 MPa (e.g., Liu et al., 2020; Poli & Prieto, 2016) and hint at a mild correlation between Δσ and $\boldsymbol{M_0}$. This correlation was already observed from both intermediate-depth and deep-focus earthquakes (e.g., Liu et al., 2020; Nishitsuji & Mori, 2014; Poli & Prieto, 2016; Prieto et al., 2013). We found very high Δσ for event 32 (~90 MPa) and relatively high Δσ for events 8, 9 and 34 (35-50 MPa), when compared to the rest of the sequence (≤ 17 MPa). Also, the Δσ found for events 8 and 9 are considerably higher than previous estimates (2.3-19.3 MPa) (Ruiz et al., 2017; Ye et al., 2016). Comparisons between Δσ from different approaches are usually difficult to make, but it is noteworthy that we determined Δσ based on well-constrained $\boldsymbol{f_c}$ and $\boldsymbol{M_0}$, which results in more reliable estimates than calculations from rupture speed (e.g., Ye et al., 2016). No depth dependency for Δσ was observed, as previously noted by Liu et al. (2020) from several globally-distributed deep-focus earthquakes in the 6.0-8.2 Mw range. Note, however, that our results are now filling a significant gap at Mw ≤ 5.8 (Figure 4) and provide observations for events smaller than those in the previous global study of Poli & Prieto (2016). Also, although Δσ is known to be difficult to constrain, our methodology was consistently applied for all events within the 2014-2022 sequence, which ensures the robustness of our comparisons.

Globally, small-to-moderate shallow earthquakes display $\boldsymbol{E_R^S}$ values that are 9-17 times that of $\boldsymbol{E_R^P}$ (Abercrombie, 1995; Boatwright et al., 1991; Prieto et al., 2004; Viegas et al., 2010), although some events in India suggest that $\boldsymbol{E_R^S}$ can reach up to 100 times $\boldsymbol{E_R^P}$ (S. Kumar et al., 2023; V. Kumar et al., 2016, 2019). Most of our events showed $\boldsymbol{E_R^S/E_R^P}$ < 20, so our observations are mostly consistent with previous estimates (Figure 5d). Events 3, 32, 34 and 41 displayed large ratios ranging between 30 and 120 (Figure 5d). Disregarding event 3, which had ~70% of its $\boldsymbol{E_R}$ extrapolated, we are thus observing 3 large-size events (Mw 6.4-7.0) with anomalously high $\boldsymbol{E_R^S/E_R^P}$ ratios. Note that the most energetic event (event 32) has an $\boldsymbol{E_R^S}$ estimate that is nearly 60 times larger than the $\boldsymbol{E_R^P}$ estimate (compare Figure 5a-c). High $\boldsymbol{E_R}$ for events 34 and 41 are also related to high $\boldsymbol{E_R^S}$, as inferred from their $\boldsymbol{E_R^S/E_R^P}$ ratios of 31 and 118, respectively. The ratio of 118 is notably higher than observed in previous studies.

To confirm that events 32, 34 and 41 are anomalously energetic, we compared their seismograms with similar-size earthquakes at select stations. We were careful to select nearby

stations away from nodal planes. It is worth noting that focal mechanisms from the Peru-Brazil segment usually show a consistent normal faulting pattern (Leite Neto & Julià, 2022). For the Mw 7.0 event 32, we compared its waveforms with those from the Mw 6.7 event 34 (Figure 8). We observe that, for frequencies above 0.05 Hz, the S-wave amplitude content relative to the P-wave amplitude content is larger for event 32 than for event 34. This observation explains the disproportionate $\boldsymbol{E_R^S/E_R^P}$ value for event 32 and why it was anomalously energetic (Figure 5c-d). We also compared its waveforms with those from the Mw 7.4 event 8 (Figure S7), with similar conclusions. Other comparisons (event 34 with the Mw 6.6 events 19, and event 41 with Mw 6.3 event 30) further confirmed this anomalous S-wave energy release at higher frequencies (Figures S5-S8). It is tempting to infer that events with magnitude above 6.4 Mw tend to release more energy compared to smaller ones.

We observe that, in general, our $\boldsymbol{E_R}$ estimates tend to increase with $\boldsymbol{M_0}$, as predicted by the empirical relationship derived from globally distributed shallow earthquakes of Choy & Boatwright (1995) (Figure 5c). However, events 8, 9, 32, 33, 34 and 41 are at odds with this observation, although event 33 had almost 70% of its energy estimate extrapolated. Overall, scaled energies are all below 10^{-4}, in agreement with independent compilations (e.g., Kanamori & Brodsky, 2004), and suggest that they are proportional to earthquake magnitude, although it is less apparent if we disregard the two extreme values (events 33 and 32). However, as demonstrated above, event 32 was indeed very energetic and yields a robust observation for an anomalously high scaled energy. In any case, the scaling (or lack thereof) between $\boldsymbol{E_R}$ and $\boldsymbol{M_0}$ remains inconclusive due to large uncertainties in $\boldsymbol{E_R}$, with some authors advocating for it (Abercrombie, 1995; Mayeda & Walter, 1996) and others arguing against it (Choy & Boatwright, 1995; Ide et al., 2003; Ide & Beroza, 2001; Prieto et al., 2004). If the scaling were real, it would imply that larger ruptures are more efficient in releasing energy as seismic waves (Prieto et al., 2004).

The variation in source parameters reported in the previous sections results in a notable variability in seismic efficiency within the DFE sequence under study. We found that most of the sequence showed $\boldsymbol{\eta_R} < 0.4$, but some discrepant values were observed. Discrepant events included: (i) Mw 6.4 event 41 and Mw 7.0 event 32 with $\boldsymbol{\eta_R} \geq 1.3$; and (ii) Mw 5.1 event 35 and Mw 6.7 event 34 with $\boldsymbol{\eta_R} \sim 0.6$. We also found no size dependency. The very high $\boldsymbol{\eta_R}$ obtained for events 41 and 32 resulted from their high scaled energies (Figure 6), produced by the disproportionate release of $\boldsymbol{E_R}$ during their ruptures (Figure 5). It is noteworthy that event 32 also involved the highest $\Delta\sigma$ within the sequence, and thus $\boldsymbol{E_R}$ for this event was remarkably

high and yielded an also high $\boldsymbol{\eta_R}$ = 1.3. The relatively high $\boldsymbol{\eta_R}$ found for event 34 can also be explained through its high scaled energy (Figure 6). Realize that, in spite of events 34 and 41 having similar scaled energies, $\boldsymbol{\eta_R}$ for event 34 is smaller because of its higher Δσ of 34.8 MPa. Similarly, a high $\boldsymbol{\eta_R}$ for event 35 is also related to a high $\boldsymbol{E_R}$, especially when compared to events with similar sizes and Δσ (events 24 and 42). Events 42 and 30 presented the lowest $\boldsymbol{\eta_R}$ among our DFEs, resulting from their relatively low scaled energies compared to the rest of the sequence (Figure 6). The $\boldsymbol{\eta_R}$ estimated for the 2015 doublet are in agreement with previous estimates (Ruiz et al., 2017).

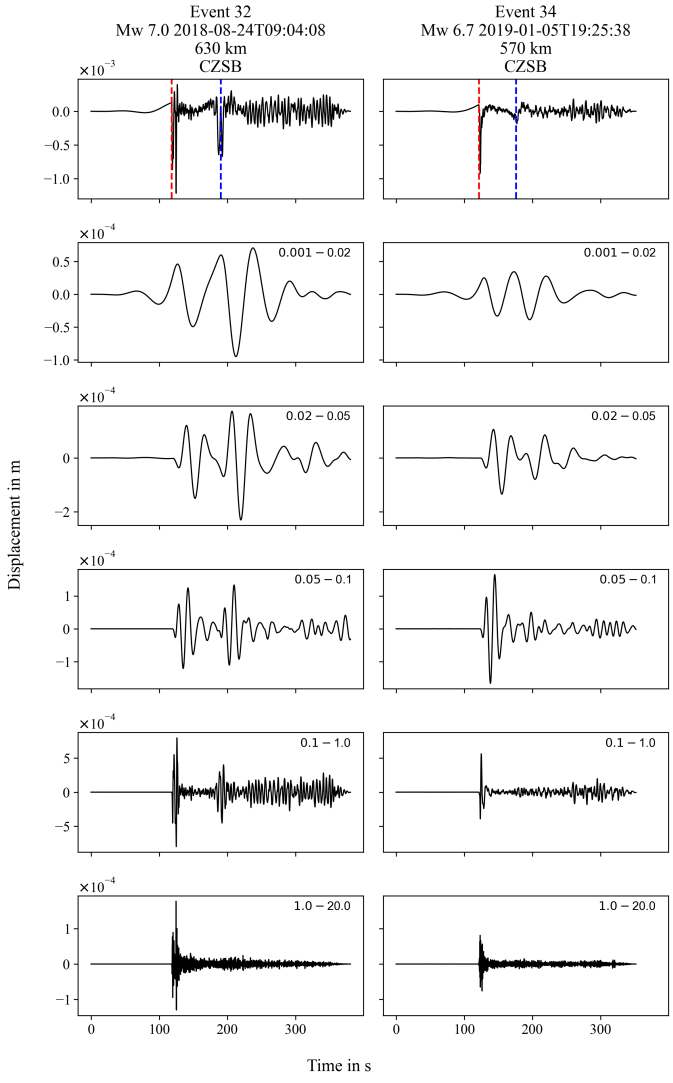

Figure 8. Comparison between vertical seismograms for event 32 and event 34 at station CZSB at different frequency ranges. P- and S-wave arrivals are shown as dashed red and blue lines on the broadband seismograms (upper panels). The frequency ranges used for filtering are shown in the upper right corner of each panel.

3.5.2. Nucleation of DFEs along the Peru-Brazil segment

Large DFEs (Mw > 7) in South America (Nazca), and in other warm subjecting plates such as Japan, are usually the product of very dissipative ruptures characterized by very low efficiencies (η_R < 0.1) (Estabrook, 1999; Tibi et al., 2003; Venkataraman & Kanamori, 2004). For instance, because the 1994 Mw 8.2 Bolivia earthquake was characterized by a very low η_R of ~0.04, high Δσ of 110-283 MPa and slow rupture velocity of 1-2 km/s, it is widely accepted that melting assisted such large slip over a relatively small area (40x40 km^2) (Goes & Ritsema, 1995; Ihmlé, 1998; Kanamori et al., 1998; Kikuchi & Kanamori, 1994; Zhan et al., 2014). The 1970 Mw 8.1 Colombia earthquake and the 1963 Mw 7.7 Peru-Bolivia earthquake also displayed very low η_R ~0.01 and low rupture speeds (2 km/s), but low-to-moderate Δσ of 39.4 and 18 MPa, respectively (Estabrook, 1999). The 1991 Mw 7.2 Argentina earthquake, on the other hand, displayed a cold slab-like behavior. The high η_R = 0.3, high rupture speed of 3.5 km/s and low Δσ of 5 MPa reported for this event were interpreted as due to little melting during its rupture, possibly related to its nucleation in a relatively colder section of the Nazca slab (Tibi et al., 2003). For comparison, some large DFEs (Mw 7.0-7.9) in cold slabs (e.g., Fiji-Tonga, Bonin and Mariana) showed η_R ranging from 0.1 to 0.6 (e.g., Tibi et al., 2003).

Similar to the Argentina earthquake, we observed η_R in the 0.34-0.39 range for several events in the Peru-Brazil sequence under study (events 8, 9, 19, 24 and 38, 5.1-7.4 Mw). In addition, previous studies pointed to relatively large rupture speeds, between 2.25 and 3.2 km/s, for events 8 and 9 (e.g., Ruiz et al., 2017). More efficient ruptures (η_R ~ 0.6) were also observed within the Peru-Brazil sequence for event 34 (6.7 Mw) and event 35 (5.1 Mw), even events with η_R > 1 (event 32, 7.0 Mw; event 41, 6.4 Mw) that suggested two very efficient or brittle-like ruptures. Events 30 (6.3 Mw) and 42 (5.2 Mw), on the other hand, presented the lowest efficiencies ($\eta_R \leq 0.18$) within the sequence, but still higher than estimates found in Colombia and Bolivia.

The Nazca plate is often regarded as a warm plate because its thermal parameter is under 2500 km (Frohlich, 2006). Note that this parameter is obtained from plate age and subduction speed, which characterize the subducting plate at shallow depths and do not necessarily reflect its thermal structure at large depths. Indeed, most of our η_R seem consistent with a relatively cold segment of the Nazca plate as they contrast with those reported for other (warmer) segments (e.g., Colombia and Bolivia). One possibility is that this segment of the Nazca plate be thermally composite, with a warm upper half consistent with the observed thermal parameter, and a cold lower-half consistent with large efficiencies. Interestingly, a

composite thermal structure has been proposed due to either an abrupt change in the age of the subducting lithosphere (Engebretson & Kirby, 1992; Kirby et al., 1995; Okal & Bina, 1994) or to a reduction in subduction speed caused by the subduction of the Nazca ridge (Leite Neto & Julià, 2022). Both hypotheses propose the transition would occur at around 500 km depth and explain the nucleation of DFEs within a narrow 500-700 km depth range through a thin MOW preserved in the interior of the cold lower half of the slab. If this were correct, ruptures could be being nucleated through transformational faulting within a thin MOW and propagated beyond its limits via thermal runaway (Zhan, 2017).

Counterintuitively, however, we found no relationship between $\boldsymbol{\eta_R}$ and $\boldsymbol{M_0}$ suggestive of event size being related to increased viscosity reduction or melting in the fault zone. Furthermore, we found no clear spatial pattern in $\boldsymbol{\eta_R}$ that would indicate any regional patterns within the slab (Figure S9). The two $\boldsymbol{\eta_R}$~ 0.6 happened at the north end of the sequence, but the two $\boldsymbol{\eta_R}$ > 1 happened at distant locations separated by events with $\boldsymbol{\eta_R}$ < 0.4. It is thus possible that very local physical conditions within the source region be controlling the dissipative (lower $\boldsymbol{\eta_R}$) or brittle-like (higher $\boldsymbol{\eta_R}$) character of the ruptures. We thus propose that the character of the rupture depends on small-scale heterogeneities within the source region (Figure 9). Such heterogeneities could be related to localized hydrated mantle rocks formed by deep hydration at outer rise faults (e.g., Fujie et al., 2018; Kita & Ferrand, 2018; Mao et al., 2022; Ranero et al., 2003). In this model, the observed brittle-like ruptures would occur in specific regions of the slab where little or no dehydration is expected to occur, thus involving little or no melting during its propagation via thermal runaway. Regions where considerable amounts of water can be released by dehydration, on the other hand, could explain less efficient ruptures through increased amounts of melt.

Moreover, note that dehydration reactions could assist transformational faulting through either water precipitation around the grains and/or through the release of elevated stresses that would be transmitted to the MOW (Ferrand, 2019; Ferrand et al., 2017; Mao et al., 2022). Conversely, transformational faulting itself could promote dehydration reactions through the release of latent heat or through temperature increase near the fault zone by shear heating. The water and heat released from these processes would allow for more or less melting in the fault zone, which would depend on the amount of fluids that can be released. This interplay between heat released by transformational faulting and water released by dehydration reactions would ultimately be responsible for the short-scale variations in seismic efficiency.

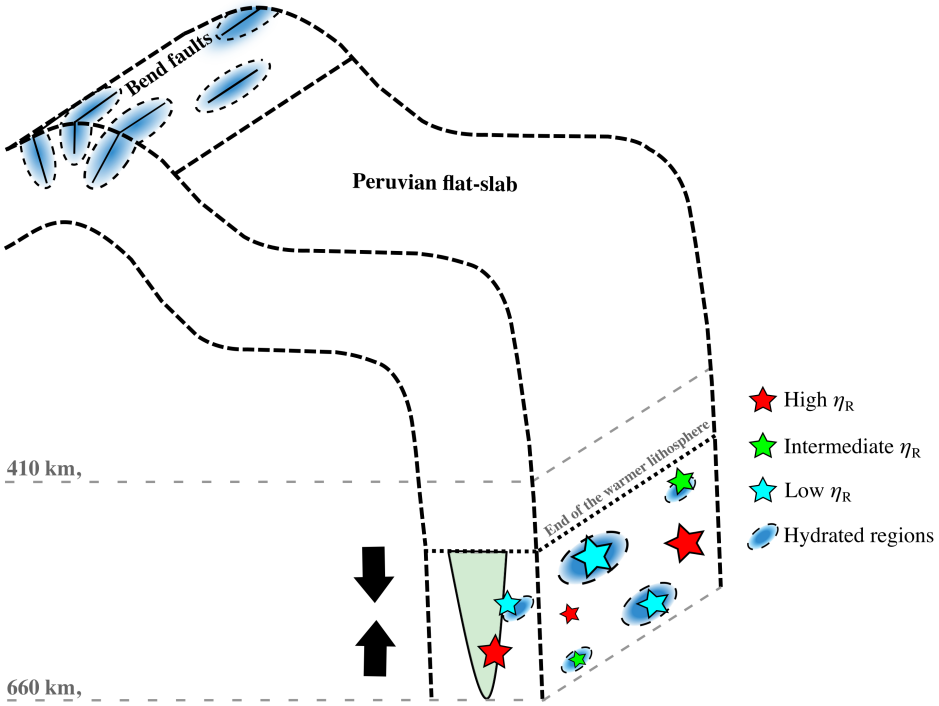

Figure 9. Schematic model proposed to explain variable $\boldsymbol{\eta_R}$ for DFEs in the Peru-Brazil segment. Outer rise faults promote localized deep hydration of mantle rocks that can survive down to MTZ depths in the form of small-scale slab heterogeneities. DFEs are explained as the result of transformational faulting and thermal runaway controlled by the dehydration reactions in such hydrated regions near the source. Transformational faulting in a preserved MOW could explain the confinement of DFEs to a narrow depth range (~500-700 km). The more or less dissipative behavior of the rupture is thus explained by the amount of melting involved in the thermal runaway step, which is possibly controlled by the amount of fluids released by the dehydration reactions when available.

As a final note, because water enhances olivine phase transformations (e.g., Du Frane et al., 2013; Hosoya et al., 2005; Kubo et al., 1998), it has been assumed that the presence of a MOW must necessarily be linked to a dry oceanic lithosphere, suggesting the simultaneous occurrence of dehydration and transformational faulting is incompatible (Du Frane et al., 2013; Kawakatsu & Yoshioka, 2011; Shen & Zhan, 2020; Zhan, 2020). However, there has been evidence that hydrous phase A in the subducting lithosphere may act as a sponge in the MTZ up to ~1000 º C, thus avoiding saturation of olivine and wadsleyite and preserving the MOW (Ishii & Ohtani, 2021). The eventual dehydration of hydrous phase A under high enough temperatures would favor the fast exothermic reactions required for transformational faulting to occur. In this case, water could play a role in the nucleation of anticracks and in allowing for more melting in the fault zone. Water as a catalyst of DFEs was already proposed by Mao et

al. (2022) to explain higher b-values found in regions of Japan where the lithospheric mantle of the Pacific plate is expected to be highly hydrated. Also, sublithospheric diamonds originated from the MTZ are strong evidence that water is being released at depths where DFEs occur (Pearson et al., 2014; Shirey et al., 2021; Wiens, 2021).

3.6. Conclusions

We determined seismic source parameters ($\boldsymbol{M_0}$, $\boldsymbol{f_c}$, Δσ, $\boldsymbol{E_R}$ and $\boldsymbol{\eta_R}$) for a total of 13 DFEs (4.8 ≤ Mw ≤ 7.4) between 2014 and 2022 in the Peru-Brazil branch. The obtained $\boldsymbol{f_c}$ (0.13-3.7 Hz) tend to decrease with $\boldsymbol{M_0}$, but not as predicted by self-similarity, resulting in notable variations in $\boldsymbol{\Delta\sigma}$ (5.1-89.8 MPa). $\boldsymbol{E_R}$ estimates are within the 6.8×10^{10}-1.9×10^{16} J range and are generally proportional to $\boldsymbol{M_0}$, although some large events (Mw > 6.4) displayed a disproportional release of $\boldsymbol{E_R}$. $\boldsymbol{\eta_R}$ presented remarkable variability within the sequence, ranging from 0.1 to 1.4. Particularly, two events showed $\boldsymbol{\eta_R} > 1$, implying in very efficient ruptures, while other two events presented $\boldsymbol{\eta_R} \leq 0.18$, evidencing more dissipative events. Given the relatively small source area we argue that, at the least, our relative efficiency estimates are robust, meaning that the large variability of seismic efficiency is a real feature. We thus propose that earthquakes are able to occur in this region due to the presence of a MOW preserved within a cold slab segment attached to the warm Nazca plate at MTZ depths. Faulting would then initiate by transformational faulting and then further propagate by thermal runaway. In the propagation stage, more or less melting in the fault zone could explain variable $\boldsymbol{\eta_R}$, and the amount of melting would depend on the presence of small-scale hydrated regions near the source. These hypothesized heterogeneities could be possibly linked to deep hydration promoted by bend faults at the outer rise.

Acknowledgments

GSLN expresses gratitude to the Coordenação de Aperfeiçoamento de Pessoal de Nível Superior (CAPES) for his PhD scholarship and for his exchange scholarship (Programa de Doutorado Sanduíche no Exterior - PDSE/CAPES). JJ is grateful to the Conselho Nacional de Desenvolvimento Científico e Tecnológico (CNPq) for their support, provided through a research grant (award n. 434807/2018-4) and a continuing research fellowship (award n. 310261/2023-6). We thank the Instituto de Astronomia, Geofísica e Ciências Atmosféricas of the Universidade de São Paulo (IAG/USP) for providing access to data from the 3-Basin Project network (XC).

Open Research

All data used in this work are made available as a Zenodo dataset (https://doi.org/10.5281/zenodo.10685298). This dataset comprises stations from different networks distributed over the South American continent, which are summarized in Table S2. In Brazil, we used data from the University of Brasilia Seismic Network (BR), the Rede Sismográfica do Nordeste do Brasil (NB), both belonging to the Brazilian Seismic Network (RSBR), and data from the temporary 3-Basin Project (XC) (Assumpção & Bianchi, 2016), which also includes a station in Bolívia. Data from both RSBR and XC are open and can be obtained through the FDSNWS server (http://seisrequest.iag.usp.br/fdsnws/dataselect/1/) from the USP Seismological Center (USPSC). In Chile, we used data from three networks: the Red Sismológica Nacional (C1) (Universidad de Chile, 2012), the Chilean National Seismic Network (C), and the Plate Boundary Observatory Network Northern Chile/IPOC seismic network (CX) (GFZ German Research Centre for Geosciences; Institut des Sciences De l'Univers-Centre National de la Recherche CNRS-INSU, 2006). We also used stations from the Red Sismológica Nacional de Colombia (CM) (Servicio Geológico Colombiano, 1993) and the Ecuador Seismic Network (EC). Data from international networks were also included: GEOFON (GE) (GEOFON Data Centre, 1993), and GSN (II and IU) (Scripps Institution of Oceanography, 1986; Albuquerque Seismological Laboratory/USGS, 2014). Data from C1, C, CX, CM, EC, GE, II, and IU can be requested through the EarthScope Consortium Wilber 3 system (https://ds.iris.edu/wilber3/).

References

Abercrombie, R. E. (1995). Earthquake source scaling relationships from −1 to 5 ML using seismograms recorded at 2.5-km depth. *Journal of Geophysical Research: Solid Earth*, *100*(B12), 24015–24036. https://doi.org/10.1029/95JB02397

Albuquerque Seismological Laboratory/USGS. (2014). Global Seismograph Network (GSN - IRIS/USGS) [Dataset]. International Federation of Digital Seismograph Networks. https://doi.org/10.7914/SN/IU

Assumpção, M. S., & Bianchi, M. B. (2016). Pantanal, Chaco and Paraná (PCPB) structural studies network [Dataset]. USP Seismological Center (USPSC). https://doi.org/10.7914/8scf-yd39

Baltay, A., Prieto, G. A., & Beroza, G. C. (2010). Radiated seismic energy from coda measurements and no scaling in apparent stress with seismic moment. *Journal of Geophysical Research*, *115*(B08314). https://doi.org/10.1029/2009JB006736

Bianchi, M. B., Assumpção, M., Rocha, M. P., Carvalho, J. M., Azevedo, P. A., Fontes, S. L., et al. (2018). The Brazilian Seismographic Network (RSBR): Improving Seismic Monitoring in Brazil. *Seismological Research Letters*, *89*(2A), 452–457. https://doi.org/10.1785/0220170227

Boatwright, J., & Fletcher, J. B. (1984). The partition of radiated energy between P and S waves. *Bulletin of the Seismological Society of America*, *74*(2), 361–376. https://doi.org/10.1785/BSSA0740020361

Boatwright, J., Fletcher, J. B., & Fumal, T. E. (1991). A general inversion scheme for source, site, and propagation characteristics using multiply recorded sets of moderate-sized earthquakes. *Bulletin of the Seismological Society of America*, *81*(5), 1754–1782. https://doi.org/10.1785/BSSA0810051754

Booth, C. M., Forsyth, D. W., & Weeraratne, D. S. (2014). Upper mantle Q structure beneath old seafloor in the western Pacific. Journal of Geophysical Research: Solid Earth, 119(4), 3448–3461. https://doi.org/10.1002/2013JB010589

Brune, J. N. (1970). Tectonic stress and the spectra of seismic shear waves from earthquakes. *Journal of Geophysical Research*, *75*(26), 4997–5009. https://doi.org/10.1029/JB075i026p04997

Choy, G. L., & Boatwright, J. L. (1995). Global patterns of radiated seismic energy and apparent stress. *Journal of Geophysical Research: Solid Earth*, *100*(B9), 18205–18228. https://doi.org/10.1029/95JB01969

Crotwell, H. P., Owens, T. J., & Ritsema, G. (1999). The TauP Toolkit: Flexible Seismic Travel-time and Ray-path Utilities. *Seismological Research Letters*, *70*(2), 154–160. https://doi.org/https://doi.org/10.1785/gssrl.70.2.154

Devaux, J. P., Schubert, G., & Anderson, C. (1997). Formation of a metastable olivine wedge in a descending slab. *Journal of Geophysical Research: Solid Earth*, *102*(B11), 24627–24637. https://doi.org/10.1029/97JB02334

Eberhart-Phillips, D., Reyners, M., Chadwick, M., & Stuart, G. (2008). Three-dimensional attenuation structure of the Hikurangi subduction zone in the central North Island, New Zealand. Geophysical Journal International, 174(1), 418–434. https://doi.org/10.1111/j.1365-246X.2008.03816.x

Efron, B., & Tibshirani, R. (1991). Statistical Data Analysis in the Computer Age. *Science*, *253*(5018), 390–395. https://doi.org/10.1126/science.253.5018.390

Engebretson, D. C., & Kirby, S. H. (1992). Deep Nazca slab seismicity: why is it so anomalous? *Eos, Trans. Amer. Geophys. Un.*, *73*(43), 379 [abstract].

Eshelby, J. D. (1957). The determination of the elastic field of an ellipsoidal inclusion, and related problems. *Proceedings of the Royal Society of London. Series A. Mathematical and Physical Sciences*, *241*(1226). https://doi.org/10.1098/rspa.1957.0133

Estabrook, C. H. (1999). Body wave inversion of the 1970 and 1963 South American large deep-focus earthquakes. *Journal of Geophysical Research: Solid Earth*, *104*(B12), 28751–28767. https://doi.org/10.1029/1999JB900244

Ferrand, T. P. (2019). Seismicity and mineral destabilizations in the subducting mantle up to 6 GPa, 200 km depth. *Lithos*, *334–335*, 205–230. https://doi.org/10.1016/j.lithos.2019.03.014

Ferrand, T. P., Hilairet, N., Incel, S., Deldicque, D., Labrousse, L., Gasc, J., et al. (2017). Dehydration-driven stress transfer triggers intermediate-depth earthquakes. *Nature Communications*, *8*(15247). https://doi.org/10.1038/ncomms15247

Du Frane, W. L., Sharp, T. G., Mosenfelder, J. L., & Leinenweber, K. (2013). Ringwoodite growth rates from olivine with ~75ppmw H2O: Metastable olivine must be nearly anhydrous to exist in the mantle transition zone. *Physics of the Earth and Planetary Interiors*, *219*, 1–10. https://doi.org/10.1016/j.pepi.2013.04.001

Frohlich, C. (1989). The Nature Of Deep-Focus Earthquakes. *Annual Review of Earth and Planetary Sciences*, *17*, 227–254. https://doi.org/10.1146/annurev.earth.17.1.227

Frohlich, C. (2006). *Deep Earthquakes*. Cambridge: Cambridge University Press. https://doi.org/10.1017/CBO9781107297562

Fujie, G., Kodaira, S., Kaiho, Y., Yamamoto, Y., Takahashi, T., Miura, S., & Yamada, T. (2018). Controlling factor of incoming plate hydration at the north-western Pacific margin. *Nature Communications*, *9*(3844). https://doi.org/10.1038/s41467-018-06320-z

Furumura, T., Kennett, B. L. N., & Padhy, S. (2016). Enhanced waveguide effect for deep-focus earthquakes in the subducting Pacific slab produced by a metastable olivine wedge. *Journal of Geophysical Research: Solid Earth*, *121*(9), 6779–6796. https://doi.org/10.1002/2016JB013300

GEOFON Data Centre (1993). GEOFON Seismic Network [Dataset]. Deutsches GeoForschungsZentrum GFZ. https://doi.org/10.14470/TR560404

GFZ German Research Centre for Geosciences; Institut des Sciences De l'Univers-Centre National de la Recherche CNRS-INSU (2006). IPOC Seismic Network [Dataset]. Integrated Plate boundary Observatory Chile – IPOC. https://doi.org/10.14470/PK615318

Goes, S., & Ritsema, J. (1995). A broadband P wave analysis of the large deep Fiji Island and Bolivia Earthquakes of 1994. *Geophysical Research Letters*, *22*(16), 2249–2252. https://doi.org/10.1029/95GL02011

Green, H. W., & Burnley, P. C. (1989). A new self-organizing mechanism for deep-focus earthquakes. *Nature*, *341*, 733–737. https://doi.org/10.1038/341733a0

Green, H. W., & Marone, C. (2002). Instability of Deformation. *Reviews in Mineralogy and Geochemistry*, *51*(1), 181–199. https://doi.org/10.2138/gsrmg.51.1.181

Green, H. W., & Zhou, Y. (1996). Transformation-induced faulting requires an exothermic reaction and explains the cessation of earthquakes at the base of the mantle transition zone. *Tectonophysics*, *256*(1–4), 39–56. https://doi.org/10.1016/0040-1951(95)00164-6

Havskov, J., & Ottemoller, L. (2010). *Routine Data Processing in Earthquake Seismology*. https:// 10.1007/978-90-481-8697-6

Hosoya, T., Kubo, T., Ohtani, E., Sano, A., & Funakoshi, K. (2005). Water controls the fields of metastable olivine in cold subducting slabs. *Geophysical Research Letters*, *32*(L17305). https://doi.org/10.1029/2005GL023398

Houston, H. (2015). Deep Earthquakes. In *Treatise on Geophysics* (pp. 329–354). Elsevier. https://doi.org/10.1016/B978-0-444-53802-4.00079-8

Ide, S., & Beroza, G. C. (2001). Does apparent stress vary with earthquake size? *Geophysical Research Letters*, *28*(17), 3349–3352. https://doi.org/10.1029/2001GL013106

Ide, S., Beroza, G. C., Prejean, S. G., & Ellsworth, W. L. (2003). Apparent break in earthquake scaling due to path and site effects on deep borehole recordings. *Journal of Geophysical Research: Solid Earth*, *108*(B5). https://doi.org/10.1029/2001JB001617

Ihmlé, P. F. (1998). On the interpretation of subevents in teleseismic waveforms: The 1994 Bolivia deep earthquake revisited. *Journal of Geophysical Research: Solid Earth*, *103*(B8), 17919–17932. https://doi.org/10.1029/98JB00603

Ishii, T., & Ohtani, E. (2021). Dry metastable olivine and slab deformation in a wet subducting slab. *Nature Geoscience*, *14*, 526–530. https://doi.org/10.1038/s41561-021-00756-7

Jiang, G., & Zhao, D. (2011). Metastable olivine wedge in the subducting Pacific slab and its relation to deep earthquakes. *Journal of Asian Earth Sciences*, *42*(6), 1411–1423. https://doi.org/10.1016/j.jseaes.2011.08.005

Jiménez, C., Calvo, C., Saavedra, M., Moggiano, N., & Molina, W. (2021). Source characteristics of Peruvian deep focus seismic doublet of November 24, 2015. *Journal of South American Earth Sciences*, *105*(102919). https://doi.org/https://doi.org/10.1016/j.jsames.2020.102919

Kanamori, H., & Brodsky, E. E. (2004). The physics of earthquakes. *Reports on Progress in Physics*, *67*, 1429–1496. https://doi.org/10.1088/0034-4885/67/8/R03

Kanamori, H., Anderson, D. L., & Heaton, T. H. (1998). Frictional Melting During the Rupture of the 1994 Bolivian Earthquake. *Science*, *279*(5352), 839–842. https://doi.org/10.1126/science.279.5352.839

Kaneko, Y., & Shearer, P. M. (2014). Seismic source spectra and estimated stress drop derived from cohesive-zone models of circular subshear rupture. *Geophysical Journal International*, *197*(2), 1002–1015. https://doi.org/10.1093/gji/ggu030

Kawakatsu, H., & Yoshioka, S. (2011). Metastable olivine wedge and deep dry cold slab beneath southwest Japan. *Earth and Planetary Science Letters*, *303*(1–2), 1–10. https://doi.org/10.1016/j.epsl.2011.01.008

Kennett, B. L. N., Engdahl, E. R., & Buland, R. (1995). Constraints on seismic velocities in the Earth from traveltimes. *Geophysical Journal International*, *122*(1), 108–124. https://doi.org/10.1111/j.1365-246X.1995.tb03540.x

Kikuchi, M., & Kanamori, H. (1994). The mechanism of the Deep Bolivia Earthquake of June 9, 1994. *Geophysical Research Letters*, *21*(22), 2341–2344. https://doi.org/10.1029/94GL02483

Kirby, S. H., Durham, W. B., & Stern, L. A. (1991). Mantle Phase Changes and Deep-Earthquake Faulting in Subducting Lithosphere. *Science*, *252*, 216–225. https://doi.org/10.1126/science.252.5003.216

Kirby, S. H., Okal, E. A., & Engdahl, E. R. (1995). The 9 June 94 Bolivian Deep Earthquake: An exceptional event in an extraordinary subduction zone. *Geophysical Research Letters*, *22*(16), 2233–2236. https://doi.org/10.1029/95GL01802

Kirby, S. H., Stein, S., Okal, E. A., & Rubie, D. C. (1996). Metastable mantle phase transformations and deep earthquakes in subducting oceanic lithosphere. *Reviews of Geophysics*, *34*(2), 261–306. https://doi.org/10.1029/96RG01050

Kita, S., & Ferrand, T. P. (2018). Physical mechanisms of oceanic mantle earthquakes: Comparison of natural and experimental events. *Scientific Reports*, *8*(17049). https://doi.org/10.1038/s41598-018-35290-x

Ko, Y., Kuo, B., & Hung, S. (2012). Robust determination of earthquake source parameters and mantle attenuation. *Journal of Geophysical Research: Solid Earth*, *117*(B4). https://doi.org/10.1029/2011JB008759

Kubo, T., Ohtani, E., Kato, T., Shinmei, T., & Fujino, K. (1998). Effects of Water on the α-β Transformation Kinetics in San Carlos Olivine. *Science*, *281*(5373), 85–87. https://doi.org/10.1126/science.281.5373.85

Kumar, S., Kumar, D., Singh, A. P., & Rastogi, B. K. (2023). Source parameters and scaling relations for small earthquakes in the Saurashtra Horst of Western Deccan Volcanic Province, India and its seismotectonic implications. *Journal of Earth System Science*, *132*(3), 118. https://doi.org/10.1007/s12040-023-02130-0

Kumar, V., Kumar, D., & Chopra, S. (2016). Estimation of source parameters and scaling relations for moderate size earthquakes in North-West Himalaya. *Journal of Asian Earth Sciences*, *128*, 79–89. https://doi.org/10.1016/j.jseaes.2016.07.023

Kumar, V., Kumar, D., & Chopra, S. (2019). Source Parameters and Scaling Relations for Moderate Size Earthquakes in North–East India Region. *Pure and Applied Geophysics*, *176*, 45–64. https://doi.org/10.1007/s00024-018-1972-0

Lay, T., & Wallace, T. (1995). *Modern Global Seismology*. Elsevier.

Leite Neto, G. S., & Julià, J. (2022). Investigating Source Mechanisms of Deep-Focus Earthquakes at the Peru-Brazil Border with Regional and Teleseismic Data. In *EGU General Assembly 2022*. Vienna, Austria & Online. https://doi.org/10.5194/egusphere-egu22-9820

Liu, M., Huang, Y., & Ritsema, J. (2020). Stress Drop Variation of Deep-Focus Earthquakes Based on Empirical Green's Functions. *Geophysical Research Letters*, *47*(9). https://doi.org/10.1029/2019GL086055

Madariaga, R. (1976). Dynamics of an expanding circular fault. *Bulletin of the Seismological Society of America*, *66*(3), 639–666. https://doi.org/10.1785/BSSA0660030639

Mao, G. L., Ferrand, T. P., Li, J., Zhu, B., Xi, Z., & Chen, M. (2022). Unsupervised machine learning reveals slab hydration variations from deep earthquake distributions beneath the northwest Pacific. *Communications Earth & Environment*, *3:56*, 1–9. https://doi.org/10.1038/s43247-022-00377-x

Mayeda, K., & Walter, W. R. (1996). Moment, energy, stress drop, and source spectra of western United States earthquakes from regional coda envelopes. *Journal of Geophysical Research: Solid Earth*, *101*(B5), 11195–11208. https://doi.org/10.1029/96JB00112

Mosenfelder, J. L., Marton, F. C., Ross, C. R., Kerschhofer, L., & Rubie, D. C. (2001). Experimental constraints on the depth of olivine metastability in subducting lithosphere.

Physics of the Earth and Planetary Interiors, *127*(1–4), 165–180. https://doi.org/10.1016/S0031-9201(01)00226-6

Nishitsuji, Y., & Mori, J. (2014). Source parameters and radiation efficiency for intermediate-depth earthquakes in Northeast Japan. *Geophysical Journal International*, *196*(2), 1247–1259. https://doi.org/10.1093/gji/ggt458

Ohuchi, T., Higo, Y., Tange, Y., Sakai, T., Matsuda, K., & Irifune, T. (2022). In situ X-ray and acoustic observations of deep seismic faulting upon phase transitions in olivine. *Nature Communications*, *13*(5213). https://doi.org/10.1038/s41467-022-32923-8

Okal, E. A., & Bina, C. R. (1994). The deep earthquakes of 1921–1922 in Northern Peru. *Physics of the Earth and Planetary Interiors*, *87*(1-2), 33–54. https://doi.org/10.1016/0031-9201(94)90020-5

Pearson, D. G., Brenker, F. E., Nestola, F., McNeill, J., Nasdala, L., Hutchison, M. T., et al. (2014). Hydrous mantle transition zone indicated by ringwoodite included within diamond. *Nature*, *507*, 221–224. https://doi.org/10.1038/nature13080

Poli, P., & Prieto, G. A. (2016). Global rupture parameters for deep and intermediate-depth earthquakes. *Journal of Geophysical Research: Solid Earth*, *121*(12), 8871–8887. https://doi.org/10.1002/2016JB013521

Prieto, G. A. (2022). The Multitaper Spectrum Analysis Package in Python. *Seismological Research Letters*, *93*(3), 1922–1929. https://doi.org/10.1785/0220210332

Prieto, G. A., Shearer, P. M., Vernon, F. L., & Kilb, D. (2004). Earthquake source scaling and self-similarity estimation from stacking P and S spectra. *Journal of Geophysical Research: Solid Earth*, *109*(B08310). https://doi.org/10.1029/2004JB003084

Prieto, G. A., Thomson, D. J., Vernon, F. L., Shearer, P. M., & Parker, R. L. (2007). Confidence intervals for earthquake source parameters. *Geophysical Journal International*, *168*(3), 1227–1234. https://doi.org/10.1111/j.1365-246X.2006.03257.x

Prieto, G. A., Florez, M., Barrett, S. A., Beroza, G. C., Pedraza, P., Blanco, J. F., & Poveda, E. (2013). Seismic evidence for thermal runaway during intermediate-depth earthquake rupture. *Geophysical Research Letters*, *40*(23), 6064–6068. https://doi.org/10.1002/2013GL058109

Raleigh, C. B. (1967). Tectonic Implications of Serpentinite Weakening. *Geophysical Journal International*, *14*(1–4), 113–118. https://doi.org/10.1111/j.1365-246X.1967.tb06229.x

Ranero, C. R., Phipps Morgan, J., McIntosh, K., & Reichert, C. (2003). Bending-related faulting and mantle serpentinization at the Middle America trench. *Nature*, *425*, 367–373. https://doi.org/10.1038/nature01961

Ruiz, S., Tavera, H., Poli, P., Herrera, C., Flores, C., Rivera, E., & Madariaga, R. (2017). The deep Peru 2015 doublet earthquakes. *Earth and Planetary Science Letters*, *478*, 102–109. https://doi.org/10.1016/j.epsl.2017.08.036

Scripps Institution of Oceanography (1986). Global Seismographic Network – IRIS/IDA [Dataset]. International Federation of Digital Seismograph Networks. https://doi.org/10.7914/SN/II

Servicio Geológico Colombiano (1993). Red Sismologica Nacional de Colombia [Dataset]. International Federation of Digital Seismograph Networks. https://doi.org/10.7914/SN/CM

Shen, Z., & Zhan, Z. (2020). Metastable Olivine Wedge Beneath the Japan Sea Imaged by Seismic Interferometry. *Geophysical Research Letters*, *47*(6). https://doi.org/10.1029/2019GL085665

Shirey, S. B., Wagner, L. S., Walter, M. J., Pearson, D. G., & van Keken, P. E. (2021). Slab Transport of Fluids to Deep Focus Earthquake Depths—Thermal Modeling Constraints and Evidence From Diamonds. *AGU Advances*, *2*(2). https://doi.org/10.1029/2020AV000304

Thomson, D. J. (1982). Spectrum estimation and harmonic analysis. *Proceedings of the IEEE*, *70*(9), 1055–1096. https://doi.org/10.1109/PROC.1982.12433

Tibi, R., Bock, G., & Wiens, D. A. (2003). Source characteristics of large deep earthquakes: Constraint on the faulting mechanism at great depths. *Journal of Geophysical Research: Solid Earth*, *108*(B2). https://doi.org/10.1029/2002JB001948

Tsallis, C. (1988). Possible generalization of Boltzmann-Gibbs statistics. *Journal of Statistical Physics*, *52*, 479–487. https://doi.org/10.1007/BF01016429

Tsallis, C., & Stariolo, D. A. (1996). Generalized simulated annealing. *Physica A: Statistical Mechanics and Its Applications*, *233*(1–2), 395–406. https://doi.org/10.1016/S0378-4371(96)00271-3

Universidad de Chile (2012). Red Sismologica Nacional [Dataset]. International Federation of Digital Seismograph Networks. https://doi.org/10.7914/SN/C1

Venkataraman, A., & Kanamori, H. (2004). Observational constraints on the fracture energy of subduction zone earthquakes. *Journal of Geophysical Research: Solid Earth*, *109*(B5). https://doi.org/10.1029/2003JB002549

Viegas, G., Abercrombie, R. E., & Kim, W.-Y. (2010). The 2002 M5 Au Sable Forks, NY, earthquake sequence: Source scaling relationships and energy budget. *Journal of Geophysical Research: Solid Earth*, *115*(B7). https://doi.org/10.1029/2009JB006799

Wiens, D. A. (2021). Diamonds Hold Clues About the Cause of Deep Earthquakes. *AGU Advances*, *2*(2). https://doi.org/10.1029/2021AV000434

Xiang, Y., Sun, D. Y., Fan, W., & Gong, X. G. (1997). Generalized simulated annealing algorithm and its application to the Thomson model. *Physics Letters A*, *233*(3), 216–220. https://doi.org/10.1016/S0375-9601(97)00474-X

Ye, L., Lay, T., Kanamori, H., Zhan, Z., & Duputel, Z. (2016). Diverse rupture processes in the 2015 Peru deep earthquake doublet. *Science Advances*, *2*(6). https://doi.org/10.1126/sciadv.1600581

Zahradník, J., Čížková, H., Bina, C. R., Sokos, E., Janský, J., Tavera, H., & Carvalho, J. (2017). A recent deep earthquake doublet in light of long-term evolution of Nazca subduction. *Scientific Reports*, *7*(45153). https://doi.org/10.1038/srep45153

Zhan, Z. (2017). Gutenberg–Richter law for deep earthquakes revisited: A dual-mechanism hypothesis. *Earth and Planetary Science Letters*, *461*, 1–7. https://doi.org/10.1016/j.epsl.2016.12.030

Zhan, Z. (2020). Mechanisms and Implications of Deep Earthquakes. *Annual Review of Earth and Planetary Sciences*, *48*, 147–174. https://doi.org/10.1146/annurev-earth-053018-060314

Zhan, Z., Kanamori, H., Tsai, V. C., Helmberger, D. V., & Wei, S. (2014). Rupture complexity of the 1994 Bolivia and 2013 Sea of Okhotsk deep earthquakes. *Earth and Planetary Science Letters*, *385*, 89–96. https://doi.org/10.1016/j.epsl.2013.10.028

CAPÍTULO 4

CONCLUSÕES

Este estudo teve como objetivo investigar o mecanismo físico por trás de terremotos de foco profundo na região amazônica entre o Peru e o Brasil. Para isso, foram determinados mecanismos focais e parâmetros de fonte sísmica – momento sísmico, frequência de esquina, energia sísmica irradiada, *stress drop* e eficiência de irradiação – para uma sequência de 42 terremotos ocorridos entre 515-655 km de profundidade no período de 2014-2022.

Na primeira etapa do estudo, através da inversão de formas de onda P e S com o método *Cut-and-Paste*, foi possível determinar mecanismos focais para um total de 28 dos 42 eventos. Os mecanismos confirmam a predominância de falhas normais com eixo P quase vertical e eixo B quase horizontal alinhado com a direção da placa de Nazca (N-NNW). Algumas falhas normais, no entanto, mostram orientações que diferem desse padrão, sugerindo variações no campo de esforços que podem ter sido induzidas pelas maiores rupturas. Observações de falhas oblíquas transcorrentes e reversa mostram que essas variações podem ser ainda mais importantes.

Os esforços obtidos a partir da inversão desses mecanismos revelaram que eventos ($4.2 \leq Mw \leq 7.5$) na região ocorrem sob um regime de compressão ao longo do mergulho da placa, consistente com outras regiões pelo mundo que apresentam sismicidade de foco profundo. De maneira geral, os planos nodais das soluções obtidas se mostraram orientados a aproximadamente 45º do eixo principal de compressão, o que é consistente com a nucleação de novas falhas, e consequentemente, com o mecanismo de *transformational faulting*. Dessa forma, foi proposto que os eventos nessa região podem estar sendo viabilizados por uma MOW preservada por um segmento de litosfera mais fria acoplada em profundidade à placa de Nazca. Esse segmento de placa fria estaria a aproximadamente 500 km de profundidade, na zona de transição do manto. Essa hipótese poderia explicar o confinamento da zona sísmica entre 500 e 700 km, uma vez que terremotos não ocorreriam no segmento de placa quente sem MOW, explicando assim a zona assísmica entre 300 e 500 km, e no manto inferior, onde as transformações de fase da olivina ou são endotérmicas ou são muito lentas.

Na segunda etapa deste estudo, parâmetros de fonte foram estimados para 13 dos 42 eventos. Momentos sísmicos e frequências de esquina, obtidos por meio da modelação de

espectros de deslocamento usando o método *Cluster-Event* (CEM), mostraram valores entre $2.08x10^{16}$ e $1.54x10^{20}$ N.m (Mw 4.8 to 7.4) e entre 0.13 e 3.7 Hz, respectivamente. De maneira geral, essas frequências de esquina diminuem com o momento sísmico, seguindo uma inclinação que difere da proporcionalidade esperada, $M_0 \propto f_c^{-3}$. Consequentemente, observou-se uma relação de escala entre os *stress drops* e os momentos sísmicos, com os valores de *stress drop* variando consideravelmente dentro da sequência, de 5.1 a 89.8 MPa. As energias sísmicas, estimadas através da integração dos espectros de velocidade, se mostraram proporcionais ao momento sísmico, variando entre $6.8x10^{10}$ e $1.9x10^{16}$ J, embora alguns eventos Mw > 6.4 tenham sido relativamente mais energéticos que o esperado. As eficiências sísmicas, por fim, mostraram valores entre 0.1 e 1.4, sugerindo a coexistência de rupturas eficientes e dissipativas na região.

Assumindo a existência de uma MOW, é proposto que as rupturas na região estejam sendo nucleadas no volume metaestável por *transformational faulting* e, em seguida, se propagam para fora desse material por *thermal runaway*. Nesse estágio de propagação, a ocorrência de maior ou menor grau de derretimento na zona de falha poderia explicar a variabilidade nas eficiências. Sugere-se então que o grau de derretimento envolvido no falhamento esteja sendo controlado pela presença de regiões hidratadas de pequena escala próximas à falha. Nesse sentido, é possível que a liberação de calor latente pelas transformações de fase ou o aumento local da temperatura na zona de falha por cisalhamento possa induzir a desidratação de fases hídricas próximas à fonte. Como resultado, a água liberada dessas reações facilitaria a fusão parcial durante o estágio de *thermal runaway*. Por outro lado, se as temperaturas na placa forem altas o suficiente, também é possível que a desidratação de fases hídricas atue de maneira ativa no processo de ruptura, induzindo *transformational faulting* no volume metaestável.

Para melhor entender o mecanismo gerador de terremotos de foco profundo na América do Sul, recomenda-se que trabalhos futuros:

- Determinem mecanismos focais e parâmetros de fonte para os eventos do segmento Bolívia-Argentina. Como apenas os segmentos Peru-Brasil e Bolívia-Argentina apresentam atividade sísmica regular, comparar os parâmetros dessas duas zonas pode ajudar a entender as condições sob as quais terremotos de foco profundo ocorrem na América do Sul. Em particular a análise de eficiências sísmicas pode confirmar se há variações laterais significativas na estrutura térmica da placa subduzida;

- Investiguem se há relação entre a subducção de dorsais e as variações laterais na sismicidade profunda ao longo da placa de Nazca subduzida. É importante compreender por que os terremotos de foco profundo na zona de subducção: i – ocorrem de forma segmentada; ii – são mais frequentes nos segmentos Peru-Brasil e Bolívia-Argentina; e iii – acontecem de maneira isolada e com grandes magnitudes nos segmentos Peru-Bolívia e Colômbia-Peru.

APÊNDICE A

Este manuscrito foi publicado em 6/12/2022 no periódico *Journal of South American Earth Sciences.* O material suplementar associado pode ser encontrado no Apêndice B.

Determination of intraplate focal mechanisms with the Brazilian Seismic Network: a simplified Cut-and-Paste approach

Gilberto S. Leite Neto[1] and Jordi Julià[1,2]

[1]Programa de Pós-Graduação em Geodinâmica e Geofísica, Universidade Federal do Rio Grande do Norte, Campus Universitário, Natal, RN 59078-970, Brazil
[2]Departamento de Geofísica, Universidade Federal do Rio Grande do Norte, Campus Universitário, Natal, RN 59078-970, Brazil

[*]Corresponding author.
E-mail address: leitenetogs@gmail.com (G. S. Leite Neto)

Summary

The feasibility of a simplified Cut-and-Paste approach (CAP) for routine determination of intraplate earthquake mechanisms in Brazil is demonstrated with data acquired by the Brazilian Seismographic Network (RSBR). Our approach models three-component seismic recordings through: (i) computation of synthetics seismograms with a single, average velocity model, and (ii) independent alignment of observed and synthetic waveforms through waveform cross-correlation. No partitioning of regional waveforms into their corresponding body- and surface-wave trains is considered. The empirical alignment successfully accounts for lateral variations along specific source-station paths, along with location uncertainties and timing errors, and effectively augments the number of waveforms available for inversion. The performance of the proposed approach is demonstrated through modeling of two recent intraplate earthquakes: the Mw 4.4 2017 Maranhão earthquake and the Mw 4.1 2020 Amargosa earthquake. For the Maranhão event, we obtain a strike-slip focal mechanism (340°±0°,70°±0°,0°±0°) and a centroid depth of 9 km with magnitude of Mw 4.4, fully consistent with previous studies. For the Amargosa earthquake, we obtain a normal-fault mechanism (20°±4.6°,60°±16.9°,-30°±14.4°) with a preferred centroid depth of 10 km, which is in general agreement with P-wave polarity data and the orientation of the nearby Salvador Shear Zone. We thus conclude that our simplified CAP approach is an effective tool for modeling regional waveforms in Brazil and, most likely, in sparse networks in general.

Keywords: South America; Regional waveform inversion; Focal mechanism; Sparse networks; Stress field.

1. Introduction

Brazil covers 54% of the South American continent and, being located away from plate boundaries, it is regarded as a region of low-to-moderate seismicity. Intraplate earthquakes in Brazil, nonetheless, can generate significant damage and alarm to society. The 5.1 mb João Câmara earthquake, for instance, took place on November 30, 1986, and resulted in thousands of properties damaged or, in some cases, destroyed. And, the 5.2 mb Cascavel earthquake, which occurred on November 20, 1980, caused the collapse of structures near the epicenter and was felt at distances of up to 600 km (Assumpção et al., 2014; Ferreira et al., 1998; Takeya et al., 1989). The origin of intraplate earthquakes in Brazil has often invoked a vague mixture of preexisting zones of weakness within the continental interior and/or favorable concentration

of stresses (e.g. Johnston, 1989; Sykes, 1978; Talwani, 1989; Talwani and Rajendran, 1991), as correlation of intraplate seismicity with surface geology has often proven difficult (Assumpção et al., 2004; Talwani and Rajendran, 1991). Although a picture is emerging in which seismicity tends to occur in regions of hot and weakened lithosphere, such as Neoproterozoic fold belts, that presumably act as stress concentrators in the brittle upper crust (e.g. Agurto-Detzel et al., 2015a; Assumpção et al., 2004), determination of reliable constraints from robust focal solutions is still needed.

The Brazilian Seismographic Network (RSBR) has been in operation since 2011 and comprises 82 permanent broadband stations unevenly distributed over the entire national territory (Fig. 1). Its operation and maintenance is carried out through four main sub-networks: *Rede Sismográfica do Nordeste do Brasil* (network code NB), *Rede Sismográfica Integrada do Brasil* (network code BL), *Rede Sismográfica do Centro e Norte do Brasil* (network code BR) and *Rede Sismográfica do Sul e do Sudeste do Brasil* (network code ON). The stations consist of either RefTek RT131B (NB), Nanometrics Trillium 120PA (BL and BR) or Streckeisen STS-2.5 (ON) sensors with flat velocity response in the 120 s – 50 Hz range attached to high-gain (24 bit) digitizers sampling continuously at 100 sps (Bianchi et al., 2018). Locations and magnitudes determined with RSBR data are routinely reported in the Brazilian Seismic Bulletin (http://rsbr.on.br); focal mechanisms, however, are seldom included. As shown in Fig. 1, RSBR stations are sparsely distributed throughout Brazil, so regional waveforms are commonly available at just a few seismic stations. Moreover, lateral variations in Earth structure have proven important when modeling regional waveforms in Brazil (Dias et al., 2018), further limiting the use of RSBR stations for routine moment tensor determination.

A number of studies have attempted the determination of individual focal mechanisms for moderate-size (Mw < 5) intraplate earthquakes in Brazil (e.g. Agurto-Detzel et al., 2015b; Assumpção et al., 2011; Barros et al., 2015; Carvalho et al., 2019, 2020; Dias et al., 2018; Fonsêca et al., 2021). Those studies considered a variety of approaches, and contemplated the use of either regional waveforms and/or first-motion polarities. Regional waveform modeling in particular proved quite challenging, because modeling of moderate-size earthquakes requires relatively high frequency contents and velocity models that predict body- and surface-wave travel-times with enough accuracy for waveform alignment. Dias et al. (2018) circumvented those difficulties by using 1D, path-specific velocity models from continental-scale surface-wave tomography at regional distances and receiver functions at more local distances. The downside of their approach was the significant time and effort devoted in

developing velocity models for each source-station pair. Additionally, assessing the validity of their models for regional waveform modeling was also challenging, as it resulted in the use of just 4 seismic stations out of 14 openly available. Carvalho et al. (2019), on the other hand, considered inversion of waveform envelopes, which are less sensitive to lateral variations in Earth structure than the waveforms themselves. Envelopes were calculated by means of a Hilbert Transform, and the inversion was performed through a grid-search for fault angles and minimization of the misfit between observed and synthetic envelopes. As envelopes do not carry phase information, however, considerable effort had to be spent in visually assigning polarities to tightly constrain the radiation pattern (Carvalho et al., 2019).

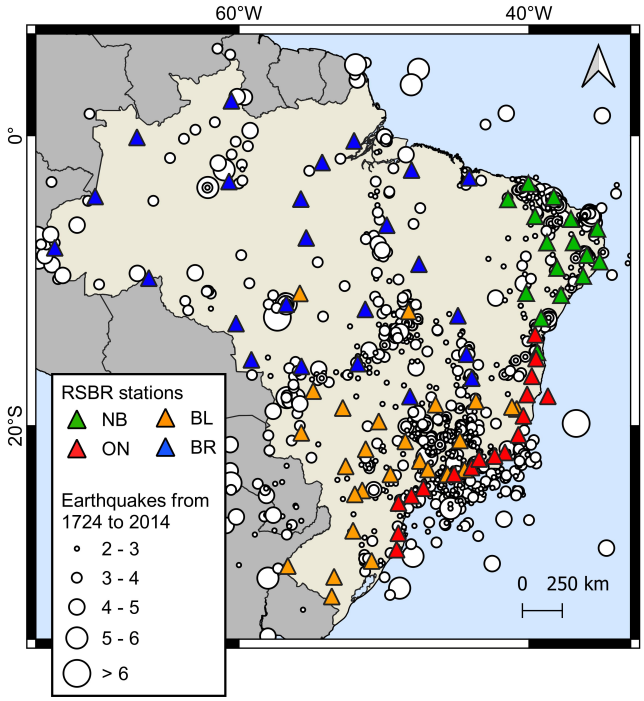

Fig. 1. Brazilian Seismic Network (RSBR) stations and crustal seismicity in Brazil and surrounding regions. RSBR subnets (codes NB, BL, BR and ON) are color-coded in the map. Earthquakes are shown as white circles scaled by magnitude (mb). Seismic locations and magnitudes were taken from the Brazilian Seismic Bulletin (available at http://rsbr.on.br/), which includes historical data from Berrocal et al. (1984).

Here, we propose the use of a simpler approach inspired in the Cut-and-Paste method (CAP) of Zhao & Helmberger (1994). The CAP method is based on the partition of seismograms into their corresponding body (typically, Pnl) and surface-wave train portions, which are then modeled separately during inversion. The partition allows for a full use of the broadband character of seismic recordings and facilitates accounting for inaccuracies in the velocity model (as well as inaccuracies in earthquake location and origin time), as synthetic

seismograms for individual segments are allowed to be time-shifted independently before misfit computation (Zhao and Helmberger, 1994; Zhu and Helmberger, 1996). Typically, time-shifts are determined through waveform cross-correlation and differ among waveform segments, resulting in an efficient alignment between observed and synthetic seismograms. This methodology has proven effective in determining focal mechanisms from regional waveforms in other intraplate regions worldwide (e.g. Chen et al., 2021, 2016; D'Amico et al., 2014; He et al., 2018; He and Ni, 2018; Luo et al., 2010; Pang et al., 2018; Singh et al., 2016; Tape et al., 2013; Zhao et al., 2013; Zhu et al., 2006).

The original CAP method assumed a double-couple (DC) source and, since its development, a number of adaptions were developed. For example, the generalized CAP (gCAP) extended the method to non-double-couple (NDC) mechanisms, which is especially useful in man-related settings (e.g. mine collapses and explosions) and natural events occurring near volcanic and geothermal areas (Zhu and Ben-Zion, 2013). The CAPjoint method proposed the use of both regional (Pnl and surface waves) and teleseismic (vertical P and transverse SH) waveforms, thus ensuring a better sampling of the focal sphere (Chen et al., 2015). And a combination of those two approaches, the so-called generalized CAP joint method (gCAPjoint), uses local and teleseismic data to retrieve the full moment tensor of earthquakes (Bai et al., 2020). Despite such improvements, those extensions are not especially relevant for our inversions, as most earthquakes in Brazil are relatively small and of tectonic origin.

Moreover, in sparse networks such as the RSBR, surface waves are the most prominent and sometimes the only signal with enough signal-to-noise ratio to be utilized for waveform modeling. Thus, our approach does not separate body from surface-wave segments in the seismograms, and simply considers separate alignments for the vertical, radial and transverse components at each station. To illustrate the performance of our approach, RSBR stations at less than ~10° from the epicenter were selected to perform inversions for two moderate-size intraplate events. The first event was the Mw 4.4 2017 January 3rd Maranhão earthquake, for which we obtained a strike-slip mechanism (340°±0°,70°±0°,0°±0°) at 9 km depth, fully compatible with previous estimates from two independent studies using either path-specific velocity models or waveform envelopes (Carvalho et al., 2019; Dias et al., 2018). The second event was the Mw 4.1 2020 August 30th Amargosa earthquake, for which we obtained a normal mechanism (20°±4.6°, 60°±16.9°, -30°±14.4°) at 10 km depth. Because no previous solution was available for this event, we verified this normal mechanism with regional P-wave polarities and surface geology. Our results thus demonstrate that our simplified CAP approach

is an effective alternative to path-specific velocity models or inversion of waveform envelopes for routine determination of focal mechanisms of shallow intraplate earthquakes in Brazil.

2. Simplified CAP method

The CAP method, as originally presented in Zhao and Helmberger (1994), takes full advantage of broadband regional recordings by separately modeling Pnl and surface-wave segments in individual seismograms. The method assumes a pure DC source, which means that the radiation pattern is to be fully described through three fault angles: strike, dip and rake. Thus, to solve the inverse problem, a grid-search is conducted by computing synthetics for every possible fault orientation, and the best fit is assessed through an amplitude-normalized average of the root-mean-square difference between observed and predicted segments. An estimate of the scalar seismic moment (M_0) is obtained from the ratio between maximum observed and synthetic waveform amplitudes.

Our implementation is simpler and considers the full wave trains contained in the vertical, radial and transverse components, with no partitioning of the corresponding body and surface-wave trains. The grid-search is performed by varying the strike from 0º to 360º, the dip from 0º to 90º and the rake from -90º to 90º, at 10º steps. M_0 is obtained from the average scale factor between observed and predicted waveforms for all components, from which moment magnitude (Mw) can be calculated (Hanks and Kanamori, 1979). Note that the limited range for the rake angle does not prevent a full mapping of all fault orientations, as the Green's functions for rake angles that are 180º apart simply display flipped polarity and can be accounted for through negative scale factors. For each fault solution, the average misfit is calculated through the L2-norm of the difference between observed and predicted waveforms, normalized by the corresponding number of data points. This normalization ensures that longer time windows do not dominate the average misfit. It is important to note that, differently from the original CAP approach, we do not consider amplitude normalization. Zhao and Helmberger (1994) normalized seismogram amplitudes to a unit value before misfit computation to ensure similar weight was given to both Pnl and surface-wave segments during inversion, which is not important in our approach. Moreover, as later noted by Zhu & Helmberger (1996), amplitude normalization introduces severe singularities in the inversion, especially when stations are close to nodal planes, and important information about source depth and fault orientation is lost because information on the relative amplitudes between phases (Pnl to surface-waves and SV to SH waves) is erased.

Following the original CAP approach, however, observed and synthetic waveforms are still cross-correlated and empirically aligned before misfit computation. A pre-defined correlation window equal to 75% of the full time-window is considered, and the time-shift that maximizes the cross-correlation coefficient is determined. The time-shift can be either positive, implying an advancement of the prediction over the observation, or negative, implying a delay. Shifting the predictions through the empirically determined time-shift optimally aligns the waveforms and effectively reduces artifacts due to inaccuracies in the velocity model, earthquake location and origin time (e.g. D'Amico et al. 2010, 2013, Bai et al. 2020). Note that this approach represents a computationally faster alternative to path-specific velocity models (e.g., Dias et al., 2018) or the use of waveform envelopes (e.g., Carvalho et al., 2019), as all synthetic seismograms are computed from the same average velocity model and no visual assessment of waveform polarity is necessary. In practice, the approach was implemented after modifying C.J. Ammon's grid-search algorithm (http://eqseis.geosc.psu.edu/cammon/) to include time-shifts from cross-correlation and the normalization by the number of data points during misfit computation.

We stress that our simplified CAP approach differs from the original one in two important aspects: (i) we do not separate the Pnl and surface-wave portions of the seismograms; and (ii) we do not normalize waveform amplitudes to unit value. Different from other intraplate regions, earthquakes in Brazil are of moderate size and the recording stations are sparse and distant, so surface-waves are generally the only portion of the seismogram with a signal-to-noise ratio (SNR) high enough within the frequency range suitable for waveform modeling. We acknowledge that no amplitude normalization may result in closer stations dominating the inversion when a wide range of distances is used. Due to the sparse character of our network, however, near-source stations represented a very small fraction of our dataset. Thus, in those few instances where near-source stations were available, we simply opted for avoiding their use in our inversions.

3. The Mw 4.4 January 3rd 2017 Maranhão earthquake

On January 3rd, 2017 (12:43:45.700 UTC), a 4.5 mb earthquake took place in the equatorial margin of Brazil (3.14°S;43.86°W), along the northern border of the cratonic Parnaíba basin (Fig. 2a). The earthquake was large enough to be well recorded at regional distances. A moment tensor was developed by Dias et al. (2018) using regional seismic waveforms and their solution revealed a left-lateral, strike-slip mechanism (strike = 339°, dip

= 83°, rake = -2°), which was verified through P-wave polarities and aftershock location, with an optimal source-depth of 7.5 km and magnitude of 4.3 Mw. The same focal mechanism (340°, 80°, -10°) and magnitude were obtained from the inversion of waveform envelopes performed by Carvalho et al. (2019).

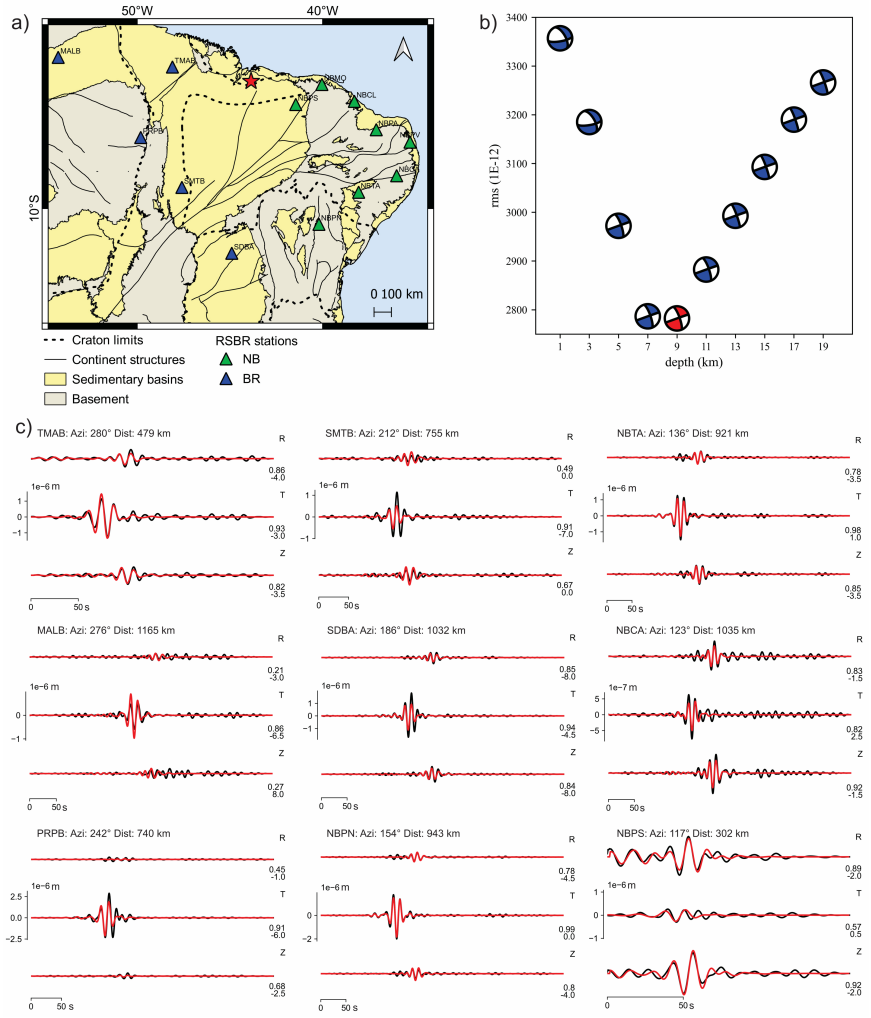

Fig. 2. Modeling results for the Mw 4.4 January 3rd, 2017 intraplate Maranhão earthquake. A) epicenter (red star) and locations of the 13 RSBR broadband stations utilized in this study (triangles). The stations have been color-coded by subnets. The map also outlines sedimentary basins, cratons and other continental structures. The epicenter is the same of Dias et al. (2018); B) Focal mechanism solutions obtained from the inversion of RSBR waveforms within the investigated depth range, showing the preferred solution in red; and C) Waveform fits for select stations produced by the preferred solution in B. The match for all 13 RSBR stations can be verified in the Supplementary Material (Fig. S1). Black traces denote observations while red traces denote predictions. On the upper right corner of each pair of observed and predicted seismograms the radial (R), transverse (T) or vertical (Z) component is indicated. On the lower right the cross-correlation coefficient (top) and the time shift required to align predictions with respect to observations (bottom) are noted.

3.1. Focal mechanism from RSBR data

Regional seismic waveforms for the 2017 Maranhão earthquake were retrieved for 13 RSBR stations. We considered only stations at less than ~10°, to stay within the flat Earth approximation, but excluded station ROSB due to its close proximity (~40 km) to the epicenter. The selected stations thus had epicentral distances in the 302–1165 km range. Retrieved time windows were 10 minutes long, starting at the earthquake's origin time, to ensure that the entire surface-wave train was included. After removing the mean and trend, the waveforms were converted to displacement through removal of the instrument response, and rotated into the great-circle-path. P-wave arrivals were visually picked on the vertical component after filtering with a nominal, short-period WWSSN response. For each station, only traces with SNR above 10 were considered for further analysis.

Green's functions were developed from a simple, 3-layer over a half-space model based on the seismic wide-angle reflection and refraction (WARR) survey of Soares et al. (2018) in the central Parnaíba Basin. Our velocity model included a 2 km thick sedimentary cover, a 38 km thick crust consisting of a 20 km thick upper crust and an 18 km-thick lower crust, and a mantle half-space (Table 1). Thicknesses and seismic velocities were averaged over the entire WARR profile, while densities were estimated from P-velocity trough an empirical relationship (Berteussen, 1977). We determined S-wave velocities from the P-wave velocities assuming a Poisson solid. To account for attenuation, we used typical values for the continental crust although, at low enough frequencies, these values proved not to be critical (D'Amico et al. 2010).

Green's functions were obtained as Langston's fundamental fault responses (Langston and Helmberger, 1975), using the spectral reflectivity matrix approach for layered media of Kennett (1983). The responses were computed at frequencies up to 1 Hz, with a sampling interval of 0.5 s and a maximum number of points of 1024. A range for the ray parameter of 0.025-0.96 s/km was employed, which accounts from waves travelling almost horizontally to waves travelling almost vertically. These parameters produced Green's functions with suitable time windows and frequency content to model the surface-wave train. The synthetics were calculated for epicentral distances and azimuths consistent with the epicenter latitude and longitude of Dias et al. (2018) (3.14°S;43.86°W) and for source depths between 1 and 19 km at 2 km depth intervals. The predicted P-wave arrival time was marked in the Greens functions after ray-tracing through the velocity model (Table 1) and was utilized to initially align observed and synthetic waveforms.

Table 1. Velocity model utilized for the 2017 Maranhão earthquake.

Thickness (km)	V_P (km/s)	V_S (km/s)	Density (g/cm³)	Q_P	Q_S
2.0	5.50	3.17	2.53	250.0	125.0
20.0	6.25	3.61	2.77	500.0	250.0
18.0	6.80	3.93	2.95	500.0	250.0
-	8.15	4.70	3.38	500.0	250.0

Before inversion, we defined shorter time windows by cutting 2 seconds before the P-wave arrival time and a theoretical time given by epicentral distance over 1.5 km/s. This value was estimated experimentally to provide a time window long enough to include the entire surface wave train. Then, we band-pass filtered both waveforms between 0.05 and 0.1 Hz to remove low-frequency noise from observations while reducing the effect of small-scale crustal heterogeneities (e.g. D'Amico et al. 2010, Chen et al. 2016). This same frequency range was used by Carvalho et al. (2019) and it is wider than that used by Dias et al. (2018) for distant stations. Finally, we decimated the observed waveforms down to a sampling interval of 0.5 s, which was sufficient for modeling purposes.

During inversion, we attributed equal weights to all waveforms, and time-shifts were constrained to ±8 seconds to avoid miscorrelation with coda complexities. Inverted focal mechanisms were produced for a range of source-depths (Fig. 2b), together with their respective average misfits. Our results reveal a strike-slip mechanism (340°±0°, 70°±0°, 0°±0°) with an M_0 of 3.91 ± 0.13 E22 dyne-cm (4.4 Mw) at an optimal depth of 9 km (Table 2). The radiation pattern appears quite robust for almost the entire depth range, and centroid depth displays acceptable values between 7 and 9 km (Fig. 2b). Uncertainties were determined through jackknife resampling after systematically removing each station, one at a time. Note that an error of 0° merely indicates that the angle did not change with jackknife resampling, so that uncertainties actually are within one grid-search interval (i.e. < 10°). The match between observations and predictions is excellent for most of the 39 traces used in this inversion (see Fig. 2c and S1), demonstrating that the empirical time-shifts succeeded in aligning observations and predictions. We achieved reasonable fits even for waveforms recorded by stations over sedimentary basins (e.g., NBPS), which naturally produce more complexity in surface-wave recordings.

Table 2. Summary of the inversion results for the 2017 Maranhão earthquake with jackknife uncertainties.

Data	Cross-correlation threshold	Number of traces	Centroid depth (km)	s°/d°/r°	M0 (E22 dyne-cm)	Mw	Reference figure
RSBR	-	39	9	340±0/70±0/ 0±0[a]	3.91±0.13	4.4	Fig. 2b
RSBR + temporary networks	-	87	11	340±3.5/80±0/ 0±3.5	4.91±0.10	4.4	Fig. 3b
RSBR	60%	30	9	340±3.7/70±3.7/ 0±3.7	3.98±0.14	4.4	Fig. S5
RSBR + temporary networks	60%	72	9	330±2.6/70±0/ -10±2.6	4.57±0.05	4.4	Fig. S7

[a]Uncertainties of 0° indicate that errors are within one grid-search step (i.e. < 10°).

3.2. Focal mechanism with an expanded dataset

The 2017 Maranhão earthquake was additionally recorded at 16 broadband stations from two nearby temporary deployments (Fig. 3a), which were part of two independent regional studies that targeted crustal structure. The Parnaíba Basin Analysis Project (PBAP) was a multi-disciplinary effort funded by BP Energy do Brazil aimed at understanding the origin and evolution of the cratonic Parnaíba Basin (Daly et al., 2018). It included a small array of 11 Meridian Compact PH seismometers that were deployed for about 2 years (2016-2017) along an approximately E-W line in the central portion of the basin. The Borborema Deep Electromagnetic and Seismic (BODES) experiment was also a multi-disciplinary effort, funded by the *Conselho Nacional de Desenvolvimento Científico e Tecnológico* (CNPq), aimed at unraveling the tectonic inversion mechanism of the Araripe Basin (Garcia et al., 2019; Nemocón et al., 2021). It included a linear array of 9 RefTek 151-120A sensors attached to RT130 digitizers that were deployed between 2015 and 2017 in an approximately N-S direction across the basin. Like the permanent RSBR stations, these temporary networks recorded continuously at 100 s.p.s.

The availability of these additional stations provides a unique opportunity for assessing the performance of the sparse RSBR network, as they improve azimuthal coverage around the epicenter significantly (compare Figs 3a and 2a). Additional inversions were thus performed through combination of the 13 RSBR stations and the 16 temporary stations. We followed the same selection criteria as outlined before (see Section 3.1), resulting in 87 waveforms available for inversion. Synthetic seismograms were computed using the same velocity model (Table 1) as before, and inversion was performed with identical frequency contents, window lengths,

time-shift ranges, and weights. The resulting focal mechanism led to the same radiation pattern (340°±3.5°, 80°±0°, 0°±3.5°) obtained with RSBR stations only, but suggested a somewhat wider range of source depths (7-11 km), in which the 11 km source-depth provided the smallest misfit (Fig. 3b). This optimal solution had a M0 of 4.91±0.10 E22 dyne-cm (4.4 Mw), somewhat larger than that obtained with RSBR stations only (Table 2).

3.3. Comparison to other focal solutions

Our focal solutions are fully consistent with solutions reported in the independent studies of Carvalho et al. (2019) and Dias et al. (2018). Regarding the focal mechanism obtained with RSBR data only, our solution is in close agreement with that of Dias et al. (2018) (339°,83°,-2°) and Carvalho et al. (2019) (340°, 80°, -10°) (Fig. S2 and S4). In terms of earthquake size, our estimate of 4.4 Mw is also compatible with that of 4.3 Mw from the two previous studies, and is relatively smaller than those attributed by the RSBR bulletin (4.6 mR) and by the USGS catalog (4.5 mb). Our optimal source-depth range (7-9 km) is within the 5-14 km range estimated by Dias et al. (2018), although our preferred value of 9 km is slightly deeper than theirs (7.5 km). The addition of 16 temporary stations further supports these findings, but suggests a somewhat larger optimal depth at 11 km. Interestingly, this depth estimate is close to the source depth reported by Dias et al. (2018) from aftershock locations (12 km) and from analysis of main-shock teleseismic recordings (12 or 13 km). It is also close to the estimate provided by the USGS catalog (10 km).

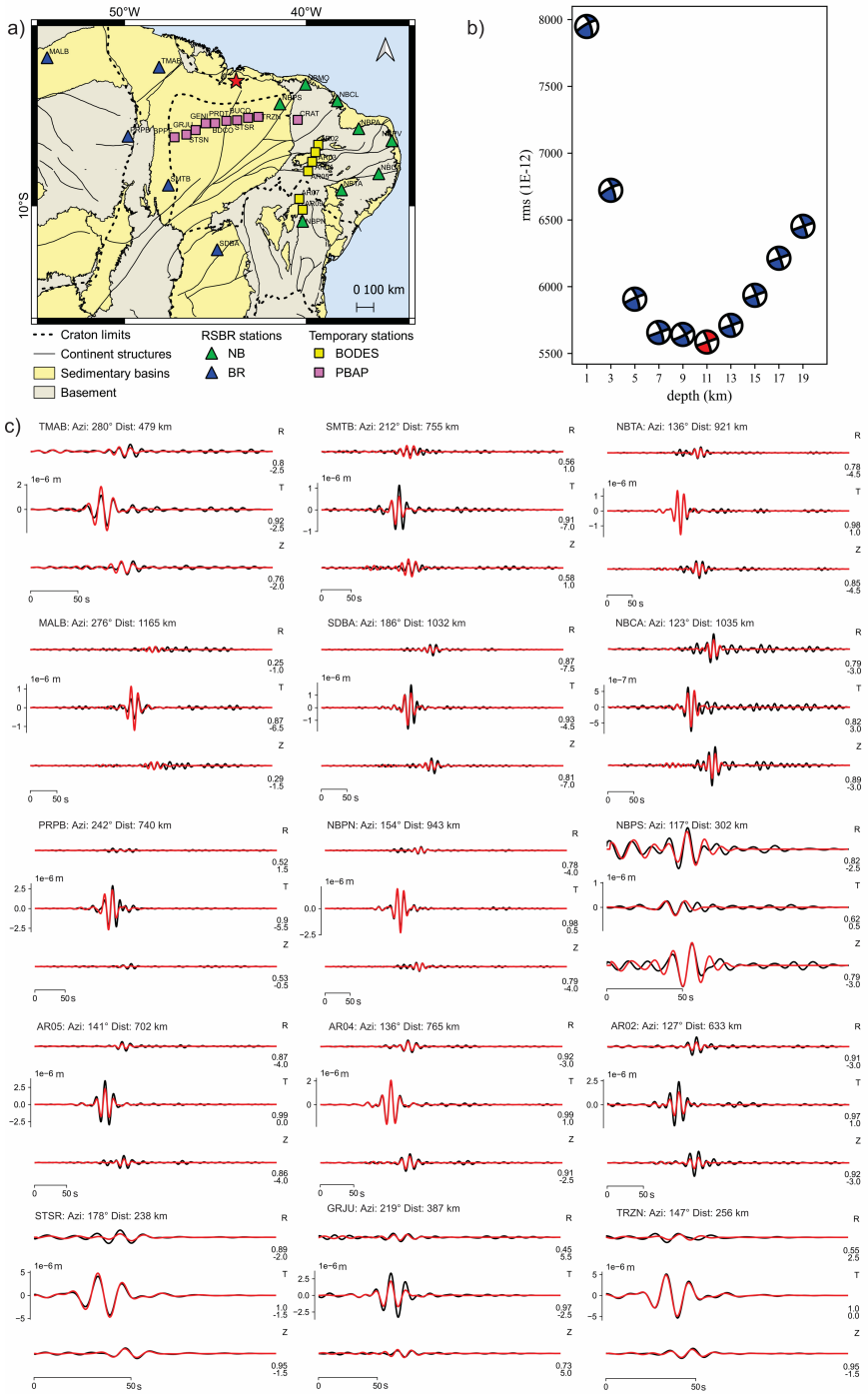

Fig. 3. Inversion results for the Mw 4.4 2017 Maranhão earthquake with an expanded dataset. A) epicenter (red star) and locations of the 13 RSBR and 16 temporary broadband seismic stations (triangles) utilized for waveform inversion. The stations have been color-coded; B) Focal mechanisms obtained from the inversion of the expanded dataset for the investigated depth-range; the preferred mechanism is shown in red; and C) Waveform fit at select stations produced by the preferred solution in B. The match between all waveforms can be checked in the Supplementary Material (Fig. S3).

4. The Mw 4.1 August 30th, 2020 Amargosa earthquake

Another moderate-size intraplate earthquake occurred on August 30th, 2020 near the municipality of Amargosa, BA. The USGS catalog listed epicentral coordinates of 13.24°S and 39.53°W and an origin time at 10:44:31.253 (UTC) for this event. Focal depth was reported at 10±1.9 km and magnitude at 4.6 mb. This epicentral location differed by about 27 km from that provided by the RSBR bulletin (13.01°S;39.60°W), which is significant (Fig. 4a). The RSBR bulletin attributed a regional magnitude of 4.2 mR for this event, while depth was fixed at 0 km.

4.1. Focal mechanism with RSBR data

This earthquake was well recorded by 25 RSBR stations located at distances below 10º from the epicenter. As before, we excluded a station (GDU01) that was in close proximity (50 km) to the source, yielding a total of 24 stations with epicentral distances between 234-1100 km available for inversion (Fig. 4a). The corresponding seismograms were windowed and processed in exactly the same manner as explained for the previous example. To perform the inversions, however, we selected traces with SNR > 20. Phase picking, which is utilized for initial waveform alignment, was especially difficult for this event. Although the P-wave onset was clear at a few closer stations, it was obscured by noise for the most distant stations or emergent at stations placed over sedimentary basins. In those cases, we used the theoretical travel-times as a guide. This proved to be an effective strategy, as the empirical time-shifts from our simplified CAP approach helped with waveform misalignment due to imprecise first-arrival pickings.

During processing, we discovered a timing issue with station NBCL; however, since the first arrival was clearly observable, we were able to pick the P-wave onset and include it in our inversions. Furthermore, we observed that station, CAM01 reported incoherent channel orientations, so only the vertical component was utilized.

We computed Green's functions for this event as we did for the 2017 Maranhão earthquake, but using the velocity model outlined in Table 3. This velocity model was based on the results of an onshore-offshore seismic refraction profile (SL09) close to the epicentral area (Pinheiro et al., 2018). As with the previous earthquake, S-wave velocities were obtained from the P-wave velocities in the seismic profile by assuming a Poisson solid, densities were estimated from an empirical relationship, and typical values for attenuation were assumed. The Green's function responses for this event were calculated at a maximum frequency of 1 Hz,

which corresponds to a sampling rate of 0.5 s. We used 4096 points, which provided a long enough time window for our synthetics. We considered the epicenter coordinates and origin time taken from the USGS catalog and calculated synthetics for source depths between 2 and 20 km at 2 km depth intervals. It is important to realize that empirical time-shifts from our simplified CAP approach will absorb potentially large uncertainties in both earthquake location and origin time.

Table 3. Simplified velocity model for computation of the Greens functions of the 2020 Amargosa earthquake.

Thickness (km)	V_P (km/s)	V_S (km/s)	Density (g/cm³)	Q_P	Q_S
16.3	6.08	3.51	2.71	500	250
13.3	6.25	3.61	2.77	500	250
11.2	6.85	3.95	2.96	500	250
19.2	8.10	4.68	3.36	500	250
-	8.30	4.79	3.43	500	250

To determine the focal mechanisms for each source-depth, we initially aligned data and Green's functions by cutting 2 s before the P-wave onset. For inversion, we considered time windows with variable length obtained after dividing epicentral distance by 1.8 km/s, 2.0 km/s and 2.2 km/s, depending on distance. Waveforms were then band-pass filtered in the 0.04-0.1 Hz frequency range and decimated down to 0.5 s.p.s. To perform the inversions, we attributed equal weights to all waveforms. Because of presumably large uncertainties in the preliminary alignment between observed and predicted waveforms, we defined a wider range of ±21 seconds for the empirical time-shifts. This wide range was thoroughly tested and found necessary to produce time-shifts that satisfactorily aligned observed and predicted waveforms.

From the solutions obtained for each depth (Fig. 4b), it was determined that the Amargosa mainshock probably occurred between 8 and 10 km depth, where the 10 km depth solution produced the overall minimum misfit. The match between observation and predictions was visually satisfying for all waveforms (Figs 4d and S9). The focal solution revealed an oblique normal fault (20°±4.6°, 60°±16.9°, -30°±14.4°) and yielded a M_0 of 1.54±0.04 E22 dyne-cm (4.1 Mw) (Table 4). A similar normal fault mechanism was also obtained for centroid depths of 8 km or larger; for shallower depths, however, the source mechanism was more variable but still suggests oblique normal rupture.

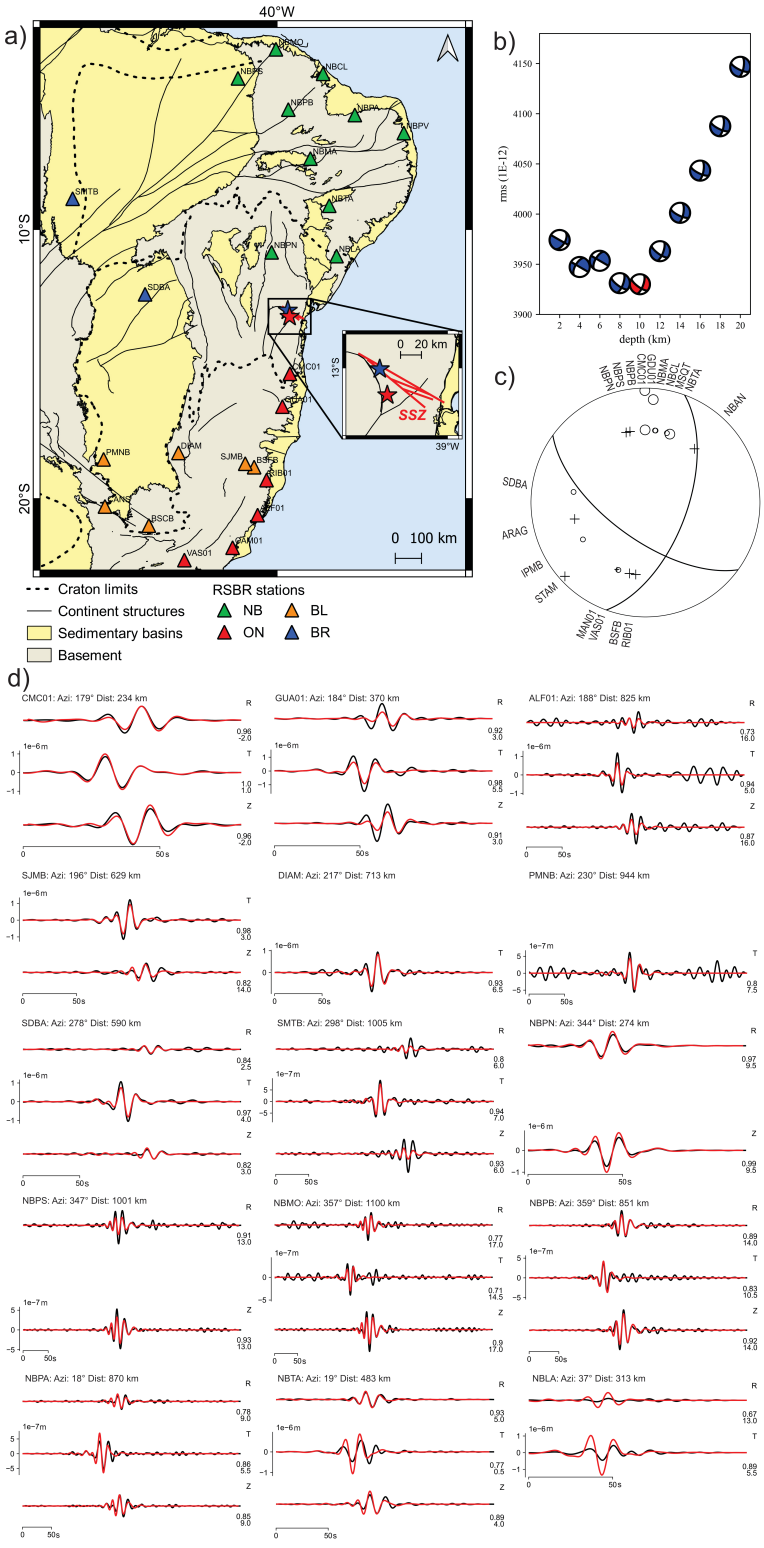

Fig. 4. Results for the Mw 4.1 August 30th, 2020 intraplate Amargosa earthquake with RSBR stations. A) Map showing the USGS epicenter (red star) along with the 24 permanent RSBR stations (triangles) considered for waveform inversion. The inset zooms on the epicentral area and shows that the Salvador Shear Zone (SSZ) lineaments overlay the epicentral location from the RSBR catalog (blue star); B) Focal mechanisms inverted for a range of source depths, with the preferred solution in red (10 km); C)

P-wave polarities plotted on the focal sphere of the preferred focal mechanism for this earthquake. Crosses denote compression while circles denote dilatation. The symbols are sized using the quality assigned for the polarity observation (see Fig. S15); D) Waveform fits at select stations produced by the preferred solution in B. Waveforms fits for all stations can be found in Figure S9.

4.2. Focal mechanism with an expanded dataset

As with the Maranhão earthquake, the Amargosa earthquake was recorded by a set of temporary stations. Those were part of a deployment funded by Petrobras that operated between 2019 and 2020, with the aim to study the architecture of syn-rift sedimentary basins in NE Brazil (Fig. 5a). Overall, 6 temporary broadband stations recorded this earthquake, but we excluded one of them because of its close proximity to the epicenter. The stations consisted of Meridian Compact PH seismometers, identical to those used in the PBAP experiment, and sampled continuously at 100 s.p.s.

An additional set of inversions was thus performed with the temporary stations added, following identical processing and inversion criteria as for the inversion with RSBR stations only. The new results indicated the same preferred source-depth and focal mechanism (20°±1.9°, 60°±0°, -30°±1.9°), with a similar M_0 of 1.68±0.04 E22 dyne-cm (4.1 Mw) (Table 4). The main difference was that the uncertainties for this last solution, as expected, were significantly smaller than those estimated with RSBR data only. Fig. 5b, demonstrates that focal depth is better resolved when including those additional stations, and that the focal mechanism is robust for a slightly wider range of depths (6-20 km) when compared to the set with RSBR stations only (8-20 km). The optimal centroid depth of 10 km obtained from both sets of inversions (Table 4) agrees with that reported in the USGS catalog. Our inferred magnitude of 4.1 Mw, on the other hand, is closer to the 4.2 mR attributed by the RSBR bulletin than that of 4.6 mb reported in the USGS catalog. Because of its relatively low magnitude, there were no available preliminary solutions from either the USGS nor the GCMT catalogs to compare with.

Table 4. Summary of the inversion results for the 2020 Amargosa earthquake with uncertainties estimated from the jackknife resampling method.

Data	Cross-correlation threshold	Number of traces	Centroid depth (km)	s°/d°/r°	M0 (E22 dyne-cm)	Mw	Reference figure
RSBR	-	55	10	20±4.6/60±16.9/ -30±14.4	1.54±0.04	4.1	Fig. 4b

RSBR + temporary networks	-	66	10	20±1.9/60±0/ -30±1.9	1.68±0.04	4.1	Fig. 5b
RSBR	60%	52	6	210±2.9/50±2.1/ 0±8.0	1.52±0.05	4.1	Fig. S11a
RSBR + temporary networks	60%	64	10	20±2.7/60±0/ -30±4.2	1.68±0.04	4.1	Fig. S13

4.3. Comparison with P-wave polarities and local tectonics

Because no independent focal mechanisms exist for this event, we validated our solution through analysis of the P-wave radiation pattern. To this effect, we read P-wave polarities from the same regional recordings that were used for waveform modeling (Fig. S15). Determining polarities proved challenging because, as mentioned earlier, P-wave onsets for the Amargosa earthquake were generally emergent or obscured by noise. In spite of those difficulties, we still managed to determine 18 polarities with various degrees of confidence. Figs. 4c and 5c overlay those polarities to the focal mechanism determined from our simplified CAP inversion. Note that polarity symbols were scaled to visually-assigned quality, with large symbols denoting high-quality and small symbols denoting low-quality. Most polarities (12 out of 18) agree with our preferred mechanism, with eight corresponding to high-quality observations and four to low-quality observations. We realize that there are three high-quality observations that disagree with our focal mechanism, perhaps resulting from a NDC contribution to the focal mechanism.

Additional validation of our preferred focal solution was achieved by correlating our fault-plane orientations with surface geology. A technical report from the Brazilian Geologic Survey (CPRM) indicated a spatial correlation between the earthquake's epicenter and the Salvador Shear Zone (SSZ) (Sobrinho et al., 2020). The SSZ is composed of a number of NW-SE-oriented lineaments associated to the Precambrian rocks making the basement of the marginal Camamu-Almada sedimentary basin (Ferreira et al., 2009; Gordon et al., 2017). Indeed, the location given by the RSBR catalog nicely overlaps with the lineaments mapped for the SSZ (Fig. 4a). Moreover, our NW-SE nodal plane (126°, 64°, 214°) is in close agreement with the orientations of the SSZ lineaments (see Figs. 4a and 5a), suggesting this might be the actual fault plane.

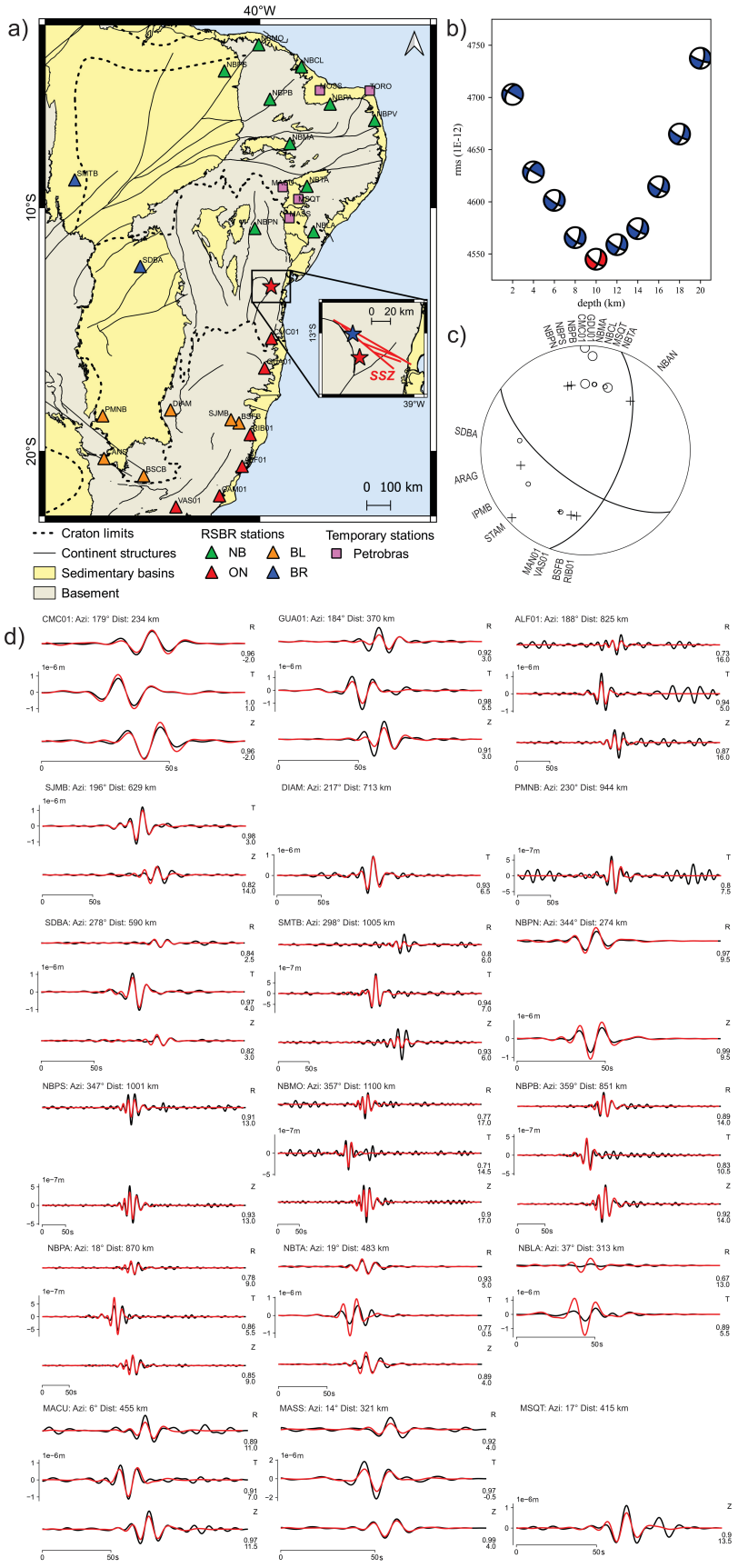

Fig. 5. Inversion results for the Mw 4.1 2020 Amargosa earthquake with an expanded dataset. A) Distribution of the 24 permanent (RSBR) and 5 temporary stations used for waveform inversion. B)

Focal mechanisms determined from the inversion of the expanded dataset for a range of source depths. The preferred mechanism is shown in red; C) Overlay of P-wave polarities on the focal sphere of the best focal mechanism. Crosses denote compression while circles denote dilation. The symbols are sized according to quality; D) Waveform fits at select stations produced by the best solution in B. The fit to all waveforms can be found in Figure S10.

5. Discussion

5.1. General performance of the simplified CAP method

The two intraplate earthquakes considered in this work showed that reliable focal mechanisms, magnitudes and depths can be determined with our simplified CAP approach. Moreover, they also demonstrated that satisfactory results are obtained from RSBR stations alone. Our solution for the 2017 Maranhão earthquake, for instance, is fully compatible with the independent studies of Dias et al. (2018) and Carvalho et al. (2019), and with an inversion with additional azimuthal coverage from two temporary deployments. The main difference was perhaps observed in the M_0 estimate, which was somewhat larger for the inversion including the temporary stations (Table 2); moment magnitude, however, was virtually the same. And, for the 2020 Amargosa earthquake, our solutions with or without additional temporary stations was also found fully compatible with the solution with additional station coverage, although uncertainties were a bit larger when using RSBR stations only (Table 4). Moreover, our solutions displayed overall consistency with the P-wave radiation pattern from first-motion polarities and with local tectonics.

We find it remarkable that we were able to achieve satisfactory waveform fits for stations as far as 1000 km by using two simple velocity models based on local seismic experiments near the epicentral region. These velocity models were simple in the sense that they did not include 3D spatial variations around the average velocity structure, such as those expected between geologic provinces and sedimentary basins. This observation corroborates that the empirical time-shifts developed through the simplified CAP approach successfully account for lateral variations in Earth structure during alignment.

We also find it remarkable that, for the inversion of the 2017 Maranhão earthquake, our study included a much larger number of stations than those reported in independent studies of the same event. Dias et al. (2018), for instance, determined their preferred solution after modeling waveforms from just four RSBR stations: SMTB, PRPB, NBCL, at 600-750 km distance, and ROSB, at 40 km; and Carvalho et al. (2019) also considered four RSBR stations

(ROSB, TMAB, PAL1 and TUC4), located at 470-640 km from the epicenter, when inverting waveform envelopes. Our inversion with RSBR data, on the other hand, included a total of 13 stations. We must therefore conclude that empirical time shifts account for lateral variations in velocity structure more effectively than path-specific Green's functions or waveforms envelopes, and that our simplified CAP approach represents a more efficient alternative for retrieving focal mechanisms for shallow intraplate earthquakes in Brazil.

5.2. Removal of low-correlation waveforms

During regional waveform modeling, it is common practice to remove traces with low cross-correlation coefficients (e.g., Luo et al., 2015; Singh et al., 2016). In this approach, the correlation between observed and predicted waveforms is assessed after inversion and those below a given threshold are removed. The inversion is then repeated and the correlation assessed again until all waveforms fall above the threshold. To test whether this approach results in any improvement in our inversions, we iteratively removed traces with low cross-correlation coefficients (< 60%) until all used waveforms were above the defined threshold. We defined this threshold based on the values used by other studies, typically ranging from 60% to 70% (e.g. Luo et al., 2015; Singh et al., 2016).

For the Maranhão earthquake, when applied to the inversion with RSBR data only, this procedure resulted in the use of 30 waveforms (out of 39 available from RSBR stations) and required two iterations. Most of the traces that were removed were Rayleigh waves recorded in radial components from stations located on sedimentary basins, or waveforms with small amplitudes (i.e., close to nodal planes). We obtained the same focal solution, magnitude and preferred depth (Figs. S5 and S6) when compared to that obtained from the inversion of all RSBR data (Table 2). Perhaps, the main difference was that the source-depth was better constrained after the iterative removal, clearly indicating a preferred depth of 9 km. The same procedure was then applied to the set of inversions including the two temporary networks. It required just one iteration and resulted in the use of 72 traces (out of 87 available). It again yielded a focal mechanism fully consistent with our original solution, but with a preferred depth of 9 km (Figs. S7 and S8). It is notable that, in all cases, the mechanism for each depth did not change after the iterative removal of low-correlation traces, which means the mechanism is robust even when including traces with low correlation coefficients.

As for the Maranhão event, we iteratively removed traces with low cross-correlation coefficients for the 2020 Amargosa earthquake. Again, a threshold of 60% was considered.

For the inversions using data from RSBR stations only, we retained 52 traces (23 stations) out of 55 originally available (24 stations), and just one iteration sufficed. This procedure yielded a normal-fault mechanism described by (210°±2.9°,50°±2.1°,0°±8.0°) with a M_0 of 1.52±0.05 E22 dyne-cm (4.1 Mw) at an optimal depth of 6 km (Figs. S11 and S12), which differs significantly from the mechanism originally obtained (Fig. 4b and Table 4). Interestingly, when we plotted the polarities against this focal mechanism, we observed that most polarities are at odds with the predicted radiation pattern (Fig. S11b). Finally, we applied the same removal procedure to the dataset that includes the temporary stations (Figure S13). After just one pass, 64 waveforms were retained from the initial 66 traces and we observed again a preferred 10 km centroid depth with the same mechanism obtained in the inversions shown in Figs. 4b and 5b (Table 4). M_0 was virtually the same (Fig. 5b, Table 4).

We conclude that, in general, the iterative removal does not make much of a difference during the inversion of regional waveforms. However, the instability detected for the Amargosa earthquake when inverting RSBR data only merits further investigation.

By comparing the inversions for the 2020 Amargosa earthquake obtained with and without the iterative removal of low-correlated traces (RSBR data only), we observe some similarities. Both inversions showed the same mechanism for each investigated depth (Fig. 4b and S11a), and both display a minimum at 10 km, depth. The main difference among the inversion schemes is that the removal of poorly-correlated waveforms led to the formation of another minimum around 6 km depth, turning the 10 km depth a local minimum. Moreover, the focal solution for the 6 km depth minimum indicates a quite different radiation pattern when compared to that for the 10 km depth minimum (Fig. S11a). In fact, the new minimum forms after the removal of just one trace, the radial component of station NBLA, with a correlation coefficient of ~58% and very close to the target threshold. Station NBLA was also removed when the inversion was performed on the expanded dataset, but only for depths of 2 and 4 km (Fig. S13). We observed that a minimum was formed at 4 km depth (Fig. S13), but such decrease in rms was not enough to form a new, absolute minimum (Fig. S11a).

We further tested the stability of the preferred 10 km focal mechanism indicated in Figs. 4b and 5b by removing traces for station NBLA only. For the set without temporary stations, we observed that the same mechanism (20°,60°,-30°) is obtained after removing the radial component only. However, after removing the transverse component as well, the focal mechanism at this depth goes to (210°,60°,-10°). For the inversion including the temporary network stations, we performed the same test and obtained the same source mechanism of (20°,60°,-30).

Thus, it seems that there is a strong dependence on the waveforms recorded at station NBLA when considering RSBR data only. The inclusion of temporary stations at azimuths and distances relatively close to that of the permanent station NBLA improved depth resolution and considerably reduced uncertainties in the preferred focal mechanism (Table 4). We thus interpret this instability (i.e., the abrupt decrease in the rms after the removal of a single station) as an artifact due to the major influence of a relatively close station (~313 km) at a poorly sampled azimuth (~37° Az) (Fig. 4a), which can be compensated by including additional coverage in that direction (Fig. 5a). These results also highlight that it is important to be careful when removing low cross-correlated traces and to always check the inverted solution with available first-motion polarities.

5.3. Limitations of the simplified CAP method

The main difficulty when using the simplified CAP approach is to correctly define the correlation window and the acceptable range for the empirical time-shifts. Obviously, the correlation window must be defined to include the portion of the seismogram that one wants to model in the inversion. The range for the acceptable time shifts can be determined after experimenting with several values and then observing which one provided a visually satisfying alignment between observed and predicted waveforms. Also, because we are using stations 1000 km away from the epicenter, this range must be wide enough to compensate for cumulative time inaccuracies with distance. Realize that we used ±8 s for the 2017 Maranhão event, while the 2020 Amargosa event required ±21 s. Inaccuracies in epicenter location and depth were larger for the Amargosa event but, most probably, large inaccuracies in P-wave picking for initial alignment played a major role. On the other hand, allowing synthetics to shift excessively might result in an incorrect alignment with coda complexities when waveforms, for example, are noisy. Thus, it is important to test the range of acceptable time shifts and to visually check if acceptable alignment is achieved.

Another limitation of our simplified CAP approach is that it does not normalize for geometrical spreading when inverting traces from a wide range of epicentral distances. This limitation results in a bigger contribution of nearby stations to the total RMS and, consequently, in constraining depth and focal mechanism. Zhu and Helmberger (1996) introduced a distance range scaling factor during misfit evaluation to correct for this effect. The authors showed that such an amplitude normalization would be more important when including recordings from stations placed at epicentral distances down to ~200 km for surface waves (see their Fig. 3).

Due to the uneven distribution of the RSBR stations, however, only a few or no stations at all are generally available at close distances for moment tensor determination of moderate intraplate earthquakes in Brazil (recall the two examples discussed in previous sections). Thus, our approach to geometrical spreading normalization was to just discard data from stations placed at less than ~200 km from the epicenter.

Finally, we have observed that azimuthal coverage is especially concerning, as demonstrated when waveforms from a poorly sampled azimuth were removed for the Amargosa event (recall station NBLA). This was possibly due to the fact that the inversion of surface-waves is more dependent on good azimuthal coverage than body waves (e.g., D'Amico et al., 2014). Thus, it seems more sensible to keep stations in poorly sampled azimuths, even when the correlation coefficient is not especially large. This limitation also highlights the importance of verifying the inverted solution with P-wave polarities – or any other means - whenever possible.

6. Conclusions

We assessed the performance of a simplified CAP approach for routine determination of earthquake focal mechanisms in Brazil using the Brazilian national seismic network (RSBR). Like the original CAP approach, alignment between observations and predictions is achieved through empirical time-shifts from cross-correlation; different from the original CAP approach, no partition of body and surface-waves and no amplitude normalization is considered. Our simplified approach successfully inverted for the focal mechanisms of two Mw ~4.0 intraplate earthquakes using regional waveforms recorded by the permanent RSBR network. One of the intraplate examples was the well-investigated 2017 January 3rd Maranhão event (4.4 Mw), for which results were verified through comparison with those presented in two independent works. The second one was the 2020 August 30th Amargosa event (4.1 Mw), for which we confirmed our solution by comparing with first-motion polarities and surface geology.

Data availability

Parts of the dataset are proprietary. Code can be shared upon request.

Acknowledgments

This research was funded through a grant awarded by the Conselho Nacional de Desenvolvimento Científico e Tecnológico (CNPq - grant no 434807/2018-4). GSLN thanks

the Coordenação de Aperfeiçoamento de Pessoal de Nível Superior (CAPES) for granting a scholarship to conduct his PhD at the Universidade Federal do Rio Grande do Norte. JJ additionally thanks CNPq for his research fellowship (CNPq – 308644/2019-0). We express our gratitude to Charles J. Ammon for making his inversion codes freely available to the public, and to Mikael Evain for providing the velocity profile used in the inversions of the Amargosa earthquake. We also thank the Geological Survey of Brazil – CPRM for providing the shapefiles used in this work.

References

Agurto-Detzel, H., Assumpção, M., Bianchi, M., Pirchiner, M., 2015a. Intraplate seismicity in mid-plate South America: correlations with geophysical lithospheric parameters. Geol. Soc. London, Spec. Publ. 432, 73–90. https://doi.org/10.1144/SP432.5

Agurto-Detzel, H., Assumpção, M., Ciardelli, C., Albuquerque, D.F., Barros, L. V., França, G.S.L., 2015b. The 2012–2013 Montes Claros earthquake series in the São Francisco Craton, Brazil: new evidence for non-uniform intraplate stresses in mid-plate South America. Geophys. J. Int. 200, 216–226. https://doi.org/10.1093/gji/ggu333

Assumpção, M., Dourado, J.C., Ribotta, L.C., Mohriak, W.U., Dias, F.L., Barbosa, J.R., 2011. The São Vicente earthquake of 2008 April and seismicity in the continental shelf off SE Brazil: Further evidence for flexural stresses. Geophys. J. Int. https://doi.org/10.1111/j.1365-246X.2011.05198.x

Assumpção, M., Ferreira, J.M., Barros, L. V., Bezerra, F.H.R., França, G.S., Barbosa, J.R., Menezes, E., Ribotta, L.C., Pirchiner, M., do Nascimento, A.F., Dourado, J.C., 2014. Intraplate Seismicity in Brazil, in: Talwani, P. (Ed.), Intraplate Earthquakes. Cambridge University Press, pp. 50–71. https://doi.org/10.1017/CBO9781139628921.004

Assumpção, M., Schimmel, M., Escalante, C., Roberto Barbosa, J., Rocha, M., Barros, L. V., 2004. Intraplate seismicity in SE Brazil: stress concentration in lithospheric thin spots. Geophys. J. Int. 159, 390–399. https://doi.org/10.1111/j.1365-246X.2004.02357.x

Bai, Q., Ni, S., Chu, R., Jia, Z., 2020. gCAPjoint, A Software Package for Full Moment Tensor Inversion of Moderately Strong Earthquakes with Local and Teleseismic Waveforms. Seismol. Res. Lett. 91, 3550–3562. https://doi.org/10.1785/0220200031

Barros, L. V., Assumpção, M., Chimpliganond, C., Carvalho, J.M., Von Huelsen, M.G., Caixeta, D., França, G.S., de Albuquerque, D.F., Ferreira, V.M., Fontenele, D.P., 2015. The Mara Rosa 2010 GT-5 earthquake and its possible relationship with the continental-scale transbrasiliano lineament. J. South Am. Earth Sci. 60, 1–9. https://doi.org/10.1016/j.jsames.2015.02.002

Berrocal, J., Assumpçao, M., Antezana, R., Dias Neto, C.M., Ortega, R., França, H., Veloso, J.A.V., 1984. Sismicidade do Brasil.

Berteussen, K.-A., 1977. Moho depth determinations based on spectral-ratio analysis of NORSAR long-period P waves. Phys. Earth Planet. Inter. 15, 13–27. https://doi.org/10.1016/0031-9201(77)90006-1

Bianchi, M.B., Assumpção, M., Rocha, M.P., Carvalho, J.M., Azevedo, P.A., Fontes, S.L., Dias, F.L., Ferreira, J.M., Nascimento, A.F., Ferreira, M. V., Costa, I.S.L., 2018. The Brazilian Seismographic Network (RSBR): Improving Seismic Monitoring in Brazil. Seismol. Res. Lett. 89, 452–457. https://doi.org/10.1785/0220170227

Carvalho, J., Barros, L.V., Zahradník, J., 2019. Inversion for Focal Mechanisms Using Waveform Envelopes and Inaccurate Velocity Models: Examples from Brazil. Bull. Seismol. Soc. Am. 109, 138–151. https://doi.org/10.1785/0120180119

Carvalho, J.M., Barros, L.V., Zahradník, J., Von Huelsen, M.G., Ferreira, V.M., 2020. Earthquake relocation, focal mechanism and stress field determination in central Brazil. J. South Am. Earth Sci. 97. https://doi.org/https://doi.org/10.1016/j.jsames.2019.102411

Chen, H., He, X., Yang, H., Zhang, J., 2021. Fault-Plane Determination of the 4 January 2020 0ffshore Pearl River Delta Earthquake and Its Implication for Seismic Hazard Assessment. Seismol. Res. Lett. 92, 1913–1925. https://doi.org/https://doi.org/10.1785/0220200232

Chen, J., Carpenter, N.S., Wang, Z., Zuo, K., Yang, L., 2016. Evidence of Complex Faulting near the Huangcheng-Shuangta Fault, Gansu, China, from the 11 May 2012 M w 4.8 Sunan Earthquake. Bull. Seismol. Soc. Am. 106, 2258–2265. https://doi.org/10.1785/0120160094

Chen, W., Ni, S., Kanamori, H., Wei, S., Jia, Z., Zhu, L., 2015. CAPjoint, A Computer Software Package for Joint Inversion of Moderate Earthquake Source Parameters with Local and Teleseismic Waveforms. Seismol. Res. Lett. 86, 432–441. https://doi.org/https://doi.org/10.1785/0220140167

D'Amico, S., Cammarata, L., Cangemi, M., Cavallaro, D., Di Martino, R.M., Carlino, M.F., 2014. Seismic moment tensors and regional stress in the area of the December 2013–January 2014, Matese earthquake sequence (Italy). J. Geodyn. 82, 118–124. https://doi.org/https://doi.org/10.1016/j.jog.2014.09.008

D'Amico, S., Orecchio, B., Presti, D., Neri, G., Wu, W.-N., Sandu, I., Zhu, L., Herrmann, R.B., 2013. Source parameters of small and moderate earthquakes in the area of the 2009 L'Aquila earthquake sequence (central Italy). Phys. Chem. Earth, Parts A/B/C 63, 77–91. https://doi.org/10.1016/j.pce.2013.02.005

D'Amico, S., Orecchio, B., Presti, D., Zhu, L., Herrmann, R.B., Neri, G., 2010. Broadband waveform inversion of moderate earthquakes in the Messina Straits, southern Italy. Phys. Earth Planet. Inter. 179, 97–106. https://doi.org/10.1016/j.pepi.2010.01.012

Daly, M.C., Fuck, R.A., Julià, J., Macdonald, D.I.M., Watts, A.B., 2018. Cratonic basin formation: a case study of the Parnaíba Basin of Brazil. Geol. Soc. London, Spec. Publ. 472, 1–15. https://doi.org/10.1144/SP472.20

Dias, F.L., Assumpção, M., Bianchi, M.B., Barros, L. V., Carvalho, J.M., 2018. The intraplate Maranhão earthquake of 2017 January 3, northern Brazil: evidence for uniform regional stresses along the Brazilian equatorial margin. Geophys. J. Int. 213, 387–396. https://doi.org/10.1093/gji/ggx560

Ferreira, J.M., Oliveira, T., Takeya, M.K., Assumpção, M., 1998. Superposition of local and regional stresses in northeast Brazil: evidence from focal mechanisms around the Potiguar marginal basin. Geophys. J. Int. 134, 341–355. https://doi.org/10.1046/j.1365-246x.1998.00563.x

Ferreira, T.S., Caixeta, J.M., Lima, F.D., 2009. Controle do embasamento no rifteamento das bacias de Camamu e Almada. Bol. Geociências - Petrobras 17, 69–88.

Fonsêca, J.A.S., Ferreira, J.M., do Nascimento, A.F., Bezerra, F.H.R., Lima Neto, H.C., de Menezes, E.A.S., 2021. Intraplate earthquakes in the Potiguar Basin, Brazil: Evidence for superposition of local and regional stresses and implications for moderate-size earthquake occurrence. J. South Am. Earth Sci. 110. https://doi.org/10.1016/j.jsames.2021.103370

Garcia, X., Julià, J., Nemocón, A.M., Neukirch, M., 2019. Lithospheric thinning under the Araripe Basin (NE Brazil) from a long-period magnetotelluric survey: Constraints for tectonic inversion. Gondwana Res. 68, 174–184. https://doi.org/10.1016/j.gr.2018.11.013

Gordon, A., Destro, N., Heilbron, M., 2017. The Recôncavo-Tucano-Jatobá Rift and Associated Atlantic Continental Margin Basins, in: São Francisco Craton, Eastern Brazil. pp. 171–185. https://doi.org/10.1007/978-3-319-01715-0_9

Hanks, T.C., Kanamori, H., 1979. A moment magnitude scale. J. Geophys. Res. 84, 2348–2350. https://doi.org/10.1029/JB084iB05p02348

He, X., Ni, S., 2018. Resolving Horizontal Rupture Directivity of Moderate Crustal Earthquake in Sparse Network With Ambient Noise Location. J. Geophys. Res. Solid Earth 123, 533–552. https://doi.org/https://doi.org/10.1002/2017JB014735

He, X., Ni, S., Zhang, P., Freymueller, J., 2018. The 1 May 2017 British Columbia-Alaska Earthquake Doublet and Implication for Complexity Near Southern End of Denali Fault System. Geophys. Res. Lett. 45, 5937–5947. https://doi.org/https://doi.org/10.1029/2018GL078014

Johnston, A.C., 1989. The Seismicity of 'Stable Continental Interiors,' in: Earthquakes at North-Atlantic Passive Margins: Neotectonics and Postglacial Rebound. Springer Netherlands, Dordrecht, pp. 299–327. https://doi.org/10.1007/978-94-009-2311-9_18

Kennett, B.L.N., 1983. Seismic Wave Propagation in Stratified Media. Cambridge University Press.

Langston, C.A., Helmberger, D. V., 1975. A Procedure for Modelling Shallow Dislocation Sources*. Geophys. J. R. Astron. Soc. 42, 117–130. https://doi.org/10.1111/j.1365-246X.1975.tb05854.x

Luo, Y., Ni, S., Zeng, X., Zheng, Y., Chen, Q., Chen, Y., 2010. A shallow aftershock sequence in the north-eastern end of the Wenchuan earthquake aftershock zone. Sci. China Earth Sci. 53, 1655–1664. https://doi.org/https://doi.org/10.1007/s11430-010-4026-8

Luo, Y., Zhao, L., Zeng, X., Gao, Y., 2015. Focal mechanisms of the Lushan earthquake sequence and spatial variation of the stress field. Sci. China Earth Sci. 58, 1148–1158. https://doi.org/10.1007/s11430-014-5017-y

Nemocón, A.M., Julià, J., Garcia, X., 2021. Lithospheric structure of the western Borborema Province from receiver functions and surface-wave dispersion: Implications for basin inversion. Tectonophysics 816, 229024. https://doi.org/10.1016/j.tecto.2021.229024

Pang, G., Koper, K.D., Stickney, M.C., Pechmann, J.C., Burlacu, R., Pankow, K.L., Payne, S., Benz, H.M., 2018. Seismicity in the Challis, Idaho, Region, January 2014–May 2017: Late Aftershocks of the 1983 Ms 7.3 Borah Peak Earthquake. Seismol. Res. Lett. 89, 1366–1378. https://doi.org/10.1785/0220180058

Pinheiro, J.M., Schnurle, P., Evain, M., Afilhado, A., Gallais, F., Klingelhoefer, F., Loureiro, A., Fuck, R., Soares, J., Cupertino, J.A., Viana, A., Rabineau, M., Baltzer, A., Benabdellouahed, M., Dias, N., Moulin, M., Aslanian, D., Morvan, L., Mazé, J.P., Pierre, D., Roudaut-Pitel, M., Rio, I., Alves, D., Barros Junior, P., Biari, Y., Corela, C., Crozon, J., Duarte, J.L., Ducatel, C., Falcão, C., Fernagu, P., Le Piver, D., Mokeddem, Z., Pelleau, P., Rigoti, C., Roest, W., Roudaut, M., 2018. Lithospheric structuration onshore-offshore of the Sergipe-Alagoas passive margin, NE Brazil, based on wide-angle seismic data. J. South Am. Earth Sci. 88, 649–672. https://doi.org/10.1016/j.jsames.2018.09.015

Singh, A.P., Zhao, L., Kumar, S., Mishra, S., 2016. Inversions for earthquake focal mechanisms and regional stress in the Kachchh Rift Basin, western India: Tectonic implications. J. Asian Earth Sci. 117, 269–283. https://doi.org/10.1016/j.jseaes.2015.12.001

Soares, J.E.P., Stephenson, R., Fuck, Reinhardt A., de Lima, M.V.A.G., de Araújo, V.C.M., Lima, F.T., Rocha, F.A.S., da Trindade, C.R., 2018. Structure of the crust and upper mantle beneath the Parnaíba Basin, Brazil, from wide-angle reflection–refraction data, in: Daly, M.C., Fuck, R.A., Julià, J., MacDonald, D.I.M., Watts, A.B. (Eds.), Cratonic Basin Formation: A Case Study of the Parnaíba Basin of Brazil. Geological Society, London, Special Publications, pp. 67–82. https://doi.org/10.1144/SP472.9

Sobrinho, V.R.S., Cruz, S.C.P., Leite, C.M.M., Lima, C.C.U., Oliveira, J.S.S., Batista, J.C., Silva, M.G., Gomes, L.C.C., 2020. TERREMOTO NA REGIÃO DE AMARGOSA/BA. Salvador.

Sykes, L.R., 1978. Intraplate seismicity, reactivation of preexisting zones of weakness, alkaline magmatism, and other tectonism postdating continental fragmentation. Rev. Geophys. 16, 621–688. https://doi.org/10.1029/RG016i004p00621

Takeya, M., Ferreira, J.M., Pearce, R.G., Assumpçao, M., Costa, J.M., Sophia, C.M., 1989. The 1986–1988 intraplate earthquake sequence near João Câmara, northeast Brazil—evolution of seismicity. Tectonophysics 167, 117–131. https://doi.org/10.1016/0040-1951(89)90062-0

Talwani, P., 1989. Characteristic Features of Intraplate Earthquakes and the Models Proposed to Explain Them, in: Earthquakes at North-Atlantic Passive Margins: Neotectonics and Postglacial Rebound. Springer Netherlands, Dordrecht, pp. 563–579. https://doi.org/10.1007/978-94-009-2311-9_33

Talwani, P., Rajendran, K., 1991. Some seismological and geometric features of intraplate earthquakes. Tectonophysics 186, 19–41. https://doi.org/10.1016/0040-1951(91)90383-4

Tape, C., West, M., Silwal, V., Ruppert, N.A., 2013. Earthquake nucleation and triggering on an optimally oriented fault. Earth Planet. Sci. Lett. 363, 231–241. https://doi.org/10.1016/j.epsl.2012.11.060

Zhao, L.-S., Helmberger, D. V., 1994. Source estimation from broadband regional seismograms. Bull. Seismol. Soc. Am. 84, 91–104. https://doi.org/https://doi.org/10.1785/BSSA0840010091

Zhao, L., Luo, Y., Liu, T.-Y., Luo, Y.-J., 2013. Earthquake Focal Mechanisms in Yunnan and their Inference on the Regional Stress Field. Bull. Seismol. Soc. Am. 103, 2498–2507. https://doi.org/https://doi.org/10.1785/0120120309

Zhu, L., Ben-Zion, Y., 2013. Parametrization of general seismic potency and moment tensors for source inversion of seismic waveform data. Geophys. J. Int. 194, 839–843. https://doi.org/10.1093/gji/ggt137

Zhu, L., Helmberger, D. V., 1996. Advancement in source estimation techniques using broadband regional seismograms. Bull. Seismol. Soc. Am. 86, 1634–1641. https://doi.org/https://doi.org/10.1785/BSSA0860051634

Zhu, L., Tan, Y., Helmberger, D. V., Saikia, C.K., 2006. Calibration of the Tibetan Plateau Using Regional Seismic Waveforms. Pure Appl. Geophys. 163, 1193–1213. https://doi.org/10.1007/s00024-006-0073-7

APÊNDICE B

Supplementary Material

2017 Maranhão earthquake

Fig. S1: Waveform fits for the preferred solution obtained for the 2017 Maranhão earthquake with RSBR data only (Fig. 2b). Black traces denote observations while red traces denote predictions. On the upper right corner of each the radial (R), transverse (T) or vertical (Z) component is indicated. On the lower right corner the cross-correlation coefficient (top) and the time-shift required to align predictions and observations (bottom) are noted.

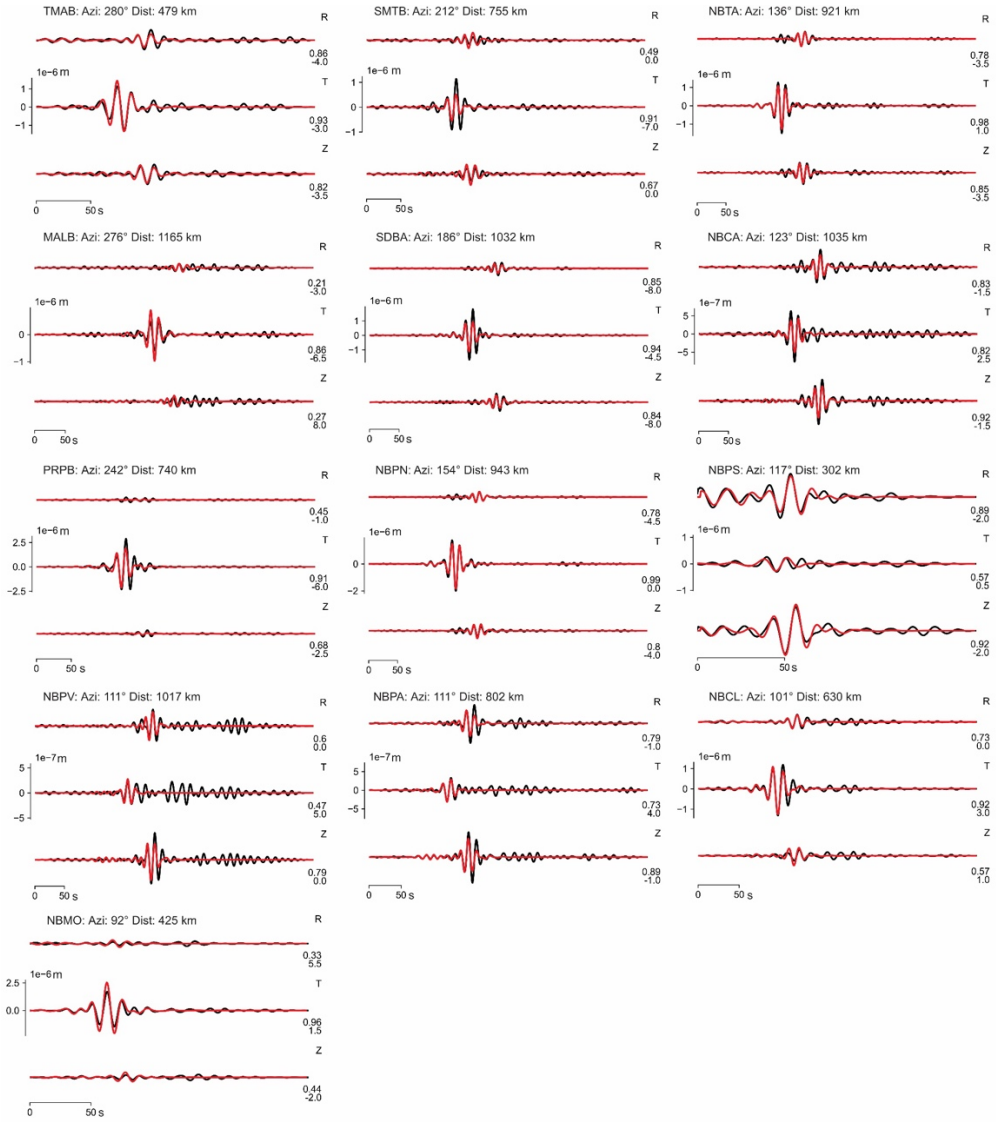

Fig. S2: Comparison of focal mechanism for the 2017 Maranhão earthquake using the simplified CAP approach and RSBR data only (Fig. 2b) with those determined by Dias et al. (2018) using path-specific velocity models, and by Carvalho et al. (2019) using the inversion of waveform envelopes.

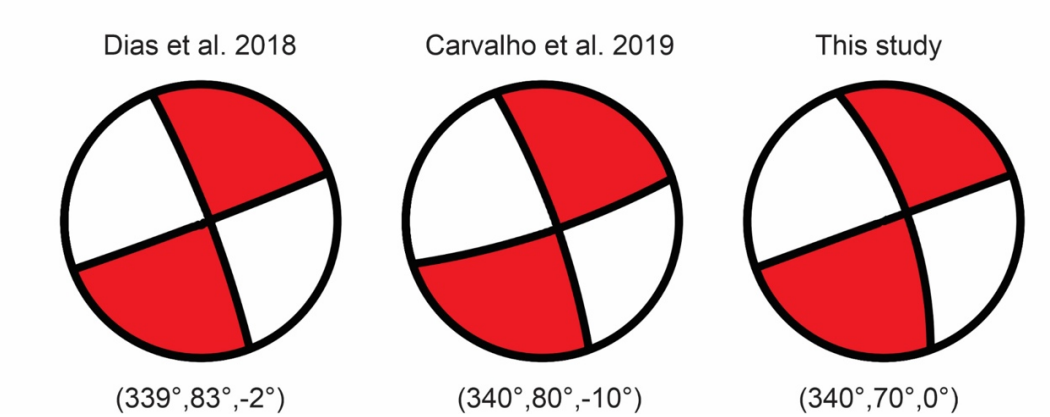

Fig. S3: Waveform fits for the preferred solution obtained for the 2017 Maranhão earthquake with an expanded dataset (Fig. 3b). Black traces denote observations while red traces denote predictions. On the upper right corner of each the radial (R), transverse (T) or vertical (Z) component is indicated. On the lower right corner the cross-correlation coefficient (top) and the time-shift required to align predictions and observations (bottom) are noted.

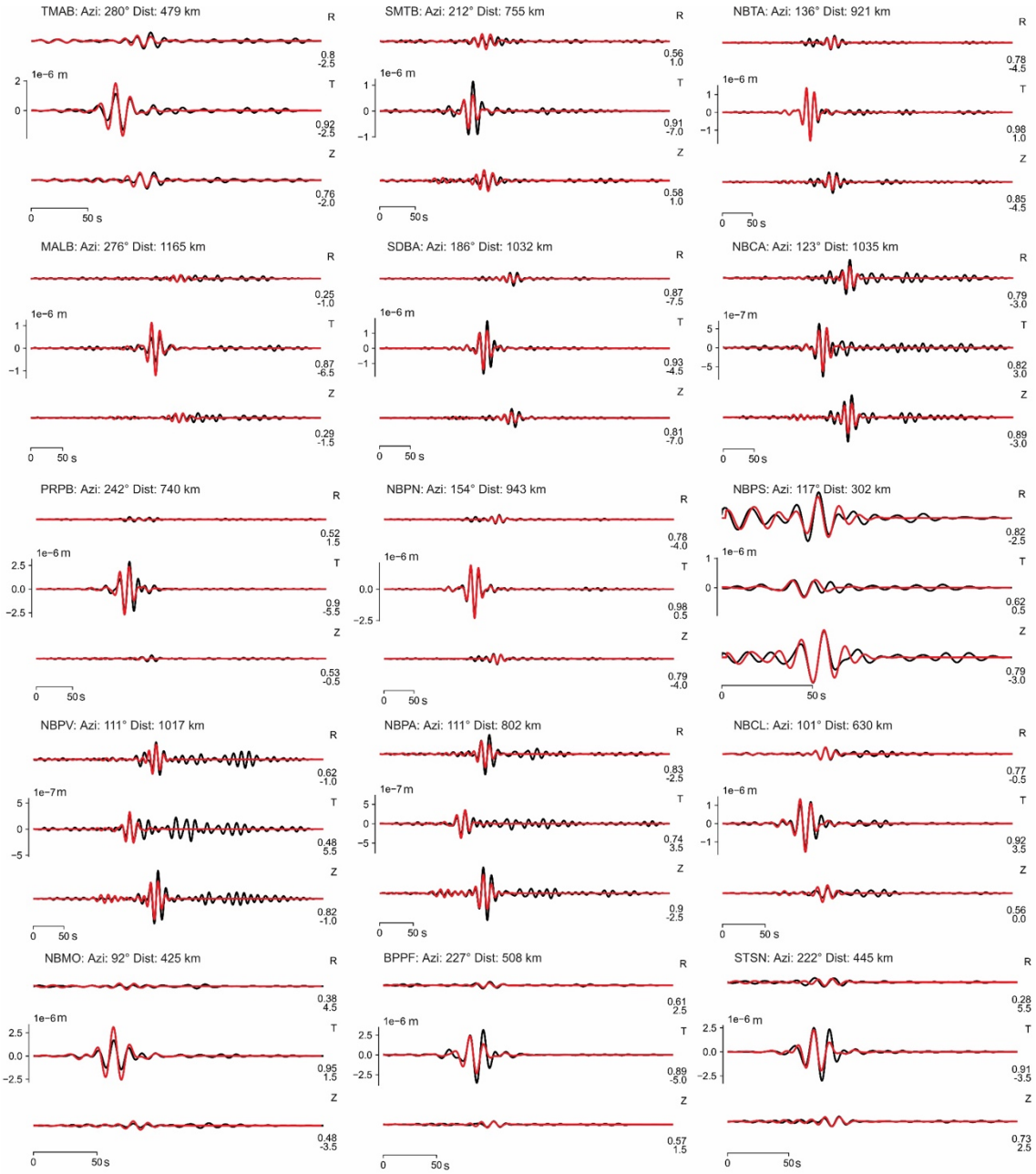

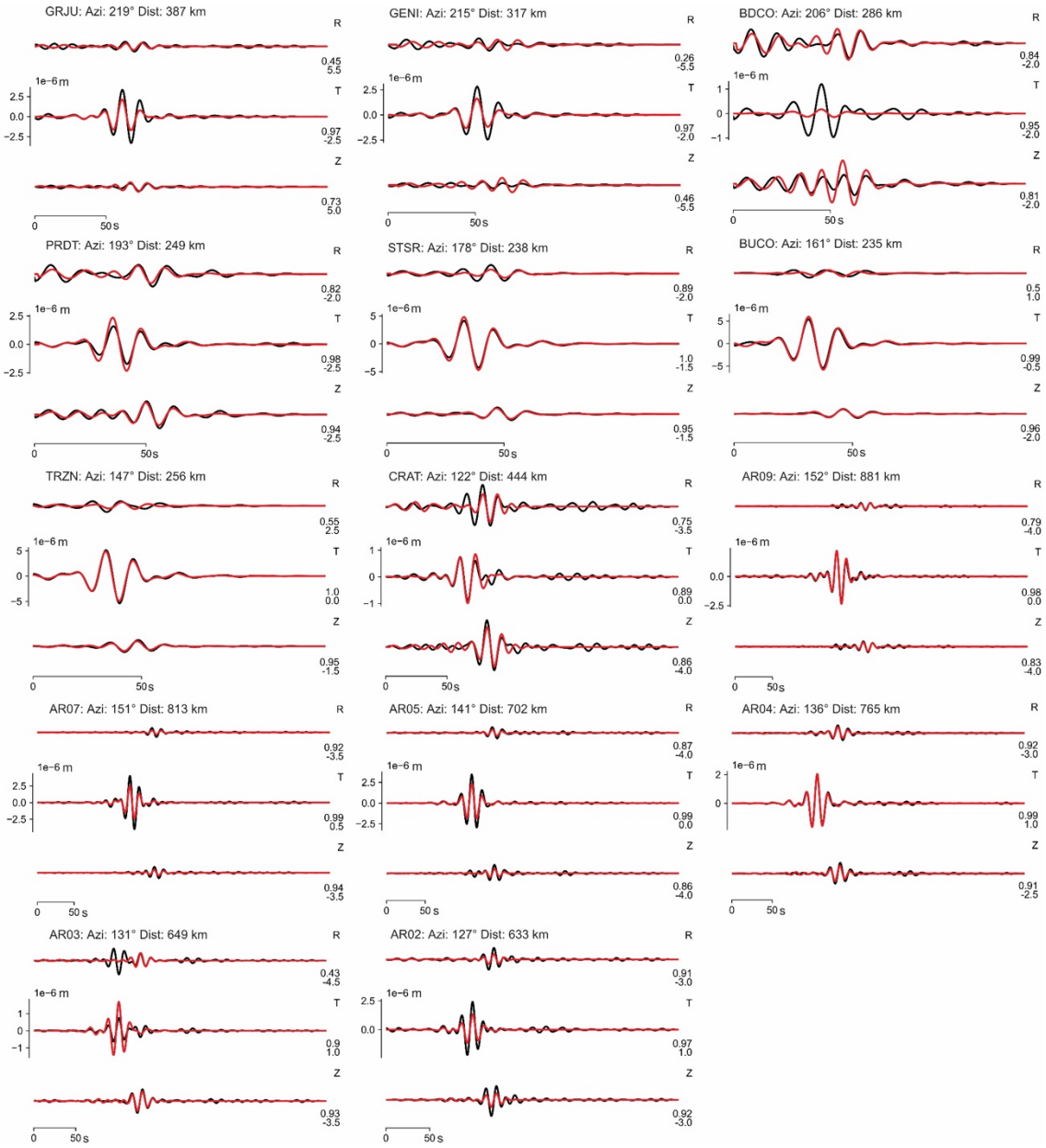
GRJU: Azi: 219° Dist: 387 km
GENI: Azi: 215° Dist: 317 km
BDCO: Azi: 206° Dist: 286 km
PRDT: Azi: 193° Dist: 249 km
STSR: Azi: 178° Dist: 238 km
BUCO: Azi: 161° Dist: 235 km
TRZN: Azi: 147° Dist: 256 km
CRAT: Azi: 122° Dist: 444 km
AR09: Azi: 152° Dist: 881 km
AR07: Azi: 151° Dist: 813 km
AR05: Azi: 141° Dist: 702 km
AR04: Azi: 136° Dist: 765 km
AR03: Azi: 131° Dist: 649 km
AR02: Azi: 127° Dist: 633 km
R
T
Z
1e−6 m
0
50 s

Fig. S4: Comparison of focal mechanism for the 2017 Maranhão earthquake using the simplified CAP approach and an expanded dataset (Fig. 3b) with those determined by Dias et al. (2018) using path-specific velocity models, and by Carvalho et al. (2019) using the inversion of waveform envelopes.

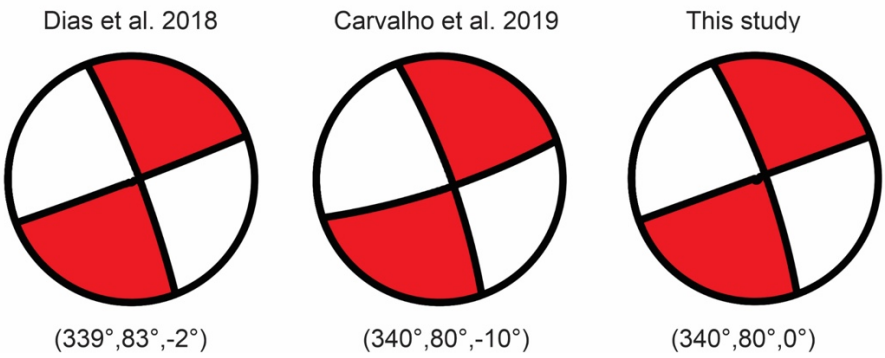

Fig. S5: Focal mechanism variation with depth for the 2017 Maranhão earthquake obtained from the inversion of RSBR data only, after iteratively removing low-correlated traces (< 60%). The final number of retained waveforms is shown on top of each solution. The match between observed and predicted waveforms for the preferred mechanism (in red) can be seen in Figure S6.

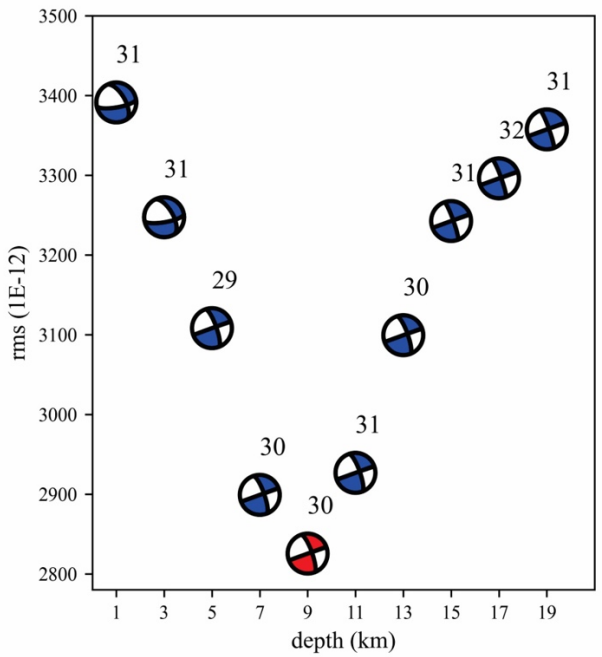

Fig. S6: Waveform fits for the preferred solution obtained for the 2017 Maranhão earthquake with RSBR data only and iterative removal of low-correlation traces. Black traces denote observations while red traces denote predictions. On the upper right corner of each the radial (R), transverse (T) or vertical (Z) component is indicated. On the lower right corner the cross-correlation coefficient (top) and the time-shift required to align predictions and observations (bottom) are noted.

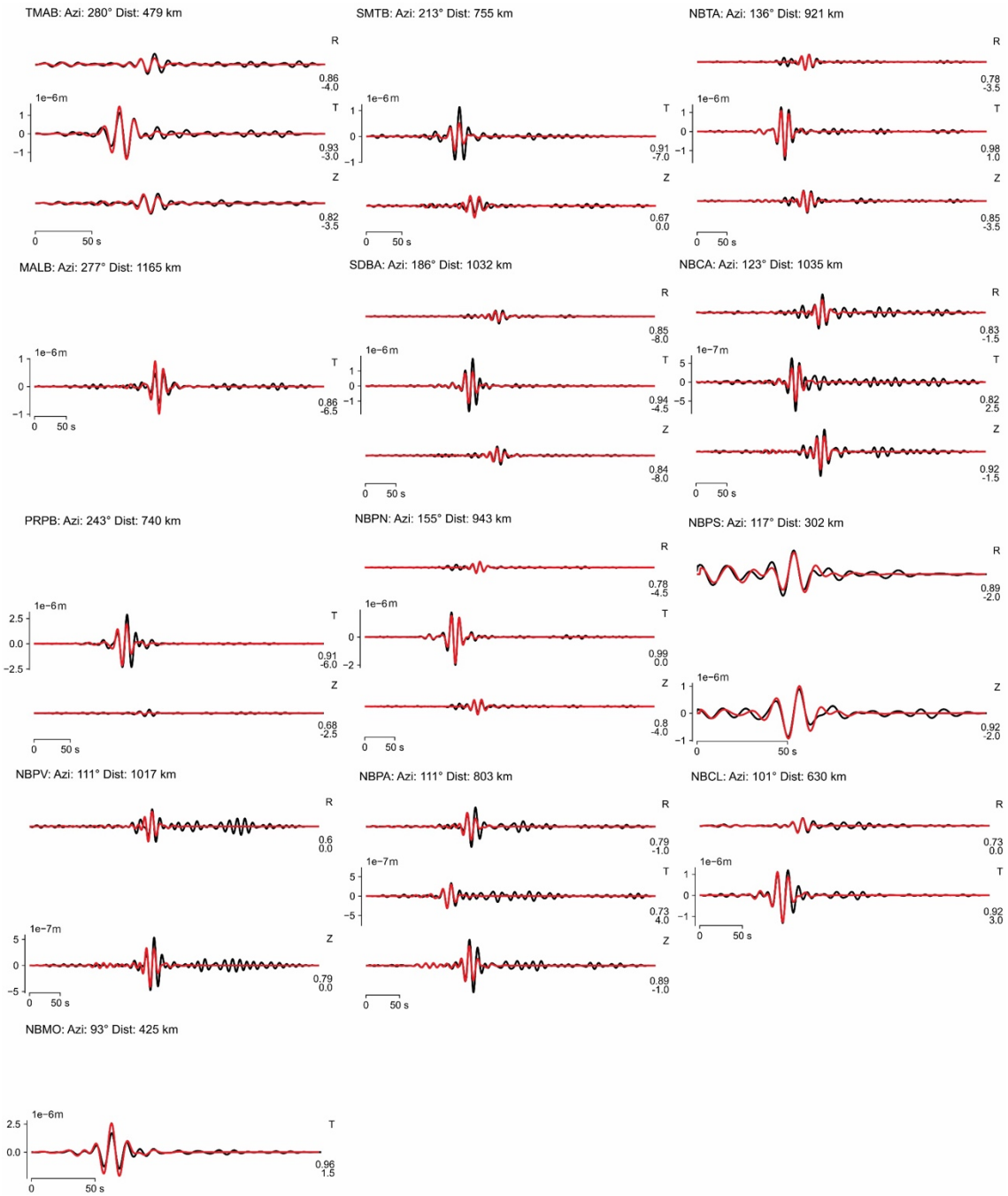

Fig. S7: Focal mechanism variation with depth for the 2017 Maranhão earthquake obtained from the inversion of an expanded dataset, after iteratively removing low-correlated traces (<60%). The final number of retained waveforms is shown on top of each solution. The match between observed and predicted waveforms for the preferred mechanism (in red) can be seen in Figure S8.

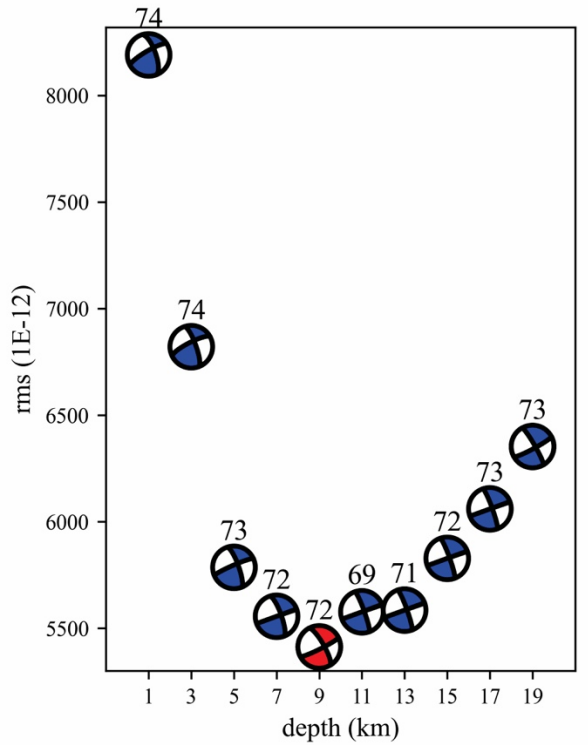

Fig. S8: Waveform fits for the preferred solution obtained for the 2017 Maranhão earthquake with an expanded dataset and iterative removal of low-correlation traces. Black traces denote observations while red traces denote predictions. On the upper right corner of each the radial (R), transverse (T) or vertical (Z) component is indicated. On the lower right corner the cross-correlation coefficient (top) and the time-shift required to align predictions and observations (bottom) are noted.

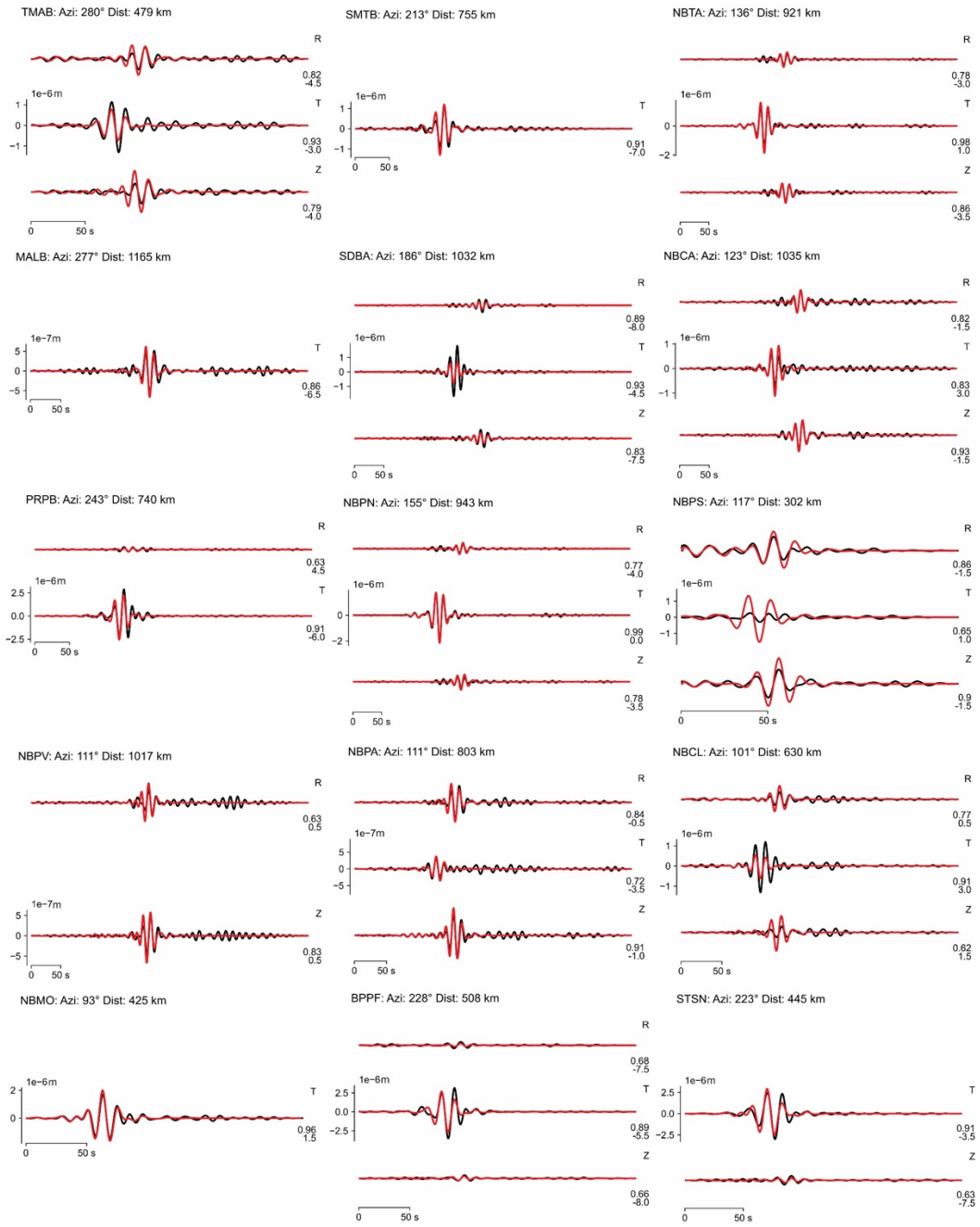

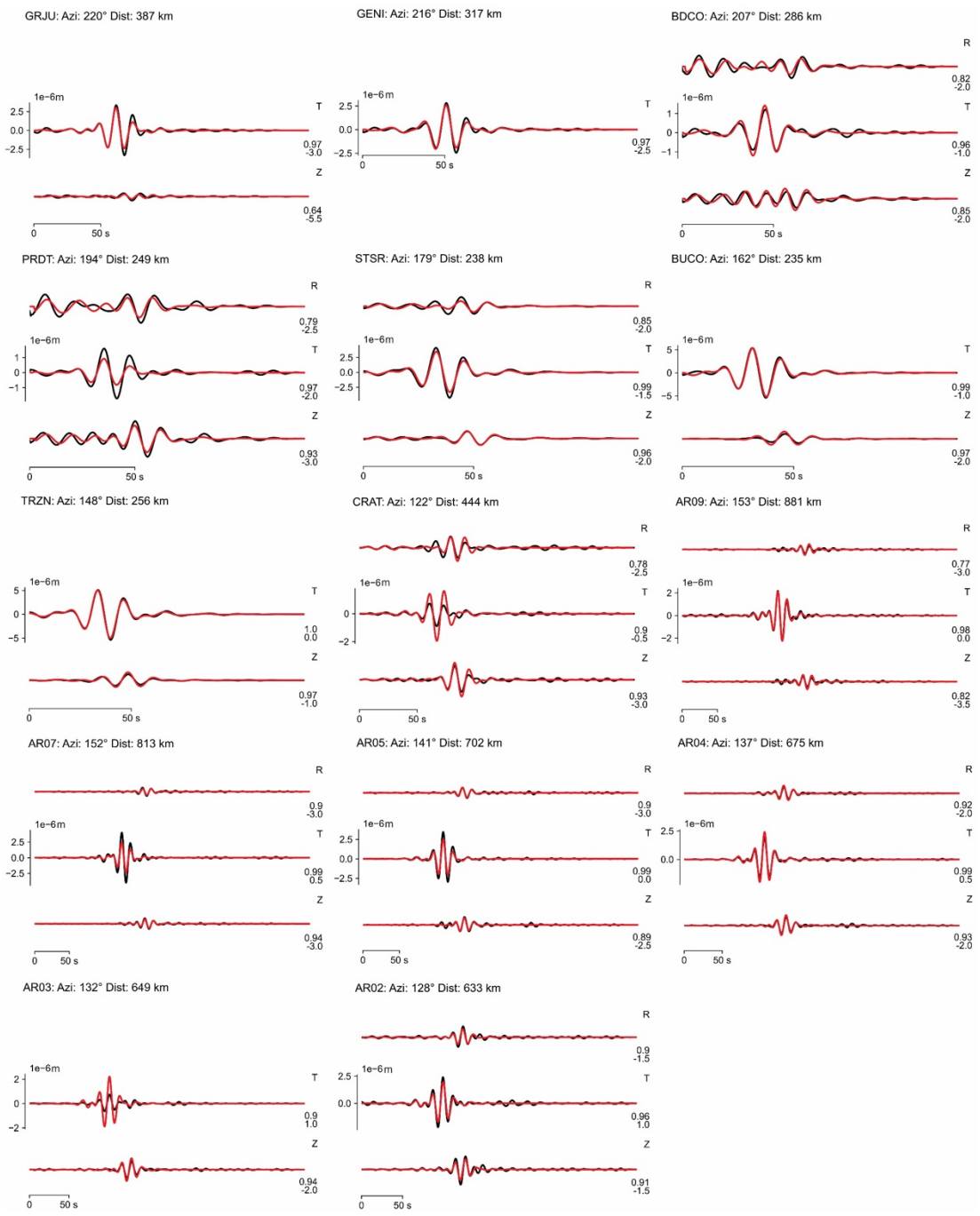
GRJU: Azi: 220° Dist: 387 km
GENI: Azi: 216° Dist: 317 km
BDCO: Azi: 207° Dist: 286 km
PRDT: Azi: 194° Dist: 249 km
STSR: Azi: 179° Dist: 238 km
BUCO: Azi: 162° Dist: 235 km
TRZN: Azi: 148° Dist: 256 km
CRAT: Azi: 122° Dist: 444 km
AR09: Azi: 153° Dist: 881 km
AR07: Azi: 152° Dist: 813 km
AR05: Azi: 141° Dist: 702 km
AR04: Azi: 137° Dist: 675 km
AR03: Azi: 132° Dist: 649 km
AR02: Azi: 128° Dist: 633 km
R
T
Z
1e−6m
0
50 s

2020 Amargosa earthquake

Fig. S9: Waveform fits for the preferred solution obtained for the 2020 Amargosa earthquake with RSBR data only (Fig. 4b). Black traces denote observations while red traces denote predictions. On the upper right corner of each the radial (R), transverse (T) or vertical (Z) component is indicated. On the lower right corner the cross-correlation coefficient (top) and the time-shift required to align predictions and observations (bottom) are noted.

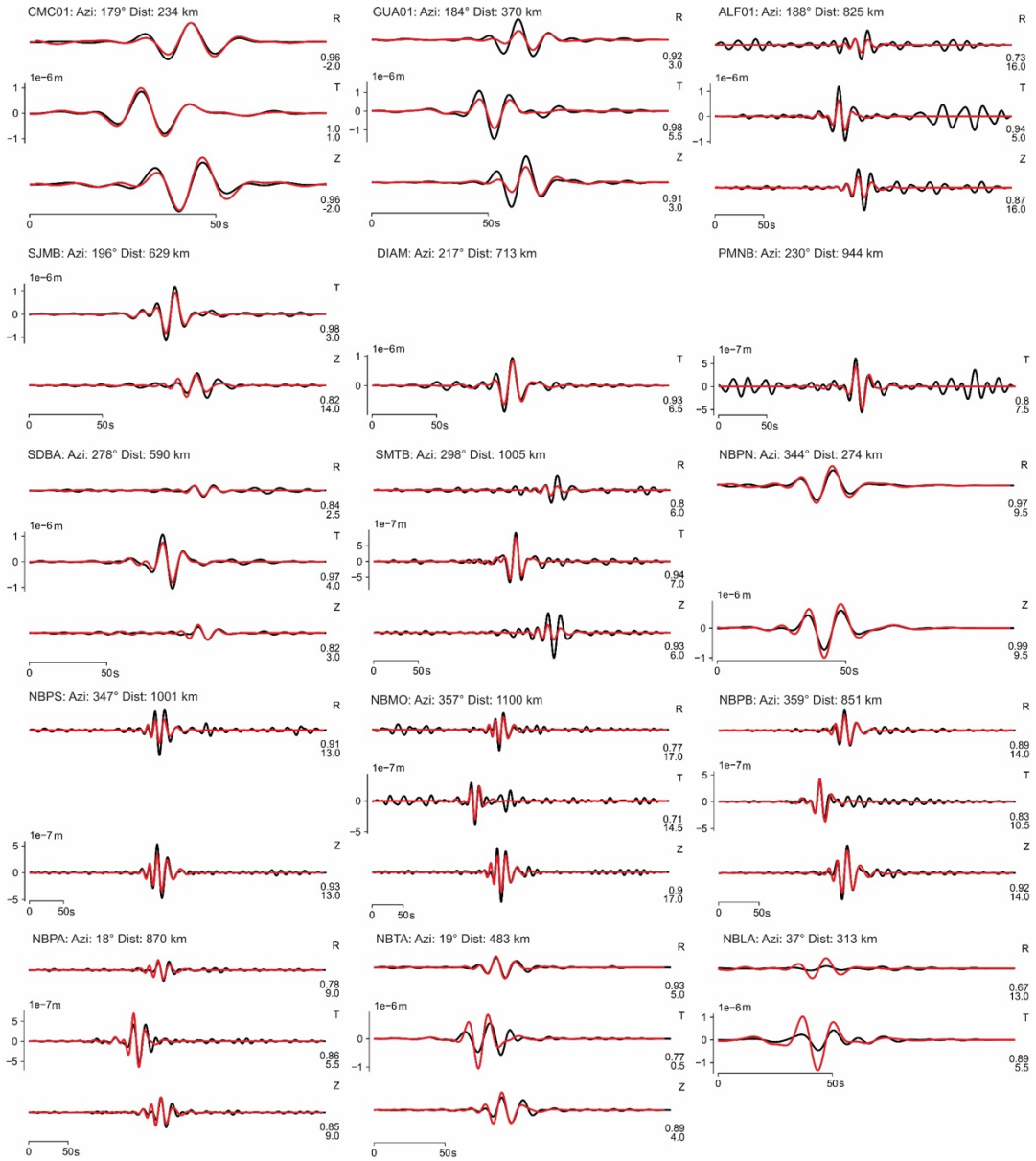

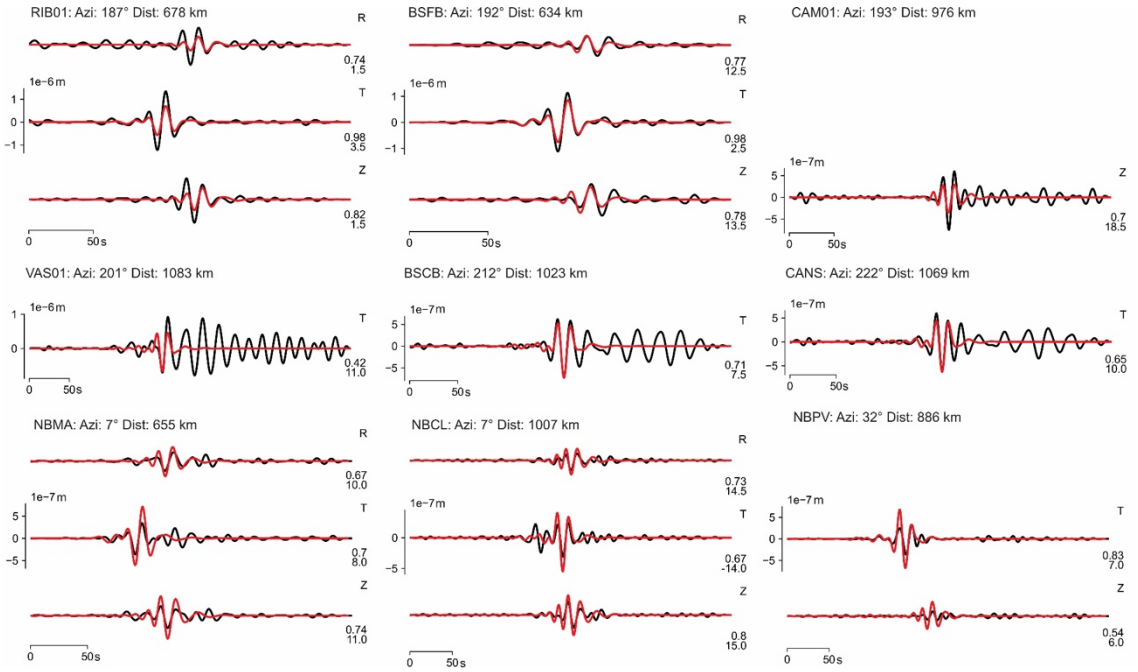
RIB01: Azi: 187° Dist: 678 km
BSFB: Azi: 192° Dist: 634 km
CAM01: Azi: 193° Dist: 976 km
VAS01: Azi: 201° Dist: 1083 km
BSCB: Azi: 212° Dist: 1023 km
CANS: Azi: 222° Dist: 1069 km
NBMA: Azi: 7° Dist: 655 km
NBCL: Azi: 7° Dist: 1007 km
NBPV: Azi: 32° Dist: 886 km
R
T
Z
1e−6 m
1e−7 m
50 s

Fig. S10: Waveform fits for the preferred solution obtained for the 2020 Amargosa earthquake with an expanded dataset (Fig. 5b). Black traces denote observations while red traces denote predictions. On the upper right corner of each the radial (R), transverse (T) or vertical (Z) component is indicated. On the lower right corner the cross-correlation coefficient (top) and the time-shift required to align predictions and observations (bottom) are noted.

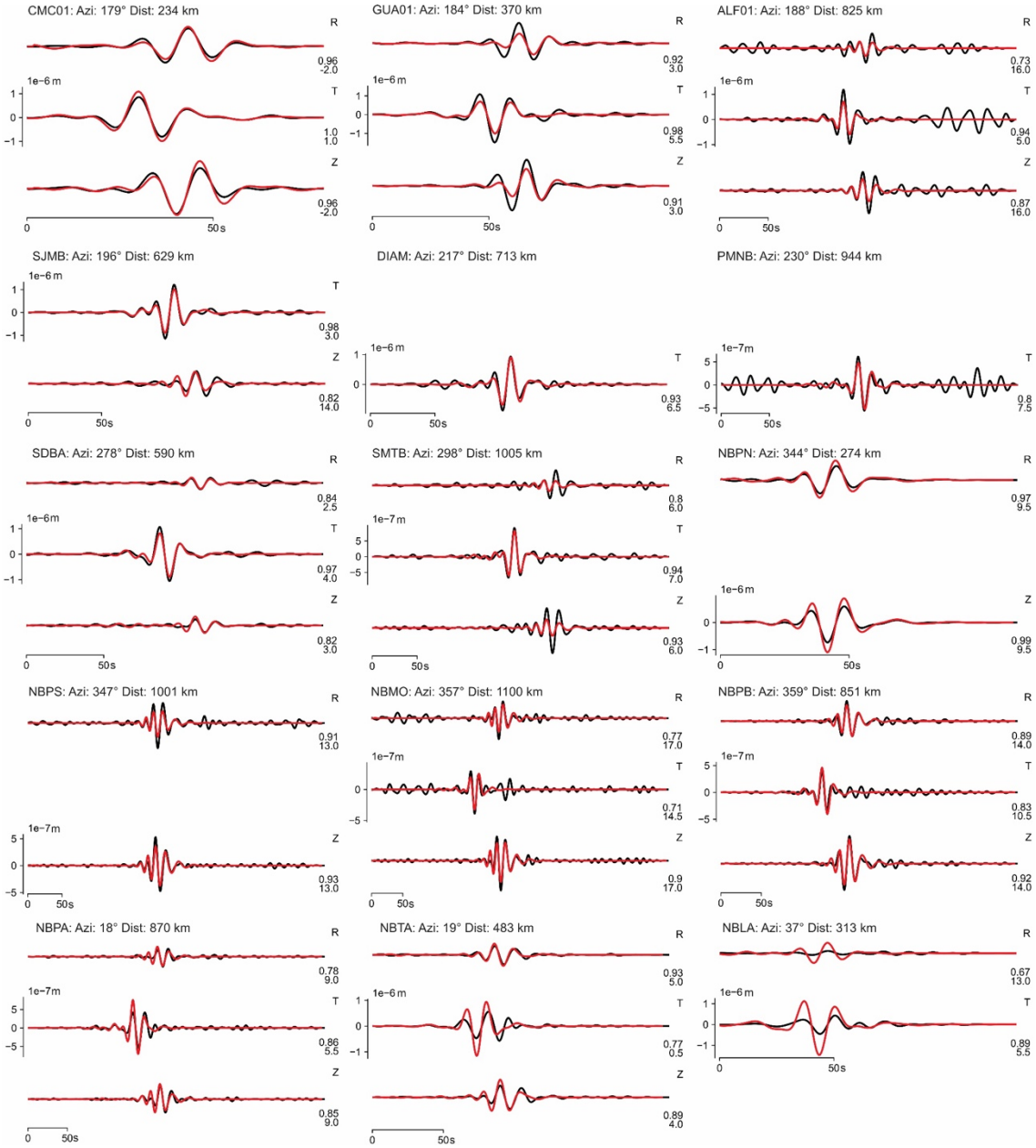

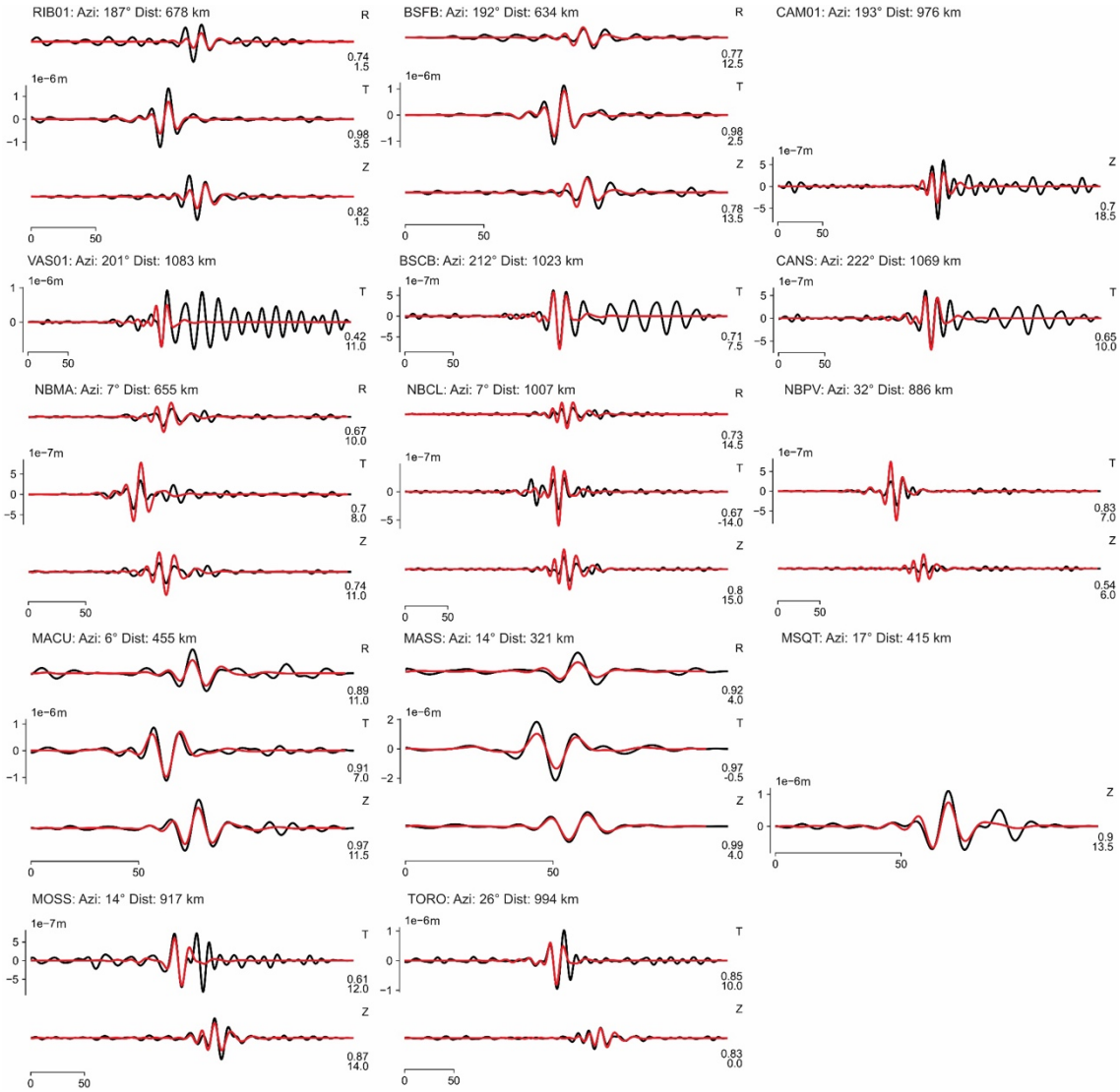
RIB01: Azi: 187° Dist: 678 km
BSFB: Azi: 192° Dist: 634 km
CAM01: Azi: 193° Dist: 976 km
VAS01: Azi: 201° Dist: 1083 km
BSCB: Azi: 212° Dist: 1023 km
CANS: Azi: 222° Dist: 1069 km
NBMA: Azi: 7° Dist: 655 km
NBCL: Azi: 7° Dist: 1007 km
NBPV: Azi: 32° Dist: 886 km
MACU: Azi: 6° Dist: 455 km
MASS: Azi: 14° Dist: 321 km
MSQT: Azi: 17° Dist: 415 km
MOSS: Azi: 14° Dist: 917 km
TORO: Azi: 26° Dist: 994 km
R
T
Z
1e−6m
1e−7m

Fig. S11: A) Focal mechanism variation with depth for the 2020 Amargosa earthquake obtained from the inversion of RSBR data only, after iteratively removing low-correlation traces (<60%). The final number of retained waveforms is shown on top of each solution. Note the two minima at 6 km and 10 km depth (in red). Also note how the absolute minimum (6 km depth) solution differs from the preferred solution displayed in Fig. 4b, while the local minimum (10 km depth) solution does not. The match between observed and predicted waveforms for the 6 km depth solution can be seen in Figure S12.; B) Minimum misfit (6 km) focal solution with regional P-wave polarities overlain.

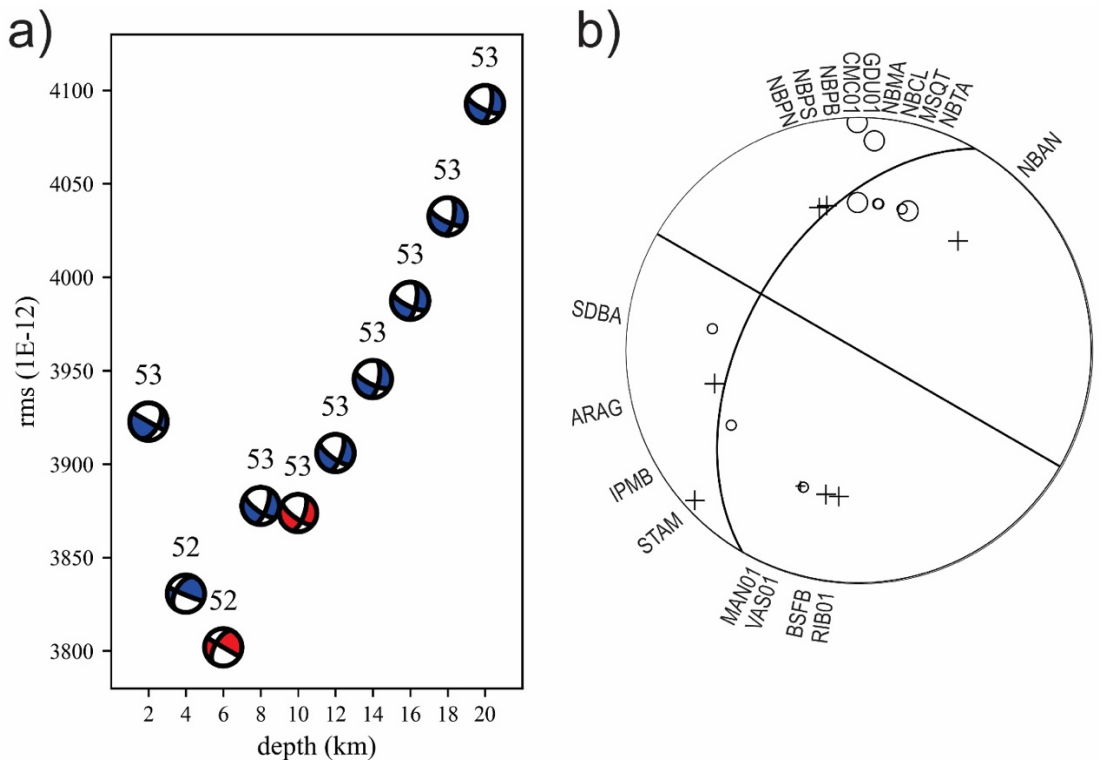

Fig. S12: Waveform fits for the 6 km-depth solution obtained for the 2020 Amargosa earthquake with RSBR data only, and iterative removal of low-correlation traces. Black traces denote observations while red traces denote predictions. On the upper right corner of each the radial (R), transverse (T) or vertical (Z) component is indicated. On the lower right corner the cross-correlation coefficient (top) and the time-shift required to align predictions and observations (bottom) are noted.

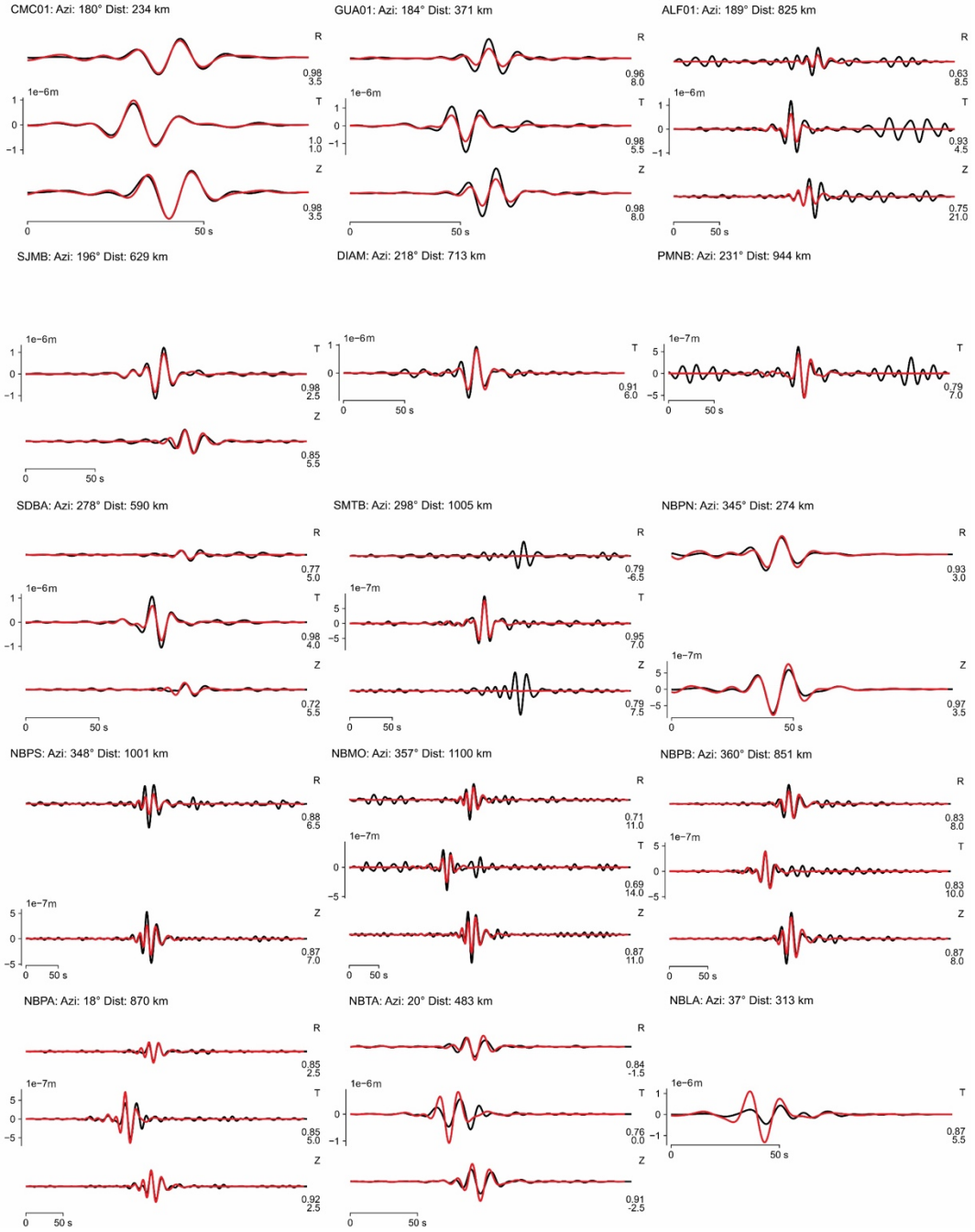

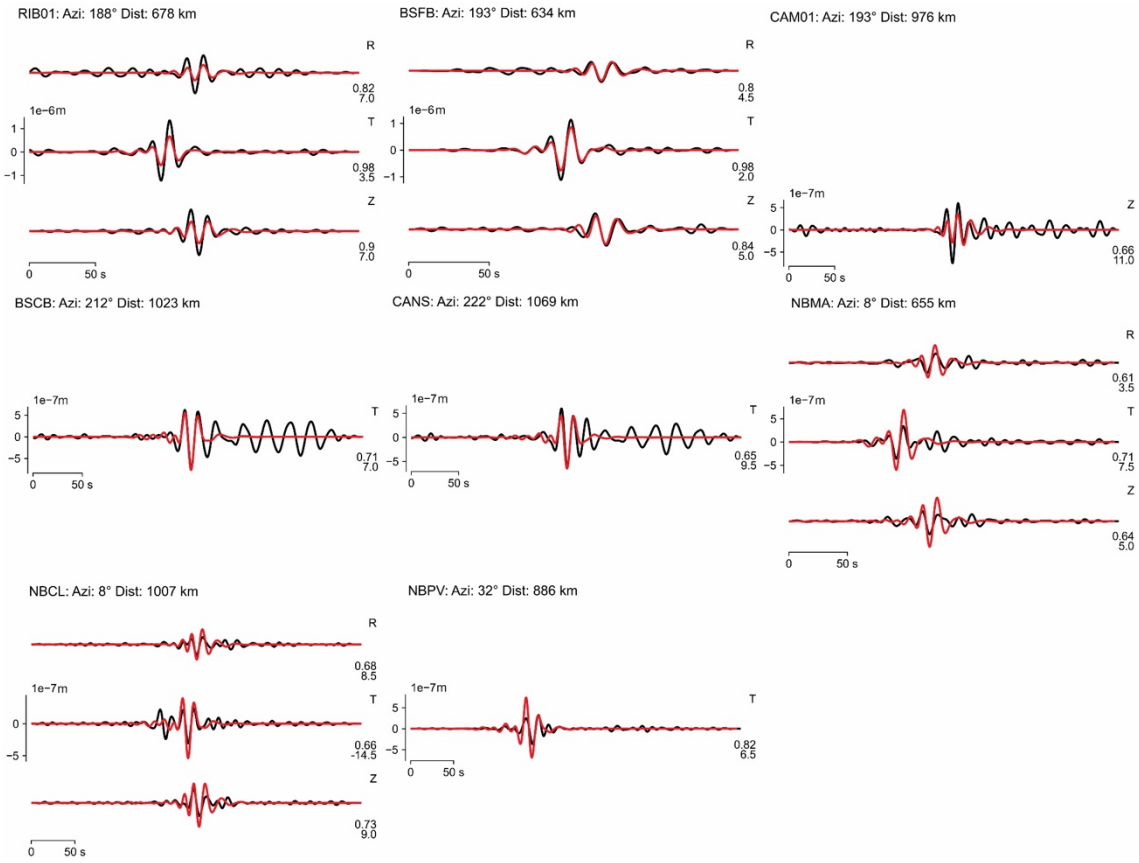
RIB01: Azi: 188° Dist: 678 km
BSFB: Azi: 193° Dist: 634 km
CAM01: Azi: 193° Dist: 976 km
BSCB: Azi: 212° Dist: 1023 km
CANS: Azi: 222° Dist: 1069 km
NBMA: Azi: 8° Dist: 655 km
NBCL: Azi: 8° Dist: 1007 km
NBPV: Azi: 32° Dist: 886 km
R
T
Z
1e−6m
1e−7m
50 s

Fig. S13: Focal mechanism variation with depth for the 2020 Amargosa earthquake obtained from the inversion of an expanded dataset, after iteratively removing low-correlation traces (<60%). The final number of retained waveforms is shown on top of each solution. The match between observed and predicted waveforms for the preferred mechanism (in red) can be seen in Figure S14.

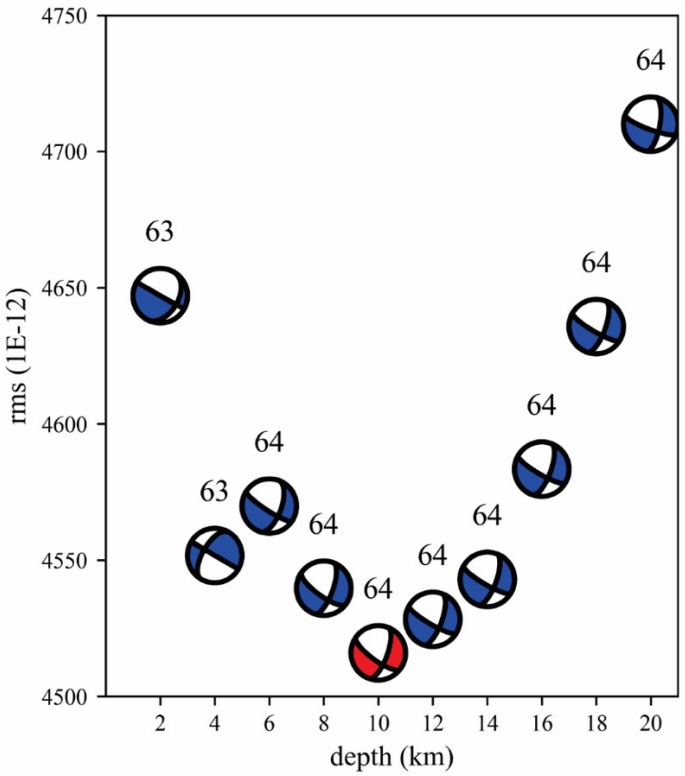

Fig. S14: Waveform fits for the preferred (10 km depth) solution obtained for the 2020 Amargosa earthquake with an expanded dataset and iterative removal of low-correlation traces. Black traces denote observations while red traces denote predictions. On the upper right corner of each the radial (R), transverse (T) or vertical (Z) component is indicated. On the lower right corner the cross-correlation coefficient (top) and the time-shift required to align predictions and observations (bottom) are noted.

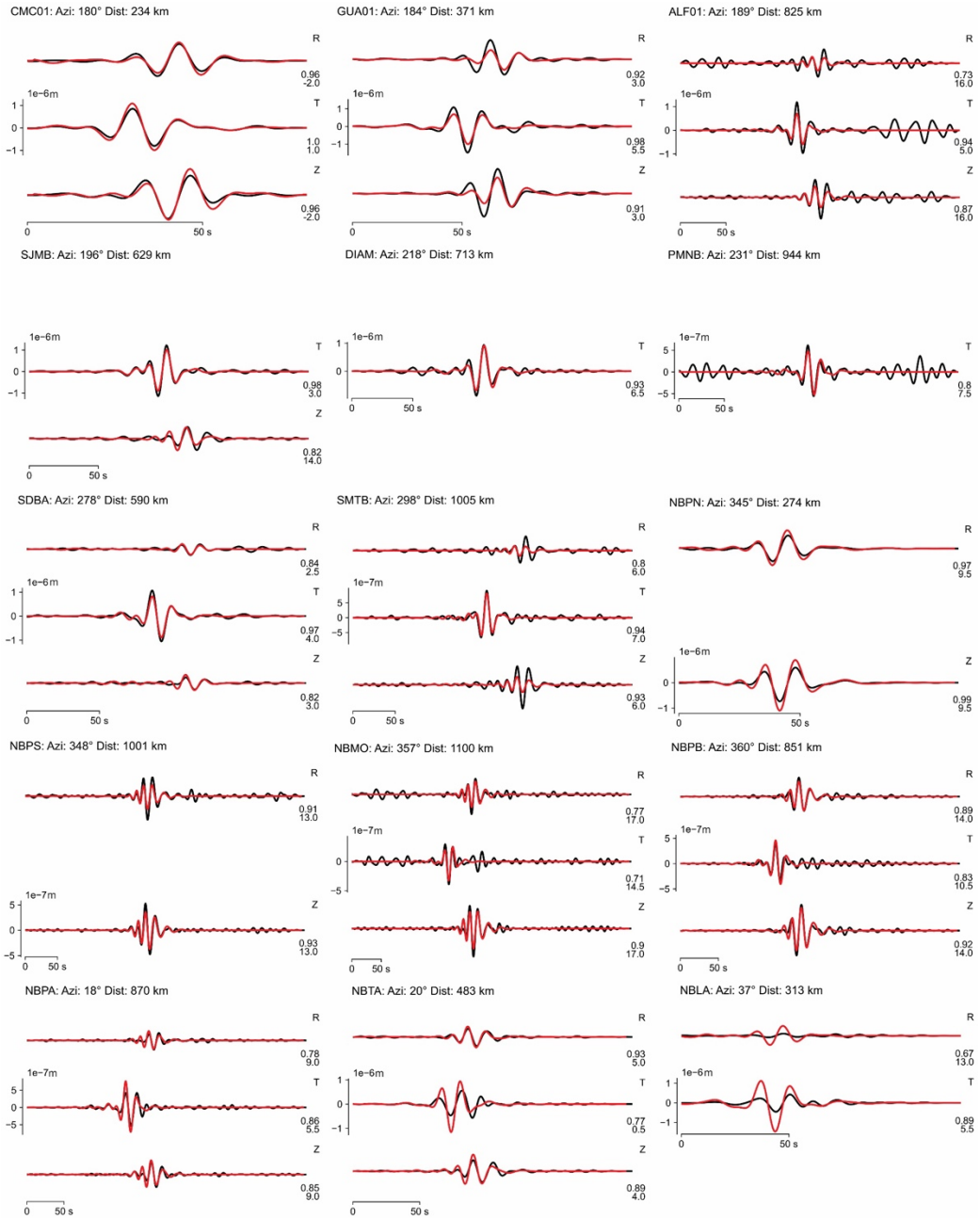

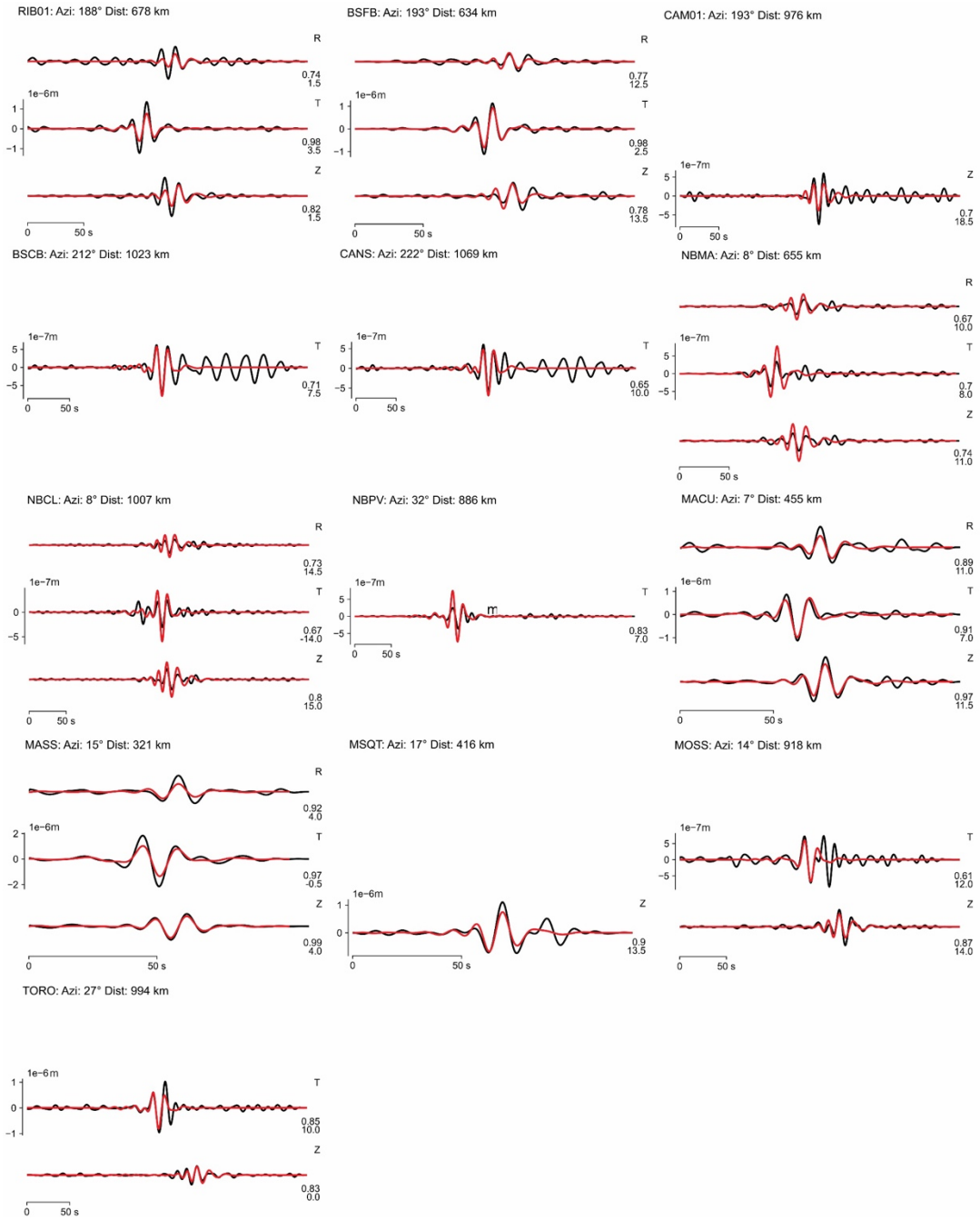
RIB01: Azi: 188° Dist: 678 km
BSFB: Azi: 193° Dist: 634 km
CAM01: Azi: 193° Dist: 976 km
BSCB: Azi: 212° Dist: 1023 km
CANS: Azi: 222° Dist: 1069 km
NBMA: Azi: 8° Dist: 655 km
NBCL: Azi: 8° Dist: 1007 km
NBPV: Azi: 32° Dist: 886 km
MACU: Azi: 7° Dist: 455 km
MASS: Azi: 15° Dist: 321 km
MSQT: Azi: 17° Dist: 416 km
MOSS: Azi: 14° Dist: 918 km
TORO: Azi: 27° Dist: 994 km
R
T
Z
1e−6m
1e−7m
50 s

Fig. S15: Regional first-motion polarities for the 2020 Amargosa earthquake measured on vertical, unfiltered seismograms. Positive (compressional) and negative (dilational) polarities are indicated as Up or Down, respectively, above each trace. Quality was assessed visually, and is indicated as clear (2) or unclear (1) in parenthesis. Amplitudes were normalized to unit value for visualization purposes only. Polarities were determined by zooming around the theoretical P-wave arrival (gray vertical dashed lines).

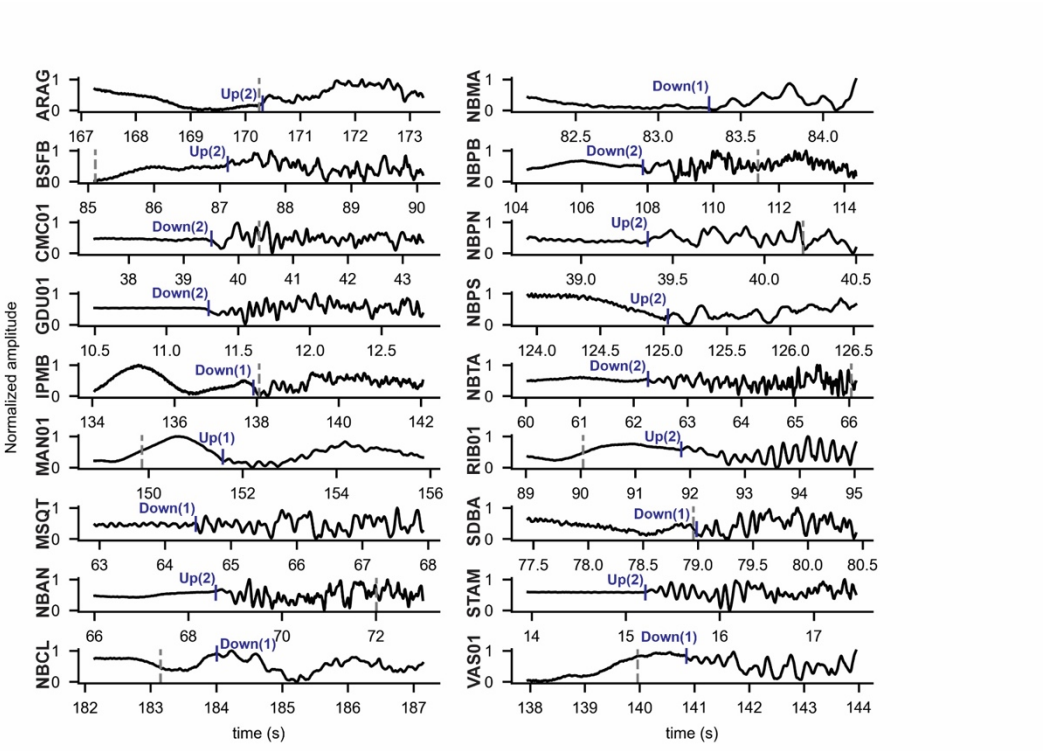

APÊNDICE C

Earth and Space Science

Supporting Information for

Deep-focus earthquake mechanisms at the subducting Nazca plate (Peru-Brazil border): Cold slab behavior in a warm plate

Leite Neto, G. S.[1], Julià, J.[1,2] and Prieto, G. A.[3]

[1]Programa de Pós-Graduação em Geodinâmica e Geofísica; [2]Departamento de Geofísica, Universidade Federal do Rio Grande do Norte; [3]Departamento de Geociencias, Universidad Nacional de Colombia

Contents of this file

Figures S1 to S39

Tables S1 to S4

Introduction

This Supporting Information contains a series of figures and tables that supports discussion in the main text.

Event Number	Date and Time (UTC)	Lat (º)	Lon (º)	Depth (km)	Magnitude	Type
1	2014-04-07 (15:27:32.600)	-8.24	-71.58	560.9	5.1	mb
2	2014-07-22 (00:53:02.260)	-6.12	-72.03	565.2	4.2	mb
3	2014-11-26 (01:26:24.340)	-6.25	-71.94	587.1	4.6	mb
4	2015-03-28 (21:48:14.380)	-9.12	-71.29	610.2	4.4	mb
5	2015-05-11 (08:21:44.350)	-9.15	-71.23	617.3	4.0	mb
6	2015-10-28 (17:10:55.290)	-9.64	-71.30	603.7	4.5	mb
7	2015-11-24 (18:10:05.040)	-10.66	-71.14	595.6	4.3	mb
8	2015-11-24 (22:45:38.880)	-10.54	-70.94	606.2	7.6	Mw
9	2015-11-24 (22:50:54.370)	-10.06	-71.02	620.6	7.6	Mw
10	2015-11-24 (23:44:14.010)	-10.56	-70.99	595.1	4.6	mb
11	2015-11-24 (23:55:20.210)	-10.29	-70.87	618.8	4.1	mb
12	2015-11-25 (00:28:16.830)	-11.03	-70.85	597.1	4.7	mb
13	2015-11-25 (04:30:29.380)	-10.08	-71.14	589.8	4.3	mb
14	2015-11-25 (09:26:22.680)	-8.53	-71.37	629.3	4.7	mb
15	2015-11-25 (11:45:25.430)	-9.30	-71.45	515.0	4.3	mb
16	2015-11-25 (16:19:24.860)	-9.85	-71.28	630.5	4.3	mb
17	2015-11-25 (18:47:56.000)	-10.40	-70.54	655.0	4.3	mb

18	2015-11-25 (23:49:34.380)	-10.52	-71.14	591.9	4.2	mb
19	2015-11-26 (05:45:18.400)	-9.18	-71.26	602.7	6.7	Mw
20	2015-11-26 (05:56:05.120)	-9.06	-71.32	602.6	4.9	mb
21	2015-11-26 (06:01:22.990)	-9.20	-71.29	602.1	4.6	mb
22	2015-11-26 (13:42:24.490)	-9.76	-71.24	605.6	4.9	mb
23	2015-11-26 (20:50:46.270)	-10.57	-71.18	601.8	4.2	mb
24	2015-11-27 (00:52:54.610)	-9.29	-71.09	617.0	5.1	mb
25	2015-11-29 (10:41:32.140)	-10.17	-71.18	625.6	4.2	mb
26	2015-12-03 (23:29:48.500)	-10.26	-71.42	622.7	4.0	mb
27	2015-12-06 (13:49:42.450)	-9.83	-71.19	638.4	4.2	mb
28	2015-12-19 (04:25:25.450)	-11.08	-71.01	601.4	4.0	mb
29	2016-01-03 (11:08:34.460)	-10.78	-70.78	633.4	4.3	mb
30	2016-12-18 (13:30:10.680)	-9.97	-70.97	612.0	6.4	Mw
31	2018-03-15 (20:13:29.710)	-8.52	-71.50	590.0	4.5	mb
32	2018-08-24 (09:04:08.250)	-11.03	-70.83	630.0	7.1	Mw
33	2018-08-26 (19:58:24.550)	-11.25	-70.59	605.7	4.5	mb
34	2019-01-05 (19:25:38.520)	-8.14	-71.59	570.4	6.8	Mw
35	2019-04-16 (03:19:30.295)	-8.11	-71.69	584.1	4.8	mb

36	2020-08-03 (03:45:57.052)	-9.38	-71.25	607.6	4.1	mb
37	2021-04-11 (04:21:02.737)	-9.22	-71.34	556.8	4.1	mb
38	2021-10-02 (12:52:34.077)	-9.59	-71.16	589.0	5.9	Mw
39	2021-10-12 (04:34:35.763)	-9.62	-71.27	605.1	4.1	mb
40	2022-05-14 (22:27:28.588)	-8.45	-71.50	580.0	4.6	mb
41	2022-06-08 (00:55:46.777)	-9.05	-71.18	622.7	6.5	Mw
42	2022-06-08 (01:53:28.974)	-9.09	-71.26	605.4	4.9	mb

Table S1. Deep-focus earthquakes in the Peru-Brazil border region from 2014 to 2022 according to the USGS catalog.

Source	Event 8 S	D	R	CD	M0	Mw	9 S	D	R	CD	M0	Mw
This study	350	40	-80	616.0	1.81e+27	7.5	350	30	-90	621.0	1.93e+27	7.5
Ye et al. 2016	354	44	-74	610.7	2.50e+27	7.5	359	36	-72	627.3	3.59e+27	7.6
Zahradnik et al. 2017	2	40	-64	590.0	2.70e+27	7.6	1	30	-73	627.0	3.10e+27	7.6
Jiménez et al. 2021	340	38	-80	655.0	1.68e+27	7.4	339	31	-88	675.0	2.63e+27	7.5
USGS	352	40	-85	590.5	2.84e+27	7.6	355	27	-74	630.5	3.19e+27	7.6
GCMT	350	39	-80	610.7	2.62e+27	7.5	350	30	-81	627.3	3.70e+27	7.6

Table S2. Mechanisms available for the 2015 deep-focus doublet (events 8 and 9 in Table S1).

	This study						USGS						GCMT					
Event	S	D	R	CD	M0	Mw	S	D	R	CD	M0	Mw	S	D	R	CD	M0	Mw
1	180±8	50±7	-80±11	571±18	7.36±1.06 e+23	5.2±0.04							315	42	-97	573.7	9.18 e+23	5.2
3	20±4	30±0	-80±4	557[b]±9	1.36±0.02 e+24	5.4± 0.004												
6	190±8	60±10	-10±6	584±13	3.28±0.77 e+23	5.0±0.07												
8	350±0	40±0	-80±0	616[b]±10	1.81±0.02 e+27	7.5± 0.003	352	40	-85	590.5	2.84 e+27	7.6	350	39	-80	610.7	2.62 e+27	7.5
9	350±0	30±0	-90±0	621±13	1.93±0.02 e+27	7.5± 0.003	355	27	-74	630.5	3.19 e+27	7.6	350	30	-81	627.3	3.70 e+27	7.6
10	110±20	50±9	-80±8	595[a]	1.63±0.34 e+23	4.8±0.05												
11	310±64	70±35	-60±28	629±17	9.61±0.76 e+22	4.6±0.03												
12	150±32	50±18	-60±35	587±8	1.82±0.27 e+23	4.8±0.04												
13	250±145	20±0	-20±67	590[a]	2.27±4.57 e+22	4.2±0.22												
14	170±4	40±0	-70±0	659±4	3.66±0.11 e+23	5.0±0.01												
17	200±41	40±5	-90±24	655[a]	1.25±0.67 e+23	4.7±0.11												
18	300±111	70±11	-80±15	592[a]	4.60±2.17 e+22	4.4±0.11												
19	350±0	30±0	-90±0	603[b]±9	1.27±0.01 e+26	6.7± 0.002	345	28	-92	610.5	1.21 e+26	6.7	344	27	-95	614.1	1.34 e+26	6.7
22	350±0	60±0	-80±0	636±15	2.75±0.03 e+23	4.9± 0.003												
24	170±2	50±2	-90±3	617±13	5.44±0.19 e+23	5.1±0.01												
29	230±131	20±23	-40±15	643±8	1.24±0.78 e+23	4.7±0.17												
30	350±0	20±0	-80±0	642[b]±19	4.72±0.01 e+25	6.4± 0.001	340	22	-90	640.5	5.36 e+25	6.4	350	18	-84	638.0	5.64 e+25	6.4
31	90±35	70±19	-90±59	590[a]	7.79±2.94 e+22	4.6±0.08												

32	340±1	40±1	-90±1	620[b]±14	4.83±0.02 e+26	7.1± 0.001	332	34	-95	640.5	5.23 e+26	7.1	335	33	-94	627.7	5.43 e+26	7.1
33	60±26	30±8	-50±9	626±8	2.58±0.55 e+23	4.9±0.06												
34	350±1	40±0	-80±2	570[b]±12	1.64±0.02 e+26	6.8± 0.003	351	36	-77	580.5	1.78 e+26	6.8	349	36	-77	588.1	1.79 e+26	6.8
35	10±4	20±0	-80±3	564±5	4.76±0.22 e+23	5.1±0.01							181	87	-76	579.0	1.36 e+24	5.4
37	180±66	20±30	-70±42	557[a]	5.59±6.04 e+22	4.5±0.17												
38	350±0	40±0	-80±0	599[b]±18	9.31±0.12 e+24	5.9± 0.004	349	43	-82	590.5	9.61 e+24	5.9	333	44	-88	609.0	1.04 e+25	5.9
39	220±21	40±28	-30±7	605±5	7.26±3.24 e+22	4.5±0.10												
40	280±58	70±30	-30±24	580[a]	1.70±0.66 e+23	4.8±0.13												
41	350±0	20±0	-80±0	623[b]±12	6.16±0.08 e+25	6.5± 0.004	346	27	-91	650.5	6.73 e+25	6.5	348	21	-89	621.0	6.7 e+25	6.5
42	350±69	80±0	60±56	605[a]	7.80±0.65 e+23	5.2±0.02												

[a]The centroid depth was fixed to be the hypocenter depth given by the USGS catalog. In these cases, there was no clear minimum in the misfit curve and thus we could not select a preferred depth. [b]Depth phases were considered in the inversion.

Table S3. Comparing the earthquake focal mechanisms determined in this study with available solutions in the USGS and GCMT catalogs. In this table, strike (S), dip (D) and rake (R), are given in degrees, centroid depth (CD) in km, and seismic moment (M0) in dyne-cm. Uncertainties are indicated next to each inverted parameter and were all calculated through jackknife resampling.

Event	Frequency range (Hz)	Number of stations	Number of waveforms	Mechanism type	Assigned quality
1	0.02-0.05	7	14	N	A
3	0.02-0.05	58	109	N	A
6	0.3-1.0	4	9	SS-N	B
8	0.02-0.05	132	332	N	A
9	0.02-0.05	57	88	N	A
10	0.3-1.0	5	12	N	B
11	0.3-1.0	2	6	N-SS	B
12	0.3-1.0	5	15	N-SS	B
13	0.3-1.0	3	6	N	D
14	0.02-0.05	5	9	N	B
17	0.3-1.0	4	13	N	B
18	0.3-1.0	3	7	N	B
19	0.02-0.05	129	353	N	A
22	0.02-0.05	7	12	N	A
24	0.02-0.05	32	53	N	A
29	0.3-1.0	3	6	N	B
30	0.02-0.05	165	392	N	A
31	0.3-1.0	9	15	N	B
32	0.02-0.05	163	411	N	A
33	0.3-1.0	6	15	N	C
34	0.02-0.05	151	375	N	A
35	0.02-0.05	10	17	N	A
37	0.3-1.0	3	8	N	B
38	0.02-0.05	81	128	N	A
39	0.3-1.0	2	6	N-SS	B
40	0.3-1.0	4	7	SS-N	B
41	0.02-0.05	125	323	N	A
42	0.3-1.0	6	10	R-SS	B

Table S4. Supplementary information for Table 1. Frequency range, number of stations and number of traces employed in our inversions. Resulting mechanism type and its quality are also shown in this table.

Figure S1. Inversion results for event 1. a) Map showing the preferred solution in b and the distribution of the 7 stations (14 traces) used in the inversion. Solution parameters are given below the map. Dashed circles indicate radii of 5º and 30º from epicenter; b) Distribution of focal mechanisms with centroid depths pointing to 571 km as the preferred solution for the event; c) Waveform fitting produced by the preferred solution. Black and red lines denote observations and synthetics, respectively. Azimuths and distances in degrees are shown above panels. Time shifts (top) and cross-correlation coefficients (bottom) are shown in blue at the lower right corner of each panel. Wave segments (Pr, Pz, SVr, SH and SVz) are identified at the upper right corners.

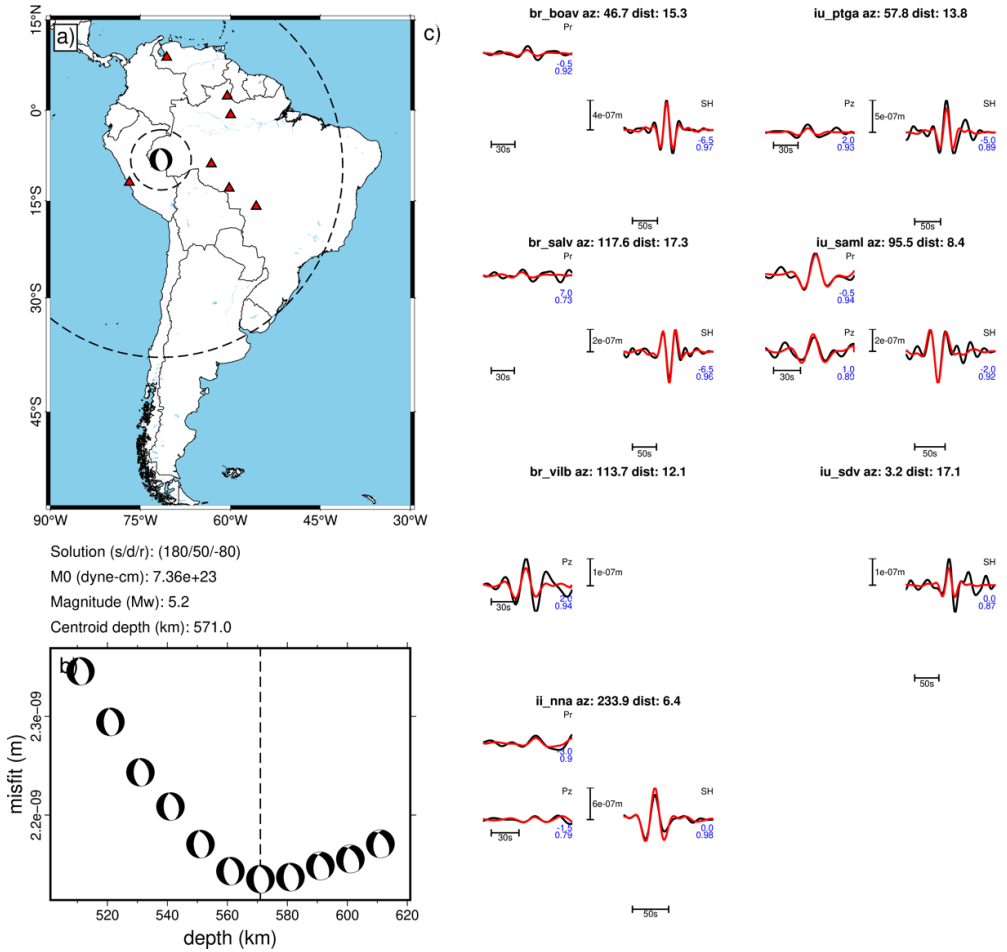

Figure S2. Inversion results for event 3. a) Map showing the preferred solution in b and the distribution of the 58 stations (109 traces) used in the inversion. Solution parameters are given below the map. Dashed circles indicate radii of 5º and 30º from epicenter; b) Distribution of focal mechanisms with centroid depths pointing to 557 km as the preferred solution for the event; c) Waveform fitting produced by the preferred solution. Black and red lines denote observations and synthetics, respectively. Azimuths and distances in degrees are shown above panels. Time shifts (top) and cross-correlation coefficients (bottom) are shown in blue at the lower right corner of each panel. Wave segments (Pr, Pz, SVr, SH and SVz) are identified at the upper right corners.

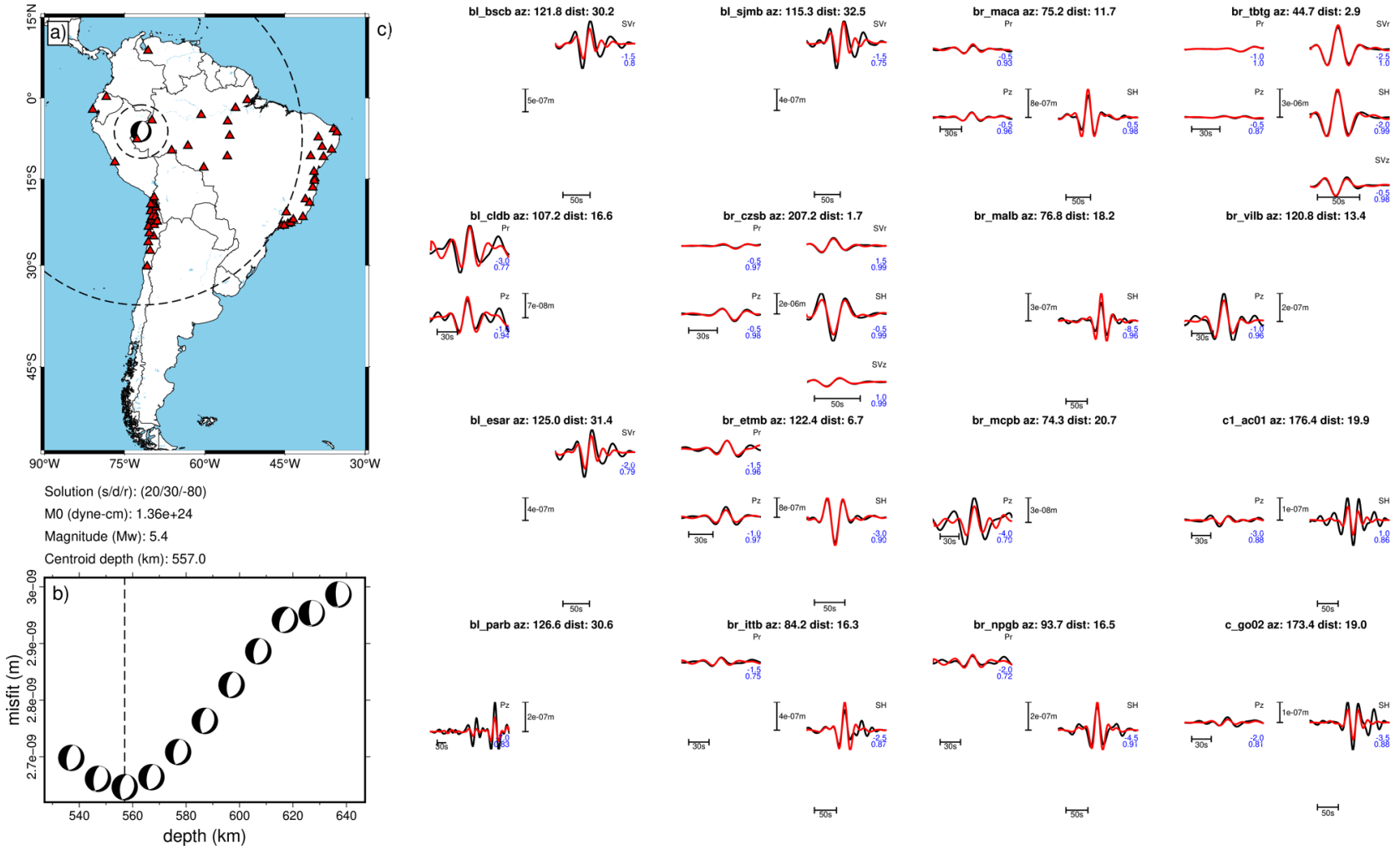

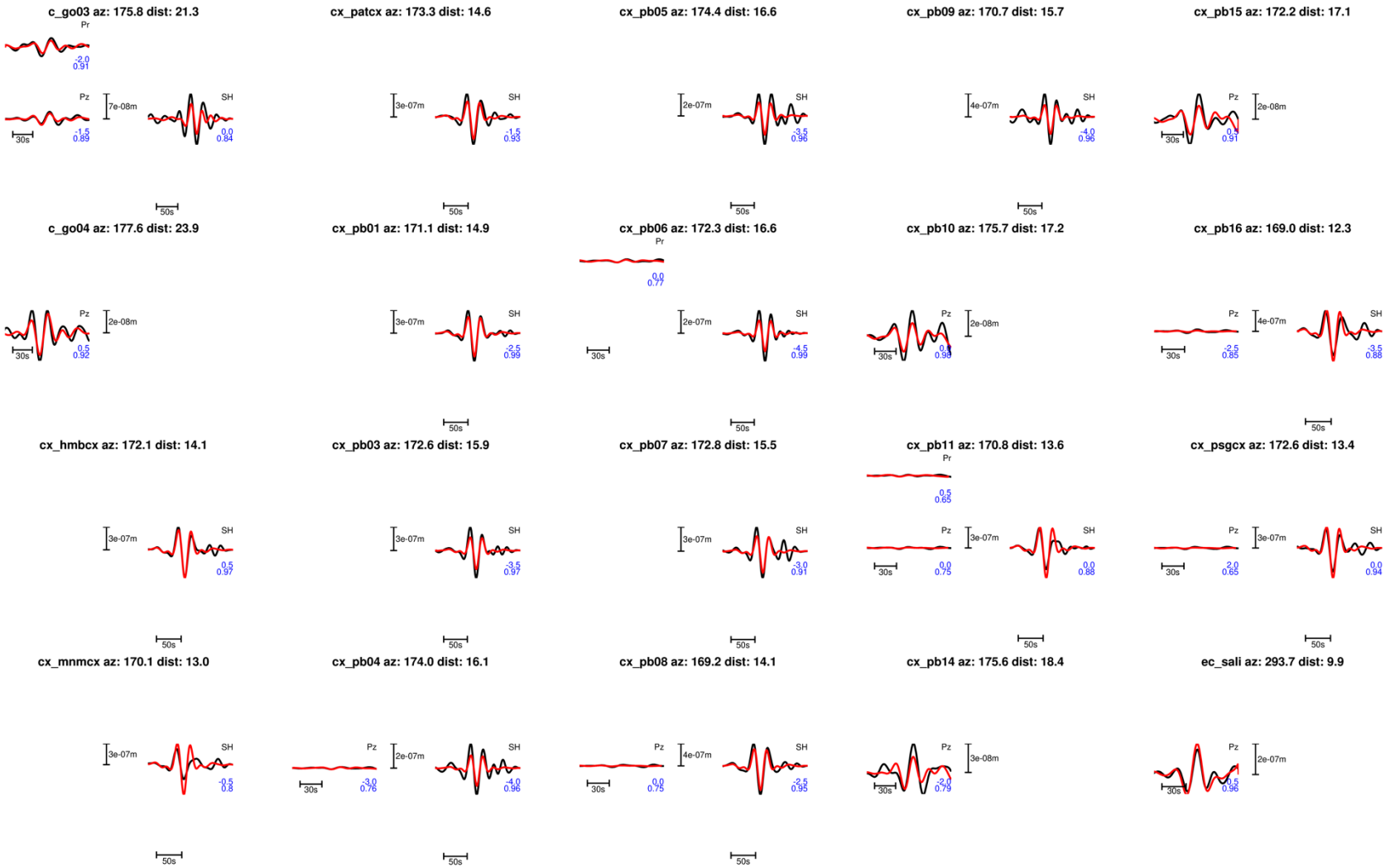
c_go03 az: 175.8 dist: 21.3
cx_patcx az: 173.3 dist: 14.6
cx_pb05 az: 174.4 dist: 16.6
cx_pb09 az: 170.7 dist: 15.7
cx_pb15 az: 172.2 dist: 17.1
c_go04 az: 177.6 dist: 23.9
cx_pb01 az: 171.1 dist: 14.9
cx_pb06 az: 172.3 dist: 16.6
cx_pb10 az: 175.7 dist: 17.2
cx_pb16 az: 169.0 dist: 12.3
cx_hmbcx az: 172.1 dist: 14.1
cx_pb03 az: 172.6 dist: 15.9
cx_pb07 az: 172.8 dist: 15.5
cx_pb11 az: 170.8 dist: 13.6
cx_psgcx az: 172.6 dist: 13.4
cx_mnmcx az: 170.1 dist: 13.0
cx_pb04 az: 174.0 dist: 16.1
cx_pb08 az: 169.2 dist: 14.1
cx_pb14 az: 175.6 dist: 18.4
ec_sali az: 293.7 dist: 9.9
Pr
Pz
SH
30s
50s

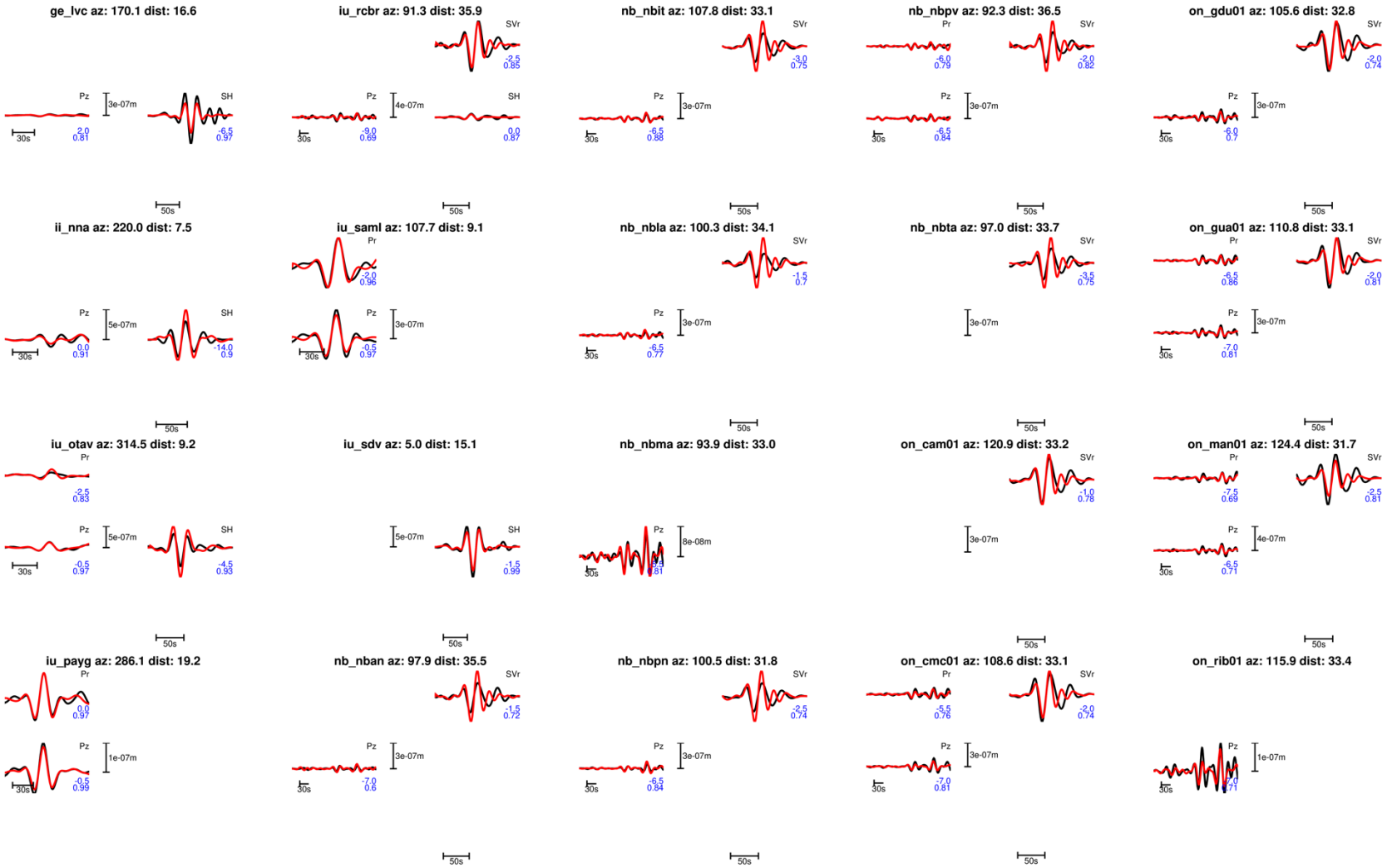
ge_lvc az: 170.1 dist: 16.6
iu_rcbr az: 91.3 dist: 35.9
nb_nbit az: 107.8 dist: 33.1
nb_nbpv az: 92.3 dist: 36.5
on_gdu01 az: 105.6 dist: 32.8
ii_nna az: 220.0 dist: 7.5
iu_saml az: 107.7 dist: 9.1
nb_nbla az: 100.3 dist: 34.1
nb_nbta az: 97.0 dist: 33.7
on_gua01 az: 110.8 dist: 33.1
iu_otav az: 314.5 dist: 9.2
iu_sdv az: 5.0 dist: 15.1
nb_nbma az: 93.9 dist: 33.0
on_cam01 az: 120.9 dist: 33.2
on_man01 az: 124.4 dist: 31.7
iu_payg az: 286.1 dist: 19.2
nb_nban az: 97.9 dist: 35.5
nb_nbpn az: 100.5 dist: 31.8
on_cmc01 az: 108.6 dist: 33.1
on_rib01 az: 115.9 dist: 33.4
Pz
Pr
SH
SVr
30s
50s

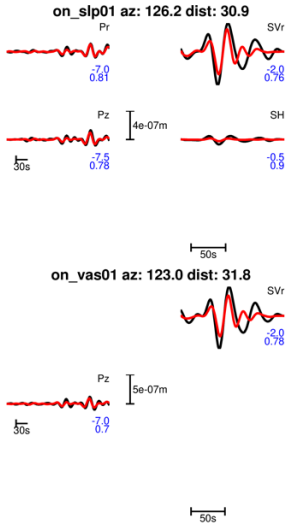
on_slp01 az: 126.2 dist: 30.9
Pr
SVr
-7.0
0.81
-2.0
0.76
Pz
4e-07m
SH
30s
-7.5
0.78
-0.5
0.9
50s
on_vas01 az: 123.0 dist: 31.8
SVr
-2.0
0.78
Pz
5e-07m
30s
-7.0
0.7
50s

Figure S3. Inversion results for event 6. a) Map showing the preferred solution in b and the distribution of the 4 stations (9 traces) used in the inversion. Solution parameters are given below the map. Dashed circles indicate radii of 5º and 30º from epicenter; b) Distribution of focal mechanisms with centroid depths pointing to 584 km as the preferred solution for the event; c) Waveform fitting produced by the preferred solution. Black and red lines denote observations and synthetics, respectively. Azimuths and distances in degrees are shown above panels. Time shifts (top) and cross-correlation coefficients (bottom) are shown in blue at the lower right corner of each panel. Wave segments (Pr, Pz, SVr, SH and SVz) are identified at the upper right corners.

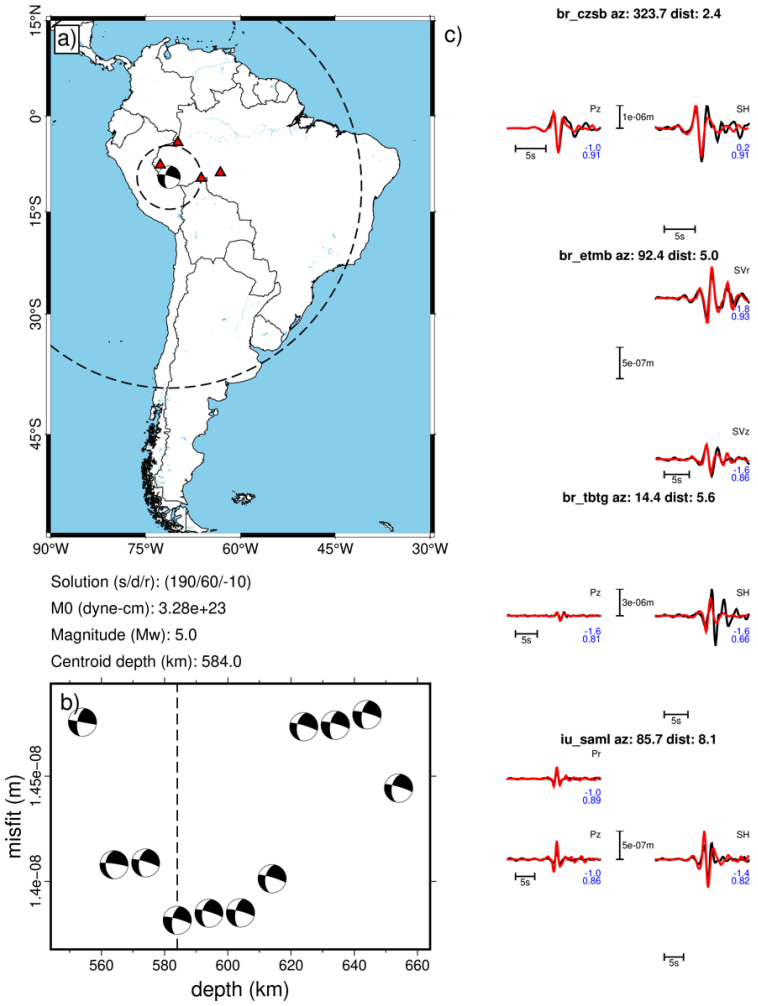

Figure S4. Inversion results for event 8. a) Map showing the preferred solution in b and the distribution of the 132 stations (332 traces) used in the inversion. Solution parameters are given below the map. Dashed circles indicate radii of 5º and 30º from epicenter; b) Distribution of focal mechanisms with centroid depths pointing to 616 km as the preferred solution for the event; c) Waveform fitting produced by the preferred solution. Black and red lines denote observations and synthetics, respectively. Azimuths and distances in degrees are shown above panels. Time shifts (top) and cross-correlation coefficients (bottom) are shown in blue at the lower right corner of each panel. Wave segments (Pr, Pz, SVr, SH and SVz) are identified at the upper right corners.

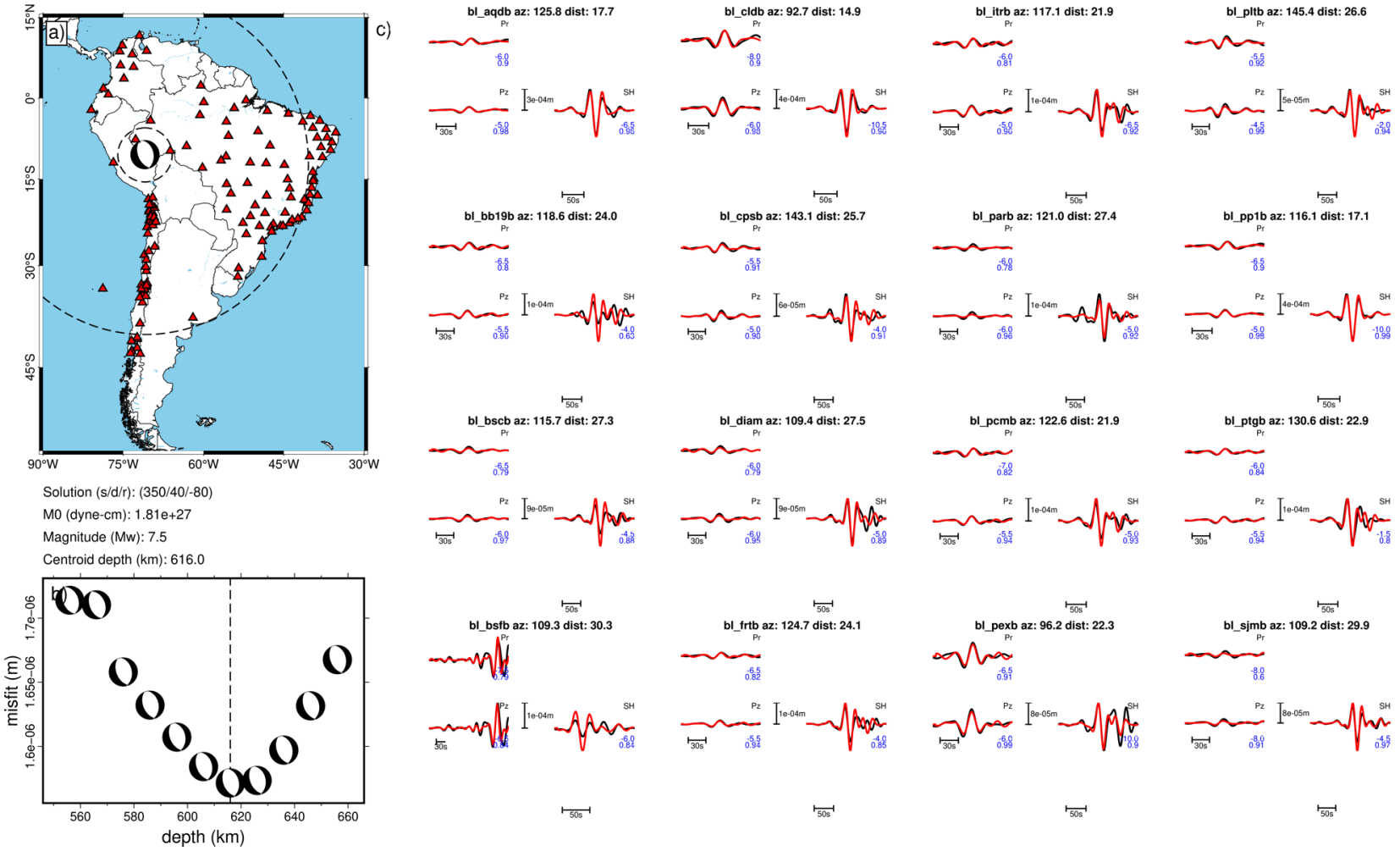

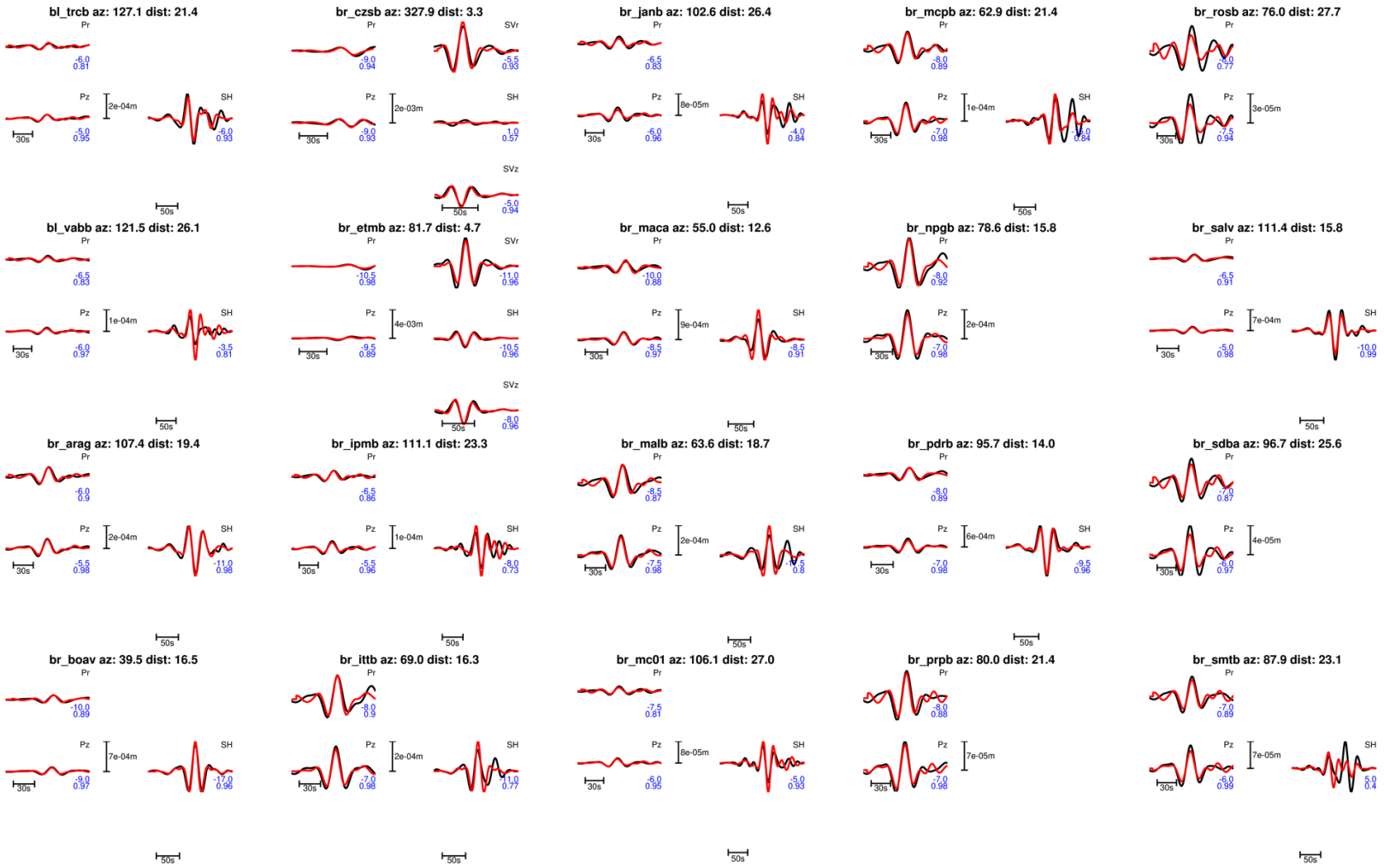
bl_trcb az: 127.1 dist: 21.4
br_czsb az: 327.9 dist: 3.3
br_janb az: 102.6 dist: 26.4
br_mcpb az: 62.9 dist: 21.4
br_rosb az: 76.0 dist: 27.7
bl_vabb az: 121.5 dist: 26.1
br_etmb az: 81.7 dist: 4.7
br_maca az: 55.0 dist: 12.6
br_npgb az: 78.6 dist: 15.8
br_salv az: 111.4 dist: 15.8
br_arag az: 107.4 dist: 19.4
br_ipmb az: 111.1 dist: 23.3
br_malb az: 63.6 dist: 18.7
br_pdrb az: 95.7 dist: 14.0
br_sdba az: 96.7 dist: 25.6
br_boav az: 39.5 dist: 16.5
br_ittb az: 69.0 dist: 16.3
br_mc01 az: 106.1 dist: 27.0
br_prpb az: 80.0 dist: 21.4
br_smtb az: 87.9 dist: 23.1
Pr
SVr
Pz
SH
SVz
30s
50s

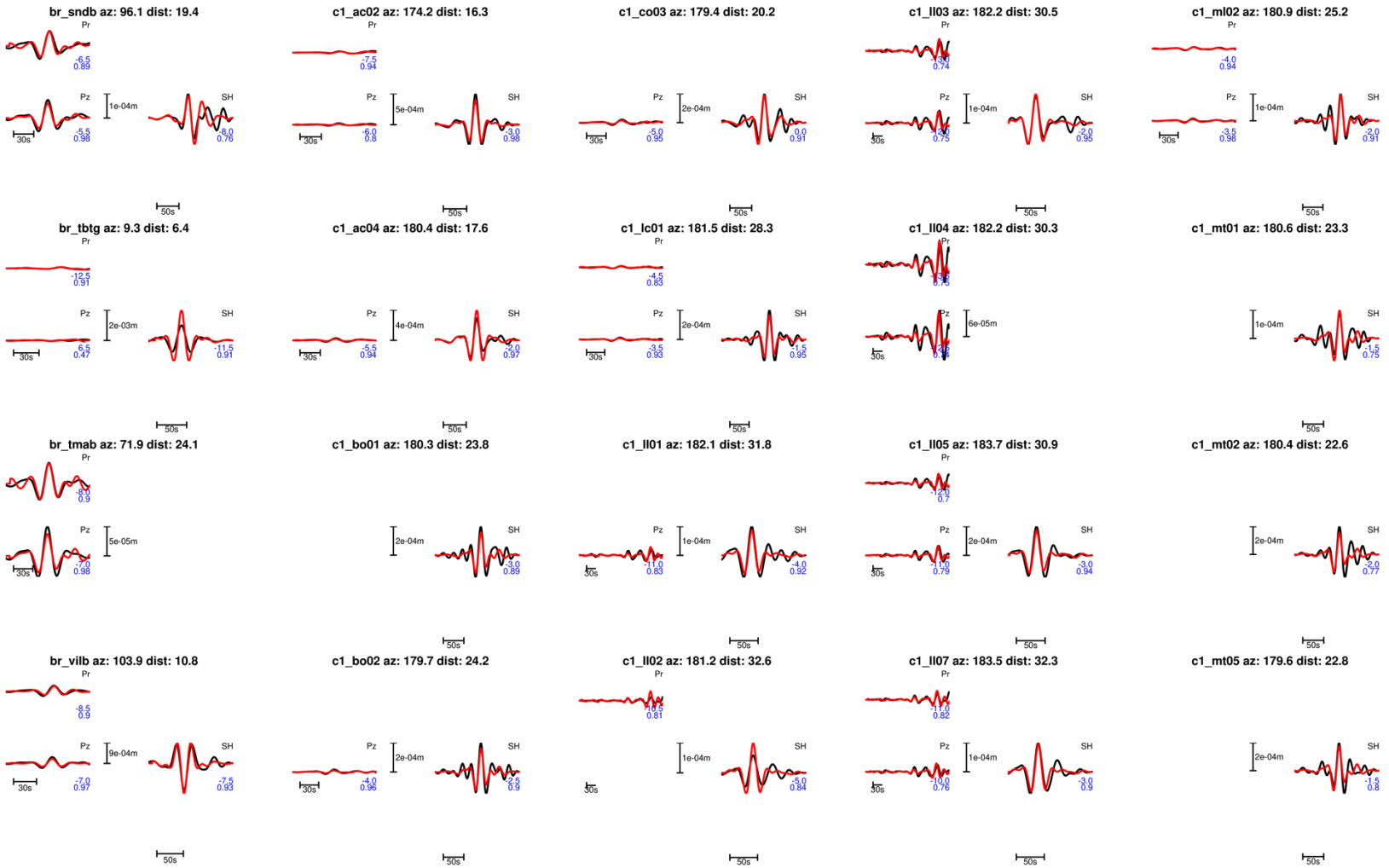
br_sndb az: 96.1 dist: 19.4
c1_ac02 az: 174.2 dist: 16.3
c1_co03 az: 179.4 dist: 20.2
c1_ll03 az: 182.2 dist: 30.5
c1_ml02 az: 180.9 dist: 25.2
br_tbtg az: 9.3 dist: 6.4
c1_ac04 az: 180.4 dist: 17.6
c1_lc01 az: 181.5 dist: 28.3
c1_ll04 az: 182.2 dist: 30.3
c1_mt01 az: 180.6 dist: 23.3
br_tmab az: 71.9 dist: 24.1
c1_bo01 az: 180.3 dist: 23.8
c1_ll01 az: 182.1 dist: 31.8
c1_ll05 az: 183.7 dist: 30.9
c1_mt02 az: 180.4 dist: 22.6
br_vilb az: 103.9 dist: 10.8
c1_bo02 az: 179.7 dist: 24.2
c1_ll02 az: 181.2 dist: 32.6
c1_ll07 az: 183.5 dist: 32.3
c1_mt05 az: 179.6 dist: 22.8
Pr
Pz
SH
30s
50s

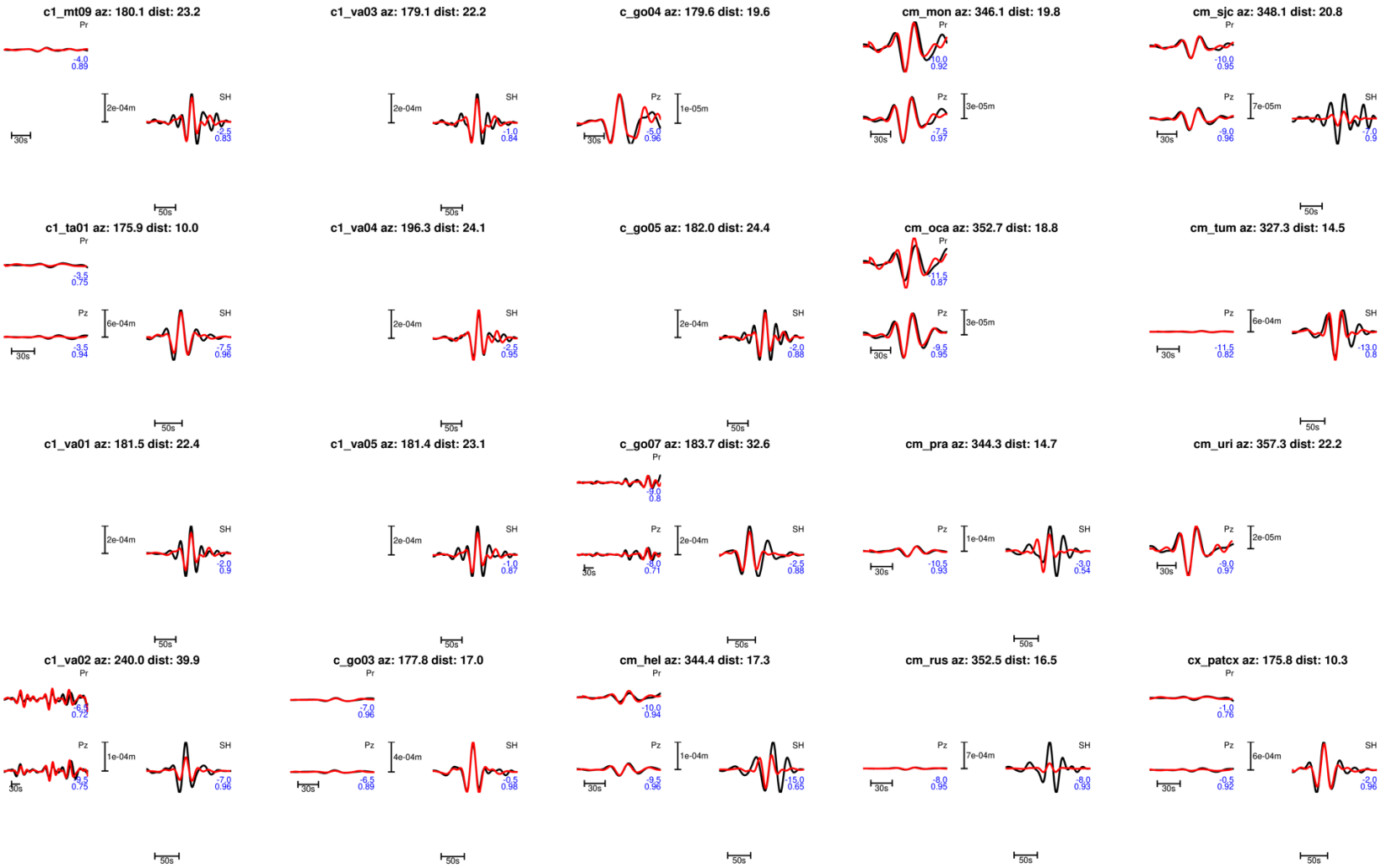
c1_mt09 az: 180.1 dist: 23.2
c1_va03 az: 179.1 dist: 22.2
c_go04 az: 179.6 dist: 19.6
cm_mon az: 346.1 dist: 19.8
cm_sjc az: 348.1 dist: 20.8
c1_ta01 az: 175.9 dist: 10.0
c1_va04 az: 196.3 dist: 24.1
c_go05 az: 182.0 dist: 24.4
cm_oca az: 352.7 dist: 18.8
cm_tum az: 327.3 dist: 14.5
c1_va01 az: 181.5 dist: 22.4
c1_va05 az: 181.4 dist: 23.1
c_go07 az: 183.7 dist: 32.6
cm_pra az: 344.3 dist: 14.7
cm_uri az: 357.3 dist: 22.2
c1_va02 az: 240.0 dist: 39.9
c_go03 az: 177.8 dist: 17.0
cm_hel az: 344.4 dist: 17.3
cm_rus az: 352.5 dist: 16.5
cx_patcx az: 175.8 dist: 10.3
Pr
Pz
SH
30s
50s

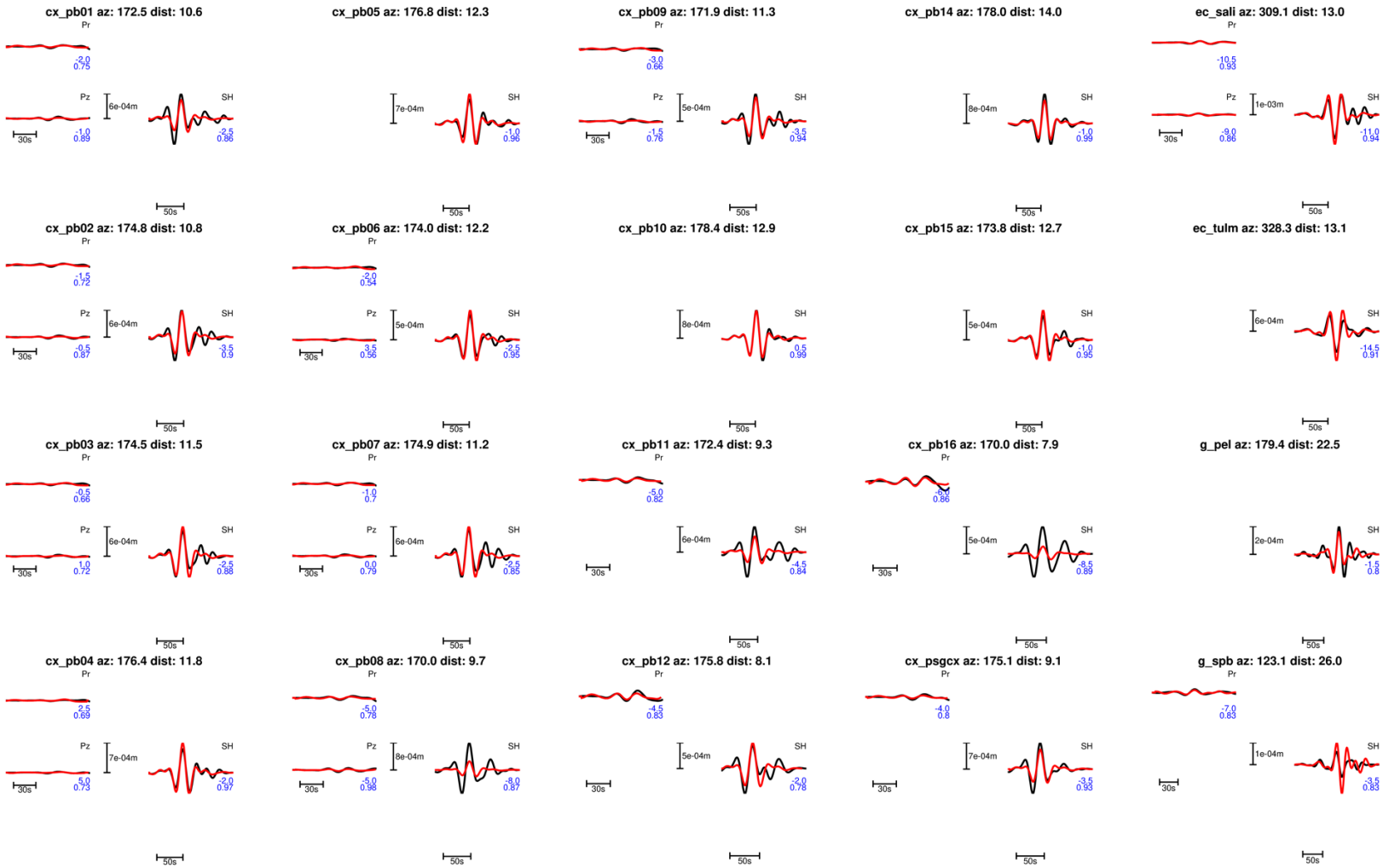
cx_pb01 az: 172.5 dist: 10.6
cx_pb05 az: 176.8 dist: 12.3
cx_pb09 az: 171.9 dist: 11.3
cx_pb14 az: 178.0 dist: 14.0
ec_sali az: 309.1 dist: 13.0
cx_pb02 az: 174.8 dist: 10.8
cx_pb06 az: 174.0 dist: 12.2
cx_pb10 az: 178.4 dist: 12.9
cx_pb15 az: 173.8 dist: 12.7
ec_tulm az: 328.3 dist: 13.1
cx_pb03 az: 174.5 dist: 11.5
cx_pb07 az: 174.9 dist: 11.2
cx_pb11 az: 172.4 dist: 9.3
cx_pb16 az: 170.0 dist: 7.9
g_pel az: 179.4 dist: 22.5
cx_pb04 az: 176.4 dist: 11.8
cx_pb08 az: 170.0 dist: 9.7
cx_pb12 az: 175.8 dist: 8.1
cx_psgcx az: 175.1 dist: 9.1
g_spb az: 123.1 dist: 26.0
Pr
Pz
SH
30s
50s

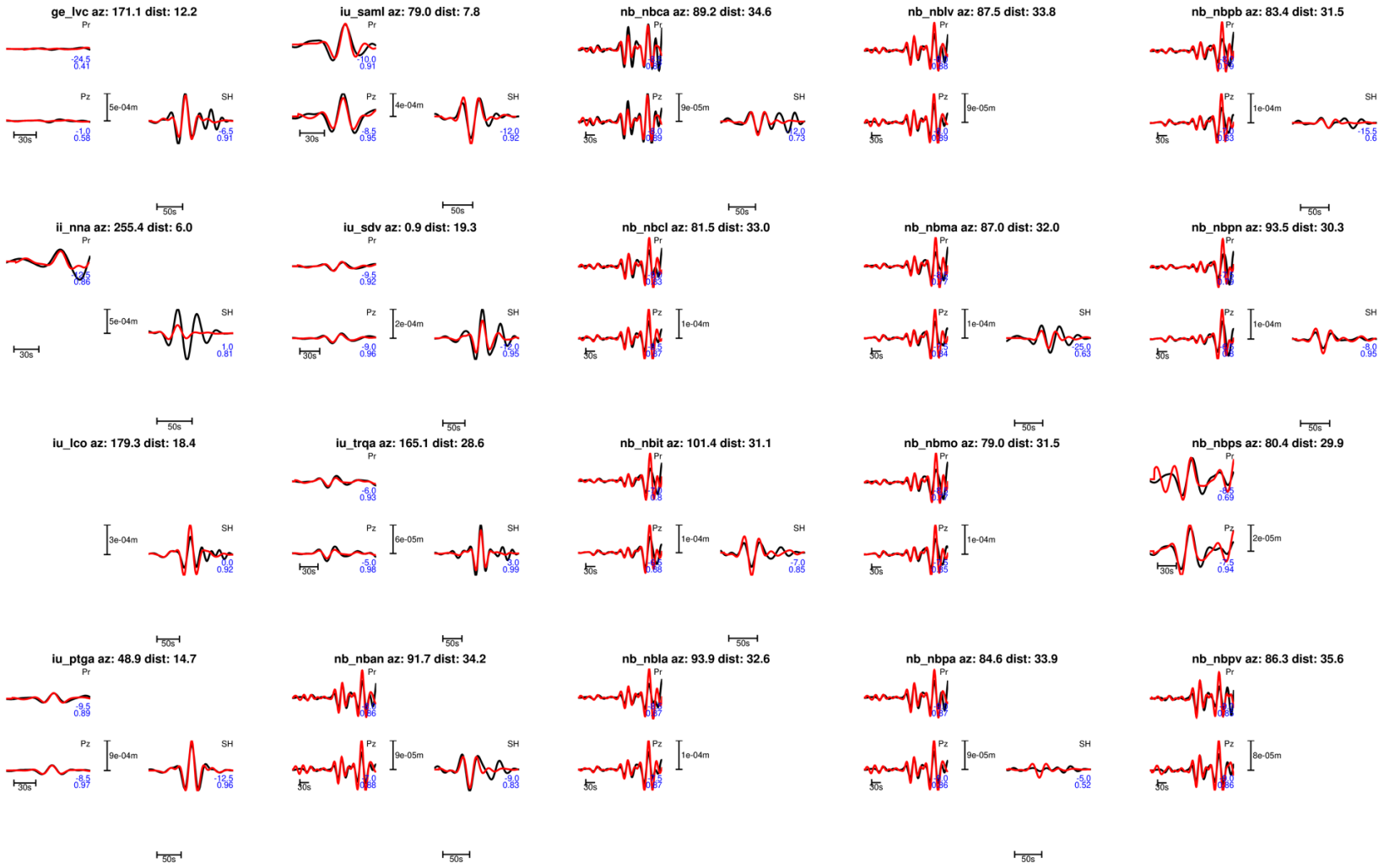
ge_lvc az: 171.1 dist: 12.2
iu_saml az: 79.0 dist: 7.8
nb_nbca az: 89.2 dist: 34.6
nb_nblv az: 87.5 dist: 33.8
nb_nbpb az: 83.4 dist: 31.5
ii_nna az: 255.4 dist: 6.0
iu_sdv az: 0.9 dist: 19.3
nb_nbcl az: 81.5 dist: 33.0
nb_nbma az: 87.0 dist: 32.0
nb_nbpn az: 93.5 dist: 30.3
iu_lco az: 179.3 dist: 18.4
iu_trqa az: 165.1 dist: 28.6
nb_nbit az: 101.4 dist: 31.1
nb_nbmo az: 79.0 dist: 31.5
nb_nbps az: 80.4 dist: 29.9
iu_ptga az: 48.9 dist: 14.7
nb_nban az: 91.7 dist: 34.2
nb_nbla az: 93.9 dist: 32.6
nb_nbpa az: 84.6 dist: 33.9
nb_nbpv az: 86.3 dist: 35.6
Pr
Pz
SH
30s
50s

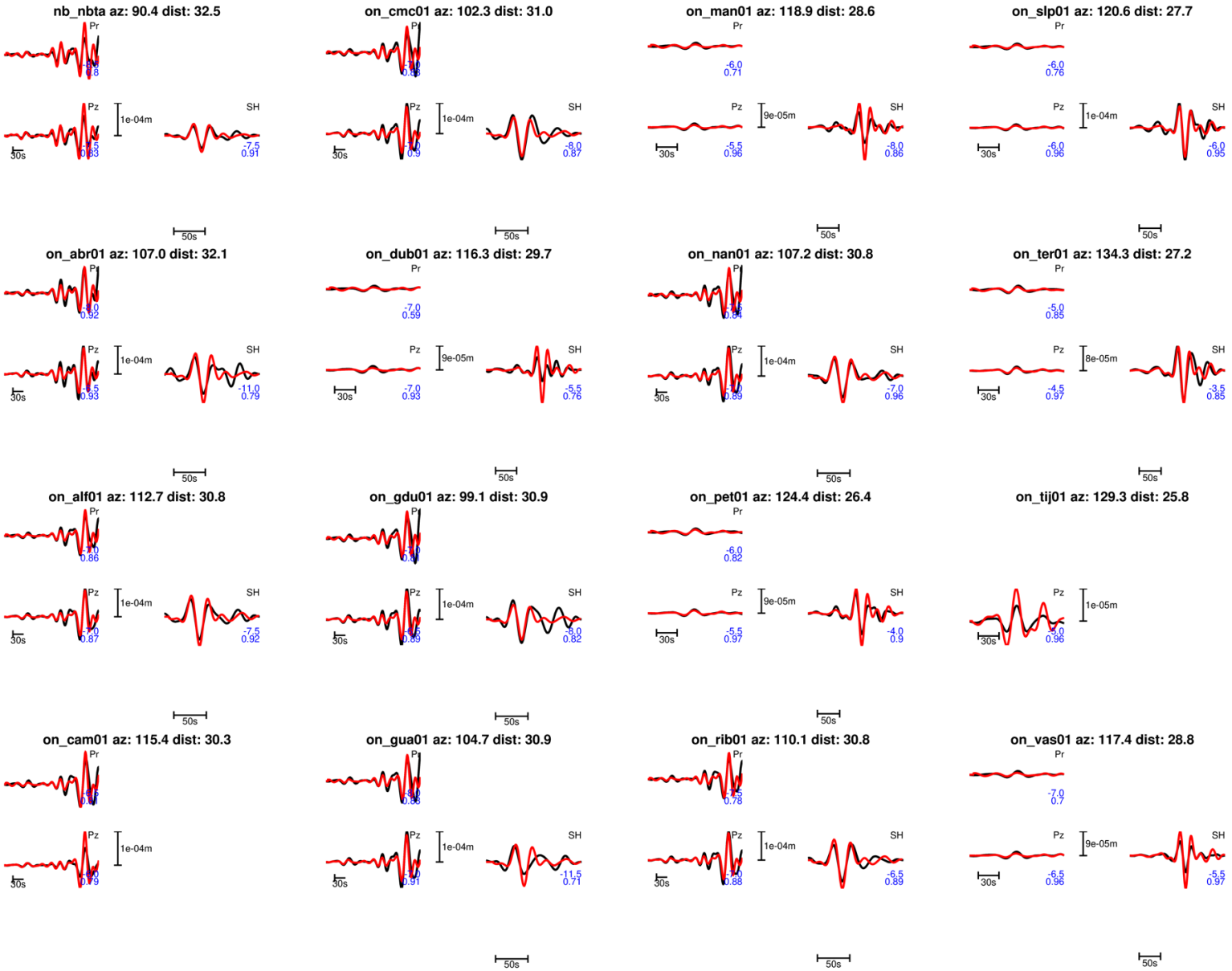
nb_nbta az: 90.4 dist: 32.5
on_cmc01 az: 102.3 dist: 31.0
on_man01 az: 118.9 dist: 28.6
on_slp01 az: 120.6 dist: 27.7
on_abr01 az: 107.0 dist: 32.1
on_dub01 az: 116.3 dist: 29.7
on_nan01 az: 107.2 dist: 30.8
on_ter01 az: 134.3 dist: 27.2
on_alf01 az: 112.7 dist: 30.8
on_gdu01 az: 99.1 dist: 30.9
on_pet01 az: 124.4 dist: 26.4
on_tij01 az: 129.3 dist: 25.8
on_cam01 az: 115.4 dist: 30.3
on_gua01 az: 104.7 dist: 30.9
on_rib01 az: 110.1 dist: 30.8
on_vas01 az: 117.4 dist: 28.8
Pr
Pz
SH
30s
50s

Figure S5. Inversion results for event 9. a) Map showing the preferred solution in b and the distribution of the 57 stations (88 traces) used in the inversion. Solution parameters are given below the map. Dashed circles indicate radii of 5º and 30º from epicenter; b) Distribution of focal mechanisms with centroid depths pointing to 621 km as the preferred solution for the event; c) Waveform fitting produced by the preferred solution. Black and red lines denote observations and synthetics, respectively. Azimuths and distances in degrees are shown above panels. Time shifts (top) and cross-correlation coefficients (bottom) are shown in blue at the lower right corner of each panel. Wave segments (Pr, Pz, SVr, SH and SVz) are identified at the upper right corners.

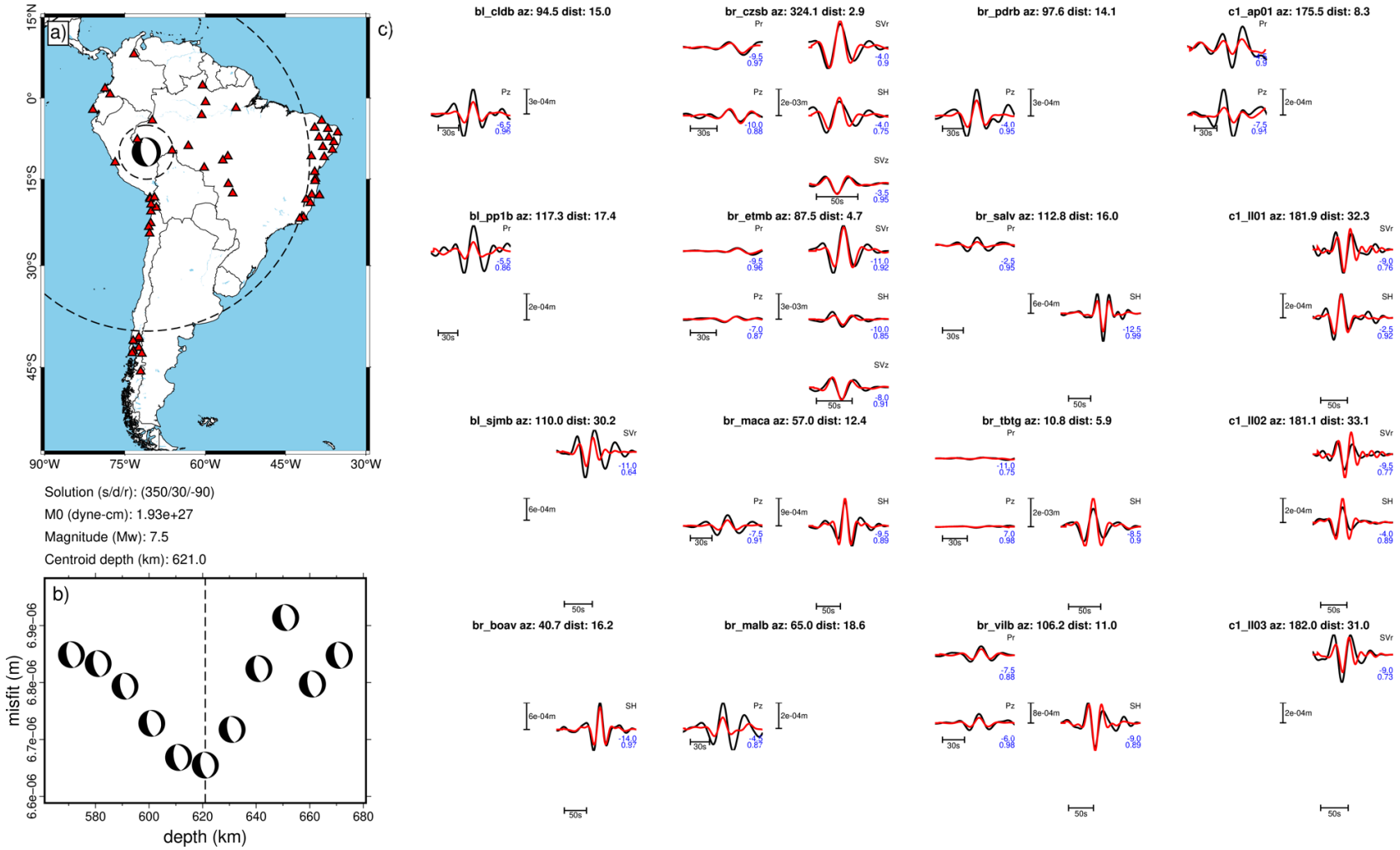

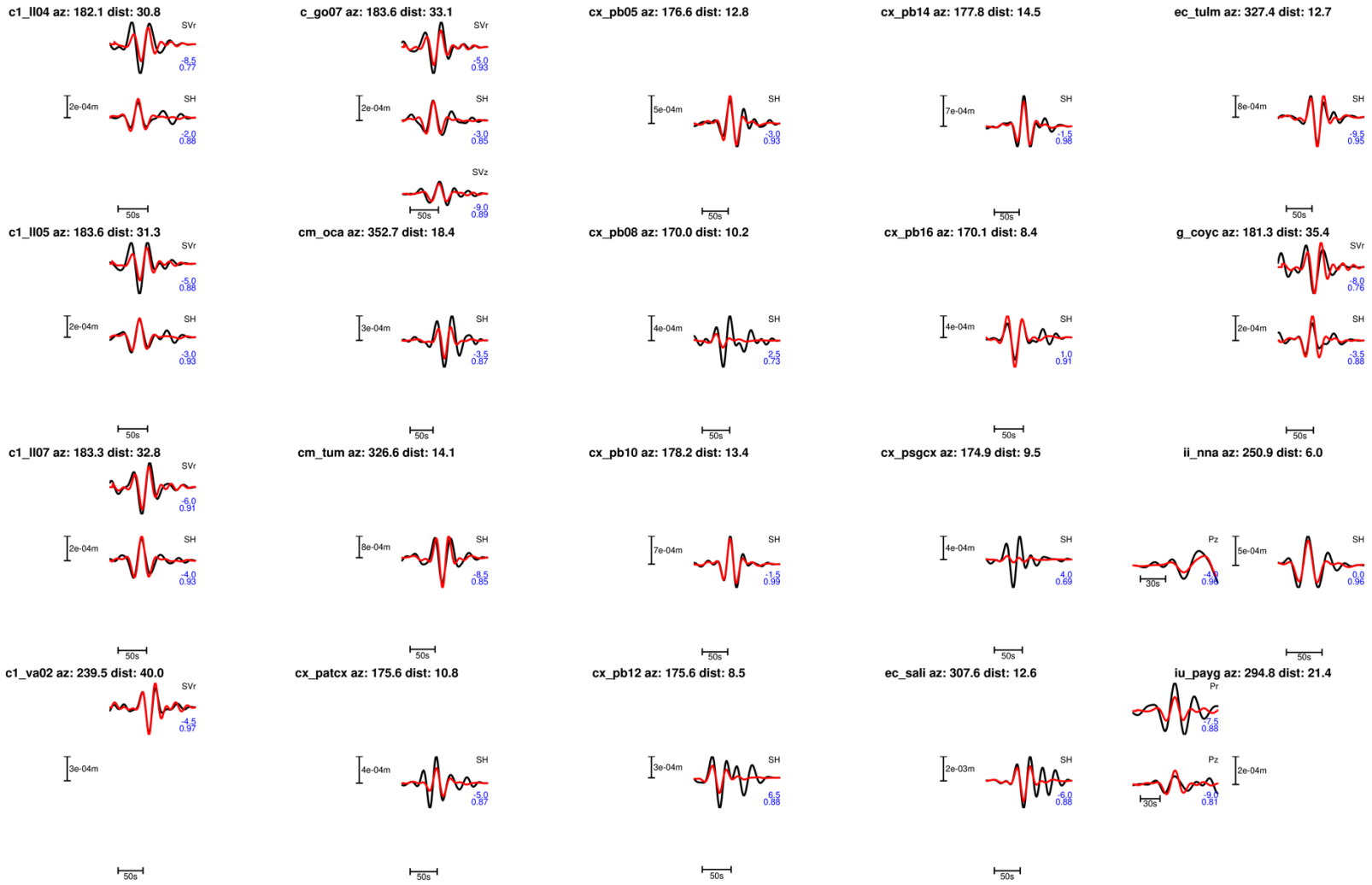
c1_ll04 az: 182.1 dist: 30.8
c_go07 az: 183.6 dist: 33.1
cx_pb05 az: 176.6 dist: 12.8
cx_pb14 az: 177.8 dist: 14.5
ec_tulm az: 327.4 dist: 12.7
c1_ll05 az: 183.6 dist: 31.3
cm_oca az: 352.7 dist: 18.4
cx_pb08 az: 170.0 dist: 10.2
cx_pb16 az: 170.1 dist: 8.4
g_coyc az: 181.3 dist: 35.4
c1_ll07 az: 183.3 dist: 32.8
cm_tum az: 326.6 dist: 14.1
cx_pb10 az: 178.2 dist: 13.4
cx_psgcx az: 174.9 dist: 9.5
ii_nna az: 250.9 dist: 6.0
c1_va02 az: 239.5 dist: 40.0
cx_patcx az: 175.6 dist: 10.8
cx_pb12 az: 175.6 dist: 8.5
ec_sali az: 307.6 dist: 12.6
iu_payg az: 294.8 dist: 21.4
SVr
SH
SVz
Pr
Pz
50s
30s

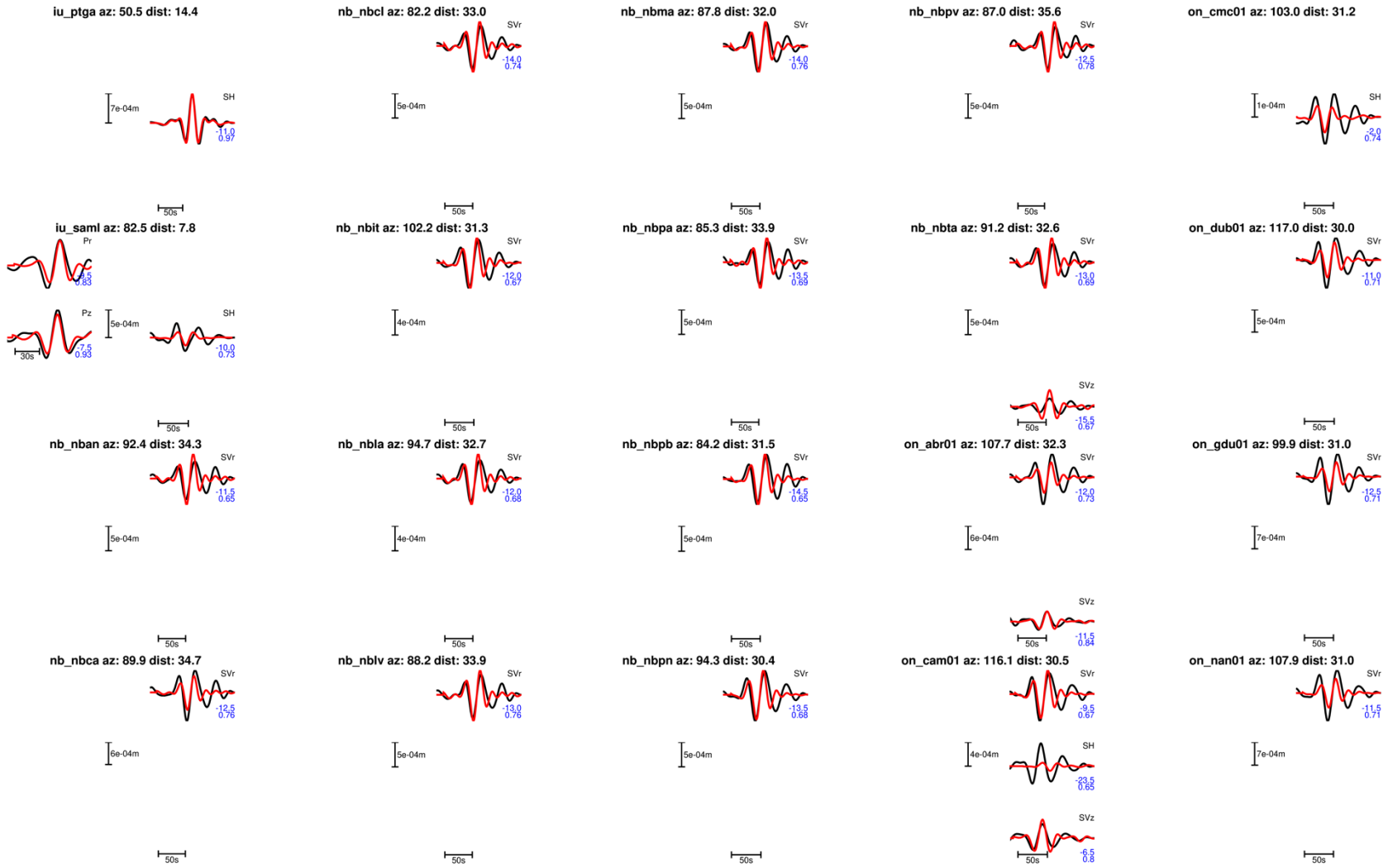
iu_ptga az: 50.5 dist: 14.4
nb_nbcl az: 82.2 dist: 33.0
nb_nbma az: 87.8 dist: 32.0
nb_nbpv az: 87.0 dist: 35.6
on_cmc01 az: 103.0 dist: 31.2
iu_saml az: 82.5 dist: 7.8
nb_nbit az: 102.2 dist: 31.3
nb_nbpa az: 85.3 dist: 33.9
nb_nbta az: 91.2 dist: 32.6
on_dub01 az: 117.0 dist: 30.0
nb_nban az: 92.4 dist: 34.3
nb_nbla az: 94.7 dist: 32.7
nb_nbpb az: 84.2 dist: 31.5
on_abr01 az: 107.7 dist: 32.3
on_gdu01 az: 99.9 dist: 31.0
nb_nbca az: 89.9 dist: 34.7
nb_nblv az: 88.2 dist: 33.9
nb_nbpn az: 94.3 dist: 30.4
on_cam01 az: 116.1 dist: 30.5
on_nan01 az: 107.9 dist: 31.0
Pr
Pz
SH
SVr
SVz
50s
30s

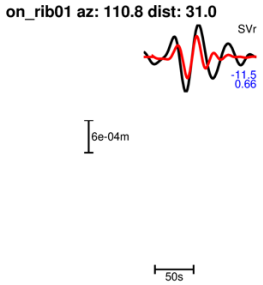
on_rib01 az: 110.8 dist: 31.0
SVr
-11.5
0.66
6e-04m
50s

Figure S6. Inversion results for event 10. a) Map showing the preferred solution in b and the distribution of the 5 stations (12 traces) used in the inversion. Solution parameters are given below the map. Dashed circles indicate radii of 5º and 30º from epicenter; b) Distribution of focal mechanisms with centroid depths. We selected 595 km as the preferred solution for the event, fixing to the hypocenter depth in Table 1; c) Waveform fitting produced by the preferred solution. Black and red lines denote observations and synthetics, respectively. Azimuths and distances in degrees are shown above panels. Time shifts (top) and cross-correlation coefficients (bottom) are shown in blue at the lower right corner of each panel. Wave segments (Pr, Pz, SVr, SH and SVz) are identified at the upper right corners.

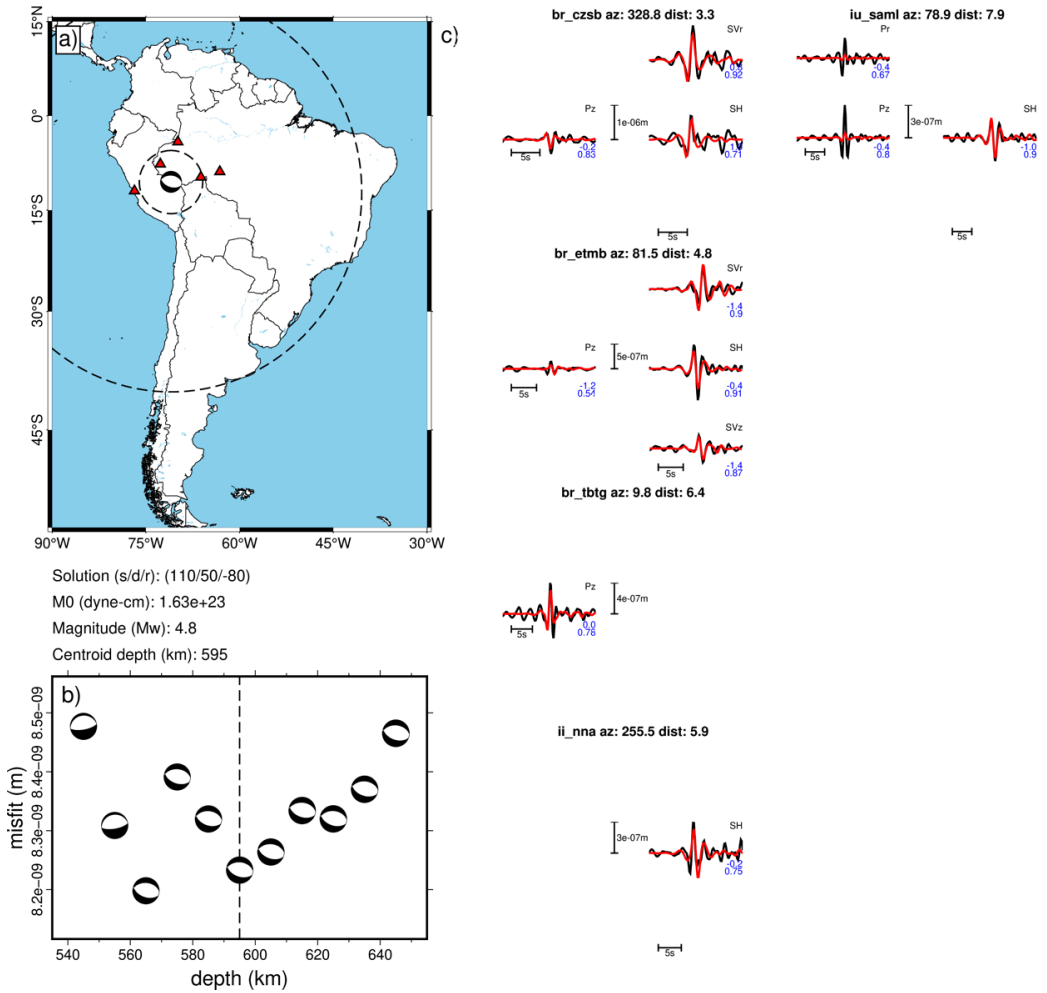

Figure S7. Inversion results for event 11. a) Map showing the preferred solution in b and the distribution of the 2 stations (6 traces) used in the inversion. Solution parameters are given below the map. Dashed circles indicate radii of 5º and 30º from epicenter; b) Distribution of focal mechanisms with centroid depths pointing to 629 km as the preferred solution for the event; c) Waveform fitting produced by the preferred solution. Black and red lines denote observations and synthetics, respectively. Azimuths and distances in degrees are shown above panels. Time shifts (top) and cross-correlation coefficients (bottom) are shown in blue at the lower right corner of each panel. Wave segments (Pr, Pz, SVr, SH and SVz) are identified at the upper right corners.

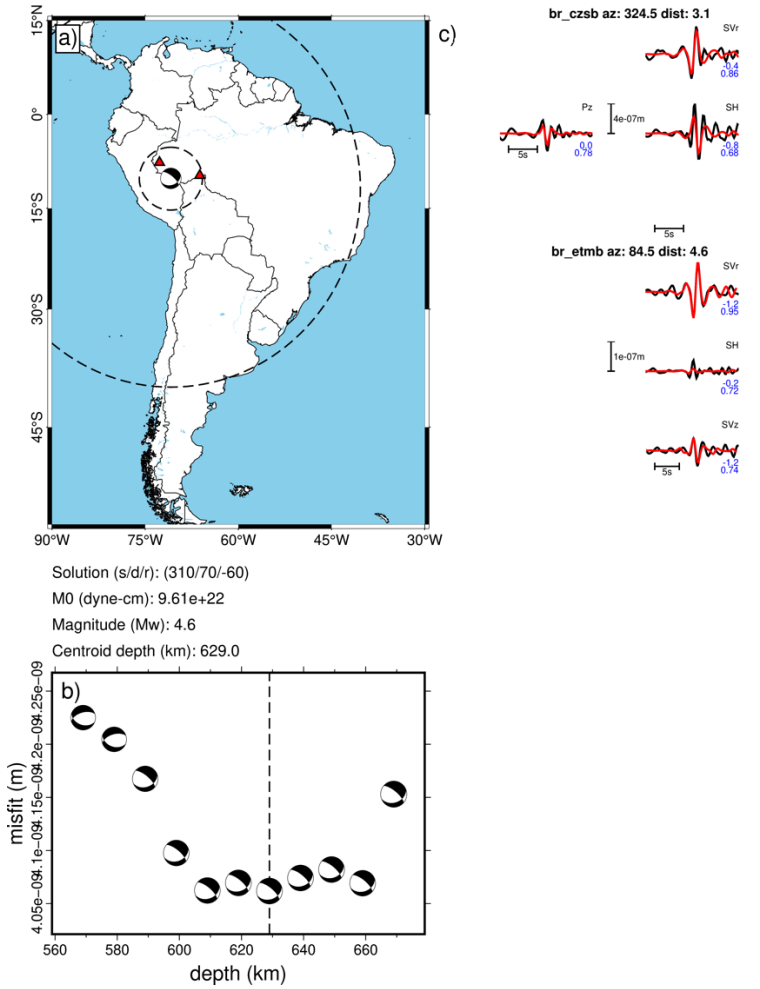

Figure S8. Inversion results for event 12. a) Map showing the preferred solution in b and the distribution of the 5 stations (15 traces) used in the inversion. Solution parameters are given below the map. Dashed circles indicate radii of 5º and 30º from epicenter; b) Distribution of focal mechanisms with centroid depths pointing to 587 km as the preferred solution for the event; c) Waveform fitting produced by the preferred solution. Black and red lines denote observations and synthetics, respectively. Azimuths and distances in degrees are shown above panels. Time shifts (top) and cross-correlation coefficients (bottom) are shown in blue at the lower right corner of each panel. Wave segments (Pr, Pz, SVr, SH and SVz) are identified at the upper right corners.

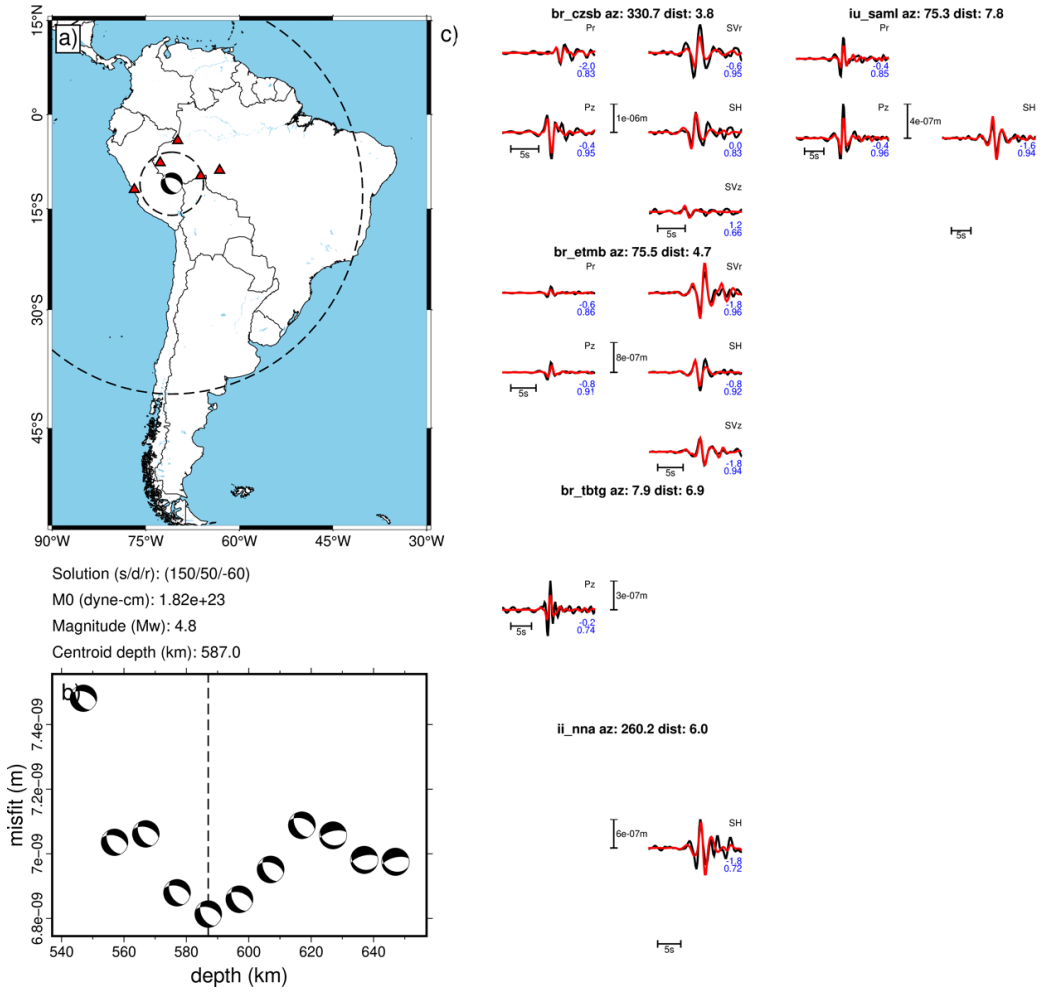

Figure S9. Inversion results for event 13. a) Map showing the preferred solution in b and the distribution of the 3 stations (6 traces) used in the inversion. Solution parameters are given below the map. Dashed circles indicate radii of 5º and 30º from epicenter; b) Distribution of focal mechanisms with centroid depths. We selected 590 km as the preferred solution for the event, fixing to the hypocenter depth in Table 1; c) Waveform fitting produced by the preferred solution. Black and red lines denote observations and synthetics, respectively. Azimuths and distances in degrees are shown above panels. Time shifts (top) and cross-correlation coefficients (bottom) are shown in blue at the lower right corner of each panel. Wave segments (Pr, Pz, SVr, SH and SVz) are identified at the upper right corners.

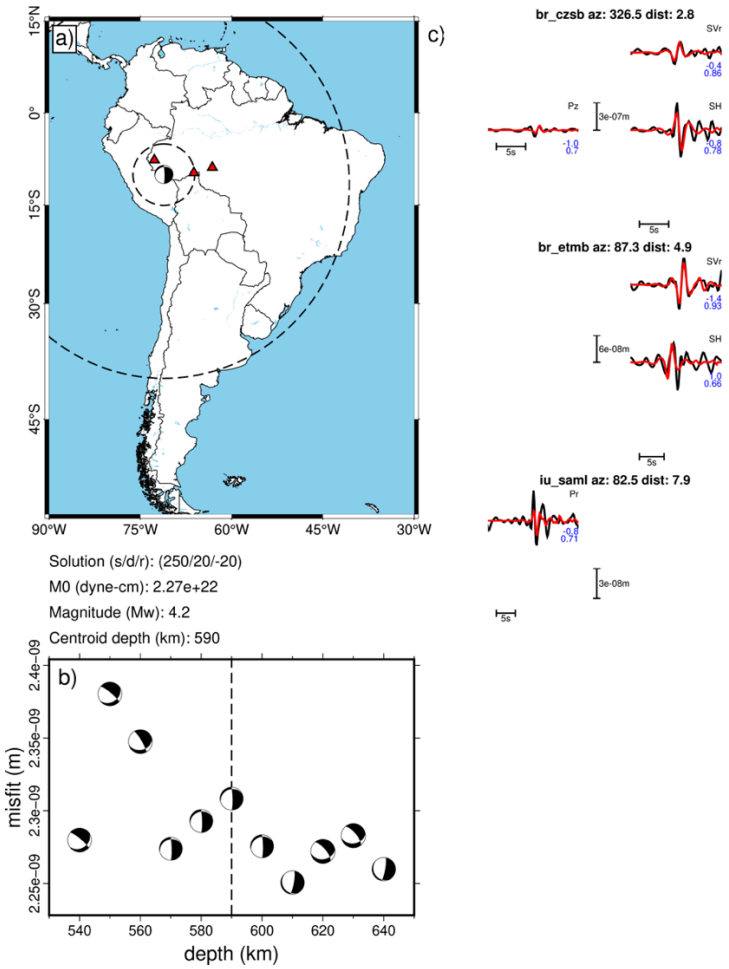

Figure S10. Inversion results for event 14. a) Map showing the preferred solution in b and the distribution of the 5 stations (9 traces) used in the inversion. Solution parameters are given below the map. Dashed circles indicate radii of 5º and 30º from epicenter; b) Distribution of focal mechanisms with centroid depths pointing to 659 km as the preferred solution for the event; c) Waveform fitting produced by the preferred solution. Black and red lines denote observations and synthetics, respectively. Azimuths and distances in degrees are shown above panels. Time shifts (top) and cross-correlation coefficients (bottom) are shown in blue at the lower right corner of each panel. Wave segments (Pr, Pz, SVr, SH and SVz) are identified at the upper right corners.

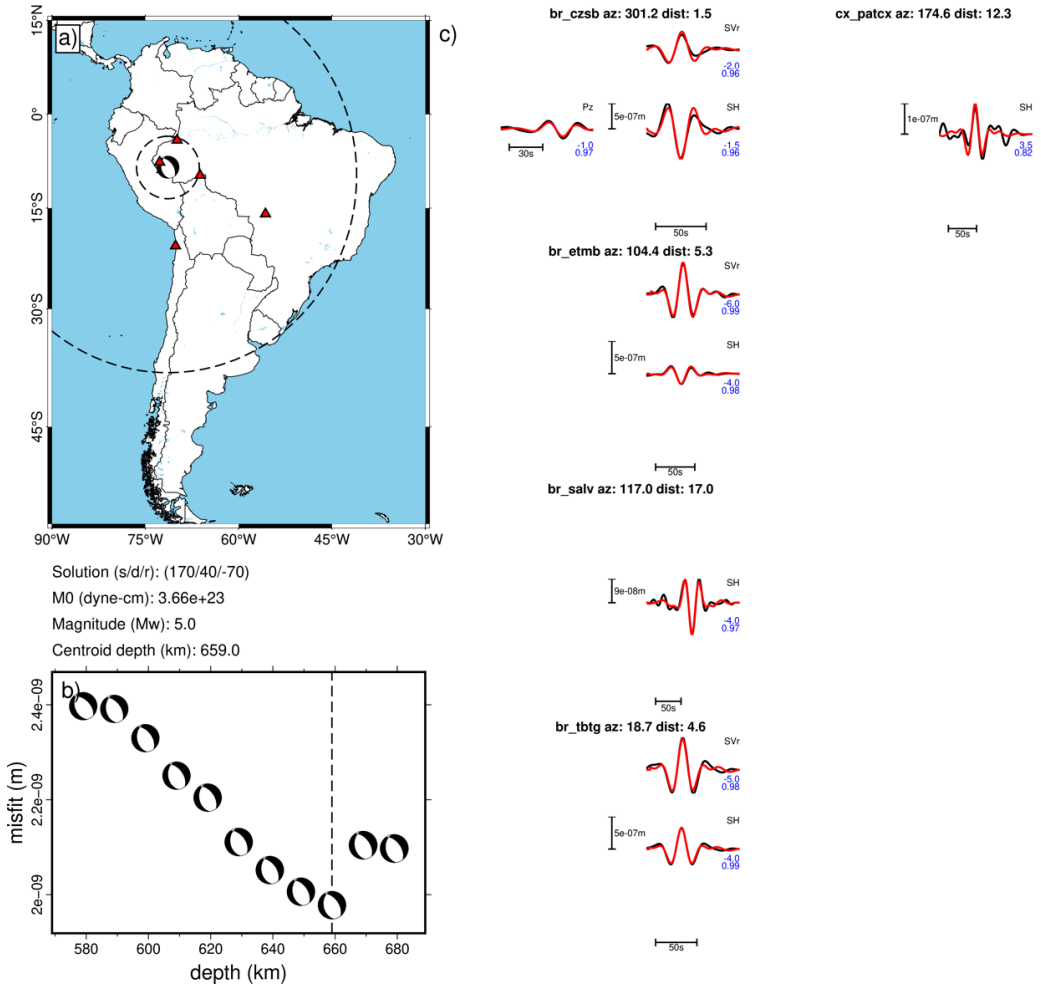

Figure S11. Inversion results for event 17. a) Map showing the preferred solution in b and the distribution of the 4 stations (13 traces) used in the inversion. Solution parameters are given below the map. Dashed circles indicate radii of 5º and 30º from epicenter; b) Distribution of focal mechanisms with centroid depths. We selected 655 km as the preferred solution for the event, fixing to the hypocenter depth in Table 1; c) Waveform fitting produced by the preferred solution. Black and red lines denote observations and synthetics, respectively. Azimuths and distances in degrees are shown above panels. Time shifts (top) and cross-correlation coefficients (bottom) are shown in blue at the lower right corner of each panel. Wave segments (Pr, Pz, SVr, SH and SVz) are identified at the upper right corners.

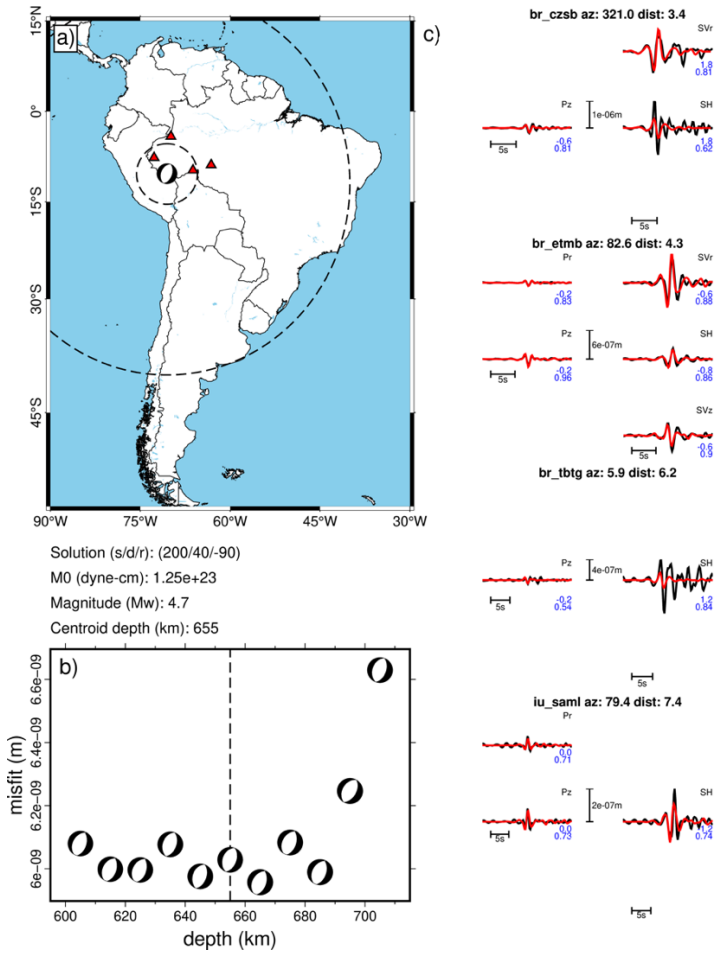

Figure S12. Inversion results for event 18. a) Map showing the preferred solution in b and the distribution of the 3 stations (7 traces) used in the inversion. Solution parameters are given below the map. Dashed circles indicate radii of 5º and 30º from epicenter; b) Distribution of focal mechanisms with centroid depths. We selected 592 km as the preferred solution for the event, fixing to the hypocenter depth in Table 1; c) Waveform fitting produced by the preferred solution. Black and red lines denote observations and synthetics, respectively. Azimuths and distances in degrees are shown above panels. Time shifts (top) and cross-correlation coefficients (bottom) are shown in blue at the lower right corner of each panel. Wave segments (Pr, Pz, SVr, SH and SVz) are identified at the upper right corners.

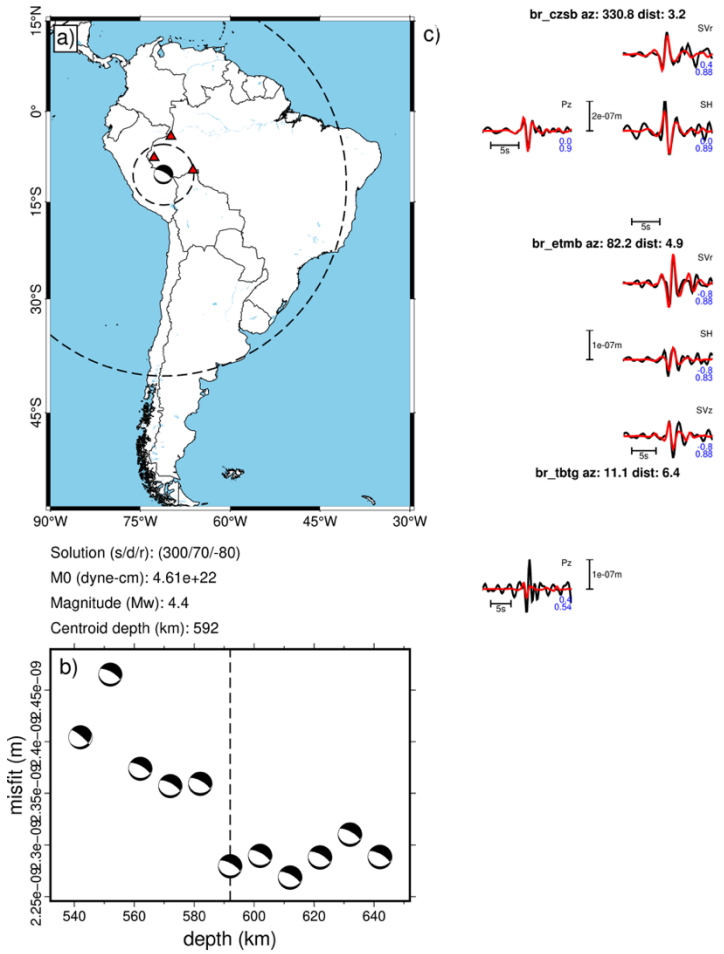

Figure S13. Inversion results for event 19. a) Map showing the preferred solution in b and the distribution of the 129 stations (353 traces) used in the inversion. Solution parameters are given below the map. Dashed circles indicate radii of 5º and 30º from epicenter; b) Distribution of focal mechanisms with centroid depths pointing to 603 km as the preferred solution for the event; c) Waveform fitting produced by the preferred solution. Black and red lines denote observations and synthetics, respectively. Azimuths and distances in degrees are shown above panels. Time shifts (top) and cross-correlation coefficients (bottom) are shown in blue at the lower right corner of each panel. Wave segments (Pr, Pz, SVr, SH and SVz) are identified at the upper right corners.

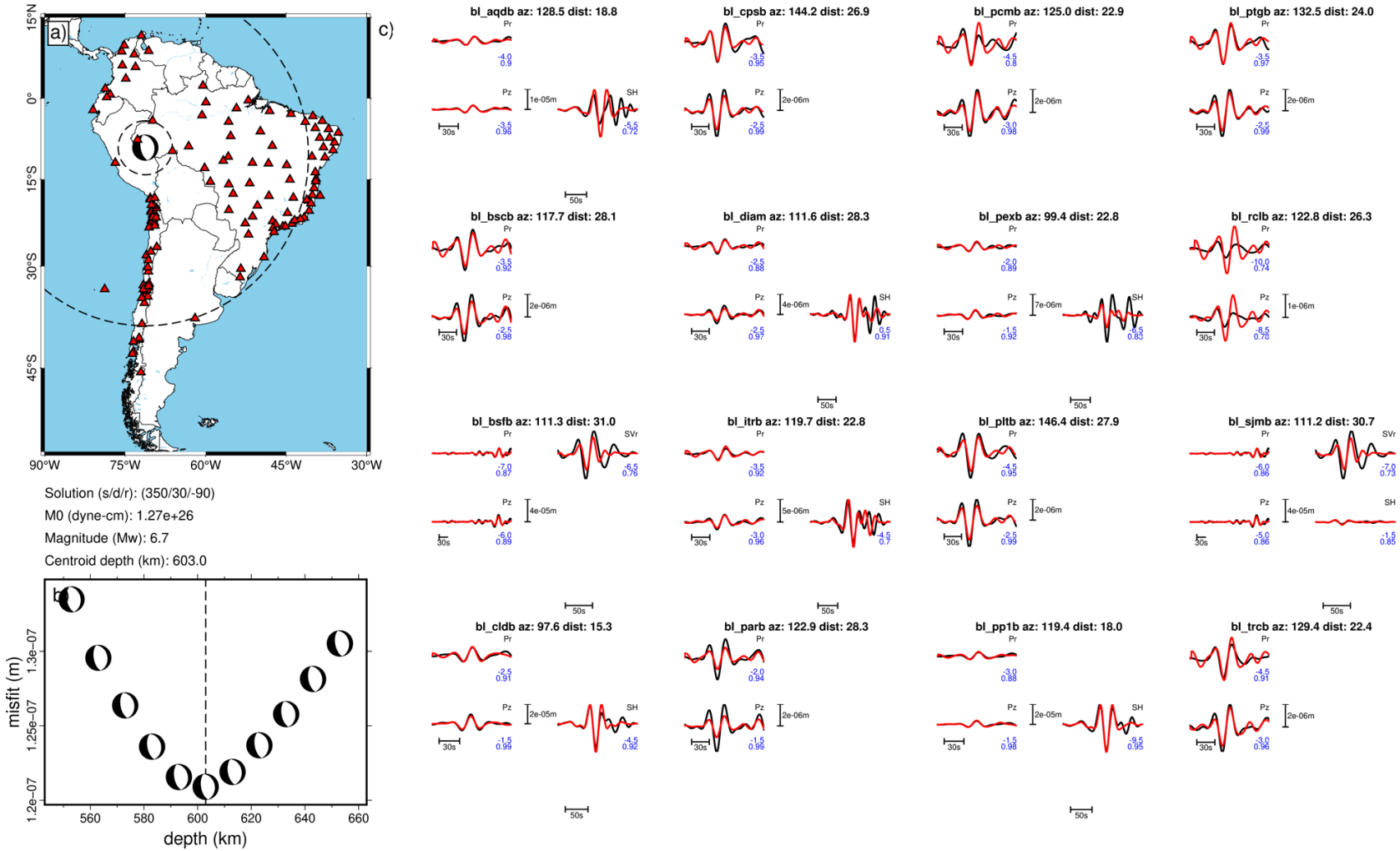

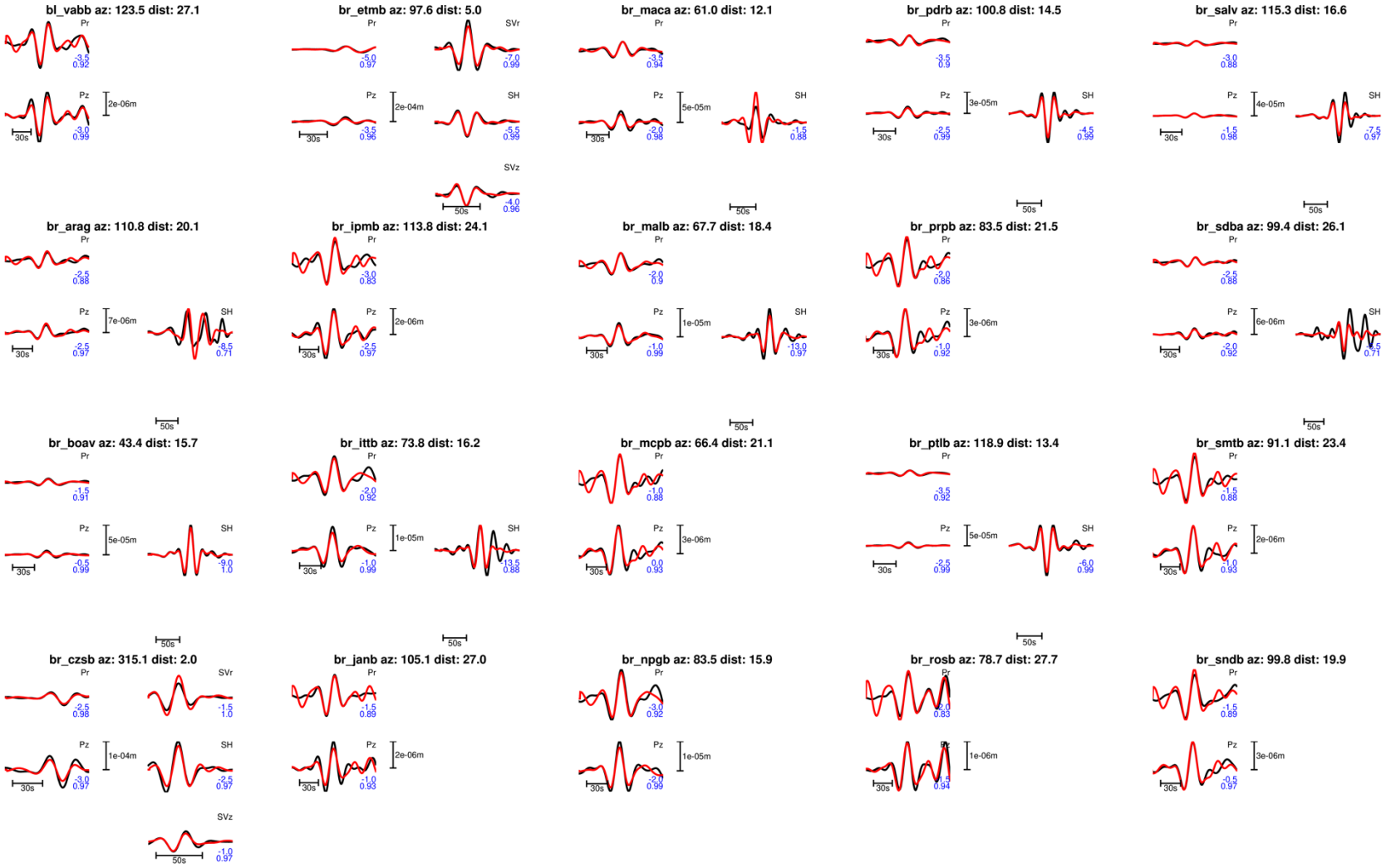
bl_vabb az: 123.5 dist: 27.1
br_etmb az: 97.6 dist: 5.0
br_maca az: 61.0 dist: 12.1
br_pdrb az: 100.8 dist: 14.5
br_salv az: 115.3 dist: 16.6
br_arag az: 110.8 dist: 20.1
br_ipmb az: 113.8 dist: 24.1
br_malb az: 67.7 dist: 18.4
br_prpb az: 83.5 dist: 21.5
br_sdba az: 99.4 dist: 26.1
br_boav az: 43.4 dist: 15.7
br_ittb az: 73.8 dist: 16.2
br_mcpb az: 66.4 dist: 21.1
br_ptlb az: 118.9 dist: 13.4
br_smtb az: 91.1 dist: 23.4
br_czsb az: 315.1 dist: 2.0
br_janb az: 105.1 dist: 27.0
br_npgb az: 83.5 dist: 15.9
br_rosb az: 78.7 dist: 27.7
br_sndb az: 99.8 dist: 19.9
Pr
Pz
SH
SVr
SVz
30s
50s

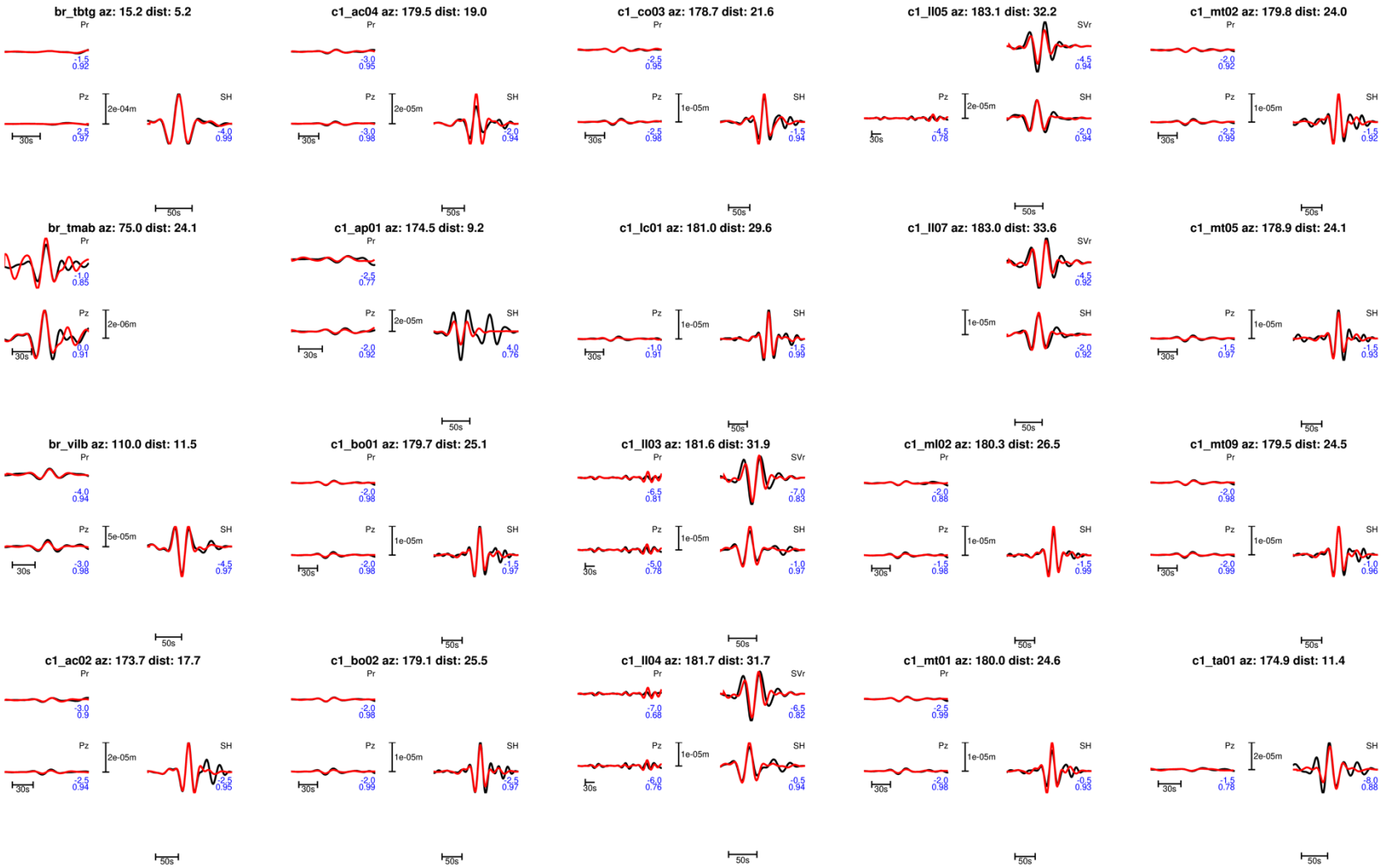
br_tbtg az: 15.2 dist: 5.2
c1_ac04 az: 179.5 dist: 19.0
c1_co03 az: 178.7 dist: 21.6
c1_ll05 az: 183.1 dist: 32.2
c1_mt02 az: 179.8 dist: 24.0
br_tmab az: 75.0 dist: 24.1
c1_ap01 az: 174.5 dist: 9.2
c1_lc01 az: 181.0 dist: 29.6
c1_ll07 az: 183.0 dist: 33.6
c1_mt05 az: 178.9 dist: 24.1
br_vilb az: 110.0 dist: 11.5
c1_bo01 az: 179.7 dist: 25.1
c1_ll03 az: 181.6 dist: 31.9
c1_ml02 az: 180.3 dist: 26.5
c1_mt09 az: 179.5 dist: 24.5
c1_ac02 az: 173.7 dist: 17.7
c1_bo02 az: 179.1 dist: 25.5
c1_ll04 az: 181.7 dist: 31.7
c1_mt01 az: 180.0 dist: 24.6
c1_ta01 az: 174.9 dist: 11.4
Pr
Pz
SH
SVr
30s
50s

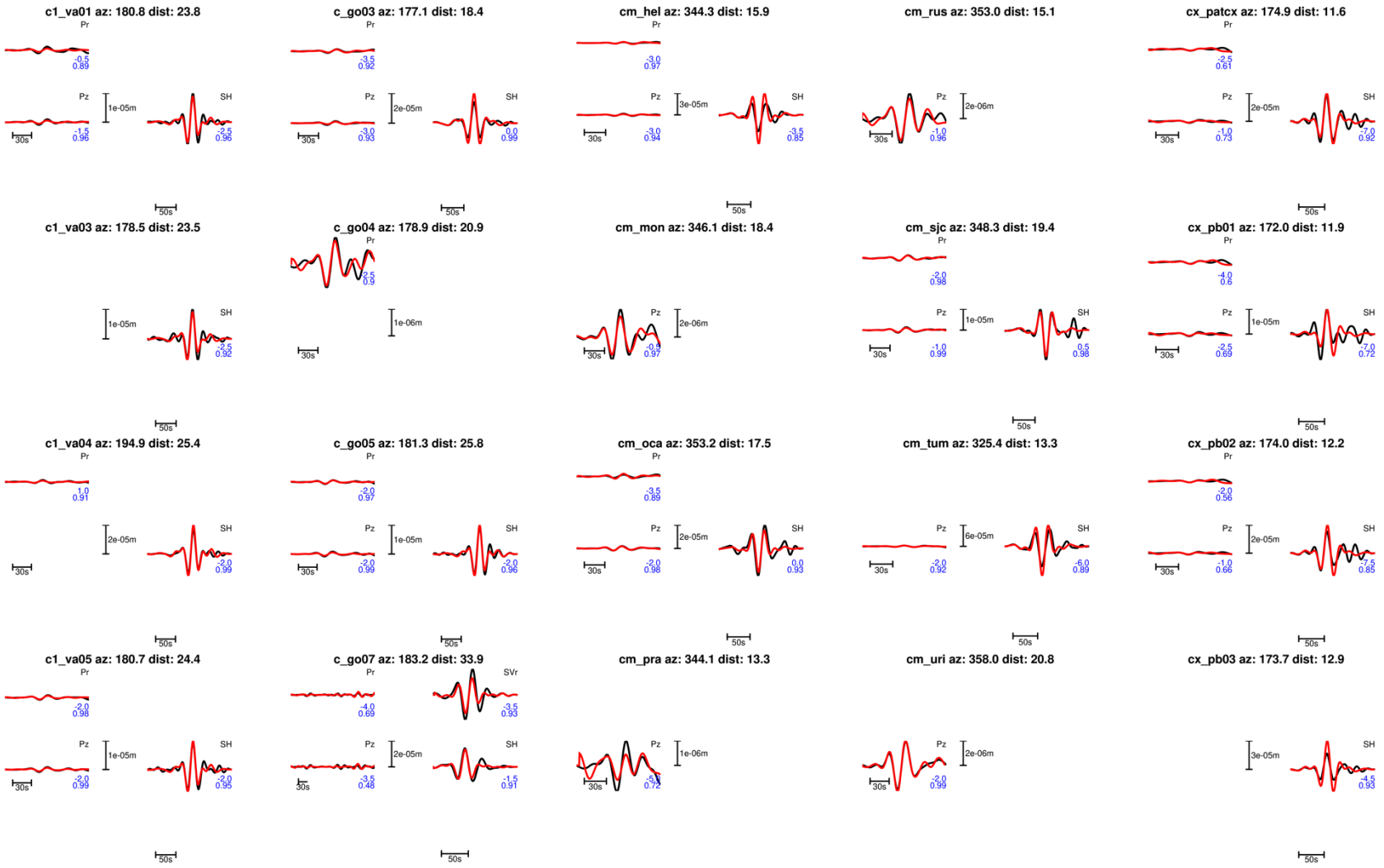
c1_va01 az: 180.8 dist: 23.8
c_go03 az: 177.1 dist: 18.4
cm_hel az: 344.3 dist: 15.9
cm_rus az: 353.0 dist: 15.1
cx_patcx az: 174.9 dist: 11.6
c1_va03 az: 178.5 dist: 23.5
c_go04 az: 178.9 dist: 20.9
cm_mon az: 346.1 dist: 18.4
cm_sjc az: 348.3 dist: 19.4
cx_pb01 az: 172.0 dist: 11.9
c1_va04 az: 194.9 dist: 25.4
c_go05 az: 181.3 dist: 25.8
cm_oca az: 353.2 dist: 17.5
cm_tum az: 325.4 dist: 13.3
cx_pb02 az: 174.0 dist: 12.2
c1_va05 az: 180.7 dist: 24.4
c_go07 az: 183.2 dist: 33.9
cm_pra az: 344.1 dist: 13.3
cm_uri az: 358.0 dist: 20.8
cx_pb03 az: 173.7 dist: 12.9
Pr
Pz
SH
SVr
30s
50s

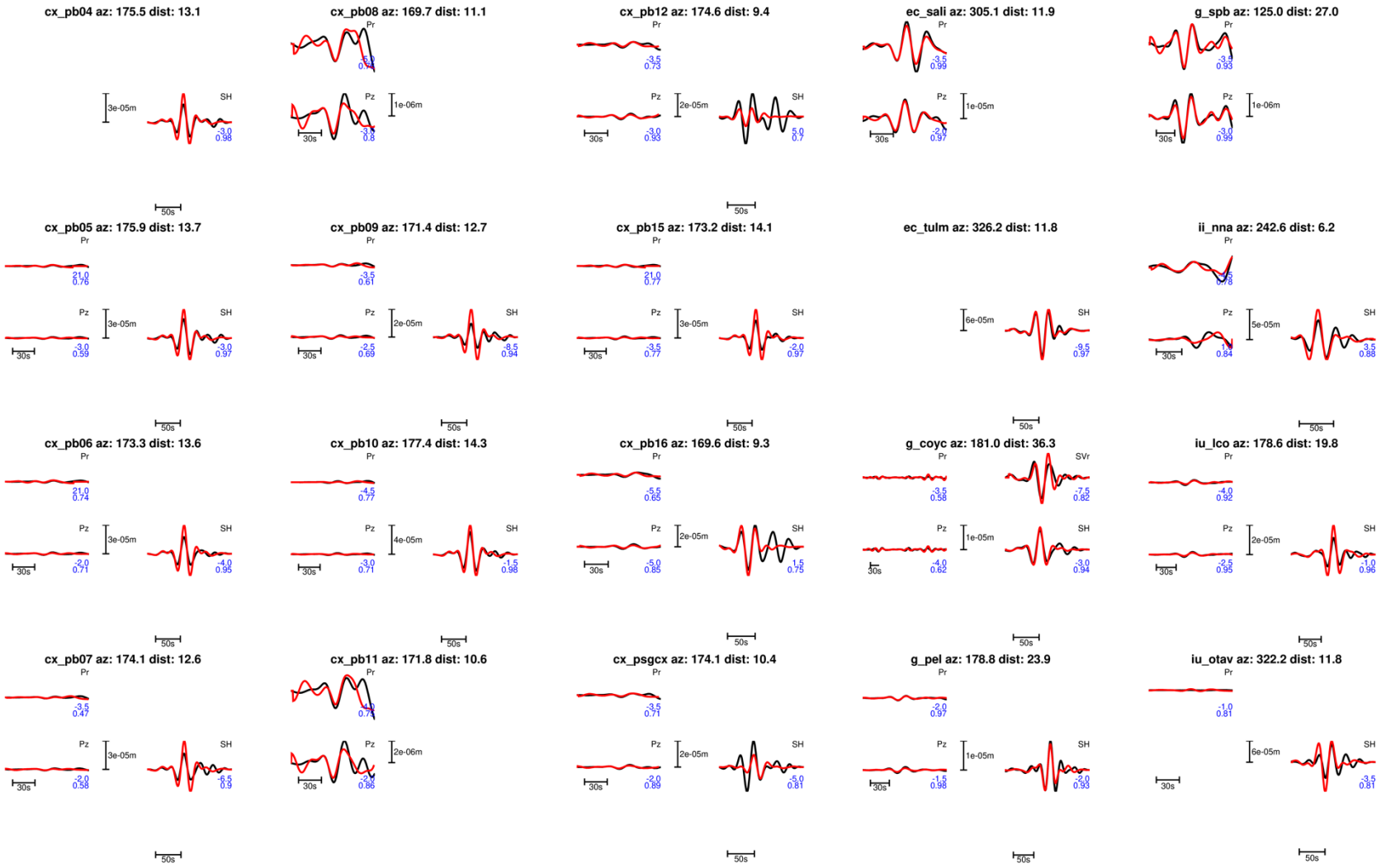
cx_pb04 az: 175.5 dist: 13.1
cx_pb08 az: 169.7 dist: 11.1
cx_pb12 az: 174.6 dist: 9.4
ec_sali az: 305.1 dist: 11.9
g_spb az: 125.0 dist: 27.0
cx_pb05 az: 175.9 dist: 13.7
cx_pb09 az: 171.4 dist: 12.7
cx_pb15 az: 173.2 dist: 14.1
ec_tulm az: 326.2 dist: 11.8
ii_nna az: 242.6 dist: 6.2
cx_pb06 az: 173.3 dist: 13.6
cx_pb10 az: 177.4 dist: 14.3
cx_pb16 az: 169.6 dist: 9.3
g_coyc az: 181.0 dist: 36.3
iu_lco az: 178.6 dist: 19.8
cx_pb07 az: 174.1 dist: 12.6
cx_pb11 az: 171.8 dist: 10.6
cx_psgcx az: 174.1 dist: 10.4
g_pel az: 178.8 dist: 23.9
iu_otav az: 322.2 dist: 11.8
Pr
Pz
SH
SVr
30s
50s

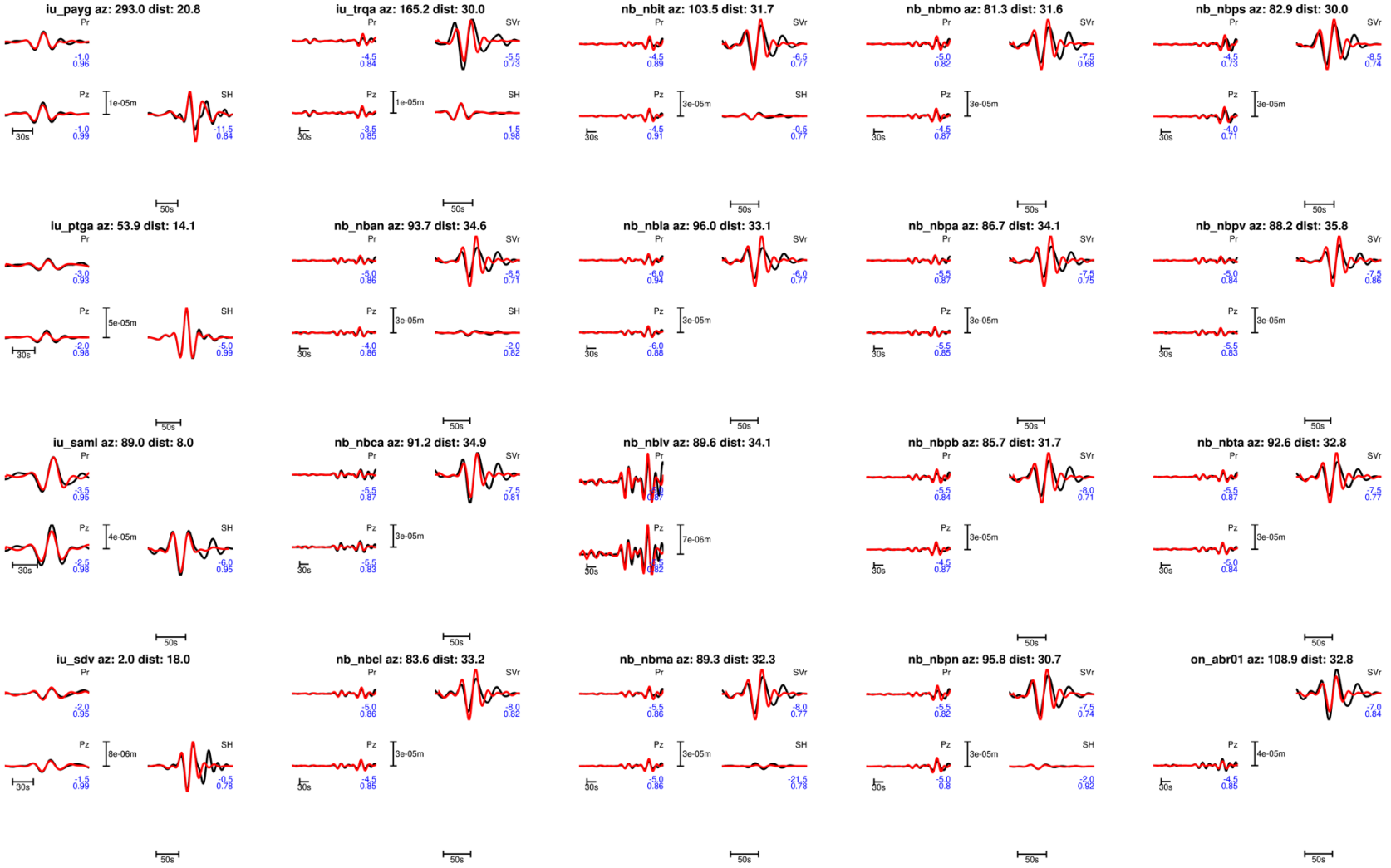
iu_payg az: 293.0 dist: 20.8
iu_trqa az: 165.2 dist: 30.0
nb_nbit az: 103.5 dist: 31.7
nb_nbmo az: 81.3 dist: 31.6
nb_nbps az: 82.9 dist: 30.0
iu_ptga az: 53.9 dist: 14.1
nb_nban az: 93.7 dist: 34.6
nb_nbla az: 96.0 dist: 33.1
nb_nbpa az: 86.7 dist: 34.1
nb_nbpv az: 88.2 dist: 35.8
iu_saml az: 89.0 dist: 8.0
nb_nbca az: 91.2 dist: 34.9
nb_nblv az: 89.6 dist: 34.1
nb_nbpb az: 85.7 dist: 31.7
nb_nbta az: 92.6 dist: 32.8
iu_sdv az: 2.0 dist: 18.0
nb_nbcl az: 83.6 dist: 33.2
nb_nbma az: 89.3 dist: 32.3
nb_nbpn az: 95.8 dist: 30.7
on_abr01 az: 108.9 dist: 32.8
Pr
SVr
Pz
SH
30s
50s

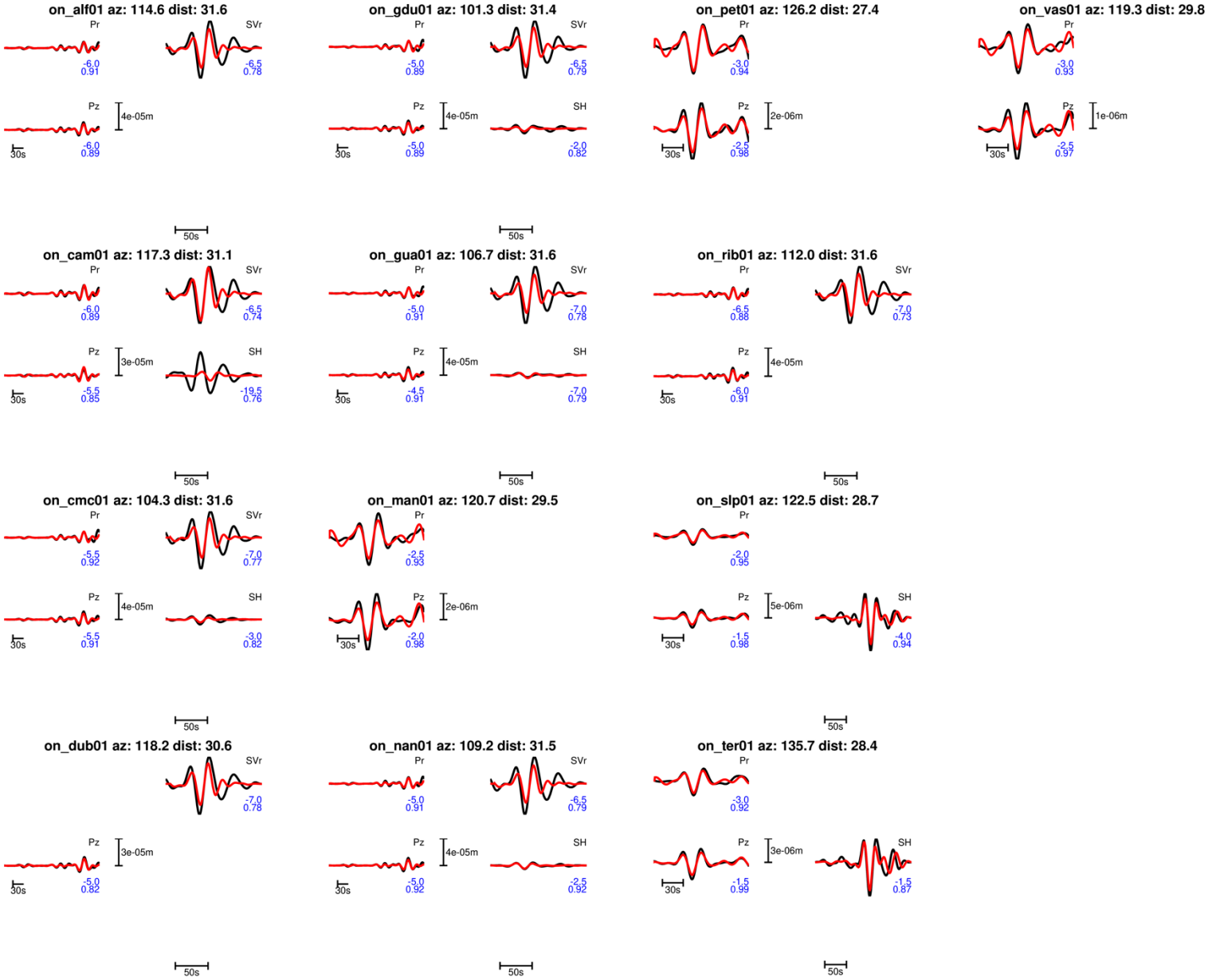
on_alf01 az: 114.6 dist: 31.6
on_gdu01 az: 101.3 dist: 31.4
on_pet01 az: 126.2 dist: 27.4
on_vas01 az: 119.3 dist: 29.8
on_cam01 az: 117.3 dist: 31.1
on_gua01 az: 106.7 dist: 31.6
on_rib01 az: 112.0 dist: 31.6
on_cmc01 az: 104.3 dist: 31.6
on_man01 az: 120.7 dist: 29.5
on_slp01 az: 122.5 dist: 28.7
on_dub01 az: 118.2 dist: 30.6
on_nan01 az: 109.2 dist: 31.5
on_ter01 az: 135.7 dist: 28.4
Pr
SVr
Pz
SH
30s
50s

Figure S14. Inversion results for event 22. a) Map showing the preferred solution in b and the distribution of the 7 stations (12 traces) used in the inversion. Solution parameters are given below the map. Dashed circles indicate radii of 5º and 30º from epicenter; b) Distribution of focal mechanisms with centroid depths pointing to 636 km as the preferred solution for the event; c) Waveform fitting produced by the preferred solution. Black and red lines denote observations and synthetics, respectively. Azimuths and distances in degrees are shown above panels. Time shifts (top) and cross-correlation coefficients (bottom) are shown in blue at the lower right corner of each panel. Wave segments (Pr, Pz, SVr, SH and SVz) are identified at the upper right corners.

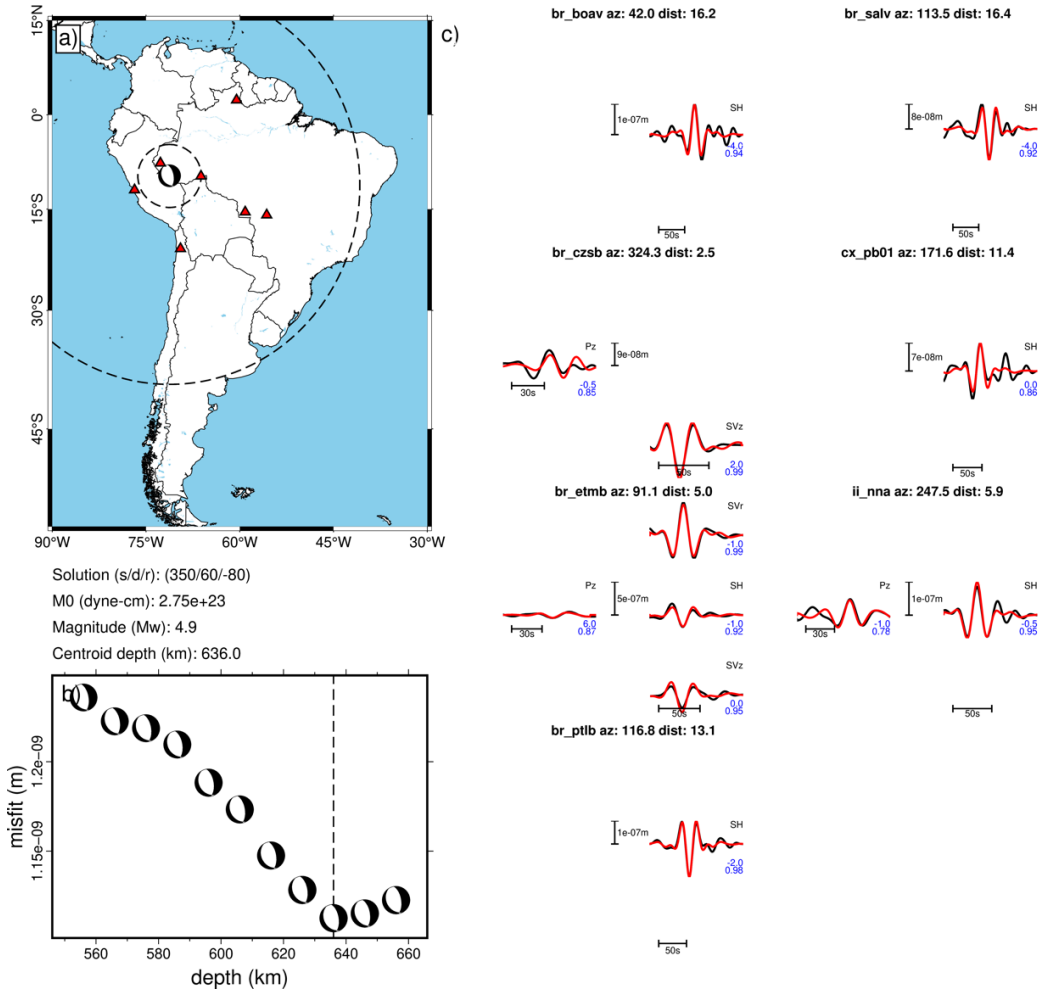

Figure S15. Inversion results for event 24. a) Map showing the preferred solution in b and the distribution of the 32 stations (53 traces) used in the inversion. Solution parameters are given below the map. Dashed circles indicate radii of 5º and 30º from epicenter; b) Distribution of focal mechanisms with centroid depths pointing to 617 km as the preferred solution for the event; c) Waveform fitting produced by the preferred solution. Black and red lines denote observations and synthetics, respectively. Azimuths and distances in degrees are shown above panels. Time shifts (top) and cross-correlation coefficients (bottom) are shown in blue at the lower right corner of each panel. Wave segments (Pr, Pz, SVr, SH and SVz) are identified at the upper right corners.

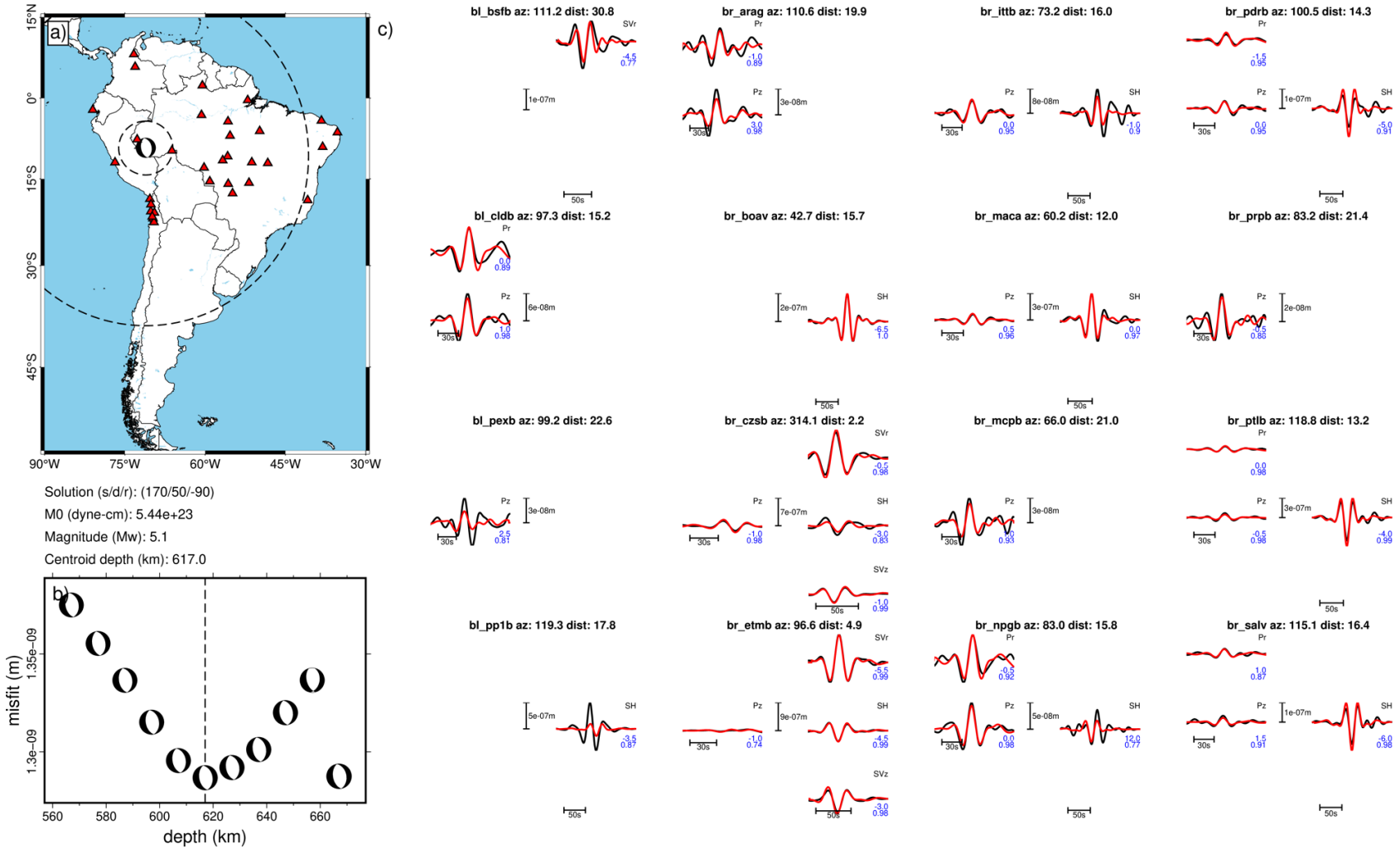

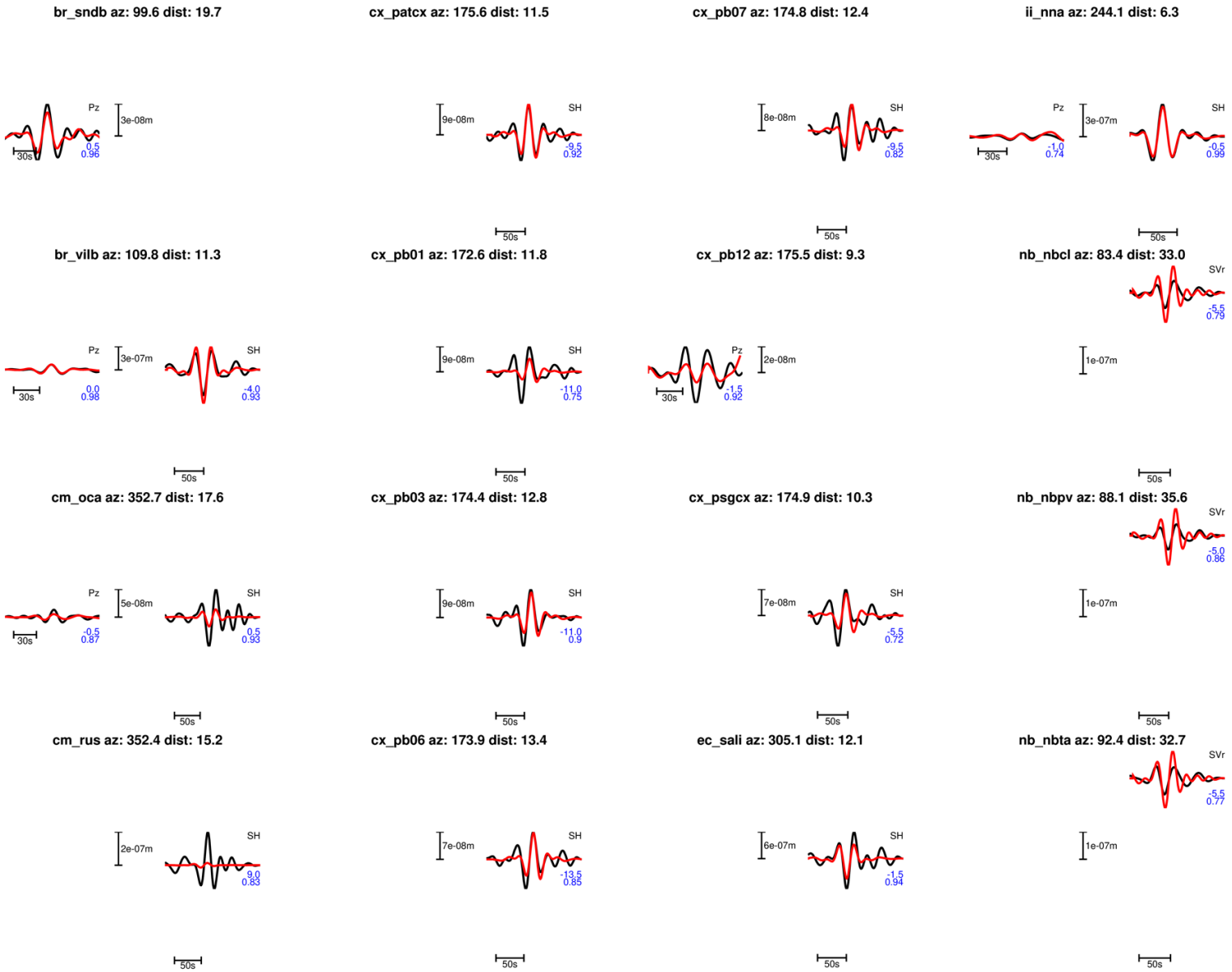
br_sndb az: 99.6 dist: 19.7
Pz
3e-08m
30s
0.5
0.96
cx_patcx az: 175.6 dist: 11.5
9e-08m
SH
-9.5
0.92
50s
cx_pb07 az: 174.8 dist: 12.4
8e-08m
SH
-9.5
0.82
50s
ii_nna az: 244.1 dist: 6.3
Pz
30s
-1.0
0.74
3e-07m
SH
-0.5
0.99
50s
br_vilb az: 109.8 dist: 11.3
Pz
3e-07m
30s
0.0
0.98
SH
-4.0
0.93
50s
cx_pb01 az: 172.6 dist: 11.8
9e-08m
SH
-11.0
0.75
50s
cx_pb12 az: 175.5 dist: 9.3
Pz
30s
-1.5
0.92
2e-08m
50s
nb_nbcl az: 83.4 dist: 33.0
SVr
-5.5
0.79
1e-07m
50s
cm_oca az: 352.7 dist: 17.6
Pz
5e-08m
30s
-0.5
0.87
SH
0.5
0.93
50s
cx_pb03 az: 174.4 dist: 12.8
9e-08m
SH
-11.0
0.9
50s
cx_psgcx az: 174.9 dist: 10.3
7e-08m
SH
-5.5
0.72
50s
nb_nbpv az: 88.1 dist: 35.6
SVr
-5.0
0.86
1e-07m
50s
cm_rus az: 352.4 dist: 15.2
2e-07m
SH
9.0
0.83
50s
cx_pb06 az: 173.9 dist: 13.4
7e-08m
SH
-13.5
0.85
50s
ec_sali az: 305.1 dist: 12.1
6e-07m
SH
-1.5
0.94
50s
nb_nbta az: 92.4 dist: 32.7
SVr
-5.5
0.77
1e-07m
50s

Figure S16. Inversion results for event 29. a) Map showing the preferred solution in b and the distribution of the 3 stations (6 traces) used in the inversion. Solution parameters are given below the map. Dashed circles indicate radii of 5º and 30º from epicenter; b) Distribution of focal mechanisms with centroid depths pointing to 643 km as the preferred solution for the event; c) Waveform fitting produced by the preferred solution. Black and red lines denote observations and synthetics, respectively. Azimuths and distances in degrees are shown above panels. Time shifts (top) and cross-correlation coefficients (bottom) are shown in blue at the lower right corner of each panel. Wave segments (Pr, Pz, SVr, SH and SVz) are identified at the upper right corners.

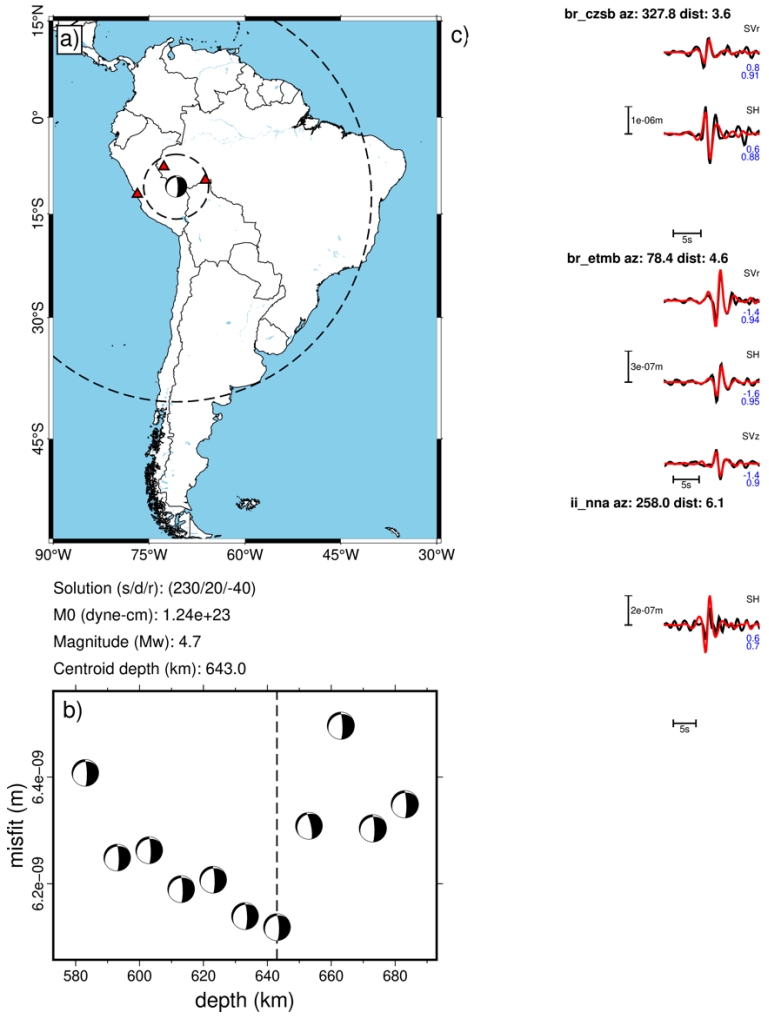

Figure S17. Inversion results for event 30. a) Map showing the preferred solution in b and the distribution of the 165 stations (392 traces) used in the inversion. Solution parameters are given below the map. Dashed circles indicate radii of 5º and 30º from epicenter; b) Distribution of focal mechanisms with centroid depths pointing to 642 km as the preferred solution for the event; c) Waveform fitting produced by the preferred solution. Black and red lines denote observations and synthetics, respectively. Azimuths and distances in degrees are shown above panels. Time shifts (top) and cross-correlation coefficients (bottom) are shown in blue at the lower right corner of each panel. Wave segments (Pr, Pz, SVr, SH and SVz) are identified at the upper right corners.

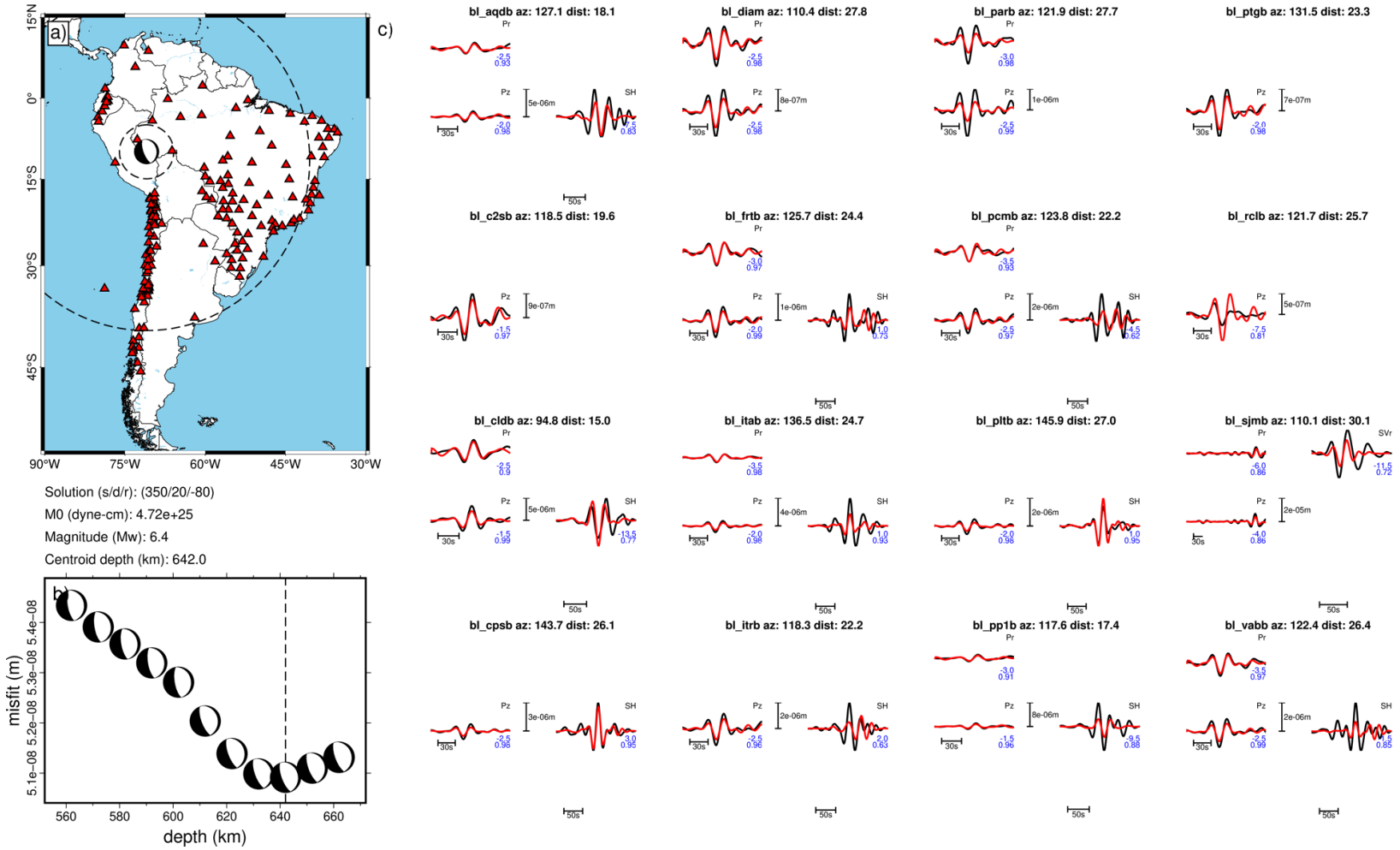

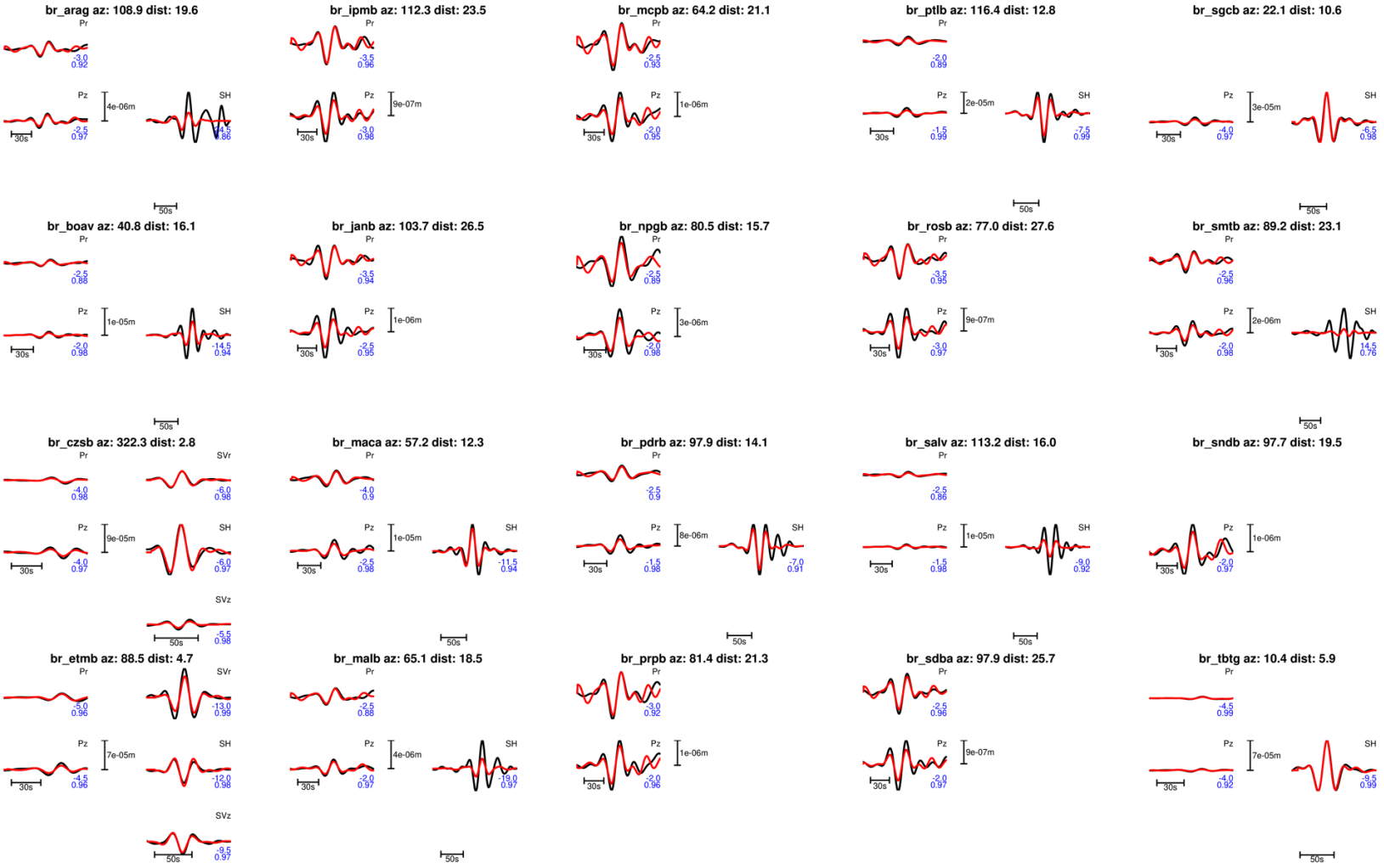
br_arag az: 108.9 dist: 19.6
br_ipmb az: 112.3 dist: 23.5
br_mcpb az: 64.2 dist: 21.1
br_ptlb az: 116.4 dist: 12.8
br_sgcb az: 22.1 dist: 10.6
br_boav az: 40.8 dist: 16.1
br_janb az: 103.7 dist: 26.5
br_npgb az: 80.5 dist: 15.7
br_rosb az: 77.0 dist: 27.6
br_smtb az: 89.2 dist: 23.1
br_czsb az: 322.3 dist: 2.8
br_maca az: 57.2 dist: 12.3
br_pdrb az: 97.9 dist: 14.1
br_salv az: 113.2 dist: 16.0
br_sndb az: 97.7 dist: 19.5
br_etmb az: 88.5 dist: 4.7
br_malb az: 65.1 dist: 18.5
br_prpb az: 81.4 dist: 21.3
br_sdba az: 97.9 dist: 25.7
br_tbtg az: 10.4 dist: 5.9
Pr
Pz
SH
SVr
SVz
30s
50s

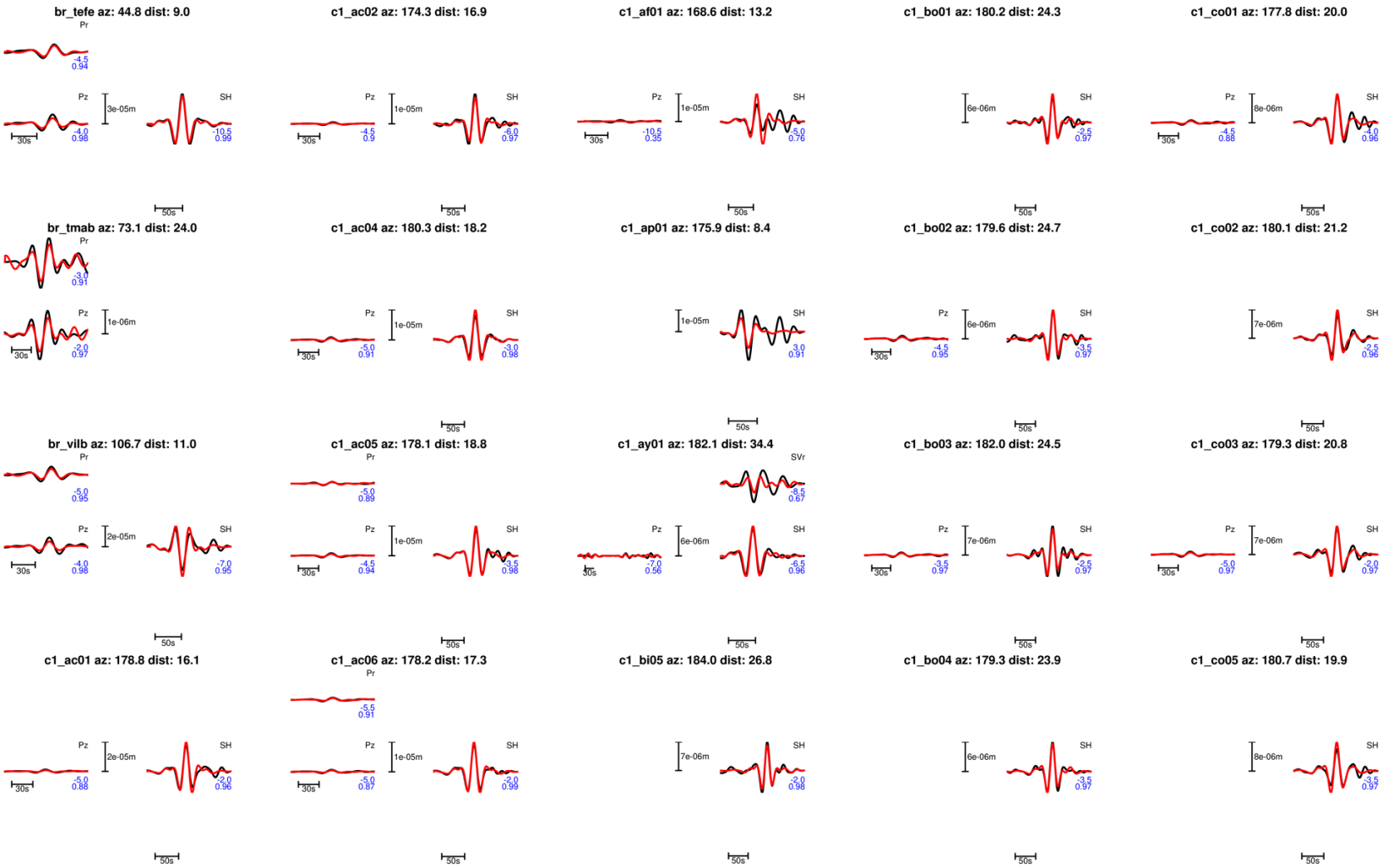
br_tefe az: 44.8 dist: 9.0
c1_ac02 az: 174.3 dist: 16.9
c1_af01 az: 168.6 dist: 13.2
c1_bo01 az: 180.2 dist: 24.3
c1_co01 az: 177.8 dist: 20.0
br_tmab az: 73.1 dist: 24.0
c1_ac04 az: 180.3 dist: 18.2
c1_ap01 az: 175.9 dist: 8.4
c1_bo02 az: 179.6 dist: 24.7
c1_co02 az: 180.1 dist: 21.2
br_vilb az: 106.7 dist: 11.0
c1_ac05 az: 178.1 dist: 18.8
c1_ay01 az: 182.1 dist: 34.4
c1_bo03 az: 182.0 dist: 24.5
c1_co03 az: 179.3 dist: 20.8
c1_ac01 az: 178.8 dist: 16.1
c1_ac06 az: 178.2 dist: 17.3
c1_bi05 az: 184.0 dist: 26.8
c1_bo04 az: 179.3 dist: 23.9
c1_co05 az: 180.7 dist: 19.9
Pr
Pz
SH
SVr
30s
50s

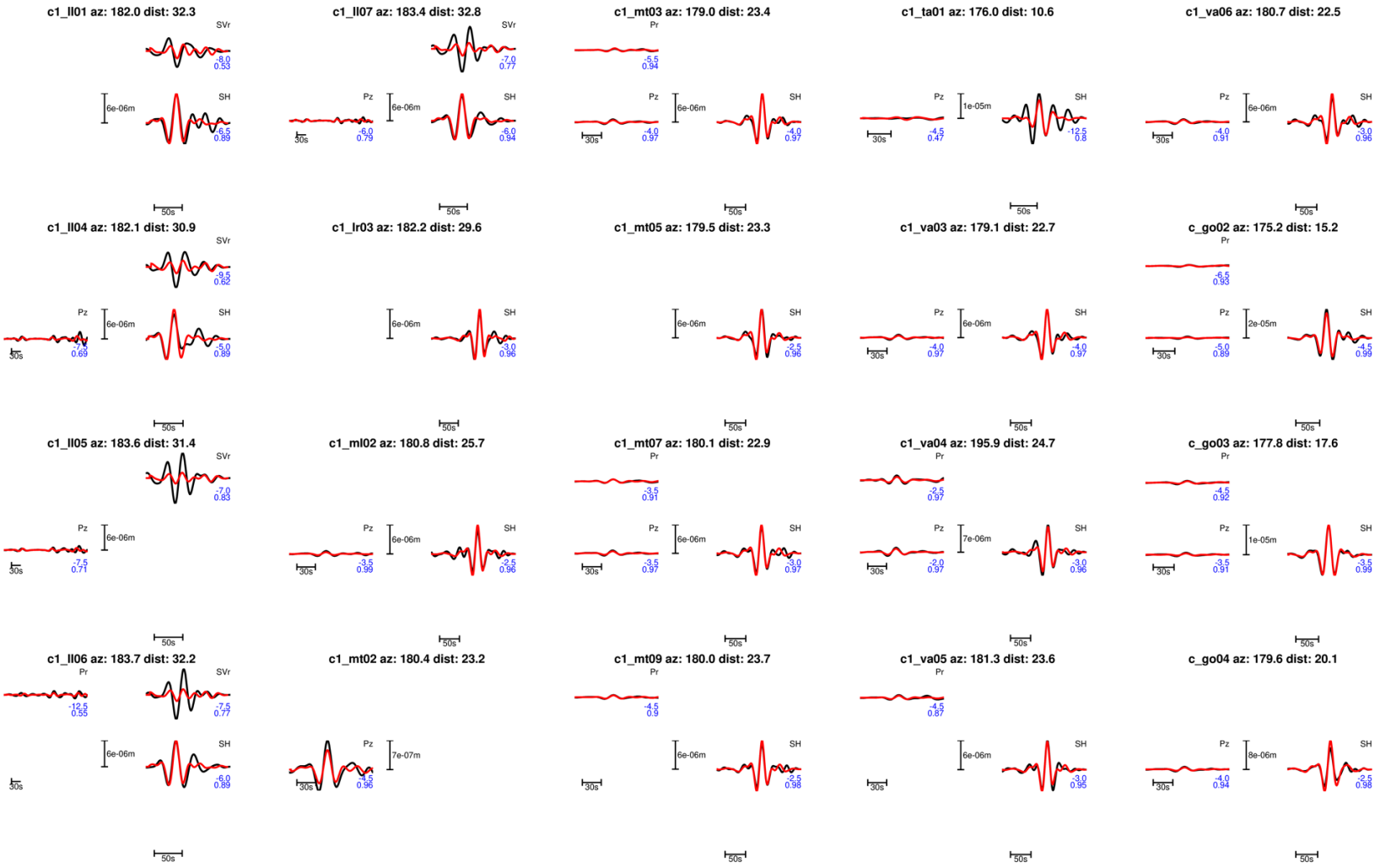
c1_ll01 az: 182.0 dist: 32.3
c1_ll07 az: 183.4 dist: 32.8
c1_mt03 az: 179.0 dist: 23.4
c1_ta01 az: 176.0 dist: 10.6
c1_va06 az: 180.7 dist: 22.5
c1_ll04 az: 182.1 dist: 30.9
c1_lr03 az: 182.2 dist: 29.6
c1_mt05 az: 179.5 dist: 23.3
c1_va03 az: 179.1 dist: 22.7
c_go02 az: 175.2 dist: 15.2
c1_ll05 az: 183.6 dist: 31.4
c1_ml02 az: 180.8 dist: 25.7
c1_mt07 az: 180.1 dist: 22.9
c1_va04 az: 195.9 dist: 24.7
c_go03 az: 177.8 dist: 17.6
c1_ll06 az: 183.7 dist: 32.2
c1_mt02 az: 180.4 dist: 23.2
c1_mt09 az: 180.0 dist: 23.7
c1_va05 az: 181.3 dist: 23.6
c_go04 az: 179.6 dist: 20.1
SVr
Pr
Pz
SH
6e-06m
1e-05m
2e-05m
7e-06m
8e-06m
7e-07m
30s
50s

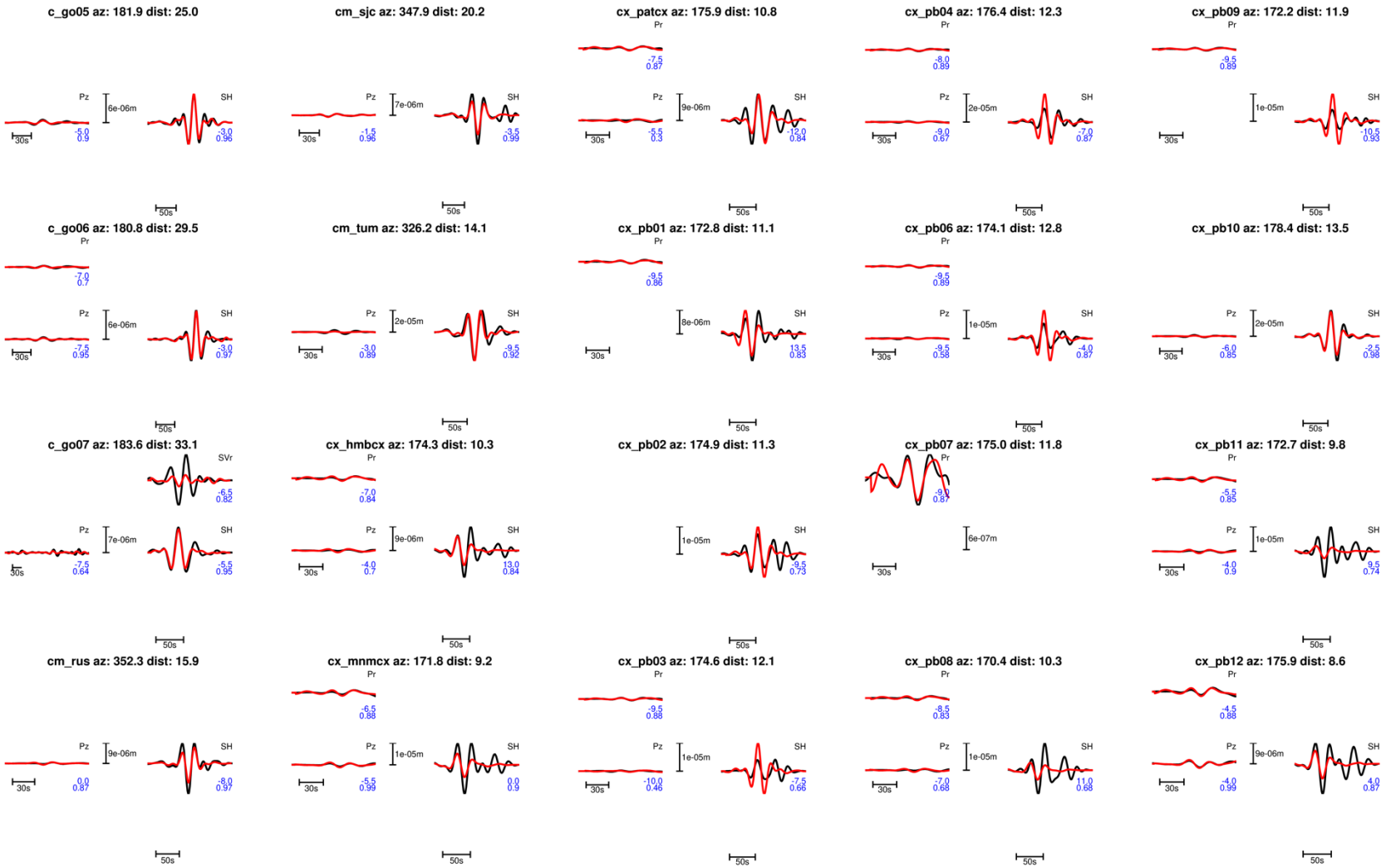
c_go05 az: 181.9 dist: 25.0
cm_sjc az: 347.9 dist: 20.2
cx_patcx az: 175.9 dist: 10.8
cx_pb04 az: 176.4 dist: 12.3
cx_pb09 az: 172.2 dist: 11.9
c_go06 az: 180.8 dist: 29.5
cm_tum az: 326.2 dist: 14.1
cx_pb01 az: 172.8 dist: 11.1
cx_pb06 az: 174.1 dist: 12.8
cx_pb10 az: 178.4 dist: 13.5
c_go07 az: 183.6 dist: 33.1
cx_hmbcx az: 174.3 dist: 10.3
cx_pb02 az: 174.9 dist: 11.3
cx_pb07 az: 175.0 dist: 11.8
cx_pb11 az: 172.7 dist: 9.8
cm_rus az: 352.3 dist: 15.9
cx_mnmcx az: 171.8 dist: 9.2
cx_pb03 az: 174.6 dist: 12.1
cx_pb08 az: 170.4 dist: 10.3
cx_pb12 az: 175.9 dist: 8.6
Pz
SH
Pr
SVr
30s
50s

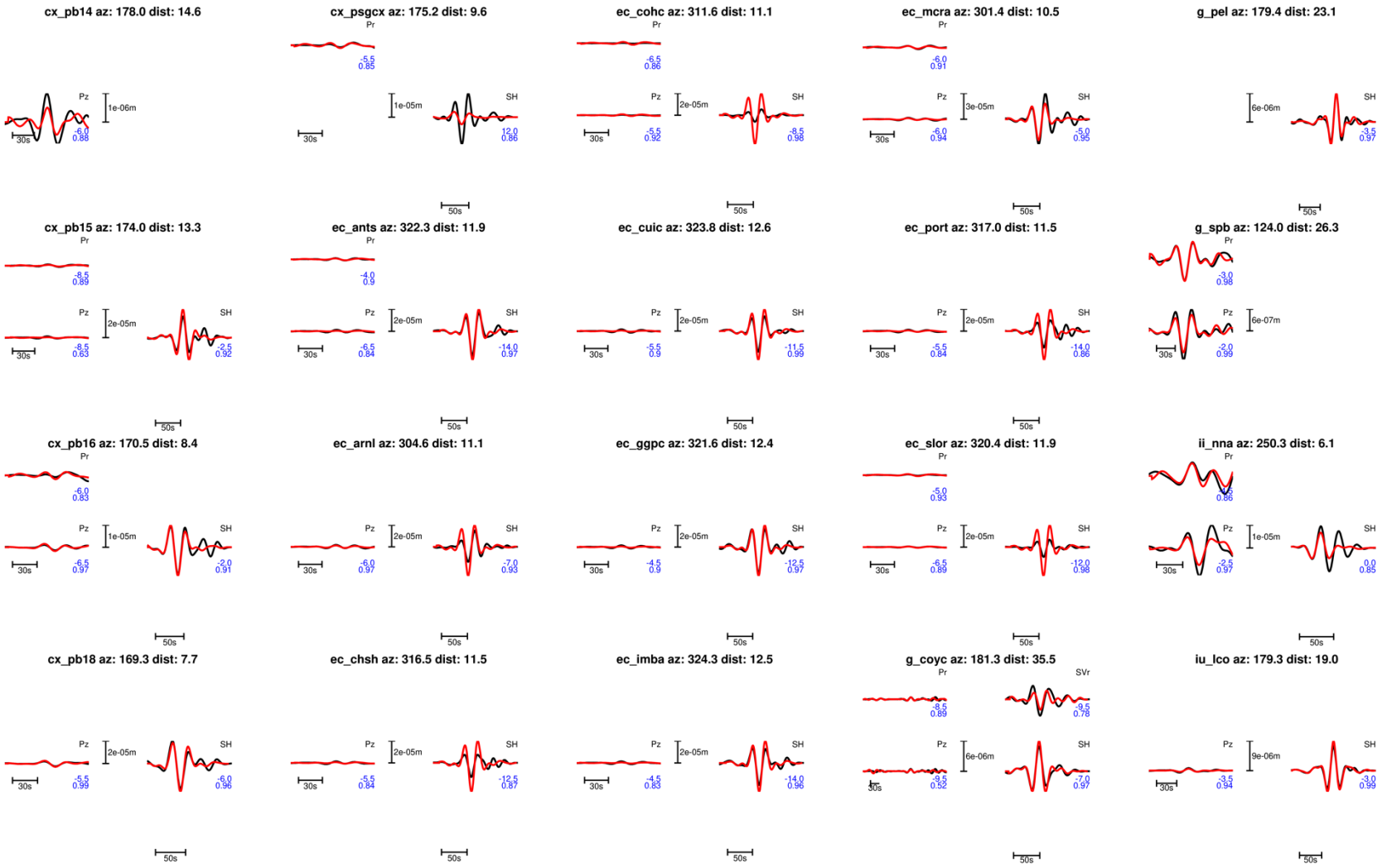
cx_pb14 az: 178.0 dist: 14.6
cx_psgcx az: 175.2 dist: 9.6
ec_cohc az: 311.6 dist: 11.1
ec_mcra az: 301.4 dist: 10.5
g_pel az: 179.4 dist: 23.1
cx_pb15 az: 174.0 dist: 13.3
ec_ants az: 322.3 dist: 11.9
ec_cuic az: 323.8 dist: 12.6
ec_port az: 317.0 dist: 11.5
g_spb az: 124.0 dist: 26.3
cx_pb16 az: 170.5 dist: 8.4
ec_arnl az: 304.6 dist: 11.1
ec_ggpc az: 321.6 dist: 12.4
ec_slor az: 320.4 dist: 11.9
ii_nna az: 250.3 dist: 6.1
cx_pb18 az: 169.3 dist: 7.7
ec_chsh az: 316.5 dist: 11.5
ec_imba az: 324.3 dist: 12.5
g_coyc az: 181.3 dist: 35.5
iu_lco az: 179.3 dist: 19.0
Pr
Pz
SH
SVr
30s
50s

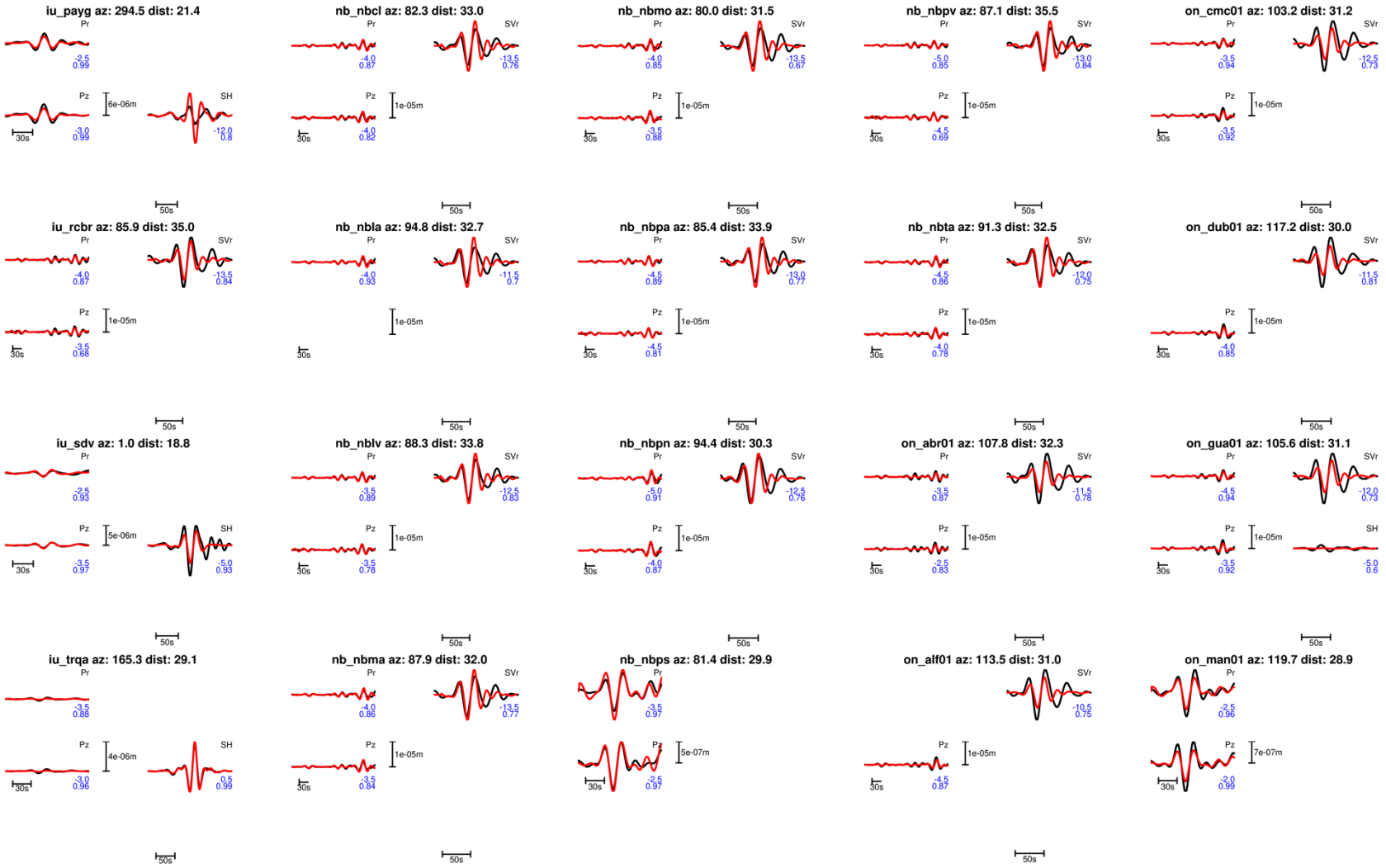
iu_payg az: 294.5 dist: 21.4
nb_nbcl az: 82.3 dist: 33.0
nb_nbmo az: 80.0 dist: 31.5
nb_nbpv az: 87.1 dist: 35.5
on_cmc01 az: 103.2 dist: 31.2
iu_rcbr az: 85.9 dist: 35.0
nb_nbla az: 94.8 dist: 32.7
nb_nbpa az: 85.4 dist: 33.9
nb_nbta az: 91.3 dist: 32.5
on_dub01 az: 117.2 dist: 30.0
iu_sdv az: 1.0 dist: 18.8
nb_nblv az: 88.3 dist: 33.8
nb_nbpn az: 94.4 dist: 30.3
on_abr01 az: 107.8 dist: 32.3
on_gua01 az: 105.6 dist: 31.1
iu_trqa az: 165.3 dist: 29.1
nb_nbma az: 87.9 dist: 32.0
nb_nbps az: 81.4 dist: 29.9
on_alf01 az: 113.5 dist: 31.0
on_man01 az: 119.7 dist: 28.9
Pr
SVr
Pz
SH
30s
50s

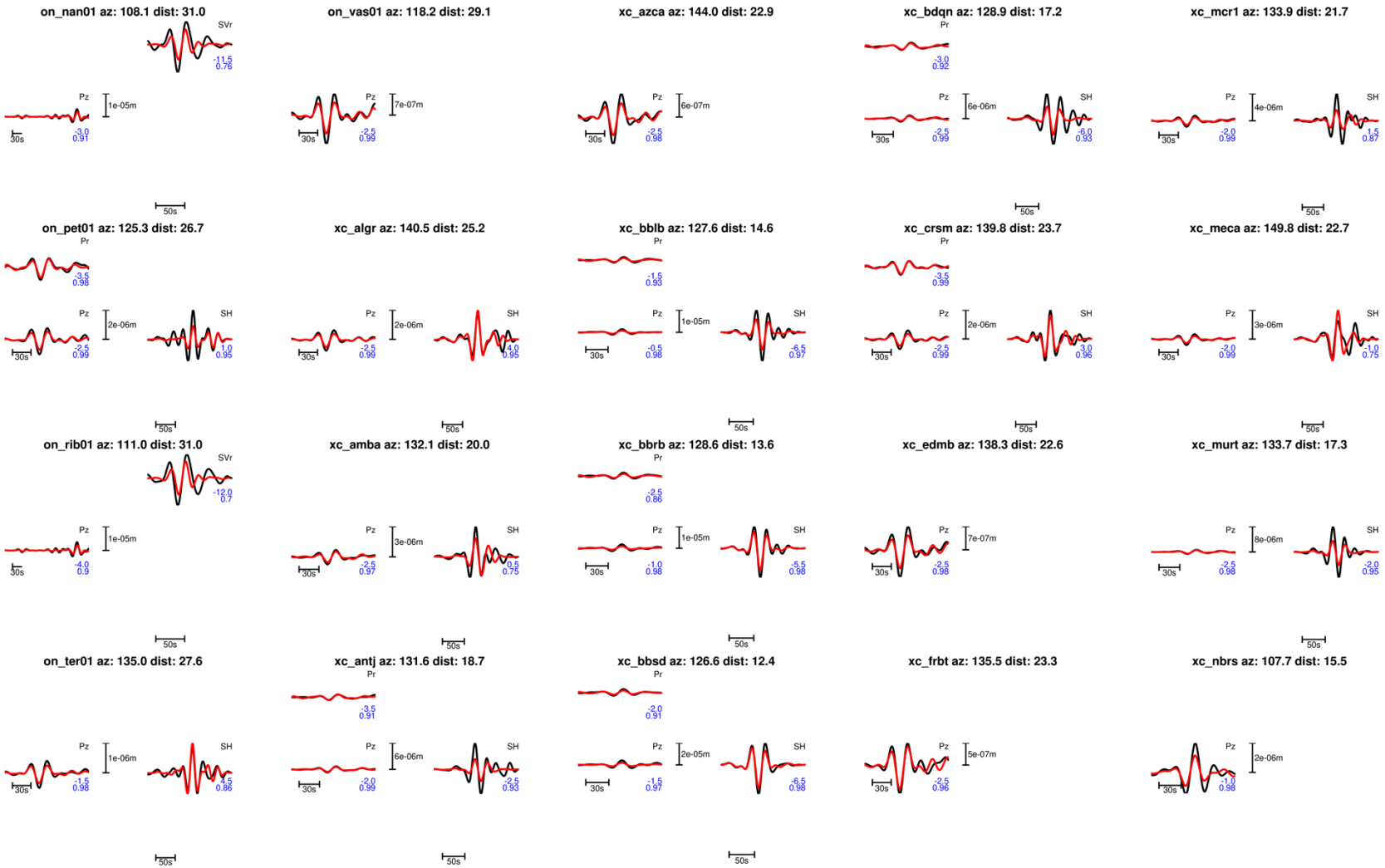
on_nan01 az: 108.1 dist: 31.0
on_vas01 az: 118.2 dist: 29.1
xc_azca az: 144.0 dist: 22.9
xc_bdqn az: 128.9 dist: 17.2
xc_mcr1 az: 133.9 dist: 21.7
on_pet01 az: 125.3 dist: 26.7
xc_algr az: 140.5 dist: 25.2
xc_bblb az: 127.6 dist: 14.6
xc_crsm az: 139.8 dist: 23.7
xc_meca az: 149.8 dist: 22.7
on_rib01 az: 111.0 dist: 31.0
xc_amba az: 132.1 dist: 20.0
xc_bbrb az: 128.6 dist: 13.6
xc_edmb az: 138.3 dist: 22.6
xc_murt az: 133.7 dist: 17.3
on_ter01 az: 135.0 dist: 27.6
xc_antj az: 131.6 dist: 18.7
xc_bbsd az: 126.6 dist: 12.4
xc_frbt az: 135.5 dist: 23.3
xc_nbrs az: 107.7 dist: 15.5
SVr
Pr
Pz
SH
30s
50s

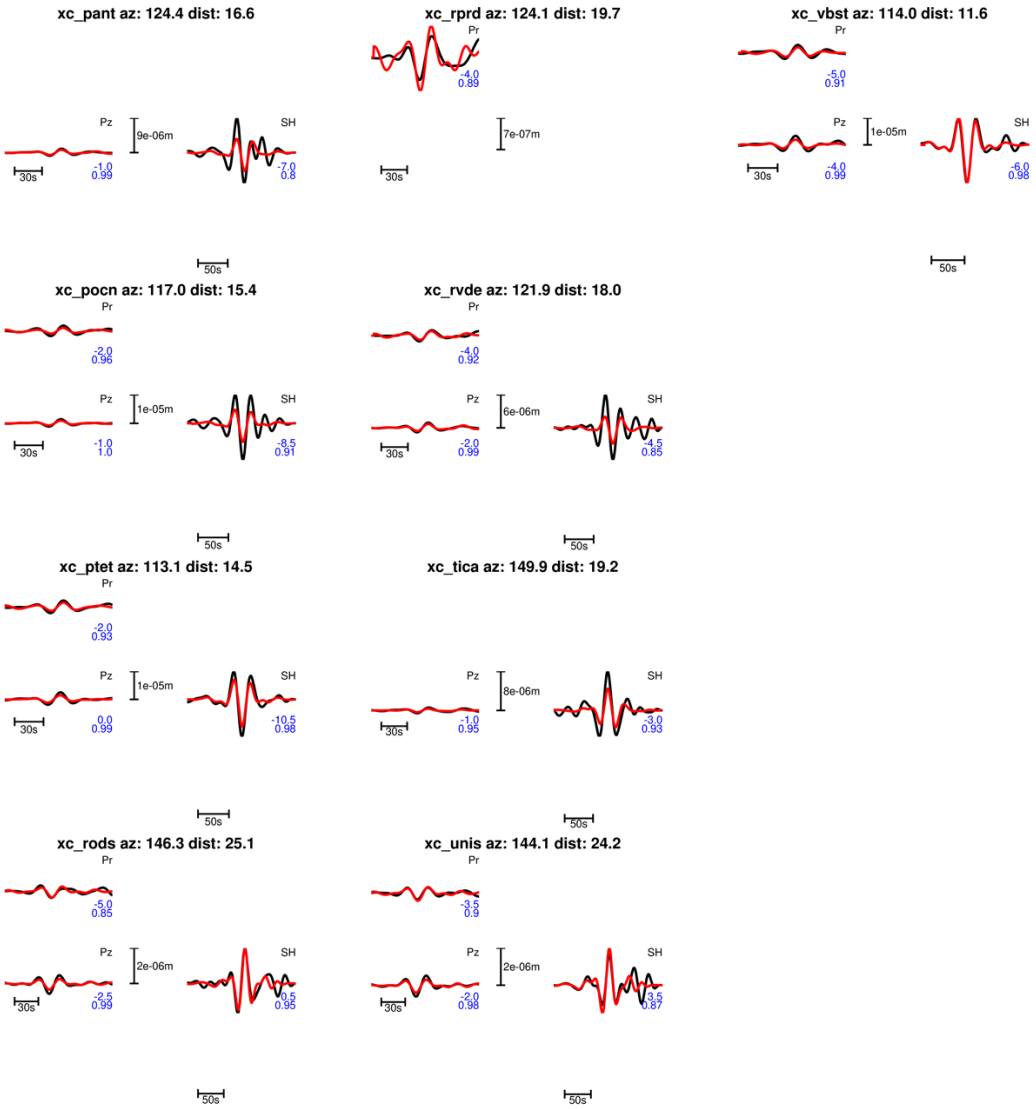
xc_pant az: 124.4 dist: 16.6
Pz
9e-06m
SH
30s
50s
xc_rprd az: 124.1 dist: 19.7
Pr
7e-07m
xc_vbst az: 114.0 dist: 11.6
1e-05m
xc_pocn az: 117.0 dist: 15.4
xc_rvde az: 121.9 dist: 18.0
6e-06m
xc_ptet az: 113.1 dist: 14.5
xc_tica az: 149.9 dist: 19.2
8e-06m
xc_rods az: 146.3 dist: 25.1
2e-06m
xc_unis az: 144.1 dist: 24.2

Figure S18. Inversion results for event 31. a) Map showing the preferred solution in b and the distribution of the 9 stations (15 traces) used in the inversion. Solution parameters are given below the map. Dashed circles indicate radii of 5º and 30º from epicenter; b) Distribution of focal mechanisms with centroid depths. We selected 590 km as the preferred solution for the event, fixing to the hypocenter depth in Table 1; c) Waveform fitting produced by the preferred solution. Black and red lines denote observations and synthetics, respectively. Azimuths and distances in degrees are shown above panels. Time shifts (top) and cross-correlation coefficients (bottom) are shown in blue at the lower right corner of each panel. Wave segments (Pr, Pz, SVr, SH and SVz) are identified at the upper right corners.

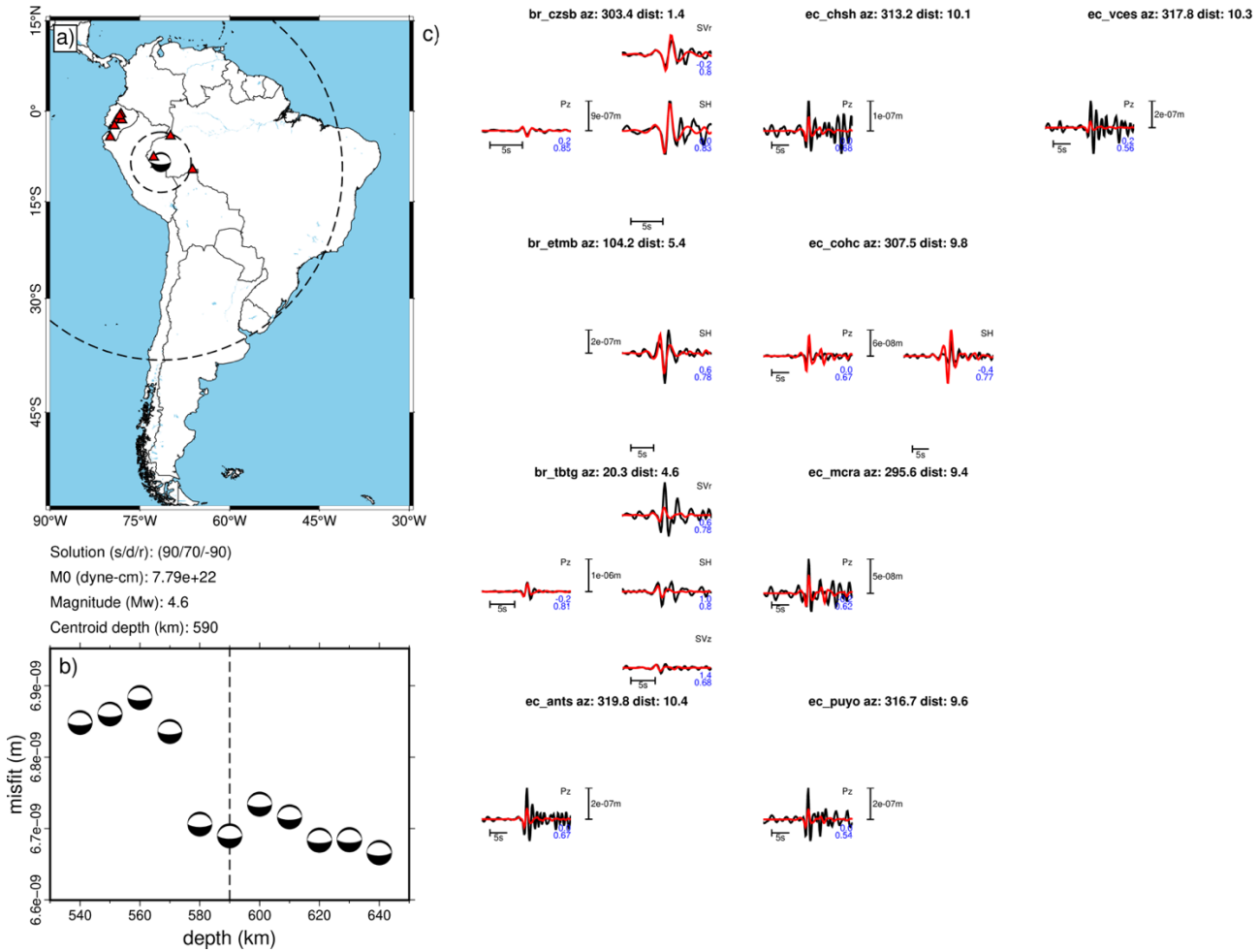

Figure S19. Inversion results for event 32. a) Map showing the preferred solution in b and the distribution of the 163 stations (411 traces) used in the inversion. Solution parameters are given below the map. Dashed circles indicate radii of 5º and 30º from epicenter; b) Distribution of focal mechanisms with centroid depths pointing to 620 km as the preferred solution for the event; c) Waveform fitting produced by the preferred solution. Black and red lines denote observations and synthetics, respectively. Azimuths and distances in degrees are shown above panels. Time shifts (top) and cross-correlation coefficients (bottom) are shown in blue at the lower right corner of each panel. Wave segments (Pr, Pz, SVr, SH and SVz) are identified at the upper right corner.

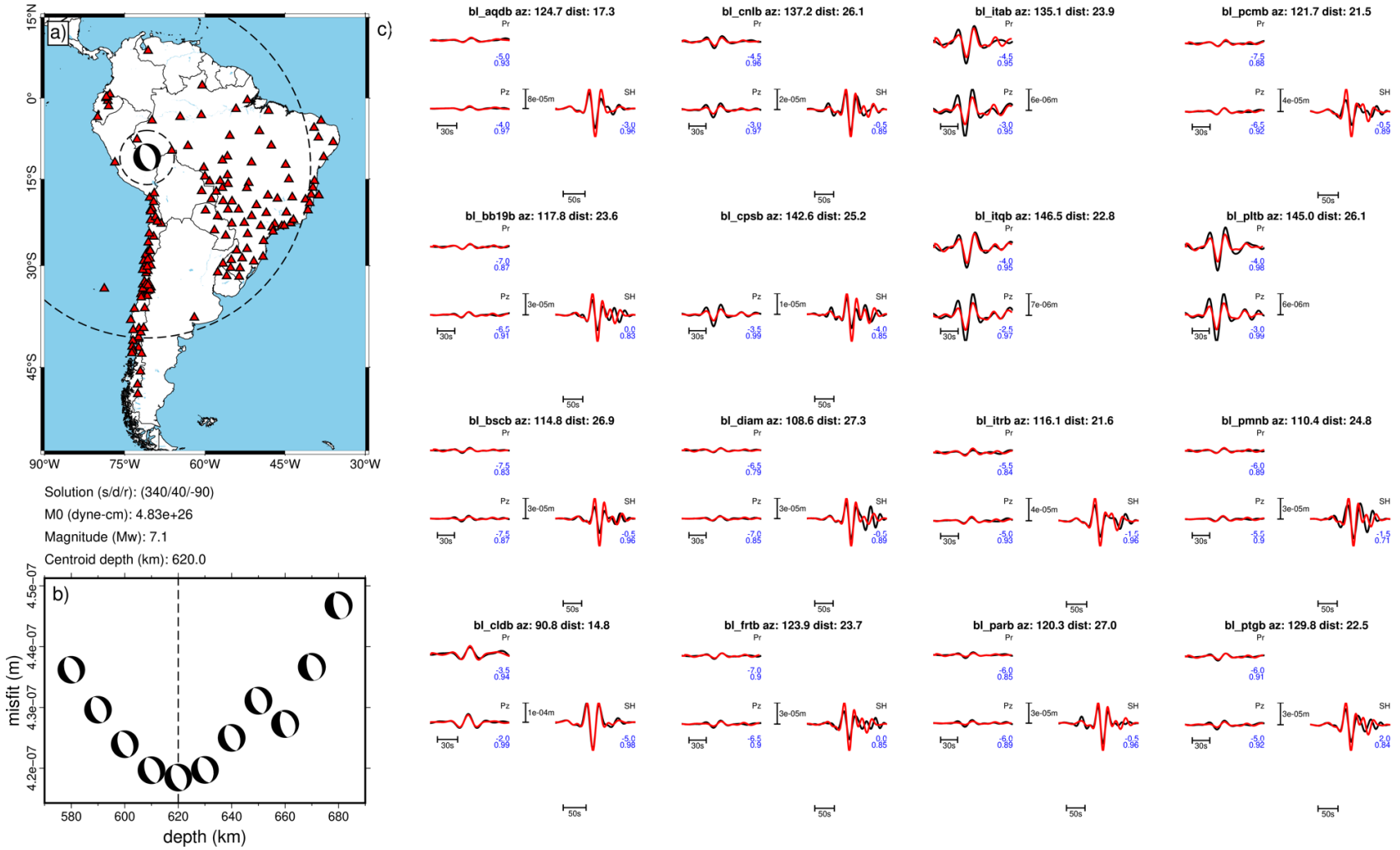

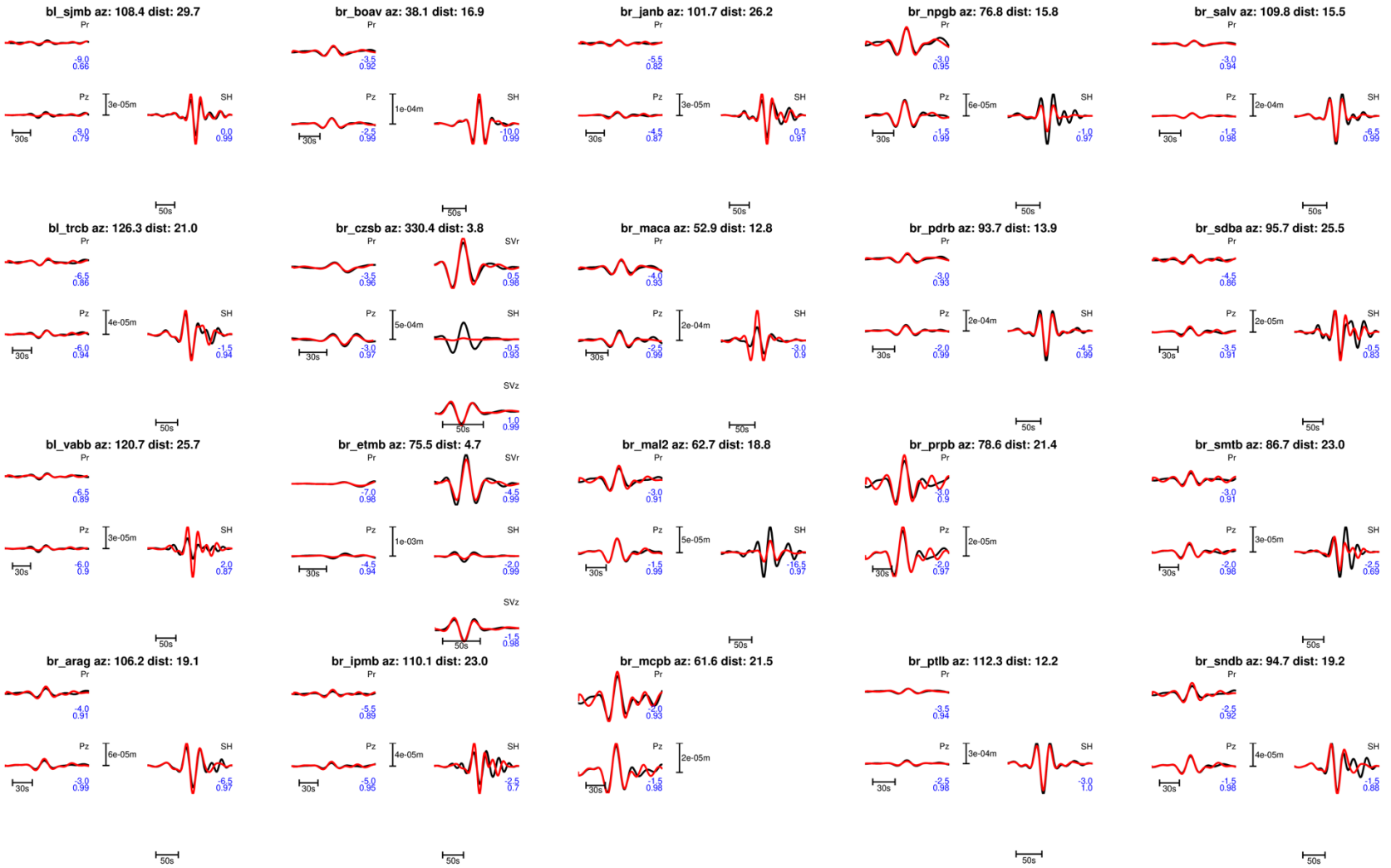
bl_sjmb az: 108.4 dist: 29.7
br_boav az: 38.1 dist: 16.9
br_janb az: 101.7 dist: 26.2
br_npgb az: 76.8 dist: 15.8
br_salv az: 109.8 dist: 15.5
bl_trcb az: 126.3 dist: 21.0
br_czsb az: 330.4 dist: 3.8
br_maca az: 52.9 dist: 12.8
br_pdrb az: 93.7 dist: 13.9
br_sdba az: 95.7 dist: 25.5
bl_vabb az: 120.7 dist: 25.7
br_etmb az: 75.5 dist: 4.7
br_mal2 az: 62.7 dist: 18.8
br_prpb az: 78.6 dist: 21.4
br_smtb az: 86.7 dist: 23.0
br_arag az: 106.2 dist: 19.1
br_ipmb az: 110.1 dist: 23.0
br_mcpb az: 61.6 dist: 21.5
br_ptlb az: 112.3 dist: 12.2
br_sndb az: 94.7 dist: 19.2
Pr
Pz
SH
SVr
SVz
30s
50s

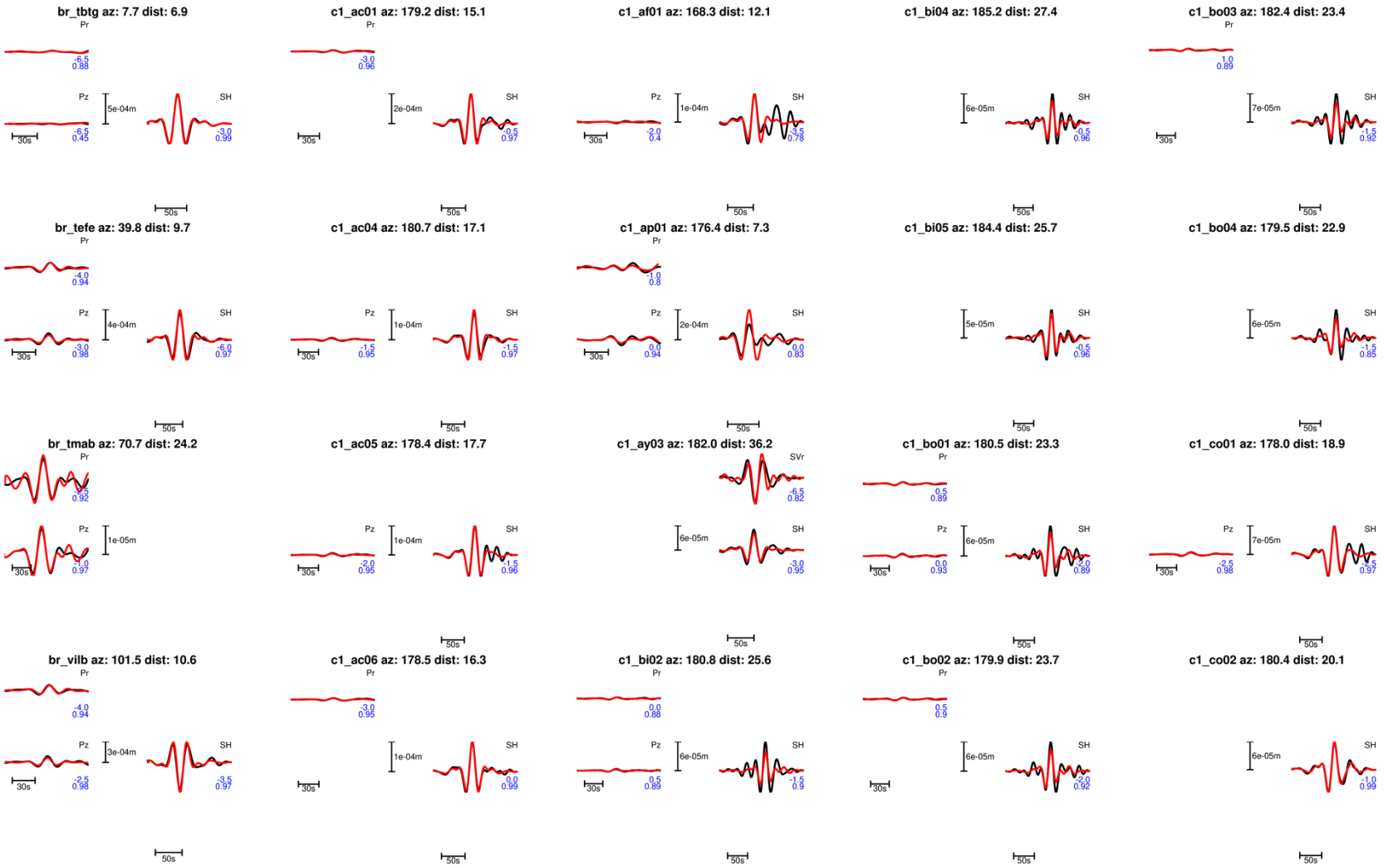
br_tbtg az: 7.7 dist: 6.9
c1_ac01 az: 179.2 dist: 15.1
c1_af01 az: 168.3 dist: 12.1
c1_bi04 az: 185.2 dist: 27.4
c1_bo03 az: 182.4 dist: 23.4
br_tefe az: 39.8 dist: 9.7
c1_ac04 az: 180.7 dist: 17.1
c1_ap01 az: 176.4 dist: 7.3
c1_bi05 az: 184.4 dist: 25.7
c1_bo04 az: 179.5 dist: 22.9
br_tmab az: 70.7 dist: 24.2
c1_ac05 az: 178.4 dist: 17.7
c1_ay03 az: 182.0 dist: 36.2
c1_bo01 az: 180.5 dist: 23.3
c1_co01 az: 178.0 dist: 18.9
br_vilb az: 101.5 dist: 10.6
c1_ac06 az: 178.5 dist: 16.3
c1_bi02 az: 180.8 dist: 25.6
c1_bo02 az: 179.9 dist: 23.7
c1_co02 az: 180.4 dist: 20.1
Pr
SVr
Pz
SH
30s
50s

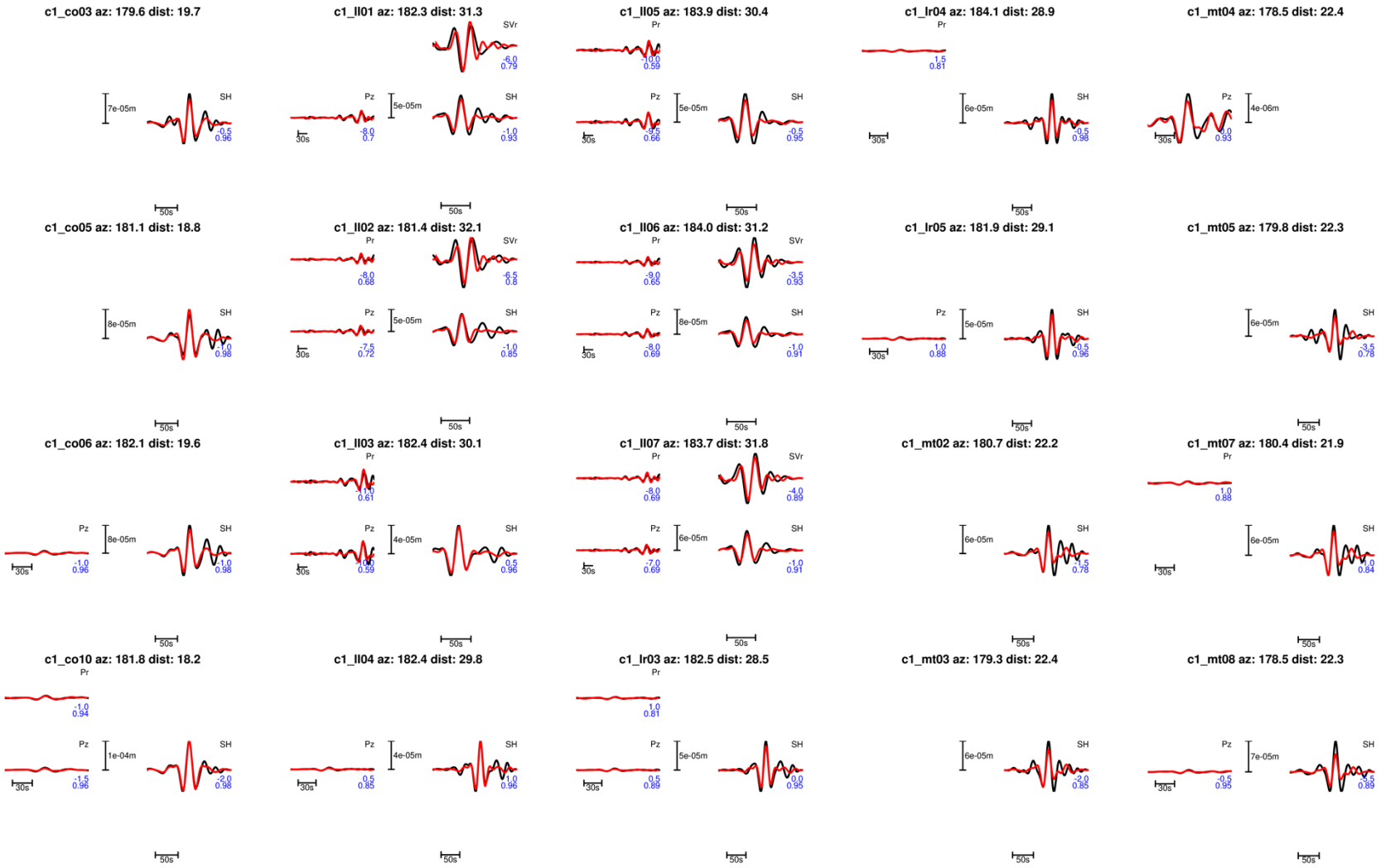
c1_co03 az: 179.6 dist: 19.7
c1_ll01 az: 182.3 dist: 31.3
c1_ll05 az: 183.9 dist: 30.4
c1_lr04 az: 184.1 dist: 28.9
c1_mt04 az: 178.5 dist: 22.4
c1_co05 az: 181.1 dist: 18.8
c1_ll02 az: 181.4 dist: 32.1
c1_ll06 az: 184.0 dist: 31.2
c1_lr05 az: 181.9 dist: 29.1
c1_mt05 az: 179.8 dist: 22.3
c1_co06 az: 182.1 dist: 19.6
c1_ll03 az: 182.4 dist: 30.1
c1_ll07 az: 183.7 dist: 31.8
c1_mt02 az: 180.7 dist: 22.2
c1_mt07 az: 180.4 dist: 21.9
c1_co10 az: 181.8 dist: 18.2
c1_ll04 az: 182.4 dist: 29.8
c1_lr03 az: 182.5 dist: 28.5
c1_mt03 az: 179.3 dist: 22.4
c1_mt08 az: 178.5 dist: 22.3
Pr
SVr
Pz
SH
50s
30s

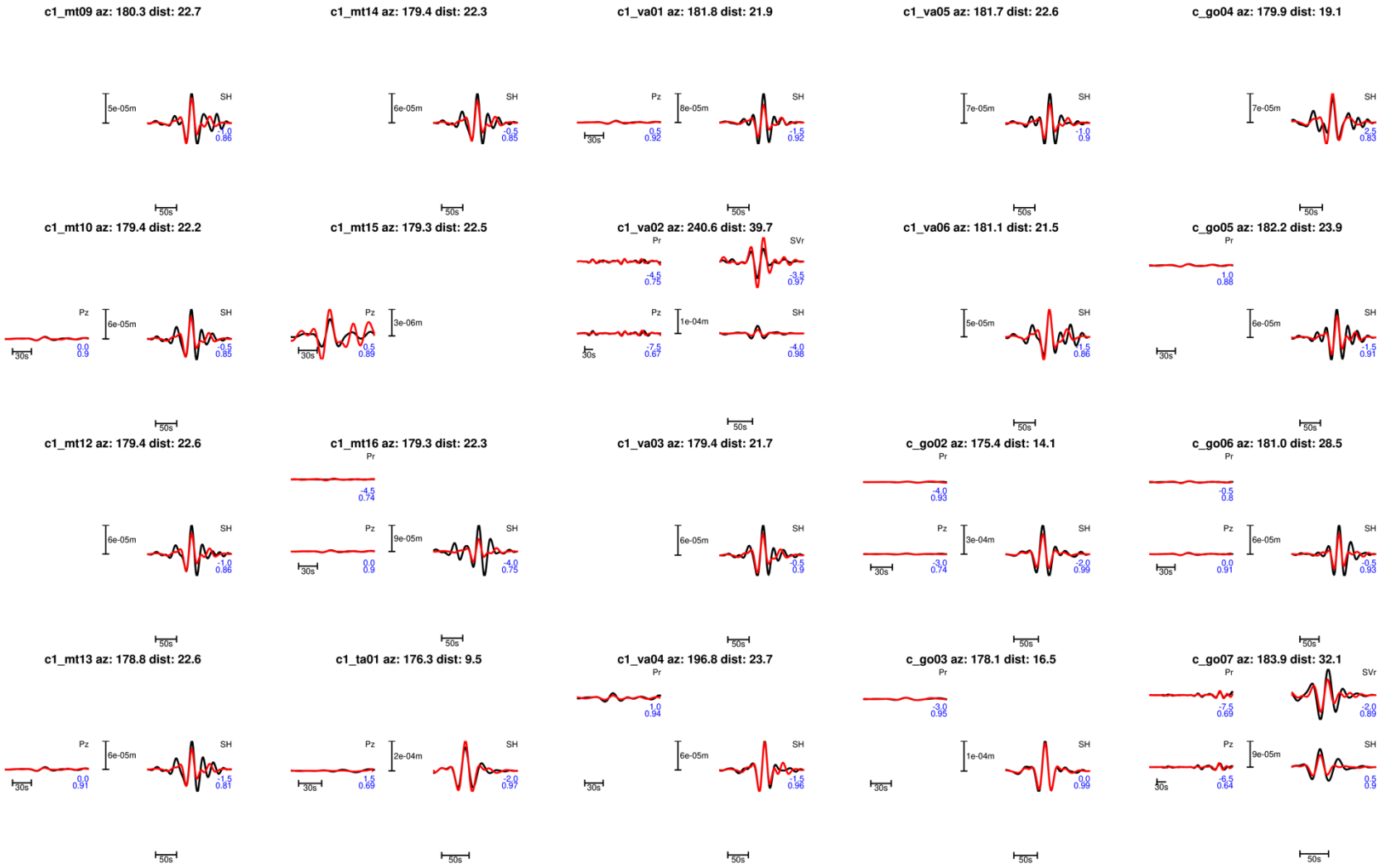
c1_mt09 az: 180.3 dist: 22.7
c1_mt14 az: 179.4 dist: 22.3
c1_va01 az: 181.8 dist: 21.9
c1_va05 az: 181.7 dist: 22.6
c_go04 az: 179.9 dist: 19.1
c1_mt10 az: 179.4 dist: 22.2
c1_mt15 az: 179.3 dist: 22.5
c1_va02 az: 240.6 dist: 39.7
c1_va06 az: 181.1 dist: 21.5
c_go05 az: 182.2 dist: 23.9
c1_mt12 az: 179.4 dist: 22.6
c1_mt16 az: 179.3 dist: 22.3
c1_va03 az: 179.4 dist: 21.7
c_go02 az: 175.4 dist: 14.1
c_go06 az: 181.0 dist: 28.5
c1_mt13 az: 178.8 dist: 22.6
c1_ta01 az: 176.3 dist: 9.5
c1_va04 az: 196.8 dist: 23.7
c_go03 az: 178.1 dist: 16.5
c_go07 az: 183.9 dist: 32.1
SH
SVr
Pr
Pz
50s
30s

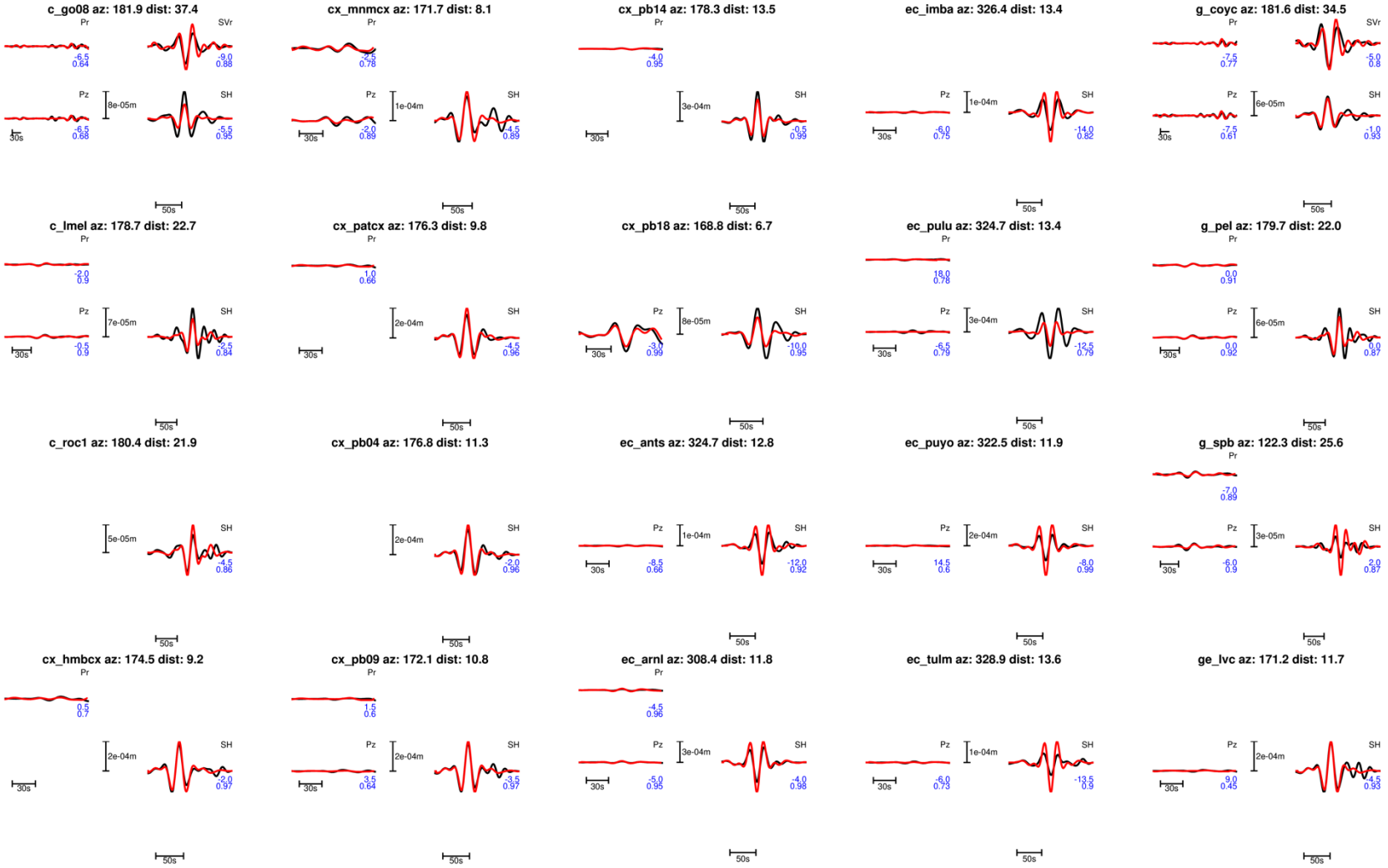
c_go08 az: 181.9 dist: 37.4
cx_mnmcx az: 171.7 dist: 8.1
cx_pb14 az: 178.3 dist: 13.5
ec_imba az: 326.4 dist: 13.4
g_coyc az: 181.6 dist: 34.5
c_lmel az: 178.7 dist: 22.7
cx_patcx az: 176.3 dist: 9.8
cx_pb18 az: 168.8 dist: 6.7
ec_pulu az: 324.7 dist: 13.4
g_pel az: 179.7 dist: 22.0
c_roc1 az: 180.4 dist: 21.9
cx_pb04 az: 176.8 dist: 11.3
ec_ants az: 324.7 dist: 12.8
ec_puyo az: 322.5 dist: 11.9
g_spb az: 122.3 dist: 25.6
cx_hmbcx az: 174.5 dist: 9.2
cx_pb09 az: 172.1 dist: 10.8
ec_arnl az: 308.4 dist: 11.8
ec_tulm az: 328.9 dist: 13.6
ge_lvc az: 171.2 dist: 11.7
Pr
SVr
Pz
SH
30s
50s

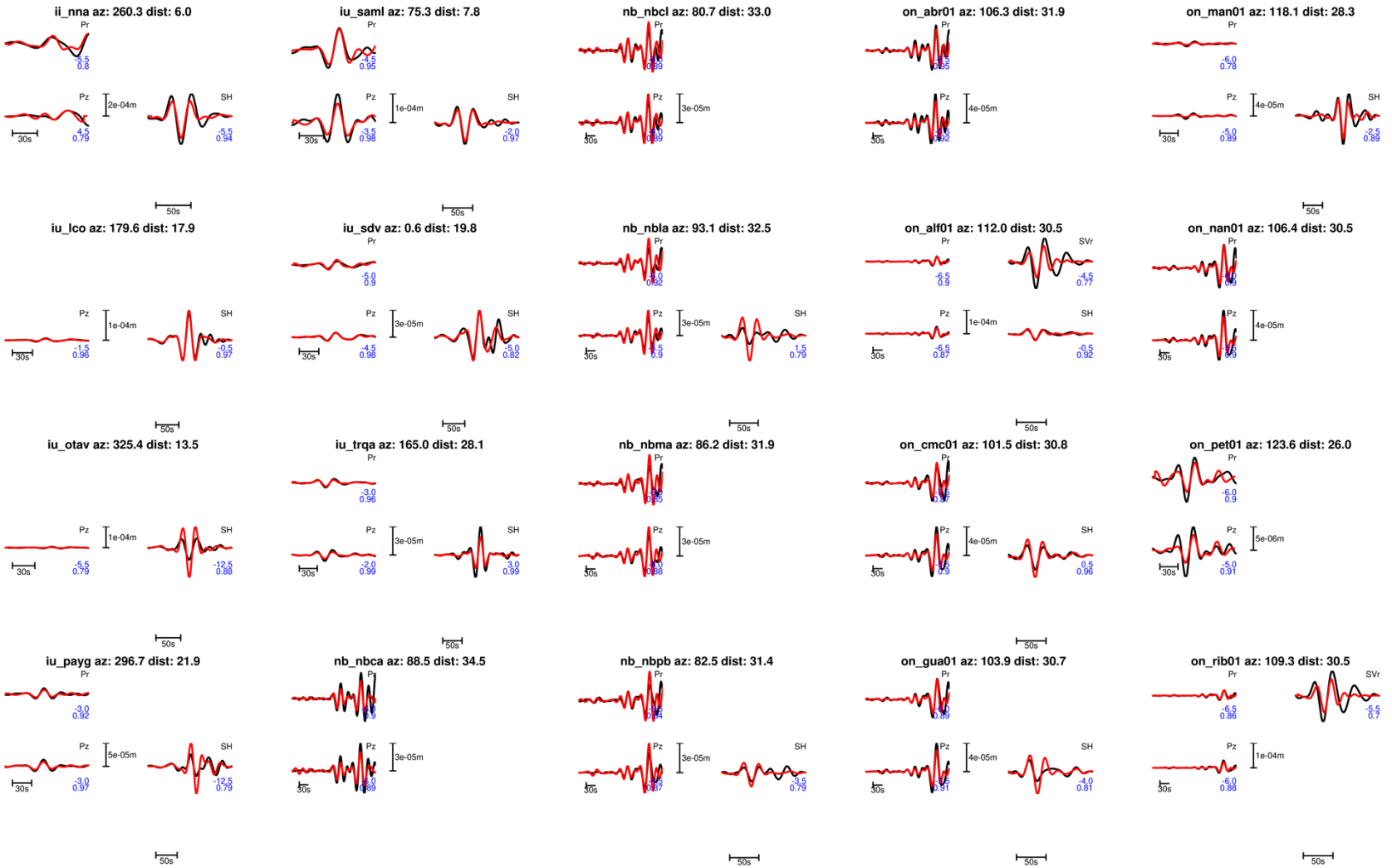
ii_nna az: 260.3 dist: 6.0
iu_saml az: 75.3 dist: 7.8
nb_nbcl az: 80.7 dist: 33.0
on_abr01 az: 106.3 dist: 31.9
on_man01 az: 118.1 dist: 28.3
iu_lco az: 179.6 dist: 17.9
iu_sdv az: 0.6 dist: 19.8
nb_nbla az: 93.1 dist: 32.5
on_alf01 az: 112.0 dist: 30.5
on_nan01 az: 106.4 dist: 30.5
iu_otav az: 325.4 dist: 13.5
iu_trqa az: 165.0 dist: 28.1
nb_nbma az: 86.2 dist: 31.9
on_cmc01 az: 101.5 dist: 30.8
on_pet01 az: 123.6 dist: 26.0
iu_payg az: 296.7 dist: 21.9
nb_nbca az: 88.5 dist: 34.5
nb_nbpb az: 82.5 dist: 31.4
on_gua01 az: 103.9 dist: 30.7
on_rib01 az: 109.3 dist: 30.5
Pr
Pz
SH
SVr
30s
50s

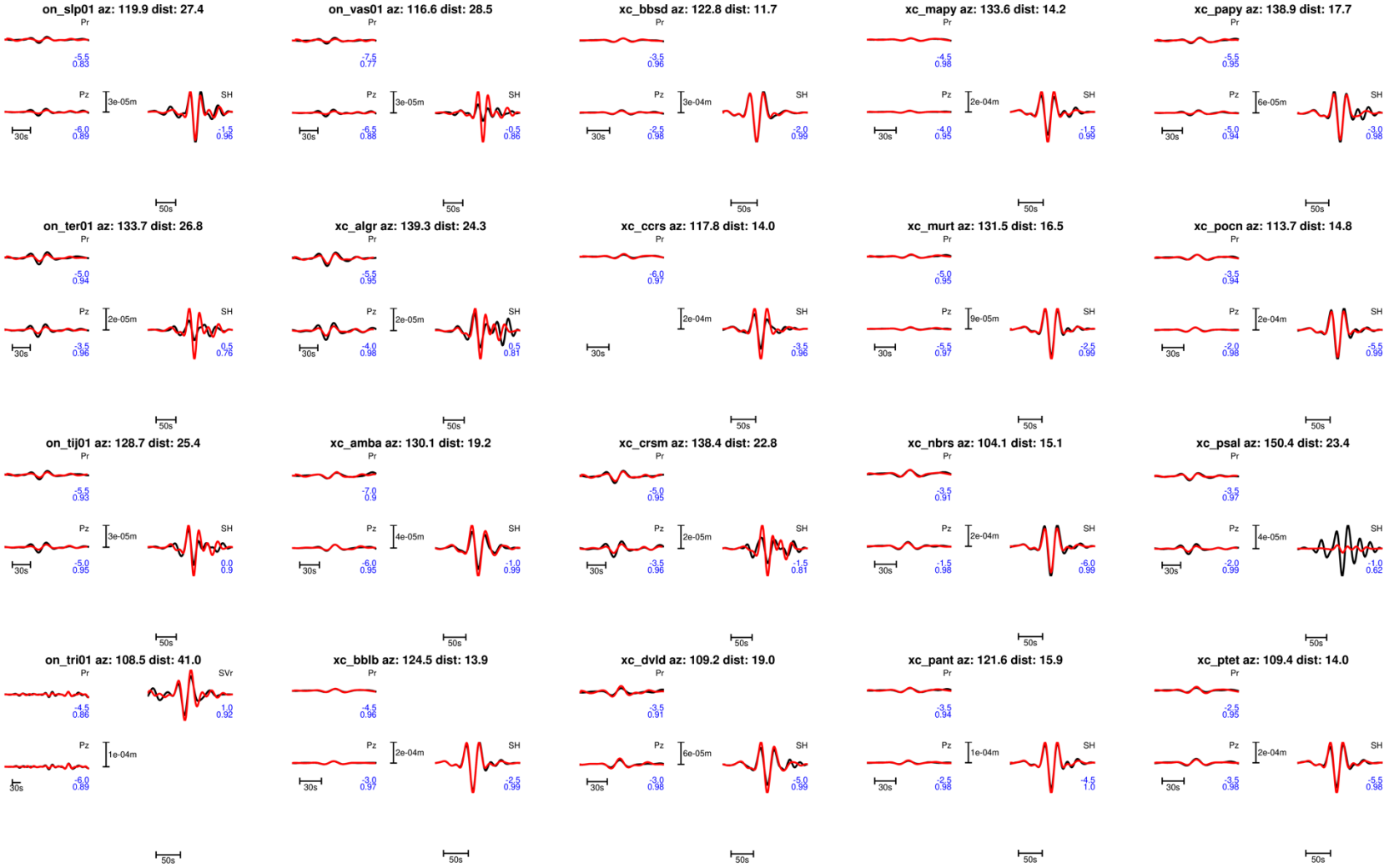
on_slp01 az: 119.9 dist: 27.4
on_vas01 az: 116.6 dist: 28.5
xc_bbsd az: 122.8 dist: 11.7
xc_mapy az: 133.6 dist: 14.2
xc_papy az: 138.9 dist: 17.7
on_ter01 az: 133.7 dist: 26.8
xc_algr az: 139.3 dist: 24.3
xc_ccrs az: 117.8 dist: 14.0
xc_murt az: 131.5 dist: 16.5
xc_pocn az: 113.7 dist: 14.8
on_tij01 az: 128.7 dist: 25.4
xc_amba az: 130.1 dist: 19.2
xc_crsm az: 138.4 dist: 22.8
xc_nbrs az: 104.1 dist: 15.1
xc_psal az: 150.4 dist: 23.4
on_tri01 az: 108.5 dist: 41.0
xc_bblb az: 124.5 dist: 13.9
xc_dvld az: 109.2 dist: 19.0
xc_pant az: 121.6 dist: 15.9
xc_ptet az: 109.4 dist: 14.0
Pr
Pz
SH
SVr
30s
50s

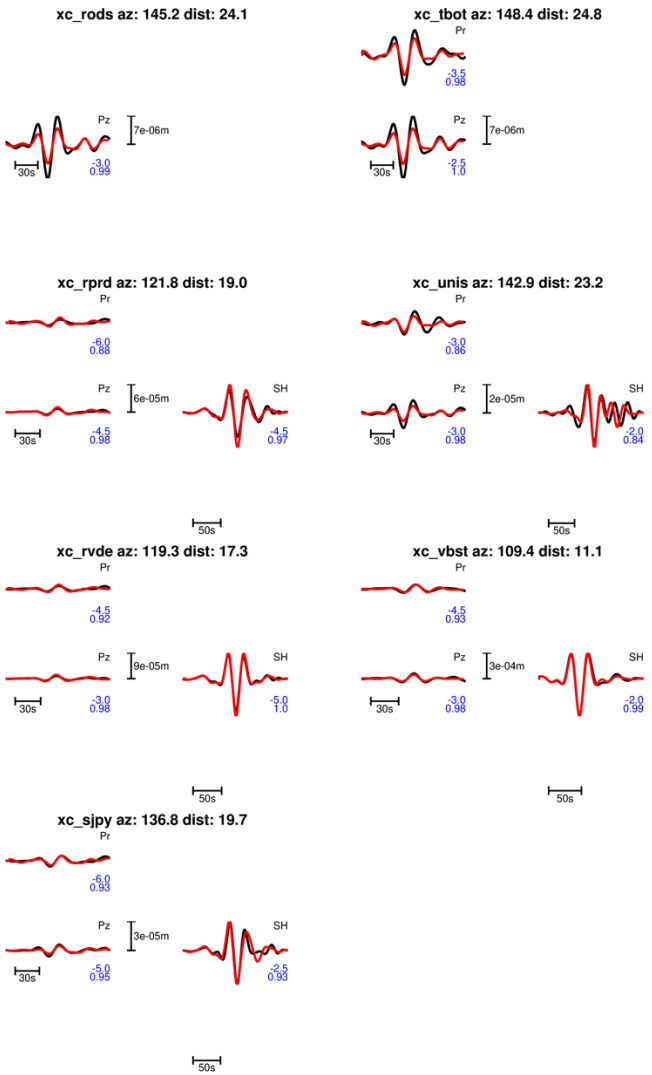
xc_rods az: 145.2 dist: 24.1
Pz
7e-06m
30s
-3.0
0.99
xc_tbot az: 148.4 dist: 24.8
Pr
-3.5
0.98
Pz
7e-06m
30s
-2.5
1.0
xc_rprd az: 121.8 dist: 19.0
Pr
-6.0
0.88
Pz
6e-05m
SH
30s
-4.5
0.98
-4.5
0.97
50s
xc_unis az: 142.9 dist: 23.2
Pr
-3.0
0.86
Pz
2e-05m
SH
30s
-3.0
0.98
-2.0
0.84
50s
xc_rvde az: 119.3 dist: 17.3
Pr
-4.5
0.92
Pz
9e-05m
SH
30s
-3.0
0.98
-5.0
1.0
50s
xc_vbst az: 109.4 dist: 11.1
Pr
-4.5
0.93
Pz
3e-04m
SH
30s
-3.0
0.98
-2.0
0.99
50s
xc_sjpy az: 136.8 dist: 19.7
Pr
-6.0
0.93
Pz
3e-05m
SH
30s
-5.0
0.95
-2.5
0.93
50s

Figure S20. Inversion results for event 33. a) Map showing the preferred solution in b and the distribution of the 6 stations (15 traces) used in the inversion. Solution parameters are given below the map. Dashed circles indicate radii of 5º and 30º from epicenter; b) Distribution of focal mechanisms with centroid depths pointing to 626 km as the preferred solution for the event; c) Waveform fitting produced by the preferred solution. Black and red lines denote observations and synthetics, respectively. Azimuths and distances in degrees are shown above panels. Time shifts (top) and cross-correlation coefficients (bottom) are shown in blue at the lower right corner of each panel. Wave segments (Pr, Pz, SVr, SH and SVz) are identified at the upper right corners.

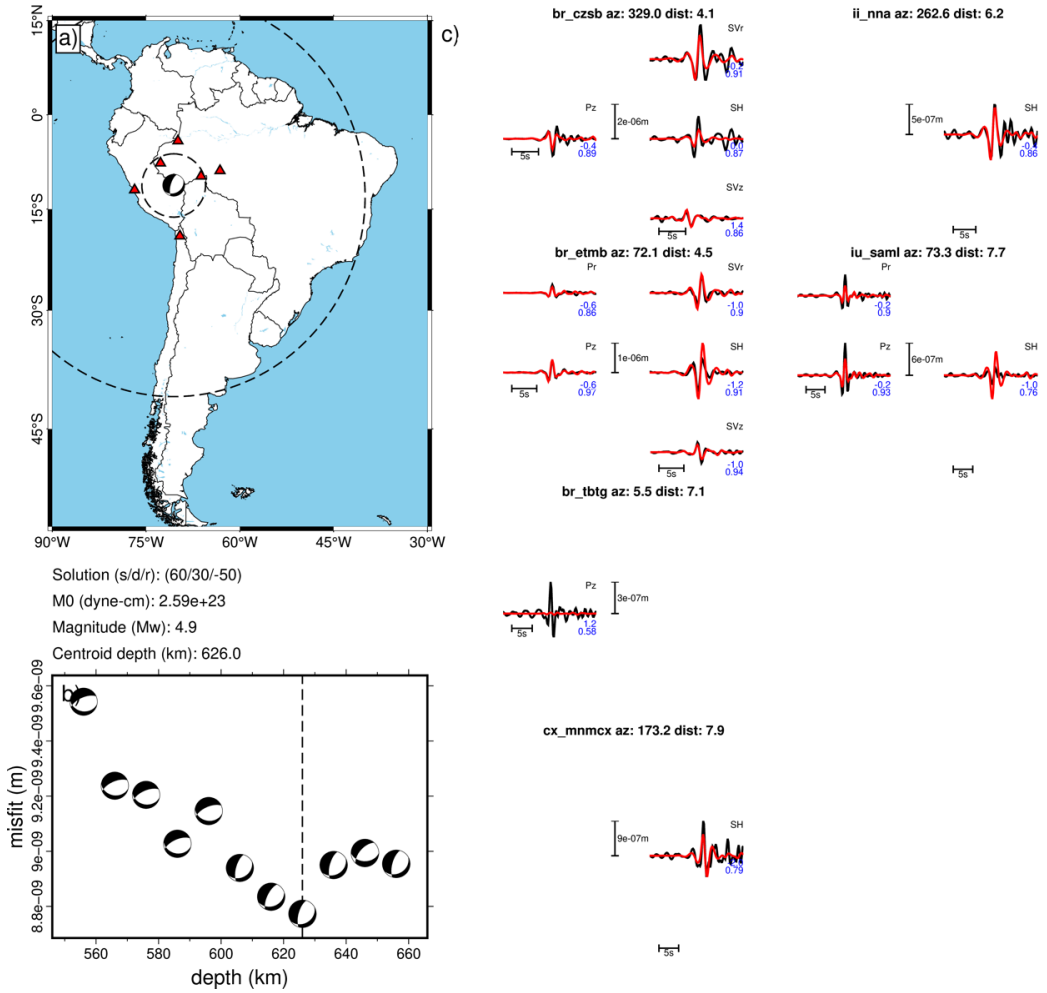

Figure S21. Inversion results for event 34. a) Map showing the preferred solution in b and the distribution of the 151 stations (375 traces) used in the inversion. Solution parameters are given below the map. Dashed circles indicate radii of 5º and 30º from epicenter; b) Distribution of focal mechanisms with centroid depths pointing to 570 km as the preferred solution for the event; c) Waveform fitting produced by the preferred solution. Black and red lines denote observations and synthetics, respectively. Azimuths and distances in degrees are shown above panels. Time shifts (top) and cross-correlation coefficients (bottom) are shown in blue at the lower right corner of each panel. Wave segments (Pr, Pz, SVr, SH and SVz) are identified at the upper right corners.

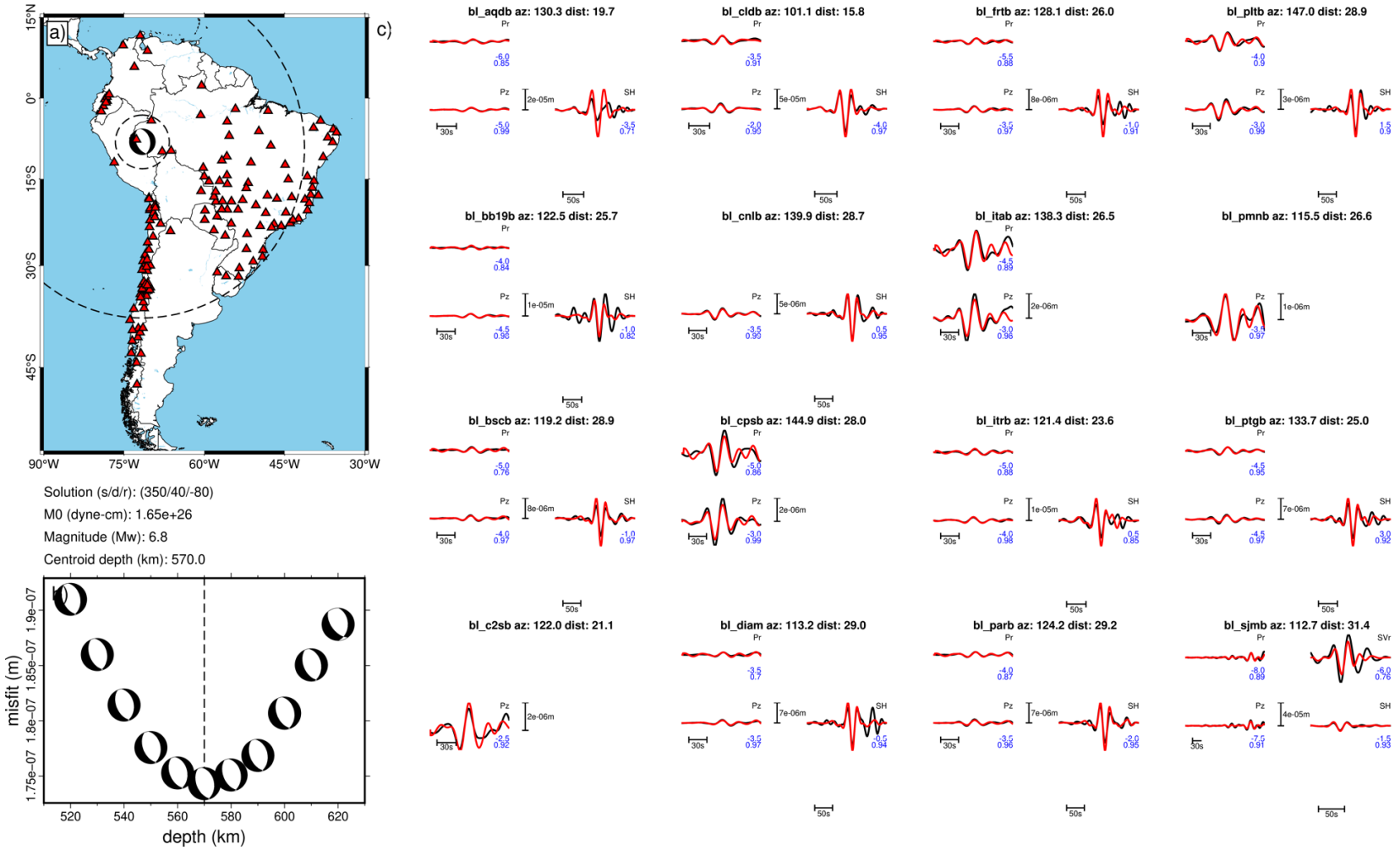

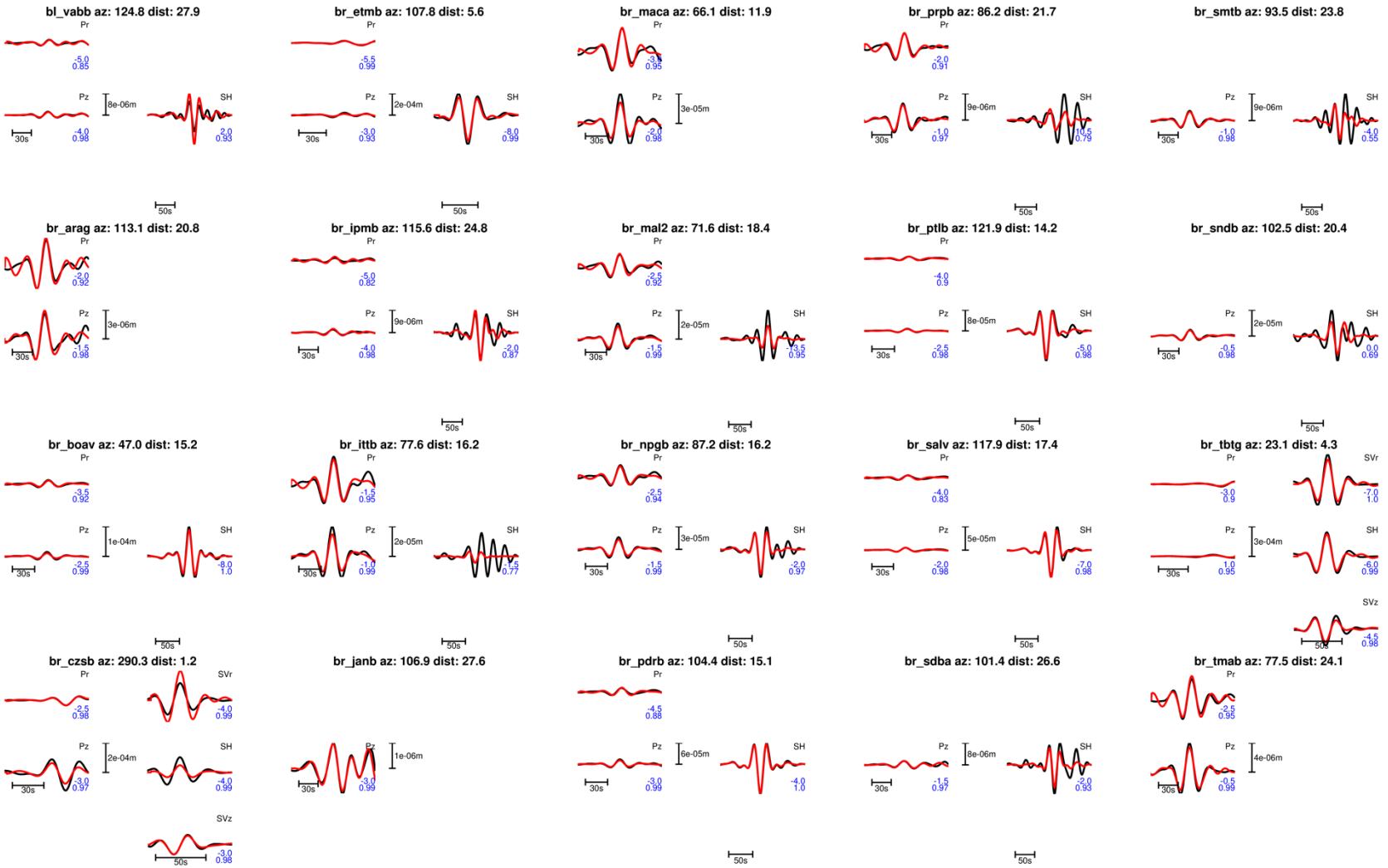
bl_vabb az: 124.8 dist: 27.9
br_etmb az: 107.8 dist: 5.6
br_maca az: 66.1 dist: 11.9
br_prpb az: 86.2 dist: 21.7
br_smtb az: 93.5 dist: 23.8
br_arag az: 113.1 dist: 20.8
br_ipmb az: 115.6 dist: 24.8
br_mal2 az: 71.6 dist: 18.4
br_ptlb az: 121.9 dist: 14.2
br_sndb az: 102.5 dist: 20.4
br_boav az: 47.0 dist: 15.2
br_ittb az: 77.6 dist: 16.2
br_npgb az: 87.2 dist: 16.2
br_salv az: 117.9 dist: 17.4
br_tbtg az: 23.1 dist: 4.3
br_czsb az: 290.3 dist: 1.2
br_janb az: 106.9 dist: 27.6
br_pdrb az: 104.4 dist: 15.1
br_sdba az: 101.4 dist: 26.6
br_tmab az: 77.5 dist: 24.1
Pr
Pz
SH
SVr
SVz
30s
50s

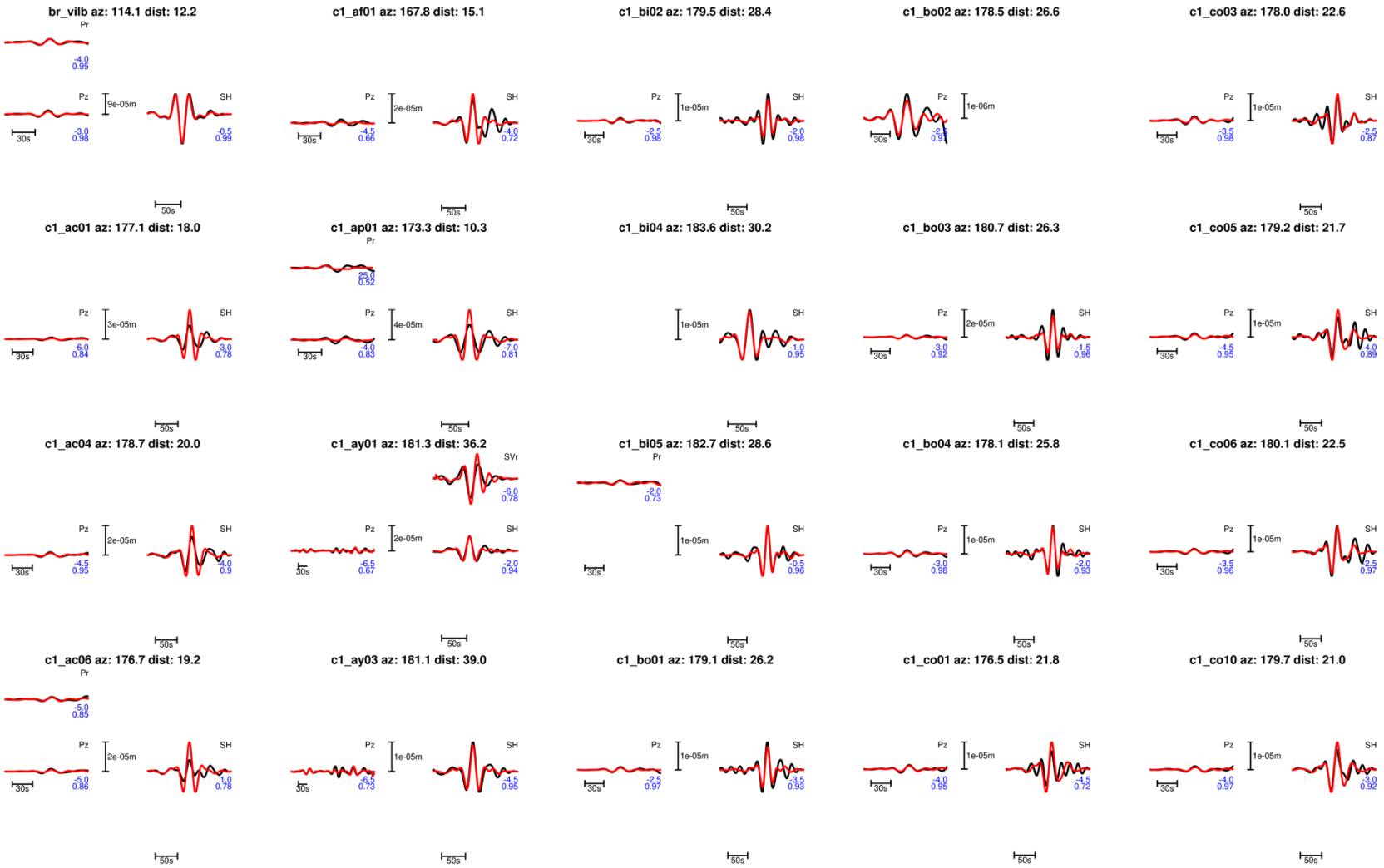
br_vilb az: 114.1 dist: 12.2
c1_af01 az: 167.8 dist: 15.1
c1_bi02 az: 179.5 dist: 28.4
c1_bo02 az: 178.5 dist: 26.6
c1_co03 az: 178.0 dist: 22.6
c1_ac01 az: 177.1 dist: 18.0
c1_ap01 az: 173.3 dist: 10.3
c1_bi04 az: 183.6 dist: 30.2
c1_bo03 az: 180.7 dist: 26.3
c1_co05 az: 179.2 dist: 21.7
c1_ac04 az: 178.7 dist: 20.0
c1_ay01 az: 181.3 dist: 36.2
c1_bi05 az: 182.7 dist: 28.6
c1_bo04 az: 178.1 dist: 25.8
c1_co06 az: 180.1 dist: 22.5
c1_ac06 az: 176.7 dist: 19.2
c1_ay03 az: 181.1 dist: 39.0
c1_bo01 az: 179.1 dist: 26.2
c1_co01 az: 176.5 dist: 21.8
c1_co10 az: 179.7 dist: 21.0
Pr
Pz
SH
SVr
30s
50s

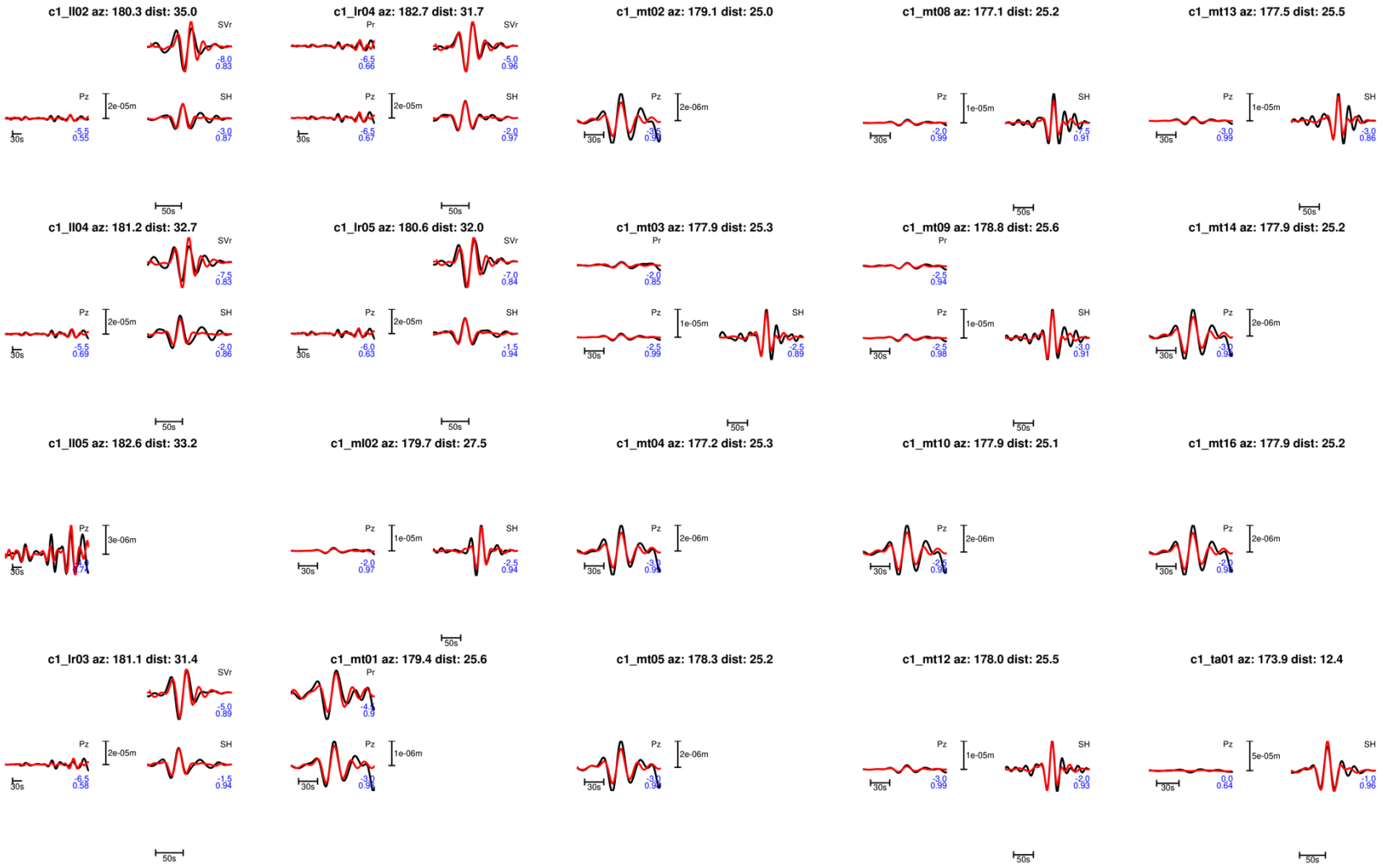
c1_ll02 az: 180.3 dist: 35.0
c1_lr04 az: 182.7 dist: 31.7
c1_mt02 az: 179.1 dist: 25.0
c1_mt08 az: 177.1 dist: 25.2
c1_mt13 az: 177.5 dist: 25.5
c1_ll04 az: 181.2 dist: 32.7
c1_lr05 az: 180.6 dist: 32.0
c1_mt03 az: 177.9 dist: 25.3
c1_mt09 az: 178.8 dist: 25.6
c1_mt14 az: 177.9 dist: 25.2
c1_ll05 az: 182.6 dist: 33.2
c1_ml02 az: 179.7 dist: 27.5
c1_mt04 az: 177.2 dist: 25.3
c1_mt10 az: 177.9 dist: 25.1
c1_mt16 az: 177.9 dist: 25.2
c1_lr03 az: 181.1 dist: 31.4
c1_mt01 az: 179.4 dist: 25.6
c1_mt05 az: 178.3 dist: 25.2
c1_mt12 az: 178.0 dist: 25.5
c1_ta01 az: 173.9 dist: 12.4
Pz
SH
SVr
Pr
30s
50s

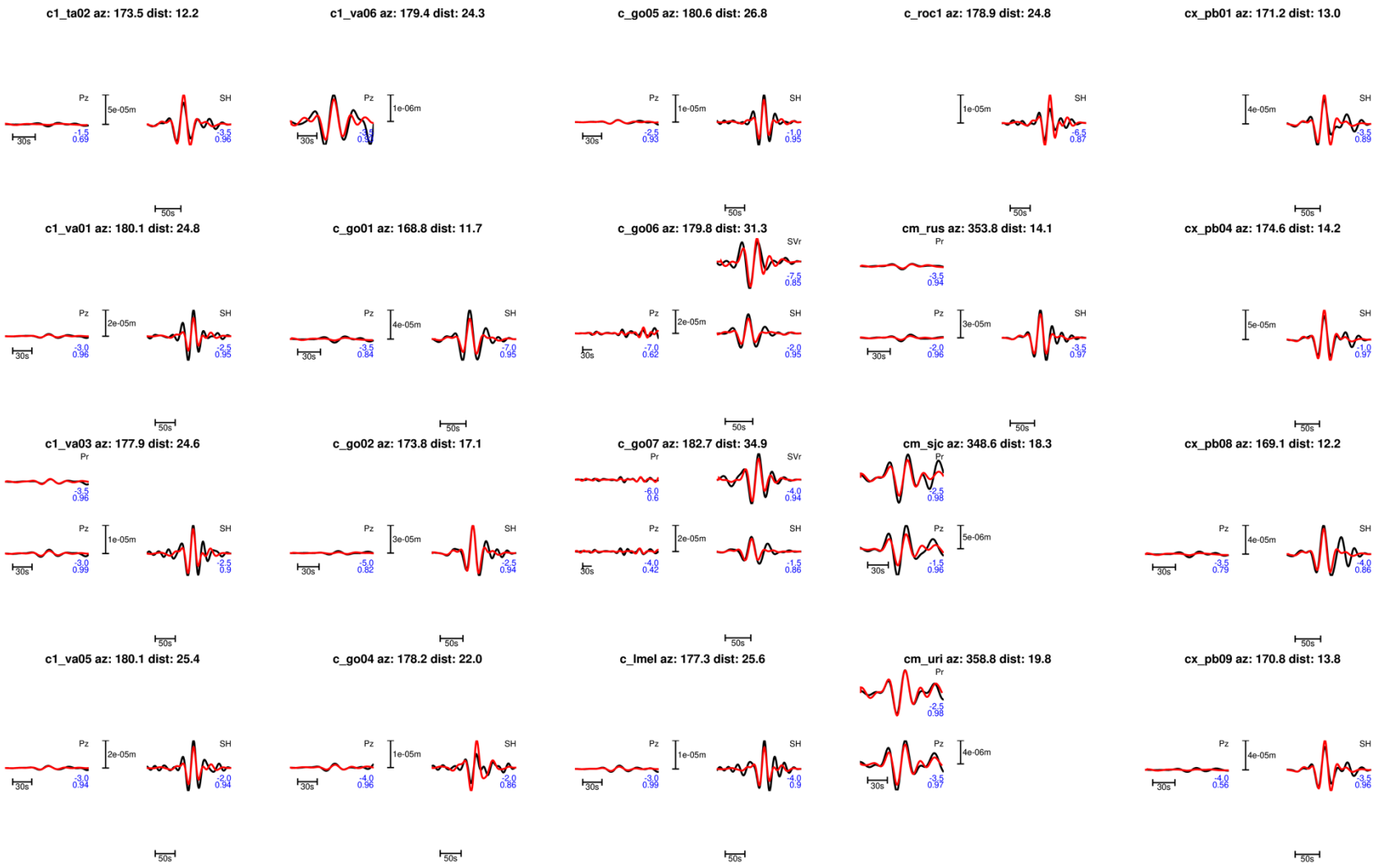
c1_ta02 az: 173.5 dist: 12.2
c1_va06 az: 179.4 dist: 24.3
c_go05 az: 180.6 dist: 26.8
c_roc1 az: 178.9 dist: 24.8
cx_pb01 az: 171.2 dist: 13.0
c1_va01 az: 180.1 dist: 24.8
c_go01 az: 168.8 dist: 11.7
c_go06 az: 179.8 dist: 31.3
cm_rus az: 353.8 dist: 14.1
cx_pb04 az: 174.6 dist: 14.2
c1_va03 az: 177.9 dist: 24.6
c_go02 az: 173.8 dist: 17.1
c_go07 az: 182.7 dist: 34.9
cm_sjc az: 348.6 dist: 18.3
cx_pb08 az: 169.1 dist: 12.2
c1_va05 az: 180.1 dist: 25.4
c_go04 az: 178.2 dist: 22.0
c_lmel az: 177.3 dist: 25.6
cm_uri az: 358.8 dist: 19.8
cx_pb09 az: 170.8 dist: 13.8
Pz
SH
Pr
SVr
30s
50s

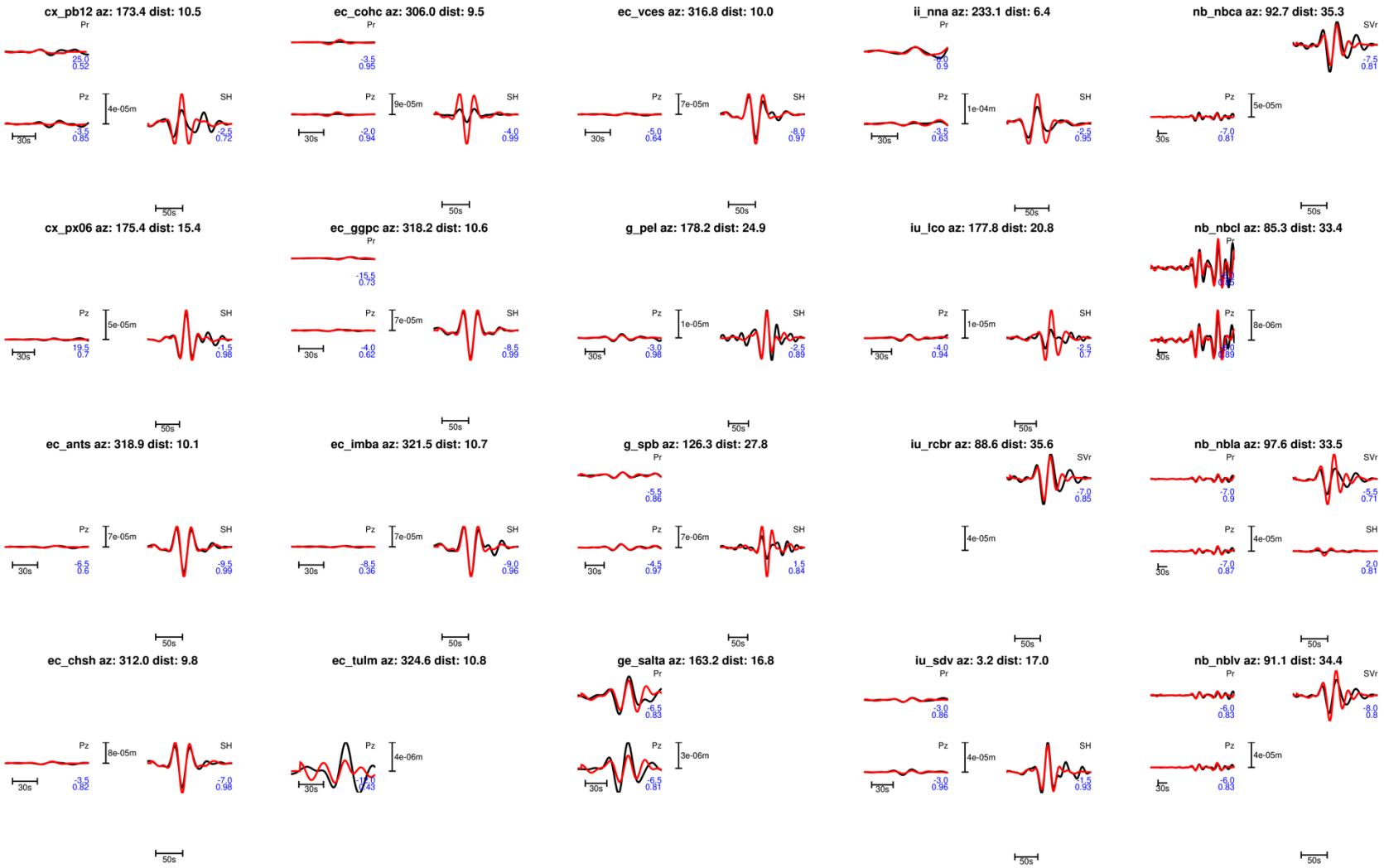
cx_pb12 az: 173.4 dist: 10.5
ec_cohc az: 306.0 dist: 9.5
ec_vces az: 316.8 dist: 10.0
ii_nna az: 233.1 dist: 6.4
nb_nbca az: 92.7 dist: 35.3
cx_px06 az: 175.4 dist: 15.4
ec_ggpc az: 318.2 dist: 10.6
g_pel az: 178.2 dist: 24.9
iu_lco az: 177.8 dist: 20.8
nb_nbcl az: 85.3 dist: 33.4
ec_ants az: 318.9 dist: 10.1
ec_imba az: 321.5 dist: 10.7
g_spb az: 126.3 dist: 27.8
iu_rcbr az: 88.6 dist: 35.6
nb_nbla az: 97.6 dist: 33.5
ec_chsh az: 312.0 dist: 9.8
ec_tulm az: 324.6 dist: 10.8
ge_salta az: 163.2 dist: 16.8
iu_sdv az: 3.2 dist: 17.0
nb_nblv az: 91.1 dist: 34.4
Pr
SVr
Pz
SH
30s
50s

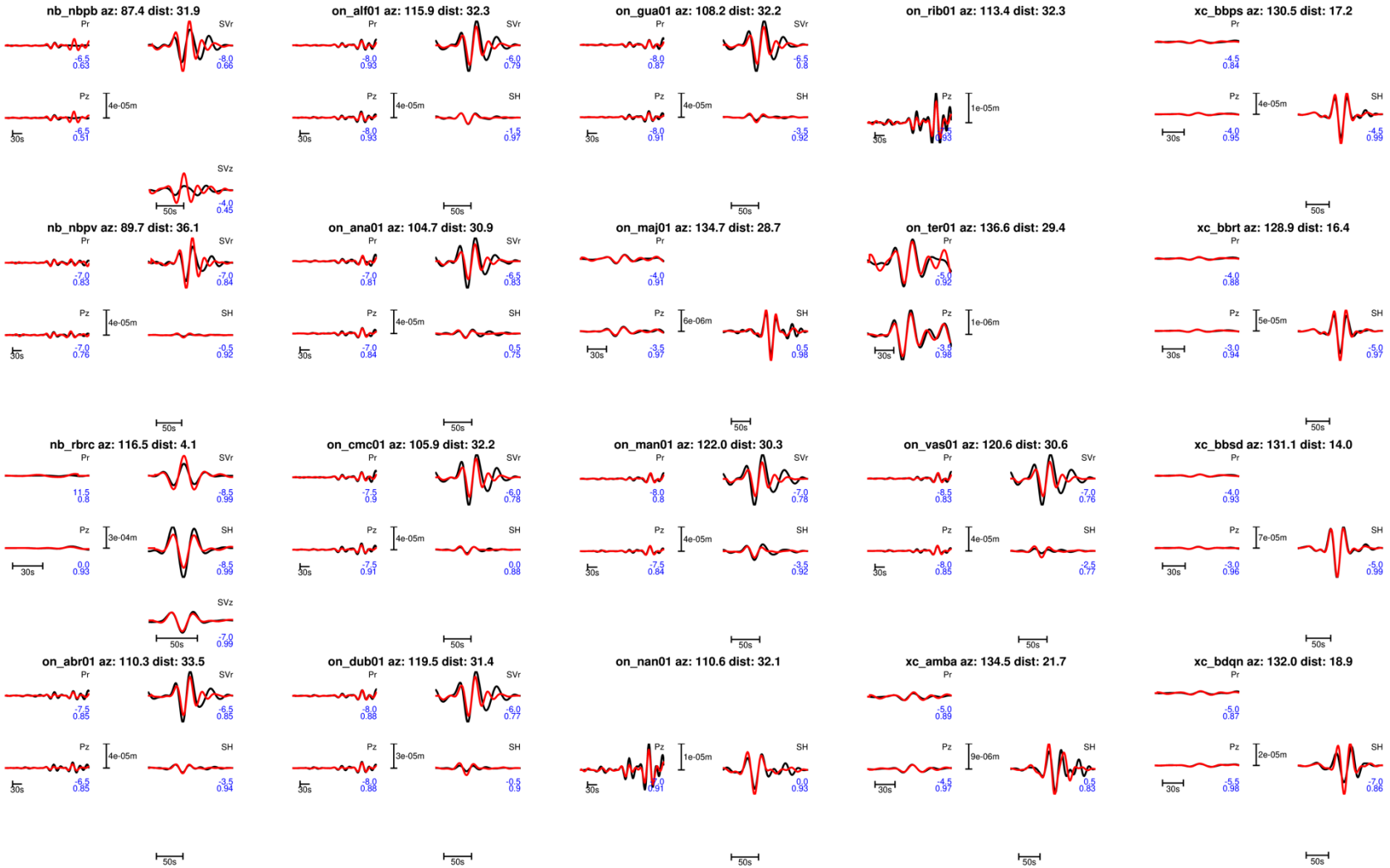
nb_nbpb az: 87.4 dist: 31.9
on_alf01 az: 115.9 dist: 32.3
on_gua01 az: 108.2 dist: 32.2
on_rib01 az: 113.4 dist: 32.3
xc_bbps az: 130.5 dist: 17.2
nb_nbpv az: 89.7 dist: 36.1
on_ana01 az: 104.7 dist: 30.9
on_maj01 az: 134.7 dist: 28.7
on_ter01 az: 136.6 dist: 29.4
xc_bbrt az: 128.9 dist: 16.4
nb_rbrc az: 116.5 dist: 4.1
on_cmc01 az: 105.9 dist: 32.2
on_man01 az: 122.0 dist: 30.3
on_vas01 az: 120.6 dist: 30.6
xc_bbsd az: 131.1 dist: 14.0
on_abr01 az: 110.3 dist: 33.5
on_dub01 az: 119.5 dist: 31.4
on_nan01 az: 110.6 dist: 32.1
xc_amba az: 134.5 dist: 21.7
xc_bdqn az: 132.0 dist: 18.9
Pr
SVr
Pz
SH
SVz
30s
50s

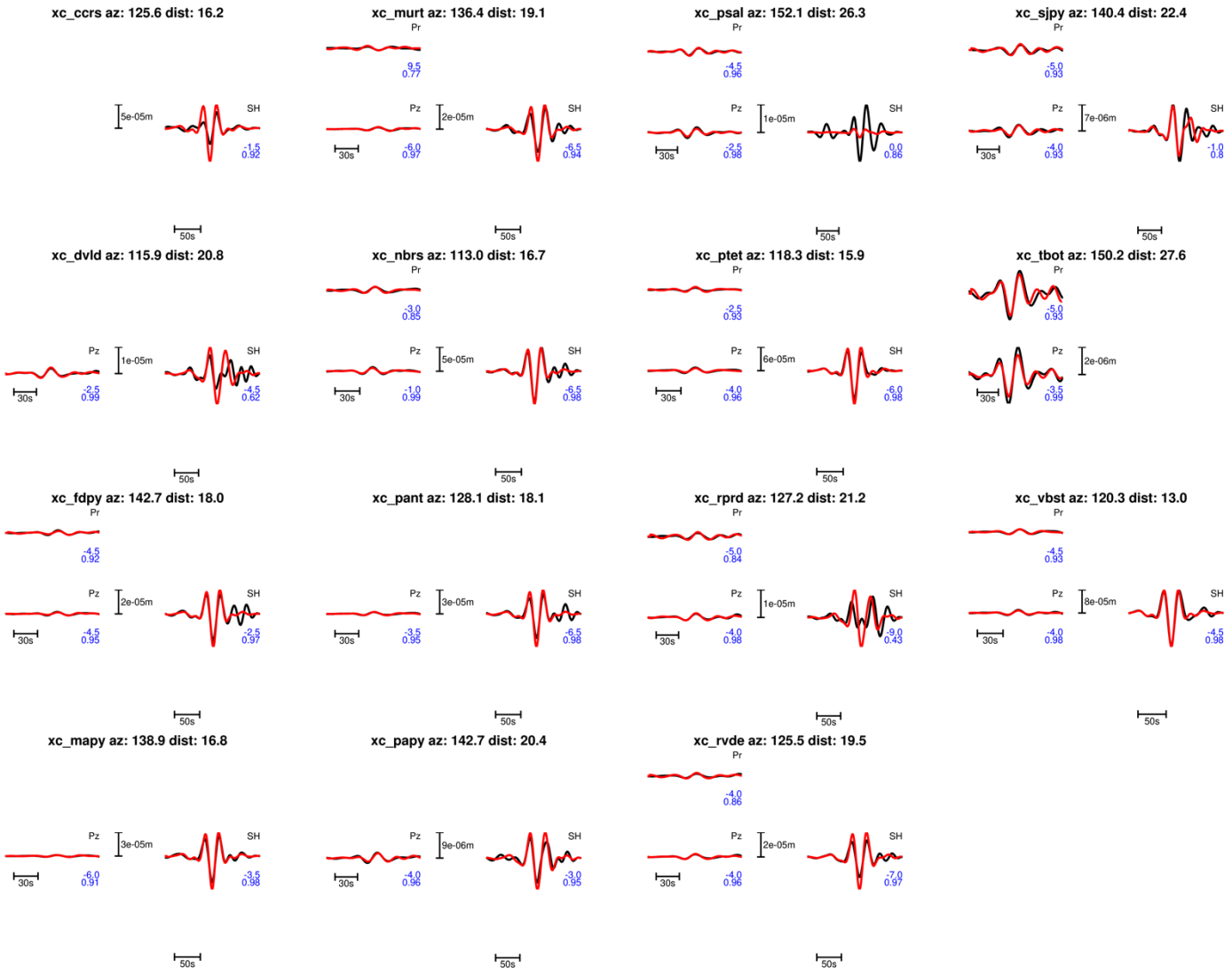
xc_ccrs az: 125.6 dist: 16.2
5e-05m
SH
-1.5
0.92
50s
xc_murt az: 136.4 dist: 19.1
Pr
9.5
0.77
Pz
2e-05m
SH
30s
-6.0
0.97
-6.5
0.94
50s
xc_psal az: 152.1 dist: 26.3
Pr
-4.5
0.96
Pz
1e-05m
SH
30s
-2.5
0.98
0.0
0.86
50s
xc_sjpy az: 140.4 dist: 22.4
Pr
-5.0
0.93
Pz
7e-06m
SH
30s
-4.0
0.93
-1.0
0.8
50s
xc_dvld az: 115.9 dist: 20.8
Pz
1e-05m
SH
30s
-2.5
0.99
-4.5
0.62
50s
xc_nbrs az: 113.0 dist: 16.7
Pr
-3.0
0.85
Pz
5e-05m
SH
30s
-1.0
0.99
-6.5
0.98
50s
xc_ptet az: 118.3 dist: 15.9
Pr
-2.5
0.93
Pz
6e-05m
SH
30s
-4.0
0.96
-6.0
0.98
50s
xc_tbot az: 150.2 dist: 27.6
Pr
-5.0
0.93
Pz
2e-06m
30s
-3.5
0.99
50s
xc_fdpy az: 142.7 dist: 18.0
Pr
-4.5
0.92
Pz
2e-05m
SH
30s
-4.5
0.95
-2.5
0.97
50s
xc_pant az: 128.1 dist: 18.1
Pz
3e-05m
SH
30s
-3.5
0.95
-6.5
0.98
50s
xc_rprd az: 127.2 dist: 21.2
Pr
-5.0
0.84
Pz
1e-05m
SH
30s
-4.0
0.98
-9.0
0.43
50s
xc_vbst az: 120.3 dist: 13.0
Pr
-4.5
0.93
Pz
8e-05m
SH
30s
-4.0
0.98
-4.5
0.98
50s
xc_mapy az: 138.9 dist: 16.8
Pz
3e-05m
SH
30s
-6.0
0.91
-3.5
0.98
50s
xc_papy az: 142.7 dist: 20.4
Pz
9e-06m
SH
30s
-4.0
0.96
-3.0
0.95
50s
xc_rvde az: 125.5 dist: 19.5
Pr
-4.0
0.86
Pz
2e-05m
SH
30s
-4.0
0.96
-7.0
0.97
50s

Figure S22. Inversion results for event 35. a) Map showing the preferred solution in b and the distribution of the 10 stations (17 traces) used in the inversion. Solution parameters are given below the map. Dashed circles indicate radii of 5º and 30º from epicenter; b) Distribution of focal mechanisms with centroid depths pointing to 564 km as the preferred solution for the event. In this case, we had to perform 5 additional inversions (644-684 km) to investigate a suspect decrease in the rms towards greater depths; c) Waveform fitting produced by the preferred solution. Black and red lines denote observations and synthetics, respectively. Azimuths and distances in degrees are shown above panels. Time shifts (top) and cross-correlation coefficients (bottom) are shown in blue at the lower right corner of each panel. Wave segments (Pr, Pz, SVr, SH and SVz) are identified at the upper right corners.

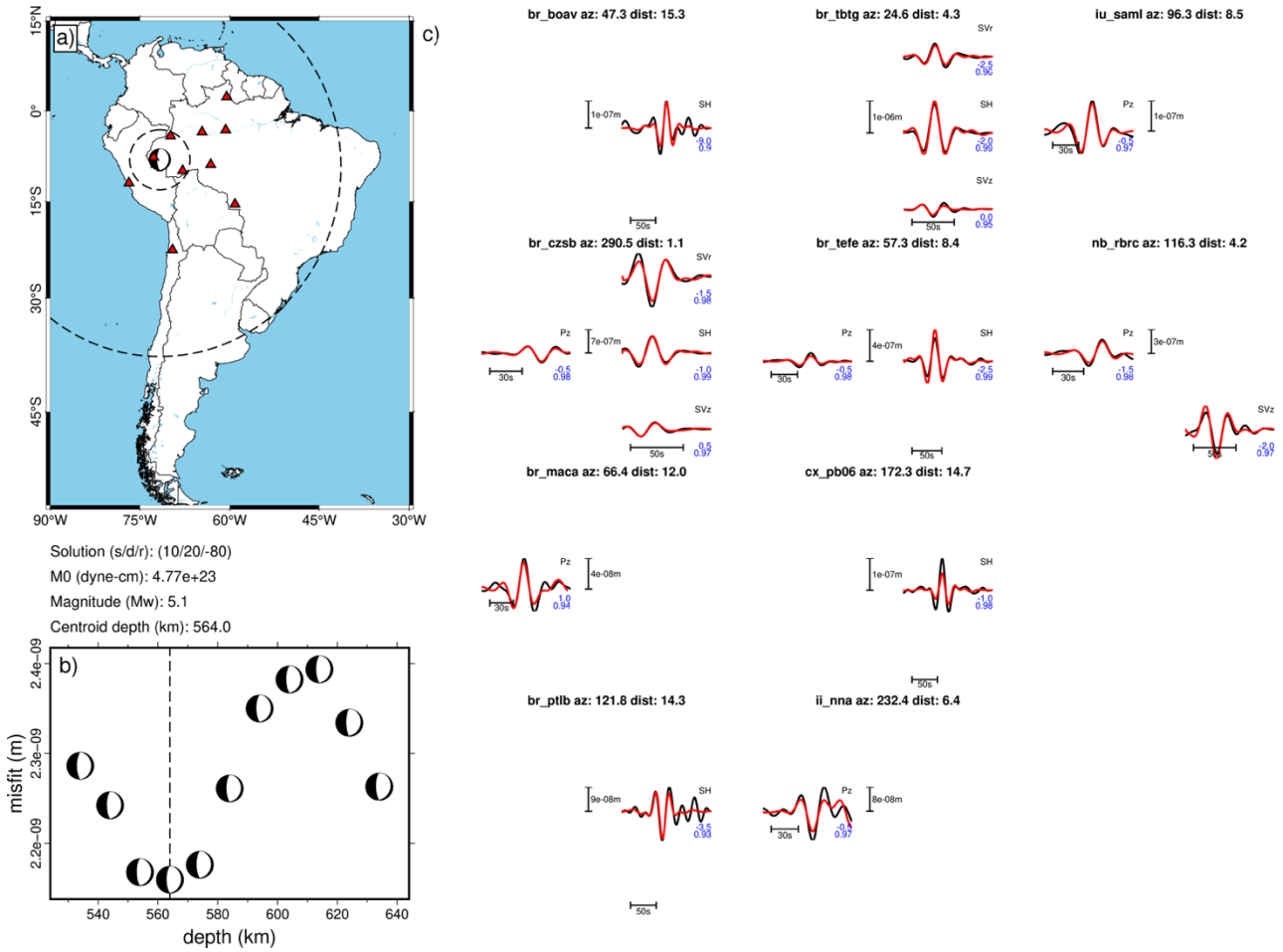

Figure S23. Inversion results for event 37. a) Map showing the preferred solution in b and the distribution of the 3 stations (8 traces) used in the inversion. Solution parameters are given below the map. Dashed circles indicate radii of 5º and 30º from epicenter; b) Distribution of focal mechanisms with centroid depths. We selected 557 km as the preferred solution for the event, fixing to the hypocenter depth in Table 1; c) Waveform fitting produced by the preferred solution. Black and red lines denote observations and synthetics, respectively. Azimuths and distances in degrees are shown above panels. Time shifts (top) and cross-correlation coefficients (bottom) are shown in blue at the lower right corner of each panel. Wave segments (Pr, Pz, SVr, SH and SVz) are identified at the upper right corners.

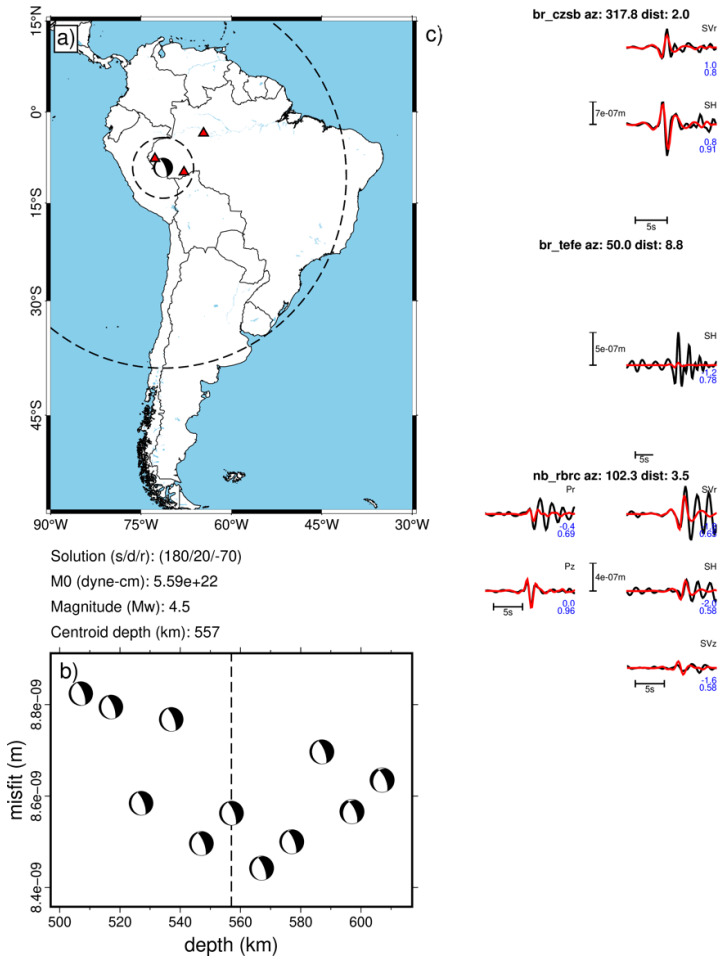

Figure S24. Inversion results for event 38. a) Map showing the preferred solution in b and the distribution of the 81 stations (128 traces) used in the inversion. Solution parameters are given below the map. Dashed circles indicate radii of 5º and 30º from epicenter; b) Distribution of focal mechanisms with centroid depths pointing to 599 km as the preferred solution for the event; c) Waveform fitting produced by the preferred solution. Black and red lines denote observations and synthetics, respectively. Azimuths and distances in degrees are shown above panels. Time shifts (top) and cross-correlation coefficients (bottom) are shown in blue at the lower right corner of each panel. Wave segments (Pr, Pz, SVr, SH and SVz) are identified at the upper right corners.

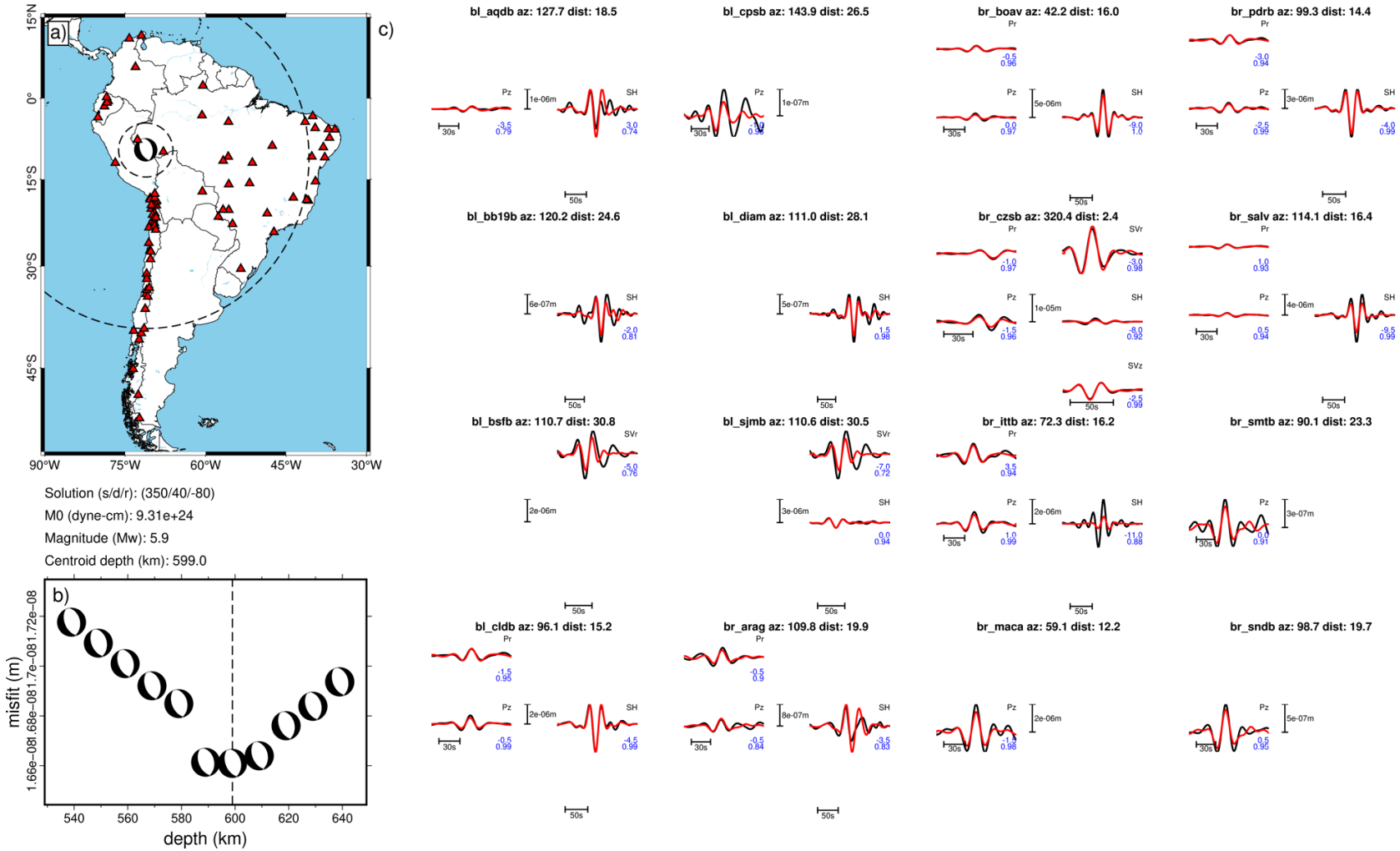

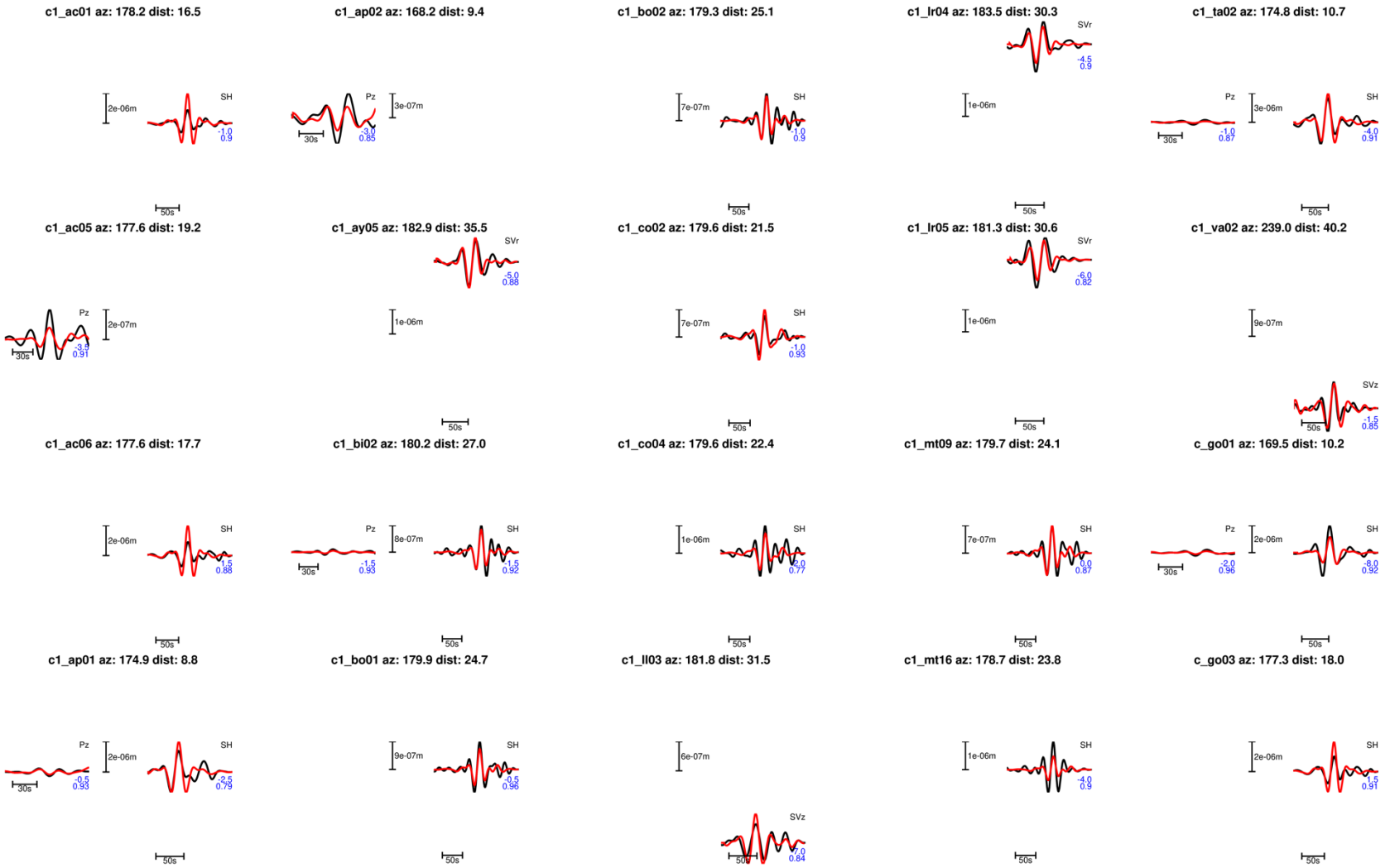
c1_ac01 az: 178.2 dist: 16.5
c1_ap02 az: 168.2 dist: 9.4
c1_bo02 az: 179.3 dist: 25.1
c1_lr04 az: 183.5 dist: 30.3
c1_ta02 az: 174.8 dist: 10.7
c1_ac05 az: 177.6 dist: 19.2
c1_ay05 az: 182.9 dist: 35.5
c1_co02 az: 179.6 dist: 21.5
c1_lr05 az: 181.3 dist: 30.6
c1_va02 az: 239.0 dist: 40.2
c1_ac06 az: 177.6 dist: 17.7
c1_bi02 az: 180.2 dist: 27.0
c1_co04 az: 179.6 dist: 22.4
c1_mt09 az: 179.7 dist: 24.1
c_go01 az: 169.5 dist: 10.2
c1_ap01 az: 174.9 dist: 8.8
c1_bo01 az: 179.9 dist: 24.7
c1_ll03 az: 181.8 dist: 31.5
c1_mt16 az: 178.7 dist: 23.8
c_go03 az: 177.3 dist: 18.0
SH
SVr
SVz
Pz
50s
30s

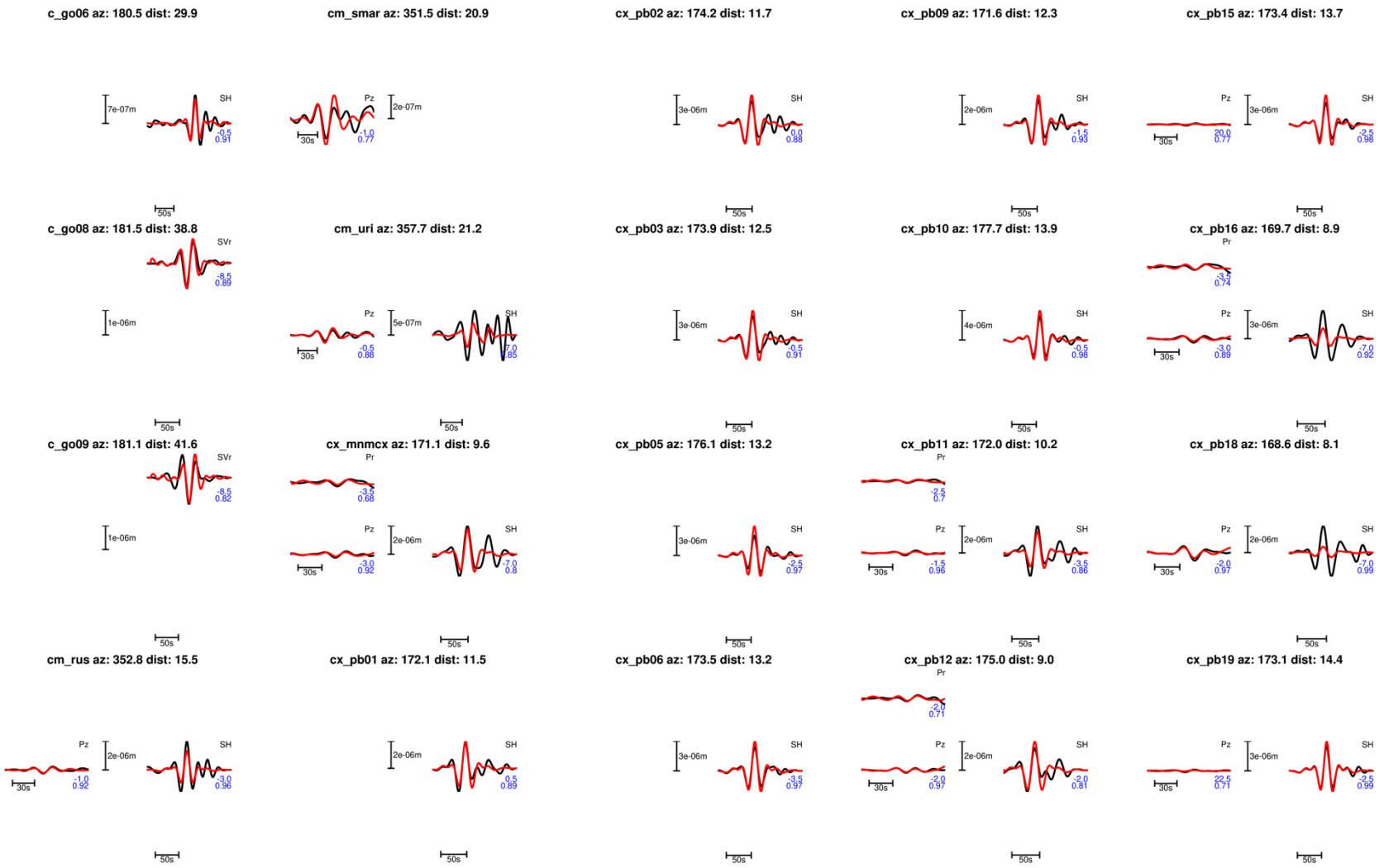
c_go06 az: 180.5 dist: 29.9
cm_smar az: 351.5 dist: 20.9
cx_pb02 az: 174.2 dist: 11.7
cx_pb09 az: 171.6 dist: 12.3
cx_pb15 az: 173.4 dist: 13.7
c_go08 az: 181.5 dist: 38.8
cm_uri az: 357.7 dist: 21.2
cx_pb03 az: 173.9 dist: 12.5
cx_pb10 az: 177.7 dist: 13.9
cx_pb16 az: 169.7 dist: 8.9
c_go09 az: 181.1 dist: 41.6
cx_mnmcx az: 171.1 dist: 9.6
cx_pb05 az: 176.1 dist: 13.2
cx_pb11 az: 172.0 dist: 10.2
cx_pb18 az: 168.6 dist: 8.1
cm_rus az: 352.8 dist: 15.5
cx_pb01 az: 172.1 dist: 11.5
cx_pb06 az: 173.5 dist: 13.2
cx_pb12 az: 175.0 dist: 9.0
cx_pb19 az: 173.1 dist: 14.4

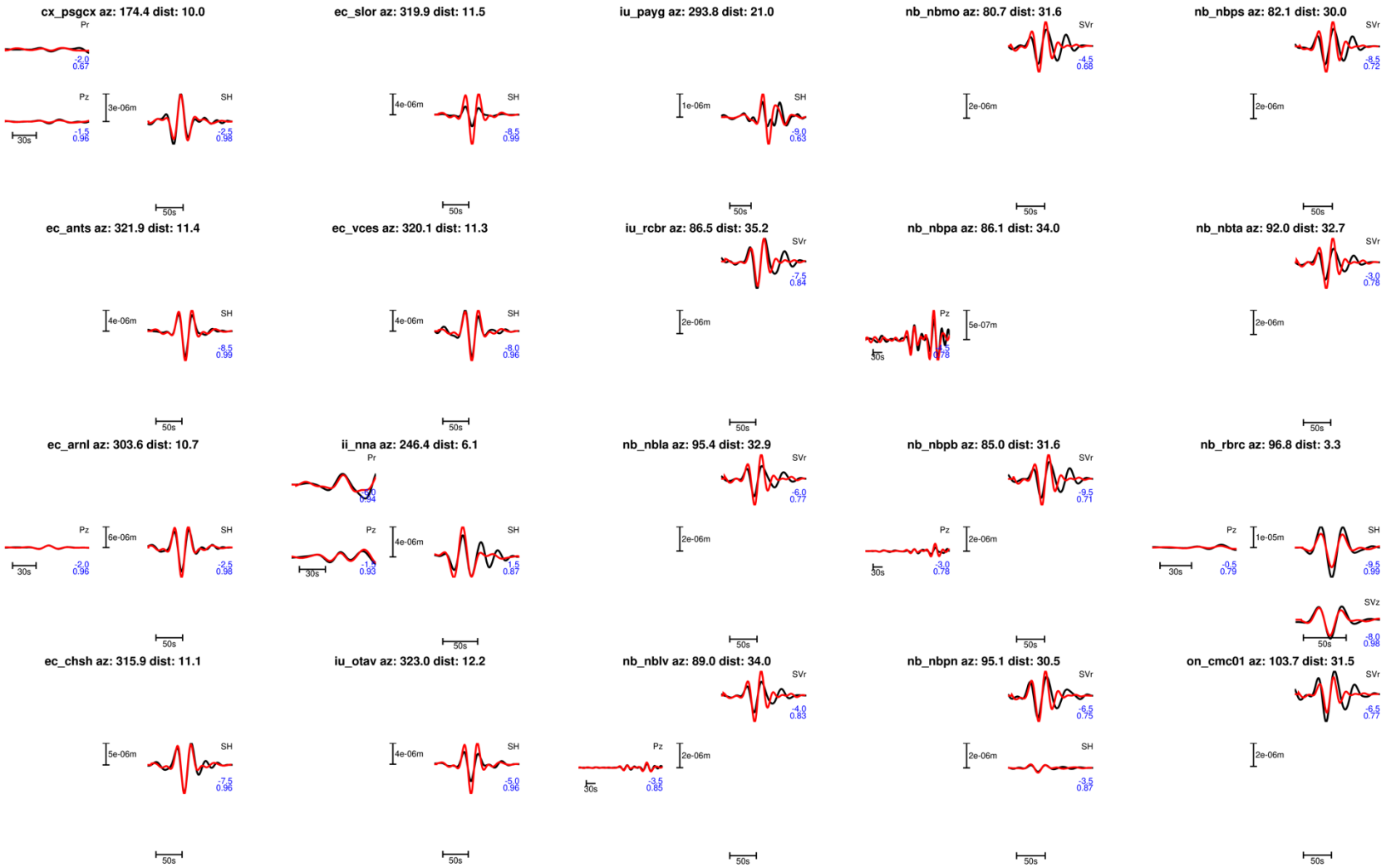
cx_psgcx az: 174.4 dist: 10.0
ec_slor az: 319.9 dist: 11.5
iu_payg az: 293.8 dist: 21.0
nb_nbmo az: 80.7 dist: 31.6
nb_nbps az: 82.1 dist: 30.0
ec_ants az: 321.9 dist: 11.4
ec_vces az: 320.1 dist: 11.3
iu_rcbr az: 86.5 dist: 35.2
nb_nbpa az: 86.1 dist: 34.0
nb_nbta az: 92.0 dist: 32.7
ec_arnl az: 303.6 dist: 10.7
ii_nna az: 246.4 dist: 6.1
nb_nbla az: 95.4 dist: 32.9
nb_nbpb az: 85.0 dist: 31.6
nb_rbrc az: 96.8 dist: 3.3
ec_chsh az: 315.9 dist: 11.1
iu_otav az: 323.0 dist: 12.2
nb_nblv az: 89.0 dist: 34.0
nb_nbpn az: 95.1 dist: 30.5
on_cmc01 az: 103.7 dist: 31.5
Pr
Pz
SH
SVr
SVz
50s
30s

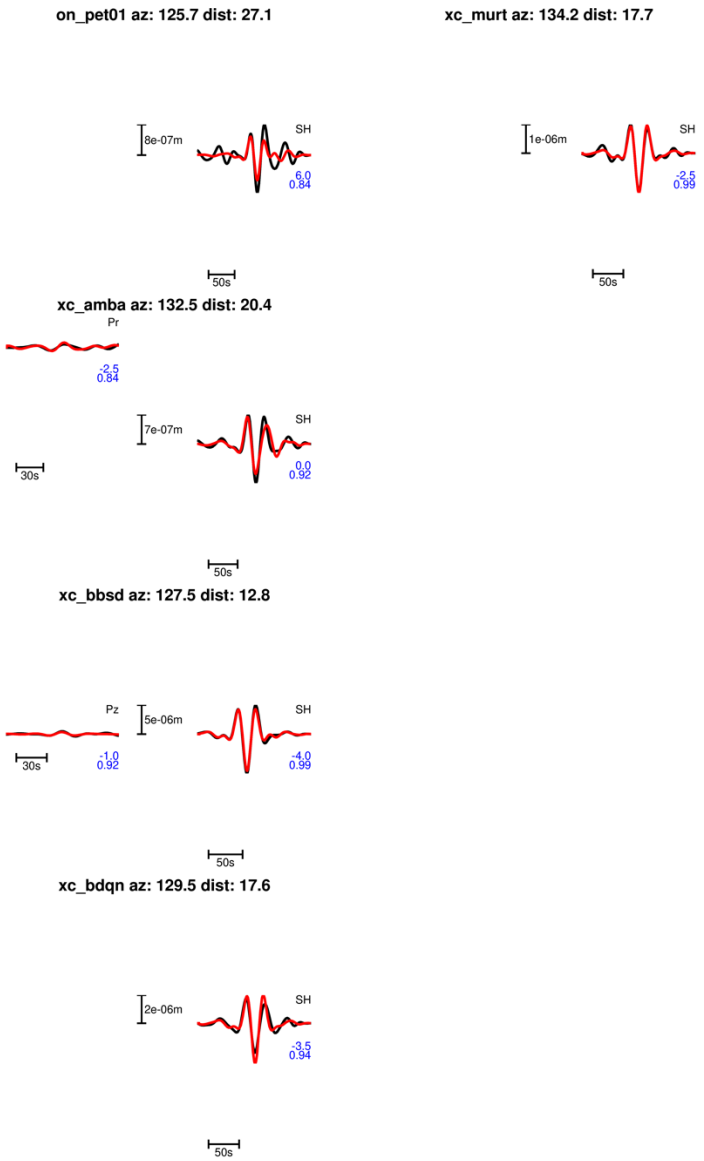
on_pet01 az: 125.7 dist: 27.1
8e-07m
SH
6.0
0.84
50s
xc_murt az: 134.2 dist: 17.7
1e-06m
SH
-2.5
0.99
50s
xc_amba az: 132.5 dist: 20.4
Pr
-2.5
0.84
7e-07m
SH
0.0
0.92
30s
50s
xc_bbsd az: 127.5 dist: 12.8
Pz
-1.0
0.92
30s
5e-06m
SH
-4.0
0.99
50s
xc_bdqn az: 129.5 dist: 17.6
2e-06m
SH
-3.5
0.94
50s

Figure S25. Inversion results for event 39. a) Map showing the preferred solution in b and the distribution of the 2 stations (6 traces) used in the inversion. Solution parameters are given below the map. Dashed circles indicate radii of 5º and 30º from epicenter; b) Distribution of focal mechanisms with centroid depths pointing to 605 km as the preferred solution for the event; c) Waveform fitting produced by the preferred solution. Black and red lines denote observations and synthetics, respectively. Azimuths and distances in degrees are shown above panels. Time shifts (top) and cross-correlation coefficients (bottom) are shown in blue at the lower right corner of each panel. Wave segments (Pr, Pz, SVr, SH and SVz) are identified at the upper right corners.

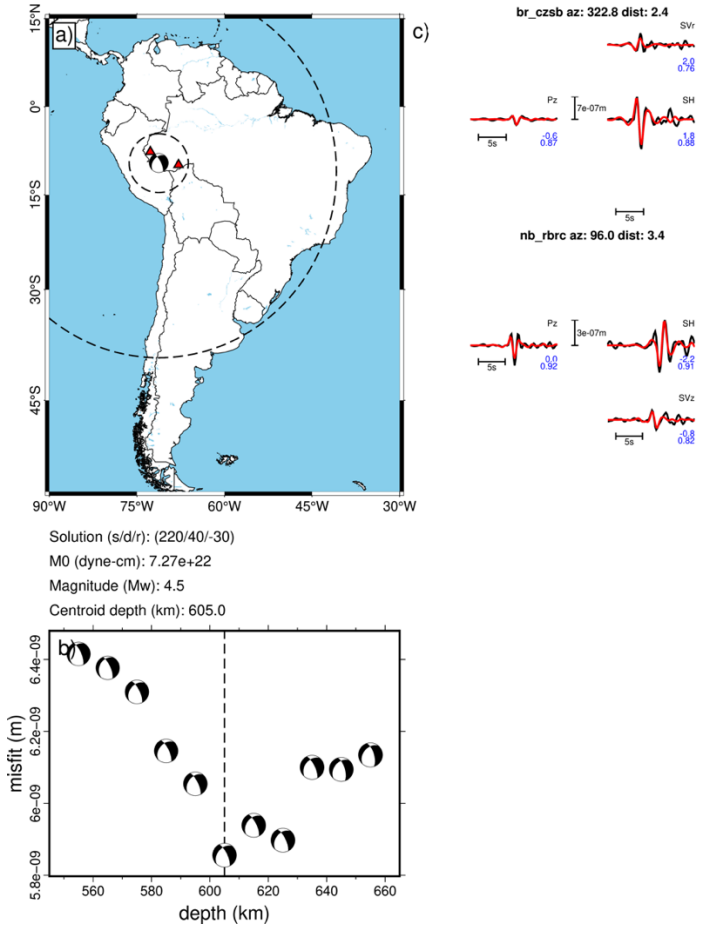

Figure S26. Inversion results for event 40. a) Map showing the preferred solution in b and the distribution of the 4 stations (7 traces) used in the inversion. Solution parameters are given below the map. Dashed circles indicate radii of 5º and 30º from epicenter; b) Distribution of focal mechanisms with centroid depths. We selected 580 km as the preferred solution for the event, fixing to the hypocenter depth in Table 1; c) Waveform fitting produced by the preferred solution. Black and red lines denote observations and synthetics, respectively. Azimuths and distances in degrees are shown above panels. Time shifts (top) and cross-correlation coefficients (bottom) are shown in blue at the lower right corner of each panel. Wave segments (Pr, Pz, SVr, SH and SVz) are identified at the upper right corners.

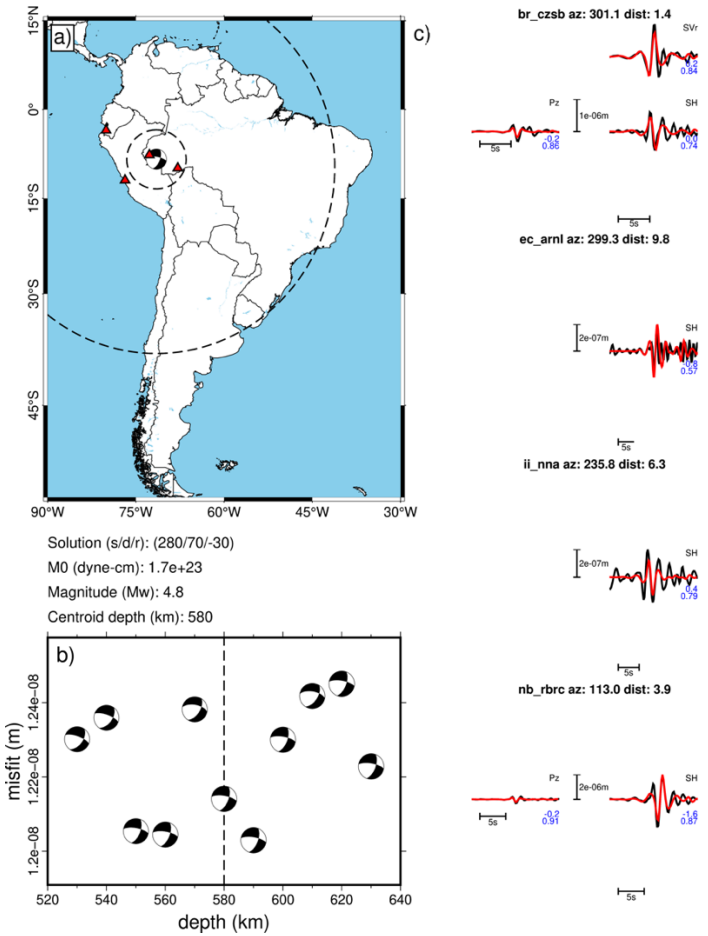

Figure S27. Inversion results for event 41. a) Map showing the preferred solution in b and the distribution of the 125 stations (323 traces) used in the inversion. Solution parameters are given below the map. Dashed circles indicate radii of 5º and 30º from epicenter; b) Distribution of focal mechanisms with centroid depths pointing to 623 km as the preferred solution for the event; c) Waveform fitting produced by the preferred solution. Black and red lines denote observations and synthetics, respectively. Time shifts (top) and cross-correlation coefficients (bottom) are shown in blue at the lower right corner of each panel. Wave segments (Pr, Pz, SVr, SH and SVz) are identified at the upper right corners.

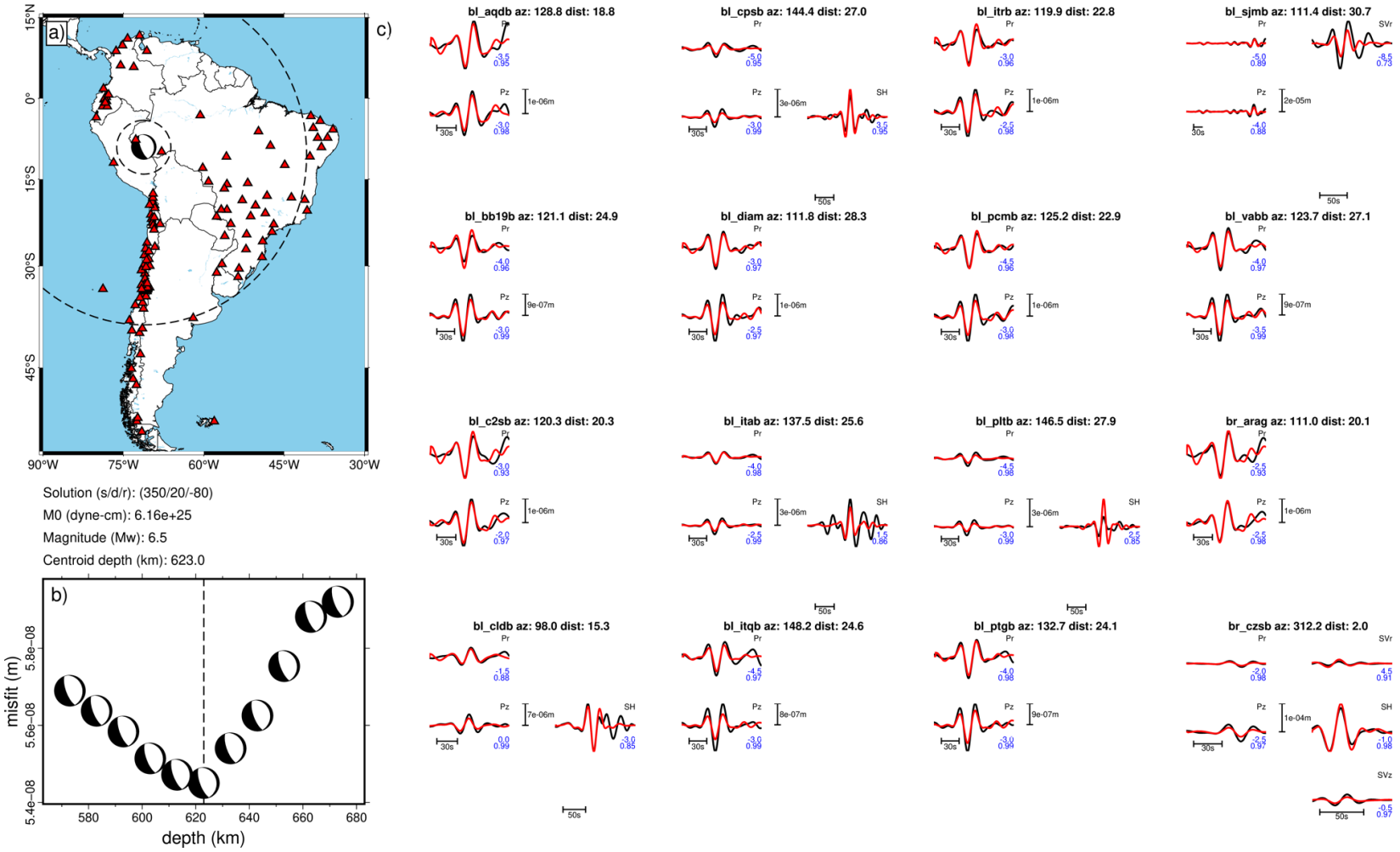

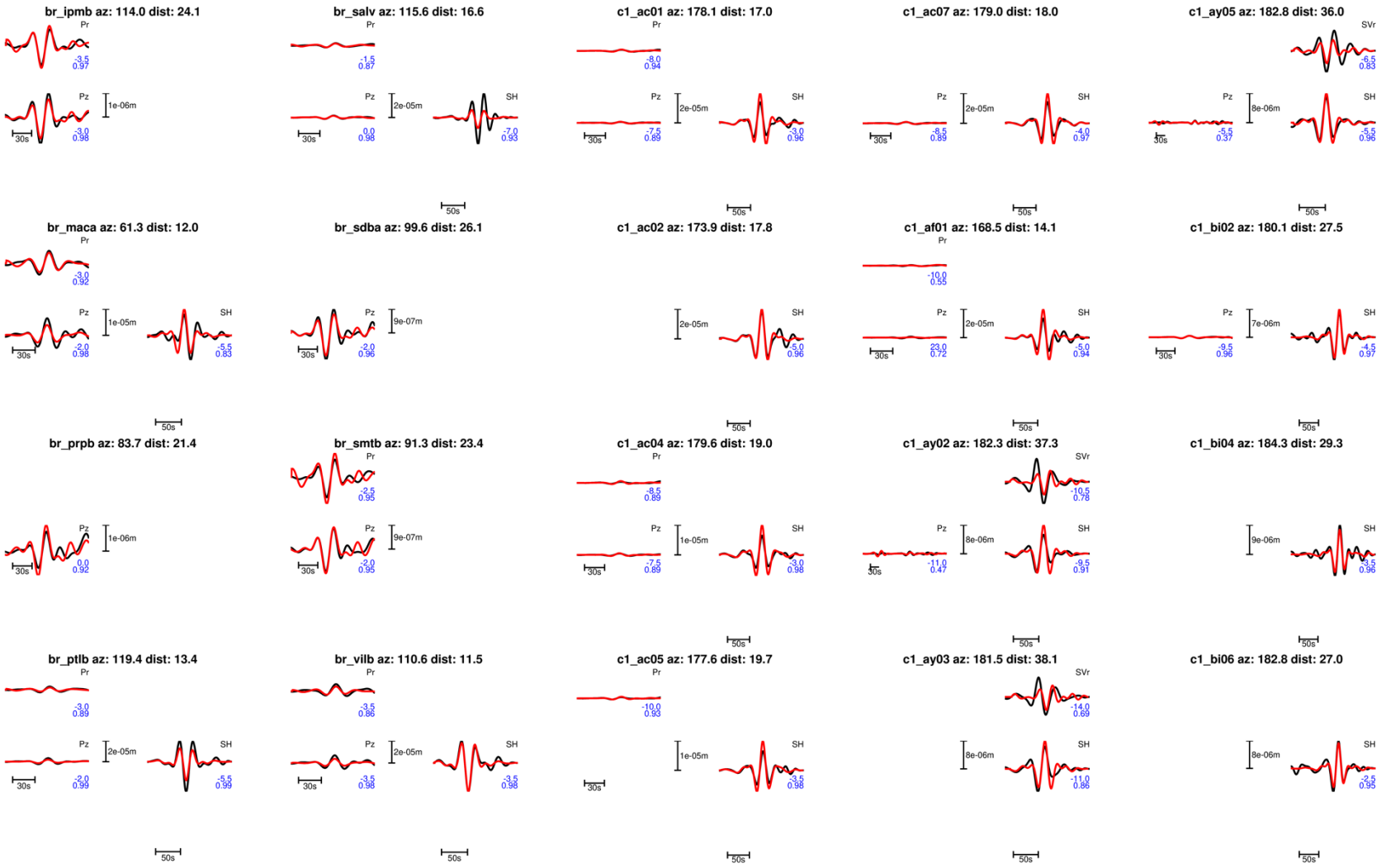
br_ipmb az: 114.0 dist: 24.1
br_salv az: 115.6 dist: 16.6
c1_ac01 az: 178.1 dist: 17.0
c1_ac07 az: 179.0 dist: 18.0
c1_ay05 az: 182.8 dist: 36.0
br_maca az: 61.3 dist: 12.0
br_sdba az: 99.6 dist: 26.1
c1_ac02 az: 173.9 dist: 17.8
c1_af01 az: 168.5 dist: 14.1
c1_bi02 az: 180.1 dist: 27.5
br_prpb az: 83.7 dist: 21.4
br_smtb az: 91.3 dist: 23.4
c1_ac04 az: 179.6 dist: 19.0
c1_ay02 az: 182.3 dist: 37.3
c1_bi04 az: 184.3 dist: 29.3
br_ptlb az: 119.4 dist: 13.4
br_vilb az: 110.6 dist: 11.5
c1_ac05 az: 177.6 dist: 19.7
c1_ay03 az: 181.5 dist: 38.1
c1_bi06 az: 182.8 dist: 27.0
Pr
Pz
SH
SVr
30s
50s

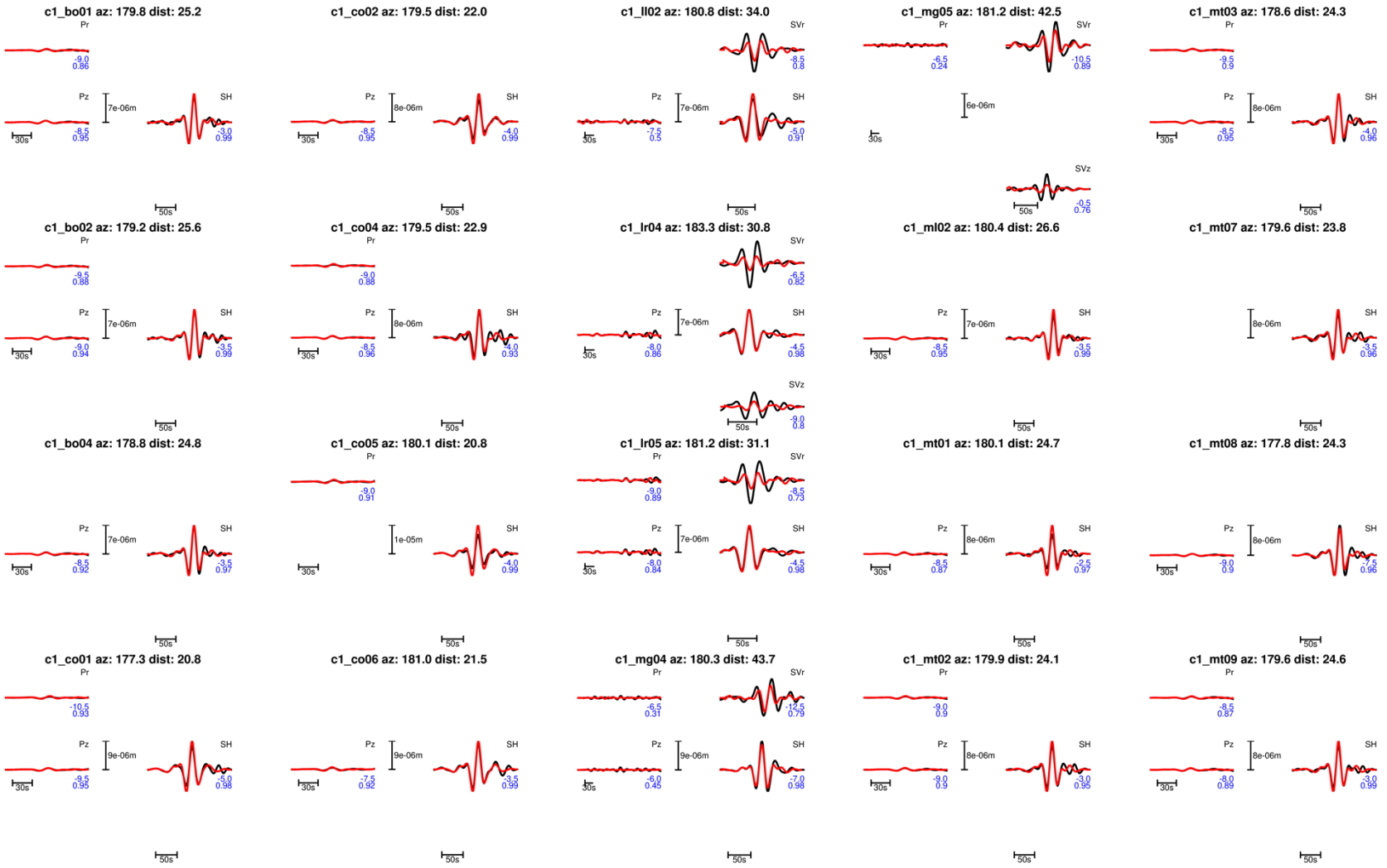
c1_bo01 az: 179.8 dist: 25.2
c1_co02 az: 179.5 dist: 22.0
c1_ll02 az: 180.8 dist: 34.0
c1_mg05 az: 181.2 dist: 42.5
c1_mt03 az: 178.6 dist: 24.3
c1_bo02 az: 179.2 dist: 25.6
c1_co04 az: 179.5 dist: 22.9
c1_lr04 az: 183.3 dist: 30.8
c1_ml02 az: 180.4 dist: 26.6
c1_mt07 az: 179.6 dist: 23.8
c1_bo04 az: 178.8 dist: 24.8
c1_co05 az: 180.1 dist: 20.8
c1_lr05 az: 181.2 dist: 31.1
c1_mt01 az: 180.1 dist: 24.7
c1_mt08 az: 177.8 dist: 24.3
c1_co01 az: 177.3 dist: 20.8
c1_co06 az: 181.0 dist: 21.5
c1_mg04 az: 180.3 dist: 43.7
c1_mt02 az: 179.9 dist: 24.1
c1_mt09 az: 179.6 dist: 24.6
Pr
Pz
SH
SVr
SVz
30s
50s

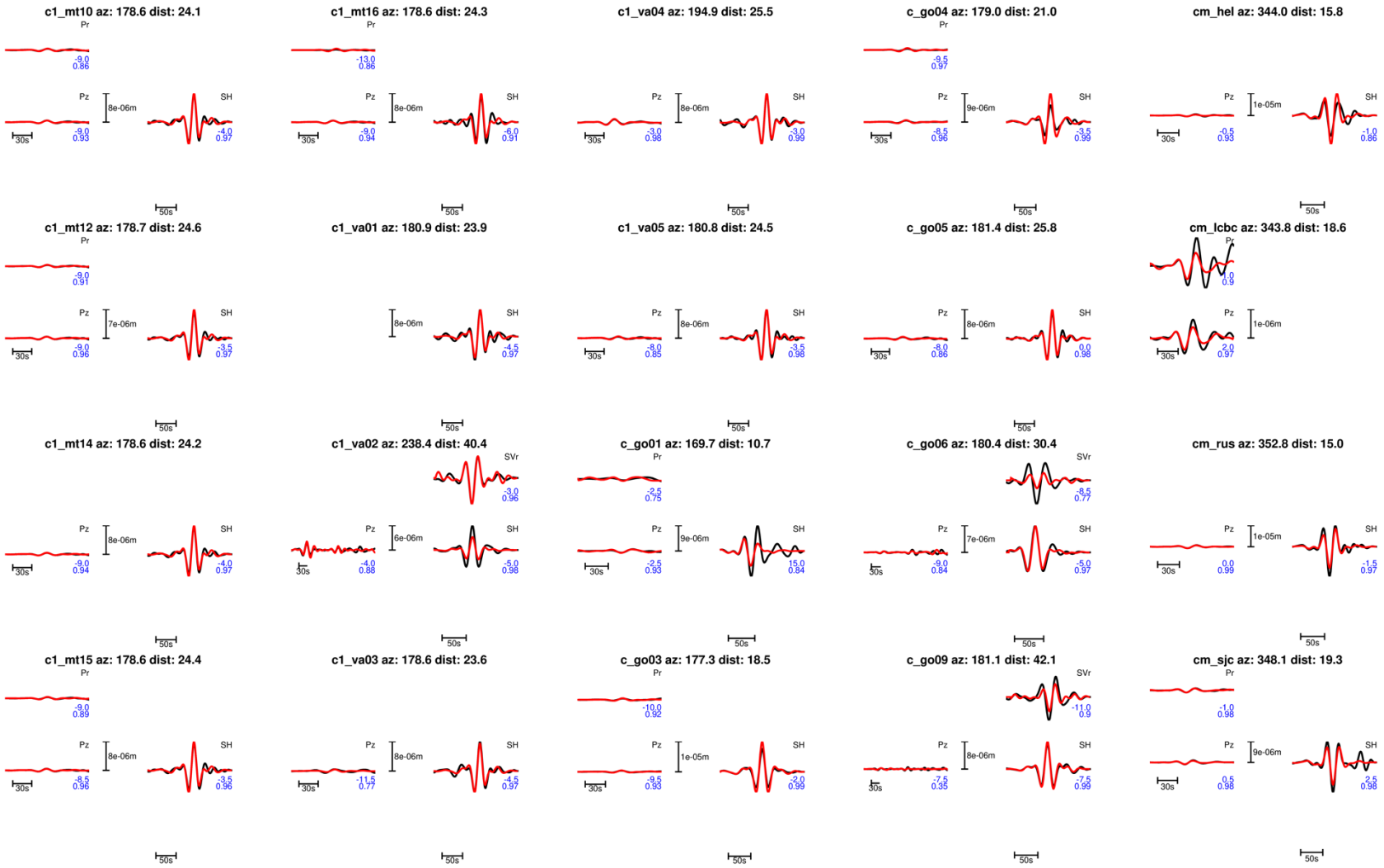
c1_mt10 az: 178.6 dist: 24.1
c1_mt16 az: 178.6 dist: 24.3
c1_va04 az: 194.9 dist: 25.5
c_go04 az: 179.0 dist: 21.0
cm_hel az: 344.0 dist: 15.8
c1_mt12 az: 178.7 dist: 24.6
c1_va01 az: 180.9 dist: 23.9
c1_va05 az: 180.8 dist: 24.5
c_go05 az: 181.4 dist: 25.8
cm_lcbc az: 343.8 dist: 18.6
c1_mt14 az: 178.6 dist: 24.2
c1_va02 az: 238.4 dist: 40.4
c_go01 az: 169.7 dist: 10.7
c_go06 az: 180.4 dist: 30.4
cm_rus az: 352.8 dist: 15.0
c1_mt15 az: 178.6 dist: 24.4
c1_va03 az: 178.6 dist: 23.6
c_go03 az: 177.3 dist: 18.5
c_go09 az: 181.1 dist: 42.1
cm_sjc az: 348.1 dist: 19.3
Pr
Pz
SH
SVr
30s
50s

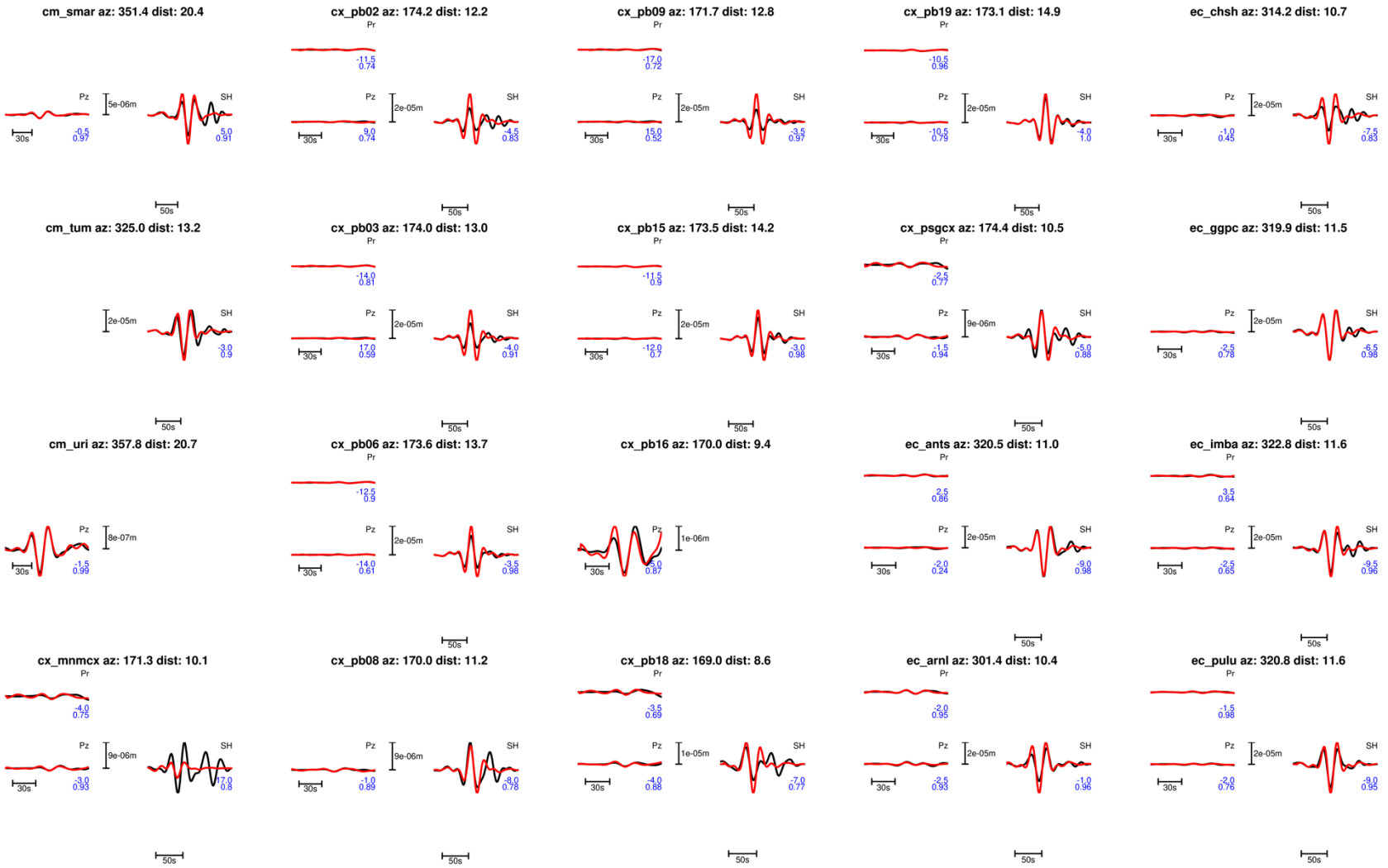
cm_smar az: 351.4 dist: 20.4
cx_pb02 az: 174.2 dist: 12.2
cx_pb09 az: 171.7 dist: 12.8
cx_pb19 az: 173.1 dist: 14.9
ec_chsh az: 314.2 dist: 10.7
cm_tum az: 325.0 dist: 13.2
cx_pb03 az: 174.0 dist: 13.0
cx_pb15 az: 173.5 dist: 14.2
cx_psgcx az: 174.4 dist: 10.5
ec_ggpc az: 319.9 dist: 11.5
cm_uri az: 357.8 dist: 20.7
cx_pb06 az: 173.6 dist: 13.7
cx_pb16 az: 170.0 dist: 9.4
ec_ants az: 320.5 dist: 11.0
ec_imba az: 322.8 dist: 11.6
cx_mnmcx az: 171.3 dist: 10.1
cx_pb08 az: 170.0 dist: 11.2
cx_pb18 az: 169.0 dist: 8.6
ec_arnl az: 301.4 dist: 10.4
ec_pulu az: 320.8 dist: 11.6
Pr
Pz
SH
30s
50s

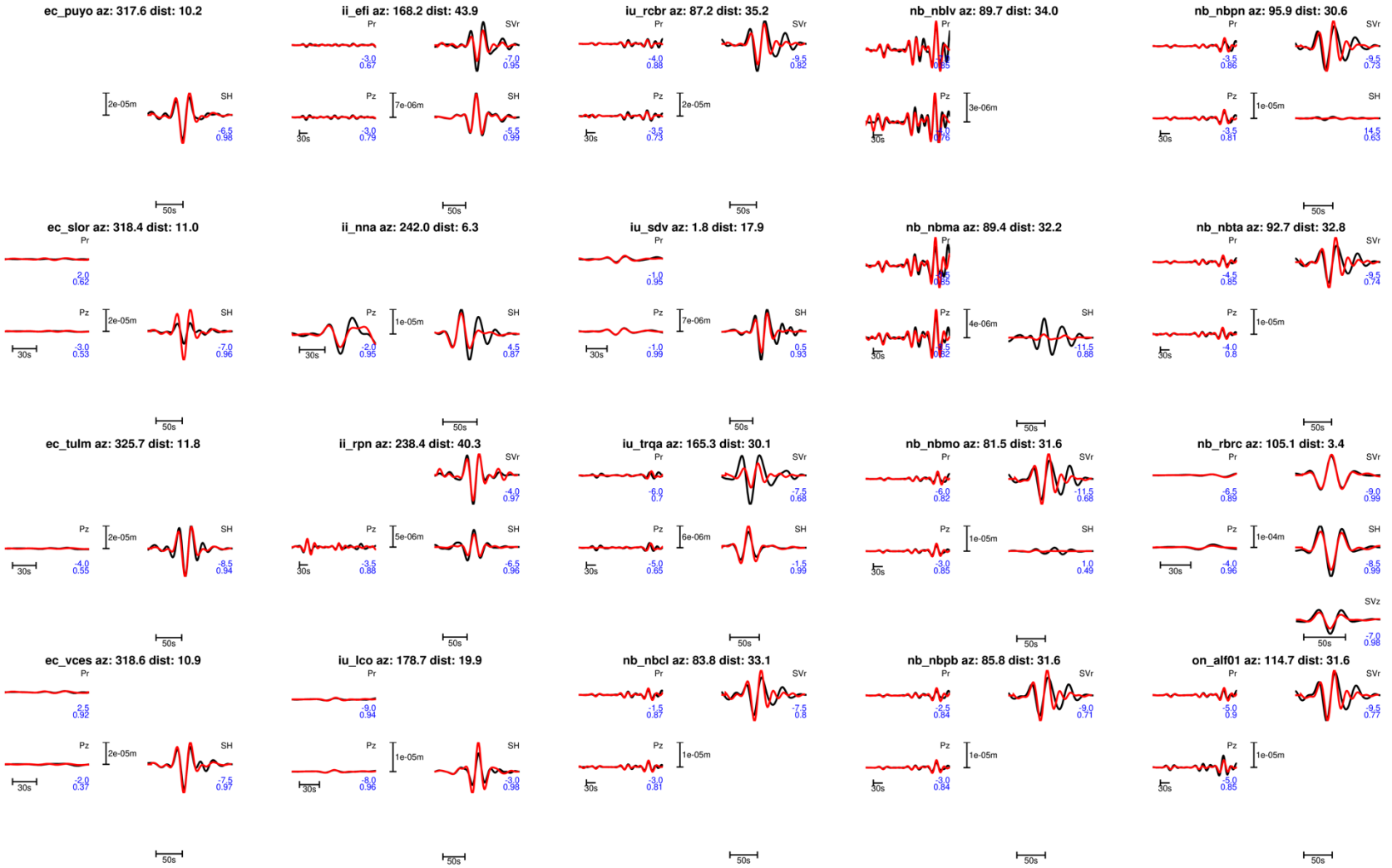
ec_puyo az: 317.6 dist: 10.2
ii_efi az: 168.2 dist: 43.9
iu_rcbr az: 87.2 dist: 35.2
nb_nblv az: 89.7 dist: 34.0
nb_nbpn az: 95.9 dist: 30.6
ec_slor az: 318.4 dist: 11.0
ii_nna az: 242.0 dist: 6.3
iu_sdv az: 1.8 dist: 17.9
nb_nbma az: 89.4 dist: 32.2
nb_nbta az: 92.7 dist: 32.8
ec_tulm az: 325.7 dist: 11.8
ii_rpn az: 238.4 dist: 40.3
iu_trqa az: 165.3 dist: 30.1
nb_nbmo az: 81.5 dist: 31.6
nb_rbrc az: 105.1 dist: 3.4
ec_vces az: 318.6 dist: 10.9
iu_lco az: 178.7 dist: 19.9
nb_nbcl az: 83.8 dist: 33.1
nb_nbpb az: 85.8 dist: 31.6
on_alf01 az: 114.7 dist: 31.6
Pr
SVr
Pz
SH
SVz
50s
30s

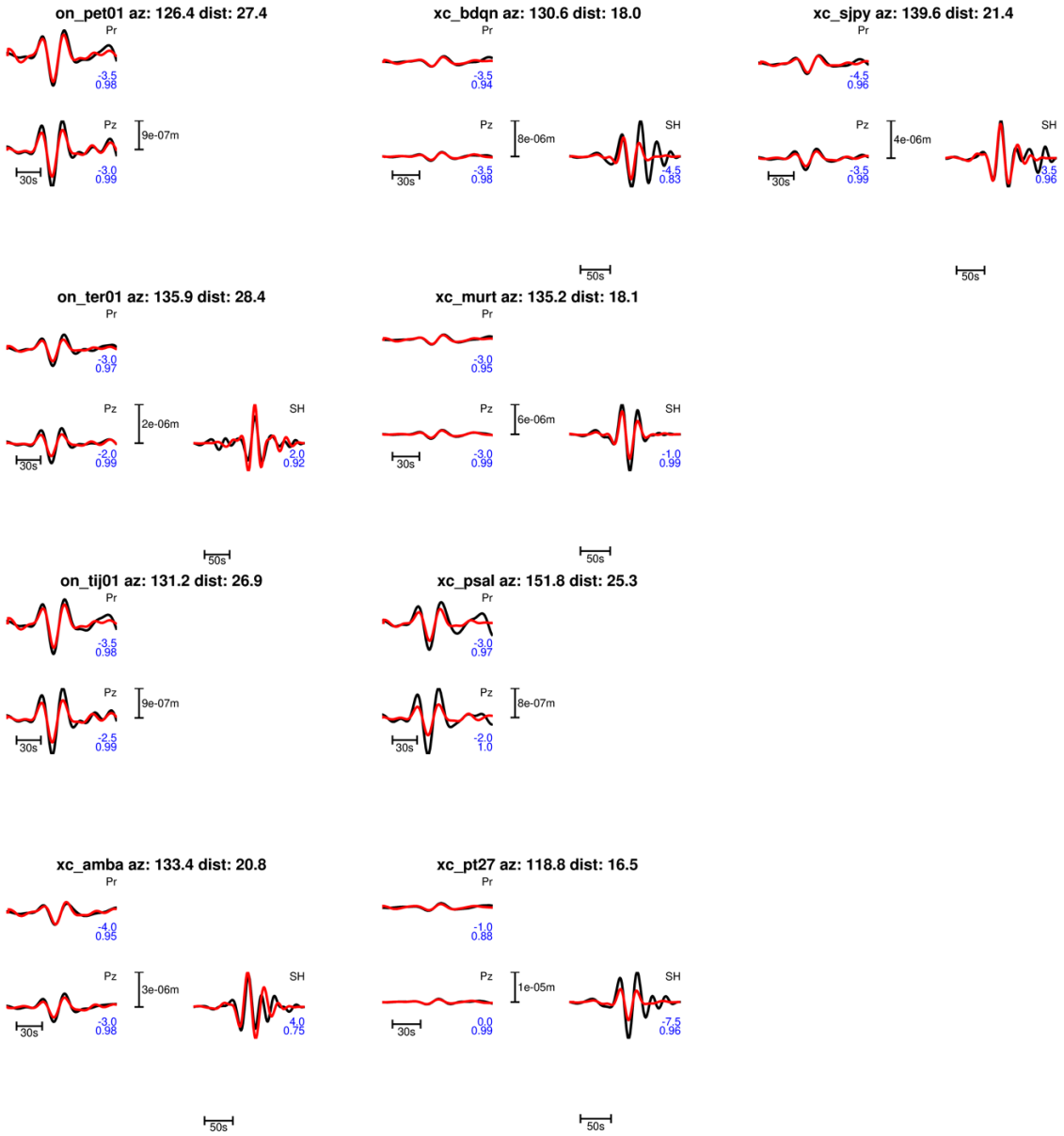
on_pet01 az: 126.4 dist: 27.4
Pr
-3.5
0.98
Pz
9e-07m
-3.0
0.99
30s
xc_bdqn az: 130.6 dist: 18.0
Pr
-3.5
0.94
Pz
8e-06m
SH
-3.5
0.98
-4.5
0.83
30s
50s
xc_sjpy az: 139.6 dist: 21.4
Pr
-4.5
0.96
Pz
4e-06m
SH
-3.5
0.99
-3.5
0.96
30s
50s
on_ter01 az: 135.9 dist: 28.4
Pr
-3.0
0.97
Pz
2e-06m
SH
-2.0
0.99
2.0
0.92
30s
50s
xc_murt az: 135.2 dist: 18.1
Pr
-3.0
0.95
Pz
6e-06m
SH
-3.0
0.99
-1.0
0.99
30s
50s
on_tij01 az: 131.2 dist: 26.9
Pr
-3.5
0.98
Pz
9e-07m
-2.5
0.99
30s
xc_psal az: 151.8 dist: 25.3
Pr
-3.0
0.97
Pz
8e-07m
-2.0
1.0
30s
xc_amba az: 133.4 dist: 20.8
Pr
-4.0
0.95
Pz
3e-06m
SH
-3.0
0.98
4.0
0.75
30s
50s
xc_pt27 az: 118.8 dist: 16.5
Pr
-1.0
0.88
Pz
1e-05m
SH
0.0
0.99
-7.5
0.96
30s
50s

Figure S28. Inversion results for event 42. a) Map showing the preferred solution in b and the distribution of the 6 stations (10 traces) used in the inversion. Solution parameters are given below the map. Dashed circles indicate radii of 5º and 30º from epicenter; b) Distribution of focal mechanisms with centroid depths. We selected 605 km as the preferred solution for the event, fixing to the hypocenter depth in Table 1; c) Waveform fitting produced by the preferred solution. Black and red lines denote observations and synthetics, respectively. Azimuths and distances in degrees are shown above panels. Time shifts (top) and cross-correlation coefficients (bottom) are shown in blue at the lower right corner of each panel. Wave segments (Pr, Pz, SVr, SH and SVz) are identified at the upper right corners.

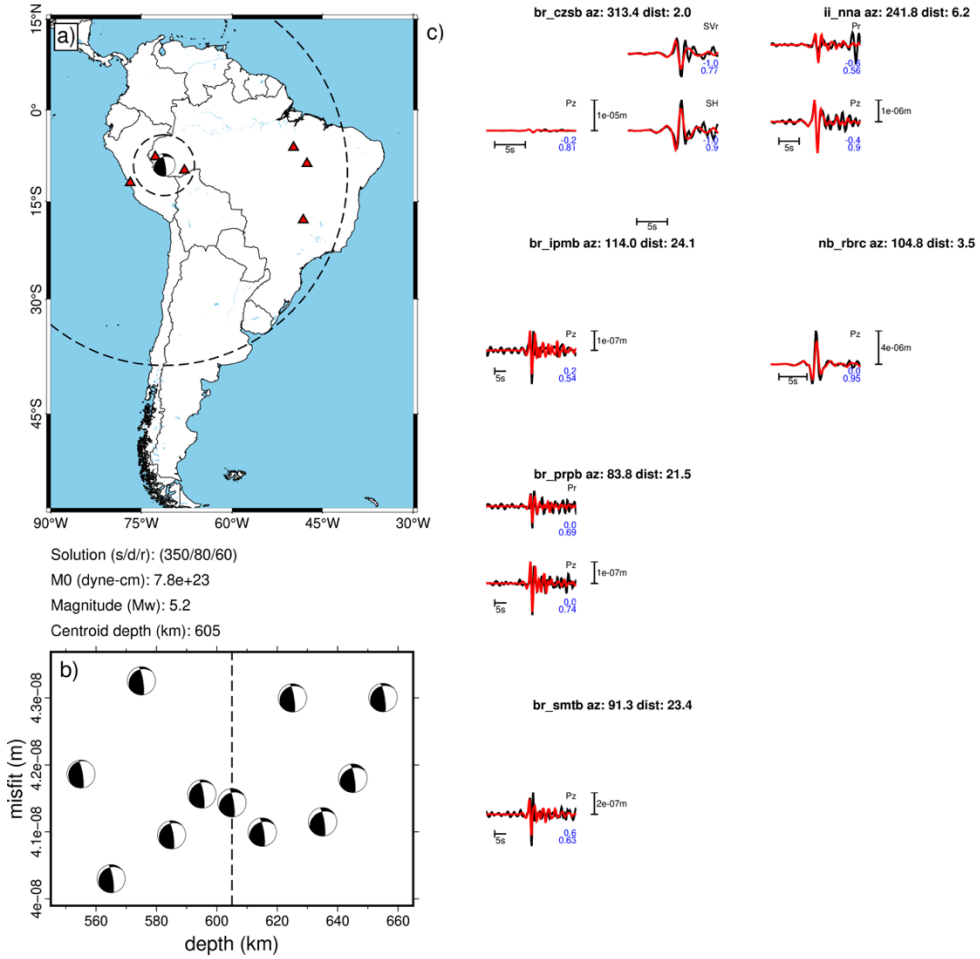

Table S5. M0 estimates obtained from the inversion of event 1 at the optimal depth of 571 km after systematically reducing both P and S attenuations in the AK135-F model in 10% steps. The tests began using the original attenuation model (100%) and ended using only 50% of the original model. Note that we applied the same percentage reduction for both P and S attenuations in each run.

Q (%)	M0 (dyne-cm)	Mw
100	7.357e+23	5.21
90	7.508e+23	5.22
80	7.687e+23	5.22
70	7.931e+23	5.23
60	8.116e+23	5.24
50	8.730e+23	5.26

Figure S29. Comparison between focal mechanisms from GCMT catalog and this study. A) South America map with GCMT solutions (period of 1976-2022 with d > 70 km and Mw > 5) colored according to fault style and sized based on moment magnitude; B) The same as in A but with a zoom in the Peru-Brazil border segment of deep-focus seismicity; and C) all 28 solutions obtained in this study colored by faulting style and sized by magnitude (period of 2014-2022 with Mw ≥ 4.2). The other map features are the same described in Figure 1.

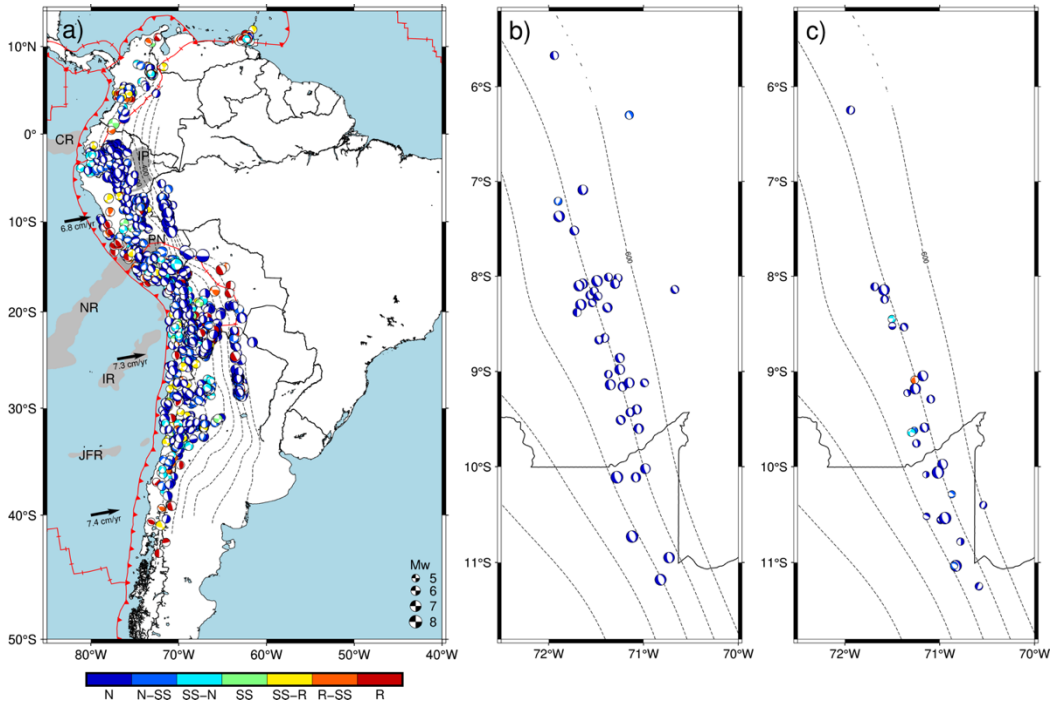

Figure S30. The 28 focal solutions determined in this work with epicenters colored by centroid depth and beachballs colored by faulting style. Other features are described in the main text Figure 3.

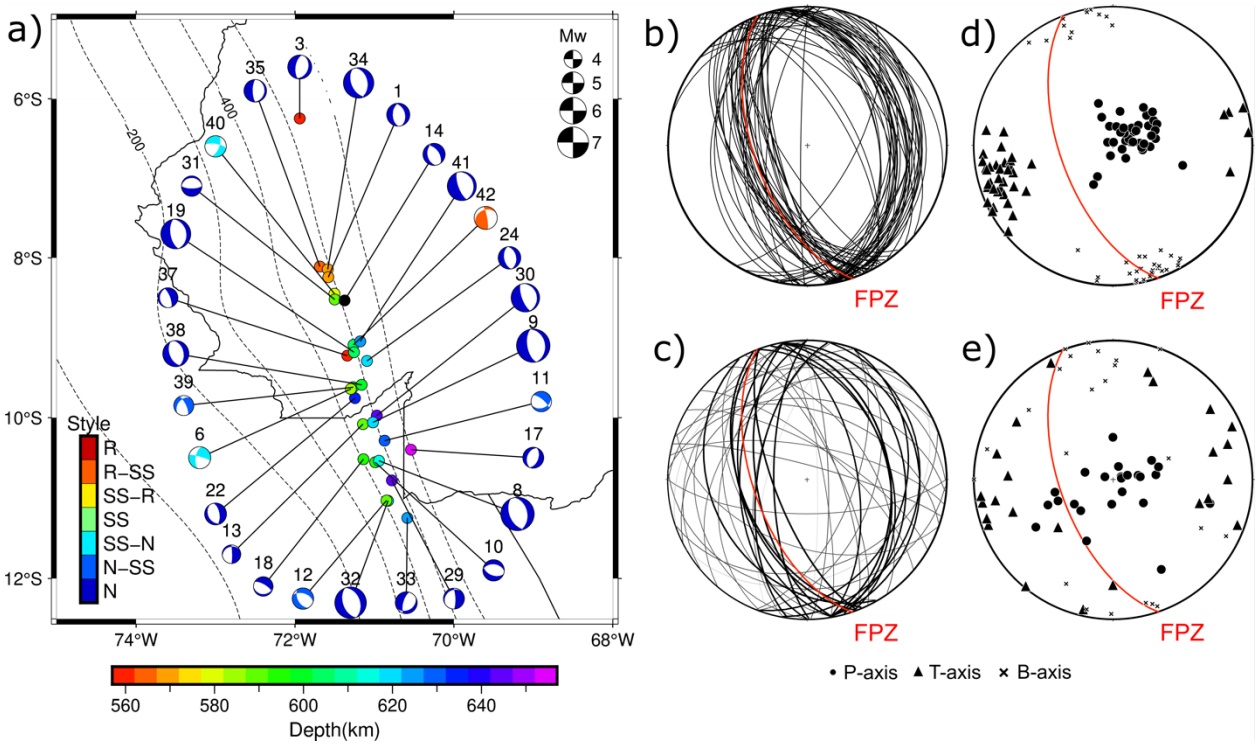

Figure S31. Focal solutions determined for the event 6. From a to c, the mechanism obtained considering all possible fault orientations, as in Figure S3; and from d to e, the mechanism obtained after restricting fault orientation before the grid search. In this restriction, strike is allowed to vary from 330º to 30º, dip from 25º to 65º and rake from -90º to -40º, which should comprise normal fault mechanisms reasonably consistent with the regional stress pattern.

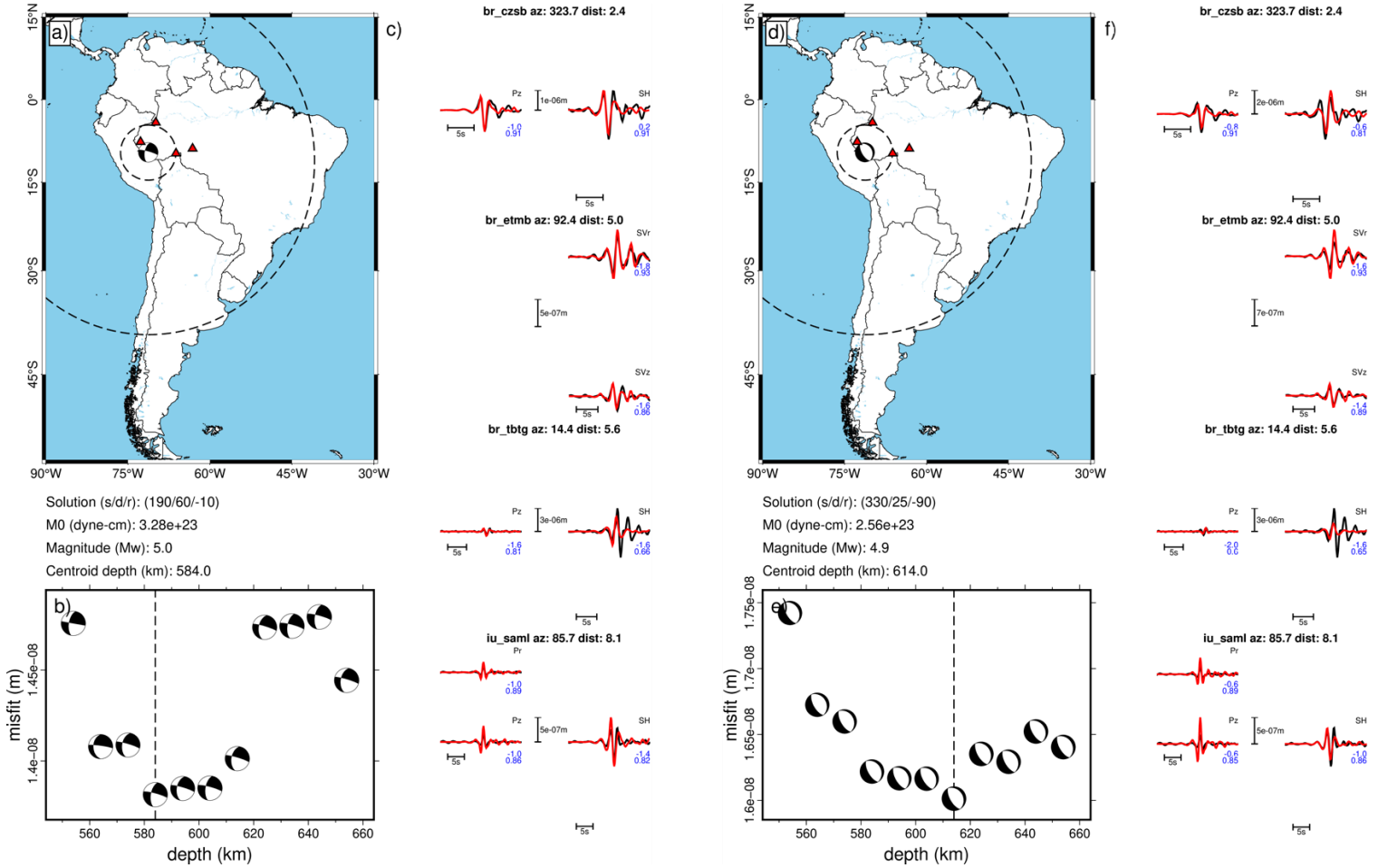

Figure S32. Comparison between synthetics produced by the two solutions in Fig. S31 with observations. a) Focal solution for event 6 obtained by this study (M1) with black circles indicating the stations used in the inversion; b) Alternative focal solution obtained after constraining the mechanism to be normal faulting (M2); and c) comparison between synthetics (in red) produced by M1 (top) and M2 (bottom) with the observed seismogram (in black), for each phase and component used in the event inversion, indicated at the upper right corner of each panel. The waveforms were filtered using the same frequency range used in the inversion but with a causal Butterworth filter and were aligned based on the picked P or S arrival time.

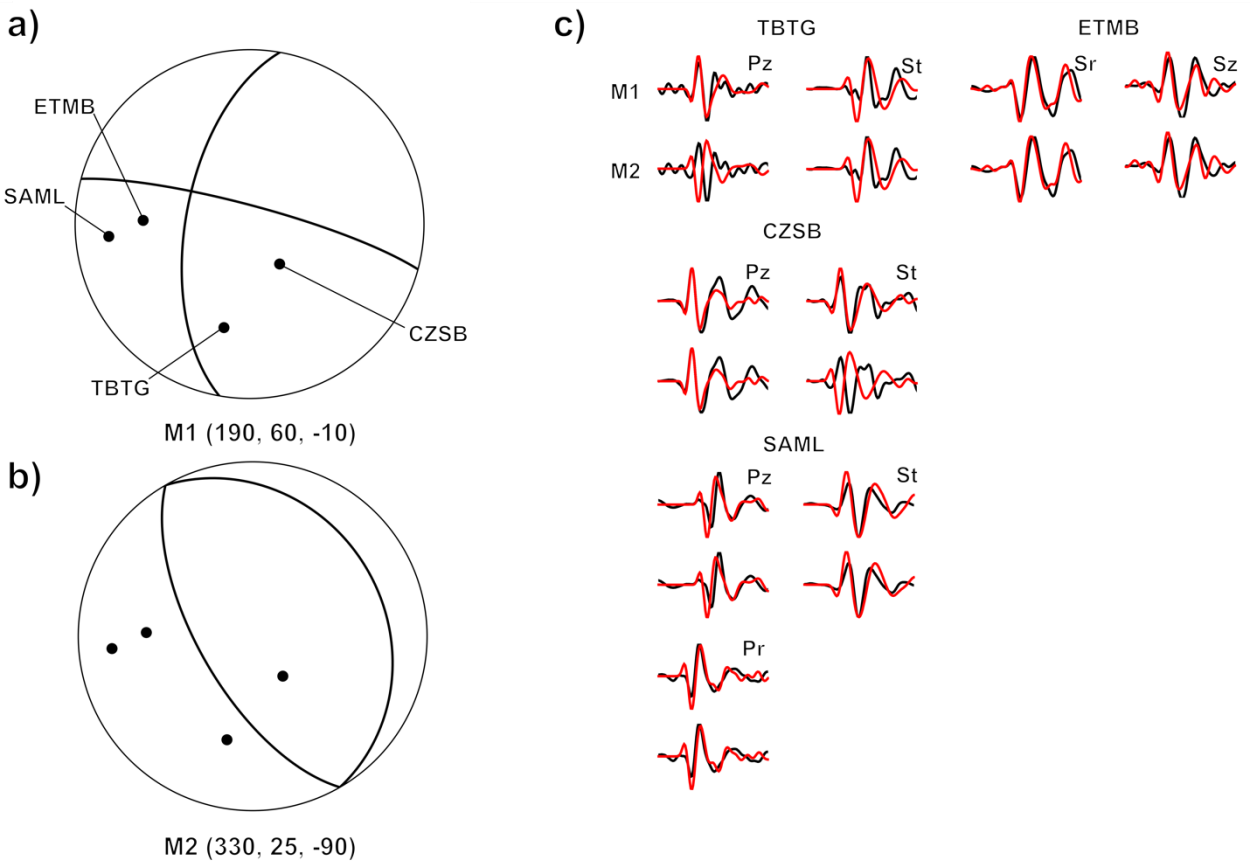

Figure S33. Focal solutions determined for the event 10. From a to c, the mechanism obtained considering all possible fault orientations, as in Fig. S6; and from d to e, the mechanism obtained after restricting fault orientation before the grid search. In this restriction, strike is allowed to vary from 330º to 30º, dip from 25º to 65º and rake from -90º to -40º, which should comprise normal fault mechanisms reasonably consistent with the regional stress pattern.

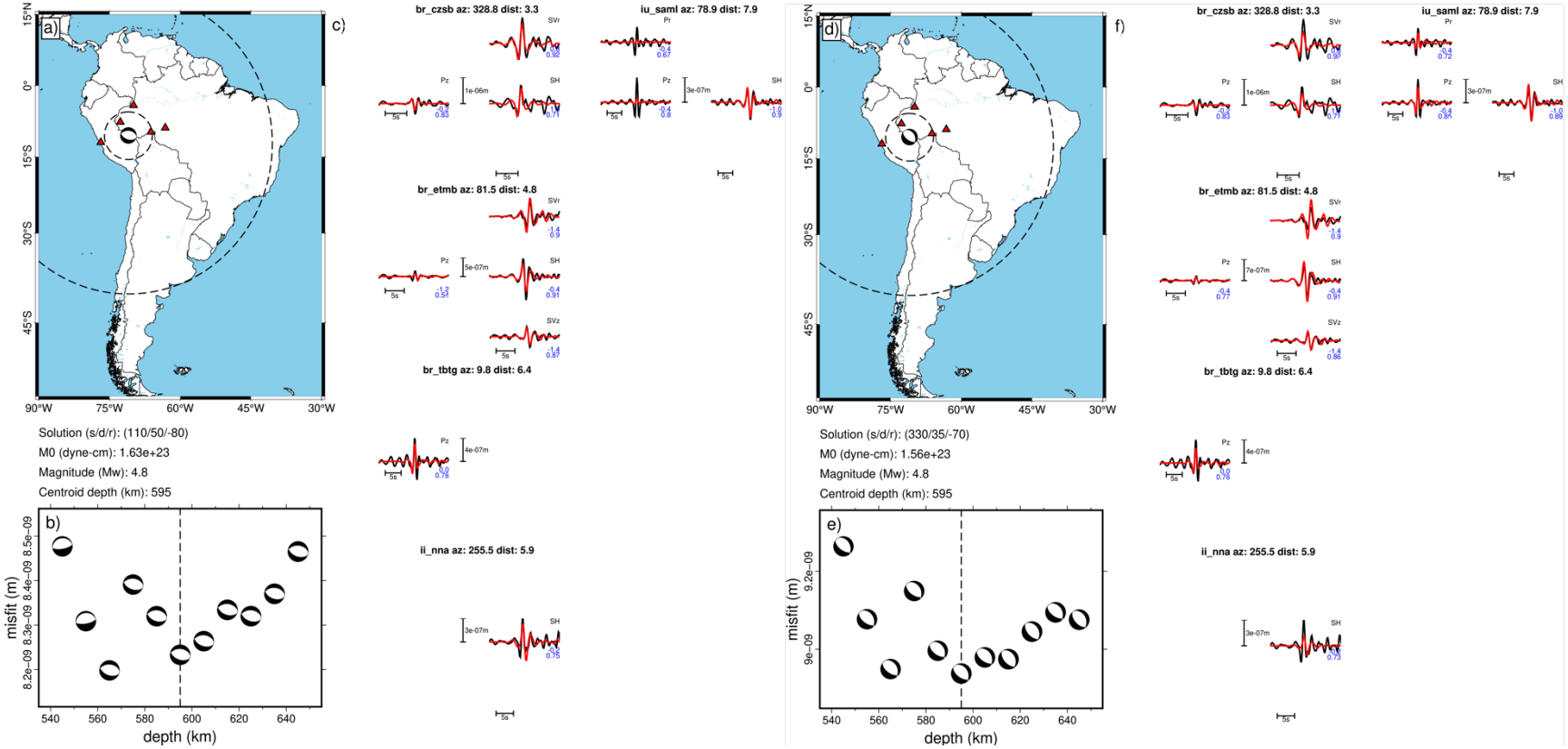

Figure S34. Comparison between synthetics produced by the two solutions in Fig. S33 with observations. a) Focal solution for event 10 obtained by this study (M1) with black circles indicating the stations used in the inversion; b) Alternative focal solution obtained after constraining the mechanism to be normal faulting (M2); and c) comparison between synthetics (in red) produced by M1 (top) and M2 (bottom) with the observed seismogram (in black), for each phase and component used in the event inversion, indicated at the upper right corner of each panel. The waveforms were filtered using the same frequency range used in the inversion but with a causal Butterworth filter and were aligned based on the picked P or S arrival time.

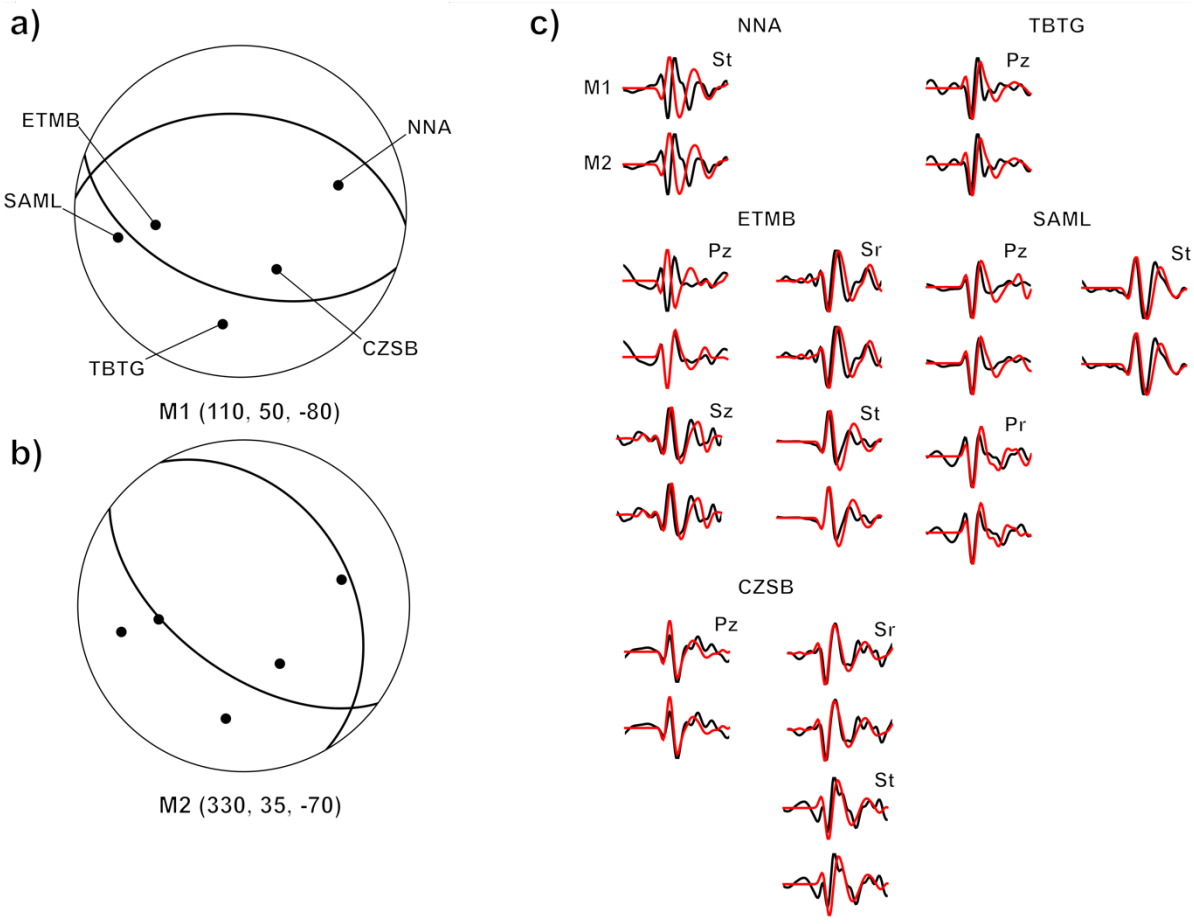

Figure S35. Focal solutions determined for the event 31. From a to c, the mechanism obtained considering all possible fault orientations, as in Fig. S18; and from d to e, the mechanism obtained after restricting fault orientation before the grid search. In this restriction, strike is allowed to vary from 330º to 30º, dip from 25º to 65º and rake from -90º to -40º, which should comprise normal fault mechanisms reasonably consistent with the regional stress pattern.

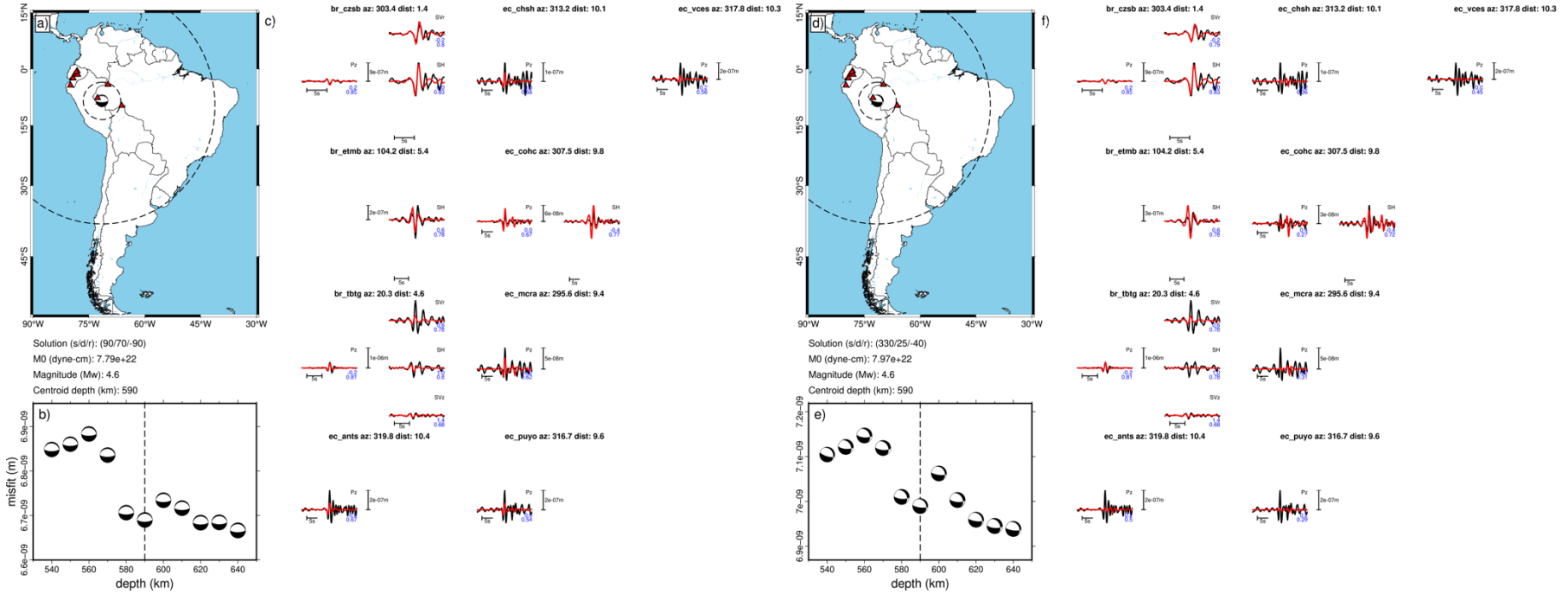

Figure S36. Comparison between synthetics produced by the two solutions in Fig. S35 with observations. a) Focal solution for event 31 obtained by this study (M1) with black circles indicating the stations used in the inversion; b) Alternative focal solution obtained after constraining the mechanism to be normal faulting (M2); and c) comparison between synthetics (in red) produced by M1 (top) and M2 (bottom) with the observed seismogram (in black), for each phase and component used in the event inversion, indicated at the upper right corner of each panel. The waveforms were filtered using the same frequency range used in the inversion but with a causal Butterworth filter and were aligned based on the picked P or S arrival time.

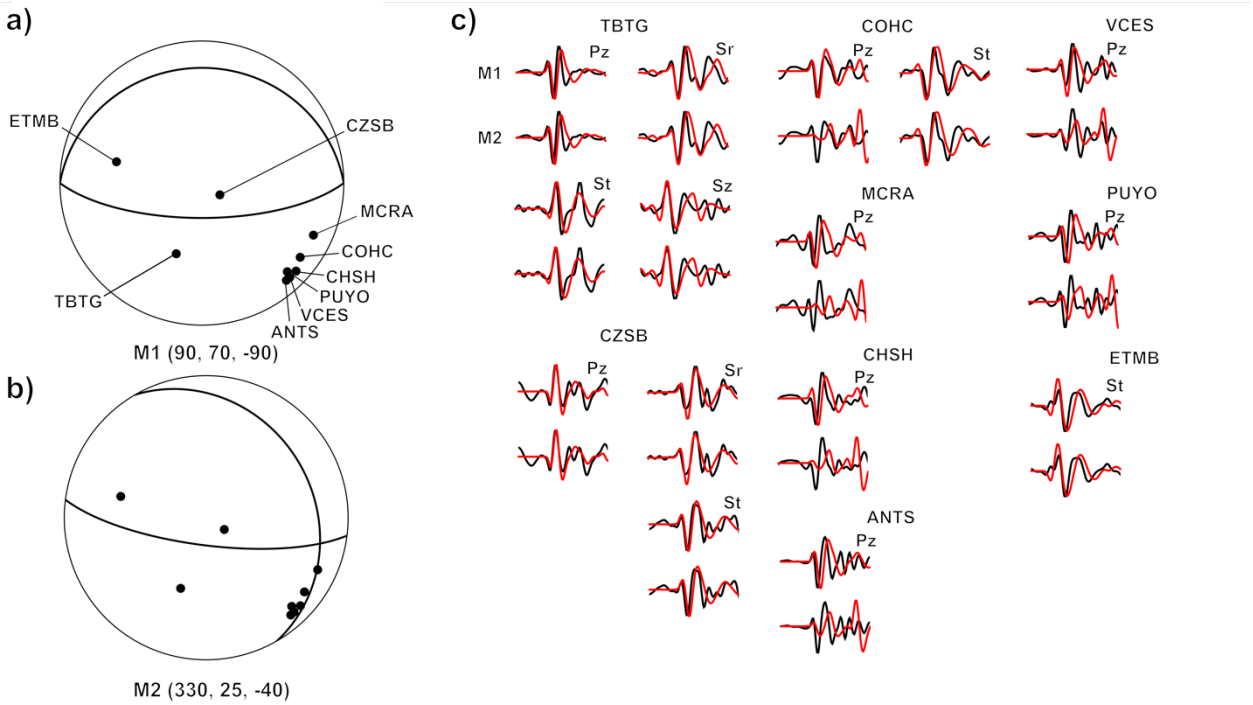

Figure S37. Focal solutions determined for the event 42. From a to c, the mechanism obtained considering all possible fault orientations, as in Fig. S28; and from d to e, the mechanism obtained after restricting fault orientation before the grid search. In this restriction, strike is allowed to vary from 330º to 30º, dip from 25º to 65º and rake from -90º to -40º, which should comprise normal fault mechanisms reasonably consistent with the regional stress pattern.

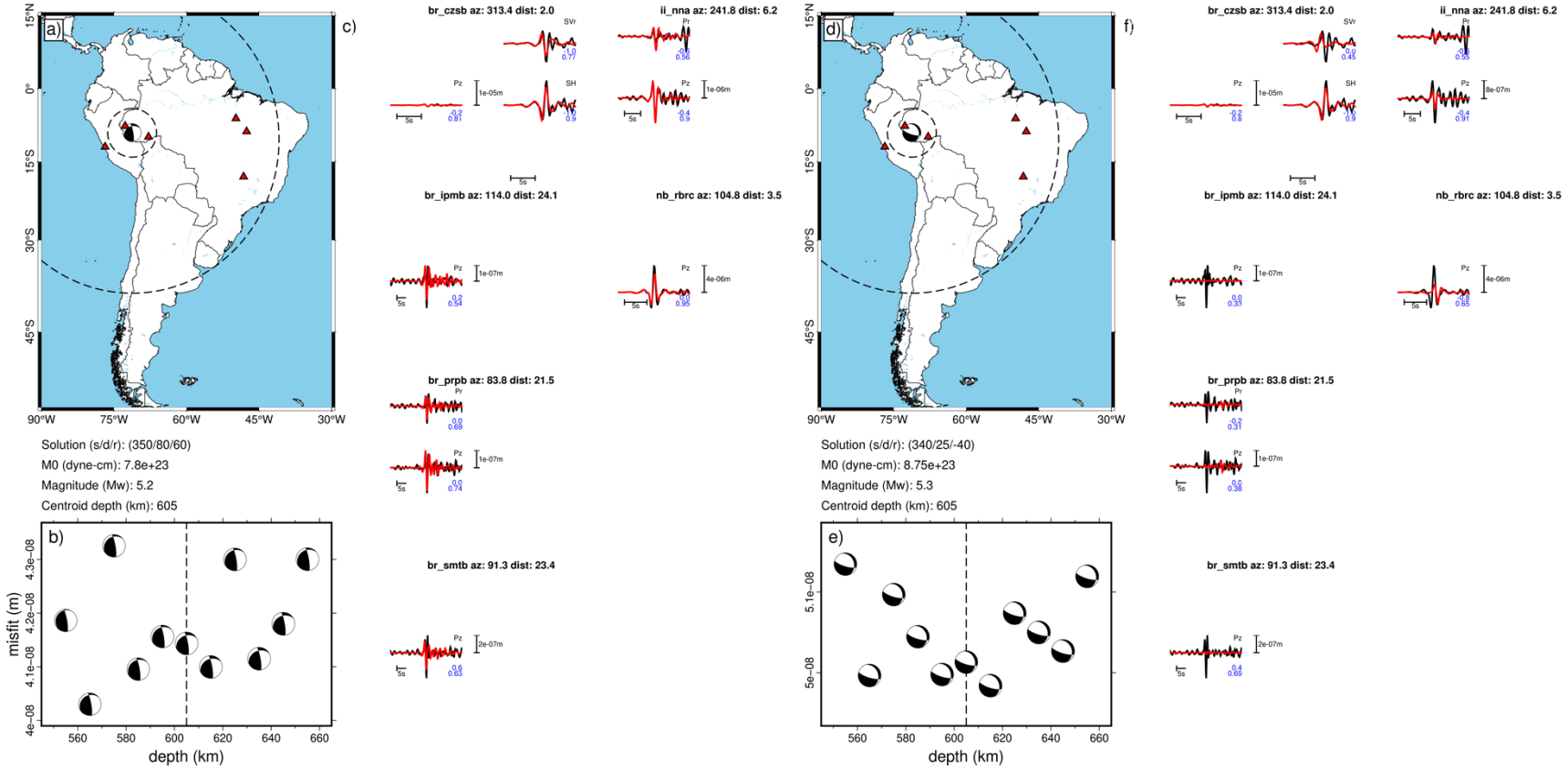

Figure S38. Comparison between synthetics produced by the two solutions in Fig. S37 with observations. a) Focal solution for event 42 obtained by this study (M1) with black circles indicating the stations used in the inversion; b) Alternative focal solution obtained after constraining the mechanism to be normal faulting (M2); and c) comparison between synthetics (in red) produced by M1 (top) and M2 (bottom) with the observed seismogram (in black), for each phase and component used in the event inversion, indicated at the upper right corner of each panel. The waveforms were filtered using the same frequency range used in the inversion but with a causal Butterworth filter and were aligned based on the picked P or S arrival time.

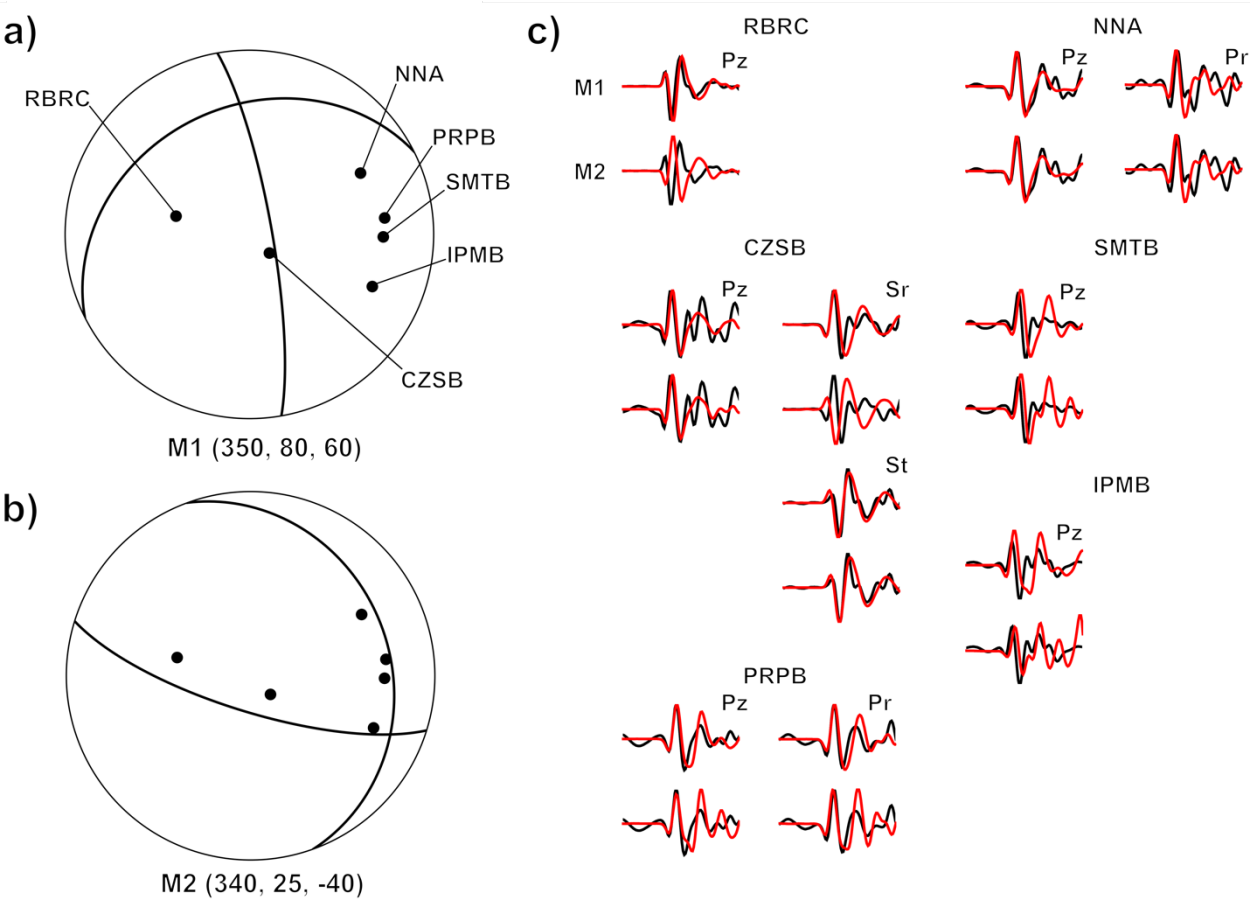

Figure S39. Deep-focus earthquakes in the Peru-Brazil border between 2014 and 2022. a) distribution of earthquake magnitude over time; b) number of earthquakes per year, highlighting relatively higher seismic activity in 2015 compared to other years; c) earthquake magnitudes per month during 2015, demonstrating that most events occurred during the end of November; and d) magnitudes per day around the time of the 2015 Mw 7.6 doublet, displaying its foreshock and aftershocks.

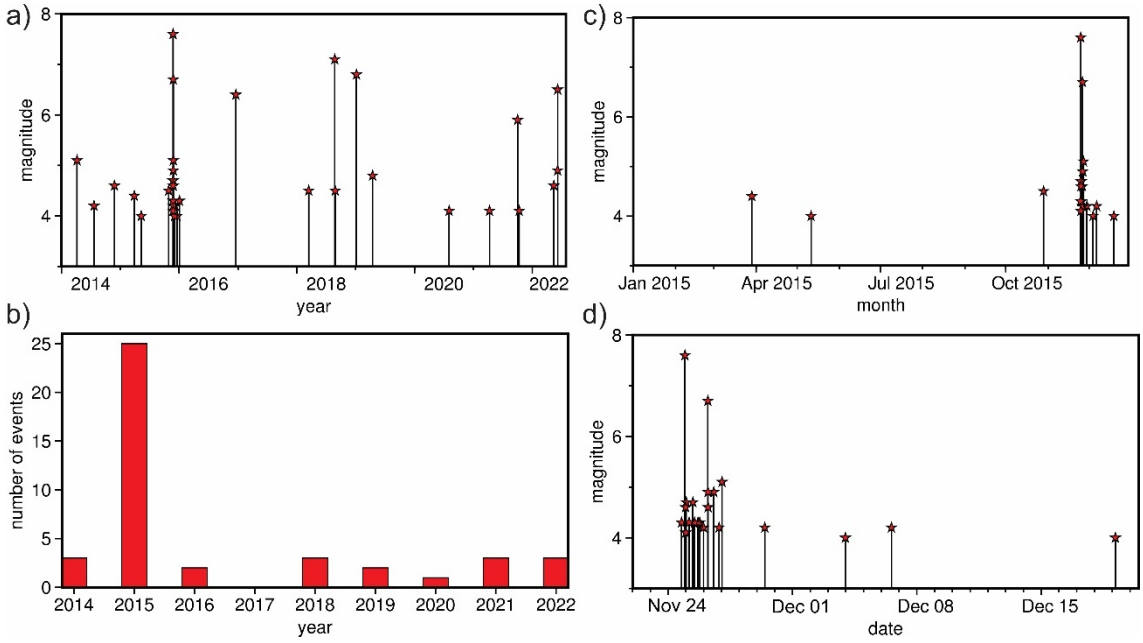

APÊNDICE D

Journal of Geophysical Research: Solid Earth

Supporting Information for

Deep-Focus Earthquakes in Warm Slabs: Seismic Source Parameters in the Peru-Brazil Region

G. S. Leite Neto[1]*, G. A. Prieto[2], and J. Julià[1,3]

[1]Programa de Pós-Graduação em Geodinâmica e Geofísica, Universidade Federal do Rio Grande do Norte, Natal, Brasil.

[2]Departamento de Geociencias, Universidad Nacional de Colombia, Bogotá, Colombia.

[3]Departamento de Geofísica, Universidade Federal do Rio Grande do Norte, Natal, Brasil.

*Corresponding author: Gilberto S. Leite Neto (leitenetogs@gmail.com)

Contents of this file

Text S1

Figures S1 to S23

Tables S1 to S2

Introduction

This material includes text, figures and tables that complement the primary content.

Event Number	Date and Time (UTC)	Lat (º)	Lon (º)	Depth (km)	Magnitude	Type
1	2014-04-07 (15:27:32.600)	-8.24	-71.58	560.9	5.2*	Mw
2	2014-07-22 (00:53:02.260)	-6.12	-72.03	565.2	4.2	mb
3	2014-11-26 (01:26:24.340)	-6.25	-71.94	587.1	5.4*	Mw
4	2015-03-28 (21:48:14.380)	-9.12	-71.29	610.2	4.4	mb
5	2015-05-11 (08:21:44.350)	-9.15	-71.23	617.3	4.0	mb
6	2015-10-28 (17:10:55.290)	-9.64	-71.30	603.7	5.0*	Mw
7	2015-11-24 (18:10:05.040)	-10.66	-71.14	595.6	4.3	mb
8	2015-11-24 (22:45:38.880)	-10.54	-70.94	606.2	7.5*	Mw
9	2015-11-24 (22:50:54.370)	-10.06	-71.02	620.6	7.5*	Mw
10	2015-11-24 (23:44:14.010)	-10.56	-70.99	595.1	4.8*	Mw
11	2015-11-24 (23:55:20.210)	-10.29	-70.87	618.8	4.6*	Mw
12	2015-11-25 (00:28:16.830)	-11.03	-70.85	597.1	4.8*	Mw
13	2015-11-25 (04:30:29.380)	-10.08	-71.14	589.8	4.2*	Mw
14	2015-11-25 (09:26:22.680)	-8.53	-71.37	629.3	5.0*	Mw
15	2015-11-25 (11:45:25.430)	-9.30	-71.45	515.0	4.3	mb
16	2015-11-25 (16:19:24.860)	-9.85	-71.28	630.5	4.3	mb
17	2015-11-25 (18:47:56.000)	-10.40	-70.54	655.0	4.7*	Mw
18	2015-11-25 (23:49:34.380)	-10.52	-71.14	591.9	4.4*	Mw
19	2015-11-26 (05:45:18.400)	-9.18	-71.26	602.7	6.7*	Mw

20	2015-11-26 (05:56:05.120)	-9.06	-71.32	602.6	4.9	mb
21	2015-11-26 (06:01:22.990)	-9.20	-71.29	602.1	4.6	mb
22	2015-11-26 (13:42:24.490)	-9.76	-71.24	605.6	4.9*	Mw
23	2015-11-26 (20:50:46.270)	-10.57	-71.18	601.8	4.2	mb
24	2015-11-27 (00:52:54.610)	-9.29	-71.09	617.0	5.1*	Mw
25	2015-11-29 (10:41:32.140)	-10.17	-71.18	625.6	4.2	mb
26	2015-12-03 (23:29:48.500)	-10.26	-71.42	622.7	4.0	mb
27	2015-12-06 (13:49:42.450)	-9.83	-71.19	638.4	4.2	mb
28	2015-12-19 (04:25:25.450)	-11.08	-71.01	601.4	4.0	mb
29	2016-01-03 (11:08:34.460)	-10.78	-70.78	633.4	4.7*	Mw
30	2016-12-18 (13:30:10.680)	-9.97	-70.97	612.0	6.4*	Mw
31	2018-03-15 (20:13:29.710)	-8.52	-71.50	590.0	4.6*	Mw
32	2018-08-24 (09:04:08.250)	-11.03	-70.83	630.0	7.1*	Mw
33	2018-08-26 (19:58:24.550)	-11.25	-70.59	605.7	4.9*	Mw
34	2019-01-05 (19:25:38.520)	-8.14	-71.59	570.4	6.8*	Mw
35	2019-04-16 (03:19:30.295)	-8.11	-71.69	584.1	5.1*	Mw
36	2020-08-03 (03:45:57.052)	-9.38	-71.25	607.6	4.1	mb
37	2021-04-11 (04:21:02.737)	-9.22	-71.34	556.8	4.5*	Mw
38	2021-10-02 (12:52:34.077)	-9.59	-71.16	589.0	5.9*	Mw
39	2021-10-12 (04:34:35.763)	-9.62	-71.27	605.1	4.5*	Mw
40	2022-05-14 (22:27:28.588)	-8.45	-71.50	580.0	4.8*	Mw

41	2022-06-08 (00:55:46.777)	-9.05	-71.18	622.7	6.5*	Mw
42	2022-06-08 (01:53:28.974)	-9.09	-71.26	605.4	5.2*	Mw

Table S1. USGS catalog information for the 42 deep-focus earthquakes occurred between 2014 and 2022 in the Peru-Brazil region. Magnitudes marked with an asterisk are estimates from a waveform inversion study (Leite Neto & Julià, 2022).

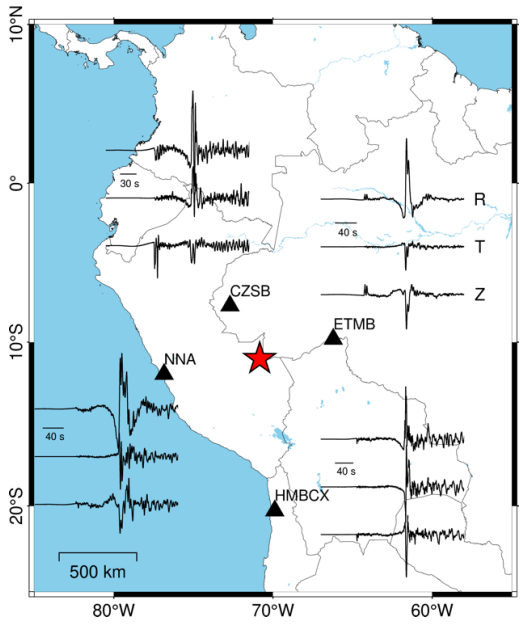

Figure S1. Examples of seismograms from nearby stations (CZSB, ETMB, NNA, and HMBCX) recording the Mw 7.0 event 32 at a depth of 630 km. Seismograms are labeled as radial (R), transverse (T), or vertical (Z). Amplitudes at each station are scaled relative to each other.

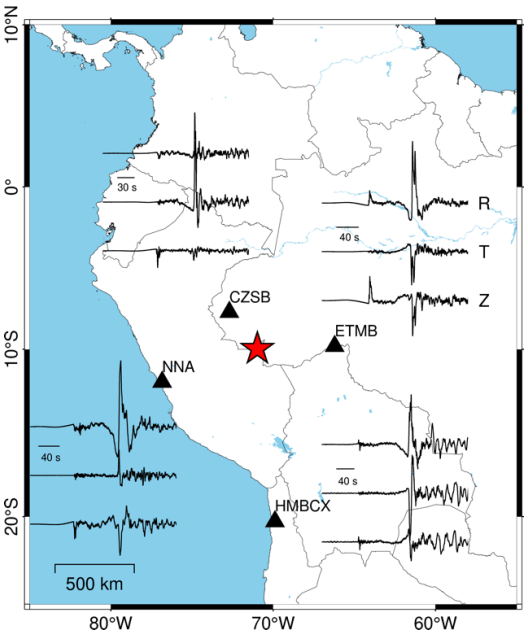

Figure S2. Examples of seismograms from nearby stations (CZSB, ETMB, NNA, and HMBCX) recording the Mw 6.3 event 30 at a depth of 612 km. Seismograms are labeled as radial (R), transverse (T), or vertical (Z). Amplitudes at each station are scaled relative to each other.

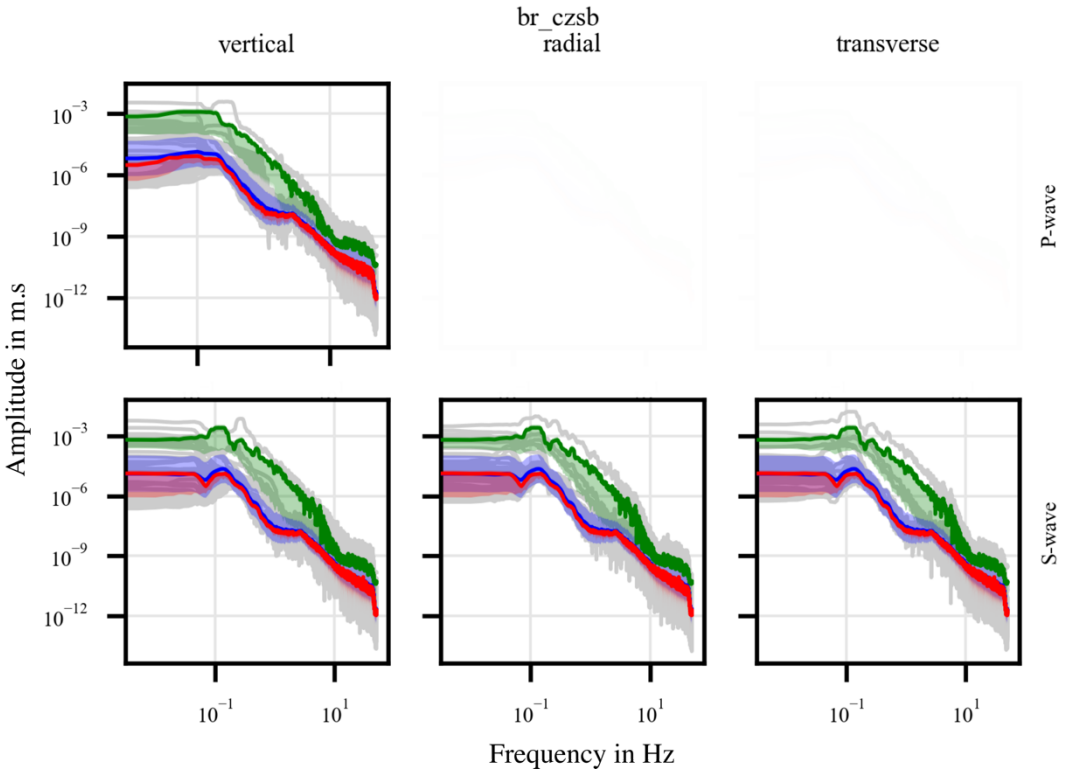

Figure S3. Example of the background noise calculation. Gray lines are the individual noise spectra observed for the CZSB station. Gray, blue, and red lines denote the arithmetic mean, geometric mean and median, respectively. Shaded regions around the lines represent the standard deviation. Note that the arithmetic mean is usually affected by the small number of high-amplitude noise spectra, while the geometric mean and median provide a better representation of the overall noise level in the station.

Text S1. Inability to determine the attenuation (Q) with the CEM method.

While conducting the inversion, we noted that Q assumed very high values for most of the stations, usually reaching the limit value set to 2000. In fact, we noted the same behavior after changing this maximum to 3000, 4000, and even 5000. We then proceeded to investigate how misfit behaves as a function of P- and S-wave attenuation for a given event. We selected event 8 (Table S1) because it is one of the largest ruptures in our sequence (Mw 7.4), consequently producing more data with sufficient SNR, thus being ideal for this kind of examination.

Figure S4 depicts a broad minimum evident across most stations, posing a significant obstacle to accurately determining Q during the inversion process. As Q values increase, the estimates for corner frequencies tend to decrease, due to the trade-off between these parameters (e.g., Ko et al., 2012). Only PRA, shown in Figure S4l, exhibited a relatively well-constrained minimum out of 54 stations.

Thus, to avoid an incorrect determination of the corner frequencies, we simply decided to assume Q equal to 1000 for both P and S waves. After considerable testing, we observed that this value, although large, is good enough to model the fall-off of most of the spectra, as can be attested by the modeled spectra in Figure 2. This value

is consistent with the very high values found at MTZ depths beneath the Pacific seafloor (Booth et al., 2014), and agrees with estimates for the subducting Pacific plate in New Zealand (Eberhart-Phillips et al., 2008).

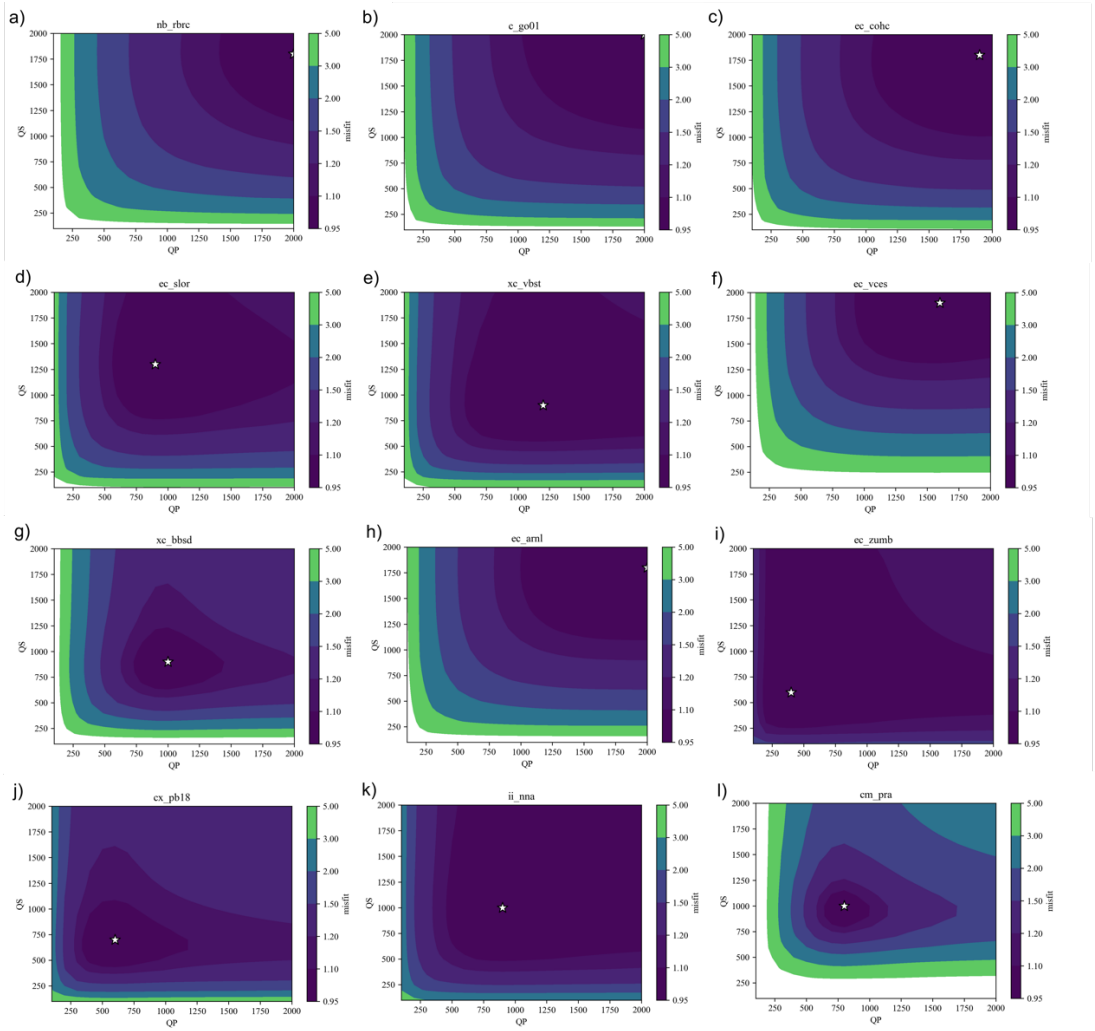

Figure S4. Error surface as a function of P- and S-wave attenuation, $\boldsymbol{Q_P}$ and $\boldsymbol{Q_S}$ respectively, for some example stations. White star indicates the overall minimum of each misfit surface.

Network	Name	Longitude (º)	Latitude (º)
BR	VILB	-60.2	-12.95
	MACA	-60.68	-3.16
	CZSB	-72.7	-7.73
	ETMB	-66.21	-9.81
	TBTG	-69.9	-4.18
	PTLB	-59.14	-15.45
	TEFE	-64.63	-3.51
C1	AP01	-70.34	-18.37
	TA01	-70.18	-20.57
	TA02	-70.13	-20.27
	AF01	-68.18	-22.95
CX	MNMCX	-69.6	-19.13
	PSGCX	-70.12	-19.6
	PB16	-69.51	-18.34
	PB09	-69.24	-21.8
	PB07	-69.89	-21.73
	PB01	-69.49	-21.04
	PB08	-69.15	-20.14
	PB04	-70.15	-22.33
	PATCX	-70.15	-20.82
	PB03	-69.75	-22.05
	HMBCX	-69.89	-20.28
	PB02	-69.9	-21.32
	PB05	-70.2	-22.85

	PB06	-69.57	-22.71
	PB11	-69.66	-19.76
	PB10	-70.55	-23.51
	PB12	-70.33	-18.61
	PB15	-69.47	-23.21
	PB18	-69.48	-17.59
C	GO01	-69.19	-19.67
CM	TUM	-78.73	1.82
	PRA	-74.89	3.71
EC	SALI	-80.99	-2.19
	SAGO	-78.67	-1.15
	TULM	-77.79	0.72
	GGPC	-78.59	-0.18
	IMBA	-78.2	0.28
	CHSH	-78.87	-1.49
	PUYO	-78.02	-1.49
	ANTS	-78.17	-0.5
	COHC	-79.26	-2.47
	SLOR	-78.5	-0.73
	VCES	-78.39	-0.8
	MCRA	-79.95	-4.37
	ARNL	-80.07	-3.55
	ZUMB	-79.14	-4.86
	PULU	-78.5	0.02
GE	LVC	-68.91	-22.61

II	NNA	-76.84	-11.99
IU	SAML	-63.18	-8.95
	OTAV	-78.45	0.24
NB	RBRC	-67.88	-9.96
XC	BBSD	-60.61	-17.19
	VBST	-60.02	-14.53

Table S2. Networks, names, and coordinates of all 55 stations used in this work as in the FDSN.

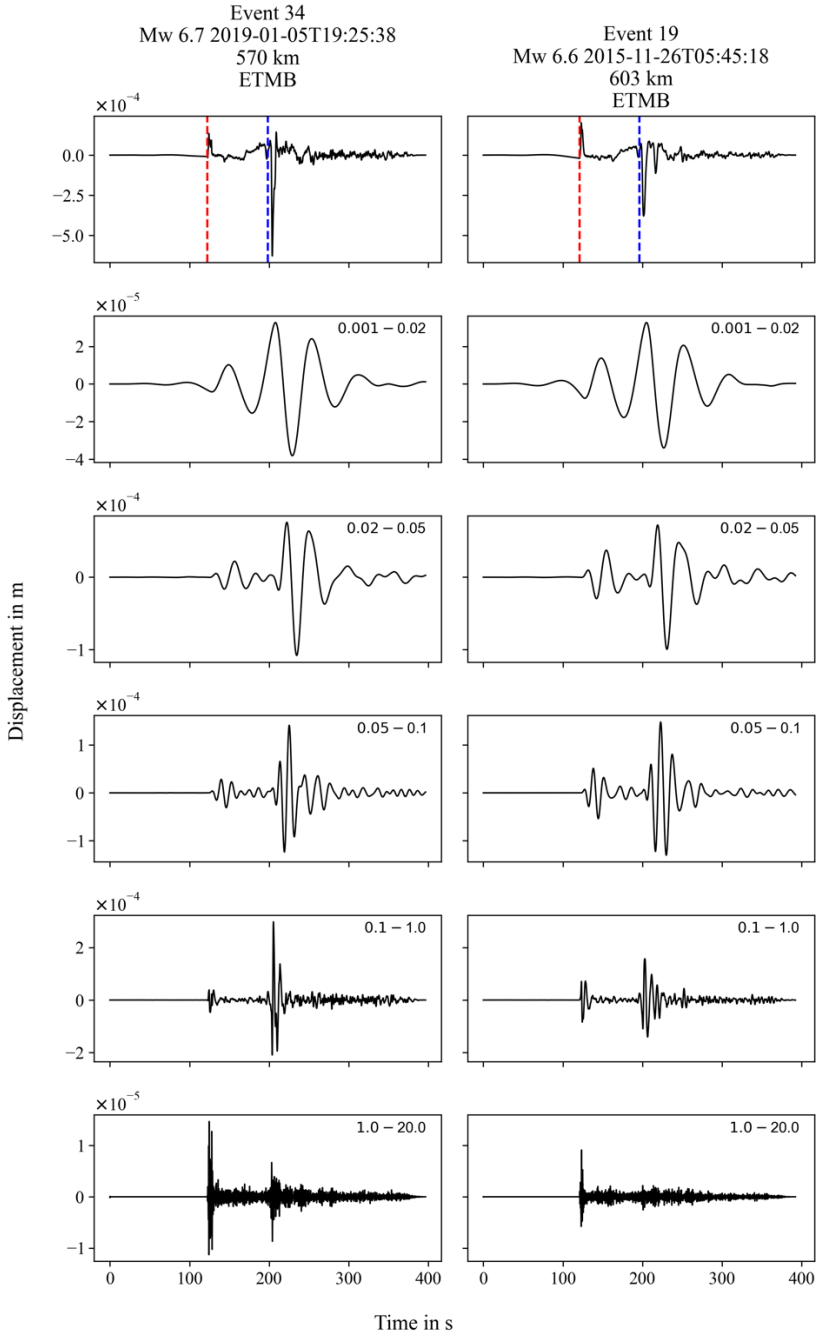

Figure S5. Comparing vertical seismograms from Mw 6.7 event 34 and Mw 6.6 event 19 at ETMB in different frequency ranges. The onsets of the P and S waves are shown in the broadband signal (upper panels) as vertical red and blue lines, respectively. The frequency ranges are shown in the upper right corner of each panel. To facilitate comparisons, we equalized amplitudes in the 0.001 – 0.02 Hz frequency range and applied the amplitude factor to the other frequency ranges.

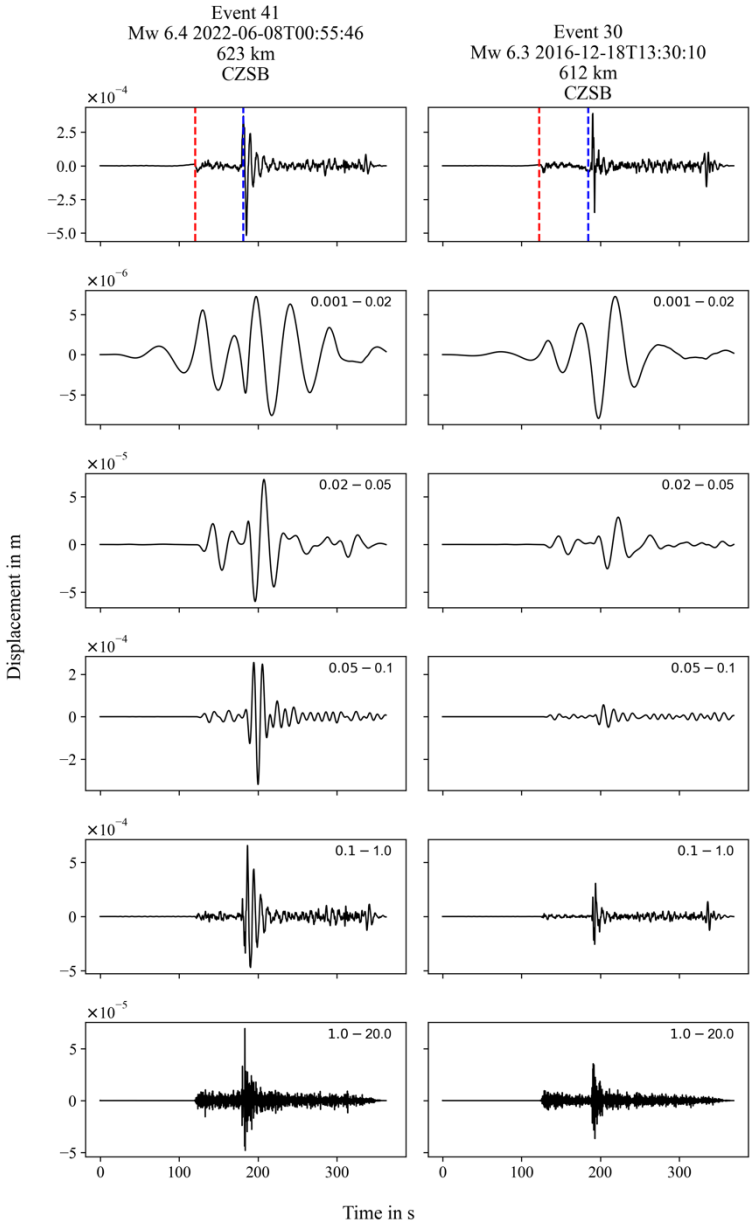

Figure S6. Comparing radial seismograms from Mw 6.4 event 41 and Mw 6.3 event 30 at CZSB in different frequency ranges. The onsets of the P and S waves are shown in the broadband signal (upper panels) as vertical red and blue lines, respectively. The frequency ranges are shown in the upper right corner of each panel. To facilitate comparisons, we equalized amplitudes in the 0.001 – 0.02 Hz frequency range and applied the amplitude factor to the other frequency ranges.

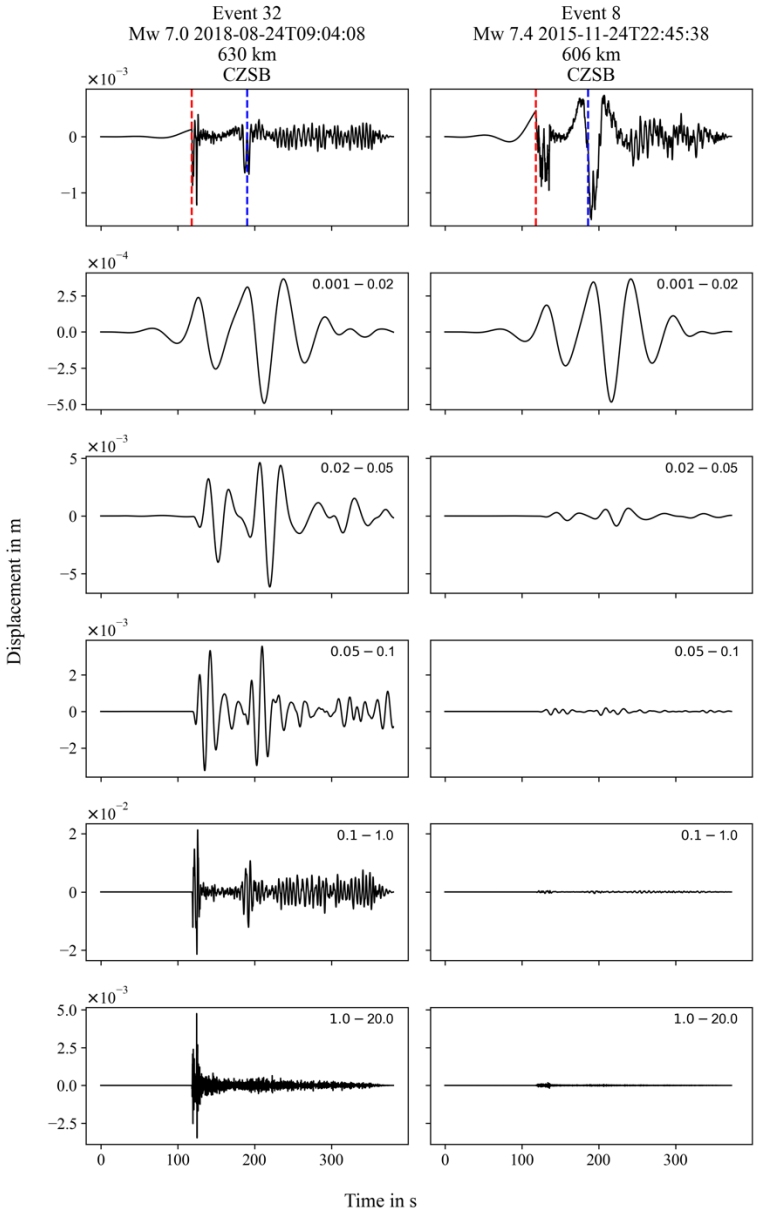

Figure S7. Comparing vertical seismograms from Mw 7.0 event 32 and Mw 7.4 event 8 at CZSB in different frequency ranges. The onsets of the P and S waves are shown in the broadband signal (upper panels) as vertical red and blue lines, respectively. The frequency ranges are shown in the upper right corner of each panel. To facilitate comparisons, we equalized amplitudes in the 0.001 – 0.02 Hz frequency range and applied the amplitude factor to the other frequency ranges.

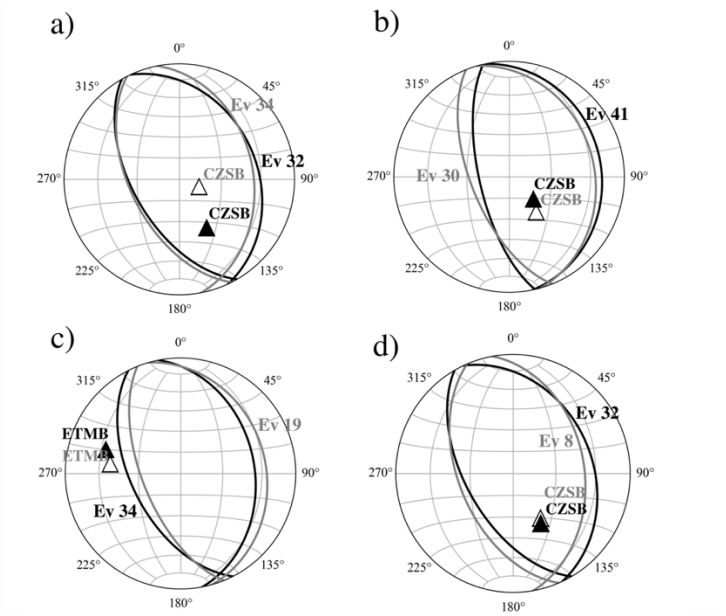

Figure S8. Stereonets with focal mechanisms represented by black and gray planes, and stations represented by solid and open triangles, respectively. The focal mechanism for an event, as described in the GCMT catalog, is depicted by the black planes and solid triangles, with the station located at the corresponding azimuth and take-off angle. The gray planes and open triangles represent the focal mechanism and the same station for a comparative event.

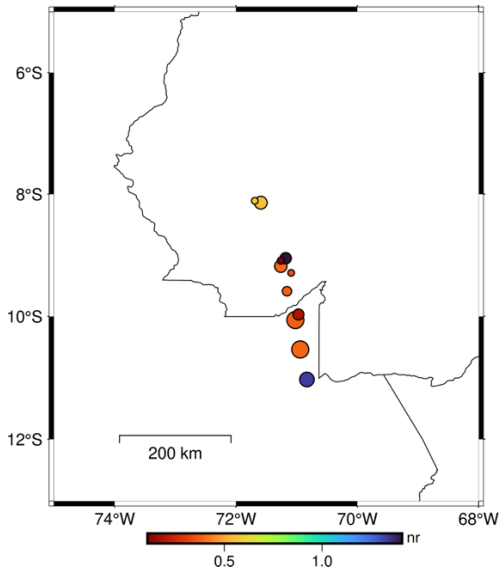

Figure S9. Epicenters from the 13 events listed in Table 1 colored by their radiation efficiencies.

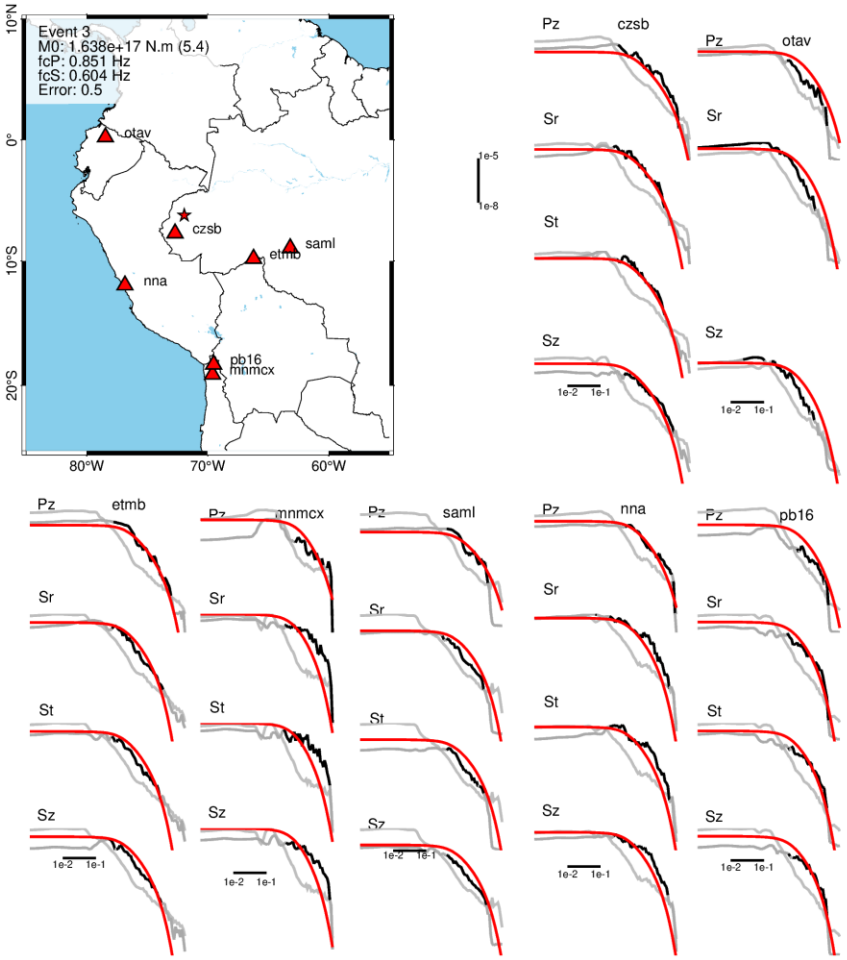

Figure S10. Observed and predicted spectra for event 3 (5.4 Mw). On the map, the red star represents the epicenter, while black and red triangles indicate the stations used in the inversion, with red triangles denoting the stations selected for display in the figure. For each selected station, the black, red and light gray lines respectively represent the observed, modeled and background noise spectra, respectively. Segments of the observed spectra with low SNR are shown in dark gray and were not considered for inversion.

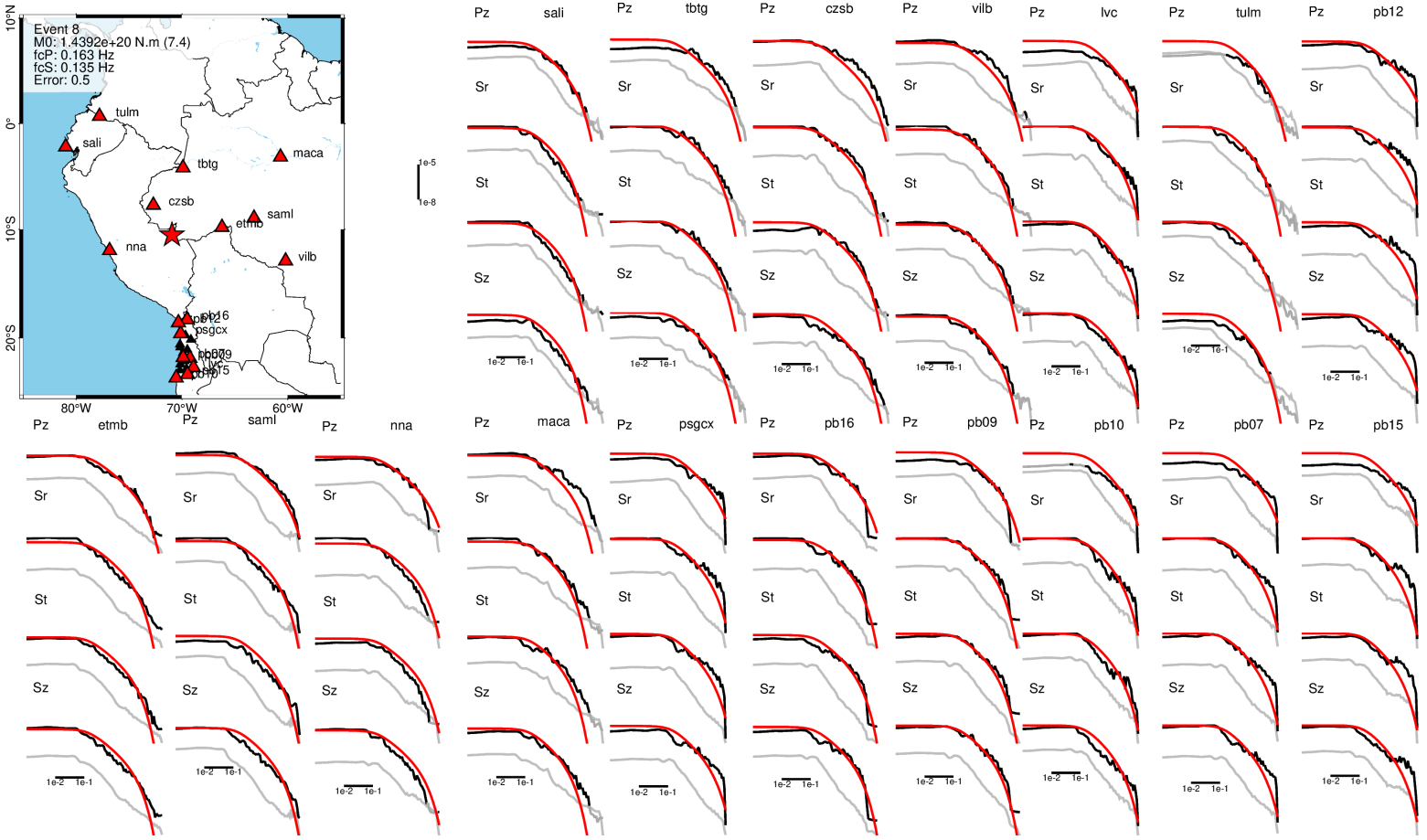

Figure S11. Observed and predicted spectra for event 8 (7.4 Mw). On the map, the red star represents the epicenter, while black and red triangles indicate the stations used in the inversion, with red triangles denoting the stations selected for display in the figure. For each selected station, the black, red and light gray lines respectively represent the observed, modeled and background noise spectra, respectively. Segments of the observed spectra with low SNR are shown in dark gray and were not considered for inversion.

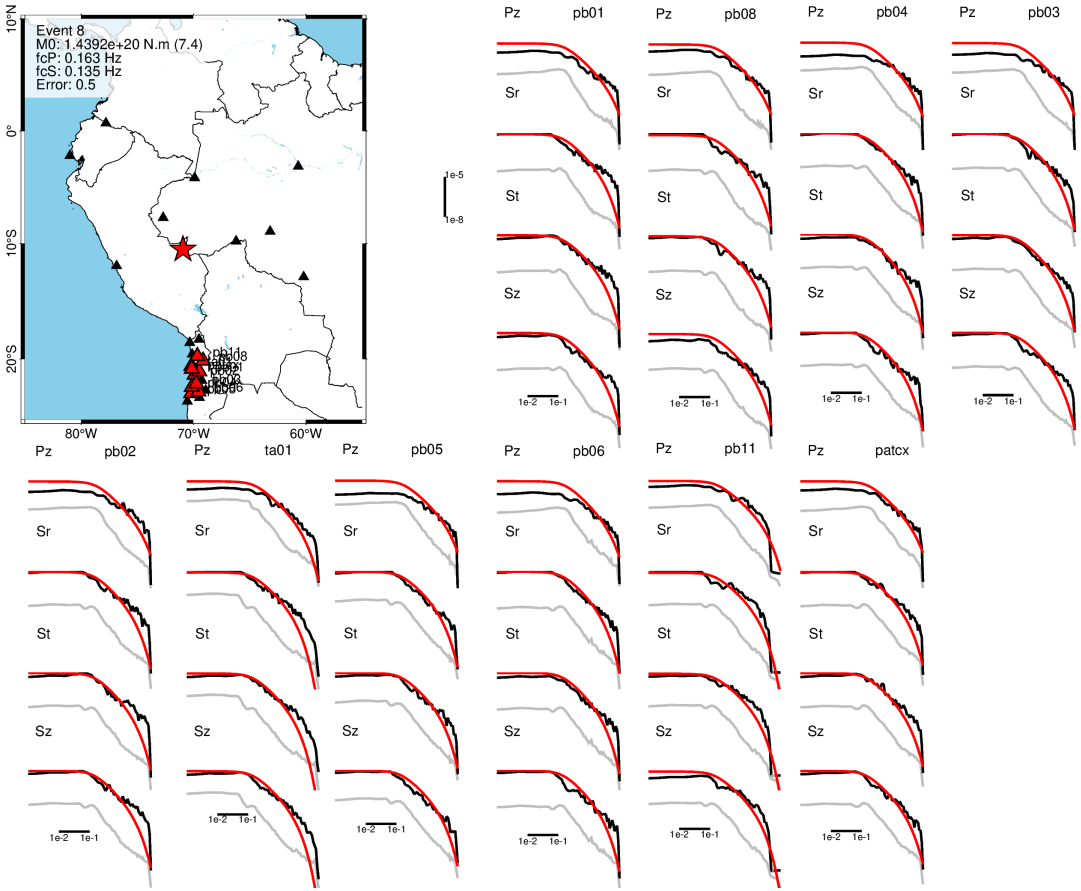

Figure S11. Continued.

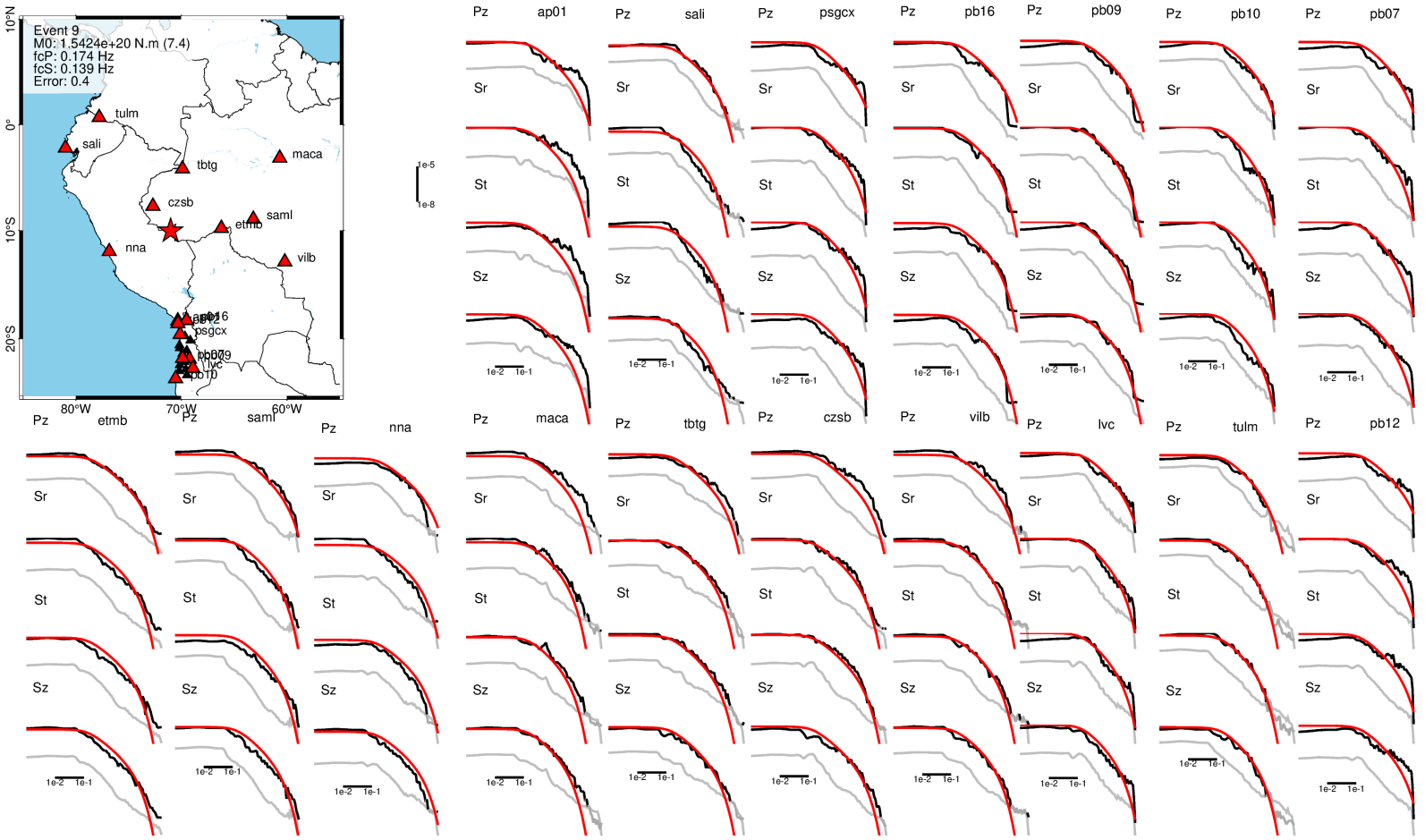

Figure S12. Observed and predicted spectra for event 9 (7.4 Mw). On the map, the red star represents the epicenter, while black and red triangles indicate the stations used in the inversion, with red triangles denoting the stations selected for display in the figure. For each selected station, the black, red and light gray lines respectively represent the observed, modeled and background noise spectra, respectively. Segments of the observed spectra with low SNR are shown in dark gray and were not considered for inversion.

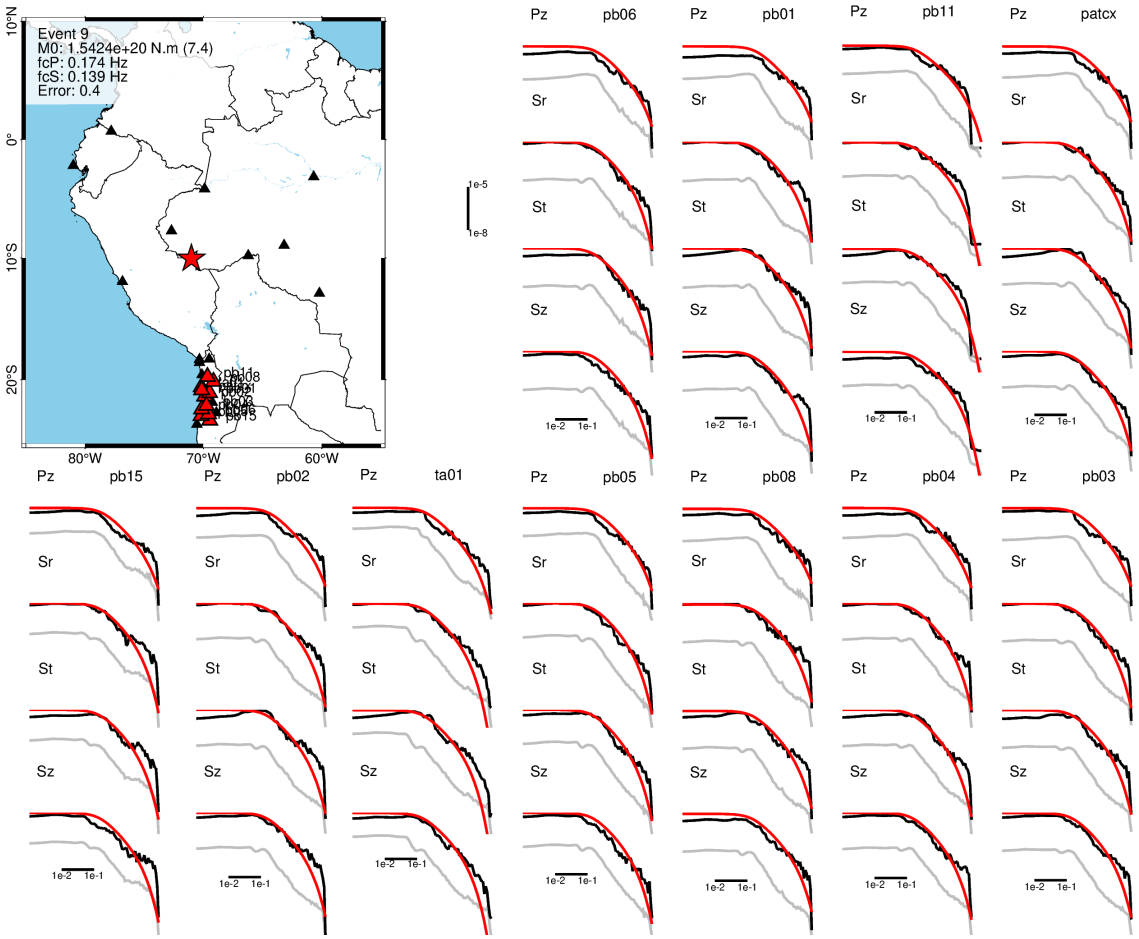

Figure S12. Continued.

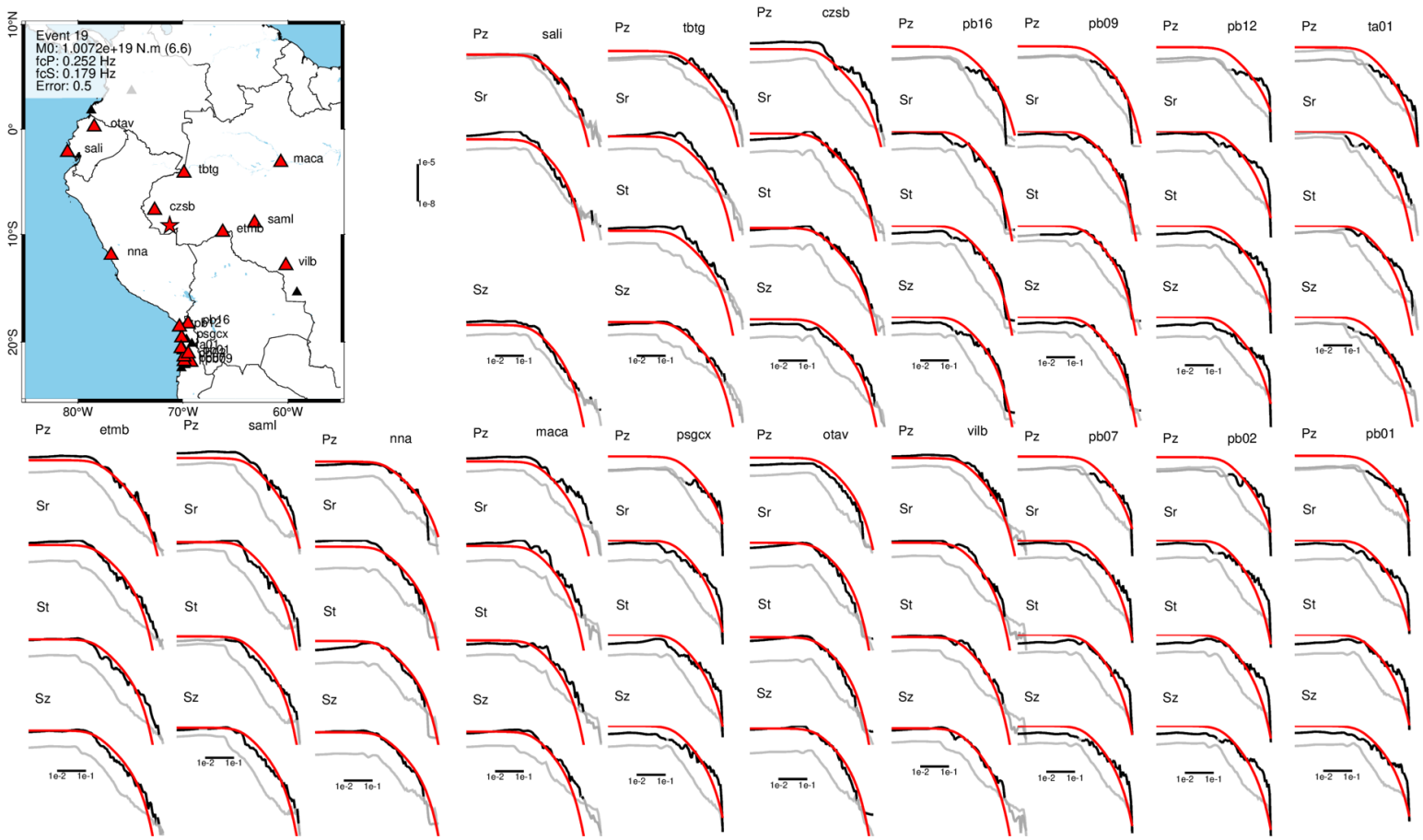

Figure S13. Observed and predicted spectra for event 19 (6.6 Mw). On the map, the red star represents the epicenter, while black and red triangles indicate the stations used in the inversion, with red triangles denoting the stations selected for display in the figure. For each selected station, the black, red and light gray lines respectively represent the observed, modeled and background noise spectra, respectively. Segments of the observed spectra with low SNR are shown in dark gray and were not considered for inversion.

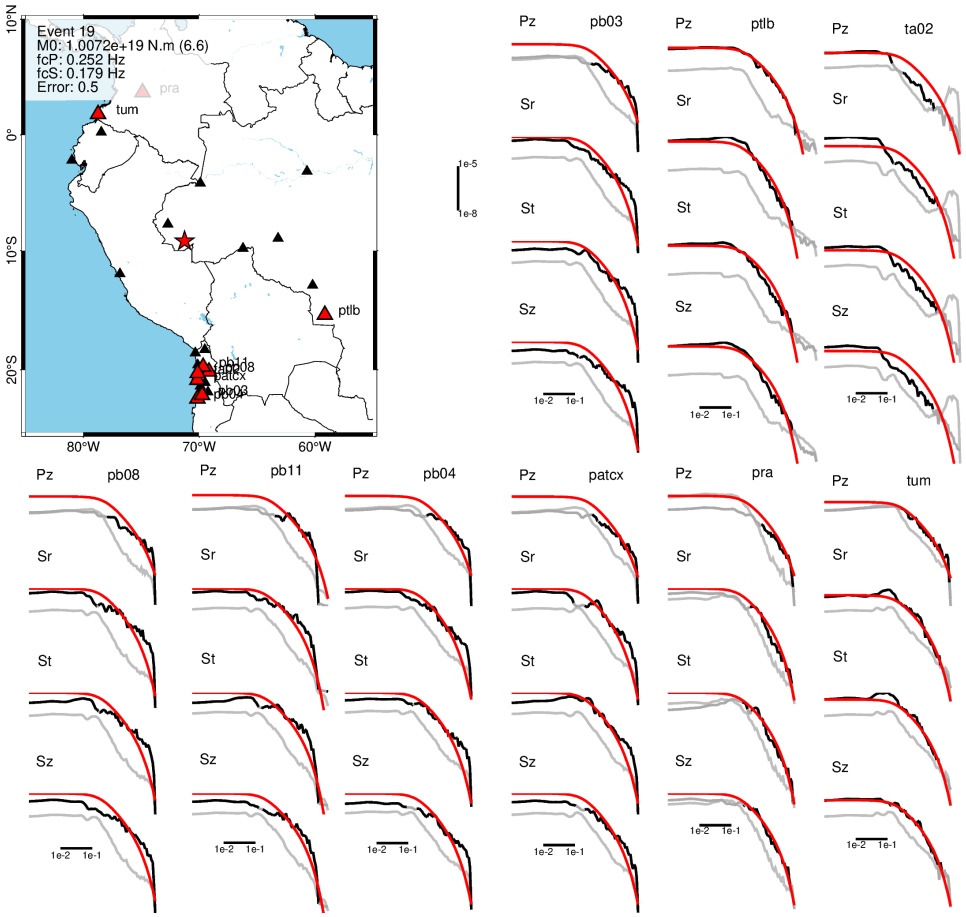

Figure S13. Continued.

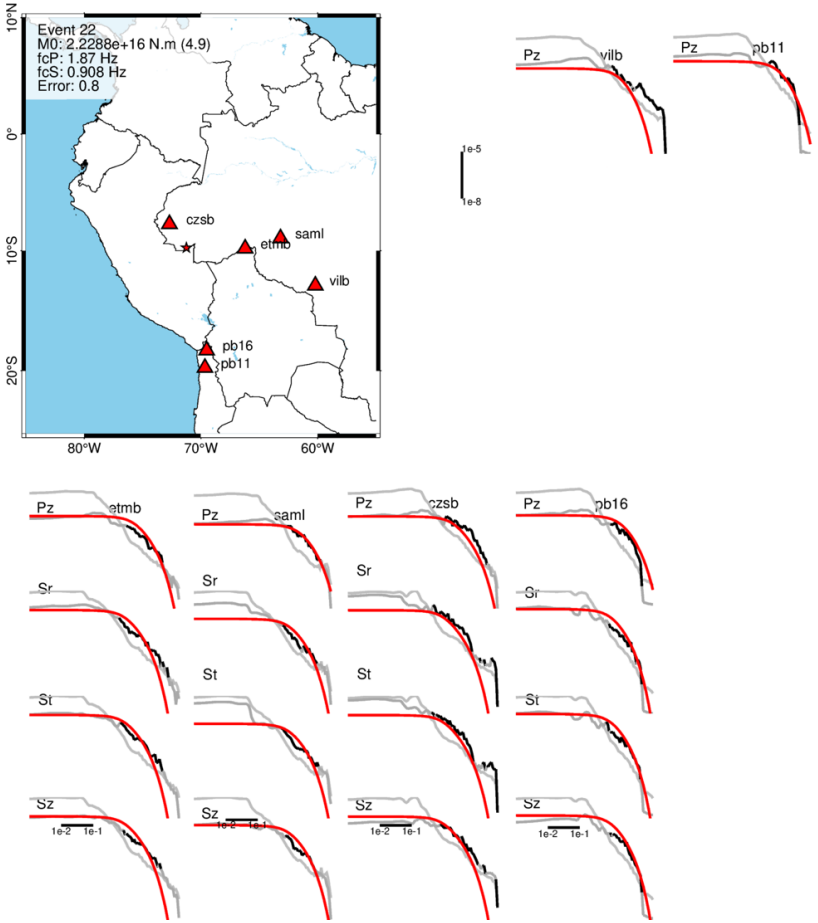

Figure S14. Observed and predicted spectra for event 22 (4.9 Mw). On the map, the red star represents the epicenter, while black and red triangles indicate the stations used in the inversion, with red triangles denoting the stations selected for display in the figure. For each selected station, the black, red and light gray lines respectively represent the observed, modeled and background noise spectra, respectively. Segments of the observed spectra with low SNR are shown in dark gray and were not considered for inversion.

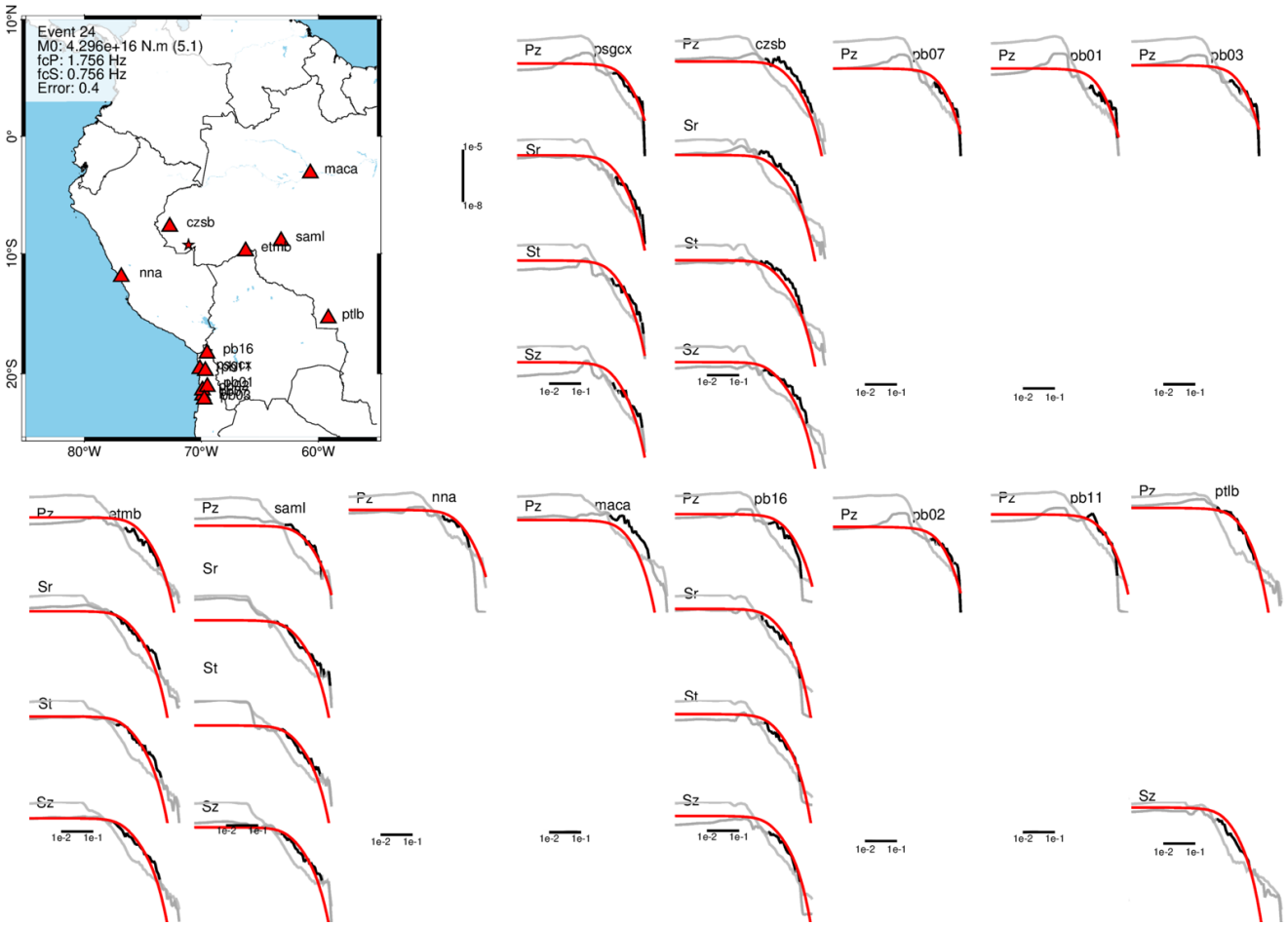

Figure S15. Observed and predicted spectra for event 24 (5.1 Mw). On the map, the red star represents the epicenter, while black and red triangles indicate the stations used in the inversion, with red triangles denoting the stations selected for display in the figure. For each selected station, the black, red and light gray lines respectively represent the observed, modeled and background noise spectra, respectively. Segments of the observed spectra with low SNR are shown in dark gray and were not considered for inversion.

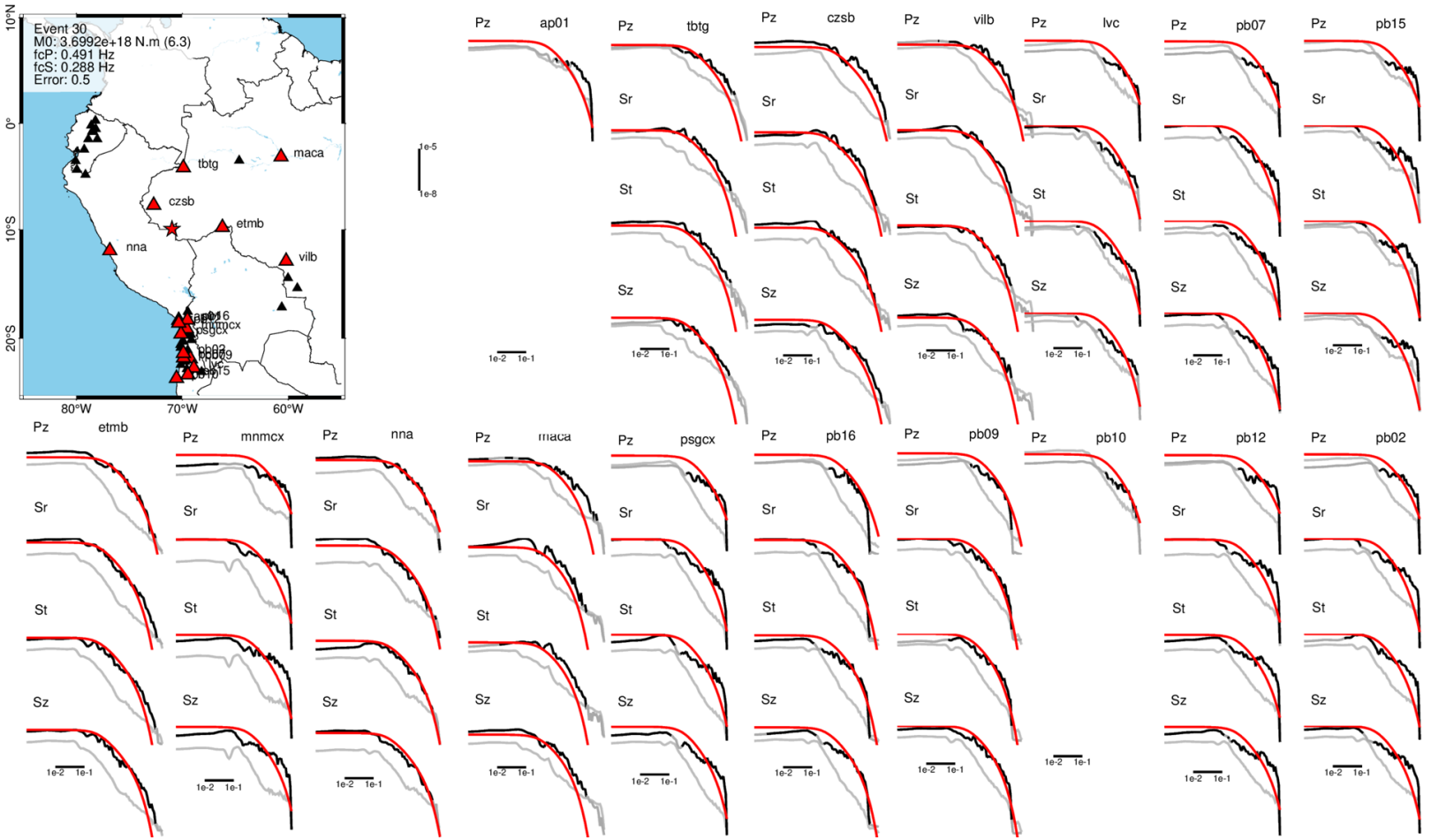

Figure S16. Observed and predicted spectra for event 30 (6.3 Mw). On the map, the red star represents the epicenter, while black and red triangles indicate the stations used in the inversion, with red triangles denoting the stations selected for display in the figure. For each selected station, the black, red and light gray lines respectively represent the observed, modeled and background noise spectra, respectively. Segments of the observed spectra with low SNR are shown in dark gray and were not considered for inversion.

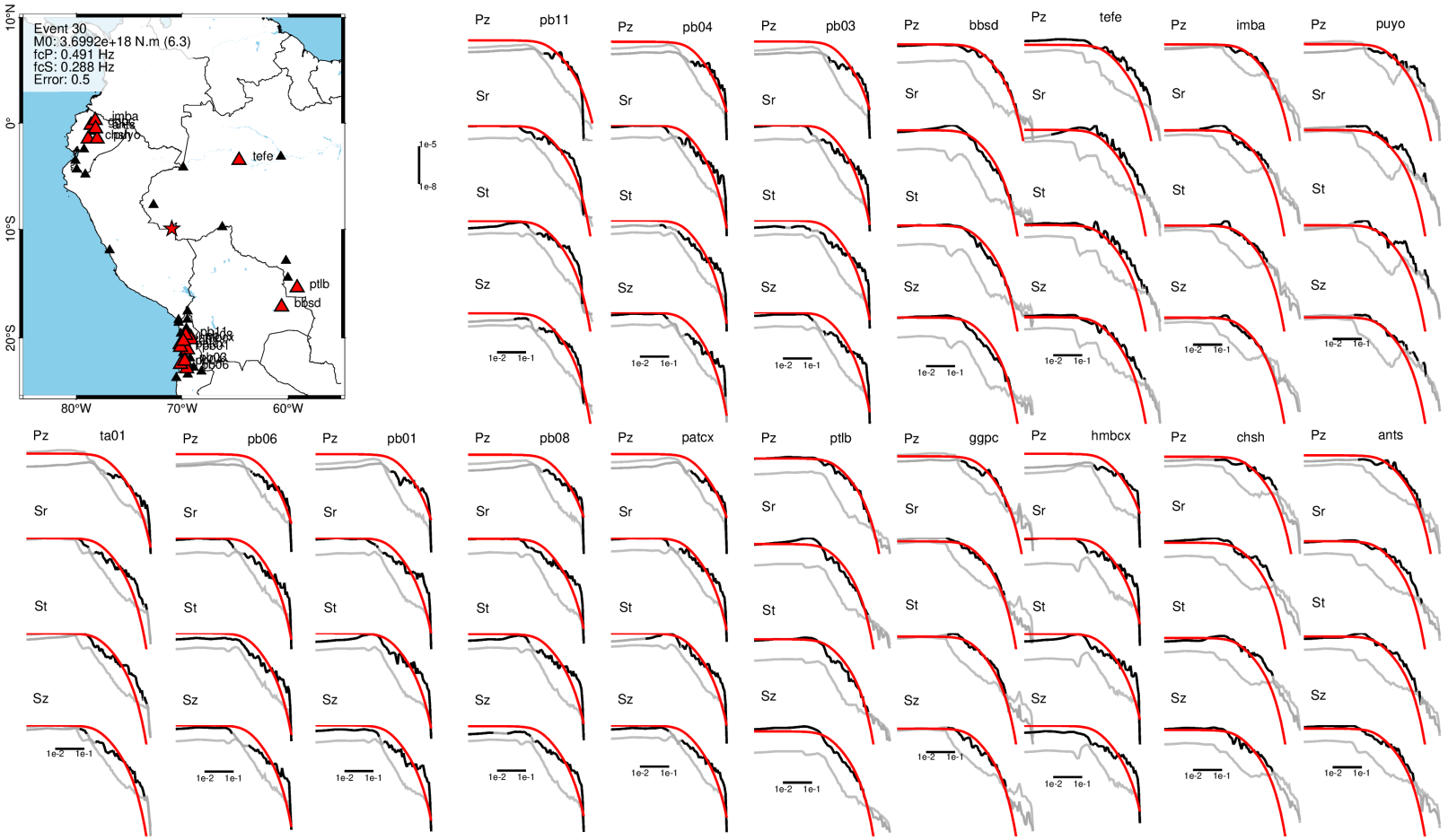

Figure S16. Continued.

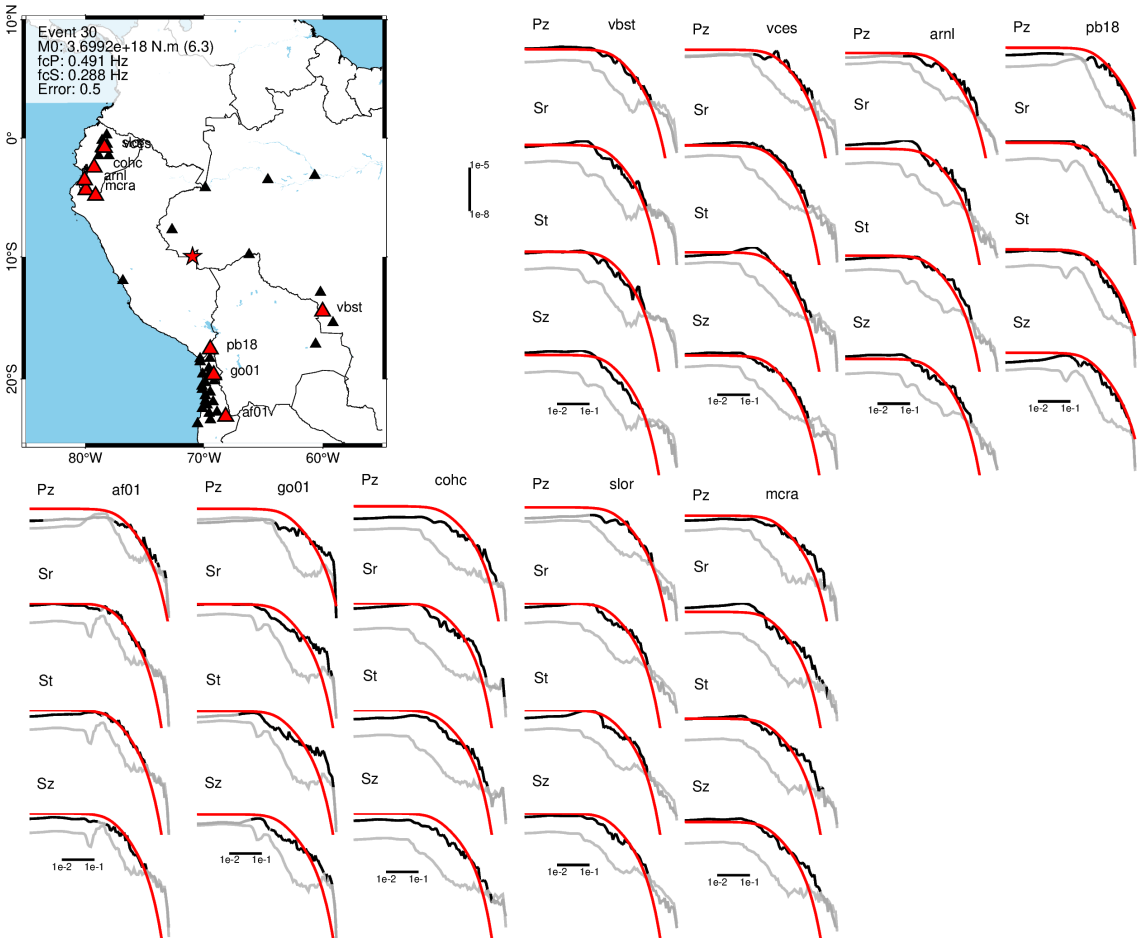

Figure S16. Continued.

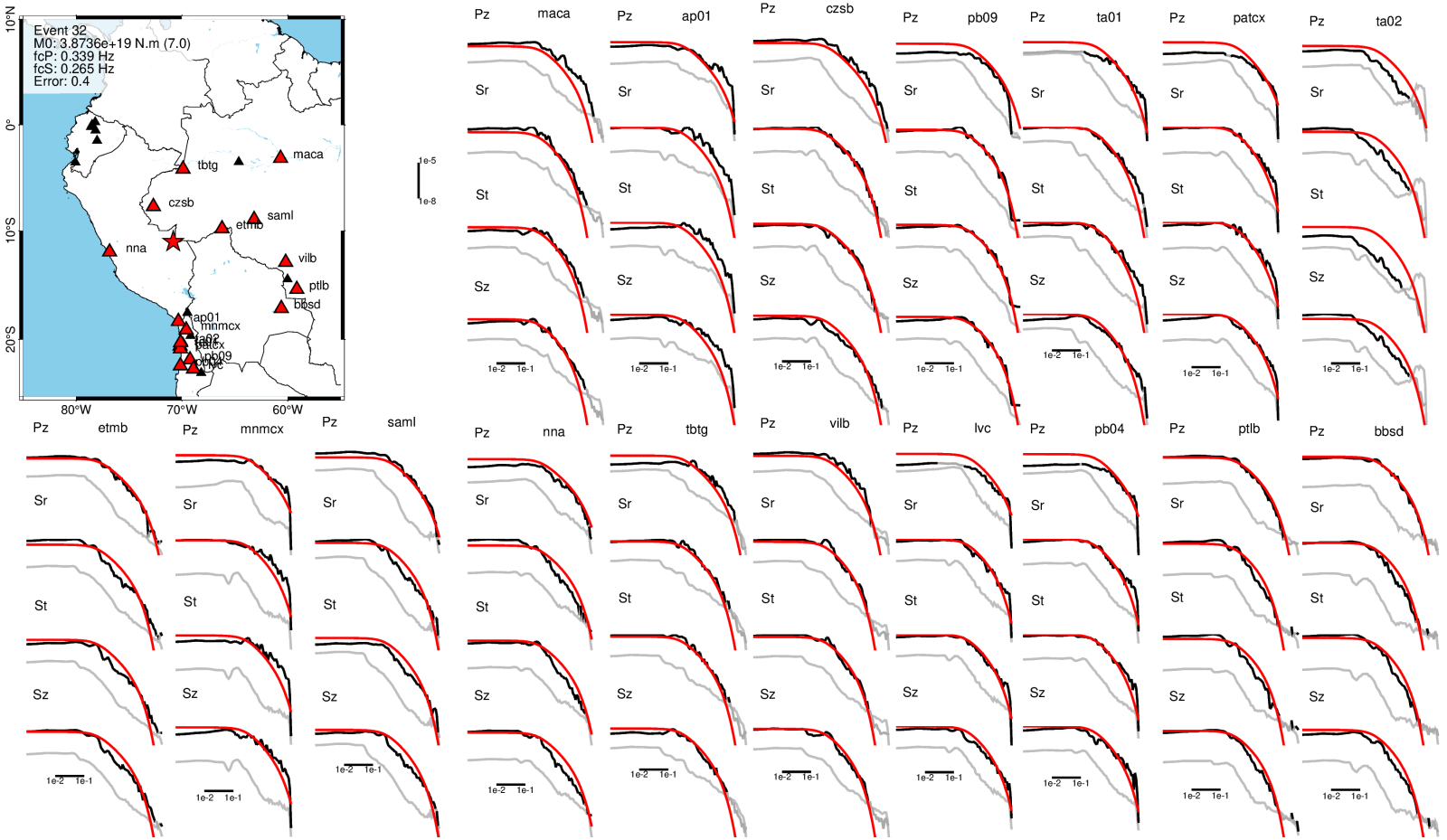

Figure S17. Observed and predicted spectra for event 32 (7.0 Mw). On the map, the red star represents the epicenter, while black and red triangles indicate the stations used in the inversion, with red triangles denoting the stations selected for display in the figure. For each selected station, the black, red and light gray lines respectively represent the observed, modeled and background noise spectra, respectively. Segments of the observed spectra with low SNR are shown in dark gray and were not considered for inversion.

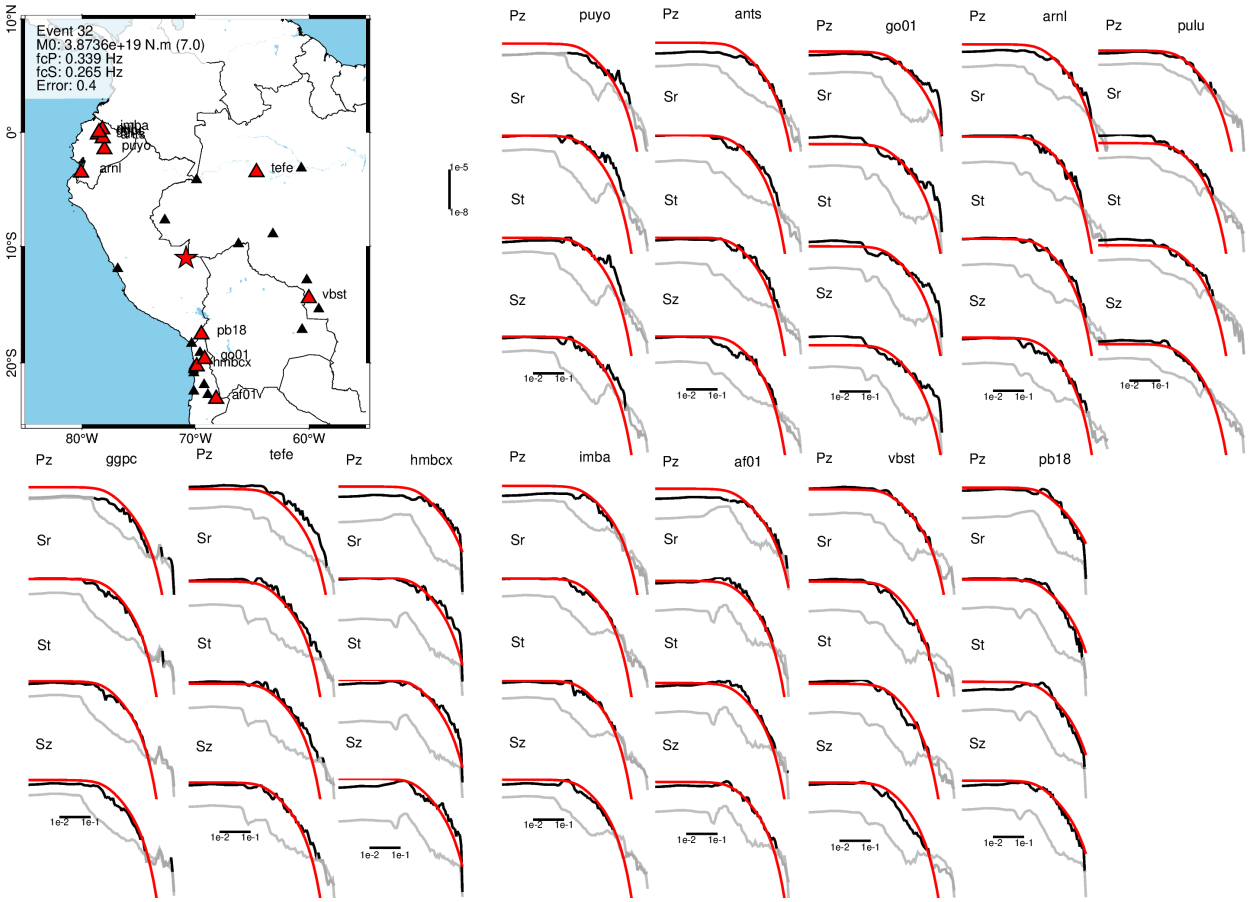

Figure S17. Continued.

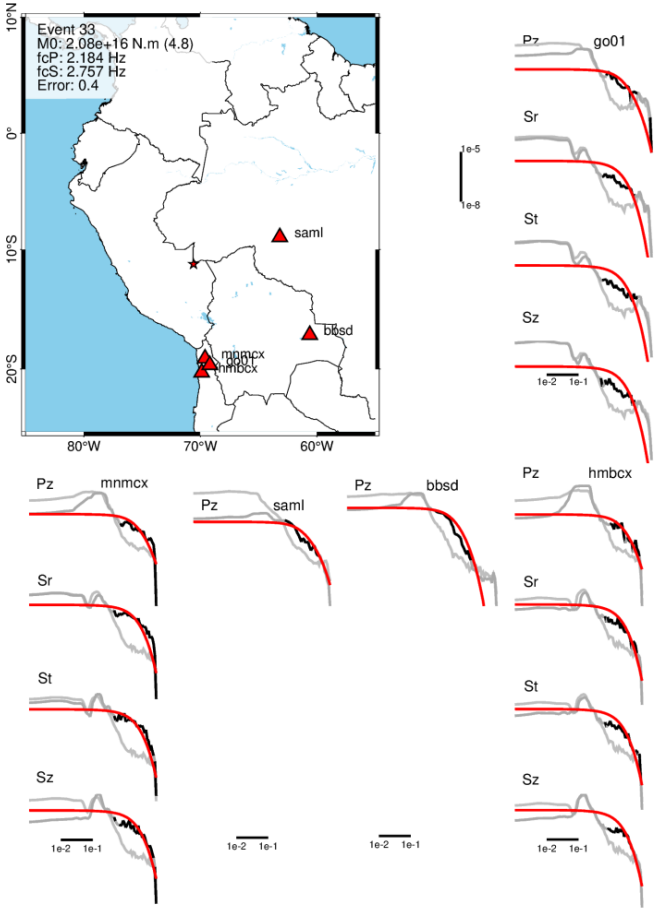

Figure S18. Observed and predicted spectra for event 33 (4.8 Mw). On the map, the red star represents the epicenter, while black and red triangles indicate the stations used in the inversion, with red triangles denoting the stations selected for display in the figure. For each selected station, the black, red and light gray lines respectively represent the observed, modeled and background noise spectra, respectively. Segments of the observed spectra with low SNR are shown in dark gray and were not considered for inversion.

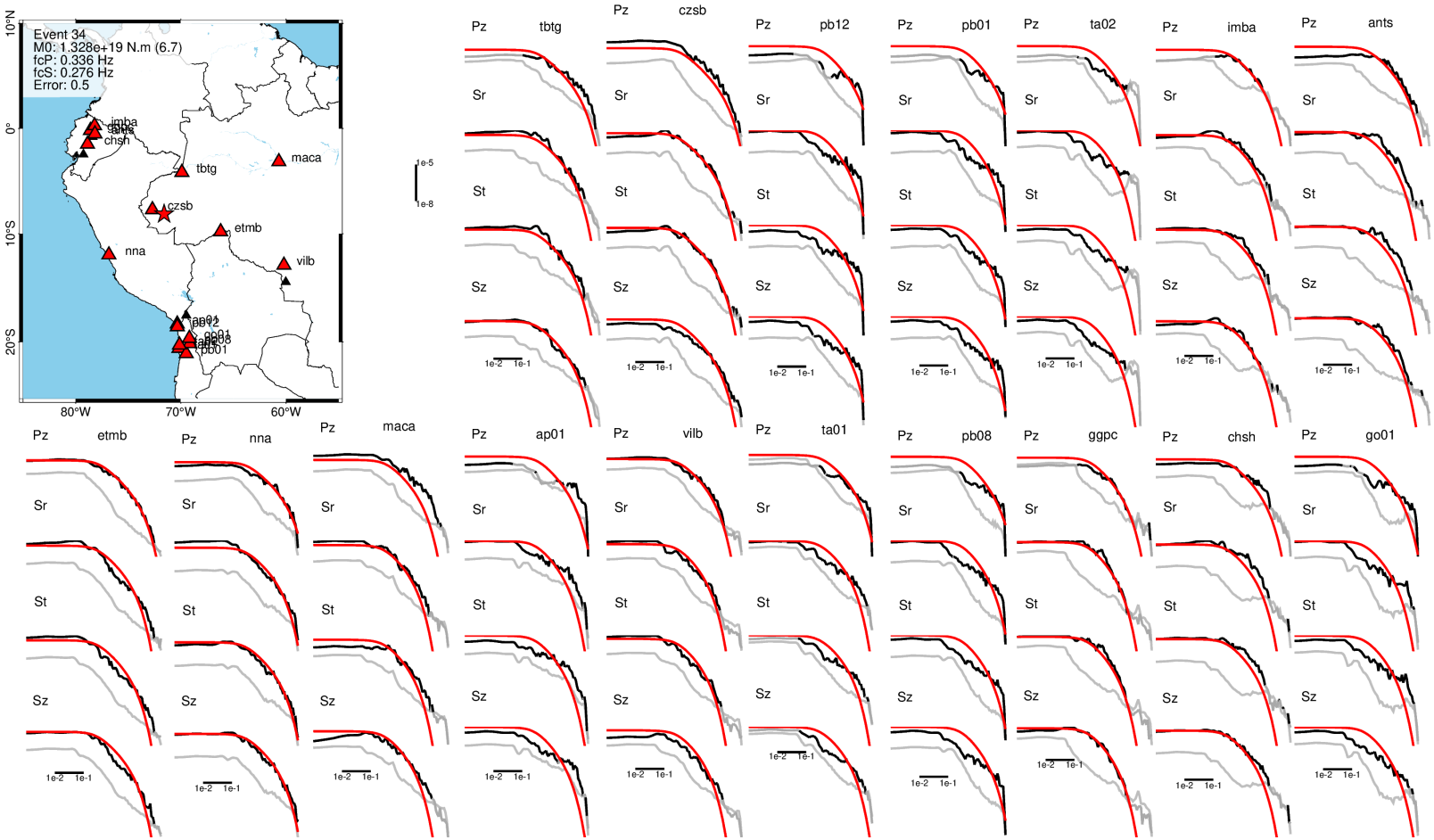

Figure S19. Observed and predicted spectra for event 34 (6.7 Mw). On the map, the red star represents the epicenter, while black and red triangles indicate the stations used in the inversion, with red triangles denoting the stations selected for display in the figure. For each selected station, the black, red and light gray lines respectively represent the observed, modeled and background noise spectra, respectively. Segments of the observed spectra with low SNR are shown in dark gray and were not considered for inversion.

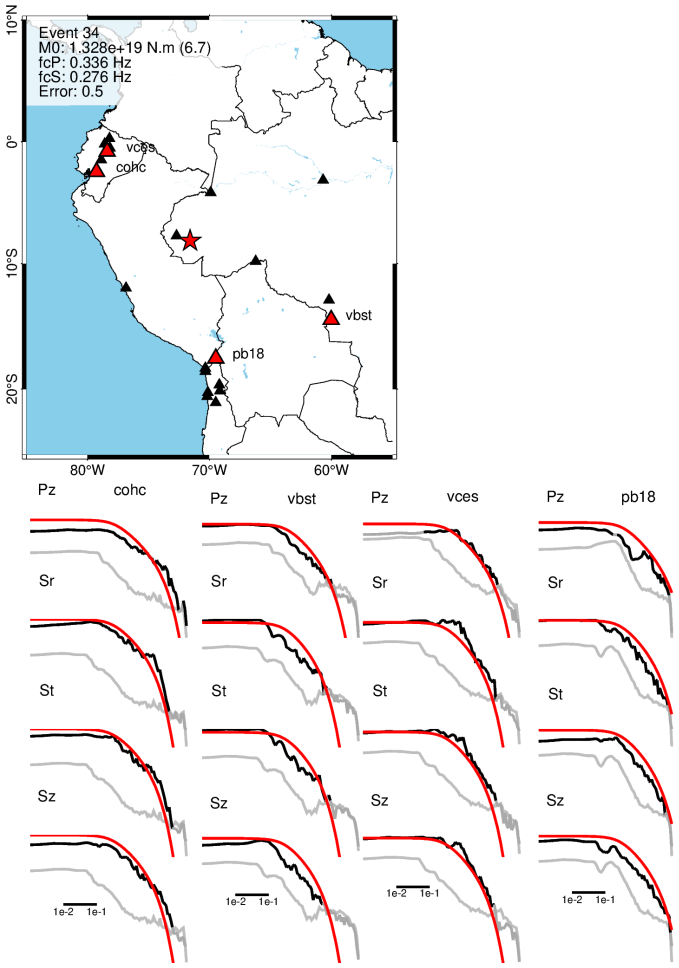

Figure S19. Continued.

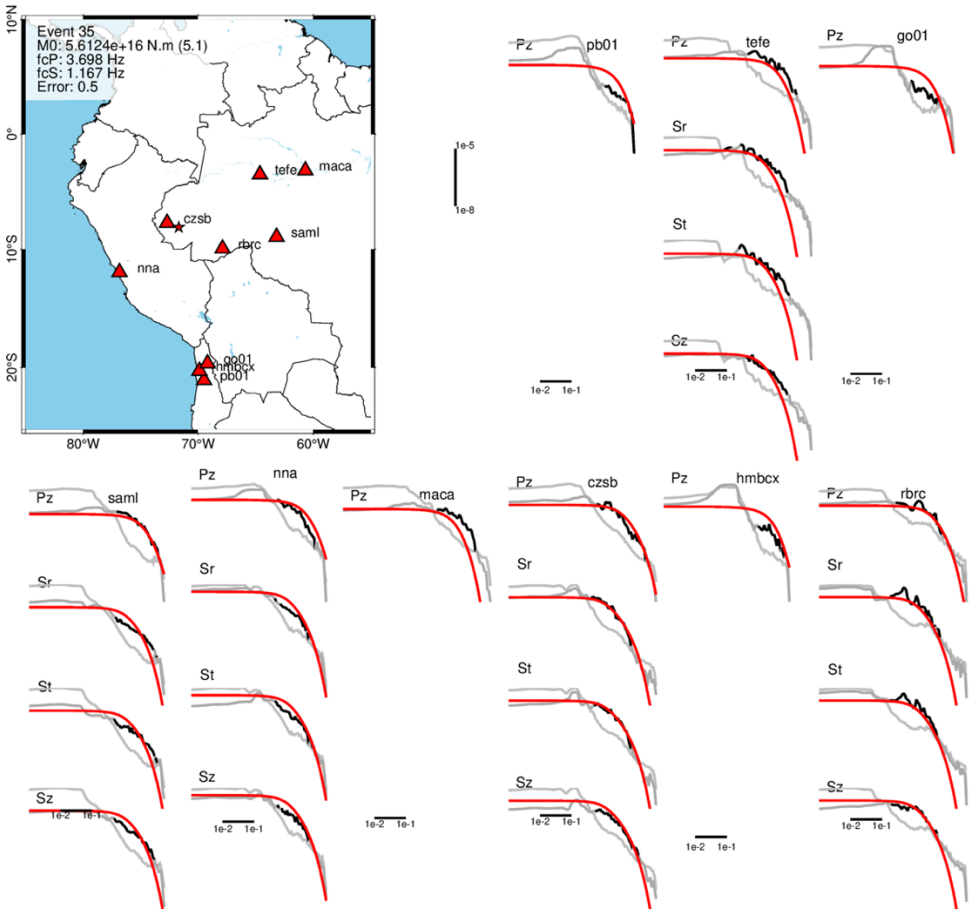

Figure S20. Observed and predicted spectra for event 35 (5.1 Mw). On the map, the red star represents the epicenter, while black and red triangles indicate the stations used in the inversion, with red triangles denoting the stations selected for display in the figure. For each selected station, the black, red and light gray lines respectively represent the observed, modeled and background noise spectra, respectively. Segments of the observed spectra with low SNR are shown in dark gray and were not considered for inversion.

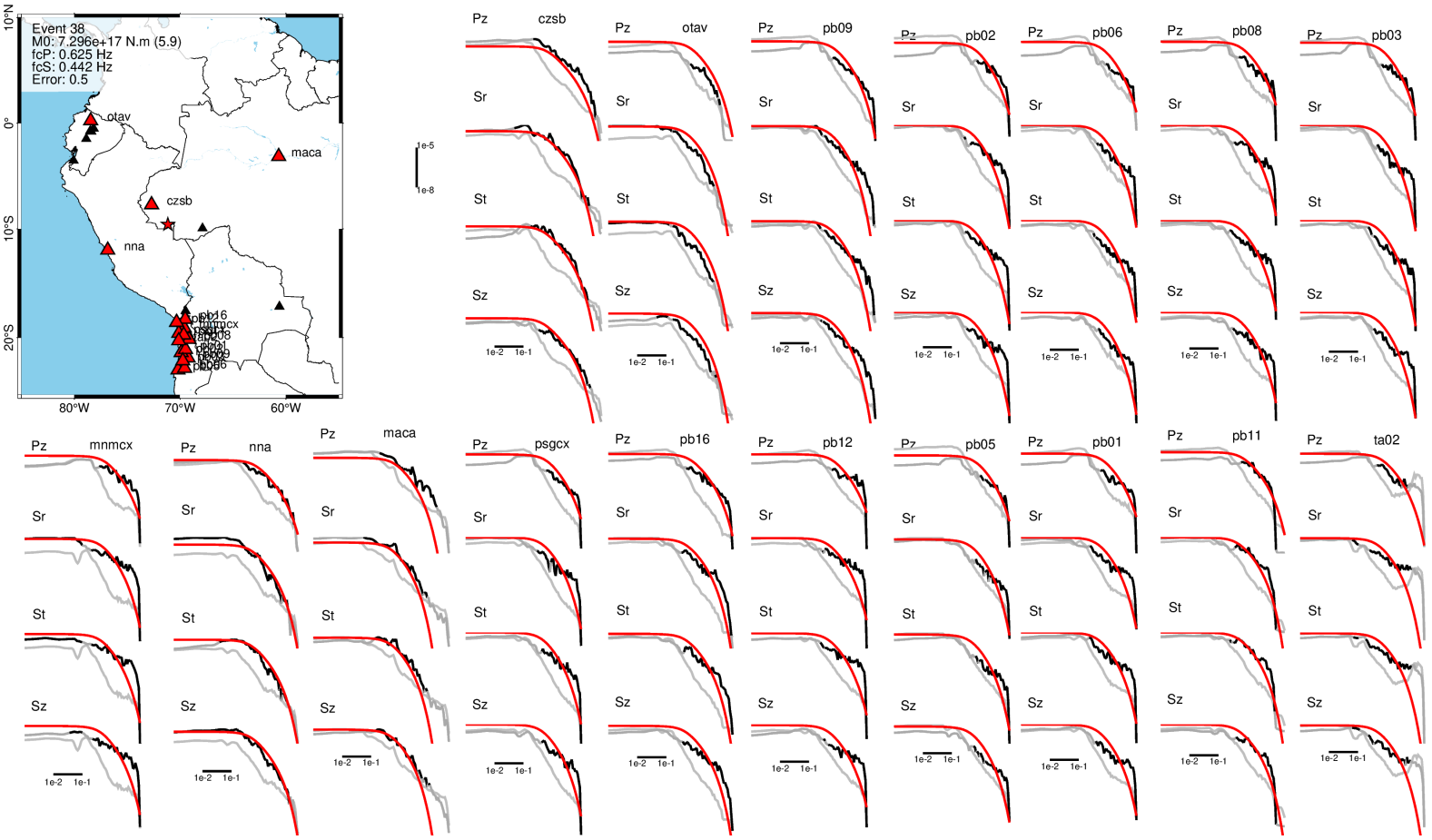

Figure S21. Observed and predicted spectra for event 38 (5.9 Mw). On the map, the red star represents the epicenter, while black and red triangles indicate the stations used in the inversion, with red triangles denoting the stations selected for display in the figure. For each selected station, the black, red and light gray lines respectively represent the observed, modeled and background noise spectra, respectively. Segments of the observed spectra with low SNR are shown in dark gray and were not considered for inversion.

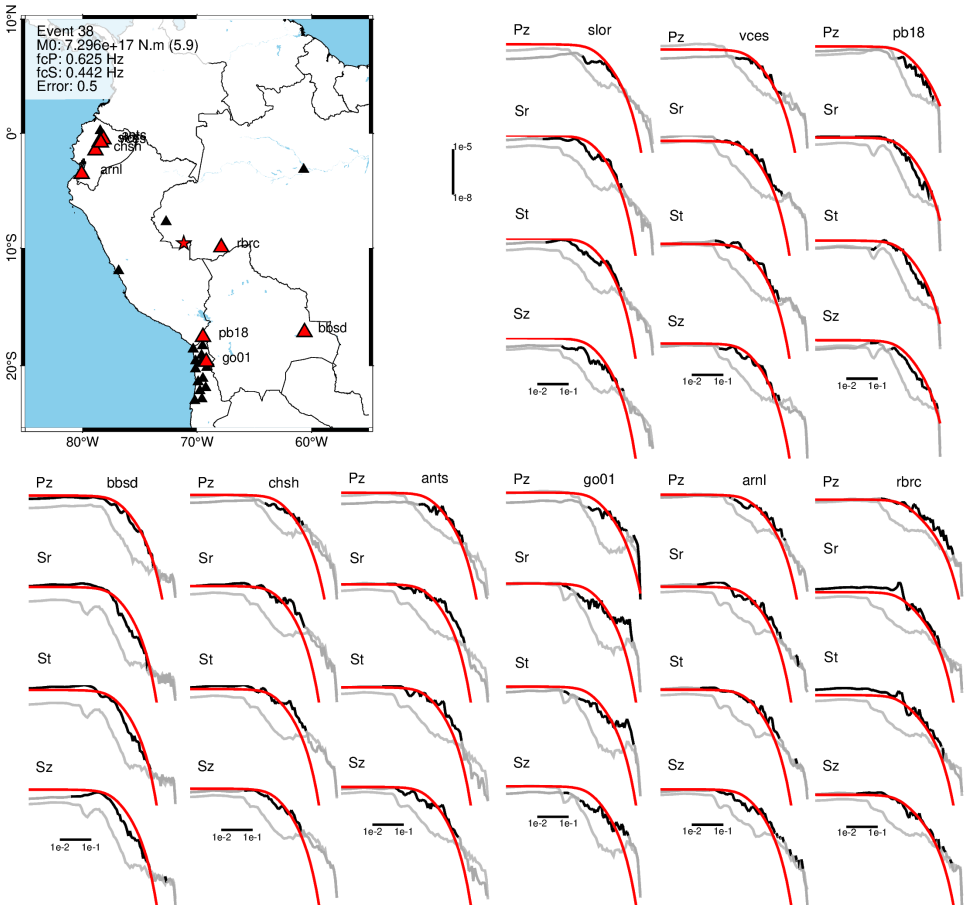

Figure S21. Continued.

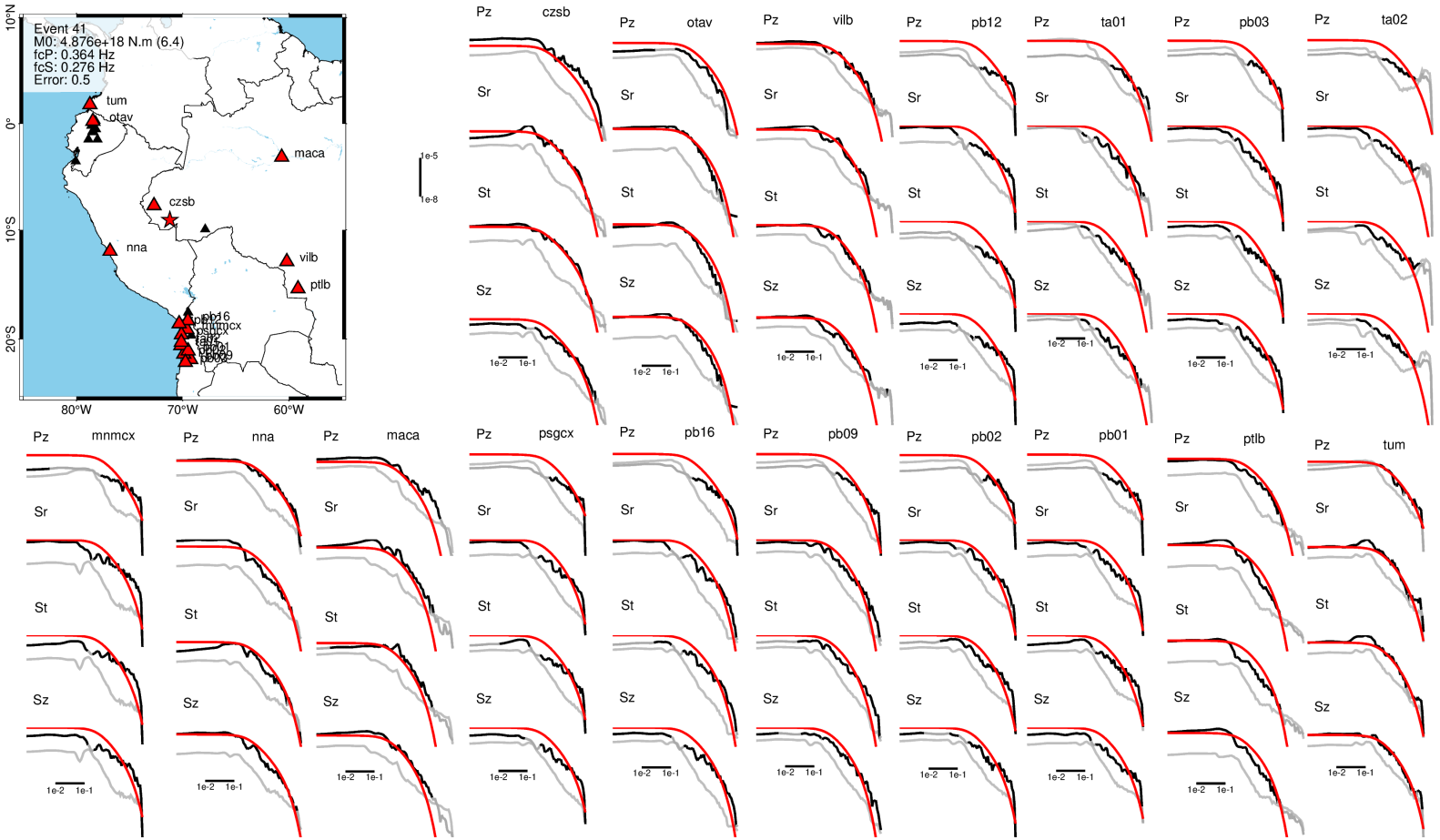

Figure S22. Observed and predicted spectra for event 41 (6.4 Mw). On the map, the red star represents the epicenter, while black and red triangles indicate the stations used in the inversion, with red triangles denoting the stations selected for display in the figure. For each selected station, the black, red and light gray lines respectively represent the observed, modeled and background noise spectra, respectively. Segments of the observed spectra with low SNR are shown in dark gray and were not considered for inversion.

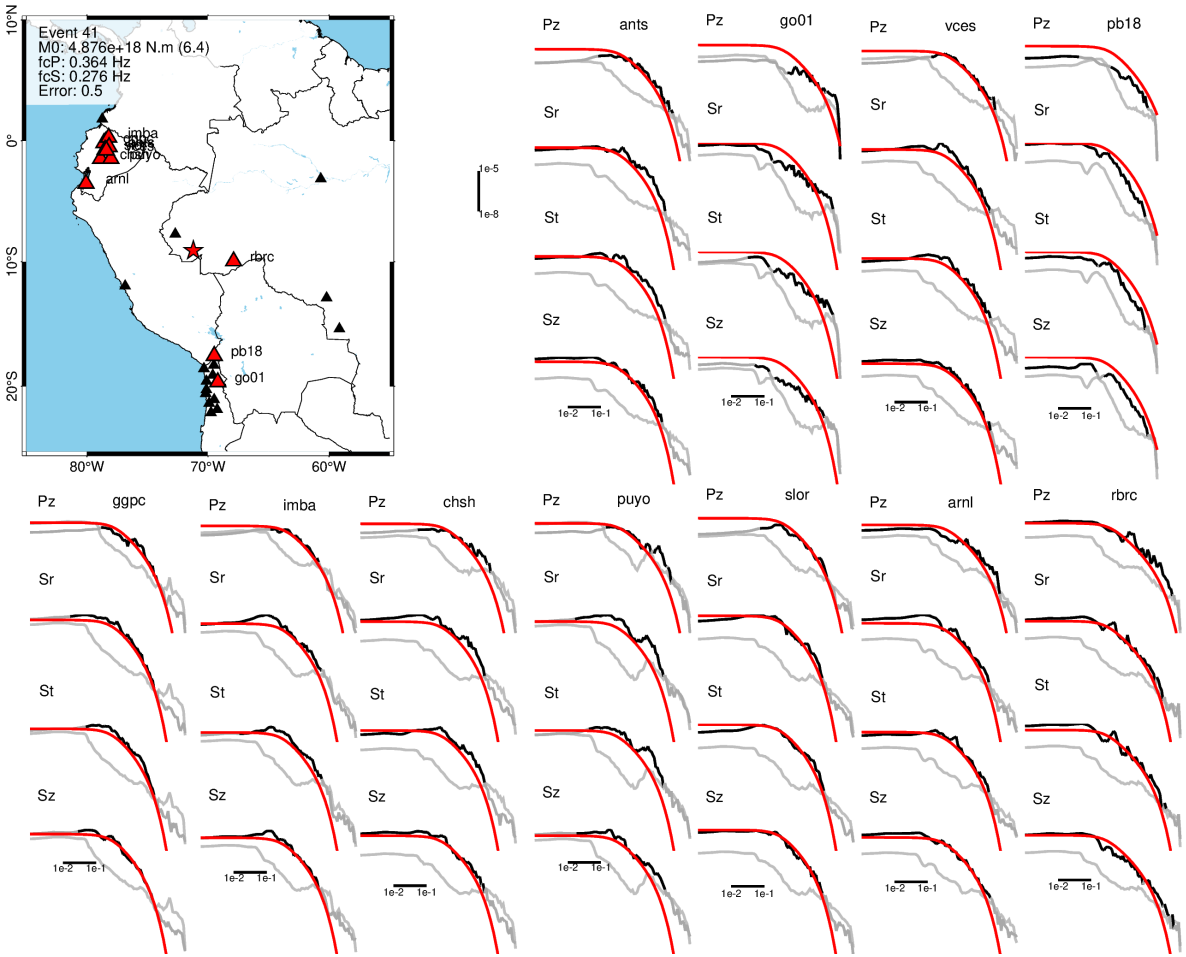

Figure S22. Continued.

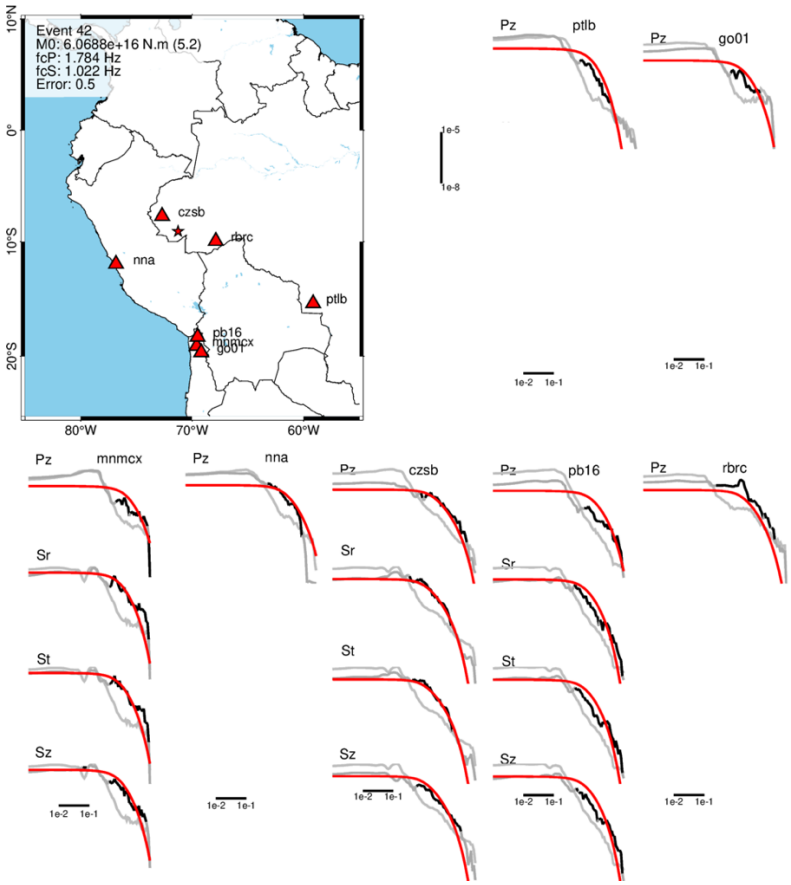

Figure S23. Observed and predicted spectra for event 42 (5.2 Mw). On the map, the red star represents the epicenter, while black and red triangles indicate the stations used in the inversion, with red triangles denoting the stations selected for display in the figure. For each selected station, the black, red and light gray lines respectively represent the observed, modeled and background noise spectra, respectively. Segments of the observed spectra with low SNR are shown in dark gray and were not considered for inversion.